nanomaterials

Special Issue Reprint

Nanomaterials for Chemical Engineering (Volume II)

Edited by
Meiwen Cao

mdpi.com/journal/nanomaterials

MDPI

Nanomaterials for Chemical Engineering (Volume II)

Nanomaterials for Chemical Engineering (Volume II)

Editor

Meiwen Cao

MDPI

Basel • Beijing • Wuhan • Barcelona • Belgrade • Novi Sad • Cluj • Manchester

Editor
Meiwen Cao
China University of
Petroleum (East China)
Qingdao
China

Editorial Office
MDPI
St. Alban-Anlage 66
4052 Basel, Switzerland

This is a reprint of articles from the Special Issue published online in the open access journal *Nanomaterials* (ISSN 2079-4991) (available at: https://www.mdpi.com/journal/nanomaterials/special_issues/RE8M789B65).

For citation purposes, cite each article independently as indicated on the article page online and as indicated below:

Lastname, A.A.; Lastname, B.B. Article Title. *Journal Name* **Year**, *Volume Number*, Page Range.

ISBN 978-3-7258-0593-8 (Hbk)
ISBN 978-3-7258-0594-5 (PDF)
doi.org/10.3390/books978-3-7258-0594-5

Contents

About the Editor . . . . . **vii**

Meiwen Cao
Recent Development of Nanomaterials for Chemical Engineering
Reprinted from: *Nanomaterials* **2024**, *14*, 456, doi:10.3390/nano14050456 . . . . . **1**

Xingjie Lu, Zhen Liu, Wentao Wang, Xin Wang, Hongchao Ma and Meiwen Cao
Synthesis and Evaluation of Peptide–Manganese Dioxide Nanocomposites as Adsorbents for the Removal of Strontium Ions
Reprinted from: *Nanomaterials* **2024**, *14*, 52, doi:10.3390/nano14010052 . . . . . **7**

Marieke Altena, Thies Jansen, Martina Tsvetanova and Alexander Brinkman
Phase Separation Prevents the Synthesis of VBi_2Te_4 by Molecular Beam Epitaxy
Reprinted from: *Nanomaterials* **2024**, *14*, 87, doi:10.3390/nano14010087 . . . . . **21**

Federica Magaletti, Gea Prioglio, Ulrich Giese, Vincenzina Barbera and Maurizio Galimberti
Hexagonal Boron Nitride as Filler for Silica-Based Elastomer Nanocomposites
Reprinted from: *Nanomaterials* **2024**, *14*, 30, doi:10.3390/nano14010030 . . . . . **30**

Alessandro Pacella, Paolo Ballirano, Maria Cristina Di Carlo, Marzia Fantauzzi, Antonella Rossi, Elisa Nardi, et al.
Dissolution Reaction and Surface Modification of UICC Amosite in Mimicked Gamble's Solution: A Step towards Filling the Gap between Asbestos Toxicity and Its Crystal Chemical Features
Reprinted from: *Nanomaterials* **2023**, *13*, 2933, doi:10.3390/nano13222933 . . . . . **57**

Jingting Wang, Mingying Lu, Yongxing Chen, Guolin Hao, Bin Liu, Pinghua Tang, et al.
Machine Learning-Assisted Large-Area Preparation of MoS_2 Materials
Reprinted from: *Nanomaterials* **2023**, *13*, 2283, doi:10.3390/nano13162283 . . . . . **69**

Adriana Saldaña-Robles, Javier Antonio Arcibar-Orozco, Luz Rocío Guerrero-Mosqueda, César Eduardo Damián-Ascencio, Alfredo Marquez-Herrera, Miguel Corona, et al.
Synthesis of Composites for the Removal of F^- Anions
Reprinted from: *Nanomaterials* **2023**, *13*, 2277, doi:10.3390/nano13162277 . . . . . **81**

Yu-Chun Chiang, Zhi-Hui Pu and Ziyi Wang
Study on Oxygen Evolution Reaction of Ir Nanodendrites Supported on Antimony Tin Oxide
Reprinted from: *Nanomaterials* **2023**, *13*, 2264, doi:10.3390/nano13152264 . . . . . **103**

José Remigio Quiñones-Gurrola, Juan Carlos Rendón-Angeles, Zully Matamoros-Veloza, Jorge López-Cuevas, Roberto Pérez-Garibay and Kazumichi Yanagisawa
Facile Preparation of $SrZr_{1-x}Ti_xO_3$ and $SrTi_{1-x}Zr_xO_3$ Fine Particles Assisted by Dehydration of Zr^{4+} and Ti^{4+} Gels under Hydrothermal Conditions
Reprinted from: *Nanomaterials* **2023**, *13*, 2195, doi:10.3390/nano13152195 . . . . . **115**

Karina Abitaev, Petia Atanasova, Joachim Bill, Natalie Preisig, Ivan Kuzmenko, Jan Ilavsky, et al.
In Situ Ultra-Small- and Small-Angle X-ray Scattering Study of ZnO Nanoparticle Formation and Growth through Chemical Bath Deposition in the Presence of Polyvinylpyrrolidone
Reprinted from: *Nanomaterials* **2023**, *13*, 2180, doi:10.3390/nano13152180 . . . . . **131**

Rollie Mills, Cameron Tvrdik, Andrew Lin and Dibakar Bhattacharyya
Enhanced Degradation of Methyl Orange and Trichloroethylene with PNIPAm-PMMA-Fe/Pd-Functionalized Hollow Fiber Membranes
Reprinted from: *Nanomaterials* **2023**, *13*, 2041, doi:10.3390/nano13142041 . . . . . **150**

Fabian Mares-Briones, América Higareda, Jose Luis Lopez-Miranda, Rubén Mendoza-Cruz and Rodrigo Esparza
Bimetallic AgPt Nanoalloys as an Electrocatalyst for Ethanol Oxidation Reaction: Synthesis, Structural Analysis, and Electro-Catalytic Activity
Reprinted from: *Nanomaterials* **2023**, *13*, 1396, doi:10.3390/nano13081396 . . . . . **177**

Adriana Marinoiu, Mircea Raceanu, Elena Carcadea and Mihai Varlam
Nitrogen-Doped Graphene Oxide as Efficient Metal-Free Electrocatalyst in PEM Fuel Cells
Reprinted from: *Nanomaterials* **2023**, *13*, 1233, doi:10.3390/nano13071233 . . . . . **193**

Algirdas Lazauskas, Mindaugas Andrulevičius, Brigita Abakevičienė, Dalius Jucius, Viktoras Grigaliūnas, Asta Guobienė and Šarūnas Meškinis
Hydrophilic Surface Modification of Amorphous Hydrogenated Carbon Nanocomposite Films via Atmospheric Oxygen Plasma Treatment
Reprinted from: *Nanomaterials* **2023**, *13*, 1108, doi:10.3390/nano13061108 . . . . . **216**

Eleonora La Greca, Tamara S. Kharlamova, Maria V. Grabchenko, Luca Consentino, Daria Yu Savenko, Giuseppe Pantaleo, et al.
Ag Catalysts Supported on CeO_2, MnO_2 and $CeMnO_x$ Mixed Oxides for Selective Catalytic Reduction of NO by C_3H_6
Reprinted from: *Nanomaterials* **2023**, *13*, 873, doi:10.3390/nano13050873 . . . . . **225**

George Barjoveanu, Carmen Teodosiu, Irina Morosanu, Ramona Ciobanu, Florin Bucatariu and Marcela Mihai
Life Cycle Assessment as Support Tool for Development of Novel Polyelectrolyte Materials Used for Wastewater Treatment
Reprinted from: *Nanomaterials* **2023**, *13*, 840, doi:10.3390/nano13050840 . . . . . **246**

Mihaela Iordache, Anisoara Oubraham, Ioan-Sorin Sorlei, Florin Alexandru Lungu, Catalin Capris, Tudor Popescu and Adriana Marinoiu
Noble Metals Functionalized on Graphene Oxide Obtained by Different Methods—New Catalytic Materials
Reprinted from: *Nanomaterials* **2023**, *13*, 783, doi:10.3390/nano13040783 . . . . . **261**

About the Editor

Meiwen Cao

Meiwen Cao currently works as a professor and doctoral supervisor in the College of Chemical Engineering, China University of Petroleum (East China). He received his Ph.D. degree in physical chemistry from the Institute of Chemistry, Chinese Academy of Sciences, in 2008. Between 2017 and 2018, he worked as a senior visiting scholar at the University of Manchester with Prof. Jianren Lu. His research focuses on the development of novel biological amphiphilic molecules and their self-assembly, and the preparation of nano/biological functional materials and their applications in daily chemical, oilfield chemistry, and pollutant control fields. He has published more than 100 SCI papers and has an H index of 30.

nanomaterials

MDPI

Editorial

Recent Development of Nanomaterials for Chemical Engineering

Meiwen Cao

State Key Laboratory of Heavy Oil Processing, Department of Biological and Energy Chemical Engineering, College of Chemistry and Chemical Engineering, China University of Petroleum (East China), Qingdao 266580, China; mwcao@upc.edu.cn

There has been an explosive growth in research on nanomaterials since the late 1980s and early 1990s. So far, massive amounts of nanomaterials have been developed and their preparation and characterization methods are relatively comprehensive and well-established [1,2]. The current most important issue is the engineering of nanomaterials in real-world applications to promote economic and social development. Based on the booming development of nanomaterials in the field of chemical engineering, we have launched two Special Issues, that is, Nanomaterials for Chemical Engineering (Volume I, 2022) and Nanomaterials for Chemical Engineering (Volume II, 2023). Detailed information on Volume I can be found via the following web link: https://www.mdpi.com/journal/nanomaterials/special_issues/nano_chemical_engineering. In the latest Special Issue (Volume II), we collected 15 original research articles and 1 comprehensive review paper written by excellent scientists from relevant fields covering the topics of nanomaterial synthesis and characterization, the engineering of nanomaterials into composites with novel properties, the development of functional nanomaterials for applications in catalysis and pollutant treatment, the evaluation of the durability and environmental friendliness of nanomaterials, etc. This Special Issue also follows closely the forefront of global scientific research and includes studies on the application of machine learning in the field of nanomaterials for chemical engineering. In what follows, I will give a brief introduction of the studies presented in this Special Issue.

The design and optimization of nanomaterial synthesis as well as performance control are eternal themes in the development of nanotechnology [3]. The rapid advancement of material preparation technology and the actual needs of specific nanomaterials with desired properties both drive the development of new synthesis methods to produce novel nanostructures. In this Special Issue, Mares-Briones et al. presented the chemical synthesis of AgPt nanoalloys by the polyol method, which used polyvinylpyrrolidone (PVP) as a surfactant in a heterogeneous nucleation approach. This study modulated well the composition, the size and morphology, the catalytic activity as well as the stability and long-term durability of the AgPt nanoparticles, providing attractive catalyst candidates for cost-effective ethanol oxidation. Abitaev et al. reported the controlled synthesis of ZnO nanoparticles via the chemical bath deposition (CBD) method. The kinetics of ZnO formation was controlled by using a methanolic precursor solution containing the organic additive polyvinylpyrrolidone (PVP) as the stabilizing and structuring agent. They also gave a nearly quantitative description of both the nucleation and growth period using the two-step Finke–Watzky model with slow, continuous nucleation followed by autocatalytic growth. This study provides valuable insights into the controlled synthesis of ZnO nanoparticles. Quiñones-Gurrola et al. carried out a systematic study of preparing perovskite-type fine particles in the binary system of $SrZrO_3$–$SrTiO_3$ with the hydrothermal method. They optimized the synthesis parameters such as temperature, the precursors and their stoichiometry, and the reaction time. The size and structural characteristics as well as the crystalline nature of the nanoparticles were also systematically investigated. This study demonstrates that soft chemistry hydrothermal processing can be employed

Citation: Cao, M. Recent Development of Nanomaterials for Chemical Engineering. *Nanomaterials* **2024**, *14*, 456. https://doi.org/10.3390/nano14050456

Received: 21 February 2024
Accepted: 22 February 2024
Published: 1 March 2024

for synthesizing inorganic perovskite binary systems for potential industrial applications. Moreover, Altena et al. reported in their work the attempt to synthesize VBi_2Te_4 by molecular beam epitaxy (MBE) as well as the detailed characterization of the material by various techniques. Noting that VBi_2Te_4 is an intrinsic magnetic topological insulator (IMTI) that has been theoretically predicted but has a lack of experimental evidence supporting it so far, this study filled in this gap by providing experimental results for its material synthesis.

How to engineer a specific nanomaterial into practical applications, that is, the development of applying techniques, is crucial. In this Special Issue, Lazauskas et al. investigated the hydrophilic surface modification of SiO_x containing amorphous hydrogenated carbon nanocomposite films (DLC:SiO_x) by using atmospheric oxygen plasma treatment. They showed that atmospheric oxygen plasma treatment can effectively modify the wetting property of the DLC:SiOx film, which can ensure practical applications such as biocompatible coatings for medical purposes, anti-fog coatings for optical components, and protective coatings to prevent corrosion and wear. Mills et al. formulated catalytic zero-valent iron/palladium (Fe/Pd) with stimuli-responsive poly-N-isopropylacrylamide (PNIPAm) and poly-methyl methacrylate (PMMA) to functionalize hollow fiber membranes, producing functional composite membranes for the reductive degradation of organic pollutants. By using trichloroethylene and methyl orange as model compounds for degradation, they proved that temperature-responsive domains and catalyst incorporation in the composited membrane provide significant advantages for toxic organic decontamination, which are promising for the efficient treatment of high-volume contaminated water. In another study included in the Special Issue, Chiang et al. synthesized nano-branched iridium nanodendrites (Ir NDs) on an antimony tin oxide (ATO) support (Ir NDs/ATO) by a surfactant-mediated method. They investigated the effect of ATO support and evaluated the electrocatalytic activity and durability of the material during an oxygen evolution reaction (OER). The authors' detailed characterization of the structural properties and catalytic performance of the Ir NDs provides solid support for the practical application of this material.

By having an extremely small size and high specific surface area, nanomaterials have more active sites for improving the reaction efficiency in catalytic processes [4–6]. This Special Issue includes several papers on the chemical engineering applications of nanocatalytic materials, providing comprehensive explorations on materials preparation, physical–chemical characterization, and catalytic performance evaluation. The hybridization of nanomaterials with different structures and properties to produce composite materials is an important approach for engineering nanomaterials in various applications [7–9]. For example, two-dimensional (2D) graphene/graphene oxide (GO) and noble metal nanoparticles are two types of nanomaterials with distinct structural characteristics and physicochemical properties. The hybridization of them into a single composite material can produce new materials with exceptional performance due to the synergism of the specific properties of each material. In this Special Issue, Iordache et al. present a comprehensive review on the most used and up-to-date methods for the synthesis and characterization of graphene/noble metal (Pt, Ag, Pd and Au) nanocomposites as well as their application as new catalysts in fuel cell and renewable technology. This paper discusses well the preparation methods, the type and amount of noble metal, the nature of the graphene support material, the type of dopant and the metal–support relationship in the synthesis of graphene/noble metal nanocomposites. The electrocatalytic activity and electrochemical stability of the nanocomposites as well as the techniques of applying the nanocomposites as catalysts are also discussed. In another research paper, Marinoiu et al. developed a microwave-based single-step synthesis method for nitrogen-doped graphene oxide preparation, which is simple, faster, scalable, and economical. By evaluating and comparing the physical and chemical properties of various materials obtained from different precursors, they concluded that ammonia allowed for a higher nitrogen doping concentration by utilizing the high vapor pressure to facilitate the functionalization reaction with graphene oxide. This study contributes well to the synthesis methodology and engineering of nitrogen-doped graphene

as a promising metal-free catalyst for the oxygen reduction reaction (ORR). Such catalysts show good electrocatalytic activity and long-term operation stability, and are excellent for practical ORR application in proton exchange membrane fuel cells (PEMFCs).

By having a high specific surface area and porosity as well as excellent catalytic capability, nanomaterials also find widespread applications in pollution treatment, that is, being used as adsorbents for the adsorptive removal of harmful substances from the environment or catalytic transformation of toxic species into nontoxic ones [10–12]. In this Special Issue, La Greca et al. synthesized composite catalysts of Ag/MnO_x and $Ag/CeMnO_x$ by using a combination of the citrate sol–gel method for support synthesis and incipient wetness impregnation with $[Ag(NH_3)_2]NO_3$ aqueous solution to deposit the active component. They systematically investigated the physical–chemical properties of the as-prepared catalysts by various characterization techniques and then studied the selective catalytic NO_x reduction with propylene. This work presents well how to develop the hybridized nanocatalysts for NO reduction applications. Saldaña-Robles et al. presented in their paper the synthesis of amine and ferrihydrite functionalized graphene oxide for the removal of fluoride from water. The comprehensive characterization of the synthesized materials was performed by using various techniques. This study is a good example of engineering composite nanomaterials for application in pollution treatment. In another work, Lu et al. [13] synthesized a novel organic–inorganic hybrid material of IIGK@MnO_2 via an environmentally friendly and simple method. They used short peptide self-assembled nanostructures as a template to assist with the formation of a fibrous IIGK@MnO_2 nanocomposite with a large specific surface area and negative charges, which can be used as an effective adsorbent for the removal of strontium ions (Sr^{2+}) from aqueous solution. This study shed light on the construction of organic–inorganic hybrid adsorbents with multiple active adsorption sites and a high adsorption efficiency for adsorbing radioactive ions from wastewater.

Nanomaterials can be composited into other materials as fillers to enhance the mechanical properties such as strength, hardness, toughness, wear resistance, etc. [8] For example, two-dimensional hexagonal boron nitride (hBN) has a stable structure and outstanding properties such as mechanical strength, thermal conductivity, electrical insulation, and lubricant behavior. However, how to utilize hBN in practical applications is a significant challenge. Magaletti et al. used hBN as a filler material to partially replace silica in elastomer composites so as to improve their rheological and mechanical properties. They found that hBN as a substitute for 30% of the silica can greatly improve the material's property, which leads to a lower Payne effect, a higher dynamic rigidity, and an increase in E′ with similar/lower hysteresis. This study paves the way for substantial improvements in the important properties of silica-based composites for tire compounds, which can be used to reduce rolling resistance and lessen environmental impacts.

For the practical application of a specific nanomaterial in chemical engineering, it is important to evaluate the performance, stability, safety, and environmental sustainability of the materials in advance [14,15]. However, such studies are relatively scarce at the current stage. In this Special Issue, Barjoveanu et al. presented in their paper how a life cycle assessment can be used to evaluate the eco-design options for early-stage material development and engineering while allowing for the environmental sustainability of novel materials. They focused on a comparison of the technical and environmental performance of two types of synthesis strategies (the classic layer-by-layer strategy and the one-pot coacervate deposition strategy) for PEI-coated silica particles (organic/inorganic composites), which were tested for Cd^{2+} ion removal from aqueous solution. This study proves the usefulness of life cycle assessments and scenario analyses as environmental support tools for engineering nanomaterials into practical applications because they can highlight environmental hotspots and point out the environmental improvement possibilities from the very early stages of material development. Pacella et al. adopted a multi-analytical approach to investigate the dissolution process and surface characterization of amosite fibers following interaction with a mimicked Gamble's solution for a long period. This study highlighted the incongruent behavior of the amosite fiber dissolution and observed a

preferential release of Mg and Ca from the amphibole structure as well the oxidation of Fe. By probing into the most important toxicity parameters, that is, the biodurability (i.e., the resistance to dissolution), this study helps us to understand the mechanisms of long-term toxicity, which is crucial for practical applications of UICC amosite.

Machine learning technology provides new ideas and methods for the research and engineering application of nanomaterials, helping to accelerate material innovation, optimize process design, and promote the practical application of nanomaterials. Wang et al. presented a good attempt of machine-learning-assisted synthesis of nanomaterials. They constructed a machine learning Gaussian regression model to assist with the preparation of molybdenum disulfide (MoS_2) semiconductors with the CVD method and to explore the growth mechanism. The optimal model can predict the size of MoS_2 synthesized under 185,900 experimental conditions in the simulation dataset, which enabled the selection of the optimal range for the synthesis of large-area MoS_2. This study verifies that machine learning is a powerful tool for the development of nanomaterials in chemical engineering.

In short, this Special Issue achieves great success by presenting all of the above high-quality original research papers and comprehensive review papers. We give our sincere thanks to the excellent scholars that have made contributions to this Special Issue. Inspired by the previous two successful Special Issue volumes, we are now launching the third volume of the Special Issue, that is, "Nanomaterials for Chemical Engineering III". We welcome even more excellent scholars to submit their original research or review papers on nanomaterials for chemical engineering to the Special Issue. Besides the topics that were covered by the previous two volumes (e.g., nanomaterials synthesis and characterization, catalytic nanomaterials, environmental protection and pollution control, biomedical applications, computational modeling studies, as well as utilization in devices and practical applications), we will welcome contributions from new fields, including, but not limited to, the following topics:

Green chemical engineering: Utilizing the special properties and effects of nanomaterials to develop green and sustainable chemical reactions and processes [16]. For example, the design and application of novel nanocatalysts will help to improve reaction selectivity and efficiency, reduce energy consumption and waste generation.

Energy applications: Nanomaterials have enormous potential in the energy field [17]. For example, nanomaterials can be used as electrodes and electrolytes for efficient energy storage devices, improving the performance of batteries and supercapacitors [18]. Nano photocatalysts can be used for photocatalytic water splitting and hydrogen production, etc.

The sustainability of nanomaterials: The preparation and application of nanomaterials need to consider their impact on the environment. The development of more sustainable and environmentally friendly preparation methods, as well as the recovery and recycling of nanomaterials, are key issues [19].

Moreover, we greatly encourage contributions from artificial intelligence and machine learning. These fast-developing artificial intelligence (AI) technologies provide great opportunities for the research and application of nanomaterials in the field of chemical engineering [20,21]. However, the design and optimization of machine learning algorithms also need to fully consider the special properties of nanomaterials themselves so as to obtain accurate and reliable results [22]. We believe that machine learning will provide many potential advantages and innovations to the engineering application of nanomaterials, including material design and prediction, reaction control and optimization, the analysis and interpretation of massive experimental data, the improvement of experimental efficiency, and so on.

Funding: This work was supported by the National Natural Science Foundation of China (22172194, 21872173).

Conflicts of Interest: The author declares no conflicts of interest.

List of Contributions

1. Mares-Briones, F.; Higareda, A.; Lopez-Miranda, J.L.; Mendoza-Cruz, R.; Esparza, R. Bimetallic AgPt Nanoalloys as an Electrocatalyst for Ethanol Oxidation Reaction: Synthesis, Structural Analysis, and Electro-Catalytic Activity. *Nanomaterials* **2023**, *13*, 1396.
2. Abitaev, K.; Atanasova, P.; Bill, J.; Preisig, N.; Kuzmenko, I.; Ilavsky, J.; Liu, Y.; Sottmann, T. In Situ Ultra-Small- and Small-Angle X-ray Scattering Study of ZnO Nanoparticle Formation and Growth through Chemical Bath Deposition in the Presence of Polyvinylpyrrolidone. *Nanomaterials* **2023**, *13*, 2180.
3. Quiñones-Gurrola, J.R.; Rendón-Angeles, J.C.; Matamoros-Veloza, Z.; López-Cuevas, J.; Pérez-Garibay, R.; Yanagisawa, K. Facile Preparation of $SrZr_{1-x}TixO_3$ and $SrTi_{1-x}ZrxO_3$ Fine Particles Assisted by Dehydration of Zr^{4+} and Ti^{4+} Gels under Hydrothermal Conditions. *Nanomaterials* **2023**, *13*, 2195.
4. Altena, M.; Jansen, T.; Tsvetanova, M.; Brinkman, A. Phase Separation Prevents the Synthesis of VBi_2Te_4 by Molecular Beam Epitaxy. *Nanomaterials* **2024**, *14*, 87.
5. Lazauskas, A.; Andrulevičius, M.; Abakevičienė, B.; Jucius, D.; Grigaliūnas, V.; Guobienė, A.; Meškinis, Š. Hydrophilic Surface Modification of Amorphous Hydrogenated Carbon Nanocomposite Films via Atmospheric Oxygen Plasma Treatment. *Nanomaterials* **2023**, *13*, 1108.
6. Mills, R.; Tvrdik, C.; Lin, A.; Bhattacharyya, D. Enhanced Degradation of Methyl Orange and Trichloroethylene with PNIPAm-PMMA-Fe/Pd-Functionalized Hollow Fiber Membranes. *Nanomaterials* **2023**, *13*, 2041.
7. Chiang, Y.-C.; Pu, Z.-H.; Wang, Z. Study on Oxygen Evolution Reaction of Ir Nanodendrites Supported on Antimony Tin Oxide. *Nanomaterials* **2023**, *13*, 2264.
8. Iordache, M.; Oubraham, A.; Sorlei, I.-S.; Lungu, F.A.; Capris, C.; Popescu, T.; Marinoiu, A. Noble Metals Functionalized on Graphene Oxide Obtained by Different Methods—New Catalytic Materials. *Nanomaterials* **2023**, *13*, 783.
9. Marinoiu, A.; Raceanu, M.; Carcadea, E.; Varlam, M. Nitrogen-Doped Graphene Oxide as Efficient Metal-Free Electrocatalyst in PEM Fuel Cells. *Nanomaterials* **2023**, *13*, 1233.
10. La Greca, E.; Kharlamova, T.S.; Grabchenko, M.V.; Consentino, L.; Savenko, D.Y.; Pantaleo, G.; Kibis, L.S.; Stonkus, O.A.; Vodyankina, O.V.; Liotta, L.F. Ag Catalysts Supported on CeO_2, MnO_2 and $CeMnO_x$ Mixed Oxides for Selective Catalytic Reduction of NO by C_3H_6. *Nanomaterials* **2023**, *13*, 873.
11. Saldaña-Robles, A.; Arcibar-Orozco, J.A.; Guerrero-Mosqueda, L.R.; Damián-Ascencio, C.E.; Marquez-Herrera, A.; Corona, M.; Gallegos-Muñoz, A.; Cano-Andrade, S. Synthesis of Composites for the Removal of F- Anions. *Nanomaterials* **2023**, *13*, 2277.
12. Lu, X.; Liu, Z.; Wang, W.; Wang, X.; Ma, H.; Cao, M. Synthesis and Evaluation of Peptide–Manganese Dioxide Nanocomposites as Adsorbents for the Removal of Strontium Ions. *Nanomaterials* **2024**, *14*, 52.
13. Magaletti, F.; Prioglio, G.; Giese, U.; Barbera, V.; Galimberti, M. Hexagonal Boron Nitride as Filler for Silica-Based Elastomer Nanocomposites. *Nanomaterials* **2024**, *14*, 30.
14. Barjoveanu, G.; Teodosiu, C.; Morosanu, I.; Ciobanu, R.; Bucatariu, F.; Mihai, M. Life Cycle Assessment as Support Tool for Development of Novel Polyelectrolyte Materials Used for Wastewater Treatment. *Nanomaterials* **2023**, *13*, 840.
15. Pacella, A.; Ballirano, P.; Di Carlo, M.C.; Fantauzzi, M.; Rossi, A.; Nardi, E.; Viti, C.; Arrizza, L.; Campopiano, A.; Cannizzaro, A. et al. Dissolution Reaction and Surface Modification of UICC Amosite in Mimicked Gamble’s Solution: A Step towards Filling the Gap between Asbestos Toxicity and Its Crystal Chemical Features. *Nanomaterials* **2023**, *13*, 2933.
16. Wang, J.; Lu, M.; Chen, Y.; Hao, G.; Liu, B.; Tang, P.; Yu, L.; Wen, L.; Ji, H. Machine Learning-Assisted Large-Area Preparation of MoS_2 Materials. *Nanomaterials* **2023**, *13*, 2283.

References

1. Vajtai, R. Science and Engineering of Nanomaterials. In *Springer Handbook of Nanomaterials*; Vajtai, R., Ed.; Springer: Berlin/Heidelberg, Germany, 2013; pp. 1–36. [CrossRef]
2. Chen, Y.; Lai, Z.; Zhang, X.; Fan, Z.; He, Q.; Tan, C.; Zhang, H. Phase engineering of nanomaterials. *Nat. Rev. Chem.* **2020**, *4*, 243–256. [CrossRef] [PubMed]
3. Sebastian, V.; Arruebo, M.; Santamaria, J. Reaction Engineering Strategies for the Production of Inorganic Nanomaterials. *Small* **2014**, *10*, 835–853. [CrossRef]
4. Qiu, L.-Q.; Li, H.-R.; He, L.-N. Incorporating Catalytic Units into Nanomaterials: Rational Design of Multipurpose Catalysts for CO_2 Valorization. *Acc. Chem. Res.* **2023**, *56*, 2225–2240. [CrossRef] [PubMed]
5. Chen, Z.; Li, Y.; Cai, Y.; Wang, S.; Hu, B.; Li, B.; Ding, X.; Zhuang, L.; Wang, X. Application of covalent organic frameworks and metal–organic frameworks nanomaterials in organic/inorganic pollutants removal from solutions through sorption-catalysis strategies. *Carbon Res.* **2023**, *2*, 8. [CrossRef]
6. Ansari, S.A.; Parveen, N.; Rahman, M.M. Nanomaterials for Catalysis and Energy Storage. *Nanomaterials* **2023**, *13*, 360. [CrossRef] [PubMed]
7. Yang, G.; Kong, H.; Chen, Y.; Liu, B.; Zhu, D.; Guo, L.; Wei, G. Recent advances in the hybridization of cellulose and carbon nanomaterials: Interactions, structural design, functional tailoring, and applications. *Carbohydr. Polym.* **2022**, *279*, 118947. [CrossRef]
8. Qin, T.; Li, X.; Yang, A.; Wu, M.; Yu, L.; Zeng, H.; Han, L. Nanomaterials-enhanced, stretchable, self-healing, temperature-tolerant and adhesive tough organohydrogels with long-term durability as flexible sensors for intelligent motion-speech recognition. *Chem. Eng. J.* **2023**, *461*, 141905. [CrossRef]
9. Liu, B.; Wang, Y.; Chen, Y.; Guo, L.; Wei, G. Biomimetic two-dimensional nanozymes: Synthesis, hybridization, functional tailoring, and biosensor applications. *J. Mater. Chem. B* **2020**, *8*, 10065–10086. [CrossRef]
10. Mazari, S.A.; Ali, E.; Abro, R.; Khan, F.S.A.; Ahmed, I.; Ahmed, M.; Nizamuddin, S.; Siddiqui, T.H.; Hossain, N.; Mubarak, N.M.; et al. Nanomaterials: Applications, waste-handling, environmental toxicities, and future challenges—A review. *J. Environ. Chem. Eng.* **2021**, *9*, 105028. [CrossRef]
11. Cao, M.; Zhuang, Z.; Liu, Y.; Zhang, Z.; Xuan, J.; Zhang, Q.; Wang, W. Peptide-mediated green synthesis of the MnO_2@ZIF-8 core–shell nanoparticles for efficient removal of pollutant dyes from wastewater via a synergistic process. *J. Colloid Interface Sci.* **2022**, *608*, 2779–2790. [CrossRef]
12. Adeleye, A.S.; Conway, J.R.; Garner, K.; Huang, Y.; Su, Y.; Keller, A.A. Engineered nanomaterials for water treatment and remediation: Costs, benefits, and applicability. *Chem. Eng. J.* **2016**, *286*, 640–662. [CrossRef]
13. Lu, X.; Liu, Z.; Wang, X.; Liu, Y.; Ma, H.; Cao, M.; Wang, W.; Yan, T. Construction of MnO_2@ZIF-8 core-shell nanocomposites for efficient removal of Sr^{2+} from aqueous solution. *Colloids Surf. A Physicochem. Eng. Asp.* **2024**, *685*, 133317. [CrossRef]
14. Ahmed, S.F.; Mofijur, M.; Rafa, N.; Chowdhury, A.T.; Chowdhury, S.; Nahrin, M.; Islam, A.B.M.S.; Ong, H.C. Green approaches in synthesising nanomaterials for environmental nanobioremediation: Technological advancements, applications, benefits and challenges. *Environ. Res.* **2022**, *204*, 111967. [CrossRef]
15. Shafiq, M.; Anjum, S.; Hano, C.; Anjum, I.; Abbasi, B.H. An Overview of the Applications of Nanomaterials and Nanodevices in the Food Industry. *Foods* **2020**, *9*, 148. [CrossRef]
16. Gómez-López, P.; Puente-Santiago, A.; Castro-Beltrán, A.; Santos do Nascimento, L.A.; Balu, A.M.; Luque, R.; Alvarado-Beltrán, C.G. Nanomaterials and catalysis for green chemistry. *Curr. Opin. Green Sustain. Chem.* **2020**, *24*, 48–55. [CrossRef]
17. Mishra, K.; Devi, N.; Siwal, S.S.; Gupta, V.K.; Thakur, V.K. Hybrid Semiconductor Photocatalyst Nanomaterials for Energy and Environmental Applications: Fundamentals, Designing, and Prospects. *Adv. Sustain. Syst.* **2023**, *7*, 2300095. [CrossRef]
18. Zhu, Y.; Peng, L.; Fang, Z.; Yan, C.; Zhang, X.; Yu, G. Structural Engineering of 2D Nanomaterials for Energy Storage and Catalysis. *Adv. Mater.* **2018**, *30*, 1706347. [CrossRef]
19. Khalaj, M.; Kamali, M.; Aminabhavi, T.M.; Costa, M.E.V.; Dewil, R.; Appels, L.; Capela, I. Sustainability insights into the synthesis of engineered nanomaterials—Problem formulation and considerations. *Environ. Res.* **2023**, *220*, 115249. [CrossRef]
20. Scott-Fordsmand, J.J.; Amorim, M.J.B. Using Machine Learning to make nanomaterials sustainable. *Sci. Total Environ.* **2023**, *859*, 160303. [CrossRef]
21. Shirokii, N.; Din, Y.; Petrov, I.; Seregin, Y.; Sirotenko, S.; Razlivina, J.; Serov, N.; Vinogradov, V. Quantitative Prediction of Inorganic Nanomaterial Cellular Toxicity via Machine Learning. *Small* **2023**, *19*, 2207106. [CrossRef]
22. Kløve, M.; Sommer, S.; Iversen, B.B.; Hammer, B.; Dononelli, W. A Machine-Learning-Based Approach for Solving Atomic Structures of Nanomaterials Combining Pair Distribution Functions with Density Functional Theory. *Adv. Mater.* **2023**, *35*, 2208220. [CrossRef] [PubMed]

nanomaterials

MDPI

Article

Synthesis and Evaluation of Peptide–Manganese Dioxide Nanocomposites as Adsorbents for the Removal of Strontium Ions

Xingjie Lu [1,2], Zhen Liu [1], Wentao Wang [2], Xin Wang [1], Hongchao Ma [1,*] and Meiwen Cao [1,*]

[1] State Key Laboratory of Heavy Oil Processing, Department of Biological and Energy Chemical Engineering, College of Chemical Engineering, China University of Petroleum (East China), 66 Changjiang West Road, Qingdao 266580, China; 17864272242@163.com (X.L.); lassiezhen@163.com (Z.L.); z21030169@s.upc.edu.cn (X.W.)

[2] Department of Radiochemistry, China Institute of Atomic Energy, Beijing 102413, China; wentaowang001@163.com

* Correspondence: mahc@upc.edu.cn (H.M.); mwcao@upc.edu.cn (M.C.)

Abstract: In this study, a novel organic–inorganic hybrid material IIGK@MnO_2 (2-naphthalenemethyl-isoleucine-isoleucine-glycine-lysine@manganese dioxide) was designed as a novel adsorbent for the removal of strontium ions (Sr^{2+}). The morphology and structure of IIGK@MnO_2 were characterized using TEM, AFM, XRD, and XPS. The results indicate that the large specific surface area and abundant negative surface charges of IIGK@MnO_2 make its surface rich in active adsorption sites for Sr^{2+} adsorption. As expected, IIGK@MnO_2 exhibited excellent adsorbing performance for Sr^{2+}. According to the adsorption results, the interaction between Sr^{2+} and IIGK@MnO_2 can be fitted with the Langmuir isotherm and pseudo-second-order equation. Moreover, leaching and desorption experiments were conducted to assess the recycling capacity, demonstrating significant reusability of IIGK@MnO_2.

Keywords: peptide assembly; MnO_2; Sr^{2+} removal

Citation: Lu, X.; Liu, Z.; Wang, W.; Wang, X.; Ma, H.; Cao, M. Synthesis and Evaluation of Peptide–Manganese Dioxide Nanocomposites as Adsorbents for the Removal of Strontium Ions. *Nanomaterials* **2024**, *14*, 52. https://doi.org/10.3390/nano14010052

Academic Editor: Diego Cazorla-Amorós

Received: 1 December 2023
Revised: 19 December 2023
Accepted: 21 December 2023
Published: 23 December 2023

1. Introduction

Nuclear energy is widely used due to its ability to reduce greenhouse effects, high energy density, and ease of storing nuclear fuel [1]. However, in nuclear disasters such as Chernobyl and Fukushima, the release of large amounts of radioactive isotopes and waste has had a catastrophic impact on ecosystems, causing significant damage. In terms of radioactive safety, strontium (^{90}Sr), cobalt (^{60}Co), and cesium (^{137}Cs) are considered the main radioactive isotopes due to their relatively long half-lives, high solubility, and easy transfer [2]. Among them, ^{90}Sr is a carcinogen and hazardous pollutant that has chemical properties similar to calcium and is easily absorbed by the human body [3]. Therefore, the development of new materials for removing strontium ions (Sr^{2+}) from aqueous solutions has received great attention. At present, various methods have been developed to remove radioactive toxic ions from aqueous solutions, including chemical precipitation, membrane, solvent extraction, ion exchange, and adsorption [4–8]. Among them, the adsorption method is the most used and highly efficient technology. Up to now, a large number of nanomaterials, such as hydroxyapatite nanoparticles, metal sulfide, metallic oxide, graphene oxide (GO), and MOFs, have been employed as adsorbents for removing Sr^{2+} [9–13]. Attributed to their larger specific surface area and more active sites, MnO_2 nanoparticles have been widely studied and applied as effective adsorbents for Sr^{2+} [14]. Moreover, MnO_2 particles also exhibit selectivity for Sr^{2+} in the presence of competing ions, including Na^+, K^+, Ca^{2+}, and Mg^{2+} [15]. However, MnO_2 nanoparticles have drawbacks such as susceptibility to van der Waals forces, which may lead to aggregation and a decrease in their adsorption performance [16]. Therefore, it is necessary to fix MnO_2 nanoparticles

on the carrier to improve their dispersion stability as well as adsorption performance and reusability for Sr^{2+} removal.

Due to the presence of abundant functional groups such as hydroxyl groups, thiol groups, and carboxyl groups as adsorption sites, along with diverse secondary structures, a series of peptides has been studied for their binding to various metallic materials, including metal oxides, metal sulfides, and metals [17,18]. Moreover, some specifically designed peptides demonstrate a selective affinity for particular metal ions, which can serve as effective metal-binding moieties in aqueous solutions and promote selective metal ion adsorption [19]. For example, Mondal et al. confirmed the affinity of a tripeptide gel for metal ions, including lead and cadmium [20]. Besides direct metal ion adsorption, the peptides can be used to composite with other materials to achieve synergistic metal ion adsorption. At present, various peptide sequences have been used for biomimetic synthesis of ceramics, metal sulfides, metal oxides, and metal nanoparticles, and composite materials with low dispersion, good crystallinity, diverse morphology, and excellent biological functions have been constructed in mild water environments [21,22]. In addition, peptides have excellent assembly performance and can form different functional structures through covalent and noncovalent interactions (such as hydrophilicity and hydrophobicity, π-π stacking, hydrogen bonding, and electrostatic interactions). These peptide assembly structures can regulate the structure of peptide–inorganic nanoparticles by inducing the nucleation and growth process of inorganic nanoparticles and selectively binding to certain crystal planes. This makes peptides an excellent template for in situ loading and construction of inorganic nanomaterials.

As mentioned in the above text, though MnO_2 nanoparticles are good candidates for Sr^{2+} absorption and removal, they easily experience severe agglomeration and poor dispersibility in aqueous solution, which influences the adsorption performance. To address this issue, we chose the self-assembled nanofibrils of short peptide 2-naphthalenemethyl-isoleucine-isoleucine-glycine-lysine (IIGK) (Figure 1) as templates to mediate the mineralization of MnO_2 on their surface, which can greatly enhance the dispersibility of MnO_2 nanoparticles. Compared with other methods for synthesizing MnO_2, such as electrodeposition, demulsification, and hydrothermal methods, this method is environmentally friendly, mild, and easy to operate. The physicochemical properties of the as-prepared IIGK@MnO_2 were systematically characterized first by using various techniques. Then, experiments were performed to investigate the adsorption performance of the IIGK@MnO_2 nanocomposites towards Sr^{2+}. The results show that the IIGK@MnO_2 nanocomposites have a strong affinity and adsorption capacity for Sr^{2+}, and a synergistic effect on the adsorption of Sr^{2+} with IIGK@MnO_2 can be concluded. This study demonstrated the merits of IIGK@MnO_2 as a promising adsorbent to remove Sr^{2+} from nuclear wastewater.

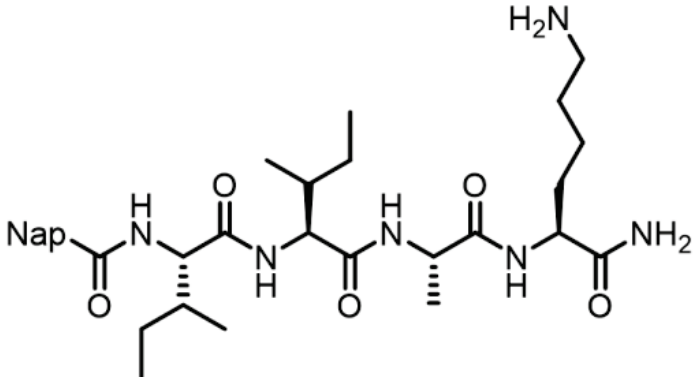

Figure 1. Molecular structure of the short peptide IIGK.

2. Materials and Methods

2.1. Materials

Manganese chloride tetrahydrate ($MnCl_2{\cdot}4H_2O$), potassium permanganate ($KMnO_4$), sodium nitrate ($NaNO_3$), potassium nitrate (KNO_3), strontium nitrate ($Sr(NO_3)_2$), sodium hydroxide (NaOH), and potassium hydroxide (KNO_3) were acquired from Sinopharm Chemical Reagent Co., Ltd. (Shanghai, China). All working solutions were prepared using distilled water. The pH was adjusted using NaOH and HCl as needed and monitored with a digital pH meter. All adsorption experiments were conducted at ambient temperature.

2.2. Preparation of IIGK@MnO_2 Nanocomposite

First, 300 mg IIGK powder was dissolved in 250 mL ultrapure water, which was then subjected to ultrasonic dispersion for approximately 10 min. Then, the mixture was left to stand overnight, followed by adding another 225.6 mL ultrapure water. Subsequently, 9.6 mL $KmnO_4$ (30 mM) aqueous solution and 9.6 mL $MnCl_2{\cdot}4H_2O$ (42 mM) aqueous solution were added to the mixture, which was then stirred for 24 h. Finally, the samples were centrifuged, washed three times with ultrapure water, and subsequently freeze-dried to obtain IIGK@MnO_2 powder for further use.

2.3. Characterization

The morphology of samples was characterized using a scanning electron microscope (SEM, Hitachi S-4800, Tokyo, Japan) and transmission electron microscope (TEM, JOEL JEM1400 Plus, Tokyo, Japan). The SEM equipped with an Oxford Instruments energy-dispersive X-ray spectroscopy (EDS) system was used for analyzing elemental composition. The thickness of materials was measured using atomic force microscopy (AFM, Santa Babara Vecco Nanoscope Iva, Santa Barbara, CA, USA). The size and zeta potential of samples were determined on a Zetasizer Nano (DLS, Malvern NANO ZS, Marvin City, UK). The element analysis of the samples before and after Sr^{2+} adsorption was carried out using X-ray photoelectron spectroscopy (XPS, Thermo Scientific Esclab 250Xi, Waltham, MA, USA) with a monochromatic Al Kα X-ray source (15 KV). Fourier-transform infrared spectroscopy (FT-IR, Thermo Scientific Nicolet iS5, Waltham, MA, USA) was performed to investigate the interaction between MnO_2 and IIGK. X-ray diffraction (XRD, PANalitical X'Pert PRO MPD, Almelo, The Netherland) was performed to study the crystal structure of the samples using Cu-Kα radiation in the 2θ range of 10°–80° at room temperature. N_2 adsorption–desorption isotherm was conducted on the gas sorption analyzer at 373.15 K (Malvern PANalitical Autosorb-6B, Marvin City, UK), and the specific area and the average pore diameters were stimulated using the Brunauer-Emmett-Teller (BET) and Barrett–Joyner–Halenda (BJH) method. Inductively coupled plasma optical emission spectroscopy (ICP-OES, HORIBA JY 2000-2, Loos, Naples, FL, USA) was employed to determine the concentration of residual metal ions in the solution.

2.4. Adsorption Performance of IIGK@MnO_2

All adsorption experiments were carried out in 15 mL polyethylene centrifuge tubes. After mixing 1 mg IIGK@MnO_2 with 10 mL Sr^{2+} aqueous solution, the pH of the mixture was adjusted to a suitable value. The mixture was left in a constant-temperature shaker for a certain time, followed by centrifugation at 12,000 rpm for 20 min to extract the supernatant. Finally, the residue Sr^{2+} concentration in the adsorbed solution was measured using ICP-OES. The equilibrium adsorption amount (q_e, mg/g) and removal rate (R, %) of IIGK@MnO_2 towards Sr^{2+} can be calculated by the following equations:

$$q_e = (c_0 - c_e) \times \frac{V}{M} \quad (1)$$

$$R = \frac{c_0 - c_e}{c_0} \times 100\% \quad (2)$$

where c_0 (mg/L) and c_e (mg/L) are the initial and equilibrium concentrations of Sr^{2+} in the solution, respectively. V (mL) represents the volume of the adsorbed solution, and M (g) is the quantity of adsorbent.

2.5. Desorption of Strontium Ions from IIGK@MnO$_2$

The desorption behavior of the IIGK@MnO_2 was investigated by treating IIGK-MnO_2-Sr composites with 1 M HCl aqueous solution. The amount of Sr^{2+} desorbed from the IIGK@MnO_2, Q_{D_Sr}, was determined according to Equation (3), while the desorption efficiency (De, %) was obtained from Equation (4).

$$Q_{D\_Sr} = \frac{C_D \times V_D}{M_D} \tag{3}$$

$$De = \frac{Q_{D\_Sr}}{q_e} \times 100 \tag{4}$$

where C_D (mg/L) is the equilibrium desorption concentrations of Sr^{2+}, V_D (mL) represents the volume of the eluent, and M_D (g) is the weight of adsorbent after Sr^{2+} adsorption.

3. Results and Discussion

3.1. Synthesis and Characterization of IIGK@MnO$_2$ Nanocomposite

In this work, the IIGK@MnO_2 nanocomposite was synthesized by depositing MnO_2 nanoparticles along peptide fibers using a green, simple, and easy-to-operate biomimetic mineralization method. For comparison, pure manganese dioxide nanoparticles without peptide involvement were also synthesized. The morphology of MnO_2 nanoparticles and IIGK@MnO_2 nanocomposites was characterized using SEM, TEM, and AFM. As shown in Figure 2a,b, the MnO_2 nanoparticles generated without peptide show a disordered flower shape with a diameter of 400–500 nm, while the IIGK@MnO_2 nanocomposites took on elongated structures with many MnO_2 nanoparticles aligned in an axial direction (Figure 2c,d). The TEM result (Figure 2e) shows more clearly the one-dimensional nanowire/nanosheet composited structure. The results indicate that MnO_2 is generated through biomimetic mineralization using IIGK short peptides as templates. The inner core should be the IIGK fibrils, while the outer layer sheets should be MnO_2 nanostructures. The results demonstrate clearly the template role of the peptide fibrils in mediating MnO_2 mineralization. The formation of fibrous IIGK@MnO_2 nanocomposite can be confirmed with an AFM image (Figure 2f).

The surface zeta potential of the one-dimensional fiber-like IIGK@MnO_2 nanocomposites at different pH was then measured, as shown in Figure 3a. It can be observed that the isoelectric point of IIGK@MnO_2 appears at pH 1.7. While the pH value increases from 0.9 to 10.5, the zeta potential of IIGK@MnO_2 decreases gradually from 10 mV to −40 mV. Notably, when the pH value is greater than 1.7, IIGK@MnO_2 undergoes charge reversal, changing from a positively charged surface to a negatively charged surface. Moreover, the excess negative charges on the IIGK@MnO_2 surface are beneficial for the subsequent adsorption of Sr^{2+}. The particle size distribution of MnO_2 and IIGK@MnO_2 was measured using the dynamic light scattering measurement. As shown in Figure 3b, the size of IIGK-induced IIGK@MnO_2 nanocomposites is about 100–400 nm, while that of MnO_2 produced in the absence of peptide is above 1000 nm. This result indicates that the IIGK@MnO_2 nanocomposites induced with IIGK have a higher dispersion stability in the solution and a larger specific surface area, which is beneficial for the adsorption of Sr^{2+}.

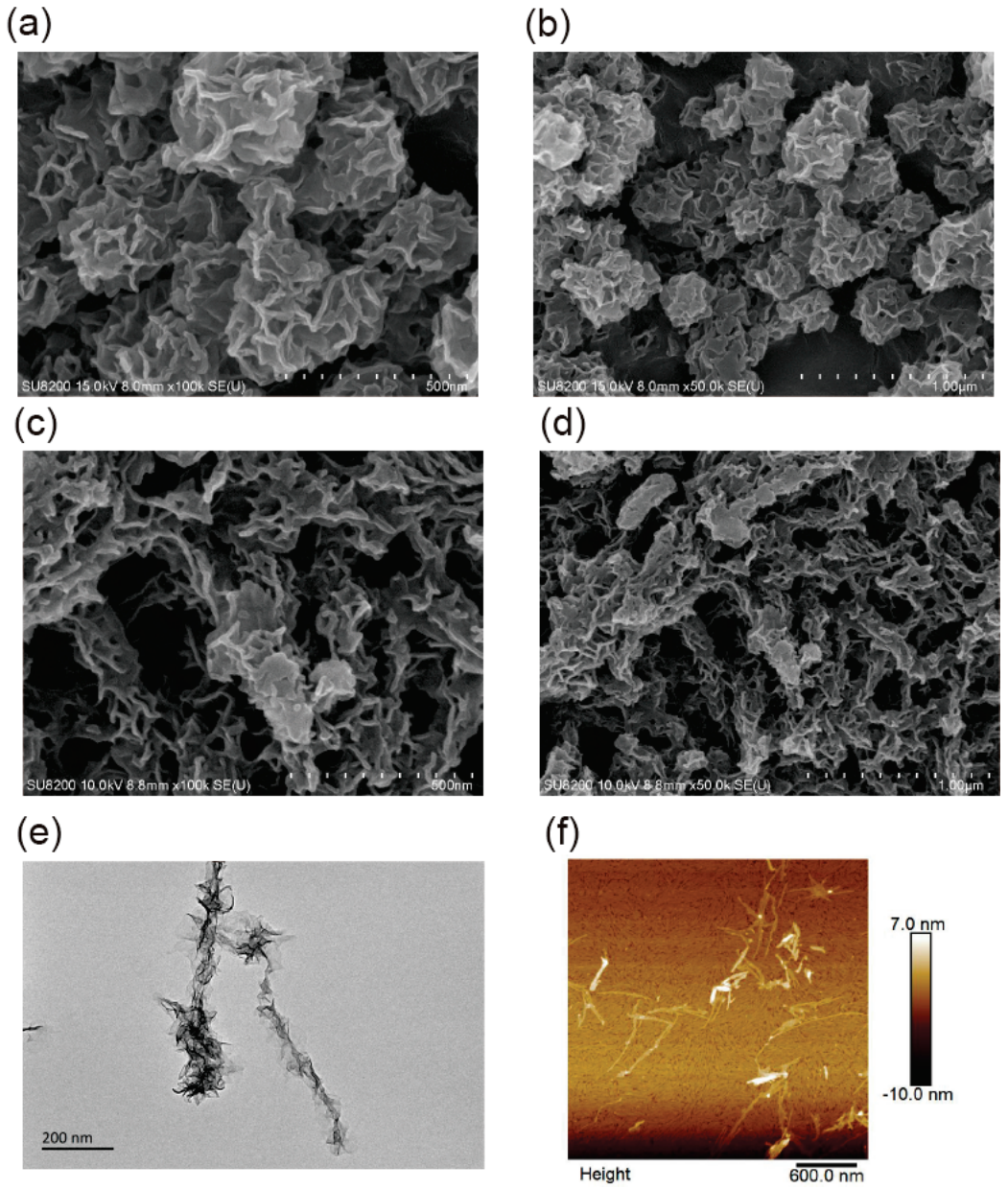

Figure 2. (**a**,**b**) SEM images of MnO_2, (**c**,**d**) SEM images of IIGK@MnO_2, (**e**) TEM, and (**f**) AFM images of IIGK@MnO_2 nanocomposite.

In order to investigate the crystal structure, X-ray powder diffraction (XRD) was employed to characterize IIGK@MnO_2 and MnO_2. The XRD patterns of the IIGK@MnO_2 nanocomposites and MnO_2 itself are shown in Figure 3c. For MnO_2, the peaks are found at $2\theta = 22.8°$, 36.5°, and 65.7°. These crystalline microregions correspond to δ-standard diffraction patterns (002), (111), and (311) of MnO_2 (JCPDS 80-1098), respectively. The same peaks were found in the XRD patterns of IIGK@MnO_2, indicating that MnO_2 was successfully loaded on the IIGK fibril's surface. Moreover, as indicated by the weak XRD peaks, the IIGK@MnO_2 nanocomposites show a low crystallinity level. The reason for the poor crystallinity may be due to the fast reaction rate during the interaction between $KMnO_4$ and $MnCl_2$, which leads to the rapid formation and precipitation of MnO_2 [23]. This rapid process may have hindered the formation of an orderly atomic arrangement.

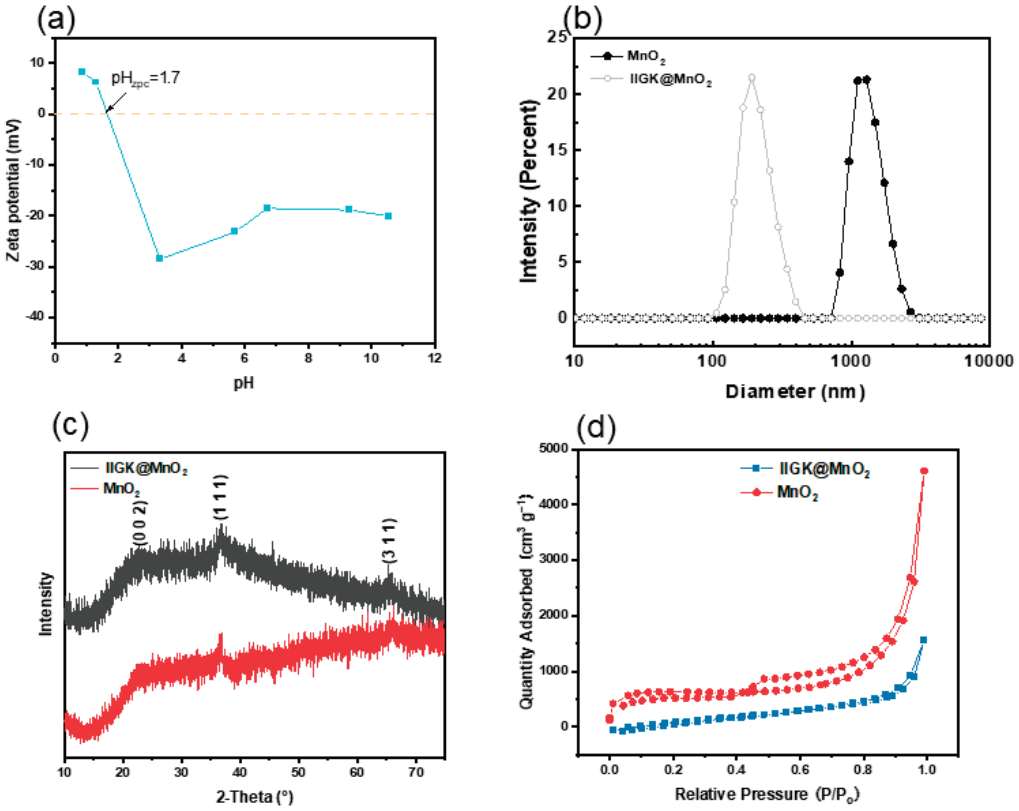

Figure 3. (**a**) Zeta potential of IIGK@MnO_2, (**b**) diameter distribution of MnO_2 and IIGK@MnO_2, (**c**) XRD spectra of IIGK@MnO_2 and MnO_2, and (**d**) N_2 adsorption–desorption isotherms of IIGK@MnO_2 and MnO_2.

Subsequently, the surface area, pore size, as well as pore volume of the IIGK@MnO_2 and MnO_2 were determined using BET analysis and the BJH method. According to the adsorption–desorption isotherms shown in Figure 3d, the surface area of IIGK@MnO_2 is approximately 46.19 $m^2 \cdot g^{-1}$. In addition, the pore volume and average pore size of IIGK@MnO_2 are calculated to be 2.40 $cm^3 \cdot g^{-1}$ and 14.02 nm, respectively. The whole results also indicate that the IIGK@MnO_2 nanocomposite has suitable physical properties as an adsorbent and is suitable for the adsorption of Sr^{2+} [24].

Furthermore, Fourier transform infrared spectroscopy (FTIR) was used to characterize IIGK@MnO_2 at a molecular level (Figure S1). The broad band at about 3421.6 cm^{-1} belongs to the stretching vibration of -OH, which may be attributed to the adsorption of a small amount of water by IIGK@MnO_2 and the presence of hydroxyl groups on the Mn surface [25]. In addition, the characteristic absorption peaks at 1628.2 cm^{-1}, 1383.7 cm^{-1}, and 1022.8 cm^{-1} can be attributed to the bending vibration of the hydroxyl group (Mn-OH) directly connected to the Mn atom. The peak appearing at 500 cm^{-1} indicates the presence of [MnO_6] octahedra, which is caused by the stretching of Mn-O and Mn-O-Mn bonds in the octahedral structure [26]. The elements' valence states of IIGK@MnO_2 were further characterized using XPS spectroscopy. As shown in Figure 4a, the XPS spectrum of Mn 2p exhibits two peaks at 642.7 eV and 654.4 eV, corresponding to Mn 2p 3/2 and Mn 2p 1/2, respectively. The spin energy range of 11.7 eV indicates that the IIGK short peptide fibers are mainly used as templates for the deposition of MnO_2 [27]. In addition, the weak peak appearing at 645.6 eV indicates the presence of a small amount of unreacted Mn^{2+} in the system. According to Chigane et al., the XPS spectrum of Mn 3s can split into two weaker peaks, which are located at 84.6 eV and 89.5 eV, corresponding to Mn^{4+} and Mn^{3+}, respectively [28]. The difference in binding energy between these two peaks increases with the decrease in the valence state of Mn. As shown in Figure 4b, a 4.9 eV difference can be observed between the two peaks, indicating that Mn in IIGK@MnO_2 is mainly composed of

Mn^{4+}, with a small amount of Mn^{3+} present. The O 1s peak exhibits three resolved peaks, with binding energies concentrated at 530.1 eV, 531.4 eV, and 533.12 eV (Figure 4c). These peaks are attributed to Mn-O-Mn, Mn-O, and O-H, respectively [29]. Figure 4d shows the complete XPS spectrum of IIGK@MnO_2, including Mn 3s, Mn 2p, C 1s, O 1s, and N 1s signals, indicating the successful mineralization of MnO_2.

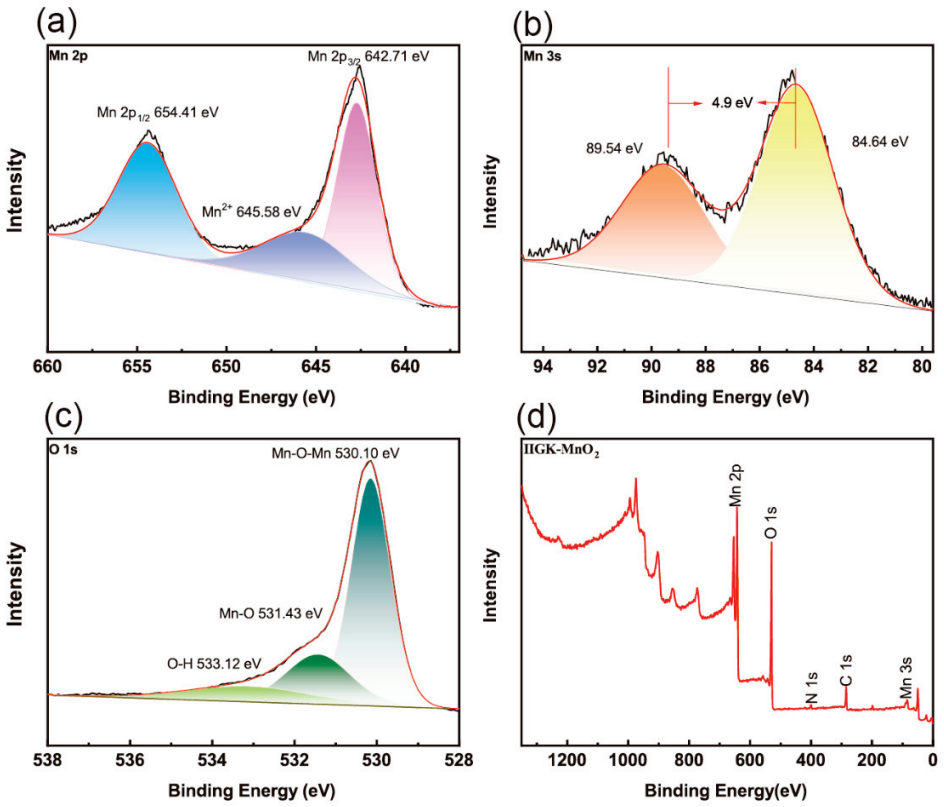

Figure 4. XPS spectra of (**a**) Mn 2p, (**b**) Mn 3s, and (**c**) O 1s of IIGK@MnO_2. (**d**) XPS full survey spectra of IIGK@MnO_2. The fitting data of spectra (**a**–**c**) are shown by different colors.

3.2. Sr^{2+} Adsorption Studies

Previous reports have indicated that MnO_2 possesses excellent adsorbing performance for Sr^{2+}. Then, the performance of IIGK@MnO_2 in adsorbing Sr^{2+} was studied. The ability of IIGK@MnO_2 to adsorb Sr^{2+} at different pH values was first evaluated. As shown in Figure 5a, the adsorption efficiency of Sr^{2+} increases with the increase in pH value and then tends to equilibrium. The low adsorption efficiency of IIGK@MnO_2 for Sr^{2+} in acidic pH environments may be caused by the competitive interaction between H^+ and Sr^{2+}. At higher pH conditions, the concentration of H^+ is lower; thus, there are more active sites left on IIGK@MnO_2 for the adsorption of Sr^{2+}. In addition, under high pH conditions, the surface of IIGK@MnO_2 carries more negative charges, which has a stronger electrostatic force on positively charged Sr^{2+}, thereby improving the adsorption efficiency of Sr^{2+} [30]. Except for pH, temperature also affects the adsorption efficiency of IIGK@MnO_2 for Sr^{2+}. As shown in Figure 5b, IIGK@MnO_2 has the highest adsorption efficiency for Sr^{2+} at room temperature. When the temperature rises above 40 °C, the adsorption efficiency sharply decreases. This phenomenon may be due to the weakening of the interaction between IIGK@MnO_2 and Sr^{2+} at higher temperatures, resulting in the desorption of Sr^{2+} [31].

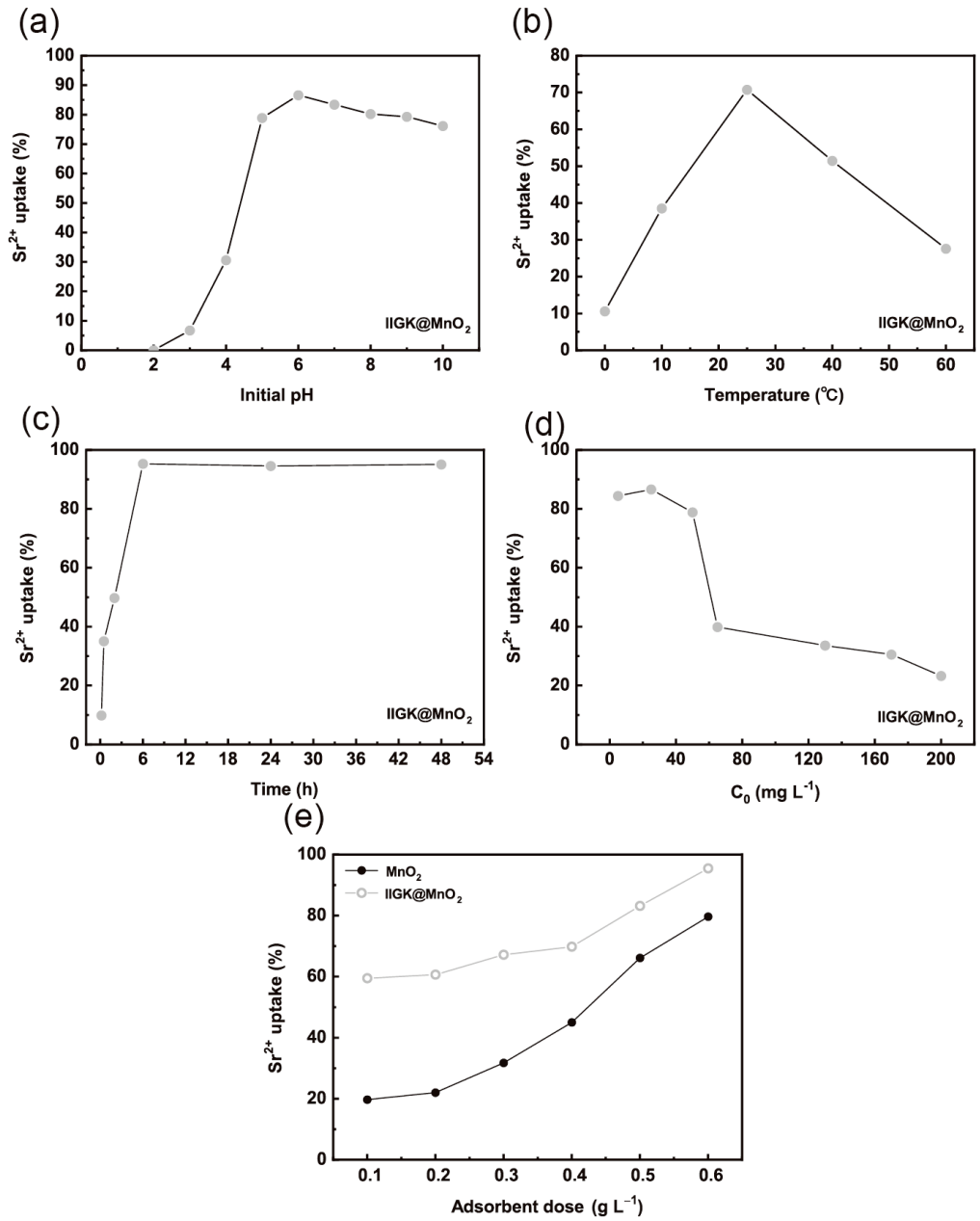

Figure 5. Sr^{2+} removal efficiency of the IIGK@MnO_2 nanocomposite at different (**a**) pH, (**b**) temperature, (**c**) contact time, (**d**) initial Sr^{2+} concentration, and (**e**) different adsorbent dosage.

The contact time between IIGK@MnO_2 and Sr^{2+} would also affect the adsorption efficiency. As shown in Figure 5c, the adsorption of Sr^{2+} by IIGK@MnO_2 rapidly reaches equilibrium at 6 h. The initial rapid adsorption may be attributed to the large number of available adsorption sites exposed on the surface of IIGK@MnO_2. Then, the adsorption process reached equilibrium after 6 h, indicating that most of the available adsorption sites were occupied. The whole adsorption process was assessed using both the pseudo-first-order and pseudo-second-order kinetic models. The equations are as follows [32]:

$$lg(q_e - q_t) = lgq_e - \frac{k_1}{2.303} \tag{5}$$

$$\frac{t}{q_t} = \frac{1}{k_2 q_e^2} + \frac{1}{q_e} \tag{6}$$

where q_e and q_t represent the Sr^{2+} adsorption capacity (mg/g) at equilibrium or at time t (adsorption time), respectively; k_1 (min^{-1}) and k_2 (g/(mg·min)) represent the rate constants for the pseudo-first-order and pseudo-second-order models. The fitted parameters are summarized in Table 1. Comparing the R^2 value of these models, the pseudo-second-order model fits better than the pseudo-first-order model [33].

Table 1. Fitted parameters of pseudo-first-order and pseudo-second-order kinetic models.

Model	Parameters	Value
Pseudo-First-Order	q_e (mg/g)	238.94
	k_1 (min^{-1})	0.489
	R^2	0.939
Pseudo-Second-Order	q_e (mg/g)	252.542
	k_2 (g/mg·min)	0.003
	R^2	0.936

For adsorbents, the initial concentration of the adsorbed substance often affects the adsorption rate and efficiency. Therefore, the effect of initial Sr^{2+} concentration on the adsorption efficiency of IIGK@MnO_2 was further studied. According to Figure 5d, the adsorption efficiency of IIGK@MnO_2 for Sr^{2+} shows a trend of first increasing and then decreasing with the increase in initial Sr^{2+} concentration. The maximum adsorption efficiency occurs when the Sr^{2+} concentration is 25 mg·L^{-1}. When the initial Sr^{2+} concentration reaches 40 mg·L^{-1}, the adsorption efficiency sharply decreases. When the Sr^{2+} concentration increases to 60 mg·L^{-1}, the adsorption efficiency tends to stabilize. The adsorption isotherms of Sr^{2+} on IIGK@MnO_2 were studied using Freundlich and Langmuir isotherm models. The model is shown as follows [34]:

$$q_e = \frac{q_m b C_e}{1 + b C_e} \tag{7}$$

$$q_e = K_f C_e^{\frac{1}{n}} \tag{8}$$

where q_m (mg/g) represents the maximum adsorption capacity at the isotherm temperature, b (L/mg) is the Langmuir constant associated with the free energy or net enthalpy of adsorption, C_e (mg/L) and q_e (mg/g) denote the concentration of the adsorbate in the equilibrated solution and the amount adsorbed on the adsorbent, respectively, K_f and n are equilibrium constants that provide information about the adsorption capacity and intensity. Shown in Table 2 is the fitting effect of equilibrium data, and the Langmuir isotherm model (R^2 = 0.991) is better than that of the Freundlich model (R^2 = 0.982). Furthermore, the Sr^{2+} adsorption performance of the IIGK@MnO_2 nanocomposite was compared with that of other reported materials (Table 3). Compared to other adsorbents, IIGK@MnO_2 showed better performance in the aspects of higher adsorption capacity (748.2 mg/g), which is beneficial for the treatment of nuclear wastewater. Therefore, the adsorbent surface is considered homogeneous and monolayer in terms of adsorption energy [35]. Compared with pure MnO_2, IIGK@MnO_2 composites exhibit significantly stronger adsorption efficiency for Sr^{2+} (Figure 5e). As previously speculated, after combing IIGK peptide with MnO_2, the obtained IIGK@MnO_2 composites contain more adsorption active sites due to their high dispersion, large specific surface area, and high negative charge, which is beneficial for the adsorption of Sr^{2+}.

Table 2. The parameters calculated from the Langmuir and Freundlich for Sr^{2+} adsorption by the IIGK@MnO_2 nanocomposite.

Models	Parameters		
Langmuir isotherm	q_m (mg/g) 748.193	b (L/mg) 0.015	R^2 0.991
Freundlich isotherm	k 33.542	1/n 0.55	R^2 0.982

Table 3. Comparison of the adsorption performance of IIGK@MnO_2 nanocomposite and other adsorbents for removal of Sr^{2+}.

Adsorbent	Maximum Adsorption Capacity (mg/g)	Optimal pH	Equilibrium Time (min)	Reference
IIGK@MnO_2	748.193	6	360	This study
bentonite	63.01	-	-	[36]
zeolite 4A	252.5	4–9	5	[37]
K_2SbPO_6	175.9	3	1440	[38]
SBA-15	17.67	10	100	[39]
A-ZrP	300	3–11	240	[40]
NaTS	80.0	5	0.083	[10]
SZ-6	61.4	10	50	[41]
MnO_2	53.5	10	0.25	[24]

3.3. Desorption and Reusability Studies

When evaluating the economy and applicability of an adsorbent, the reusability is an important indicator that plays a crucial role in the practical application of adsorbents. Herein, the adsorption/desorption process was repeated to assess the reusability of IIGK@MnO_2. Firstly, IIGK@MnO_2 was used to adsorb Sr^{2+}, and then the IGK@MnO_2-Sr^{2+} composite was treated with 1M HCl solution for Sr^{2+} desorption. The whole adsorption/desorption process was repeated three times. As shown in Figure 6, when the regeneration cycle is repeated three times, the adsorption efficiency of IIGK@MnO_2 for Sr^{2+} is still higher than 64%, indicating that 1M HCl solution can effectively desorb Sr^{2+} from IIGK@MnO_2. Moreover, the adsorption capacity of IIGK@MnO_2 for Sr^{2+} decreased with the increase in cycling number, which may be due to H^+ occupying some adsorption sites. However, it can also be noted that the adsorption efficiency of IIGK@MnO_2 for Sr^{2+} can still reach over 60% at the end of three cycles, indicating that IIGK@MnO_2 has good reusability.

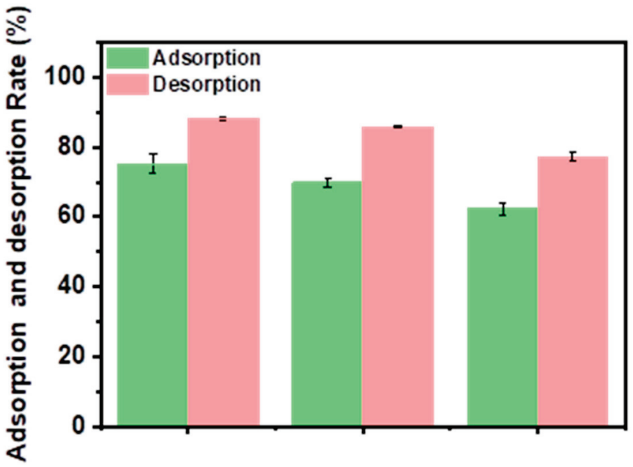

Figure 6. Reusability of the IIGK@MnO_2 nanocomposite during three cycles of Sr^{2+} adsorption and desorption.

3.4. Adsorption Mechanism of Sr^{2+} by the IIGK@MnO_2 Nanocomposite

The adsorption mechanism of IIGK@MnO_2 for Sr^{2+} was studied. Figure 7a shows the morphology and distribution of various elements of IIGK@MnO_2 after the adsorption of Sr^{2+}. After adsorbing Sr^{2+}, there was no significant change in the morphology of IIGK@MnO_2. The mapping of IIGK@MnO_2-Sr elements shows that the adsorbed Sr^{2+} is evenly distributed on the surface of IIGK@MnO_2, indicating that the adsorption sites on IIGK@MnO_2 are relatively uniform. XPS data confirmed the presence of strontium on IIGK@MnO_2 after adsorption (Figure 7b). The deconvolution peaks located at 133.5 eV and 135.4 eV belong to Sr 3d 5/2 and Sr 3d 3/2, respectively (Figure 7c) [10]. There is a shift in binding energy in the high-resolution spectrum of O1s in Figure 7d. The binding energy of the O1s-Mn-OH peak decreased from 531.4 eV to 531.0 eV, and the binding energy of the O 1s O-H peak decreased from 533.1 eV to 532.8 eV. This result indicates that oxygen atoms interact with Sr^{2+} and play a dominant role in the Sr^{2+} adsorption process.

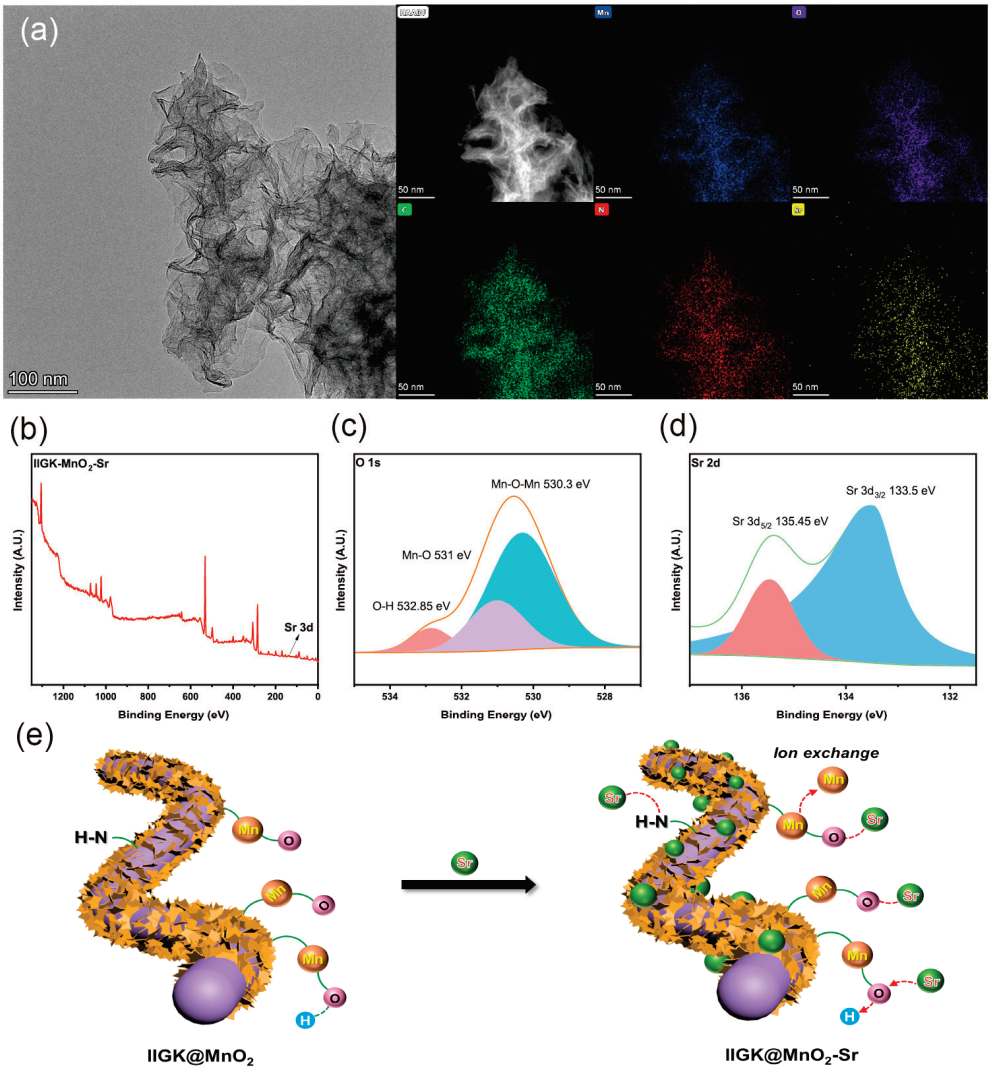

Figure 7. (**a**) TEM imagine and EDS element-mapping of IIGK@MnO_2-Sr composite. (**b**) XPS full survey spectra of the IIGK@MnO_2-Sr nanocomposite. (**c**,**d**) XPS fine spectra of O 1s and Sr 3d of the IIGK@MnO_2-Sr nanocomposite. (**e**) Schematic diagram of the adsorption mechanism of Sr^{2+} by IIGK@MnO_2.

From the above results, the mechanism of Sr^{2+} adsorption by IIGK@MnO_2 can be proposed, as schemed in Figure 7e. On the one hand, the peptide IIGK can bind with Sr^{2+} through coordination or electrostatic interactions. On the other hand, the MnO_2

nanoparticles on the IIGK fibrils' surface have many absorption sites, which can adsorb Sr^{2+} by either coordination interaction or ion exchange reaction. Therefore, IIGK and MnO_2 work synergistically to enhance the removal efficiency of the IIGK@MnO_2 nanocomposites.

4. Conclusions

In this work, the IIGK@MnO_2 nanocomposites were synthesized using environmentally friendly and mild methods. Using the short peptide IIGK as a template leads to the formation of a one-dimensional fibrous structure of IIGK@MnO_2 nanocomposite, which not only gives the mineralized IIGK@MnO_2 complex a large specific surface area but also makes the overall IIGK@MnO_2 negatively charged. These unique properties are conducive to the adsorption and removal of Sr^{2+} from wastewater. According to the adsorption performance of IIGK@MnO_2 towards Sr^{2+}, it can be observed that the IIGK@MnO_2 hybrid adsorbents possess excellent Sr^{2+} adsorption effects in a large range of temperature and pH values and show much higher Sr^{2+} adsorption efficiency than pure MnO_2 nanoparticles. In addition, IIGK@MnO_2 also exhibits good reusability, achieving a Sr^{2+} adsorption efficiency of over 60% after three cycles of adsorption–desorption processes. By analyzing the element distribution and valence states of IIGK@MnO_2-Sr after the adsorbing process, the mechanism of Sr^{2+} adsorption was proposed. The interaction between N-H groups on IIGK and oxygen atoms on MnO_2 with Sr^{2+} may play an important role in the adsorption of strontium ions. In conclusion, the designed IIGK@MnO_2 nanocomposite in this work exhibits excellent adsorption performance towards Sr^{2+} and will shed light on the construction of organic–inorganic hybrid adsorbents with multiple active adsorption sites and high adsorption efficiency for adsorbing radioactive ions in wastewater.

Supplementary Materials: The following supporting information can be downloaded at: https://www.mdpi.com/article/10.3390/nano14010052/s1, Figure S1. FTIR spectra of IIGK@MnO_2 and MnO_2.

Author Contributions: Conceptualization, M.C. and W.W.; software, X.L., Z.L., X.W. and H.M.; resources, M.C. and W.W.; writing—original draft preparation, X.L., Z.L., X.W. and H.M.; writing—review and editing, H.M. and M.C.; supervision, M.C.; project administration, M.C.; funding acquisition, W.W. and M.C. All authors have read and agreed to the published version of the manuscript.

Funding: This research was funded by the National Natural Science Foundation of China (22172194, 21972167, 21872173).

Data Availability Statement: All data generated or analyzed during this study are contained within the article and Supplementary Materials.

Conflicts of Interest: The authors declare no conflict of interest.

References

1. Davis, L.W. Prospects for nuclear power. *J. Econ. Perspect.* **2012**, *26*, 49–66. [CrossRef]
2. Park, Y.; Lee, Y.C.; Shin, W.S. Removal of cobalt, strontium and cesium from radioactive laundry wastewater by ammonium molybdophosphate–polyacrylonitrile (AMP-PAN). *Chem. Eng. J.* **2010**, *162*, 685–695. [CrossRef]
3. Chen, Y.; Wang, J. Removal of radionuclide Sr^{2+} ions from aqueous solution using synthesized magnetic chitosan beads. *Nucl. Eng. Des.* **2012**, *242*, 445–451. [CrossRef]
4. Chen, Q.; Yao, Y.; Li, X.; Lu, J.; Zhou, J.; Huang, Z. Comparison of heavy metal removals from aqueous solutions by chemical precipitation and characteristics of precipitates. *J. Water Process Eng.* **2018**, *26*, 289–300. [CrossRef]
5. Abdullah, N.; Yusof, N.; Lau, W.J.; Jaffar, J.; Ismail, A.F. Recent trends of heavy metal removal from water/wastewater by membrane technologies. *J. Ind. Eng. Chem.* **2019**, *76*, 17–38. [CrossRef]
6. Wang, J.; Zhuang, S. Extraction and adsorption of U (VI) from aqueous solution using affinity ligand-based technologies: An overview. *Rev. Environ. Sci. Biotechnol.* **2019**, *18*, 437–452. [CrossRef]
7. Rae, I.B.; Pap, S.; Svobodova, D.; Gibb, S.W. Comparison of sustainable biosorbents and ion-exchange resins to remove Sr^{2+} from simulant nuclear wastewater: Batch, dynamic and mechanism studies. *Sci. Total Environ.* **2019**, *650*, 2411–2422. [CrossRef]
8. Mironyuk, I.; Tatarchuk, T.; Vasylyeva, H.; Gun'ko, V.M.; Mykytyn, I. Effects of chemosorbed arsenate groups on the mesoporous titania morphology and enhanced adsorption properties towards Sr (II) cations. *J. Mol. Liq.* **2019**, *282*, 587–597. [CrossRef]
9. Ma, B.; Shin, W.S.; Oh, S.; Park, Y.J.; Choi, S.J. Adsorptive removal of Co and Sr ions from aqueous solution by synthetic hydroxyapatite nanoparticles. *Sep. Sci. Technol.* **2010**, *45*, 453–462. [CrossRef]

10. Zhang, Z.; Gu, P.; Zhang, M.; Yan, S.; Dong, L.; Zhang, G. Synthesis of a robust layered metal sulfide for rapid and effective removal of Sr^{2+} from aqueous solutions. *J. Chem. Eng.* **2019**, *372*, 1205–1215. [CrossRef]
11. Villard, A.; Siboulet, B.; Toquer, G.; Merceille, A.; Grandjean, A.; Dufrêche, J. Strontium selectivity in sodium nonatitanate $Na_4Ti_9O_{20}{\cdot}xH_2O$. *J. Hazard. Mater.* **2015**, *283*, 432–438. [CrossRef] [PubMed]
12. Qi, H.; Liu, H.; Gao, Y. Removal of Sr (II) from aqueous solutions using polyacrylamide modified graphene oxide composites. *J. Mol. Liq.* **2015**, *208*, 394–401. [CrossRef]
13. Asgari, P.; Mousavi, S.H.; Aghayan, H.; Ghasemi, H.; Yousefi, T. Nd-BTC metal-organic framework (MOF); synthesis, characterization and investigation on its adsorption behavior toward cesium and strontium ions. *Microchem. J.* **2019**, *150*, 104–188. [CrossRef]
14. Valsala, T.P.; Joseph, A.; Sonar, N.L.; Sonavane, M.; Shah, J.; Raj, K.; Venugopal, V. Separation of strontium from low level radioactive waste solutions using hydrous manganese dioxide composite materials. *J. Nucl. Mater.* **2010**, *404*, 138–143. [CrossRef]
15. Bondar, Y.V.; Alekseev, S.A. Synthesis and evaluation of manganese dioxide with layered structure as an adsorbent for selective removal of strontium ions from aqueous solution. *SN Appl. Sci.* **2020**, *2*, 1379. [CrossRef]
16. Fei, J.B.; Cui, Y.; Yan, X.H.; Qi, W.; Yang, Y.; Wang, K.W.; He, Q.; Li, J.B. Controlled preparation of MnO_2 hierarchical hollow nanostructures and their application in water treatment. *Adv. Mater.* **2008**, *20*, 452–456. [CrossRef]
17. Nair, B.; Pradeep, T. Coalescence of nanoclusters and formation of submicron crystallites assisted by Lactobacillus strains. *Cryst. Growth Des.* **2002**, *2*, 293–298. [CrossRef]
18. Xu, Y.; Yoo, I.K. Removal of lead from water solution by reusable magnetic adsorbent incorporating selective lead-binding peptide. *Appl. Sci.* **2020**, *10*, 6418.
19. Chen, C.L.; Rosi, N.L. Peptide-based methods for the preparation of nanostructured inorganic materials. *Angew. Chem. Int. Ed.* **2010**, *49*, 1924–1942. [CrossRef]
20. Mondal, B.; Bairagi, D.; Nandi, N. Peptide-based gel in environmental remediation: Removal of toxic organic dyes and hazardous Pb2+ and Cd2+ ions from wastewater and oil spill recovery. *Langmuir* **2020**, *36*, 12942–12953. [CrossRef]
21. Sweeney, R.Y.; Mao, C.B.; Gao, X.X.; Burt, J.L.; Belcher, A.M.; Georgiou, G.; Iverson, B.L. Bacterial biosynthesis of cadmium sulfide nanocrystals. *Chem. Biol.* **2004**, *11*, 1553–1559. [CrossRef] [PubMed]
22. Sewell, S.L.; Wright, D.W. Biomimetic synthesis of titanium dioxide utilizing the R5 peptide derived from Cylindrotheca fusiformis. *Chem. Mater.* **2006**, *18*, 3108–3113. [CrossRef]
23. Portehault, D.; Cassaignon, S.; Nassif, N.; Baudrin, E.; Jolivet, J.P. A core-corona hierarchical manganese oxide and its formation by an aqueous soft chemistry mechanism. *Angew. Chem. Int. Ed.* **2008**, *4*, 6441–6444. [CrossRef] [PubMed]
24. Asim, U.; Husnain, S.M.; Abbas, N.; Shahzad, F.; Khan, A.R.; Ali, T. Morphology controlled facile synthesis of MnO_2 adsorbents for rapid strontium removal. *J. Ind. Eng. Chem.* **2021**, *98*, 375–382. [CrossRef]
25. Ganesan, K.; Ghosh, S.; Krishna, N.G.; Ilango, S.; Kamruddin, M.; Tyagi, A.K. A comparative study on defect estimation using XPS and Raman spectroscopy in few layer nanographitic structures. *Phys. Chem. Chem. Phys.* **2016**, *18*, 22160–22167. [CrossRef] [PubMed]
26. Shaker, K.S.; AbdAlsalm, A.H. Synthesis and characterization nano structure of MnO_2 via chemical method. *Eng. Technol. J.* **2018**, *36*, 946–950. [CrossRef]
27. Ren, Y.; Yan, N.; Wen, Q.; Fan, Z.; Wei, T.; Zhang, M.; Ma, J. Graphene/δ-MnO_2 composite as adsorbent for the removal of nickel ions from wastewater. *Chem. Eng. J.* **2011**, *175*, 1–7. [CrossRef]
28. Sang, L.; Wang, T.K.; Chen, G.Y.; Liang, J.C.; Wei, Z.Y. A comparative study of the crystalline structure and mechanical properties of carbon fiber/polyamide 6 composites enhanced with/without silane treatment. *Rsc. Adv.* **2016**, *6*, 107739–107747. [CrossRef]
29. Nesbitt, H.; Banerjee, W.D. Interpretation of XPS Mn (2p) spectra of Mn oxyhydroxides and constraints on the mechanism of MnO_2 precipitation. *Am. Min.* **1998**, *83*, 305–315. [CrossRef]
30. Zhang, L.; Wei, J.; Zhao, X.; Li, F.; Jiang, F.; Zhang, M.; Cheng, X. Removal of strontium (II) and cobalt (II) from acidic solution by manganese antimonate. *Chem. Eng. J.* **2016**, *302*, 733–743. [CrossRef]
31. Karaseva, O.N.; Ivanova, L.I.; Lakshtanov, L.Z. Adsorption of strontium on manganese oxide (δ-MnO_2) at elevated temperatures: Experiment and modeling. *Geokhimiya. Int.* **2019**, *64*, 1091–1104. [CrossRef]
32. Lei, H.Y.; Muhammad, Y.; Wang, K.T.; Yi, M.; He, C.L.; Wei, Y.Z.; Fujita, T. Facile fabrication of metakaolin/slag-based zeolite microspheres (M/SZMs) geopolymer for the efficient remediation of Cs^+ and Sr^{2+} from aqueous media. *J. Hazard. Mater.* **2021**, *406*, 124292. [CrossRef] [PubMed]
33. Hua, M.; Zhang, S.J.; Pan, B.C.; Zhang, W.M.; Lv, L.; Zhang, Q.X. Heavy metal removal from water/wastewater by nanosized metal oxides: A review. *J. Hazard. Mater.* **2012**, *211*, 317–331. [CrossRef] [PubMed]
34. Fu, H.; Wang, Q. Removal of heavy metal ions from wastewaters: A review. *J. Environ. Manage.* **2011**, *92*, 407–418. [CrossRef] [PubMed]
35. Zhang, H.; Li, C.M.; Chen, X.J.; Fu, H.; Chen, Y.L.; Ning, S.Y.; Fujita, T.; Wei, Y.Z.; Wang, X.P. Layered ammonium vanadate nanobelt as efficient adsorbents for removal of Sr^{2+} and Cs^+ from contaminated water. *J. Colloid Interface Sci.* **2022**, *615*, 110–123. [CrossRef] [PubMed]
36. Lee, C.P.; Tsai, S.C.; Wu, M.C.; Tsai, T.L. A study on removal of Cs and Sr from aqueous solution by bentonite–alginate microcapsules. *J. Radioanal. Nucl. Chem.* **2018**, *318*, 2381–2387. [CrossRef]

37. Smiciklas, I.; Coha, I.; Jovic, M.; Nodilo, M.; Sljivic-Ivanovic, M.; Smiljanic, S.; Grahek, Z. Efficient separation of strontium radionuclides from high-salinity wastewater by zeolite 4A synthesized from Bayer process liquids. *Sci. Rep.* **2021**, *11*, 1738. [CrossRef]
38. Guo, Y.L.; Sun, H.Y.; Zeng, X.; Lv, T.T.; Yao, Y.X.; Zhuang, T.H.; Feng, M.L.; Huang, X.Y. Efficient removal of Sr^{2+} ions by a one-dimensional potassium phosphatoantimonate. *Chem. Eng. J.* **2023**, *460*, 141697. [CrossRef]
39. Zhang, N.; Liu, S.J.; Jiang, L.; Luo, M.B.; Chi, C.X.; Ma, J.G. Adsorption of strontium from aqueous solution by silica mesoporous SBA-15. *J. Radioanal. Nucl. Chem.* **2015**, *303*, 1671–1677. [CrossRef]
40. Li, Z.Q.; Vivas, E.L.; Suh, Y.J.; Cho, K. Highly efficient and selective removal of Sr^{2+} from aqueous solutions using ammoniated zirconium phosphate. *J. Environ. Chem. Eng.* **2022**, *10*, 107333. [CrossRef]
41. Li, G.D.; Ji, G.X.; Liu, W.; Zhang, J.R.; Song, L.P.; Cheng, L.W.; Wang, X.; Wang, Y.L.; Liu, J.J.; Chen, X.D.; et al. A hydrolytically stable anionic layered indium–organic framework for the efficient removal of ^{90}Sr from seawater. *Dalton Trans.* **2019**, *48*, 17858–17863. [CrossRef] [PubMed]

nanomaterials

MDPI

Article

Phase Separation Prevents the Synthesis of VBi_2Te_4 by Molecular Beam Epitaxy

Marieke Altena *, Thies Jansen *, Martina Tsvetanova and Alexander Brinkman

MESA+ Institute for Nanotechnology, University of Twente, 7500 AE Enschede, The Netherlands
* Correspondence: m.w.altena@utwente.nl (M.A.); t.jansen@utwente.nl (T.J.)

Abstract: Intrinsic magnetic topological insulators (IMTIs) have a non-trivial band topology in combination with magnetic order. This potentially leads to fascinating states of matter, such as quantum anomalous Hall (QAH) insulators and axion insulators. One of the theoretically predicted IMTIs is VBi_2Te_4, but experimental evidence of this material is lacking so far. Here, we report on our attempts to synthesise VBi_2Te_4 by molecular beam epitaxy (MBE). X-ray diffraction reveals that in the thermodynamic phase space reachable by MBE, there is no region where VBi_2Te_4 is stably synthesised. Moreover, scanning transmission electron microscopy shows a clear phase separation to Bi_2Te_3 and VTe_2 instead of the formation of VBi_2Te_4. We suggest the phase instability to be due to either the large lattice mismatch between VTe_2 and Bi_2Te_3 or the unfavourable valence state of vanadium.

Keywords: molecular beam epitaxy; VBi_2Te_4; magnetic topological insulator; phase separation; crystal growth

1. Introduction

Over the last decade, the introduction of magnetic order into 3D topological insulators (TIs) has attracted considerable interest. The bandstructure of a TI is characterised by a gapless Dirac cone at the surface, resulting in conducting surface states that are protected by time-reversal symmetry [1]. Magnetism breaks the time-reversal symmetry via exchange interaction and opens a gap in the conducting surface states [1–4]. This exchange gap can give rise to interesting phases such as the quantum anomalous Hall (QAH) state [2,5–11] and the axion insulating state [12–15].

To introduce magnetism into TIs, the following methods are currently used [16]: doping magnetic ions into the TI [6,7,11,17], bringing the TI in proximity with ferromagnetic materials [10,16,18–20] and incorporating intrinsic magnetic moments in the crystal structure, which results in an intrinsic magnetic topological insulator (IMTI) [8,9,14,21,22]. All three methods are successful in realising the QAH state; however, with the former two methods the temperatures at which this state arises is very low in the light of applications. It is interesting to compare the temperature at which the QAH effect is observed to the Curie temperature (T_C) of the materials. Remarkably, the temperatures for observing the QAH effect are an order of magnitude smaller than T_C [16]. The explanation for this difference in temperature depends on the method used to introduce the magnetism. In the magnetically doped system, the the high level of disorder caused by the random distribution of magnetic dopants may reduce the effective exchange gap [16], form a conducting bulk or create regions without ferromagnetic ordering [11]. In the magnetic proximity system, the sensitivity to the interface between the TI and the magnetic material is the main problem [14].

These challenges are overcome in IMTIs because in these materials the magnetic moment is intrinsically embedded in the unit cell. In 2019, Li et al. [9] theoretically predicted a class of materials acting as IMTIs, called the MBT family (M = transition-metal or rare-earth element, B = Bi or Sb and T = Te or Se). The materials in the MBT family

Citation: Altena, M.; Jansen, T.; Tsvetanova, M.; Brinkman, A. Phase Separation Prevents the Synthesis of VBi_2Te_4 by Molecular Beam Epitaxy. *Nanomaterials* **2024**, *14*, 87. https://doi.org/10.3390/nano14010087

Academic Editor: Meiwen Cao

Received: 24 November 2023
Revised: 17 December 2023
Accepted: 26 December 2023
Published: 28 December 2023

have the same crystal structure, but their behaviour differs depending on the magnetic element (transition-metal or rare-earth element, M) in the MBT structure. The unit cell of the MBT family can be viewed as the unit cell of the well studied family of Bi_2Te_3 TIs, with a structural intercalated layer containing a magnetic element. The addition of magnetism within the unit cell results in periodic magnetic layers, which results in a large magnetic exchange gap [9,21]. A representative material of the MBT family is $MnBi_2Te_4$, for which the crystal structure is shown in Figure 1a. Like other materials in the MBT family, it crystallises in the $\overline{R}3m$ space group with a rhombohedral structure. Each monolayer has a triangular lattice with ABC stacking along the out-of-plane direction. A monolayer is structured as a septuple layer (SL) with T-B-T-M-T-B-T stacking and a Van der Waals (VdW) gap separates consecutive SLs. The Mn atoms introduce a magnetic moment of 5 μB per atom with an out-of-plane easy axis [9]. The exchange coupling within a single SL ($J_{||}$) is ferromagnetic (FM), while the coupling between consecutive SLs ($J_{\perp}$) is antiferromagnetic (AFM) [9,23–25]. In these VdW materials, the $J_{||}$ is much stronger than $J_{\perp}$ [23,26].

Another potential member of the MBT family of IMTIs is the theoretically predicted VBi_2Te_4 [9]. In contrast to $MnBi_2Te_4$, VBi_2Te_4 has a predicted in-plane easy axis (Figure 1b), the V-atoms introduce a magnetic moment of 3 μB per atom [9,26] and a stronger $J_{\perp}$ is expected in VBi_2Te_4 leading to a higher T_C [26]. The latter could potentially result in a higher temperature at which topological phases such as QAH can be observed, opening up possibilities for applications. However, to the best of our knowledge, no experimental evidence of VBi_2Te_4 has been published so far.

In this work, we report on a structural MBE study to synthesise VBi_2Te_4. The crystal structure of the films was analysed by X-ray diffraction (XRD), scanning transmission electron microscopy (STEM) and energy dispersive diffraction (EDX), which are suitable techniques to detect the presence of the SL structure of VBi_2Te_4. The surface morphology of the films was characterised by reflective high energy electron diffraction (RHEED) and atomic force microscopy (AFM). The analysis of the crystal structure indicates a phase separation to Bi_2Te_3 and VTe_2 instead of the SL structure of VBi_2Te_4. This observation suggests VBi_2Te_4 to be unstable in the deposition conditions of MBE.

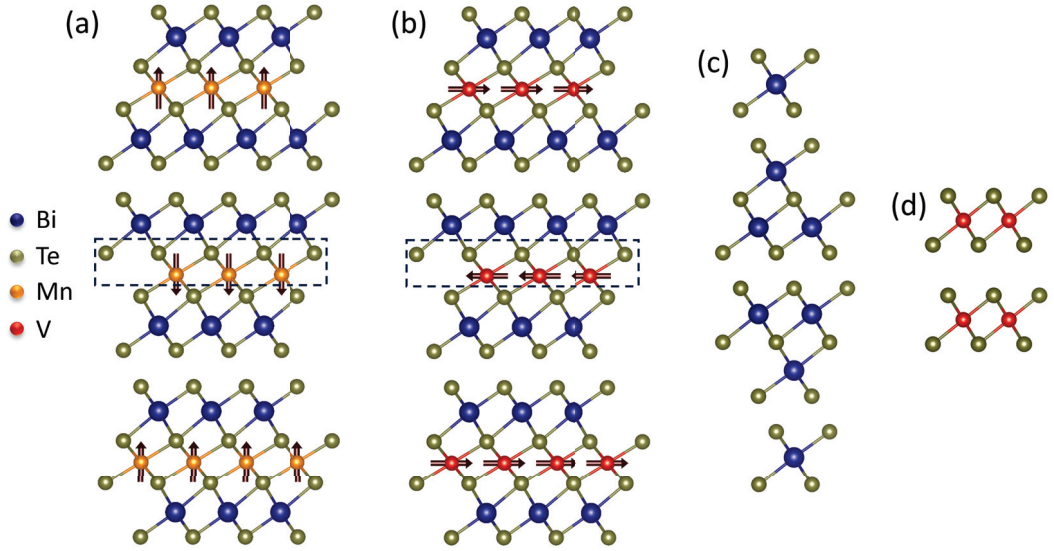

Figure 1. (**a**) $MnBi_2Te_4$ and (**b**) VBi_2Te_4 have a unit cell structured as SLs separated by a VdW gap. The dashed boxes indicate the relative intercalated layers of MnTe and VTe in Bi_2Te_3. $J_{||}$ is FM with either an (**a**) out-of-plane or (**b**) in-plane easy axis. $J_{\perp}$ is AFM. (**c**) Bi_2Te_3 structured in QLs separated by a VdW gap. (**d**) VTe_2.

2. Materials and Methods

The deposition of VBi_2Te_4 is performed on (0001)-Al_2O_3 substrates in an ultrahigh vacuum Octoplus 300 MBE system from Dr. Eberl MBE Komponenten with a base pressure

of 5.0×10^{-11} mbar. High-purity (6N) bismuth (Bi) and tellurium (Te) are evaporated from standard Knudsen effusion cells and their fluxes are calibrated by a quartz crystal monitor. The Bi- and Te-flux are kept constant during the depositions at $\phi_{Bi} = 0.0027$ Å/s and $\phi_{Te} = 0.072$ Å/s. ϕ_{Te} is set to a high flux to prevent Te vacancies. High-purity (5N) vanadium (V) is evaporated from a custom high-temperature Knudsen effusion cell. The flux, ϕ_V, is indicated by the heating temperature of the Knudsen cell and is varied from 1750 °C to 1900 °C. The combination of the V-pocket size and the high evaporation temperature result in a large flux instability measured with the quartz crystal monitor, and therefore the pocket temperature will be kept as a reference for ϕ_V. An estimate for the flux variation in this temperature range is from 0.001 Å/s to 0.0080 Å/s. The substrate temperature T_{sub} was kept constant at 150 °C. Before the deposition of VBi_2Te_4, a buffer layer of Bi_2Te_3 was deposited of ≈1 nm. The samples discussed in this article are deposited using the co-evaporation method, meaning all elemental beams are opened simultaneously during the full deposition. In addition to these results, some attempts were made to use a beam-shuttering method to interrupt the V- and Bi-beams during the deposition. First, Bi and Te are opened to deposit a monolayer of Bi_2Te_3. Second, V and Te are opened to deposit a monolayer of VTe on top of the Bi_2Te_3 layer. Third, an annealing step is applied during which the VTe layer should diffuse into Bi_2Te_3 to form the SL of VBi_2Te_4. These three steps were repeated to form a multilayered VBi_2Te_4 film. This method was previously used to successfully deposit $MnBi_2Te_4$ by MBE [27], but for VBi_2Te_4 the beam-shuttered method resulted in the same observations discussed here for the co-evaporation method showing a phase separation to VTe_2 and Bi_2Te_3. Right after deposition, a RHEED image of the diffraction pattern is taken. From the RHEED image the in-plane lattice constant can be deduced by comparing the diffraction pattern of the film to a known substrate.

The crystal structure of the films is measured with XRD, STEM and EDX. The XRD measurements are performed with a Bruker D8 Discover system (Bruker, Billerica, MA, USA) with a two-dimensional Eiger2 500K detector and a two-bounce channel-cut germanium monochromator. Symmetric 2θ-ω scans were performed along the surface normal direction. The STEM measurements are made with a Thermo Scientific Spectra 300 STEM (Thermo Fisher Scientific, Waltham, MA, USA) with an electron beam voltage of 300 kV and a high-angle annular dark-field (HAADF) detector.

3. Results

The crystal structure of the films is analysed with STEM, EDX and XRD. STEM is performed on a sample deposited with ϕ_V = 1800 °C (Figure 2a). The image shows the V-Bi-Te film and the Al_2O_3 substrate. These STEM results clearly indicate two regions by looking at the contrast. These variations are caused by the Z-contrast related to the atomic weight of the present elements. For a V-Bi-Te sample, the atomic weights are arranged as $m_{Bi} > m_{Te} > m_V$. Therefore, the bright areas in Figure 2a are Bi-rich regions. These results clearly indicate a phase separation between a Bi-compound and a non-Bi compound. EDX (Figure 2b) shows a clear separation between a Bi/Te region and a V/Te region. Figure 2c shows a detailed STEM scan of the sample. The atoms in the bright areas are structured as a QL separated by a VdW-gap. This structure is consistent with Bi_2Te_3 (Figure 1c). In the darker area the bright atoms form the typical Te octahedra of VTe_2 which are separated by a VdW gap as shown in Figure 1d. The in-plane lattice constant a is related to the distance between the atoms in the x-direction, dx. Figure 2d shows the distribution of dx as extracted from Figure 2c. This distribution indicates two clearly separated regions. The in-plane lattice constants related to these two regions are calculated from the dx value with maximum intensity as $a = 2dx$ for both Bi_2Te_3 and VTe_2. This calculation results in the lattice constants a_1 = 3.82 Å, corresponding to VTe_2, and a_2 = 4.65 Å, corresponding to Bi_2Te_3.

Figure 2e presents the 2θ-ω scans of films deposited with different ϕ_V. The peaks in the 2θ-ω scans can be identified as the (00l)-Bi_2Te_3 and (00l)-VTe_2 peaks. The dotted arrow at the (006)-Bi_2Te_3 peak indicates the dominance of Bi_2Te_3 at low ϕ_V, but the intensity of

this phase decreases as ϕ_V increases. The dashed arrow at the (001)-VTe_2 peak indicates the dominance of VTe_2 at high ϕ_V, but this phase disappears as ϕ_V decreases. VBi_2Te_4 is absent in all 2θ-ω scans.

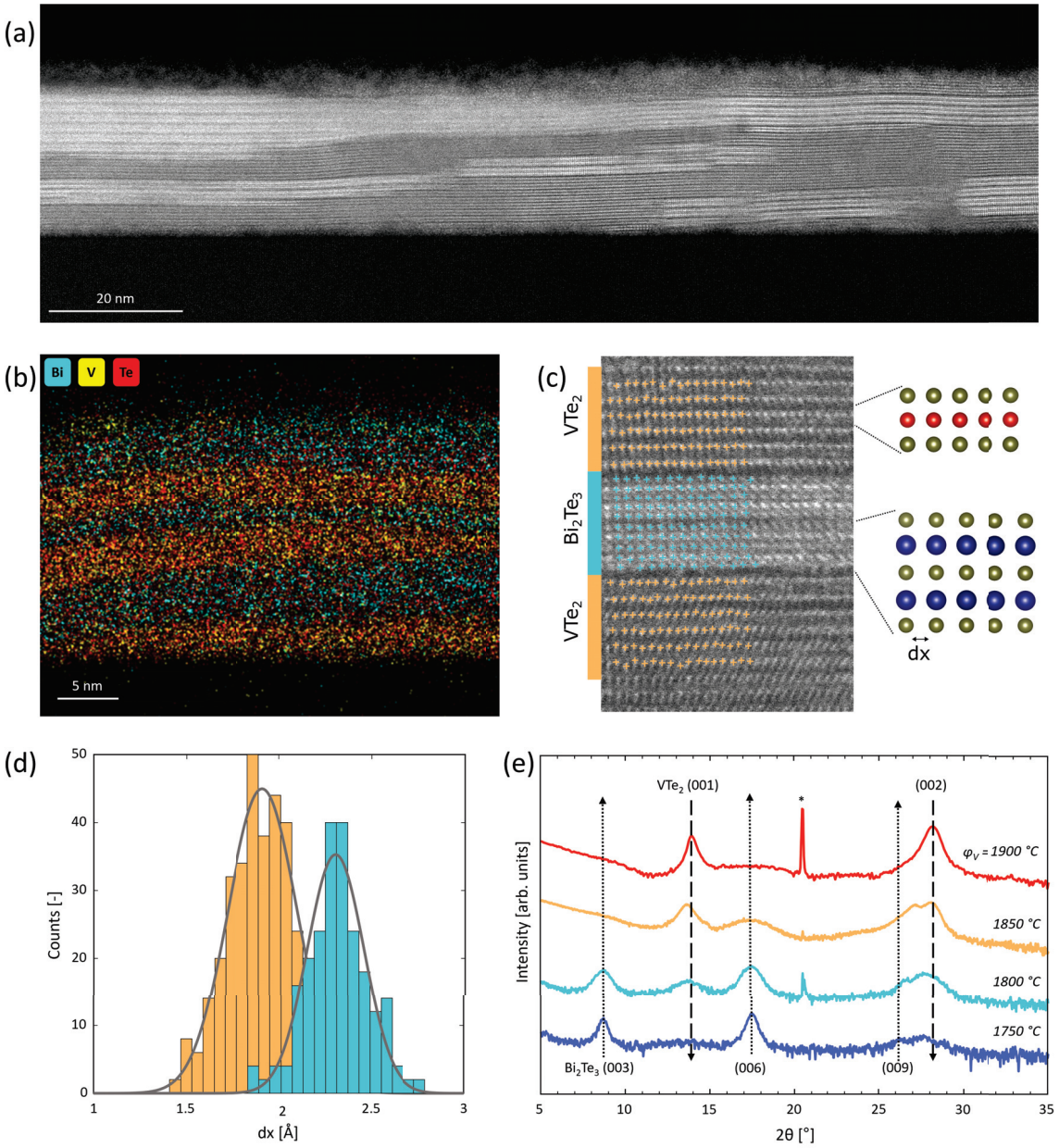

Figure 2. (**a**) STEM image of a V-Bi-Te sample. The image is taken with a HAADF detector at 300 keV. A clear phase separation between bright and dark areas can be observed. (**b**) EDX scan of the V-Bi-Te sample. A strong separation between V-regions and Bi-regions can be observed. (**c**) STEM image of a smaller region on a V-Bi-Te sample. The bright areas (blue) show the QL structure of Bi_2Te_3 and the dark areas (orange) the VTe_2 structure. (**d**) Histogram of the atomic distance in the x-direction. (**e**) 2θ-ω scans indicating (00l)-Bi_2Te_3 being dominant at low ϕ_V, while (00l)-VTe_2 is dominant at high ϕ_V. The arrows indicate the disappearance of the respective phases as a function of ϕ_V. * indicates the Al_2O_3 substrate peak.

The surface of the films is analysed with RHEED and AFM. Figure 3a presents the in situ RHEED pattern of a film deposited with ϕ_V = 1750 °C. The RHEED pattern consists of a double streak pattern as indicated by the blue and white arrows. This doubled pattern indicates the presence of two separate crystal phases at the surface. The in-plane lattice

constants related to these streaks are a_1 = 4.31 Å (white arrows) and a_2 = 3.59 Å (blue arrows). These values correspond well with the lattice constants of Bi_2Te_3 and VTe_2, respectively.

The surface morphology is measured by AFM. Figure 3b shows the height distribution as measured with AFM for films deposited with different ϕ_V. The insets show the surface morphology of the films with ϕ_V = 1750 °C and ϕ_V = 1900 °C. At low ϕ_V, the morphology shows strong island formation and the triangular crystals typically observed for Bi_2Te_3. The results at high ϕ_V show a relative flat film without any sharp crystals. The height distributions indicate a strong influence of the ϕ_V on the distribution spread. With an increasing ϕ_V, the height variation becomes smaller, indicating a flatter surface.

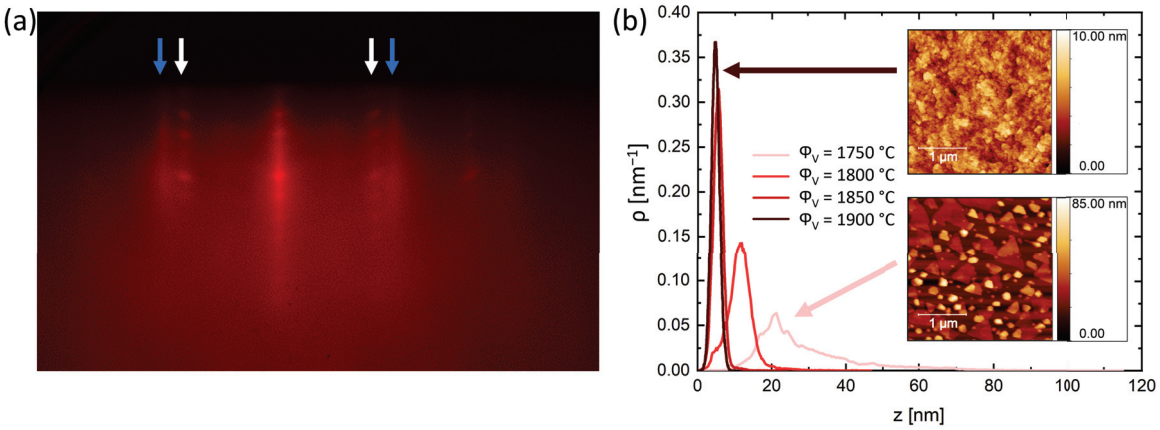

Figure 3. (**a**) RHEED pattern for ϕ_V = 1750 °C showing a double streak pattern related to the phases Bi_2Te_3 with a_1 = 4.31 Å and VTe_2 with a_2 = 3.59 Å, indicated by the blue and white arrows, respectively. (**b**) Height distribution at the surface as a function of the ϕ_V. The insets show the surface morphology of the samples with ϕ_V = 1750 °C and ϕ_V = 1900 °C.

4. Discussion

VBi_2Te_4 is a SL structure requiring the embedding of VTe within the QL structure of Bi_2Te_3. According to our results, the formation of VBi_2Te_4 is unstable with respect to phase separated Bi_2Te_3 and VTe_2 within the thermodynamic conditions of the MBE. The instability of VBi_2Te_4 can have various causes.

First, a large in-plane lattice mismatch, Δ_a, between VTe_2 and Bi_2Te_3 might prohibit the formation of VBi_2Te_4 [28]. Our STEM results indicate Δ_a = 0.83 Å between the two phases. The theoretically predicted lattice constant of VBi_2Te_4, a = 4.37 Å, is close to the lattice constant of Bi_2Te_3, a = 4.65 Å. Therefore, the VTe_2 lattice has to overcome Δ_a to form VBi_2Te_4. Table 1 gives an overview of different materials structured as a SL with the relevant lattice constants and whether the material was successfully observed in experiments. The intercalated layer is presented as XTe or XTe_2, depending on the experimental stability of the phases. The experimentally successful materials match $\Delta_a < 0.6$ Å, while the experimentally unsuccessful materials match $\Delta_a > 0.5$ Å. This difference can indicate a limit to the maximum allowed Δ_a of 0.5 Å to 0.6 Å between the SL material and the intercalated layer, possibly explaining the phase separation in VBi_2Te_4. However, this observation does not match with the stability of $PbBi_2Te_4$ and $SnBi_2Te_4$ [29]. Therefore, the lattice mismatch between the intercalated layer and Bi_2Te_3 does not completely explain the instability of the SL structure in general, and another factor should be considered.

Second, the elemental valence states in the intercalated layer might prohibit the formation of the SL. In the SL, the preferred valence states are $M^{(+2)}Bi_2{}^{(+3)}Te_4{}^{(-2)}$ (M = transition metal or rare-earth element), which matches well with the valence states of an intercalated layer structure of $M^{(+2)}Te^{(-2)}$ [30]. However, when the stable compound of the intercalated layer is structured as $M^{(+4)}Te_2{}^{(-2)}$ the valence states of the intercalated layer and the SL do not match. A mismatch between the preferred valence state of the intercalated layer and the SL indicates the instability of the SL. Table 1 reflects this instability, showing that every

experimentally observed intercalated layer bulk compound with a valence structure of $M^{(+2)}Te^{(-2)}$ also has a stable SL counterpart, but a valence structure of $M^{(+4)}Te_2{}^{(-2)}$ does not. This is in agreement with our study on VBi_2Te_4, because VTe_2 is thermodynamically more stable than VTe [31].

Furthermore, ref. [32] studied the preferred valence states of V, Cr, Mn and Fe in Bi_2Te_3. In Te-rich conditions, only V^{3+} and Cr^{3+} can substitute neutrally for Bi^{+3} atoms in Bi_2Te_3. In contrast, Mn and Fe mostly form Mn^{2+} and Fe^{2+}, which create energetically unfavourable states when mixed with Bi^{3+} [9,32]. This additionally shows the unfavourable V^{2+} valence state. Therefore, Mn and Fe can more easily form a neutral SL structure with respect to V and Cr.

Table 1. Overview of materials with a unit cell structured as a SL. The table presents whether the material is successfully synthesised experimentally, the lattice constants found in the literature for these materials (either experimental or theoretical values), the intercalated layer with the corresponding lattice constant and the lattice mismatch between the SL and the intercalated layer. The intercalated layer is presented as XTe or XTe_2, depending on the experimental stability of the phases.

Material	Experimentally Observed?	a_{SL} [Å]	Intercalated Layer	$a_{int.}$ [Å]	Lattice Structure	Δ_a [Å]
VBi_2Te_4	No	4.34–4.37 [9,26,33–35]	VTe_2	3.59	Hexagonal, $P\bar{3}m1$	0.75–0.78
$MnBi_2Te_4$	Yes [8,21–23,27,36]	4.33 [36]	MnTe	4.13 [37]	Hexagonal, $P6_3/mmc$	0.20
$FeBi_2Te_4$	Yes [38]	4.39 [9,38]	FeTe	3.83 [38,39]	Tetragonal, P4/nmm	0.56
			$FeTe_2$	3.77 [40]	Hexagonal, $P\bar{3}m1$	0.63
$EuBi_2Te_4$	No	4.50 [9,33]	EuTe	6.60 [41,42]	Cubic, $Fm\bar{3}m$	2.10
			$EuTe_2$	6.97 [43]	Tetragonal, I4/mcm	2.47
$NiBi_2Te_4$	Yes *	4.30 [9,33]	$NiTe_2$	3.86 [44]	Hexagonal, $P\bar{3}m1$	0.44
$CrBi_2Te_4$	No	4.32 [45]	$CrTe_2$	3.79 [46]	Hexagonal, $P\bar{3}m1$	0.53
$TiBi_2Te_4$	No	4.39 [9]	$TiTe_2$	3.78 [47]	Hexagonal, $P\bar{3}m1$	0.61
$PbBi_2Te_4$	Yes [48,49]	4.44 [49]	PbTe	6.46 [50]	Cubic, $Fm\bar{3}m$	2.02
$SnBi_2Te_4$	Yes [51–53]	4.40 [51,53]	SnTe	6.32 [50]	Cubic, $Fm\bar{3}m$	1.92
$GeBi_2Te_4$	Yes [54,55]	4.33 [54,55]	GeTe	4.16 [50,56]	Rhombohedral, $R\bar{3}m$	0.17

* Not observed as multilayered/bulk material. Ref. [57] observed the SL structure as an intercalated layer between Bi_2Te_3 and Ni-doped Bi_2Te_3.

In conclusion, the influence of the ϕ_V during MBE depositions was investigated on the synthesis of the VBi_2Te_4 phase. The resulting films do not show any indication of VBi_2Te_4 but rather a phase separation into Bi_2Te_3 and VTe_2. These results show VBi_2Te_4 is unstable within the deposition conditions of MBE.

Author Contributions: Conceptualization, T.J. and A.B.; methodology, M.A. and T.J.; validation, M.A. and T.J.; formal analysis, M.A., T.J. and M.T.; investigation, M.A. and T.J.; resources, M.T. and A.B.; data curation, M.A., T.J. and A.B.; writing—original draft preparation, M.A.; writing—review and editing, M.A., T.J., M.T. and A.B.; visualization, M.A. and T.J.; supervision, A.B.; project administration, M.A. and T.J.; funding acquisition, A.B. All authors have read and agreed to the published version of the manuscript.

Funding: This research was funded by the research program "Materials for the Quantum Age" (QuMat) and the Dutch Research Council (NWO). QuMat (registration number 024.005.006) is part of the Gravitation program financed by the Dutch Ministry of Education, Culture and Science (OCW). The NWO supports this research via the TOPCORE project (registration number OCENW.GROOT.2019.048).

Data Availability Statement: The data presented in this study are openly available in 4TU.ResearchData at 10.4121/95ee6f7b-3cf7-4c01-a461-860e6f9485bf.

Acknowledgments: We would like to acknowledge Daan Wielens and Frank Roesthuis for technical support and Anna Isaeva for sharing her expertise on the synthesis of septuple-layered materials.

Conflicts of Interest: The authors declare no conflicts of interest.

References

1. Hasan, M.Z.; Kane, C.L. Colloquium: Topological insulators. *Rev. Mod. Phys.* **2010**, *82*, 3045–3067. [CrossRef]
2. Yu, R.; Zhang, W.; Zhang, H.J.; Zhang, S.C.; Dai, X.; Fang, Z. Quantized anomalous Hall effect in magnetic topological insulators. *Science* **2010**, *329*, 61–64. [CrossRef]
3. Liu, C.X.; Qi, X.L.; Dai, X.; Fang, Z.; Zhang, S.C. Quantum anomalous Hall effect in $Hg_{1-y}Mn_yTe$ quantum wells. *Phys. Rev. Lett.* **2008**, *101*, 146802. [CrossRef] [PubMed]
4. Liu, Q.; Liu, C.X.; Xu, C.; Qi, X.L.; Zhang, S.C. Magnetic impurities on the surface of a topological insulator. *Phys. Rev. Lett.* **2009**, *102*, 156603. [CrossRef] [PubMed]
5. Haldane, F.D.M. Model for a quantum Hall effect without Landau levels: Condensed-matter realization of the "parity anomaly". *Phys. Rev. Lett.* **1988**, *61*, 2015–2018. [CrossRef] [PubMed]
6. Chang, C.Z.; Zhang, J.; Feng, X.; Shen, J.; Zhang, Z.; Guo, M.; Ou, Y.; Wei, P.; Jun, L.; Ji, Z.; et al. Experimental observation of the quantum anomalous Hall effect in a magnetic topological insulator. *Science* **2013**, *340*, 167–170. [CrossRef] [PubMed]
7. Chang, C.Z.; Zhao, W.; Kim, D.Y.; Zhang, H.; Assaf, B.A.; Heiman, D.; Zhang, S.C.; Liu, C.; Chan, M.H.W.; Moodera, J.S. High-precision realization of robust quantum anomalous Hall state in a hard ferromagnetic topological insulator. *Nat. Mater.* **2015**, *14*, 473–477. [CrossRef] [PubMed]
8. Deng, Y.; Yu, Y.; Shi, M.Z.; Guo, Z.; Xu, Z.; Wang, J.; Chen, X.H.; Zhang, Y. Quantum anomalous Hall effect in intrinsic magnetic topological insulator $MnBi_2Te_4$. *Science* **2020**, *367*, 895–900. [CrossRef]
9. Li, J.; Li, Y.; Du, S.; Wang, Z.; Gu, B.L.; Zhang, S.C.; He, K.; Duan, W.; Xu, Y. Intrinsic magnetic topological insulators in van der Waals layered $MnBi_2Te_4$-family materials. *Sci. Adv.* **2019**, *5*, eaaw5685. [CrossRef]
10. Watanabe, R.; Yoshimi, R.; Kawamura, M.; Mogi, M.; Tsukazaki, A.; Yu, X.Z.; Nakajima, K.; Takahashi, K.S.; Kawasaki, M.; Tokura, Y. Quantum anomalous Hall effect driven by magnetic proximity coupling in all-telluride based heterostructure. *Appl. Phys. Lett.* **2019**, *115*, 102403. [CrossRef]
11. Ou, Y.; Liu, C.; Jiang, G.; Feng, Y.; Zhao, D.; Wu, W.; Wang, X.X.; Li, W.; Song, C.; Wang, L.L.; et al. Enhancing the quantum anomalous Hall effect by magnetic codoping in a topological insulator. *Adv. Mater.* **2018**, *30*, 1703062. [CrossRef]
12. Qi, X.L.; Hughes, T.L.; Zhang, S.C. Topological field theory of time-reversal invariant insulators. *Phys. Rev. B* **2008**, *78*, 195424. [CrossRef]
13. Li, R.; Wang, J.; Qi, X.L.; Zhang, S.C. Dynamical axion field in topological magnetic insulators. *Nat. Phys.* **2010**, *6*, 284–288. [CrossRef]
14. Wang, P.; Ge, J.; Li, J.; Liu, Y.; Xu, Y.; Wang, J. Intrinsic magnetic topological insulators. *Innovation* **2021**, *2*, 100098. [CrossRef] [PubMed]
15. Mogi, M.; Kawamura, M.; Yoshimi, R.; Tsukazaki, A.; Kozuka, Y.; Shirakawa, N.; Takahashi, K.S.; Kawasaki, M.; Tokura, Y. A magnetic heterostructure of topological insulators as a candidate for an axion insulator. *Nat. Mater.* **2017**, *16*, 516–521. [CrossRef] [PubMed]
16. Grutter, A.J.; He, Q.L. Magnetic proximity effects in topological insulator heterostructures: Implementation and characterization. *Phys. Rev. Mater.* **2021**, *5*, 090301. [CrossRef]
17. Hor, Y.S.; Roushan, P.; Beidenkopf, H.; Seo, J.; Qu, D.; Checkelsky, J.G.; Wray, L.A.; Hsieh, D.; Xia, Y.; Xu, S.Y.; et al. Development of ferromagnetism in the doped topological insulator $Bi_{2-x}Mn_xTe_3$. *Phys. Rev. B* **2010**, *81*, 195203. [CrossRef]
18. Katmis, F.; Lauter, V.; Nogueira, F.S.; Assaf, B.A.; Jamer, M.E.; Wei, P.; Satpati, B.; Freeland, J.W.; Eremin, I.; Heiman, D.; et al. A high-temperature ferromagnetic topological insulating phase by proximity coupling. *Nature* **2016**, *533*, 513–516. [CrossRef] [PubMed]
19. Tang, C.; Chang, C.Z.; Zhao, G.; Liu, Y.; Jiang, Z.; Liu, C.X.; McCartney, M.R.; Smith, D.J.; Chen, T.; Moodera, J.S.; et al. Above 400-K robust perpendicular ferromagnetic phase in a topological insulator. *Sci. Adv.* **2017**, *3*, e1700307. [CrossRef]
20. He, Q.L.; Yin, G.; Yu, L.; Grutter, A.J.; Pan, L.; Chen, C.Z.; Che, X.; Yu, G.; Zhang, B.; Shao, Q.; et al. Topological transitions induced by antiferromagnetism in a thin-film topological insulator. *Phys. Rev. Lett.* **2018**, *121*, 096802. [CrossRef]
21. Rienks, E.D.L.; Wimmer, S.; Sánchez-Barriga, J.; Caha, O.; Mandal, P.S.; Růžička, J.; Ney, A.; Steiner, H.; Volobuev, V.V.; Groiss, H.; et al. Large magnetic gap at the Dirac point in $Bi_2Te_3/MnBi_2Te_4$ heterostructures. *Nature* **2019**, *576*, 423–428. [CrossRef] [PubMed]
22. Liu, C.; Wang, Y.; Li, H.; Wu, Y.; Li, Y.; Li, J.; He, K.; Xu, Y.; Zhang, J.; Wang, Y. Robust axion insulator and Chern insulator phases in a two-dimensional antiferromagnetic topological insulator. *Nat. Mater.* **2020**, *19*, 522–527. [CrossRef] [PubMed]
23. Otrokov, M.M.; Klimovskikh, I.I.; Bentmann, H.; Estyunin, D.; Zeugner, A.; Aliev, Z.S.; Gaß, S.; Wolter, A.U.B.; Koroleva, A.V.; Shikin, A.M.; et al. Prediction and observation of an antiferromagnetic topological insulator. *Nature* **2019**, *576*, 416–422. [CrossRef]

24. Otrokov, M.M.; Rusinov, I.P.; Blanco-Rey, M.; Hoffmann, M.; Vyazovskaya, A.Y.; Eremeev, S.V.; Ernst, A.; Echenique, P.M.; Arnau, A.; Chulkov, E.V. Unique thickness-dependent properties of the van der Waals interlayer antiferromagnet $MnBi_2Te_4$ films. *Phys. Rev. Lett.* **2019**, *122*, 107202. [CrossRef] [PubMed]
25. Zhang, D.; Shi, M.; Zhu, T.; Xing, D.; Zhang, H.; Wang, J. Topological axion states in the magnetic insulator $MnBi_2Te_4$ with the quantized magnetoelectric effect. *Phys. Rev. Lett.* **2019**, *122*, 206401. [CrossRef]
26. Petrov, E.K.; Men'shov, V.N.; Rusinov, I.P.; Hoffmann, M.; Ernst, A.; Otrokov, M.M.; Dugaev, V.K.; Menshchikova, T.V.; Chulkov, E.V. Domain wall induced spin-polarized flat bands in antiferromagnetic topological insulators. *Phys. Rev. B* **2021**, *103*, 235142. [CrossRef]
27. Gong, Y.; Guo, J.; Li, J.; Zhu, K.; Liao, M.; Liu, X.; Zhang, Q.; Gu, L.; Tang, L.; Feng, X.; et al. Experimental realization of an intrinsic magnetic topological insulator. *Chin. Phys. Lett.* **2019**, *36*, 076801. [CrossRef]
28. Jiao, F.; Wang, J.; Wang, X.; Tian, Q.; Chang, M.; Cai, L.; Zhu, S.; Zhang, D.; Lu, Q.; Wang, C.; et al. The Layer-Inserting Growth of Antiferromagnetic Topological Insulator $MnBi_2Te_4$ Based on Symmetry and Its X-ray Photoelectron Spectroscopy. *J. Supercond. Nov. Magn.* **2021**, *34*, 1485–1493. [CrossRef]
29. Sans, J.A.; Vilaplana, R.; da Silva, E.L.; Popescu, C.; Cuenca-Gotor, V.P.; Andrada-Chacón, A.; Sánchez-Benitez, J.; Gomis, O.; Pereira, A.L.J.; Rodríguez-Hernández, P.; et al. Characterization and Decomposition of the Natural van der Waals $SnSb_2Te_4$ under Compression. *Inorg. Chem.* **2020**, *59*, 9900–9918. [CrossRef]
30. Zeugner, A.; Nietschke, F.; Wolter, A.U.B.; Gaß, S.; Vidal, R.C.; Peixoto, T.R.F.; Pohl, D.; Damm, C.; Lubk, A.; Hentrich, R.; et al. Chemical Aspects of the Candidate Antiferromagnetic Topological Insulator $MnBi_2Te_4$. *Chem. Mater.* **2019**, *31*, 2795–2806. [CrossRef]
31. Parker, D.S.; Yin, L.; Samolyuk, G.D.; Sanjeewa, L.D.; Wang, X.; Cooper, V.R.; Liu, Y.; Bud'ko, S.; Sefat, A.S. Insulating antiferromagnetism in VTe. *Phys. Rev. B* **2022**, *105*, 174414. [CrossRef]
32. Zhang, J.M.; Ming, W.; Huang, Z.; Liu, G.B.; Kou, X.; Fan, Y.; Wang, K.L.; Yao, Y. Stability, electronic, and magnetic properties of the magnetically doped topological insulators Bi_2Se_3, Bi_2Te_3, and Sb_2Te_3. *Phys. Rev. B* **2013**, *88*, 235131. [CrossRef]
33. Li, Z.; Li, J.; He, K.; Wan, X.; Duan, W.; Xu, Y. Tunable interlayer magnetism and band topology in van der Waals heterostructures of $MnBi_2Te_4$-family materials. *Phys. Rev. B* **2020**, *102*, 081107. [CrossRef]
34. Zhang, Y.; Wang, Y.; Yang, W.; Zhang, H.; Jia, J. Strain-tunable magnetism and topological states in layered VBi_2Te_4. *Phys. Chem. Chem. Phys.* **2023**, *25*, 28189–28195. [CrossRef] [PubMed]
35. Zhu, W.; Song, C.; Liao, L.; Zhou, Z.; Bai, H.; Zhou, Y.; Pan, F. Quantum anomalous Hall insulator state in ferromagnetically ordered $MnBi_2Te_4/VBi_2Te_4$ heterostructures. *Phys. Rev. B* **2020**, *102*, 085111. [CrossRef]
36. Lee, D.S.; Kim, T.H.; Park, C.H.; Chung, C.Y.; Lim, Y.S.; Seo, W.S.; Park, H.H. Crystal structure, properties and nanostructuring of a new layered chalcogenide semiconductor, Bi_2MnTe_4. *CrystEngComm* **2013**, *15*, 5532–5538. [CrossRef]
37. Kriegner, D.; Reichlova, H.; Grenzer, J.; Schmidt, W.; Ressouche, E.; Godinho, J.; Wagner, T.; Martin, S.Y.; Shick, A.B.; Volobuev, V.V.; et al. Magnetic anisotropy in antiferromagnetic hexagonal MnTe. *Phys. Rev. B* **2017**, *96*, 214418. [CrossRef]
38. Saxena, A.; Rani, P.; Nagpal, V.; Patnaik, S.; Felner, I.; Awana, V.P.S. Crystal growth and characterization of possible new magnetic topological insulators $FeBi_2Te_4$. *J. Supercond. Nov. Magn.* **2020**, *33*, 2251–2256. [CrossRef]
39. Oyler, K.D.; Ke, X.; Sines, I.T.; Schiffer, P.; Schaak, R.E. Chemical Synthesis of Two-Dimensional Iron Chalcogenide Nanosheets: FeSe, FeTe, Fe(Se,Te), and FeTe2. *Chem. Mater.* **2009**, *21*, 3655–3661. [CrossRef]
40. Wu, H.; Feng, Z.; Pal, A.; Dong, H.; Jing, C.; Wang, K.; Zhang, S.; Deng, W.; Li, S.; Feng, J.; et al. Evolution of Temperature-Induced Isostructural Phase Transition in a Newly Grown Layered $FeTe_2$ Single Crystal. *Chem. Mater.* **2021**, *33*, 4927–4935. [CrossRef]
41. Radomska, A.; Balcerzak, T. Calculations of EuTe magnetic phase diagram for external pressure. *Acta Phys. Pol. A* **2000**, *98*, 83–91. [CrossRef]
42. Fornari, C.I.; Bentmann, H.; Morelhão, S.L.; Peixoto, T.R.F.; Rappl, P.H.O.; Tcakaev, A.V.; Zabolotnyy, V.; Kamp, M.; Lee, T.L.; Min, C.H.; et al. Incorporation of Europium in Bi_2Te_3 topological insulator epitaxial films. *J. Phys. Chem. C* **2020**, *124*, 16048–16057. [CrossRef]
43. Yin, J.; Wu, C.; Li, L.; Yu, J.; Sun, H.; Shen, B.; Frandsen, B.A.; Yao, D.X.; Wang, M. Large negative magnetoresistance in the antiferromagnetic rare-earth dichalcogenide $EuTe_2$. *Phys. Rev. Mater.* **2020**, *4*, 013405. [CrossRef]
44. Xu, C.; Li, B.; Jiao, W.; Zhou, W.; Qian, B.; Sankar, R.; Zhigadlo, N.D.; Qi, Y.; Qian, D.; Chou, F.C.; et al. Topological type-II Dirac fermions approaching the Fermi level in a transition metal dichalcogenide $NiTe_2$. *Chem. Mater.* **2018**, *30*, 4823–4830. [CrossRef]
45. Petrov, E.K.; Ernst, A.; Menshchikova, T.V.; Chulkov, E.V. Intrinsic magnetic topological insulator state induced by the Jahn–Teller effect. *J. Phys. Chem. Lett.* **2021**, *12*, 9076–9085. [CrossRef] [PubMed]
46. Freitas, D.C.; Weht, R.; Sulpice, A.; Remenyi, G.; Strobel, P.; Gay, F.; Marcus, J.; Núñez-Regueiro, M. Ferromagnetism in layered metastable 1T-$CrTe_2$. *J. Phys. Condens. Matter* **2015**, *27*, 176002. [CrossRef] [PubMed]
47. Chen, P.; Pai, W.W.; Chan, Y.H.; Takayama, A.; Xu, C.Z.; Karn, A.; Hasegawa, S.; Chou, M.Y.; Mo, S.K.; Fedorov, A.V.; et al. Emergence of charge density waves and a pseudogap in single-layer $TiTe_2$. *Nat. Commun.* **2017**, *8*, 516. [CrossRef]
48. Kuroda, K.; Miyahara, H.; Ye, M.; Eremeev, S.V.; Koroteev, Y.M.; Krasovskii, E.E.; Chulkov, E.V.; Hiramoto, S.; Moriyoshi, C.; Kuroiwa, Y.; et al. Experimental verification of $PbBi_2Te_4$ as a 3D topological insulator. *Phys. Rev. Lett.* **2012**, *108*, 206803. [CrossRef]
49. Xu, X.; Ni, D.; Xie, W.; Cava, R.J. Superconductivity in electron-doped $PbBi_2Te_4$. *Phys. Rev. B* **2023**, *108*, 054525. [CrossRef]

50. Bauer Pereira, P.; Sergueev, I.; Gorsse, S.; Dadda, J.; Müller, E.; Hermann, R.P. Lattice dynamics and structure of GeTe, SnTe and PbTe. *Phys. Status Solidi (B)* **2013**, *250*, 1300–1307. [CrossRef]
51. Saxena, A.; Karn, N.K.; Sharma, M.M.; Awana, V.P.S. Detailed structural and topological analysis of $SnBi_2Te_4$ single crystal. *J. Phys. Chem. Solids* **2023**, *174*, 111169. [CrossRef]
52. Zou, Y.C.; Chen, Z.G.; Zhang, E.; Kong, F.; Lu, Y.; Wang, L.; Drennan, J.; Wang, Z.; Xiu, F.; Cho, K.; et al. Atomic disorders in layer structured topological insulator $SnBi_2Te_4$ nanoplates. *Nano Res.* **2018**, *11*, 696–706. [CrossRef]
53. Vilaplana, R.; Sans, J.A.; Manjón, F.J.; Andrada-Chacón, A.; Sánchez-Benítez, J.; Popescu, C.; Gomis, O.; Pereira, A.L.J.; García-Domene, B.; Rodríguez-Hernández, P.; et al. Structural and electrical study of the topological insulator $SnBi_2Te_4$ at high pressure. *J. Alloys Compd.* **2016**, *685*, 962–970. [CrossRef]
54. Marcinkova, A.; Wang, J.K.; Slavonic, C.; Nevidomskyy, A.H.; Kelly, K.F.; Filinchuk, Y.; Morosan, E. Topological metal behavior in $GeBi_2Te_4$ single crystals. *Phys. Rev. B* **2013**, *88*, 165128. [CrossRef]
55. Frolov, A.S.; Usachov, D.Y.; Tarasov, A.V.; Fedorov, A.V.; Bokai, K.A.; Klimovskikh, I.; Stolyarov, V.S.; Sergeev, A.I.; Lavrov, A.N.; Golyashov, V.A.; et al. Magnetic Dirac semimetal state of $(Mn,Ge)Bi_2Te_4$. *arXiv* **2023**, arXiv:2306.13024.
56. Serrano-Sánchez, F.; Funes, M.; Nemes, N.M.; Dura, O.J.; Martínez, J.L.; Prado-Gonjal, J.; Fernández-Díaz, M.T.; Alonso, J.A. Low lattice thermal conductivity in arc-melted GeTe with Ge-deficient crystal structure. *Appl. Phys. Lett.* **2018**, *113*, 083902. [CrossRef]
57. Bhattacharjee, N.; Mahalingam, K.; Fedorko, A.; Lauter, V.; Matzelle, M.; Singh, B.; Grutter, A.; Will-Cole, A.; Page, M.; McConney, M.; et al. Topological antiferromagnetic Van der Waals phase in topological insulator/ferromagnet heterostructures synthesized by a CMOS-compatible sputtering technique. *Adv. Mater.* **2022**, *34*, 2108790. [CrossRef] [PubMed]

nanomaterials

MDPI

Article

Hexagonal Boron Nitride as Filler for Silica-Based Elastomer Nanocomposites

Federica Magaletti [1], Gea Prioglio [1], Ulrich Giese [2], Vincenzina Barbera [1,*] and Maurizio Galimberti [1,*]

[1] Department of Chemistry, Materials and Chemical Engineering "G. Natta", Politecnico di Milano, Via Mancinelli 7, 20131 Milano, Italy; federica.magaletti@polimi.it (F.M.); gea.prioglio@polimi.it (G.P.)
[2] Deutsches Institut für Kautschuktechnologie e. V., Eupener Straße 33, 30519 Hannover, Germany
* Correspondence: vincenzina.barbera@polimi.it (V.B.); maurizio.galimberti@polimi.it (M.G.)

Abstract: Two-dimensional hexagonal boron nitride (hBN) has attracted tremendous attention over the last few years, thanks to its stable structure and its outstanding properties, such as mechanical strength, thermal conductivity, electrical insulation, and lubricant behavior. This work demonstrates that hBN can also improve the rheological and mechanical properties of elastomer composites when used to partially replace silica. In this work, commercially available pristine hBN (hBN-p) was exfoliated and ball-mill treated in air for different durations (2.5, 5, and 10 h milling). Functionalization occurred with the -NH and -OH groups (hBN-OH). The functional groups were detected using Fourier-Transform Infrared pectroscopy (FT-IR) and were estimated to be up to about 7% through thermogravimetric analysis. The presence of an increased amount of oxygen in hBN-OH was confirmed using Scanning Electron Microscopy coupled with Energy-Dispersive X-ray Spectroscopy. (SEM-EDS). The number of stacked layers, estimated using WAXD analysis, decreased to 8–9 in hBN-OH (10 h milling) from about 130 in hBN-p. High-resolution transmission electron microscopy (HR-TEM) and SEM-EDS revealed the increase in disorder in hBN-OH. hBN-p and hBN-OH were used to partially replace silica by 15% and 30%, respectively, by volume, in elastomer composites based on poly(styrene-co-butadiene) from solution anionic polymerization (S-SBR) and poly(1,4-cis-isoprene) from *Hevea Brasiliensis* (natural rubber, NR) as the elastomers (volume (mm^3) of composites released by the instrument). The use of both hBNs in substitution of 30% of silica led to a lower Payne effect, a higher dynamic rigidity, and an increase in E′ of up to about 15% at 70 °C, with similar/lower hysteresis. Indeed, the composites with hBN-OH revealed a better balance of tan delta (higher at low temperatures and lower at high temperatures) and better ultimate properties. The functional groups reasonably promote the interaction of hBN with silica and with the silica's coupling agent, sulfur-based silane, and thus promoted the interaction with the elastomer chains. The volume of the composite, measured using a high-pressure capillary viscometer, increased by about 500% and 400% after one week of storage in the presence of hBN-p and hBN-OH. Hence, both hBNs improved the processability and the shelf life of the composites. Composites obtained using hBN-OH had even filler dispersion without the detachments of the filler from the elastomer matrix, as shown through TEM micrographs. These results pave the way for substantial improvements in the important properties of silica-based composites for tire compounds, used to reduce rolling resistance and thus the improve environmental impacts.

Keywords: rubber compounds; 2D nanomaterials; h-BN functionalization; lower Payne effect

Citation: Magaletti, F.; Prioglio, G.; Giese, U.; Barbera, V.; Galimberti, M. Hexagonal Boron Nitride as Filler for Silica-Based Elastomer Nanocomposites. *Nanomaterials* **2024**, *14*, 30. https://doi.org/10.3390/nano14010030

Academic Editor: Meiwen Cao

Received: 15 September 2023
Revised: 7 December 2023
Accepted: 15 December 2023
Published: 21 December 2023

1. Introduction

Since the discovery of graphene [1] and the micromechanical isolation of single-layered graphene (the scotch tape experiment) [2], research in the field of two-dimensional (2D) nanomaterials has exponentially grown [3–8]. Their atomic thickness, their very high area/volume ratio, their significant potential for applications in performing functionalization reactions, and their remarkable physical, electrical, and optical properties have

captivated researchers from diverse domains; such domains include condensed matter physics, materials science, chemistry, and nanotechnology. Research in these fields has paved the way for a variety of applications, from the biomedical field [9] to gas sensing [10] to the tailoring of friction and wear in machine elements [11–13].

Among all the studied 2D materials, boron nitride (BN) is an extremely versatile material. BN is a ceramic material with an equal number of boron (B) and nitrogen (N) atoms. Different allotropic forms can be described: cubic BN (cBN), wurstzite BN (wBN), hexagonal boron nitride (h-BN), and turbostratic BN [14].

h-BN is the most stable allotropic form of BN and is a synthetic material. It is also called graphitic boron nitride and white graphene [15], due to its similarity to the sp^2 carbon allotrope homologue. h-BN is a layered material and is characterized by high hardness, high mechanical strength, low roughness, good thermal stability, good thermal conductivity, electrical insulation, lubricant properties, and good biocompatibility [16–23]. As a consequence, h-BN is the most widely used BN allotrope, and significant interest in this material has been developing over recent years; there are many, varied potential applications for it [24–35].

The 2030 Agenda for Sustainable Development incorporates sustainable transportation into multiple Sustainable Development Goals [36]. The energy sector is the most significant contributor to global greenhouse gas emissions (more than 70%); road transport is the most impactful sector in this contribution, accounting for about 12%. Tires play a key role in sustainable development. The worldwide tire market is expected produce 2.7 billion units in 2025 [37]. The rolling resistance (RR), defined as "the energy consumed per unit distance of travel as a tire rolls under load" [38], holds the primary responsibility for a tire's environmental impact during its use. Tire compounds must be designed in order to reduce their hysteresis and thus the rolling resistance. Nowadays, in tire compounds, precipitated silica [39,40] is the preferred filler for preparing materials with low hysteresis [39–41]. The silanol groups on its surface allow reactions to occur with sulfur-containing silanes, which act as coupling agents with the elastomer matrix through crosslinking reactions [42]. The chemical bond between silica and the polymer chains plays a key role in reducing the composite's hysteresis. However, silica has many technical drawbacks. Some of them arise from the high surface activity of silica, which promotes extensive supramolecular interactions. Silica causes increases in the viscosity of the elastomer composite, and leads to decreased processability and reduced storage time. The short storage time has a clear impact on planning for the production and transportation of the composites; in turn, there are consequences for the logistics. Ad hoc mixing equipment that is more expensive than regular equipment must be used to ensure the efficient processing of silica-based composites. The silane increases the adherence of the material to the metal parts of the mixing machines. Moreover, silica is corrosive and abrasive. Hence, special treatments of the metal surfaces and particular revision procedures must be performed. All these technical problems are remarkable at the industrial scale, in the light of the great number of tires on the market. Thus, it would be highly desirable to achieve improved (or at least the same) dynamic mechanical properties for silica-based composites; this might be possible through using a lower amount of silica; this would reduce—at least to some extent—the mentioned technical drawbacks.

To this aim, an interesting potential approach is the partial replacement of silica with a filler that is suitable for interrupting the 3D network and weakening the supramolecular interaction. From this perspective, 2D nanomaterials are of great interest. Researchers have recently reported on the use of 2D graphene nanoplatelets (GnP) in partial replacement of silica, obtaining similar dynamic mechanical characteristics and better rheological properties in comparison with the original material [43]. Due to the poor compatibility of GnP with silica, flaws were found in the elastomer composite and only the introduction of polar groups on the GnP edges, through the functionalization with a pyrrole compound such as 2-(2,5-dimethyl-1*H*-pyrrol-1-yl)propane-1,3-diol (serinol pyrrole), allowed the researchers to obtain a material with a homogenous, continuous structure. However, the functionaliza-

tion method required polluting steps, with the use of an organic solvent such as acetone and of high temperature (180 °C). hBN, as a 2D material, presents advantages with respect to GnP: lower numbers of stacked layers could promote higher efficiency—the composite ingredients and the chemical nature of hBN could favor its compatibility with silica and/or its chemical modification.

In this work, elastomer composites based on poly(styrene-co-butadiene) from anionic solution polymerization (solution styrene butadiene rubber, S-SBR) and poly(1,4-*cis*-isoprene) from *Hevea Brasiliensis* (natural rubber, NR) were prepared, with precipitated silica as the reinforcing filler. Bis(triethoxysilylpropyl)tetrasulfide (TESPT) was the organosulfur compound that was used as the coupling agent for silica with elastomer chains. Pristine hexagonal boron nitride (hBN-p) and the functionalized derivative were used in partial replacement of silica at two different levels, 15% vol and 30% vol, while maintaining the same total volume fraction of the filler. The functionalization of h-BN was performed through a simple and environmentally friendly mechanical approach: ball milling [44]. In previous studies, the functionalization of hBN has been performed with various methods [45–55]. Mechanochemistry was applied using sonication [47,48] and ball milling [49–51]. For the introduction of hydroxyl groups, hBN was treated with air plasma [52], steam (Ar flow) at 850 °C and 1000 °C [53], and hot aqueous solution of H_2SO_4/$KMnO_4$ [54]. Ball milling was performed in the presence of water solutions of either NaOH [49] or NaOH/KOH [50]. Sonication was carried out at room temperature in the presence of H_2O [47] or N-methylpyrroliperformed [48].

In this work, functionalization was used to enable the introduction of OH groups, relying on the Lewis' base character of hBN; hence, milder and scalable experimental conditions were used, without the need for any chemical substance. Mechanical treatment of hBN was performed through ball milling at a nominal room temperature in air; the samples taken from the jar were washed with water. The functionalized hBN is referred to in this paper as hBN-OH. hBN-p and hBN-OH, as taken from the milling jar and after washing with water, were characterized through thermogravimetric analysis (TGA), Fourier-transform infrared spectroscopy (FT-IR), wide-angle X-ray diffraction (WAXD), and high-resolution transmission electron microscopy (HR-TEM). The elastomer composites were prepared via melt blending in an internal mixer; they were additionally crosslinked using a system based on sulfur and a sulphenamide, such as *N*-tert-butyl-2-benzothiazyl sulfenamide (TBBS). They were characterized through studying the crosslinking reaction and determining the dynamic mechanical properties in both the shear and the axial modes; the tensile properties were also studied. Their structure was analyzed through TEM. The composites were extruded from a high-pressure capillary viscometer (HKV) to investigate their processability.

2. Materials and Methods

2.1. Materials

2.1.1. Chemicals

All reagents and solvents were purchased and used without further purification: acetone was obtained from Sigma-Aldrich.

The following chemicals were used in the preparation of the elastomeric composites: Bis(triethoxysilylpropyl)tetrasulfide (TESPT; Evonik Industries, Essen, Germany), ZnO (Zincol Ossidi, Bellusco, MB, Italy), stearic acid (Sogis, Milan, Italy), 1,3-dimethyl butyl)-*N*′-Phenyl-p-phenylenediamine (6PPD from Eastman Kingsport, TN, USA), sulfur (S from Solfotecnica, Cotignola, Italy), and *N*-tert-butyl-2-benzothiazyl sulfenamide (TBBS from Lanxess Chemical, Shangai, China).

2.1.2. Elastomeric Materials

Natural rubber (poly(1,4-*cis*-isoprene) from Hevea brasiliensis) was purchased from EQR-E.Q. Rubber, BR-THAI, Eastern GR. Thailand—Chonburi, with the trade name SIR20. The rubber has a Mooney viscosity (ML (1 + 4) 100 °C) of 73 MU. Solution styrene butadiene,

not functionalized (SPRINTAN™ SLR 4630 from Trinseo, Milano, Italy), was employed. The composition of the S-SBR was as follows: Stirene 25%, Butadiene 75% and 37.5 phr of TDAE. The Butadiene fraction has a vinyl content of 63%. Other properties of S-SBR are Tg-29C, not functionalized. Mooney viscosity (ML (1 + 4) 100 °C) of 55 MU.

2.1.3. Fillers

Hexagonal boron nitride industrial-grade A01 was kindly provided by Hoganas (Hoganas, Sweden). Data from the technical data sheet are as follows: Boron (42.5–43.5%); Oxigen 1.2% B_2O_2 (water soluble), H_2O, and C less than 0.15% each, Cristallographic Phases Hexagonal, high degree of crystallization. Specific surface area (NSA): 3.5–7.0 m^2/g. Tap density: 0.2–0.5 g/cm^3.

Silica ZEOSIL 1165MPmicropearl silica was purchased from Solvay (Brussels, Belgium). The main properties of the material, reported in the technical data sheet, were as follows: loss on drying (2 h @ 105 °C) $\leq$ 8.0%; soluble salts (as Na_2SO_4) $\leq$ 2.0%; specific surface area—140–180 m^2/g.

The BET method was used to determine the surface area through the use of a MICROACTIVE TRISTAR® II PLUS apparatus. Samples were evacuated at 200 °C for 2 h and N_2 adsorption isotherms were recorded at 77 K in a liquid nitrogen bath. The specific surface area (SSA) was found to be 160 m^2/g.

2.2. Preparation of Functionalized Boron Nitride (hBN-OH)

The white powder of hBN-p was treated using a planetary ball mill S100 from Retsch (Haan, Germany); the zirconia grinding jar moved in a horizontal plane with a volume of 0.3 L. The powder was previously kept closed in a PET jar in a room at 19 °C and a relative humidity of 47%. The grinding jar was loaded with 7 ceramic balls with a diameter of 15 mm. A measurement of 5 g of hBN-p was put into the jar at 19 °C and a relative humidity of 47%, without any liquids. Once the jar was closed, it was made to rotate at 300 rpm at nominal room temperature in air. Milling was carried out for 2.5, 5, and 10 h. When the jar was opened, the odor of ammonia was present; this was faint following 2.5 h milling and strong following 10 h milling. Since the powder was grinded without liquids, the process can be seen as a dry grinding process.

After milling, the powder was placed in a becher and washed with 300 mL of deionized water and stirred for 4 h at 300 rpm. The mixture was then filtered on a Büchner funnel with a sintered glass disc. The wet powder was finally dried in the air. A measure of 5 g of the dark-grey powder was collected.

2.3. Preparation of Elastomeric Composites

Elastomeric nanocomposites were prepared, with S-SBR 4630 as the main rubber (70 phr), and with NR (30 phr). Precipitated silica was the filler (50 phr). Partial replacement of silica at 15% vol and 30% vol was performed with either pristine hBN or with hBN-OH obtained through a 5 h ball-milling process followed by washing with water. Sulfur-based crosslinking was performed using a typical recipe that was suitable for the crosslinking of S-SBR. In particular, a relatively low amount of ZnO was used. The recipes of the composites can be found in Table 1.

Table 1. Recipes of elastomer composites.

Recipes in phr	Silica	15-hBN-p	30-hBN-p	15-hBN-OH	30-hBN-OH
	[phr]	[phr]	[phr]	[phr]	[phr]
S-SBR 4630	70	70	70	70	70
NR	30	30	30	30	30
Silica	50	42.5	35	42.5	35
hBN	0	7.5	15	0	0
BN-OH	0	0	0	7.5	15

Other ingredients: Silane TESPT 4, stearic acid 2, ZnO 2.5, 6PPD 2, sulfur 2, and TBBS 1.8.

Mixing was performed as summarized in Figure 1.

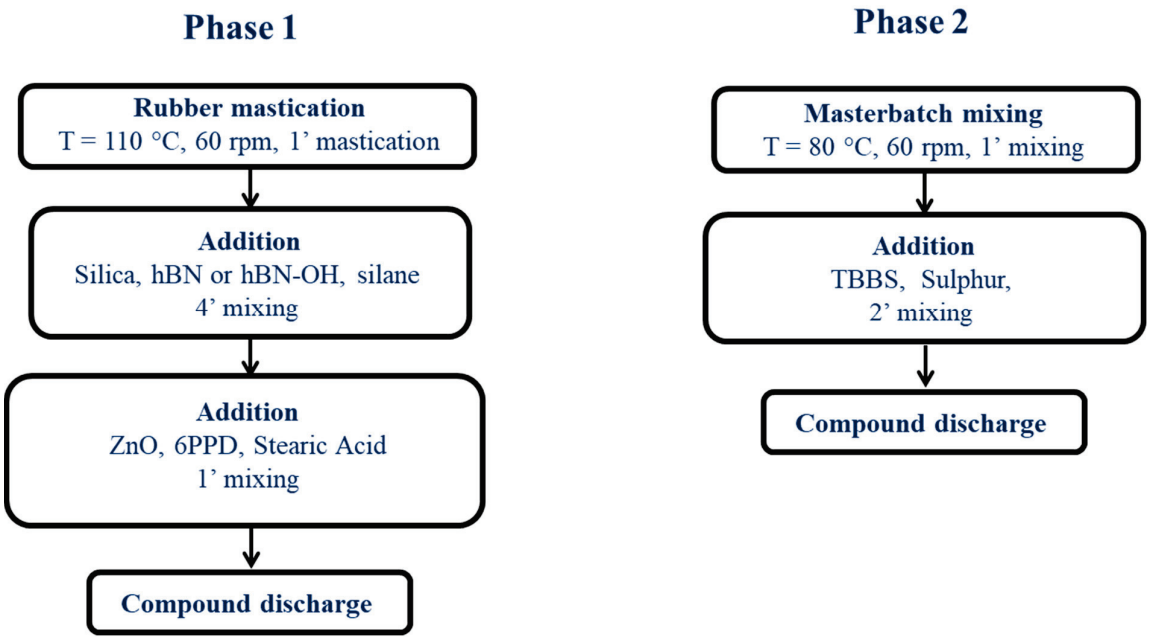

Figure 1. Block scheme of the mixing procedure.

The composites were prepared using a Brabender® internal mixer with a 55 cc chamber (Torque Rheometer Brabender® PL-2000 Plasti-Corder, from Brabender GmbH & Co. KG, Duisburg, Germany). NR and S-SBR were fed into the mixer and masticated at 110 °C and 60 rpm for 60 s. Then, silica, either hBN-p or hBN-OH, and the silane TESPT were added and mixing was performed for 4 min. ZnO, 6PPD, and stearic acid were added, and mixing was performed for 1 min. The composite was then discharged and was then fed again to the mixer at 80 °C, performing mixing for 1 min, followed by the addition of the vulcanizers. The compound was discharged after 2 min of mixing. The composites were lastly homogenized, employing a two-roll mill at 50 °C. Each compound was passed through the mill 5 times; the nip between the rolls was set to 1 cm, the rotation of the front roll was set to 30 rpm, and the rotation of the back roll was set to 38 rpm.

2.4. Characterization Techniques

2.4.1. Thermogravimetric Analysis

TGA tests were performed through heating samples (10 mg) from 30 to 900 °C with a heating rate of 10 °C/min in air (60 mL/min); these were carried out using a Mettler TGA SDTA/851 instrument following the ISO9924-1 standard [56].

TGA was used to estimate the extent of functionalization, which was considered to be the mass loss% in the T range from 150 °C to 900 °C.

2.4.2. Fourier-Transform Infrared (FT-IR)

FT-IR absorption spectra were recorded in transmission mode using a FT-IR Nicolet Nexus spectrometer coupled with a ThermoElectron FT-IR Continuμm IR microscope (Thermo Fisher Scientific, Waltham, MA, USA) (resolution: 4 cm^{-1}; scans: 30). Attenuated total reflectance ATR was carried out with a Si tip single bounce slide on an ATR accessory in a spectral range between 4000 cm^{-1} and 700 cm^{-1}. Analysis of FTIR spectra was conducted using Origin Pro 2018

2.4.3. Wide-Angle X-ray Diffraction (WAXD)

WAXD was performed with a Bruker D8 Advance automatic diffractometer (Bruker, Billerica, MA, USA)and nickel-filtered Cu-Kα radiation; wide-angle X-ray diffraction

patterns were carried out in reflection. A range of 4.7° to 90° was used to record the patterns because these angles were 2θ at the peak diffraction angles.

Spectra were developed using Origin Pro 2018.

Through the Bragg law (Equation (1)), the distance between crystallographic planes was estimated.

$$d_{hkl} = \frac{n \cdot \lambda}{2 \cdot sin\theta_{hkl}} \quad (1)$$

where n is an integer number, λ is the wavelength of the irradiating beam, and $\theta_{hk\ell}$ is the diffraction angle.

The Scherrer equation, Equation (2), was used to calculate the D_{hkl} crystallite dimensions.

$$D_{hkl} = \frac{k \cdot \lambda}{\beta_{hkl} \cdot \cos\theta_{hkl}} \quad (2)$$

where β_{hkl} is the width at half height, θ_{hkl} is the diffraction angle, K is the Scherrer constant, and λ is the wavelength of the irradiating beam.

The number of layers in a crystallite was calculated with Equation (3) by dividing the crystallite size by the interlayer distance. In this manuscript, Equation (2) was applied to the (002) reflection.

$$number\ of\ layers = \frac{D_{hkl}}{d_{hkl}} \quad (3)$$

2.4.4. Crosslinking

Crosslinking was performed in a rubber process analyzer (Monsanto R.P.A. 2000, Alpha Thechnologies, Milano, Italy). A measure of 5 g of rubber composite was weighed and put in the rheometer. Measurements were carried out at a frequency of 1.7 Hz and an oscillation angle of 6.98%. The sample, loaded at 50 °C, underwent a first strain sweep (0.2–25% strain) to cancel the thermo-mechanical history of the rubber composite; it was then maintained at 50 °C for 10 min and then underwent another strain sweep at 50 °C to measure the dynamic mechanical properties at low deformations of the uncured sample. The crosslinking reaction was then carried out at 170 °C for 20 min. A torque–time curve was obtained. The minimum achievable torque (M_L), the maximum achievable torque (M_H), the time required to have a torque equal to M_L + 1 (t_{S1}), and the time required to reach 90% of the maximum torque (t_{90}) were measured.

2.4.5. Dynamic Mechanical Analysis in the Shear Mode—Strain Sweep Test

Samples for the strain sweep test were prepared as shown in the infographic in Figure S1 in the Supplementary Materials. The uncured composites were taken from the internal mixer and were processed on a two-roll mill as described in Section 2.3 and were then placed in the rheometer.

The shear dynamic mechanical characteristics of the rubber compounds were evaluated by performing strain sweep tests in a rubber process analyzer (Monsanto R.P.A. 2000 Alpha Thechnologies, Milano, Italy). As reported in Section 2.4.3, the crude sample was subjected to a first strain sweep and held at 50 °C for ten minutes, followed by another strain sweep at 50 °C. Data from the second strain sweep were collected and are reported in the text below to discuss the behavior of the uncured samples. The crosslinking was then carried out as reported in Section 2.4.4; the shear dynamic mechanical properties of the cured samples were then assessed after 20 min at 50 °C using a 0.2–25% strain sweep at a frequency of 1 Hz. The minimum strain was 0.2%, as it was the minimum required strain value to obtain reliable data from the RPA instrument. Shear storage and loss moduli (G′, G″), and subsequently Tan δ, were the measured characteristics.

2.4.6. Dynamic Mechanical Analysis in the Axial Mode

Samples were prepared as shown in the infographic in Figure S1. After the processing on the two-roll mill, described in Section 2.3, the elastomeric compound was rolled up to

obtain a long cylinder. This cylinder was then cut into smaller cylinders and vulcanized (at 170 °C for 20 min) to produce cylindrical test pieces with dimensions of 25 mm in length and 12 mm in diameter. An Instron dynamic device, set to the traction–compression mode, was employed to perform the dynamic mechanical measurements; this was maintained at the predetermined temperatures (10, 23, and 70 °C) throughout the entire experiment. The cylinder was preloaded to a 25% longitudinal deformation with respect to the original length. The compression was subjected to a dynamic sinusoidal strain in compression with an amplitude of around 3.5% regarding the length under pre-load, at a frequency of 100 Hz. The values of dynamic storage modulus (E′), loss modulus (E″), and loss factor (tan δ) were calculated as the ratio between E″ and E′.

2.4.7. Tensile Test

Standard dumbbells made from vulcanized compound plates measuring 10 cm by 10 cm by 1 mm were used to perform the tensile tests at room temperature with a Zwick Roell Z010 (Genova, Italy) and an optical extensometer. Measurements were performed at 1 mm/min. Stresses at different elongations (σ_{50}, σ_{100}, and σ_{300}), stress at break (σ_B), elongation at break (ε_B), and the energy required to break were measured according to Standard ISO 37/UNI 6065 [57].

2.4.8. High-Pressure Capillary Viscosimeter (HKV)

HKV measurements were performed through a high-pressure capillary viscosimeter, type "Rheo-Vulkameter 78.90" (Göttfert Werkstoff-Prüfmaschinen GmbH, Buchen, Germany). The crude compound material was extruded using a 20 mm capillary with a 2 mm diameter at a pressure of 130 bar. The mold temperature was 100 °C. To obtain the correct experimental conditions, a preheating step of 180 s and an injection step of 60 s were carried out.

2.4.9. High-Resolution Transmission Electron Microscopy

hBN samples: TEM and HRTEM analyses were performed with a Philips CM 200 (Eindhoven, the Netherlands) field emission gun microscope operating at an accelerating voltage of 200 kV. A few drops of a 1 mg/mL ethyl acetate dispersion were deposited on a 200-mesh lacey carbon-coated copper grid and air-dried for several hours before analysis.

The samples were prepared with a dispersion of 1 mg/mL in ethyl acetate then sonicated to homogenize the dispersion.

Rubber nanocomposites: TEM characterizations were performed with a TEM, LIBRA® 120, Zeiss, Oberkochen (Baden-Württemberg, Germany), with an acceleration voltage of 120 kV. Layers of vulcanized rubber were cut of a thickness of approximately 100 nm under liquid nitrogen, using a diamond cutter mounted on a Leica Ultramicrotome UC6, (Leica Microsystem, Wetzlar, Germany) equipped with a stereo microscope MZ6 and a FC6 cutting system.

2.4.10. Scanning Electron Microscope Coupled with Energy-Dispersive X-ray Spectroscopy (SEM-EDS)

The SEM-EDS investigation was carried out using a Zeiss EVO 50 EP SEM (Zeis Vision Care, Castiglione Olana, Italy) coupled with an EDS spectrometer (Bruker Quantax 200 6/30, Bruker, Billerica, MA, USA). hBN powders were applied on aluminum stubs with the aid of a conductive carbon bioadhesive. The samples were subsequently coated with gold using an Ewards S150B sputter coater (Perkin Elmer, Milan, Italy) and evaluated.

3. Results and Discussion

3.1. Preparation of hBN Samples

Pristine hBN was commercially available. The functionalization of hBN-p was attempted through ball-milling the hBN-p powder, as described in the experimental section. In brief, the powder was treated in air in a planetary ball mill at nominal room temperature

and for different durations: 2.5, 5, and 10 h. All the collected powders were washed with water and filtered. The wet powder was dried for 48 h in air and then for 8 h in oven at 90 °C, under atmospheric pressure. Samples taken from the ball-milling jar—these are named, for the sake of simplicity, as hBN-OH in the paper—were characterized as such (hBN-OH_{as}); then, they were washed with water (hBN-OH_w). Characterization was performed through means of TGA, FT-IR, WAXD, and HR-TEM.

In Figure 2, a schematic representation of the procedure for the preparation of the hBN-OH samples is shown.

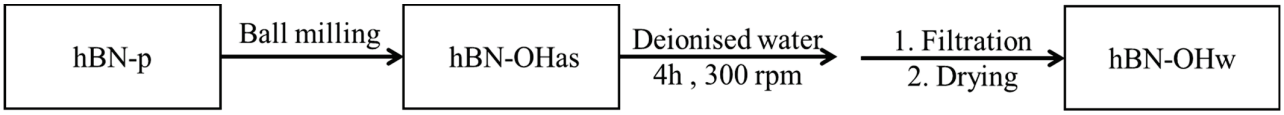

Figure 2. Block diagram describing the preparation of the hBN-OH samples as taken from the ball-milling jar (hBN-OH_{as}) and after washing with water (hBN-OH_w).

3.2. Characterization of hBN Samples

FT-IR analysis: The presence of functional groups on hBN samples, after ball milling and then after washing with water, was investigated through FT-IR vibrational spectroscopy. For the sake of clarity, the spectra of hBN-OH_{as} and hBN-OH_w, milled for 2.5, 5, and 10 h, were organized in two different figures: Figures 3 and 4, respectively. The proposed assignment of the main peaks of spectra of Figures 3 and 4 is reported in Tables 2 and 3, which show the relative abundances (%) of the bands.

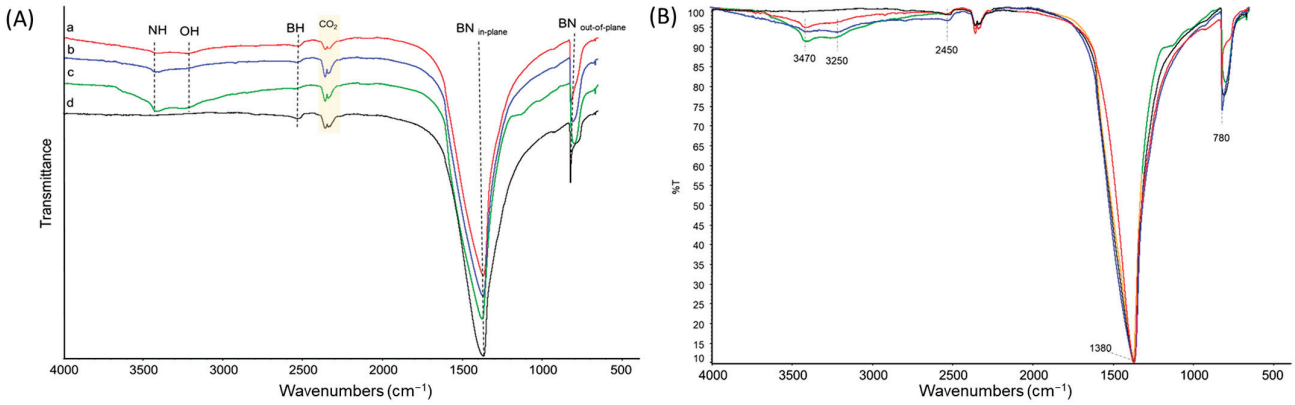

Figure 3. FT-IR spectra of hBN-OH_{as}, milled for 2.5 (a), 5 (b), and 10 (c) h; hBN-p (d). (**A**) Spectra are displayed with normalized intensity. CO_2 absorption bands are labeled. (**B**) Spectra are displayed after baseline correction and after normalization of the scale.

Table 2. Values of the wavenumbers corresponding to the absorption peaks of the most intense IR transitions for spectra in Figure 3. The relative abundance (%) is also reported.

Experimental Wavenumber (cm^{-1})	Vibrational Assignment	Relative Abundance per Sample (%)			
		hBN-Oh_{as} Milled for 2.5 h	hBN-Oh_{as} Milled for 5 h	hBN-Oh_{as} Milled for 10 h	hBN-p
3470	N-H stretching	2	3	5	0
3250	O-H stretching	2	3	4	0
2450	B-H stretching	1	1	1	1
1380	BN in-plane	100	100	100	100
780	BN out-of-plane	13	12	9	9

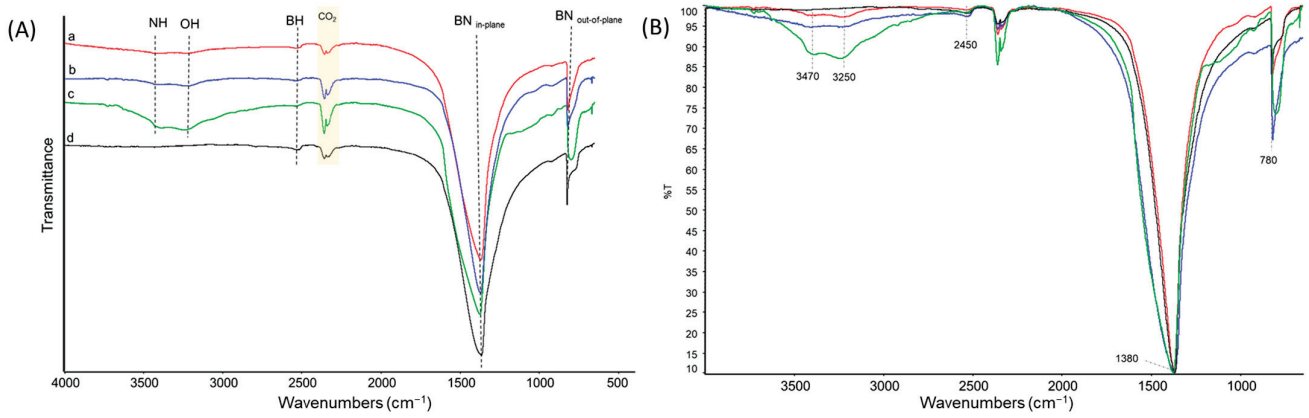

Figure 4. FT-IR spectra of hBN-OH_w, milled for 2.5 (a), 5 (b), and 10 (c) h; hBN-p (d). (**A**) Spectra are displayed with normalized intensity. CO_2 absorption bands are labeled. (**B**) Spectra are displayed after baseline correction and after normalization of the scale.

Table 3. Values of the wavenumbers corresponding to the absorption peaks of the most intense IR transitions for spectra in Figure 4. The relative abundance (%) is also reported.

Experimental Wavenumber (cm^{-1})	Vibrational Assignment	Relative Abundance per Sample (%)			
		hBN-Oh_w Milled for 2.5 h	hBN-Oh_w Milled for 5 h	hBN-Oh_w Milled for 10 h	hBN-p
3470	N-H stretching	1	2	6	0
3250	O-H stretching	1	2	6	0
2450	B-H stretching	1	1	1	1
1380	BN in-plane	100	100	100	100
780	BN out-of-plane	13	12	9	9

The IR spectra of all the hBN samples are characterized through two common strong features at 1380 cm^{-1} and 780 cm^{-1}, assigned to the conventional BN in-plane and out-of-plane vibrations, and to the signal due to the B-H stretching vibration, at 2450 cm^{-1}. These bands are typical of boron nitride samples [58,59].

In the spectra of the hBN-OH_{as} (Figure 3) and hBN-OH_w (Figure 4), new weak absorptions are detectable, at 3470 cm^{-1} and at 3250 cm^{-1}, for the samples milled for 5 (b) and 10 (c) h. They were attributed to N-H stretching and to O-H stretching, respectively. The intensity of the bands increases with the milling time. It can also be observed that the relative intensity of the bands assigned to the OH stretching and to the NH stretching is different in the hBN-OH_{as} (Figure 3) and hBN-OH_w (Figure 4) samples. The washed samples show a greater intensity of the -OH bands: this is clear through a comparison of the bands before and after the treatment and after the normalization of all spectra on the intensity of the band due to the B-N in-plane signal at 1380 cm^{-1}.

Thermogravimetric analysis: TGA analyses were performed on the hBN samples milled for 5 h and 10 h, in the 30–900 °C temperature range, with a heating rate of 10 °C/min under air. Data of mass losses, obtained from TGA analysis, are in Table 4. The thermographs are shown in Figure S2 in the Supplementary Materials.

A three-step decomposition profile can be observed. The first mass loss below 150 °C can be attributed to the loss of a low molecular mass substance: in this case, water. The second and third step, between 150 °C and 900 °C, can be attributed to defects in the polycyclic system and to the decomposition of nitrogen- and oxygen-containing functional groups. The residue at temperatures higher than 900 °C is due to the inorganic hBN. The amount of mass loss in the 150–900 °C temperature range was found to increase with the ball-milling time, as should be expected; the mechanical treatment creates defective structures which are high-energy sites—these are suitable for functionalization. By assuming a high reactivity of the defective sites, the mass loss in the 150–900 °C range could be tentatively attributed

to the thermal degradation of the functional groups. A greater amount of the mass loss in the 150–900 °C temperature range is accompanied by a greater amount of mass loss at T < 150 °C, which was attributed to water. By taking the whole amount of mass loss in the 150–900 °C temperature range, there is not an appreciable difference between the hBN-OH_{as} and hBN-OH_w samples; this might indicate that the ball-milling treatment could lead to the modification of hBN without the washing treatment. The mass loss was in a range from 3 to 4% for 5 h milling and in a range from 6% to 7% for 10 h milling. However, a different distribution of mass losses, at T < 500 °C and >500 °C, can be observed. Considering this finding in the light of the above-reported IR results, which revealed a greater amount of OH groups in the washed samples, one could assume that the mass loss in the 150–500 °C temperature range is prevailingly due to OH, as the functional groups. However, further investigations are needed to elucidate this point.

Table 4. Mass losses (mass %) for pristine of exfoliated hBN samples before (hBN-OH_{as}) and after washing (hBN-OH_w) from TGA analysis.

Sample	Milling Time (h)	Temperature Range			
		T < 150 °C	150 °C < T < 500 °C	500 °C < T < 900 °C	T > 900 °C + Residue
hBN-p	=	0	0	1.5	98.5
hBN-OH_{as}	5	1.9	2.7	1.3	96.5
hBN-OH_w	5	2.5	2.52	1	93.5
hBN-OH_{as}	10	6.8	4.5	1.6	87.2
hBN-OH_w	10	6.7	6.4	0.8	86.1

The amounts of functional groups were estimated on the basis of the mass loss in the 150 °C–900 °C T range.

WAXD analysis: Organization at the solid state of the hBN-OH samples, before and after washing, was investigated by performing WAXD analysis. WAXD patterns of the powders of the ball-milled samples which were milled for 2.5, 5, and 10 h are shown in Figure 5.

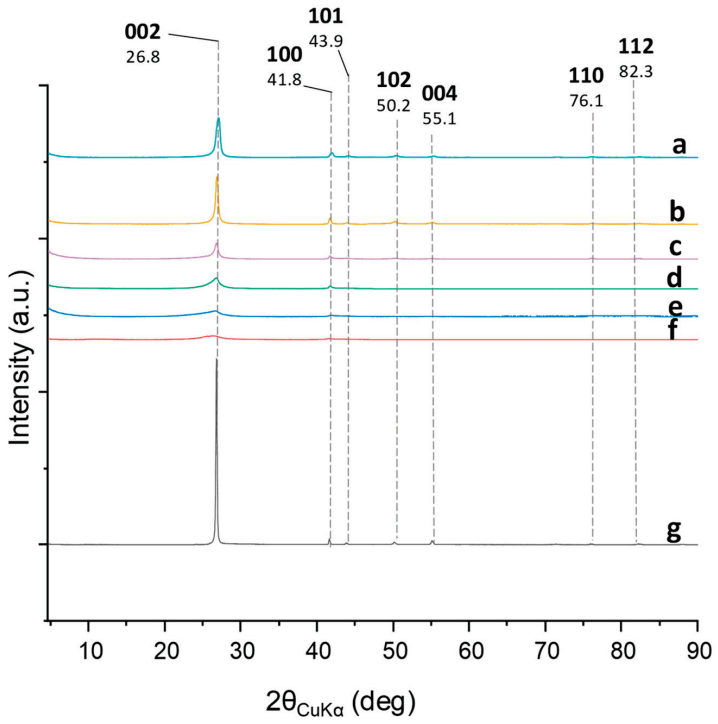

Figure 5. WAXD patterns: hBN-OH_{as}, milled for 2.5 (a), 5 (c), and 10 (e) h; hBN-OH_w, milled for 2.5 (b), 5 (d), and 10 (f) h; hBN-p (g).

In hBN, the crystalline order in the orthogonal direction to the structural layers in the hBN samples is detected through two (00ℓ) reflections: 002 at 26.8° (interlayer distance of 0.310 nm) and 004 at 55.12°. The in-plane order is shown by 100 and 110 reflections, at 41.8° and 76.1°, respectively [60].

The diffraction peaks at 2θ values of 26.8° (002), 41.8° (100), 43.91° (101), 50.20° (102), 55.12° (004), 76.1° (110), and 82.30° (112) were observed in all the patterns. The interlayer distance, the dimension of the crystallites, and the number of stacked layers were calculated by applying the Bragg's Law and the Scherrer equation, as explained in the experimental part. In brief, the perpendicular length of the crystallite ($D_{\perp}$) was obtained using the (002) reflection, while the in-plane length ($D_{//}$) was determined from the (100) reflection. The dimensional anisotropic factor of the material is given by the relation $D_{//}/D_{\perp}$. Data are given in Table 5.

Table 5. Structural parameters derived from Bragg's Law and Scherrer equation [a].

Sample	Milling Time (h)	d_{002} (nm)	$D_{\perp}$ (nm)	$D_{//}$ (nm)	$D_{//}/D_{\perp}$	Layers
hBN-p		0.31	41.53	44.56	1.07	132
hBN-OH_{as}	2.5	0.31	12.82	16.80	1.31	41
hBN-OH_{w}	2.5	0.31	18.81	26.22	1.39	60
hBN-OH_{as}	5	0.31	11.27	19.01	1.68	36
hBN-OH_{w}	5	0.32	15.01	21.61	2.32	40
hBN-OH_{as}	10	0.32	2.61	3.11	1.19	8
hBN-OH_{w}	10	0.32	2.90	3.27	1.13	9

[a] Equations (1)–(3) are reported in Section 2.

The (002) reflection was found in all the spectra and indications of intercalation of low-molar-mass chemicals do not arise from the analysis of the spectra. This could lead to the assumption that the functionalization occurred in peripheral positions, mainly on the edges.

The milling led to a reduction in the dimension of the crystallites in an orthogonal direction to the structural layers. Similar values were obtained after 2.5 and 5 h milling and a further remarkable reduction was observed after 10 h milling. As a consequence, the number of stacked layers was reduced. The sample milled for 10 h was indeed a few layers hBN, with a number of stacked layers lower than 10. Washing with water appears to promote a minor re-stacking. This can be explained with the adopted procedure, particularly the filtration, which enables the parallel placement and the overlapping of the layers.

The milling also led to a reduction in the dimension of the crystallites inside the basal plane, particularly after 10 h milling.

Transmission electron microscopy: The morphology of the hBN samples was studied through HR-TEM. Water suspensions of pristine hBN and exfoliated hBN samples (hBN-OH), with 1 mg/1 mL as the concentration, were prepared and poured on the grid. Micrographs were taken at lower and higher magnification levels and are shown in Figure 6: hBN-p in Figure 6a and hBN-OH_{as} in Figure 6b.

In the low-magnification image of thBNp, the hBN layers appear to have more similar dimensions; however, the lateral sizes for both hBN-p and hBN-OH_{as} appear to be similar, in the range from 500 to 700 nm.

Scanning Electron Microscopy Coupled with Energy-Dispersive X-ray Spectroscopy (SEM-EDS)

The morphology of hBN samples was further investigated through SEM-EDS. The powders of both hBN-p and hBN-OH_{w10h} samples were laid on aluminum stubs with the use of a conductive carbon bioadhesive. The samples were then coated in gold by a sputter coater and analyzed.

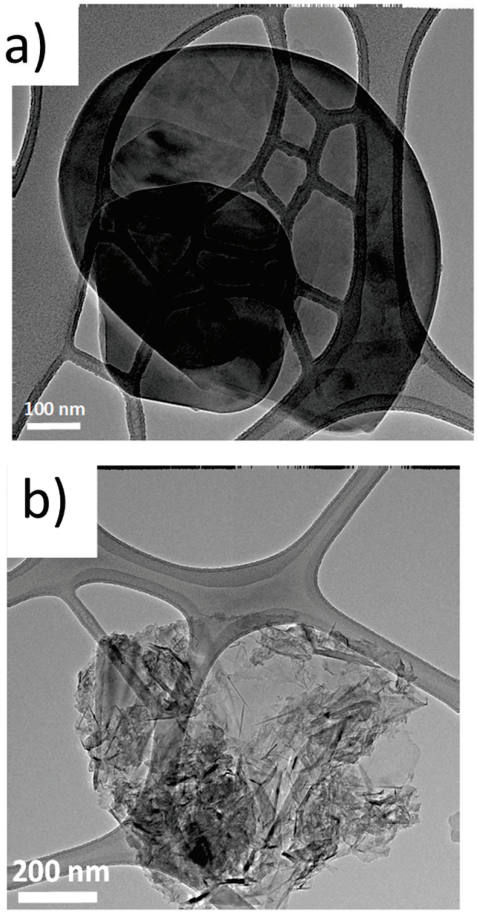

Figure 6. Micrographs of pristine hBN (**a**) and hBN-OH_{as5h} (**b**).

The elemental spectroscopy was evaluated at different points, as shown in Figure 7 for hBN-p and Figure 8 for hBN-OH_{w10h}. The EDS maps for hBN-p and hBN-OH_{w10h} are shown in Figures 9 and 10, respectively.

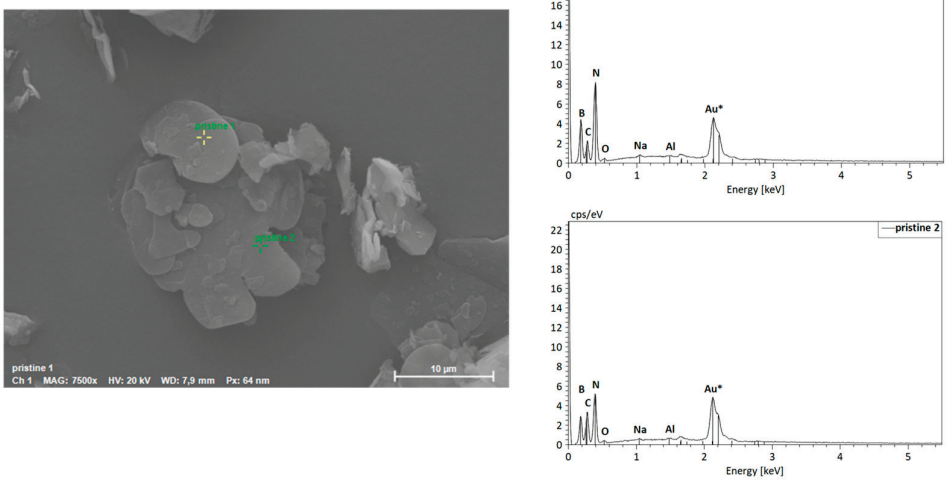

Figure 7. SEM image and EDS spectra of hBN-p.

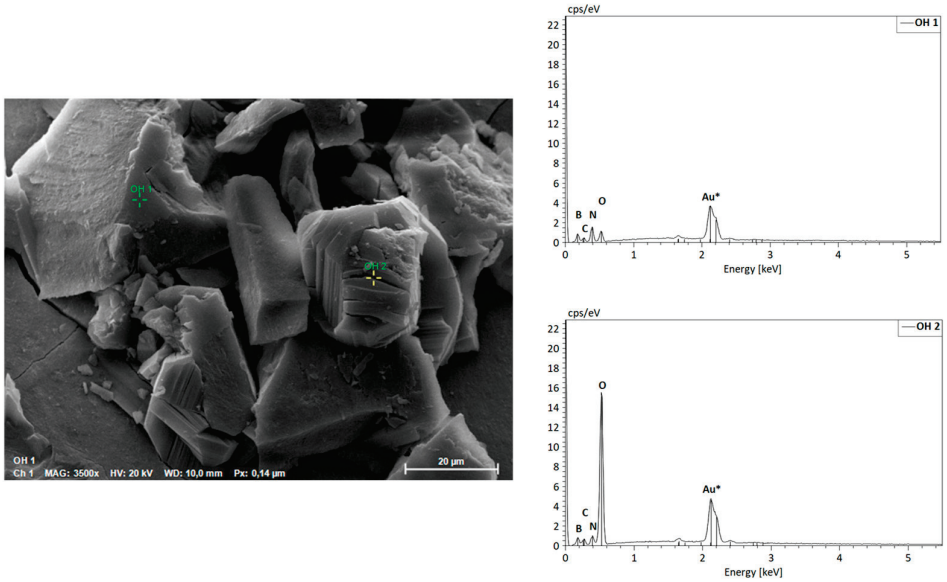

Figure 8. SEM image and EDS spectra of hBN-OH_{w10h}.

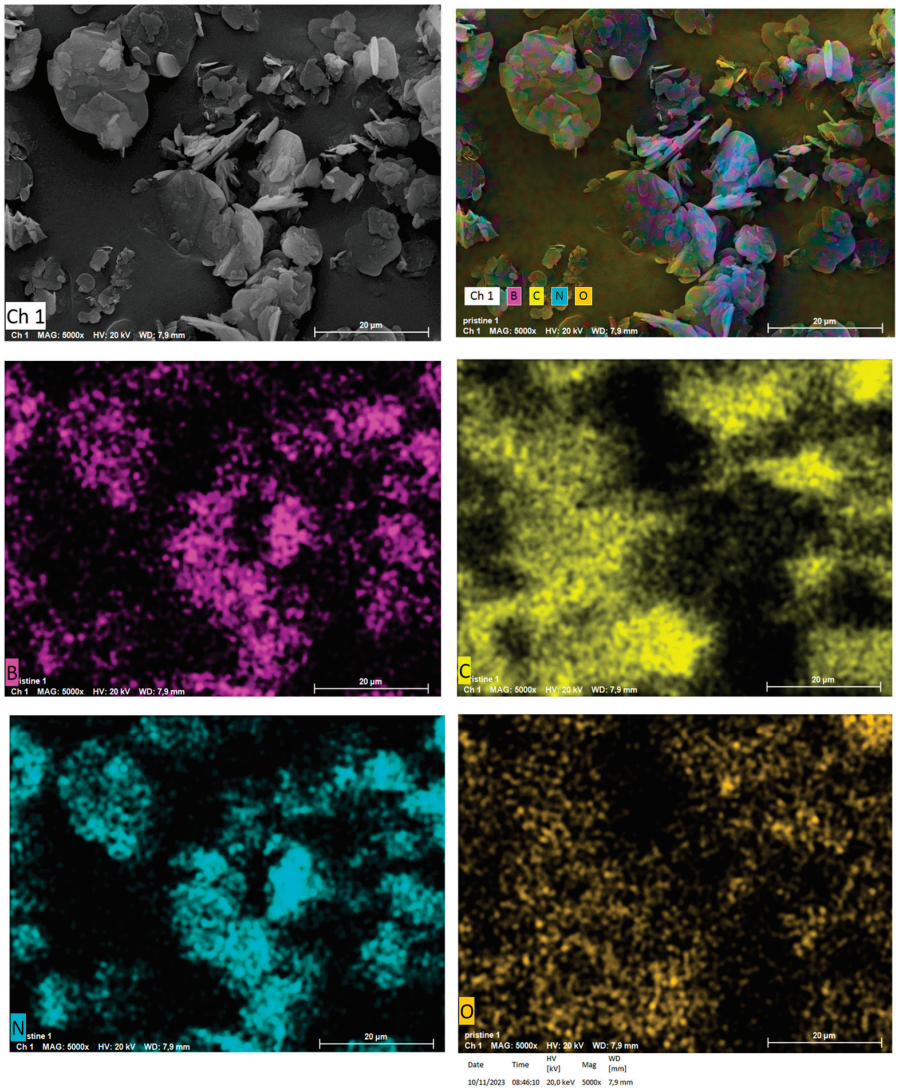

Figure 9. SEM colored image and elemental imaging of hBN pristine.

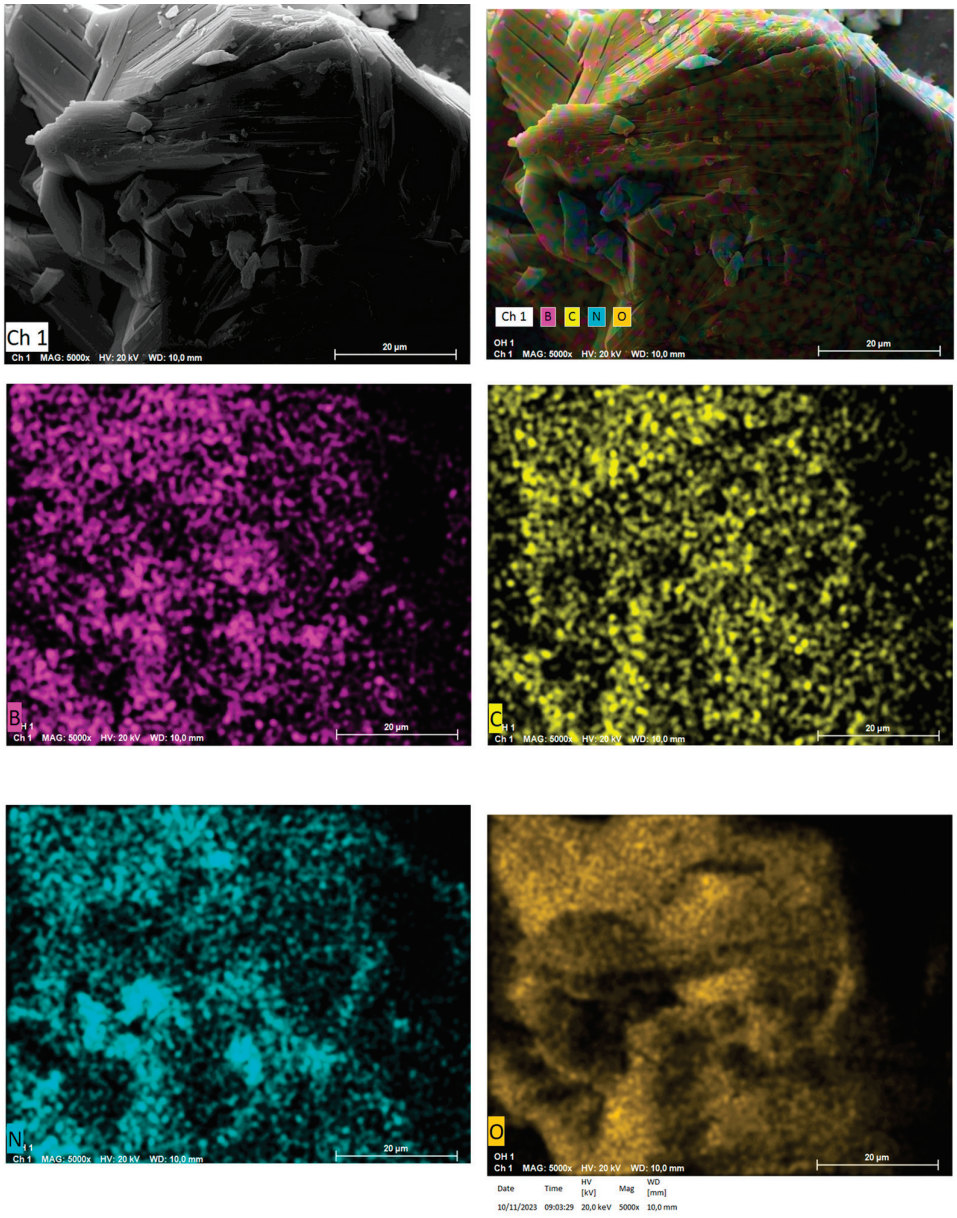

Figure 10. SEM colored image and elemental imaging of hBN-OH_{w10h}.

The morphology of the sample appears to be modified, as hBN-p results in a well-distributed flake-like appearance, while hBN-OH_{w10h} is shown to have a very coarse and compact structure.

The EDS maps and spectra, however, confirm the increased presence of oxygen in the hBN-OH_{w10h} sample with respect to the pristine powder. This result confirms the FTIR evidence of increased intensities of bands related to OH groups.

3.3. On the Functionalization of hBN with OH Groups

The experimental results reported above reveal that the milling treatment led to hBN samples with lower thermal stability, with the presence of -NH- and -OH functional groups. It can be reasonably commented that the mechanical treatment generates high-energy sites, which are able to react with the molecules present in the headspace of the jar. The formation of amino-functional groups may be a result of a reduction process. The amount of OH groups was found to increase with the milling time (see spectra b and c in Figure 3) and by washing the samples with H_2O. The OH groups could be due to the reaction of the weak nucleophile/base H_2O with boron, which acts as an acid in a Lewis acid-base

reaction. An extensive milling (10 h time) led also to a more extended rupture of the hBN structure, as suggested by the remarkable ammonia smell felt at the opening of the jar. The functionalization of hBN achieved in the present work occurred in milder and easier experimental conditions with respect to those reported in the literature [45,55].

It is indeed worth emphasizing that both the functional groups promote the interaction of hBN with silica and, in the case of OH, could also form a chemical bond. These comments must be considered as working hypotheses. Research is in progress to elucidate the mechanism of the hBN functionalization. The results of this will be reported in a future manuscript.

3.4. Elastomer Composites Containing Silica, hBN-p, and hBN-OH

Elastomer composites were prepared, with S-SBR and NR as the rubber matrix and silica as the nanostructured filler. The reason for selecting S-SBR was the high vinyl content of the butadiene fraction, which allows a high reactivity with the sulfur-based crosslinking system and silane TESPT, and the coupling agent of silica with the elastomer chains. The combination of S-SBR and NR is suitable for tire tread composites. A minor amount of silica was replaced with either hBN-p or hBN-OH: 15% and 30% by volume, maintaining the same total volume of the filler. A sample of hBN-OH was selected: the one milled for 5 h and then washed. It will be indicated as hBN-OH in the text below. As shown above by FT-IR and TGA analyses, 5 h milling allowed the introduction of a low yet appreciable amount of OH groups and did not remarkably alter the structure of the hBN layers, which maintained an order in the basal planes and lateral sizes that were similar to the one of pristine hBN. The sulfur-based crosslinking and the static and dynamic mechanical properties are discussed next.

3.4.1. Sulfur-Based Crosslinking

Sulfur-based crosslinking was performed at 170 °C for 10 min in a rubber process analyzer, as described in detail in the Experimental Section, obtaining torque vs. time curves. The minimum torque (M_L), the maximum torque (M_H), the time required to have a torque equal to M_L + 1 (t_{S1}), i.e., the induction time of crosslinking, and the time required to reach 90% of the maximum torque (t_{90}), i.e., the optimum time of crosslinking, were measured. The data are shown in Table 6. The corresponding curves are shown in Figure S3 in the Supplementary Materials.

Table 6. Vulcanization data of S-SBR 4630-based compounds.

	Silica	**15-hBN-p**	**30-hBN-p**	**15-hBN-OH**	**30-hBN-OH**
M_L [dNm]	3.8	2.5	1.9	3.4	3.1
M_H [dNm]	21.1	18.1	16.5	19.4	18.6
M_H-M_L [dNm]	17.3	15.5	14.5	16.0	15.5
t_{S1} [min]	3.1	3.4	3.4	3.2	3.4
t_{90} [min]	7.8	8.5	8.2	7.5	7.7
curing rate [dNM/min]	3.7	3.1	3.1	3.8	3.7

The curing rate was calculated by using the formula in Equation (4).

$$Curing\ rate = \frac{M_H - M_L}{T_{90} - T_{S1}} \quad (4)$$

M_L values are assumed as an index of the viscosity of the composites. The replacement of silica with hBN led to the reduction in M_L, greater for a greater amount of silica replaced. Remarkably lower M_L values were obtained with hBN-p, whereas the difference with the silica-based composites was slight in the case of hBN-OH. In the introduction, it was reported that a 2D nanomaterial such as hBN, which does not have a structure as silica [5], was supposed to interrupt the 3D network of silica and to weaken the supramolecular

interactions among the functional groups on the silica surface. It seems that this was achieved particularly with hBN-p, which has a lower compatibility with silica than hBN-OH, which bears edge -NH- and -OH groups. It is worth adding that hBN-OH has a lower number of stacked layers than hBN-p; hence, it can give rise to a more extended interaction with silica. The (M_{H-L}) values were lower for the composites with hBN and slight differences were obtained in the presence of either hBN-p or hBN-OH. This finding led the researchers to suppose that the M_H difference was mainly due to the different extents of the filler networks.

The replacement of silica did not have a remarkable effect on the induction time of crosslinking, and did not have an effect on the optimum time or on the curing rate when hBN-OH was used; in contrast, longer t_{90} and a lower curing rate were obtained with hBN-p. By taking into account the fact that the kinetics of curing are determined through measuring the torque, these findings could be explained by the ability of hBN-OH to interact with silica and to contribute to the formation of a network during the crosslinking reaction.

3.4.2. Dynamic Mechanical Properties in the Shear Mode

Dynamic mechanical properties in the shear mode were determined through strain sweep experiments at 50 °C by following the procedure described in the Experimental Section, with the strain amplitude in the range from 0.2% to 25%. The storage modulus (G′) and the loss modulus (G″) were measured and their ratio G″/G′ (=Tan δ was elaborated. Data of $G'_{\gamma min}$, $G'_{\gamma max}$, $\Delta G'$, $\Delta G'/G'_{\gamma min}$, G''_{max}, and $\tan\delta_{max}$ are presented in Table S1 in the Supplementary Materials. The curves of the G′ vs. strain and the Tan delta vs. strain are shown in Figures 11 and 12, respectively. The curve of the G″ vs. strain and the curve of the G″ vs. G′ are shown in Figure S4 and in Figure S5, respectively, in the Supplementary Materials.

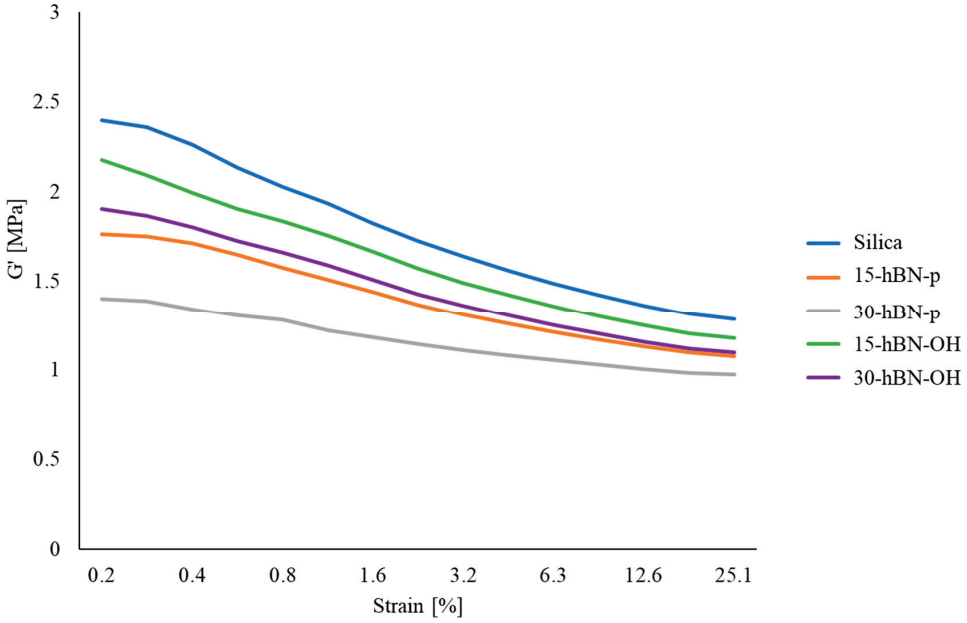

Figure 11. G′ vs. strain for composites of Table 1.

G′ at minimum strain is an index of the presence of the filler network. A filler network is formed by the interaction of filler particles, either directly or mediated by polymer chains. The reduction in G′ with the strain amplitude, i.e., the nonlinearity of the storage modulus, is known as Payne effect [61–63]; this is due to the disruption of the filler network. Parameter $\frac{\Delta G'}{G'_{\gamma min}}$ is a normalized index of the Payne effect.

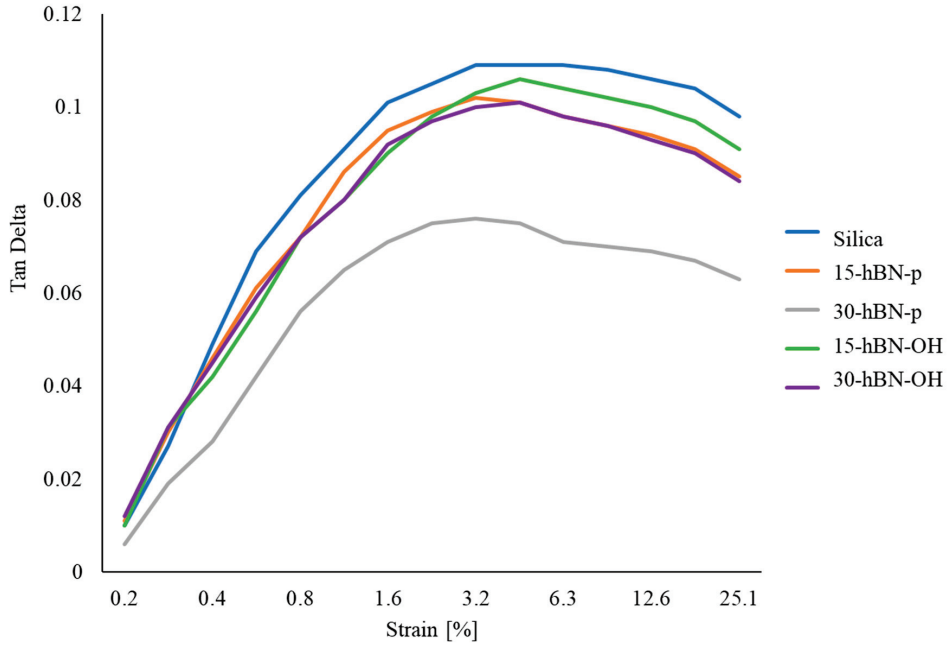

Figure 12. Tan delta vs. strain for composites of Table 1.

The replacement of silica with hBN, both pristine and functionalized, had effects—which consistently increased with the extent of the replacement—on the low-strain dynamic mechanical properties of the composites.

hBN-p in place of silica led to remarkably lower values of $G'_{\gamma min}$, $G'_{\gamma max,}$, $\Delta G'/G'_{\gamma min}$, G''_{max}, and Tan delta. These findings arise from a lower extent of the filler network and indicate a lower Payne effect and a lower dissipation of energy. They suggest the powerful effect of hBN-p for disrupting and preventing the formation of a silica-based filler network. However, to account for these results, the lamellar structure of hBN and the procedure used for preparing the specimen to be analyzed—shown in Figure S1 in the Supplementary Materials—should be taken into account. The uncured composites, taken from the internal mixer, were processed on a two-roll mill and were then placed in the rheometer. The hBN layers are reasonably arranged parallel to the plate of the rheometer. In this configuration, the layered 2D nanofiller can express its lubricant effect, which is well documented in the literature [64–66]. This behavior has also been reported for nanosized graphite nanoplatelets (GnP) [43]. The anisotropy of nanocomposites based on 1D and 2D nanofillers, such as GnP and carbon nanotubes, has been documented in the literature [67,68].

With hBN-OH in place of silica, analogous effects were observed. However, with respect to hBN-p, higher values of G′ were observed at both the minimum and the maximum strain; higher values of $G'_{\gamma max}$, $\Delta G'/G'_{\gamma min}$, G''_{max}, and Tan delta were also observed here. These findings appear to be in line with the observations from the crosslinking experiments: hBN-OH has a better interaction with silica; the extent of the filler network is lower with respect to the composite, with silica as the only filler, but it is larger than that in the presence of hBN-p. Moreover, the interaction with silica could hinder, to some extent, the parallel placement of the layers commented on above.

3.4.3. Dynamic Mechanical Properties from Axial Compression Tests

Dynamic mechanical properties were determined in the axial mode by applying the sinusoidal stress in compression, with a pre-strain of −25%, to remove the filler network or—at least—to reduce it significantly. Details of the procedure are provided in the Experimental Section. Data of E′, E″, and Tan δ, measured at 10 °C, 23 °C, and 70 °C, respectively, are provided in Table 7; the dependences of E′ and Tan δ on temperature are shown in Figure 13a and Figure 13b, respectively. The dependence of E″ on the temperature is shown in Figure S6 in the Supplementary Materials.

Table 7. Axial dynamic mechanical properties of S-SBR 4630 compounds measured in compression.

	T [°C]	Silica	15-hBN-p	30-hBN-p	15-hBN-OH	30-hBN-OH
E′ [MPa]	10	7.6	8.0	8.8	8.3	8.2
	23	6.6	6.9	7.5	7.1	7.0
	70	5.2	5.6	6.0	5.5	5.4
E″ [MPa]	10	3.8	3.8	4.1	4.0	4.1
	23	2.3	2.3	2.4	2.5	2.5
	70	0.6	0.6	0.5	0.6	0.6
Tanδ	10	0.49	0.48	0.47	0.49	0.50
	23	0.35	0.33	0.33	0.35	0.35
	70	0.12	0.10	0.09	0.11	0.11
ΔE′ (E′@10 °C–E′@70 °C) (MPa)		2.4	2.4	2.8	2.7	2.8

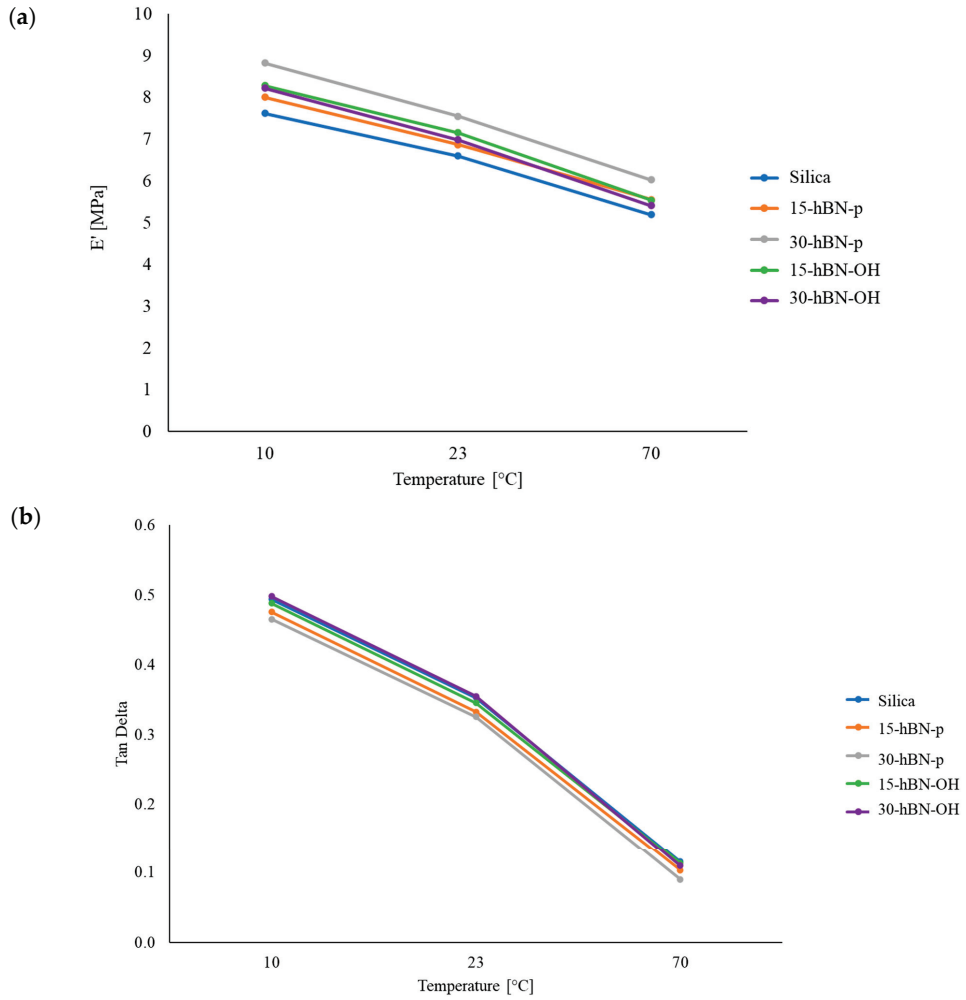

Figure 13. Axial dynamic mechanical properties of S-SBR 4630 compounds measured in compression: (**a**) storage modulus vs. temperature; (**b**) tan delta vs. temperature.

An increase in E′ was obtained at all the temperatures, with both hBN-p and hBN-OH in the place of silica. The values of E′ increased with the hBN-p content and the difference with respect to the silica composite was about 15% for 30% replacement at 70 °C. On the contrary, the E′ values were very similar in both the composites with hBN-OH. These results could be—to some extent—unexpected. In fact, it was mentioned above that hBN-p should have a poor interaction with silica, whereas hBN-OH should establish interactions

and even chemical bonds through the functional groups. However, these data could be explained by taking the procedure into consideration (procedure shown in Figure S1 in the Supplementary Materials); this procedure was used for the preparation of the specimens to be analyzed. As explained above, the uncured composite from the mixer was processed on the two-roll mill. To measure the axial dynamic mechanical properties, small cylinders were then prepared by rolling up the rubber sheet obtained from the two-roll mill. The applied sinusoidal stress was found to be parallel to the longest direction of the cylinder. Platelets lay along such a direction and experienced the applied stress. The increase in the dynamic rigidity measured in the axial mode, in the presence of the reduction in the shear moduli, could thus be explained with the anisotropy of the nanocomposites [65,66]. The results obtained with hBN-OH could be explained better with the more successful hBN-OH/silica interaction, which could also lead to a less parallel orientation of the hBN-OH layers. Dwelling upon the tan delta values of the composites with hBN-OH, they are in line or even higher at low temperatures and lower at high temperatures. This is an indication of the interaction between the filler network formed by silica and hBN-OH and the polymer chains, through the sulfur-based silane (TESPT), which acts as coupling agent.

3.4.4. Tensile Properties

Tensile properties were measured at a nominal room temperature through quasi-static measurements. The values of the stresses at different elongations, stresses, and energies at break are shown in Table 8; the curves of stress vs. strain are shown in Figure 14.

Table 8. Tensile properties of composites of Table 1.

	Silica	**15-hBN-p**	**30-hBN-p**	**15-hBN-OH**	**30-hBN-OH**
$\sigma_{50\%}$ [MPa]	1.6 ± 0.02	1.8 ± 0.03	2.1 ± 0.05	1.7 ± 0.03	1.7 ± 0.013
$\sigma_{100\%}$ [MPa]	2.9 ± 0.01	3.2 ± 0.06	3.5 ± 0.1	3.3 ± 0.07	3.1 ± 0.05
$\sigma_{300\%}$ [MPa]	7.9 ± 0.21	7.5 ± 0.13	7.6 ± 0.36	8.4 ± 0.34	6.9 ± 0.23
σ_{break} [MPa]	18.7 ± 0.65	17.8 ± 1.59	16.6 ± 1.61	16.8 ± 2.60	18.4 ± 1.28
ε_{break} [%]	361.3 ± 9.62	359.1 ± 23.24	343.2 ± 20.24	325.9 ± 22.86	401.9 ± 21.67
Energy break [MJ/m^3]	28.2 ± 1.80	26.8 ± 3.54	24.4 ± 3.54	23.2 ± 3.84	31.5 ± 3.38

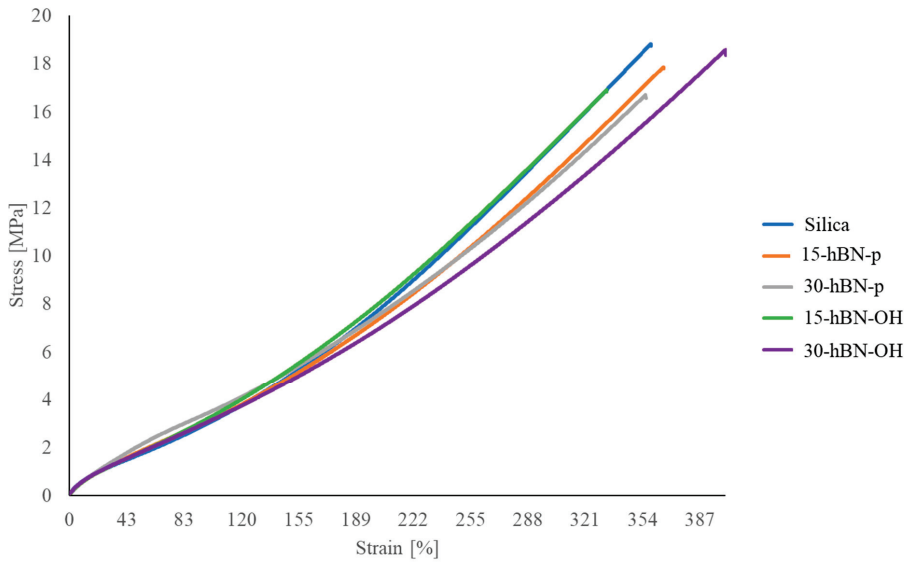

Figure 14. Tensile curves of S-SBR 4630 compounds obtained through stress–strain experiments.

The partial replacement of silica with hBN, either pristine or functionalized, brought about an increase in the stresses at low elongations, up to 100%. In the case of hBN-p, the values at 300% elongation and the ultimate properties are substantially in line with those of the reference composite for 15% replacement, whereas they are lower in the presence of

a greater amount of hBN. These findings, in particular the higher rigidity at low strains, are typical of a nanofiller with high aspect ratio and have been observed also in the case of nanofillers such as carbon nanotubes and sepiolite [68,69]. Similar behavior is shown by 15-hBN-OH, whereas the composite with 30% hBN shows better ultimate properties. Without stretching too far into making comments that are not supported by experimental data, one could hypothesize a positive role played by the tight interaction of the silica/hBN-OH system with the elastomer chains.

3.4.5. High-Pressure Capillary Viscometer (HKV)

The poor rheological properties of silica-based composites were mentioned in the Introduction. The investigation of the rheological properties of the composites shown Table 1 (i.e., the investigation of the effect of hBN, both pristine and functionalized) was performed through high-pressure capillary viscometer (HKV) tests; the methods of these are described in Section 2 The experiments were carried out on the composite with silica as the only filler and on composites with a replacement of 30% in volume of silica, with hBN-p and hBN-OH. Data were collected immediately after the compounding, at t = 0, and after 7 days of storage. Results are reported in Figure 15, Figure 15a, and Figure 15b, respectively. In the graphs, the volume (mm^3) of composites released by the instrument was plotted versus time.

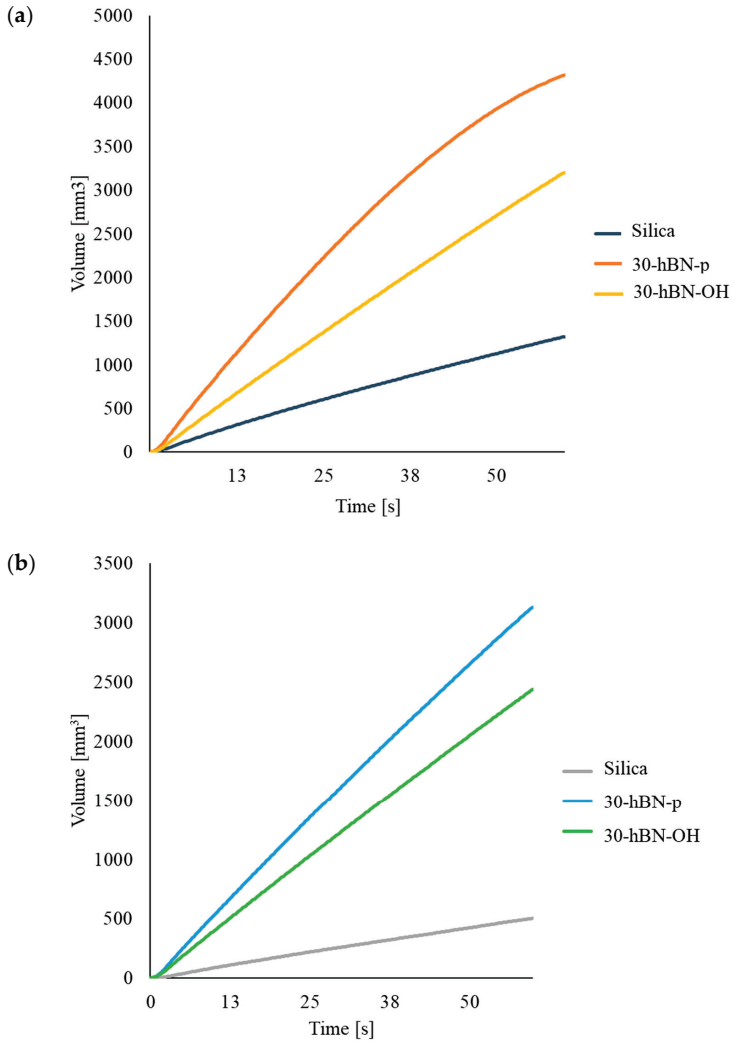

Figure 15. Measurement in mm^3 of composites released by the high-pressure capillary viscometer vs. time: (**a**) immediately after compounding, (t = 0); (**b**) after 7 days (t = 7).

At t = 0, the 30% hBN-p-based composite exhibits the best processability: the largest volume of material flows per unit of time. The lowest amount of extruded composite was obtained with the composite with only silica as the filler, whereas the 30% hBN-OH compound had an intermediate behavior.

After 7 days storage, the curves of the different composites showed the same relative placement, and those of the hBN-p- and hBN-OH-based compounds appear closer to each other. The two composites with hBN show remarkably better processability in comparison with the composite with only silica as the filler: the amount of composite extruded from the viscometer, with respect to the silica-based composite, was about 500% more with hBN-p and about 400% more with hBN-OH.

Hence, hBN-p and hBN-OH provide substantially improved rheological behavior of the silica-based elastomer composite, both immediately after compounding and after 7 days of storage. The much better processability after 7 days indicates that the shelf life of the silica-based composites can be improved by adding either hBN-p or hBN-OH. These findings are reasonably a consequence of the lower extent of the filler network. The better results obtained with hBN-p could be explained with the poorer interaction with silica.

3.4.6. Transmission Electron Microscopy Analyses (TEM) of Rubber Composites

Transmission electron microscopy (TEM) analysis was performed with the aim of investigating the filler dispersion on the vulcanized composites of Table 1, hence with silica as the only filler and with the silica/hBN-p and silica/hBN-OH as the hybrid filler systems. TEM micrographs are shown in Figure 16. Fifteen low-magnification micrographs and fifteen high-magnification micrographs were taken for each composite; representative images were selected. Low-magnification micrographs, where the TEM grid is visible, were taken to allow the observation of a larger area of sample, thus making a first evaluation of filler dispersion possible, although these are still related to a restricted sample area. Red arrows highlight sample flaws in the selected micrographs.

The micrographs of the composites with 15% silica replacement are shown in Figure 16b (hBN-p) and Figure 16d (hBN-OH); those of the composites with 30% silica replacement are shown in Figure 16c (hBN-p) and Figure 16e (hBN-OH).

Micrographs at high magnification of composites with hBN-p reveal the presence of flaws; more specifically, they show detachments of the elastomer matrix from the filler, at both levels of hBN-p content: 15% (Figure 16B) and 30% (Figure 16C). On the contrary, no large flaws are visible in the high-magnification micrographs of the composites with hBN-OH, both at 15% (Figure 16D) and 30% (Figure 16E) content.

The low-magnification micrograph of the 15% hBN-OH composite (Figure 16d) shows a level of homogeneity that is very close to the one of the reference silica composite (Figure 16a). The low-magnification micrograph of the 30% hBN-OH composite (Figure 16e) highlights a good sample homogeneity, with the presence of a few aggregates.

In general, samples containing hBN-p are characterized by micrographs with large agglomerates that induce points of detachment between the filler and the rubber matrix. Such large agglomerates, with a lamellar structure, can be attributed to hBN and led the researchers to hypothesize the presence of poor hBN-p dispersion. When hBN-OH is employed, a higher homogeneity is observable in both the low- and high-magnification micrographs. A limited number of hBN aggregates is visible with little or no rubber–filler detachments.

Overall, hBN-OH appears more homogeneously dispersed in the TEM micrographs, leading the researchers to hypothesize the presence of a generally higher level of dispersion of hBN-OH with respect to hBN-p in the considered elastomer composites, at both levels of silica replacement. The best filler dispersion in the presence of hBN seems to be achieved with a 15% replacement of silica with hBN-OH.

The OH groups in hBN-OH appear to favor the compatibilization and the dispersion of hBN-OH. The chemical modification of h-BN could promote the interaction with silica and with silica's coupling agent, the sulfur-based silane, either directly or mediated by

silica. Thus, alongside an improved interaction with silica, the interaction with the rubber matrix could be favored.

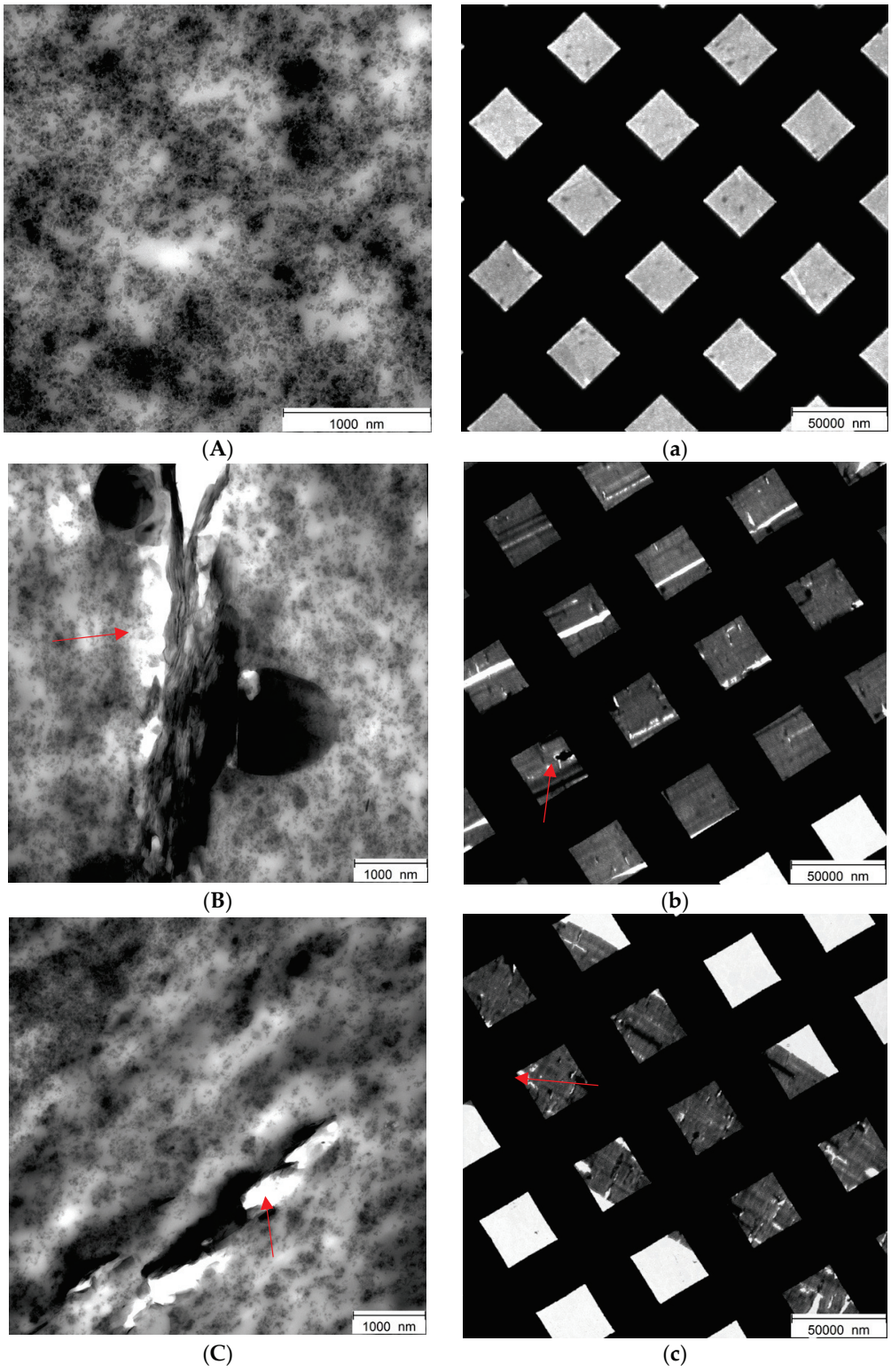

Figure 16. *Cont.*

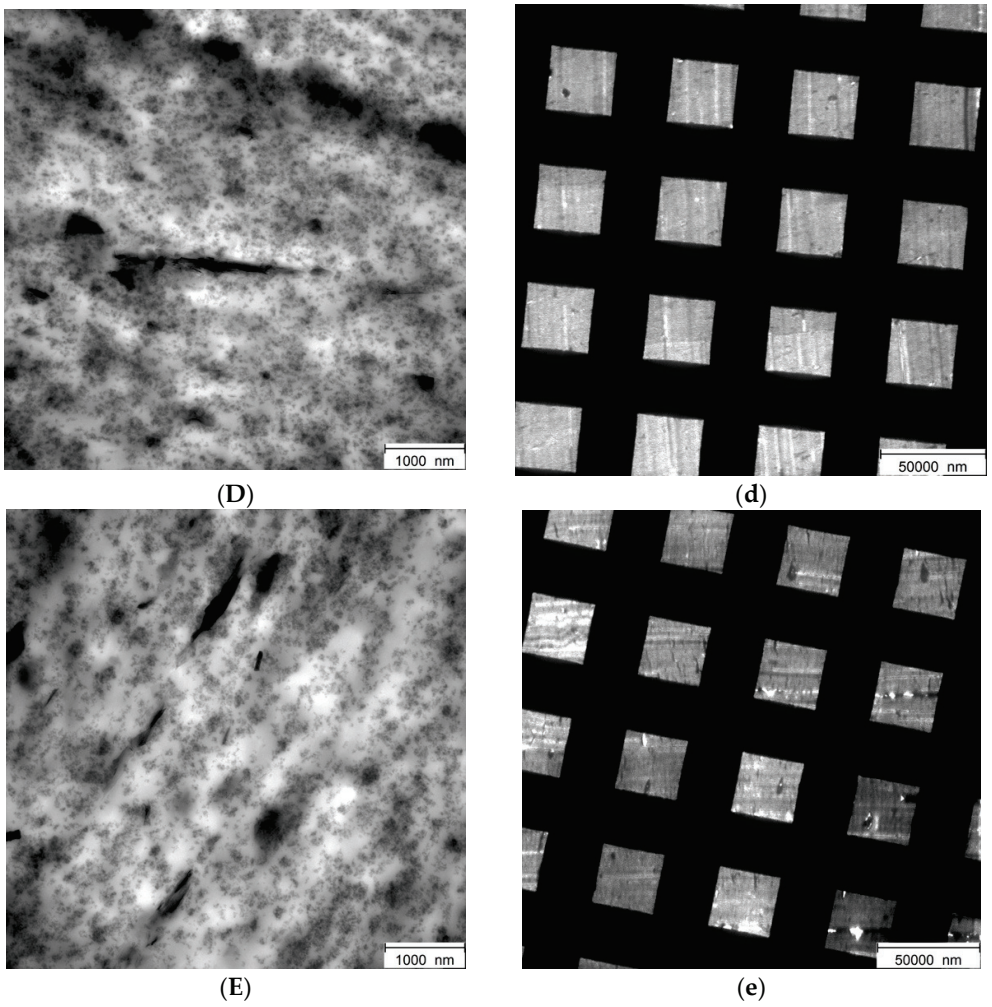

Figure 16. Micrographs of the following composites: silica (**A**,**a**), 15hBN-p (**B**,**b**), 30-hBN-p (**C**,**c**), 15-hBN-OH (**D**,**d**), 30-hBN-OH (**E**,**e**), at higher magnifications (**A**–**E**) and at lower magnifications (**a**–**e**).

4. Conclusions

This work demonstrates that a 2D nanomaterial such as hBN, which has attracted enormous interest over recent years for numerous applications in various fields, can also substantially improve the properties of a silica-based elastomer composite when used in the place of a minor amount of silica. hBN-p was a commercially available type and was exfoliated and functionalized using an ecofriendly mechanical treatment—ball milling—without any chemical substance. -NH- and -OH functional groups were introduced on hBN, as shown in the FT-IR spectra. The defective sites created by the milling were able to react with the molecules present in the headspace of the jar as well as with the water used for washing the samples. TGA revealed the lower thermal stability of the milled samples and the maximum number of functional groups was estimated to be about 6% by mass. The functional groups were in the peripheral positions, mainly on the edges, as suggested by the by X-ray analyses, which revealed the persistence of the (002) reflection and the absence of (00l) reflections at lower 2theta angles. The mechanical treatment allowed the researchers to prepare a few layers of hBN-OH. With 5 h as the milling time, the lateral size of the layers was substantially unaltered with respect to hBN-p, as revealed through HR-TEM, and the order in the basal planes was still detected, as shown by WAXD.

Silica-based elastomer composites were prepared with both hBN-p and hBN-OH, milled for 5 h, in place of 15% and 30% by volume of silica. The processability of the composite was drastically improved, particularly after one week storage at room temperature. The composite extruded using a high-pressure capillary viscometer was increased,

with respect to the reference silica composite, by about 500% and 400% using hBN-p and hBN-OH, respectively. Both hBNs, used in the place of silica, promoted a lower Payne effect, a higher dynamic rigidity and similar or lower hysteresis. The results suggest that hBN-p has a more significant ability to disrupt the silica-based network. However, homogenous composites without evidence of flaws in HR-TEM micrographs and with the best dependence on temperature of tan delta were obtained with h-BN-OH, which appears to be the best candidate for the development of elastomer composites for use on a very large scale, such as in tire tread compounds.

The simple and ecofriendly preparation of hBN-OH appears to be an appropriate solution for scaling up the whole technology.

Supplementary Materials: The following supporting information can be downloaded at: https://www.mdpi.com/article/10.3390/nano14010030/s1, Figure S1: Procedures for the preparation of specimens for axial dynamic-mechanical analyses (a) and shear dynamic mechanical analyses (b); Figure S2: TGA thermograms under air of hBN-OHas5h (a); hBN-OHw5h (b); hBN-OHas10h (c) and hBN-OHw10h; (d). Pristine hBN (e); Figure S3: Crosslinking curves of composites of Table 1; Table S1: Shear dynamic-mechanical properties from strain sweep experiments of composites of Table 1; Figure S4: G″ vs. strain for composites of Table 1; Figure S5: G plot for for composites of Table 1; Figure S6: E″ vs. Temperature for for composites of Table 1.

Author Contributions: Conceptualization, C.B and M.G.; Methodology, F.M., G.P., U.G. and V.B.; Validation, U.G. and V.B.; Formal analysis, F.M.; Investigation, F.M., G.P. and V.B.; Data curation, F.M.; Writing—original draft, F.M., G.P., V.B. and M.G.; Writing—review & editing, F.M., V.B. and M.G.; Supervision, U.G., V.B. and M.G.; Project administration, V.B. and M.G.; Funding acquisition, V.B. and M.G. All authors have read and agreed to the published version of the manuscript.

Funding: This research received no external funding.

Data Availability Statement: Data is contained within the article.

Acknowledgments: Pirelli Tire is gratefully acknowledged for the financial support to the activities of Gea Prioglio and Federica Magaletti. Thanks are due to Made in Italy—Circular and Sustainable (MICS) Extended Partnership funded by the European Union Next-Generation EU (Piano Nazionale di Ripresa e Resilienza (PNRR)—Missione 4, Componente 2, Investimento 1.3—D.D. 1551.11-10-2022, PE00000004) for financial support.

Conflicts of Interest: The authors declare no conflict of interest.

References

1. Boehm, H.P.; Clauss, A.; Fischer, G.O.; Hofmann, U. Das adsorptionsverhalten sehr dünner kohlenstoff-folien. *Z. Für Anorg. Und Allg. Chem.* **1962**, *316*, 119–127. [CrossRef]
2. Novoselov, K.S.; Geim, A.K.; Morozov, S.V.; Jiang, D.; Zhang, Y.; Dubonos, S.V.; Grigorieva, I.V.; Firsov, A.A. Electric field effect in atomically thin carbon films. *Science* **2004**, *306*, 666–669. [CrossRef]
3. Geim, A.K.; Novoselov, K.S. The rise of graphene. In *Nanoscience and Technology: A Collection of Reviews from Nature Journals*; World Scientific: Singapore, 2010; p. 11.
4. Chimene, D.; Alge, D.L.; Gaharwar, A.K. Two-dimensional nanomaterials for biomedical applications: Emerging trends and future prospects. *Adv. Mater.* **2015**, *27*, 7261–7284. [CrossRef]
5. Coleman, J.N.; Lotya, M.; O'Neill, A.; Bergin, S.D.; King, P.J.; Khan, U.; Young, K.; Gaucher, A.; De, S.; Smith, R.J.; et al. Two-dimensional nanosheets produced by liquid exfoliation of layered materials. *Science* **2011**, *331*, 568–571. [CrossRef]
6. Khan, K.; Tareen, A.K.; Aslam, M.; Wang, R.; Zhang, Y.; Mahmood, A.; Ouyang, Z.; Zhang, H.; Guo, Z. Recent developments in emerging two-dimensional materials and their applications. *J. Mater. Chem. C* **2019**, *8*, 387–440. [CrossRef]
7. Wang, Z.; Zhu, W.; Qiu, Y.; Yi, X.; Bussche, A.v.D.; Kane, A.; Gao, H.; Koski, K.; Hurt, R. Biological and environmental interactions of emerging two-dimensional nanomaterials. *Chem. Soc. Rev.* **2016**, *45*, 1750–1780. [CrossRef]
8. Zhang, H. Ultrathin Two-Dimensional Nanomaterials. *ACS Nano* **2015**, *9*, 9451–9469. [CrossRef]
9. Murali, A.; Lokhande, G.; Deo, K.A.; Brokesh, A.; Gaharwar, A.K. Emerging 2D nanomaterials for biomedical applications. *Mater. Today* **2021**, *50*, 276–302. [CrossRef]
10. Bhati, V.S.; Kumar, M.; Banerjee, R. Gas sensing performance of 2D nanomaterials/metal oxide nanocomposites: A review. *J. Mater. Chem. C* **2021**, *9*, 8776–8808. [CrossRef]
11. Marian, M.; Berman, D.; Rota, A.; Jackson, R.L.; Rosenkranz, A. Layered 2D nanomaterials to tailor friction and wear in machine elements—A review. *Adv. Mater. Interfaces* **2021**, *9*, 2101622. [CrossRef]

12. Chen, W.; Shi, H.; Xin, H.; He, N.R.; Yang, W.; Gao, H. Friction and wear properties of Si3N4-hBN ceramic composites using different synthetic lubricants. *Ceram. Int.* **2018**, *44*, 16799–16808. [CrossRef]
13. Cho, D.-H.; Kim, J.-S.; Kwon, S.-H.; Lee, C.; Lee, Y.-Z. Evaluation of hexagonal boron nitride nano-sheets as a lubricant additive in water. *Wear* **2013**, *302*, 981–986.
14. Corrigan, F.R.; Bundy, F.P. Direct transitions among the allotropic forms of boron nitride at high pressures and temperatures. *J. Chem. Phys.* **1975**, *63*, 3812–3820. [CrossRef]
15. Corso, M.; Auwärter, W.; Muntwiler, M.; Tamai, A.; Greber, T.; Osterwalder, J. Boron nitride nanomesh. *Science* **2004**, *303*, 217–220. [CrossRef] [PubMed]
16. Zhan, Y.; Lago, E.; Santillo, C.; Castillo, A.E.E.D.R.; Hao, S.; Buonocore, G.G.; Chen, Z.; Xia, H.; Lavorgna, M.; Bonaccorso, F. An anisotropic layer-by-layer carbon nanotube/boron nitride/rubber composite and its application in electromagnetic shielding. *Nanoscale* **2020**, *12*, 7782–7791. [CrossRef] [PubMed]
17. Ooi, N.; Rajan, V.; Gottlieb, J.; Catherine, Y.; Adams, J.B. Structural properties of hexagonal boron nitride. *Model. Simul. Mater. Sci. Eng.* **2006**, *14*, 515. [CrossRef]
18. Bao, J.; Jeppson, K.; Edwards, M.; Fu, Y.; Ye, L.; Lu, X.; Liu, J. Synthesis and applications of two-dimensional hexagonal boron nitride in electronics manufacturing. *Electron. Mater. Lett.* **2016**, *12*, 1–16. [CrossRef]
19. Shang, Y.; Yang, G.; Su, F.; Feng, Y.; Ji, Y.; Liu, D.; Yin, R.; Liu, C.; Shen, C. Multilayer polyethylene/hexagonal boron nitride composites showing high neutron shielding efficiency and thermal conductivity. *Compos. Commun.* **2020**, *19*, 147–153. [CrossRef]
20. Fan, Y.; Cho, U.R. Effects of graphite and boron nitride based fillers on mechanical, thermal conductive, and thermo-physical properties in solution styrene–butadiene rubber. *Polym. Compos.* **2019**, *40*, E1426–E1433. [CrossRef]
21. Weng, Q.; Wang, B.; Wang, X.; Hanagata, N.; Li, X.; Liu, D.; Wang, X.; Jiang, X.; Bando, Y.; Golberg, D. Highly water-soluble, porous, and biocompatible boron nitrides for anticancer drug delivery. *ACS Nano* **2014**, *8*, 6123–6130. [CrossRef]
22. Mukheem, A.; Shahabuddin, S.; Akbar, N.; Miskon, A.; Sarih, N.M.; Sudesh, K.; Khan, N.A.; Saidur, R.; Sridewi, N. Boron nitride doped polyhydroxyalkanoate/chitosan nanocomposite for antibacterial and biological applications. *Nanomaterials* **2019**, *9*, 645. [CrossRef]
23. Hui, S.; Ji, R.; Zhang, H.; Huang, C.; Xu, F.; Sun, L.; Xia, Y.; Lin, X.; Ma, L.; Peng, H.; et al. N-Octadecane Encapsulated by Assembled BN/GO Aerogels for Highly Improved Thermal Conductivity and Energy Storage Capacity. *Nanomaterials* **2023**, *13*, 2317. [CrossRef] [PubMed]
24. Kim, H.; Uddin, I.; Watanabe, K.; Taniguchi, T.; Whang, D.; Kim, G.-H. Conversion of Charge Carrier Polarity in $MoTe_2$ Field Effect Transistor via Laser Doping. *Nanomaterials* **2023**, *13*, 1700. [CrossRef] [PubMed]
25. Peng, Y.; Yang, Y.; Xiao, K.; Yang, Y.; Ding, H.; Deng, J.; Sun, W. Direct Synthesis of Vertical Self-Assembly Oriented Hexagonal Boron Nitride on Gallium Nitride and Ultrahigh Photoresponse Ultraviolet Photodetectors. *Nanomaterials* **2023**, *13*, 1546. [CrossRef] [PubMed]
26. Ye, X.; Du, Y.; Wang, M.; Liu, B.; Liu, J.; Jafri, S.H.M.; Liu, W.; Papadakis, R.; Zheng, X.; Li, H. Advances in the field of two-dimensional crystal-based photodetectors. *Nanomaterials* **2023**, *13*, 1379. [CrossRef] [PubMed]
27. Li, S.; Shen, Y.; Jia, X.; Xu, M.; Zong, R.; Liu, G.; Liu, B.; Huai, X. Dopamine-Mediated Graphene Bridging Hexagonal Boron Nitride for Large-Scale Composite Films with Enhanced Thermal Conductivity and Electrical Insulation. *Nanomaterials* **2023**, *13*, 1210. [CrossRef] [PubMed]
28. Chen, P.; Ge, X.; Zhang, Z.; Yin, S.; Liang, W.; Ge, J. Silicone-Based Thermally Conductive Gel Fabrication via Hybridization of Low-Melting-Point Alloy–Hexagonal Boron Nitride–Graphene Oxide. *Nanomaterials* **2023**, *13*, 490. [CrossRef]
29. Sun, L.; Zou, Y.; Ma, M.; Li, G.; Wang, X.; Zhang, X.; Zhao, Z. Synthesis of cBN-hBN-SiCw Nanocomposite with Superior Hardness, Strength, and Toughness. *Nanomaterials* **2022**, *13*, 37. [CrossRef]
30. Mballo, A.; Srivastava, A.; Sundaram, S.; Vuong, P.; Karrakchou, S.; Halfaya, Y.; Gautier, S.; Voss, P.L.; Ahaitouf, A.; Salvestrini, J.P.; et al. Towards P-type conduction in hexagonal boron nitride: Doping study and electrical measurements analysis of hBN/AlGaN heterojunctions. *Nanomaterials* **2021**, *11*, 211. [CrossRef]
31. Roy, S.; Zhang, X.; Puthirath, A.B.; Meiyazhagan, A.; Bhattacharyya, S.; Rahman, M.M.; Ajayan, P.M. Structure, properties and applications of two-dimensional hexagonal boron nitride. *Adv. Mater.* **2021**, *33*, 2101589. [CrossRef]
32. Molaei, M.J.; Younas, M.; Rezakazemi, M. A comprehensive review on recent advances in two-dimensional (2d) hexagonal boron nitride. *ACS Appl. Electron. Mater.* **2021**, *3*, 5165–5187. [CrossRef]
33. Li, M.; Huang, G.; Chen, X.; Yin, J.; Zhang, P.; Yao, Y.; Shen, J.; Wu, Y.; Huang, J. Perspectives on environmental applications of hexagonal boron nitride nanomaterials. *Nano Today* **2022**, *44*, 101486. [CrossRef]
34. Cao, X.; Zhang, R.; Zhang, N.; Chen, L.; Li, X. Flexible composite phase change material with improved hydrophobicity and thermal conductivity characters for thermal management. *J. Energy Storage* **2023**, *72*, 108641. [CrossRef]
35. Transforming Our World: The 2030 Agenda for Sustainable Development | Department of Economic and Social Affairs. Available online: https://un.org/ (accessed on 4 September 2023).
36. World Tire Market Outlook 2020–2025—Global Market Forecast to Reach 2.7 Billion Units by 2025. Available online: https://prnewswire.com/ (accessed on 4 September 2023).
37. Hall, D.E.; Moreland, J.C. Fundamentals of rolling resistance. *Rubber Chem. Technol.* **2001**, *74*, 525–539. [CrossRef]
38. Chevalier, Y.; Morawski, J.C. Precipitated Silica with Morphological Properties, Process for Producing It and Its Application, Especially as a Filler. Patent EP 0157703 B1, 29 March 1985.

39. Legrand, A.P. On the silica edge. In *The Surface Properties of Silicas*; Legrand, A.P., Ed.; Wiley and Sons: New York, NY, USA, 1998; pp. 1–20.
40. Locatelli, D.; Bernardi, A.; Rubino, L.R.; Gallo, S.; Vitale, A.; Bongiovanni, R.; Barbera, V.; Galimberti, M. Biosourced *Janus* Molecules as Silica Coupling Agents in Elastomer Composites for Tires with Lower Environmental Impact. *ACS Sustain. Chem. Eng.* **2023**, *11*, 2713–2726. [CrossRef]
41. Ramier, J.; Chazeau, L.; Gauthier, C.; Guy, L.; Bouchereau, M.N. Influence of silica and its different surface treatments on the vulcanization process of silica filled SBR. *Rubber Chem. Technol.* **2007**, *80*, 183–193. [CrossRef]
42. Guerra, S.; Barbera, V.; Galimberti, M.; Giese, U. Effect of the Functionalization of graphene Nanoplatelets with a Janus Pyrrole Molecule on mechanical and electrical properties of natural Rubber Nanocomposites. *KGK Kautsch. Gummi Kunststoffe* **2020**, *2020*, 17–25.
43. Friščić, T.; Mottillo, C.; Titi, H.M. Mechanochemistry for synthesis. *Angew. Chem.* **2020**, *132*, 1030–1041. [CrossRef]
44. Weng, Q.; Wang, X.; Wang, X.; Bando, Y.; Golberg, D. Functionalized hexagonal boron nitride nanomaterials: Emerging properties and applications. *Chem. Soc. Rev.* **2016**, *45*, 3989–4012. [CrossRef]
45. Zhang, K.; Feng, Y.; Wang, F.; Yang, Z.; Wang, J. Two dimensional hexagonal boron nitride (2D-hBN): Synthesis, properties and applications. *J. Mater. Chem. C* **2017**, *5*, 11992–12022. [CrossRef]
46. Lin, Y.; Williams, T.V.; Xu, T.-B.; Cao, W.; Elsayed-Ali, H.E.; Connell, J.W. Aqueous dispersions of few-layered and monolayered hexagonal boron nitride nanosheets from sonication-assisted hydrolysis: Critical role of water. *J. Phys. Chem. C* **2011**, *115*, 2679–2685. [CrossRef]
47. Sainsbury, T.; Satti, A.; May, P.; Wang, Z.; McGovern, I.; Gun'ko, Y.K.; Coleman, J. Oxygen radical functionalization of boron nitride nanosheets. *J. Am. Chem. Soc.* **2012**, *134*, 18758–18771. [CrossRef] [PubMed]
48. Lee, D.; Lee, B.; Park, K.H.; Ryu, H.J.; Jeon, S.; Hong, S.H. Scalable exfoliation process for highly soluble boron nitride nanoplatelets by hydroxide-assisted ball milling. *Nano Lett.* **2015**, *15*, 1238–1244. [CrossRef] [PubMed]
49. Ma, Z.-S.; Ding, H.-L.; Liu, Z.; Cheng, Z.-L. Preparation and tribological properties of hydrothermally exfoliated ultrathin hexagonal boron nitride nanosheets (BNNSs) in mixed NaOH/KOH solution. *J. Alloy. Compd.* **2019**, *784*, 807–815. [CrossRef]
50. Yan, W.; Chen, X.; Lim, J.S.K.; Chen, H.; Gill, V.; Lambourne, A.; Hu, X. Epoxy-assisted ball milling of boron nitride towards thermally conductive impregnable composites. *Compos. Part A Appl. Sci. Manuf.* **2022**, *156*, 106868. [CrossRef]
51. Pakdel, A.; Bando, Y.; Golberg, D. Plasma-assisted interface engineering of boron nitride nanostructure films. *ACS Nano* **2014**, *8*, 10631–10639. [CrossRef]
52. Xiao, F.; Naficy, S.; Casillas, G.; Khan, M.H.; Katkus, T.; Jiang, L.; Liu, H.; Li, H.; Huang, Z. Edge-hydroxylated boron nitride nanosheets as an effective additive to improve the thermal response of hydrogels. *Adv. Mater.* **2015**, *27*, 7196–7203. [CrossRef]
53. Bhimanapati, G.R.; Kozuch, D.; Robinson, J.A. Large-scale synthesis and functionalization of hexagonal boron nitride nanosheets. *Nanoscale* **2014**, *6*, 11671–11675. [CrossRef]
54. Cui, Z.; Oyer, A.J.; Glover, A.J.; Schniepp, H.C.; Adamson, D.H. Large scale thermal exfoliation and functionalization of boron nitride. *Small* **2014**, *10*, 2352–2355. [CrossRef]
55. Shen, T.; Liu, S.; Yan, W.; Wang, J. Highly efficient preparation of hexagonal boron nitride by direct microwave heating for dye removal. *J. Mater. Sci.* **2019**, *54*, 8852–8859. [CrossRef]
56. ISO9924-1 Standard. Available online: https://www.iso.org/standard/84139.html (accessed on 14 December 2023).
57. Standard ISO 37/UNI 6065. Available online: https://www.eurolab.net/it/testler/malzeme-testleri/iso-37-kaucuk-vulkanize-veya-termoplastik-cekme-gerilimi-uzama-ozelliklerinin-tayini/ (accessed on 14 December 2023).
58. Yadav, V.; Kulshrestha, V. Boron nitride: A promising material for proton exchange membranes for energy applications. *Nanoscale* **2019**, *11*, 12755–12773. [CrossRef] [PubMed]
59. Kostoglou, N.; Polychronopoulou, K.; Rebholz, C. Thermal and chemical stability of hexagonal boron nitride (h-BN) nanoplatelets. *Vacuum* **2015**, *112*, 42–45. [CrossRef]
60. Ramier, J.; Gauthier, C.; Chazeau, L.; Stelandre, L.; Guy, L. Payne effect in silica-filled styrene–butadiene rubber: Influence of surface treatment. *J. Polym. Sci. Part B Polym. Phys.* **2007**, *45*, 286–298. [CrossRef]
61. Chazeau, L.; Brown, J.D.; Yanyo, L.C.; Sternstein, S.S. Modulus recovery kinetics and other insights into the Payne effect for filled elastomers. *Polym. Compos.* **2000**, *21*, 202–222. [CrossRef]
62. Hentschke, R. The Payne effect revisited. *Express Polym. Lett.* **2017**, *11*, 278–292. [CrossRef]
63. Çelik, O.N.; Ay, N.; Göncü, Y. Effect of nano hexagonal boron nitride lubricant additives on the friction and wear properties of AISI 4140 steel. *Part. Sci. Technol.* **2013**, *31*, 501–506. [CrossRef]
64. Van Sang, L.; Yano, A.; Osaka, A.I.; Sugimura, N.; Washizu, H. Smoothed particle hydrodynamics and discrete element method coupling for influence of hexagonal boron nitride lubricant particle on friction of elastic coarse-grained micronscale iron. *J. Tribol.* **2021**, *144*, 01190.
65. Samanta, S.; Sahoo, R.R. Covalently linked hexagonal boron nitride-graphene oxide nanocomposites as high-performance oil-dispersible lubricant additives. *ACS Appl. Nano Mater.* **2020**, *3*, 10941–10953. [CrossRef]
66. Agnelli, S.; Pandini, S.; Serafini, A.; Musto, S.; Galimberti, M. Anisotropic nonlinear mechanical behavior in carbon nanotubes/poly (1, 4-cis-isoprene) nanocomposites. *Macromolecules* **2016**, *49*, 8686–8696. [CrossRef]
67. Agnelli, S.; Pandini, S.; Torricelli, F.; Romele, P.; Serafini, A.; Barbera, V.; Galimberti, M. Anisotropic properties of elastomeric nanocomposites based on natural rubber and sp2 carbon allotropes. *Express Polym. Lett.* **2018**, *12*, 713–730. [CrossRef]

68. Bokobza, L.; Chauvin, J.-P. Reinforcement of natural rubber: Use of in situ generated silicas and nanofibres of sepiolite. *Polymer* **2005**, *46*, 4144–4151. [CrossRef]
69. Locatelli, D.; Pavlovic, N.; Barbera, V.; Giannini, L.; Galimberti, M. Sepiolite as reinforcing Filler for Rubber Composites: From the chemical Compatibilization to the commercial Exploitation. *KGK Kautsch. Gummi Kunststoffe* **2020**, *73*, 26–35.

nanomaterials

MDPI

Article

Dissolution Reaction and Surface Modification of UICC Amosite in Mimicked Gamble's Solution: A Step towards Filling the Gap between Asbestos Toxicity and Its Crystal Chemical Features

Alessandro Pacella [1,*], Paolo Ballirano [1,2], Maria Cristina Di Carlo [1], Marzia Fantauzzi [3], Antonella Rossi [3], Elisa Nardi [4], Cecilia Viti [5], Lorenzo Arrizza [6], Antonella Campopiano [7], Annapaola Cannizzaro [7], Andrea Bloise [8,*] and Maria Rita Montereali [9]

1 Department of Earth Sciences, Sapienza University of Rome, Piazzale Aldo Moro 5, 00185 Rome, Italy; paolo.ballirano@uniroma1.it (P.B.); mariacristina.dicarlo@uniroma1.it (M.C.D.C.)
2 Rectoral Laboratory Fibres and Inorganic Particulate, Sapienza University of Rome, Piazzale Aldo Moro 5, 00185 Rome, Italy
3 INSTM Research Unit, Department of Chemical and Geological Sciences, University of Cagliari, 09042 Monserrato, Italy; fantauzzi@unica.it (M.F.); rossi@unica.it (A.R.)
4 Institute for Environmental Protection and Research, ISPRA, Via Vitaliano Brancati 48, 00144 Rome, Italy; elisa.nardi@isprambiente.it
5 Department of Physical, Earth and Environmental Sciences, University of Siena, Via Laterina 8, 53100 Siena, Italy; cecilia.viti@unisi.it
6 Microscopy Center, University of L' Aquila, Via Vetoio, Locality Coppito, 67100 L'Aquila, Italy; lorenzo.arrizza@univaq.it
7 Department of Medicine, Epidemiology, Occupational and Environmental Hygiene, National Institute for Insurance against Accidents at Work (INAIL), Via Fontana Candida 1, 00078 Rome, Italy; a.campopiano@inail.it (A.C.); a.cannizzaro@inail.it (A.C.)
8 Department of Biology, Ecology and Earth Sciences, University of Calabria, V. P. Bucci, 87036 Arcavacata di Rende, Italy
9 Italian National Agency for New Technologies, ENEA, Casaccia Research Centre, Via Anguillarese 301, 00123 Rome, Italy; mariarita.montereali@enea.it
* Correspondence: alessandro.pacella@uniroma1.it (A.P.); andrea.bloise@unical.it (A.B.)

Citation: Pacella, A.; Ballirano, P.; Di Carlo, M.C.; Fantauzzi, M.; Rossi, A.; Nardi, E.; Viti, C.; Arrizza, L.; Campopiano, A.; Cannizzaro, A.; et al. Dissolution Reaction and Surface Modification of UICC Amosite in Mimicked Gamble's Solution: A Step towards Filling the Gap between Asbestos Toxicity and Its Crystal Chemical Features. *Nanomaterials* **2023**, *13*, 2933. https://doi.org/10.3390/nano13222933

Academic Editor: Meiwen Cao

Received: 4 October 2023
Revised: 2 November 2023
Accepted: 10 November 2023
Published: 12 November 2023

Abstract: This study focuses on the dissolution process and surface characterization of amosite fibres following interaction with a mimicked Gamble's solution at a pH of 4.5 and T = 37 °C, up to 720 h. To achieve this, a multi-analytical approach was adopted, and the results were compared to those previously obtained on a sample of asbestos tremolite and UICC crocidolite, which were investigated under the same experimental conditions. Combining surface chemical data obtained by XPS with cation release quantified by ICP-OES, an incongruent behaviour of the fibre dissolution was highlighted for amosite fibres, similarly to asbestos tremolite and UICC crocidolite. In particular, a preferential release of Mg and Ca from the amphibole structure was observed, in agreement with their Madelung site energies. Notably, no Fe release from amosite fibres was detected in our experimental conditions (pH of 4.5 and atmospheric pO_2), despite the occurrence of Fe(II) at the *M*(4) site of the amphibole structure, where cations are expected to be rapidly leached out during mineral dissolution. Moreover, the oxidation of both the Fe centres initially present on the fibre surface and those promoted from the bulk, because of the erosion of the outmost layers, was observed. Since biodurability (i.e., the resistance to dissolution) is one of the most important toxicity parameters, the knowledge of the surface alteration of asbestos possibly occurring in vivo may help to understand the mechanisms at the basis of its long-term toxicity.

Keywords: asbestos; UICC amosite; fibre dissolution; Gamble's solution

1. Introduction

The term asbestos refers to a group including five fibrous amphiboles (amosite, i.e., the fibrous variety of cummingtonite-grunerite; tremolite; actinolite; crocidolite, i.e., the fibrous variety of riebeckite; and anthophyllite) and one fibrous serpentine mineral (chrysotile) [1]. Since the industrial age, asbestos has been intensively used in many products, mostly including building materials, friction pads, and heat-resistant fabrics, due to its physical and chemical properties, such as high mechanical strength, thermal insulation, and resistance to high temperature [2]. The global asbestos industry experienced rapid expansion during the 1960s and 1970s [3], and approximately 210 million tons of asbestos fibres were extracted worldwide between 1900 and 2015 [4]. However, after World War II, an increasing number of scientific studies revealed that the inhalation of asbestos can cause malignant mesothelioma, lung diseases like carcinoma, asbestosis, and others [5]. Accordingly, in 1989, the International Agency for Research on Cancer (IARC) classified asbestos as Group 1 "substances carcinogenic to humans" [6]. Today, asbestos use is banned in more than 50 countries (International Ban Asbestos Secretariat, 2019) [7].

Today, the toxicity of inhaled asbestos is considered the result of a complex multistep process governed by the interplay of all the physical/chemical and structural characteristics of fibres, including morphology, chemical composition, surface reactivity, and biodurability/biopersistence [8–16]. Among these factors, Fenton active iron ions exposed on the fibre surface are considered to play a primary role by yielding $HO^{\bullet}$ radicals, which have a high potency to damage DNA, proteins, and lipids, and hence to induce carcinogenicity [17–20]. Because of this complexity, there are still open issues and disputes about the molecular mechanism/s at the basis of the toxicity and carcinogenicity of mineral fibres [21].

Recently, surface reactivity studies on fibrous amphiboles (crocidolite and tremolite) carried out by some of the current authors highlighted that the $HO^{\bullet}$ production is related to specific surface Fe sites rather than the total Fe content of the minerals [22–24]. Moreover, it was established that due to leaching under physiological conditions, the surface modifications of the fibres may change the radical yield of amphibole asbestos depending on fibre crystal chemistry, surface area, and leaching solution [22,23].

Hence, the knowledge of the fibre alteration occurring in simulated biological fluids is the prerequisite step to understand how fibres may react with their biological surrounding. Notably, this piece of information may help to shed new light on the mechanisms of asbestos-induced toxicity.

This work focuses on the surface modifications of amosite fibres during incubation in a mimicked Gamble's solution (MGS) at pH 4.5, up to one month. Leached fibres were studied by using a multi-analytical approach: field-emission scanning electron microscopy (FE-SEM) was used to characterize the fibre morphology and inductively coupled plasma optical emission spectrometry (ICP-OES) was employed to measure the cation release into the leaching solution. The analytical approach based on X-ray photoelectron spectroscopy (XPS), exploited for characterizing the other asbestos fibres, was here adapted to monitoring possible changes of surface chemistry, and includes the Fe speciation of the amosite. Powder X-ray diffraction (PXRD) and high-resolution transmission electron microscopy (HR-TEM) were used to observe possible nanostructural modification of the fibres. The results are discussed comparing them with those obtained on asbestos tremolite and crocidolite previously investigated under the same experimental conditions [25].

2. Materials and Methods

2.1. Materials

A sample of amosite (fibrous grunerite) standard sample from Penge mine (South Africa), supplied by the Union International for Cancer Control (UICC), was investigated in this work. The detailed crystal chemical and structural characterization of the sample is reported in Ballirano et al. [26]. The corresponding empirical formula is: $^{A}(Na_{0.02})_{\Sigma 0.02}{}^{B}(Fe^{2+}{}_{1.54}Mn_{0.29}Na_{0.10}Ca_{0.07})_{\Sigma 2.00}{}^{C}(Fe^{2+}{}_{2.92}Mg_{1.93}Fe^{3+}{}_{0.15})_{\Sigma 5.00}{}^{T}(Si_{7.93}Al_{0.07})_{\Sigma 8.00}O_{22.00}{}^{W}(OH_{2.00})_{\Sigma 2.00}$.

Rietveld refinement results evidenced that Fe^{2+} is allocated in the octahedral layer following the site preferences $M(1) \approx M(3) > M(2)$, whereas Mg is preferentially ordered at $M(2)$. A quantitative phase analysis indicated about 10 wt.% of accessory phases including quartz (ca. 4 wt.%), ankerite (ca. 1 wt.%), and traces of stilpnomelane and biotite/annite. The surface area of the samples, measured by nitrogen physisorption (BET), resulted to be 4.5 $m^2 \times g^{-1}$.

2.2. Dissolution in MGS

Dissolution experiments were carried out under static conditions in the same experimental conditions used for UICC crocidolite and fibrous tremolite [25]. Briefly, samples were incubated (20 mg) in MGS (40 mL) at pH 4.5 and kept at 37 °C for up to 1 month with gentle shaking. Aliquots of the suspension were filtered on nitrocellulose filter membranes (porosity of 0.22 μm) and analysed by ICP-OES using a Perkin–Elmer Optima 2000 DV ICP-OES spectrometer (Perkin–Elmer, Norwalk, CT, USA). To remove any residues of the solution, the fibres deposited on filters were rinsed with ultrapure deionized water and then stored under argon prior to the SEM, TEM, XRPD, and XPS investigations.

2.3. FE-SEM Investigation

SEM images were acquired by using FESEM Thermo Fischer Apreo 2 S LoVac (Brno-Černovice, Czech Republic). Samples were mounted on a stub with conductive carbon tape, and a 5 nm of chromium film was deposited on the sample surface to make it conductive during measurements.

2.4. HR-TEM Investigation

A TEM analysis was performed using a JEOL JEM-2010 (Tokyo, Japan) microscope operating at 200 kV, equipped with a LaB6 source, an Energy Dispersive System (EDS) (Oxford ISIS, Oxford, UK) for microanalysis, and an Olympus Tengra CCD camera (2 k × 2 k × 14 bit) for image acquisition. Aliquots of the samples (pristine amosite and 1 month in MGS incubated amosite) were pipetted on 200-mesh Cu grids supported with holey carbon film, then carbon-coated to increase conductivity.

2.5. Powder X-ray Diffraction (PXRD)

X-ray powder diffraction data were collected on a D8 Advance (Bruker AXS, Karlsruhe, Germany) running in θ/θ transmission mode using a capillary as a sample holder. The sample incubated for 1 month in MGS (A-720 h) was loaded in a 0.5 mm diameter borosilicate glass capillary. The instrument is equipped with an incident beam focussing graded multilayer Göbel mirror and a PSD VÅntec-1. The diffraction pattern was measured in step-scan mode, using CuKα, in the 6–145° 2θ angular range, 0.022° 2θ step size, and 20 s counting time. Data were evaluated by the Rietveld method using Topas V6 (Bruker AXS, Billerica, MA, USA, 2016), which uses the fundamental parameters approach (FPA) [27] for describing the peak shape. Preliminary scrutiny of the pattern indicated the persistence of the same phases at the minor/trace level reported in Ballirano et al. [26], and the same computational procedure was applied. Quartz, ankerite, and garnet were included in the Rietveld refinement. Differently, the main reflections of stilpnomelane and biotite/annite were approximated by two peaks not related to any structure, whose position, intensity, and breadth were also refined following the same procedure described by Pacella et al. [25]. Only scale factors, cell parameters, and peak shapes were refined for quartz, ankerite, and garnet. The structure of amosite was refined keeping all displacement parameters fixed to reference data [28], and no restraints on bond distances and angles were imposed. Site scattering (s.s.) at $M(1)$, $M(2)$, $M(3)$, and $M(4)$ was optimized. Neither split M(4′) site nor A-type sites were observed in agreement with Ballirano et al. [26]. The refinement was performed using the normalized symmetrized spherical harmonics functions, reported by Järvinen [29], for describing the anisotropic peak broadening of the diffraction pattern. Absorption correction was performed using the equation of Sabine et al. [30] for a cylindrical

sample, and the presence of preferred orientation was modelled using normalized symmetrized spherical harmonics functions (fourth order, eight refinable parameters) following the approach of Ballirano [31]. The results of the quantitative phase analysis (QPA) are reported in Table 1. Statistical indicators of the refinement and cell parameters of A-720 h are listed in Table S1, whereas a magnified view (5–80° 2θ) of the Rietveld plots is shown in Figure S1. The CIF file of A-720 h is deposited as supporting material at the journal's site.

Table 1. QPA of the UICC amosite samples. Data of pristine samples taken from Ballirano et al. [26].

Phases	Pristine	A-720 h
Amosite	94.87(8)	95.74(8)
Quartz	3.79(5)	3.86(7)
Ankerite	0.76(4)	
Garnet	0.58(4)	0.40(4)
Stilpnomelane	traces	traces
Biotite/annite	traces	traces
Hydrated sulphates	-	traces

2.6. XPS Investigation

An XPS investigation was carried out by using a Theta Probe X-ray photoelectron spectrometer (Thermo Fisher Scientific, Waltham MA, USA) equipped with a flood gun neutralizer for charge compensation. All spectra were acquired using Al Kα1,2 source (hν = 1486.6 eV) and a 400 μm spot size. The analyser operated in the fixed analyser transmission (FAT) mode, with pass energy (PE) set at 200 eV and at 100 eV for the survey spectra and for the high-resolution spectra, respectively. The linearity of the binding energy scale was checked by periodic calibration following ISO 15472:2010 [32]. The binding energy scale was referred to the signal at 285.0 eV of adventitious aliphatic carbon. More details on the curve fitting of the spectra are reported in our previous works [33]. The surface fibre composition was reported in atomic percentages, and it was calculated correcting the peak area for Scofield's photoionization cross-sections [34], the asymmetry function [35], the transmission function correction, and the attenuation length [33]. Data are reported as the average values of three different analysed areas, with standard deviation in brackets.

3. Results

3.1. Morphological Investigation

The FE-SEM images show that amosite fibres, similarly to crocidolite fibres [25], are straight and rigid, and are arranged in bundles of variable dimensions of ca. 1–5 μm × 20–1000 μm (diameter × length) with split ends (Figure 1a). Images at high magnification (Figure 1b) show single fibrils of nanometric diameter (ca. 150–300 nm) with a partially irregular surface, indicating the possible occurrence of an amorphous layer due to weathering processes [25]. Moreover, after immersion in MGS for up to 1 month (sample A-720 h), in rare cases, some effects of the dissolution are evident on the fibres, their surface being more lobate and irregular with respect to that of the starting material (Figure 1c).

The TEM observations reveal similar nanostructures for pristine and A-720 h samples. In both samples, fibre size and aspect ratio are highly variable, with a maximum diameter of 500–600 nm (e.g., Figure 2a,c, for pristine and A-720 h samples, respectively). High-magnification images reveal the constant occurrence of an ultrathin amorphous film, approximately 10–30 nm wide, surrounding the amosite fibres (Figure 2b,d). The amorphous film also occurs at fibre terminations. The only remarkable difference between pristine amosite and A-720 h treated fibres is an average increase in the amorphous film thickness at fibre termination in the treated sample (up to 25 nm), where rare irregular, wavy lattice fringes may occur, and suggesting possible precipitation of smectite-like layers.

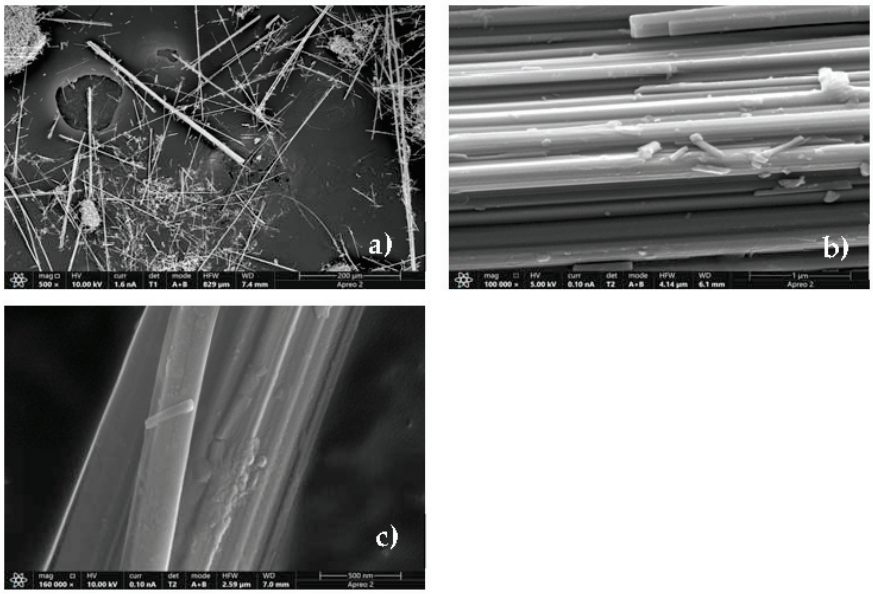

Figure 1. FE-SEM images of amosite fibres: (**a**) pristine amosite showing straight and rigid morphology arranged in bundles; (**b**) high magnification image showing pristine fibrils with nanometric diameter (ca. 150–300 nm); (**c**) high magnification image of fibres after incubation in MGS for up to 1 month showing an irregular surface due to dissolution process.

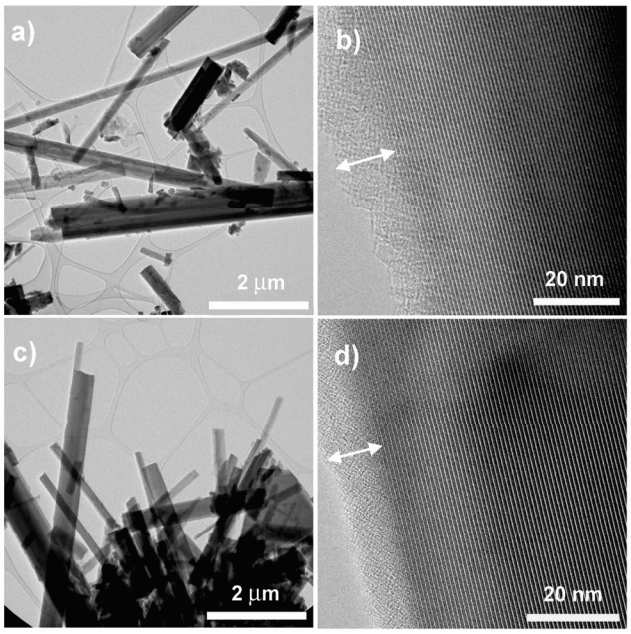

Figure 2. Bright-field TEM images of pristine amosite (**a**,**b**) and amosite after 1 month of incubation (**c**,**d**) at variable magnification. Lattice fringes in (**b**,**d**) correspond to (020) with d-spacings of 9.05–9.20 Å. Double-arrowed white lines highlight the thin amorphous film surrounding both pristine and treated amosite fibres.

3.2. Structural Analysis

The cell parameters and volume of the A-720 h sample are very close to those of the pristine one (Table S1). The QPA results testify the complete dissolution of ankerite observed in the pristine sample. Moreover, the presence of an extra reflection at ca. 18° 2θ, already observed for other amphiboles (UICC crocidolite and tremolite: [25]) upon dissolution experiments in MGS at acidic conditions, was assigned to newly precipitated hydrated sulphates. Relevant bond distances of A-720 h are reported in Table S2, where

they are compared to those of the pristine sample [26]. The differences are marginal and testify the absence of significant structural variations at the bulk level. The same applies to the site scattering (s.s.) of the cation sites (Table S3) and the site partition at the B and C sites (Table S4). Cation partition was calculated assuming that all Mn is allocated at *M*(4).

Comparison with the pristine sample possibly indicates only a minor oxidation of Fe^{2+} at C sites. The <<*M*(1), *M*(2), *M*(3)–O>> is of 2.111 Å as compared to 2.114 Å of the pristine sample [26]. The C group sites preference of Fe^{2+} follow the same *M*(1) ≈ *M*(3) > *M*(2), with Mg preferentially ordered at *M*(2), of the pristine sample, in agreement with the reference data of Hirschmann et al. [36]. An indirect Fe^{2+}/Fe^{3+} partition was performed by comparing the $<r_M>$ mean cationic radii calculated from both the refined <*M*(1,2,3)–O> bond distances and from the proposed site partition (Table S4). The results confirm the unusual preferential allocation of Fe^{3+} at *M*(1) (0.15 apfu) and *M*(3) (0.09) observed in the pristine sample, plus minor Fe^{3+} at *M*(2) (0.03 apfu) for a total of 0.27 Fe^{3+} apfu to be compared to 0.15 Fe^{3+} apfu of the untreated sample.

3.3. Dissolution Process

The results of the ICP-OES analyses after fibre incubation in the MGS are shown in Figure 3 and Table S5. Si and Mg release shows a parallel trend, both increasing with incubation time, from 57(1) mg/kg up to 2169(62), and from 394(3) mg/kg up to 985(36) mg/kg, respectively (Figure 3).

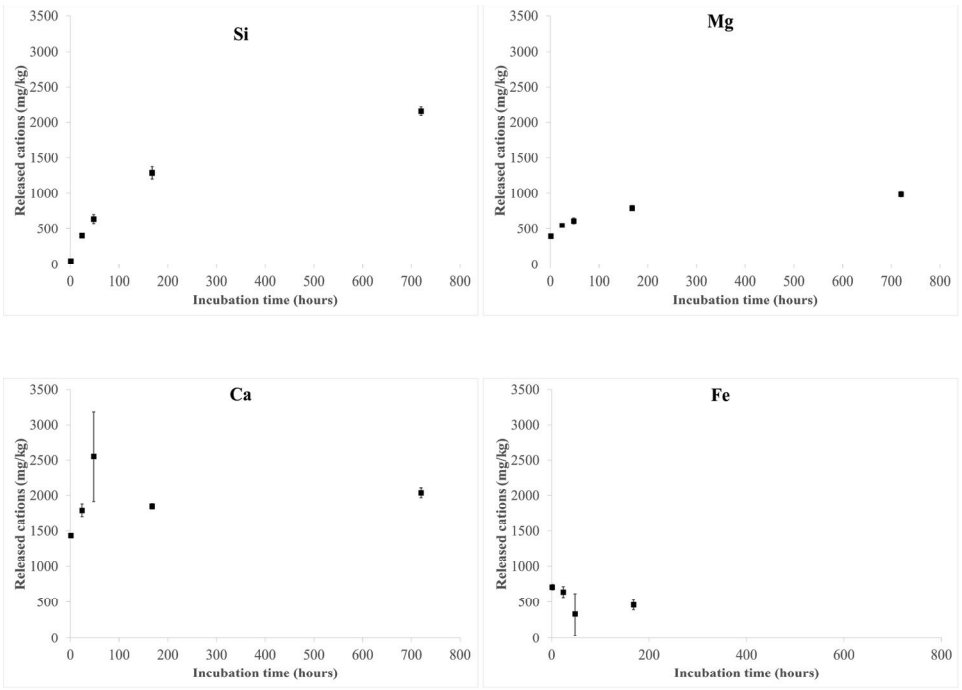

Figure 3. Released cations from the UICC amosite sample during incubation in MGS at pH 4.5 for up to 1 month (720 h).

Ca and Fe release mainly occurs in the first stages of dissolution (48 and 24 h of incubation, respectively). The observed release of Fe and Ca may be attributed to the dissolution of ankerite [calcium, iron carbonate: $CaFe(CO_3)_2$] in the hand sample, in agreement with the QPA results showing the absence of this accessory phase in the sample incubated for up to 1 month in MGS (Table 1). It must be pointed out that the concentration of released Ca is higher than that expected from the dissolution of only ankerite: considering the dissolution of ca. 0.76 wt.% of ankerite, the concentration of Ca and Fe should be roughly 1500 and 1200 mg/kg, respectively. Thus, due to the occurrence of the small content of Ca in the amosite structure, Ca leaching from the fibres cannot be ruled out. Moreover, the small amount of Fe detected in the solution (up to 720 mg/kg) indicates the possible formation

of Fe-bearing secondary phases (hydrated sulphates), as revealed by PXRD data reported in Table 1). This hypothesis is further supported by the absence of Fe in the solution for longer incubation times (1 month).

3.4. Surface Chemistry

The XPS survey spectra of the amosite samples after suspension in MGS are reported in Figure S2 and show the presence of Si, O, Fe, Mg, Ca, and Na, together with C, due to the presence of the adventitious carbon caused by the contact with the laboratory atmosphere and aqueous solutions. Specifically, no S and Cl signals that might be due to the incubating solution were found on the fibre surface. The binding energy of the principal photoelectron lines are shown in Table S6. The high-resolution spectra were processed to gain data on the chemical state of the elements.

Si 2p peaks were fitted with a doublet due to spin orbit coupling. The energy separation between the $2p_{3/2}$ and $2p_{1/2}$ components and their area ratio were constrained to 0.8 and 2:1, respectively. The binding energy of Si $2p_{3/2}$ was found to be in the range 102.5 (0.1)–102.7 (0.1) for the considered samples (Table S6) and agrees with that reported in our previous investigations [33]. The oxygen O 1s peak resulted to be multicomponent with a signal due to oxygen in oxides in the range 530.0–530.2 eV; the component due to bridging oxygen is at 532.2 eV, and the components assigned to non-bridging oxygen in silicates and -OH are found at about 531.2 eV [33]. The quantitative surface composition of both pristine and MGS-incubated fibres is reported in Table 2. Compared to the bulk composition, an enrichment in Mg and Si with respect to Fe is evident on the surface of pristine fibres (Table 2), likely due to weathering processes, as we already observed for UICC crocidolite fibres [25]. It must be pointed out that, owing to their very low amount in the hand sample, the contribution of accessory phases to the XPS measurements may be considered negligible.

Table 2. Surface quantitative composition (at%) of both pristine and amosite samples after incubation in MGS. Average values and standard deviation (in parentheses) over three measurements are reported. The composition of the bulk obtained by chemical analysis is reported for comparison.

Sample	O	Si	Mg	Fe	Na	Ca
Bulk	62.1	20.5	5.0	11.9	0.3	0.2
Pristine	57.8 (0.4)	28.4 (0.5)	7.3 (0.2)	5.9 (0.3)	n.d.	0.6 (0.2)
A-1 h	62.1 (0.7)	24.7 (0.8)	6.0 (0.8)	4.9 (0.1)	2.0 (0.3)	0.3 (0.1)
A-24 h	62.4 (0.6)	24.8 (0.7)	5.5 (0.2)	5.35 (0.05)	1.8 (0.3)	0.15 (0.03)
A-48 h	63.1 (0.5)	24.5 (0.2)	4.6 (0.4)	5.9 (0.1)	1.9 (0.4)	n.d.
A-168 h	63.6 (0.6)	23.4 (0.4)	5.3 (0.3)	6.1 (0.2)	1.5 (0.2)	n.d.
A-720 h	63.7 (0.2)	24.4 (0.7)	4.5 (0.4)	6.2 (0.2)	1.1 (0.1)	n.d.

The Fe $2p_{3/2}$ high-resolution spectra of the samples are shown in Figure S3. Following Fantauzzi et al. [33], the signals were resolved in three components assigned to: (i) Fe(II) bound to oxygen with its satellite, at about 709.0 eV; (ii) Fe(III) bound to oxygen found at 710.6 eV; and (iii) FeOOH at 711.7 eV. The percentage of each component is shown in Table 3. Significant variations of the Fe components were observed only in the first hour of sample incubation in MGS. In particular, the intensity of the Fe(II)-O signal decreases from ca. 70% of the total peak area in the pristine sample down to ca. 60%, at the expense of the Fe(III)-O signal, which increases from ca. 3% up to ca. 18%. Moreover, the signals remain almost constant up to the end of the experiment.

Table 3. Relative intensities of Fe $2p_{3/2}$ components (area%) in UICC amosite samples (A). Results of Pacella et al. [25] obtained for UICC crocidolite (C) and asbestos tremolite (T) investigated under the same experimental conditions are reported for comparison.

A: UICC Amosite (This Work)				B: UICC Crocidolite (Pacella et al. [25])				C: Tremolite (Pacella et al. [25])			
Sample	**Fe(II)-O**	**Fe(III)-O**	**Fe-OOH**	**Sample**	**Fe(II)-O**	**Fe(III)-O**	**Fe-OOH**	**Sample**	**Fe(II)-O**	**Fe(III)-O**	**Fe-OOH**
Pristine	71(3)	3(1)	26(4)	Pristine	29	10	61	Pristine	21(1)	19(1)	60(1)
A-1 h	59(3)	18(4)	23(2)	T-1 h	11(2)	5(1)	84(3)	C-1 h	24(1)	20.8(0.2)	55.3(0.2)
A-24 h	65(1)	12(1)	23(1)	T-24 h	13(1)	2(1)	85(1)	C-24 h	25(1)	23(1)	53(2)
A-48 h	59(3)	15(2)	26(4)	T-48 h	19(1)	3(1)	78(2)	C-48 h	30.5(0.2)	20.6(0.9)	49(1)
A-168 h	56(1)	18.0(0.1)	26(1)	T-168 h	13(1)	10(2)	77(3)	C-168 h	28.9(0.1)	23(3)	48(3)
A-720 h	59(5)	15(3)	26(2)	T-720 h	15(2)	8(2)	77(2)	C-720 h	29(2)	18(1)	53(1)

4. Discussion

Cation release as a function of the sample incubation time is reported in Figure 3 and Table S5. It must be pointed out that the observed release of Fe and (at least a fraction of) Ca was ascribed to the dissolution of a small amount of ankerite, a carbonate mineral soluble at acidic pH, occurring in the hand sample (Table 1).

Comparing the Si/Mg ratio of the leached cations (based on nanomoles) at the various sampling times with that retrieved from the surface chemical analysis (Figure 4), a preferential Mg release from the amosite fibres is evident, especially in the first 48 h, as already observed for the dissolution of asbestos tremolite and UICC crocidolite samples [25]. Accordingly, the incongruent behaviour of the dissolution process was also highlighted by the XPS results (Tables 2 and 4) showing a depletion of Mg and Ca on the surface of the leached fibres, in agreement with their Madelung site energies in the amphibole structure [37,38].

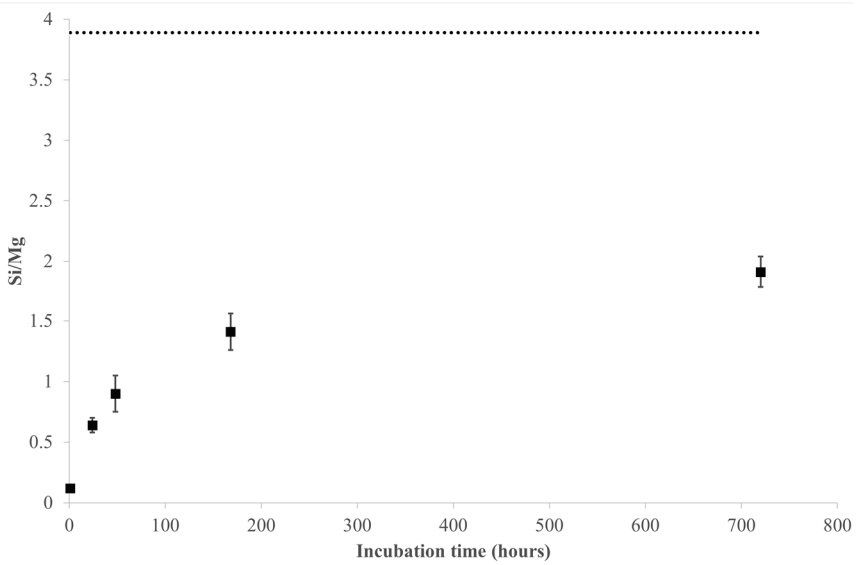

Figure 4. Dissolution of amosite fibres in MGS at pH 4.5 in the range 0–720 h: Si/Mg ratio (as nmol/mg) in the solution at each sampling time as compared to that arising from XPS analysis of the pristine sample. Dotted line shows the Si/Mg ratio on the fibre surface, retrieved from XPS analysis.

Table 4. Silicon/cation ratios on the surface of the amosite fibres as a function of the incubation time.

Sample	Si/Mg	Si/Fe	Si/O
Pristine	3.9(0.2)	4.8(0.3)	0.49(0.01)
A-1 h	4.1(0.7)	5.0(0.3)	0.40(0.02)
A-24 h	4.5(0.3)	4.6(0.2)	0.40(0.02)
A-48 h	5.3(0.5)	4.2(0.1)	0.39(0.01)
A-168 h	4.4(0.3)	3.8(0.2)	0.37(0.01)
A-720 h	5.4(0.6)	3.9(0.2)	0.38(0.01)

Notably, the selective removal of cations from the amphibole structure, leading to surface amorphization, was highlighted by Germine et al. [39] on fibrous tremolite samples following in vivo alteration. Later, Germine et al. [40] found that the neo-formed surface layer is not completely amorphous but is composed of sub-nanometer silica-rich particles with the potential to penetrate deeply into DNA interiors. The Fe enrichment on the fibre surface (Table 4) indicates no Fe leaching from the amosite fibres in the adopted experimental conditions (pH of 4.5 and atmospheric pO_2), despite significant Fe(II) occurrence at the *M*(4) site [26], where cations are expected to be rapidly leached out during amphibole dissolution on the basis of its Madelung site energy [37,38,41]. Moreover, the Na enrichment on the sample surface during incubation is likely due its adsorption on the fibre surface from the MGS solution (Table 4).

Concerning Fe speciation, pristine fibres show a more oxidized surface with respect to the bulk ($Fe(II)/Fe_{tot}$ ratios are 97% for the bulk and 71% for the surface), with Fe(III) mainly present as FeOOH (26% of the total surface Fe content). For the MGS incubated samples (Table 3), the intensity of the Fe(II)-O component decreases in the first hour of incubation, from about 71% to ca. 59% of the total Fe, and is coupled with a parallel increase in the Fe(III)-O component (from ca. 3% to ca. 15% of the total Fe). Moreover, the increase in the Fe(III)-O component on the surface is in agreement with the increased oxygen content observed in the same interval of time (Table 4). The depletion of Fe(II) centres on the surface indicates that for amosite fibres the Fe oxidation is faster than the fibre dissolution in the first hour of incubation, similarly to what was observed for samples of fibrous tremolite [25]. However, for amosite fibres, the Fe(II) reduction is less marked, being only ca. 17% of the total surface Fe(II), whereas for tremolite it is much more pronounced [ca. 62% of the total surface Fe(II) present in the pristine sample is oxidized in the same interval of time]. Moreover, in the asbestos tremolite sample, the oxidation converted Fe(II) into FeOOH (Table 3), very likely located in the outer part of the sample surface [33]. This might be attributed to the slow dissolution rate of the investigated fibres, affected by both their crystal chemical features and low surface area (ca. 2.7 $m^2 \times g^{-1}$ for Maryland tremolite, see Pacella et al. [25]). Notably, the observed trend is opposite to that of UICC crocidolite, which shows an increase in the Fe(II) component coupled with a decrease in the FeOOH component (Table 3). This is a consequence of the fast fibre dissolution that removes the outer layer and promotes the exposure of new Fe sites from the bulk, especially in the form of Fe(II) of which the bulk is enriched with respect to the surface. Considering that for amosite fibres the FeOOH component keeps constant with incubation time, the moderate conversion of Fe(II)-O to Fe(III)-O observed in the first hour of incubation (Table 3) may be interpreted as the result of both the oxidation of the Fe centres initially present on the fibre surface and those emerging from the bulk following mineral dissolution. Those interpretations are supported by the Rietveld structural analysis that indicates a minor oxidation of Fe(II) of the bulk. Notably, for amosite (ca. 4.5 $m^2 \times g^{-1}$), the lower surface area with respect to that of crocidolite (ca. 8.7 $m^2 \times g^{-1}$) likely hinders a sustained occurrence of Fe(II) centres on the fibre surface (Table 3). This agrees with previous results obtained on two fibrous tremolite samples with largely different surface areas revealing that both the processes of dissolution and surface modification are slower for the sample with the lowest surface area [23]. Moreover, starting from 24 h of sample incubation, an equilibrium between Fe oxidation rate and fibre dissolution kinetics is established (Table 3). To make a comparison of the biodurability among these amphibole asbestos samples, the dissolution rate of amosite fibres normalized to their surface area was quantified, according to Pacella et al. [25], using the Si release in the unsaturated region (0–48 h). The value obtained was $dSi/dt = 0.002$ μmol $\times h^{-1} \times m^{-2}$ ($R^2 = 0.99$), in between that retrieved from UICC crocidolite and asbestos tremolite ($dSi/dt = 0.007$ μmol $\times h^{-1} \times m^{-2}$ and 0.0004 μmol $\times h^{-1} \times m^{-2}$, respectively). This result unequivocally confirms previous findings postulating: (i) a quicker dissolution for Fe-rich silicates with respect to their isostructural, iron-free analogues [37,42]; (ii) asbestos tremolite durability is among the highest compared to any other amphibole asbestos [43–48].

5. Conclusions

In this work, the dissolution process in MGS at acidic pH (ca. 4.5), and the following chemical and structural surface alterations of UICC amosite fibres, were investigated by a well-tested multi-analytical approach. The results obtained were compared with those previously acquired, under the same experimental conditions, on asbestos tremolite and UICC crocidolite samples.

Despite a similar dissolution process (i.e., incongruent dissolution with preferential release of Mg and Ca leading to surface amorphization, and absence of Fe release), differences in biodurability among the samples were highlighted. In particular, the release of Si based on an equivalent surface area showed that amosite fibres have an intermediate biodurability between that of crocidolite (lowest biodurability) and asbestos tremolite (highest biodurability). Moreover, for both amosite and asbestos tremolite samples, the transformation of bulk Fe(II) centres to surface ions is overwhelmed by the Fe oxidation rate in the first stages of dissolution. Accordingly, a depletion of surface Fe(II) is observed for the leached samples with respect to the pristine ones.

The results of our group showed that the alteration of the fibre surface following dissolution may induce the occurrence of under-coordinated Fe ions, which primarily contribute to the overall fibre reactivity. On this basis, the fibre dissolution kinetics can drive the extent of surface alteration that in turn modulates the fibre chemical reactivity and, possibly, its ability to interact with the biological environment in vivo (i.e., radical generation by Fenton reaction, protein adsorption, etc.). Since biodurability is assumed to be a relevant toxicity parameter, the knowledge of the surface alteration fibres possibly occurring in lung fluids is of primary importance to assess the mechanisms underlying the observed long-term toxicity of asbestos. To provide a much more detailed picture of the possible surface modifications occurring in vivo, other works focusing on the treatment of fibres with real fluids present in the lungs are in progress.

Supplementary Materials: The following supporting information can be downloaded at: https://www.mdpi.com/article/10.3390/nano13222933/s1, Figure S1. Magnified view (5–80° 2θ) of the Rietveld plots of the refinement of A-720 h. Continuous blue line: experimental data; continuous red line: calculated pattern; continuous grey line: difference pattern. Vertical blue lines: single peak of annite/biotite (ca. 7.25° 2θ), stilpnomelane (ca. 8.8° 2θ), and hydrated sulphates (ca. 18° 2θ) (see text for explanation). Vertical short bars: position of calculated Bragg reflections of (from above to below): garnet, quartz, and amosite; Figure S2. Survey spectra of the investigated UICC amosite samples. X-ray source: Al Kα; Figure S3. Fe $2p_{3/2}$ peaks of the UICC amosite samples pristine and incubated in mimicked Gamble's solution for 1 h and 720 h; Table S1. Cell parameters and volume of UICC amosite fibres and agreement factors (as defined in the work of Young [28]) of the Rietveld refinements. Data of pristine samples taken from Ballirano et al. [26]; Table S2. Relevant bond distances (in Å) of UICC amosite fibres. * Calculated as in table 7 in the work of Hawthorne and Oberti [49]. Data of pristine samples taken from Ballirano et al. [26]; Table S3. Site scattering (*s.s.*) at A, B, and C sites from Rietveld refinement. Data of pristine samples taken from Ballirano et al. [26]; Table S4. Site partition at B and C sites from Rietveld refinement. Data of pristine samples taken from Ballirano et al. [26]; Table S5. Results of ICP-OES analyses of the UICC amosite sample after incubation in the mimicked Gamble's solution at pH 4.5 up to 720 h. Standard deviations (in parentheses) were calculated over three independent measurements; Table S6. Binding energy values (eV) of the main photoelectron lines in UICC amosite samples. Average values and standard deviation (in parentheses) over three measurements carried out on different areas of the same sample.

Author Contributions: Supervision, Conceptualization, Writing—original draft preparation, Project administration, Investigation, Formal analysis, Methodology, A.P.; Conceptualization, Writing—original draft preparation, Investigation, Funding acquisition, Formal analysis, Methodology, P.B.; Writing—original draft preparation, Investigation, Methodology, A.R.; Writing—original draft preparation, Investigation, Formal analysis, Methodology, M.F.; Writing—original draft preparation, Investigation, Formal analysis, M.C.D.C.; Writing—original draft preparation, Methodology, Investigation, Formal analysis, E.N.; Formal analysis, L.A.; Investigation, Writing—original draft preparation, C.V.; Conceptualization, Writing—original draft preparation, A.C. (Antonella Campopiano) and

A.C. (Annapaola Cannizzaro), A.B.; Writing—original draft preparation, Methodology, Investigation, Formal analysis, M.R.M. All authors have read and agreed to the published version of the manuscript.

Funding: This study was carried out within the RETURN Extended Partnership and received funding from the European Union Next-GenerationEU (National Recovery and Resilience Plan–NRRP, Mission 4, Component 2, Investment 1.3–D.D. 1243 2/8/2022, PE0000005).

Data Availability Statement: The data presented in this study are available on request from the corresponding author.

Acknowledgments: The authors are grateful to Maura Tomatis who provided the UICC amosite sample for the study. M.F. and A.R. acknowledge the financial support from the University of Cagliari.

Conflicts of Interest: The authors declare no conflict of interest. The funders had no role in the design of the study; in the collection, analysis, or interpretation of data; in the writing of the manuscript, or in the decision to publish the results.

References

1. Skinner, H.C.W. Mineralogy of Asbestos Minerals. *Indoor Built Environ.* **2003**, *12*, 385–389. [CrossRef]
2. Kim, S.-Y.; Kim, Y.-C.; Kim, Y.; Hong, W.-H. Predicting the Mortality from Asbestos-Related Diseases Based on the Amount of Asbestos Used and the Effects of Slate Buildings in Korea. *Sci. Total Environ.* **2016**, *542*, 1–11. [CrossRef]
3. Iwaszko, J. Making Asbestos-Cement Products Safe Using Heat Treatment. *Case Stud. Constr. Mater.* **2019**, *10*, e00221. [CrossRef]
4. Spasiano, D.; Pirozzi, F. Treatments of Asbestos Containing Wastes. *J. Environ. Manag.* **2017**, *204*, 82–91. [CrossRef] [PubMed]
5. Gualtieri, A.F. Bridging the Gap between Toxicity and Carcinogenicity of Mineral Fibres by Connecting the Fibre Crystal-Chemical and Physical Parameters to the Key Characteristics of Cancer. *Curr. Res. Toxicol.* **2021**, *2*, 42–52. [CrossRef]
6. IARC Working Group on the Evaluation of Carcinogenic Risks to Humans. Arsenic, Metals, Fibres and Dusts. In Proceedings of the IARC Monographs on the Evaluation of Carcinogenic Risks to Humans, Lion, France, 17–24 March 2009; published in 2012; No. 100C. p. 501.
7. International Ban Asbestos Secretariat. Available online: http://ibasecretariat.org/alpha_ban_list.php (accessed on 5 May 2020).
8. Fubini, B.; Mollo, L. Role of Iron in the Reactivity of Mineral Fibers. *Toxicol. Lett.* **1995**, *82–83*, 951–960. [CrossRef] [PubMed]
9. Donaldson, K.; Murphy, F.A.; Duffin, R.; Poland, C.A. Asbestos, Carbon Nanotubes and the Pleural Mesothelium: A Review of the Hypothesis Regarding the Role of Long Fibre Retention in the Parietal Pleura, Inflammation and Mesothelioma. *Part. Fibre Toxicol.* **2010**, *7*, 5. [CrossRef]
10. Bernstein, D.; Dunnigan, J.; Hesterberg, T.; Brown, R.; Velasco, J.A.L.; Barrera, R.; Hoskins, J.; Gibbs, A. Health Risk of Chrysotile Revisited. *Crit. Rev. Toxicol.* **2013**, *43*, 154–183. [CrossRef]
11. Bonneau, L.; Malard, C.; Pezerat, H. Studies on surface properties of asbestos. 2. Role of dimensional characteristics and surface properties of mineral fibers in the induction of pleural tumors. *Environ. Res.* **1986**, *41*, 268–275. [CrossRef]
12. Bonneau, L.; Suquet, H.; Malard, C.; Pezerat, H. Studies on surface properties of asbestos. 1. Active sites on surface of chrysotile and amphiboles. *Environ. Res.* **1986**, *41*, 251–267. [CrossRef]
13. Gilmour, P.S.; Brown, D.M.; Beswik, P.H.; Macnee, W.; Rahman, I.; Donaldson, K. Free radical activity of industrial fibers: Role of iron in oxidative stress and activation of transcription factors. *Environ. Health Perspect.* **1997**, *105*, 1313–1317. [PubMed]
14. Fubini, B. Physico-chemical and cell free assays to evaluate the potential carcinogenicity of fibres. In *Mechanisms of Fibre Carcinogenesis*; Kane, A.B., Boffetta, P., Saracci, R., Wilbourn, J., Eds.; IARC Scientific Publication: Lyon, France, 1996; p. 140.
15. Fubini, B.; Otero Arean, C. Chemical aspects of the toxicity of inhaled mineral dusts. *Chem. Soc. Rev.* **1999**, *28*, 373–381. [CrossRef]
16. Van Oss, C.J.; Naim, J.O.; Costanzo, P.M.; Giese Jr, R.F.; Wu, W.; Sorling, A.F. Impact of different asbestos species and other mineral particles on pulmonary pathogenesis: Clay. *Clay Min.* **1999**, *47*, 697–707. [CrossRef]
17. Hardy, J.A.; Aust, A.E. Iron in Asbestos Chemistry and Carcinogenicity. *Chem. Rev.* **1995**, *95*, 97–118. [CrossRef]
18. Fenoglio, I.; Prandi, L.; Tomatis, M.; Fubini, B. Free Radical Generation in the Toxicity of Inhaled Mineral Particles: The Role of Iron Speciation at the Surface of Asbestos and Silica. *Redox Rep.* **2001**, *6*, 235–241. [CrossRef]
19. Kamp, D.W. Asbestos-induced lung diseases: An update. *Transl. Res.* **2009**, *153*, 143–152. [CrossRef]
20. Liu, G.; Cheresh, P.; Kamp, D.W. Molecular Basis of Asbestos-Induced Lung Disease. *Annu. Rev. Pathol. Mech. Dis.* **2013**, *8*, 161–187. [CrossRef]
21. Gualtieri, A.F. Introduction. In *Mineral Fibres: Crystal Chemistry, Chemical-Physical Properties, Biological Interaction and Toxicity*; Gualtieri, A.F., Ed.; European Mineralogical Union: Brussels, Belgium, 2017; Volume 18, pp. 1–16, ISBN 9780903056656.
22. Andreozzi, G.B.; Pacella, A.; Corazzari, I.; Tomatis, M.; Turci, F. Surface Reactivity of Amphibole Asbestos: A Comparison between Crocidolite and Tremolite. *Sci. Rep.* **2017**, *7*, 14696. [CrossRef]
23. Pacella, A.; Andreozzi, G.B.; Corazzari, I.; Tomatis, M.; Turci, F. Surface Reactivity of Amphibole Asbestos. A Comparison between Two Tremolite Samples with Different Surface Area. *Period. Miner.* **2018**, *87*, 195–205. [CrossRef]
24. Pacella, A.; Tomatis, M.; Viti, C.; Bloise, A.; Arrizza, L.; Ballirano, P.; Turci, F. Thermal Inertization of Amphibole Asbestos Modulates Fe Topochemistry and Surface Reactivity. *J. Hazard. Mater.* **2020**, *398*, 123119. [CrossRef]

25. Pacella, A.; Ballirano, P.; Fantauzzi, M.; Rossi, A.; Nardi, E.; Capitani, G.; Arrizza, L.; Montereali, M.R. Surface and Bulk Modifications of Amphibole Asbestos in Mimicked Gamble's Solution at Acidic PH. *Sci. Rep.* **2021**, *11*, 14249. [CrossRef]
26. Ballirano, P.; Skogby, H.; Gianchiglia, F.; Di Carlo, M.C.; Campopiano, A.; Cannizzaro, A.; Olori, A.; Pacella, A. Chemical and Structural Characterization of UICC Amosite Fibres from Penge Mine (South Africa). *Period. Miner.* **2022**, *91*, 143–154. [CrossRef]
27. Cheary, R.W.; Coelho, A. A Fundamental Parameters Approach to X-Ray Line-Profile Fitting. *J. Appl. Crystallogr.* **1992**, *25*, 109–121. [CrossRef]
28. Young, R.A. Introduction to the Rietveld Method. In *The Rietveld Method*; Young, R.A., Ed.; Oxford University Press: Oxford, UK, 1993; Volume 8, pp. 252–254, ISBN 0198555776.
29. Järvinen, M. Application of Symmetrized Harmonics Expansion to Correction of the Preferred Orientation Effect. *J. Appl. Crystallogr.* **1993**, *26*, 525–531. [CrossRef]
30. Sabine, T.M.; Hunter, B.A.; Sabine, W.R.; Ball, C.J. Analytical expressions for the transmission factor and peak shift in absorbing cylindrical specimens. *J. Appl. Crystallogr.* **1998**, *31*, 47–51. [CrossRef]
31. Ballirano, P. Effects of the Choice of Different Ionization Level for Scattering Curves and Correction for Small Preferred Orientation in Rietveld Refinement: The $MgAl_2O_4$ Test Case. *J. Appl. Crystallogr.* **2003**, *36*, 1056–1061. [CrossRef]
32. *ISO 15472:2010*; Surface Chemical Analysis—X-ray Photoelectron Spectrometers—Calibration of Energy Scales. ISO: Geneva, Switzerland, 2010. Available online: https://www.iso.org/standard/55796.html (accessed on 2 October 2023).
33. Fantauzzi, M.; Pacella, A.; Atzei, D.; Gianfagna, A.; Andreozzi, G.B.; Rossi, A. Combined Use of X-Ray Photoelectron and Mössbauer Spectroscopic Techniques in the Analytical Characterization of Iron Oxidation State in Amphibole Asbestos. *Anal. Bioanal. Chem.* **2010**, *396*, 2889–2898. [CrossRef]
34. Scofield, J.H. Hartree-Slater Subshell Photoionization Cross-Sections at 1254 and 1487 EV. *J. Electron Spectros. Relat. Phenomena* **1976**, *8*, 129–137. [CrossRef]
35. Reilman, R.F.; Msezane, A.; Manson, S.T. Relative Intensities in Photoelectron Spectroscopy of Atoms and Molecules. *J. Electron Spectros. Relat. Phenomena* **1976**, *8*, 389–394. [CrossRef]
36. Hirschmann, M.; Evans, B.W.; Yang, H. Composition and Temperature Dependence of Fe-Mg Ordering in Cummingtonite-Grunerite as Determined by X-Ray Diffraction. *Amer. Miner.* **1994**, *79*, 862–877.
37. Schott, J.; Berner, R.A.; Sjöberg, E.L. Mechanism of Pyroxene and Amphibole Weathering—I. Experimental Studies of Iron-Free Minerals. *Geochim. Cosmochim. Acta* **1981**, *45*, 2123–2135. [CrossRef]
38. Brantley, S.L.; Chen, Y. Chemical Weathering Rates of Pyroxenes and Amphiboles. *Rev. Mineral. Geochem.* **1995**, *31*, 119–172.
39. Germine, M.; Puffer, J.H. Analytical Transmission Electron Microscopy of Amphibole Fibers From the Lungs of Quebec Miners. *Arch. Environ. Occup. Health* **2015**, *70*, 323–331. [CrossRef] [PubMed]
40. Germine, M.; Puffer, J.H. Tremolite–actinolite fiber coatings of sub-nanometer silica-rich particles in lungs from deceased Quebec miners. *Toxicol. Ind. Health.* **2020**, *36*, 146–152. [CrossRef]
41. Schott, J.; Berner, R.A. X-Ray Photoelectron Studies of the Mechanism of Iron Silicate Dissolution during Weathering. *Geochim. Cosmochim. Acta* **1983**, *47*, 2233–2240. [CrossRef]
42. Siever, R.; Woodford, N. Dissolution Kinetics and the Weathering of Mafic Minerals. *Geochim. Cosmochim. Acta* **1979**, *43*, 717–724. [CrossRef]
43. Speil, S.; Leineweber, J.P. Asbestos Minerals in Modern Technology. *Environ. Res.* **1969**, *2*, 166–208. [CrossRef]
44. Hesterberg, T.W.; Miiller, W.C.; Musselman, R.P.; Kamstrup, O.; Hamilton, R.D.; Thevenaz, P. Biopersistence of Man-Made Vitreous Fibers and Crocidolite Asbestos in the Rat Lung Following Inhalation. *Fundam. Appl. Toxicol.* **1996**, *29*, 267–279. [CrossRef]
45. Hesterberg, T.W.; Hart, G.A.; Chevalier, J.; Miiller, W.C.; Hamilton, R.D.; Bauer, J.; Thevenaz, P. The Importance of Fiber Biopersistence and Lung Dose in Determining the Chronic Inhalation Effects of X607, RCF1, and Chrysotile Asbestos in Rats. *Toxicol. Appl. Pharmacol.* **1998**, *153*, 68–82. [CrossRef]
46. Hesterberg, T.W.; Chase, G.; Axten, C.; Miller, W.C.; Musselman, R.P.; Kamstrup, O.; Hadley, J.; Morscheidt, C.; Bernstein, D.M.; Thevenaz, P. Biopersistence of Synthetic Vitreous Fibers and Amosite Asbestos in the Rat Lung Following Inhalation. *Toxicol. Appl. Pharmacol.* **1998**, *151*, 262–275. [CrossRef]
47. Bernstein, D.M.; Chevalier, J.; Smith, P. Comparison of Calidria Chrysotile Asbestos to Pure Tremolite: Inhalation Biopersistence and Histopathology Following Short-Term Exposure. *Inhal. Toxicol.* **2003**, *15*, 1387–1419. [CrossRef] [PubMed]
48. Enrico Favero-Longo, S.; Turci, F.; Tomatis, M.; Compagnoni, R.; Piervittori, R.; Fubini, B. The Effect of Weathering on Ecopersistence, Reactivity, and Potential Toxicity of Naturally Occurring Asbestos and Asbestiform Minerals. *J. Toxicol. Environ. Health Part A* **2009**, *72*, 305–314. [CrossRef] [PubMed]
49. Hawthorne, F.C.; Oberti, R. Amphiboles: Crystal Chemistry. In *Amphiboles: Crystal Chemistry, Occurrence, and Health Issues*; Hawthorne, F.C., Oberti, R., Della Ventura, G., Mottana, A., Eds.; Walter de Gruyter GmbH & Co. KG: Berlin, Germany, 2007; Volume 67, pp. 1–54, ISBN 0-939950-79-0.

nanomaterials

MDPI

Article

Machine Learning-Assisted Large-Area Preparation of MoS_2 Materials

Jingting Wang, Mingying Lu, Yongxing Chen, Guolin Hao, Bin Liu , Pinghua Tang, Lian Yu, Lei Wen and Haining Ji *

School of Physics and Optoelectronics, Xiangtan University, Xiangtan 411105, China; 202005710126@smail.xtu.edu.cn (J.W.); 202021001488@smail.xtu.edu.cn (M.L.); 202121521308@smail.xtu.edu.cn (Y.C.); guolinhao@xtu.edu.cn (G.H.); liubin@xtu.edu.cn (B.L.); pinghuatang@xtu.edu.cn (P.T.); 202005710108@smail.xtu.edu.cn (L.Y.); 202205710203@smail.xtu.edu.cn (L.W.)
* Correspondence: sdytjhn@xtu.edu.cn

Abstract: Molybdenum disulfide (MoS_2) is a layered transition metal-sulfur compound semiconductor that shows promising prospects for applications in optoelectronics and integrated circuits because of its low preparation cost, good stability and excellent physicochemical, biological and mechanical properties. MoS_2 with high quality, large size and outstanding performance can be prepared via chemical vapor deposition (CVD). However, its preparation process is complex, and the area of MoS_2 obtained is difficult to control. Machine learning (ML), as a powerful tool, has been widely applied in materials science. Based on this, in this paper, a ML Gaussian regression model was constructed to explore the growth mechanism of MoS_2 material prepared with the CVD method. The parameters of the regression model were evaluated by combining the four indicators of goodness of fit (r2), mean squared error (MSE), Pearson correlation coefficient (p) and *p*-value (*p*_val) of Pearson's correlation coefficient. After comprehensive comparison, it was found that the performance of the model was optimal when the number of iterations was 15. Additionally, feature importance analysis was conducted on the growth parameters using the established model. The results showed that the carrier gas flow rate (Fr), molybdenum sulfur ratio (R) and reaction temperature (T) had a crucial impact on the CVD growth of MoS_2 materials. The optimal model was used to predict the size of molybdenum disulfide synthesis under 185,900 experimental conditions in the simulation dataset so as to select the optimal range for the synthesis of large-size molybdenum disulfide. Furthermore, the model prediction results were verified through literature and experimental results. It was found that the relative error between the prediction results and the literature and experimental results was small. These findings provide an effective solution to the preparation of MoS_2 materials with a reduction in the time and cost of trial and error.

Keywords: machine learning; Gaussian regression model; CVD; MoS_2; area prediction

Citation: Wang, J.; Lu, M.; Chen, Y.; Hao, G.; Liu, B.; Tang, P.; Yu, L.; Wen, L.; Ji, H. Machine Learning-Assisted Large-Area Preparation of MoS_2 Materials. *Nanomaterials* **2023**, *13*, 2283. https://doi.org/10.3390/nano13162283

Academic Editor: Mads Brandbyge

Received: 27 June 2023
Revised: 5 August 2023
Accepted: 7 August 2023
Published: 9 August 2023

1. Introduction

MoS_2 is a typical layered transition metal-sulfur compound. Single-layer MoS_2 is a sandwich structure with S-Mo-S overlapping, which has a good band gap structure [1]. Under certain external conditions, it will transit from an indirect to direct bandgap semiconductor, exhibiting strong photoluminescence when confined in a 2D monolayer [2]. It is expected to be a candidate for next-generation application in the field of nanoelectronics devices, which has aroused the interest of many researchers. As early as 2011, B. Radisavljevic and A. Radenovic et al. reported that semiconductors made of single-layer MoS_2 thin films can be used to manufacture electronic chips with smaller volume, better performance and higher efficiency [3]. In recent years, the preparation of large-area, high-quality MoS_2 thin films has become the focus of research, and its application areas have been constantly expanding, with typical representatives being next-generation nanoelectronics [4,5], biosensors [6], solar cells [7,8], etc. However, the area of MoS_2 has an extremely important impact

on the characteristics of the prepared devices. For example, a new single heterojunction solar cell structure based on n-type MoS_2 and WS_2 was prepared with its photovoltaic characteristics being greatly affected by the area of MoS_2 and WS_2 [9]. At present, the common method for preparing MoS_2 is chemical vapor deposition (CVD). CVD, a method of reacting chemical gases or vapors on the surface of a matrix to synthesize coatings or nanomaterials, is the most widely used technology in the semiconductor industry for depositing a variety of materials, including a wide range of insulating materials, most metal materials and metal alloy materials. In theory, it is simple: after the introduction of two or more gaseous raw materials into a reaction chamber, they chemically react with each other to form a new material, which is deposited on the wafer surface. The single layer of MoS_2 generated on the substrate often has a certain triangular shape, and the reaction needs to be carried out under high-temperature conditions. If the reaction time is too long, certain sulfur, molybdenum and their compounds will be deposited on the generated MoS_2, which will have a considerable impact on the area of the generated MoS_2. Lee et al. obtained a continuous MoS_2 film with a size of up to 2 mm through the vulcanization of MoO_3, but the film was not a uniform monolayer [10]. Hence, the preparation of large-area and high-quality MoS_2 thin films remains a challenge.

With the deepening of computer science research, an increasing number of machine learning algorithms, such as support vector machines, naive Bayes, artificial neural networks, decision trees, etc., are being widely used. In chemical synthesis, James M. Tour et al. used the parameters of mass, capacitance, voltage, pretreatment and duration and then applied an ensemble of models to predict the yield of graphene, an extremely important material in wastewater treatment [11]. Chen et al. successfully achieved the two-step hydrothermal synthesis of VO_2 under the guidance of machine learning and evaluated the performance of the machine learning model. The RF model had the best performance, with a prediction accuracy of 87.27% [12]. Chen et al. realized the controllable synthesis of multicolor discs with the assistance of machine learning, providing new ideas for the rational design and improvement of optical disc performance in the future [13]. Our research group successfully achieved controllable preparation of MoS_2 using an extreme gradient boosting (XGBoost) model with an average prediction accuracy of over 88% and an AUC value of up to 0.91. The multilayer perceptron (MLP) model, with an average prediction accuracy of 75% and an AUC value of 0.8, was used to successfully realize the controllable preparation of MoS_2 materials [14]. Machine learning can largely compensate for the shortcomings of cumbersome experimental steps, long experimental time and high cost in the traditional material research process. However, further exploration is needed to prepare MoS_2 films with larger areas for better applications.

Therefore, a Gaussian regression model was constructed using machine learning via the collection of 200 sets of experimental data obtained in the laboratory and literature. Furthermore, the best model parameters were found to optimize the synthesis conditions and predict the experimental results by changing the iteration number of the model cross validation, thus providing theoretical support for the MoS_2 preparation of a given area.

2. Methods

Machine learning reveals the potential relationship between synthesized feature data through training and learning models and then fits the experiments to select the optimal experimental synthesis conditions. The research of machine learning in materials mainly includes, as shown in Figure 1, data acquisition and processing, feature engineering, model building, simulation data analysis and verification [15]. MoS_2 is prepared by adding precursors (molybdenum and sulfur sources) and controlling the macroscopic parameters of the reaction (such as reaction temperature, the ratio of the two molybdenum trioxide and sulfur element precursors, carrier gas flow rate, reaction time, etc.). For the purposes of this paper, the larger the side-length size of the synthesized triangle MoS_2 is, the larger its area.

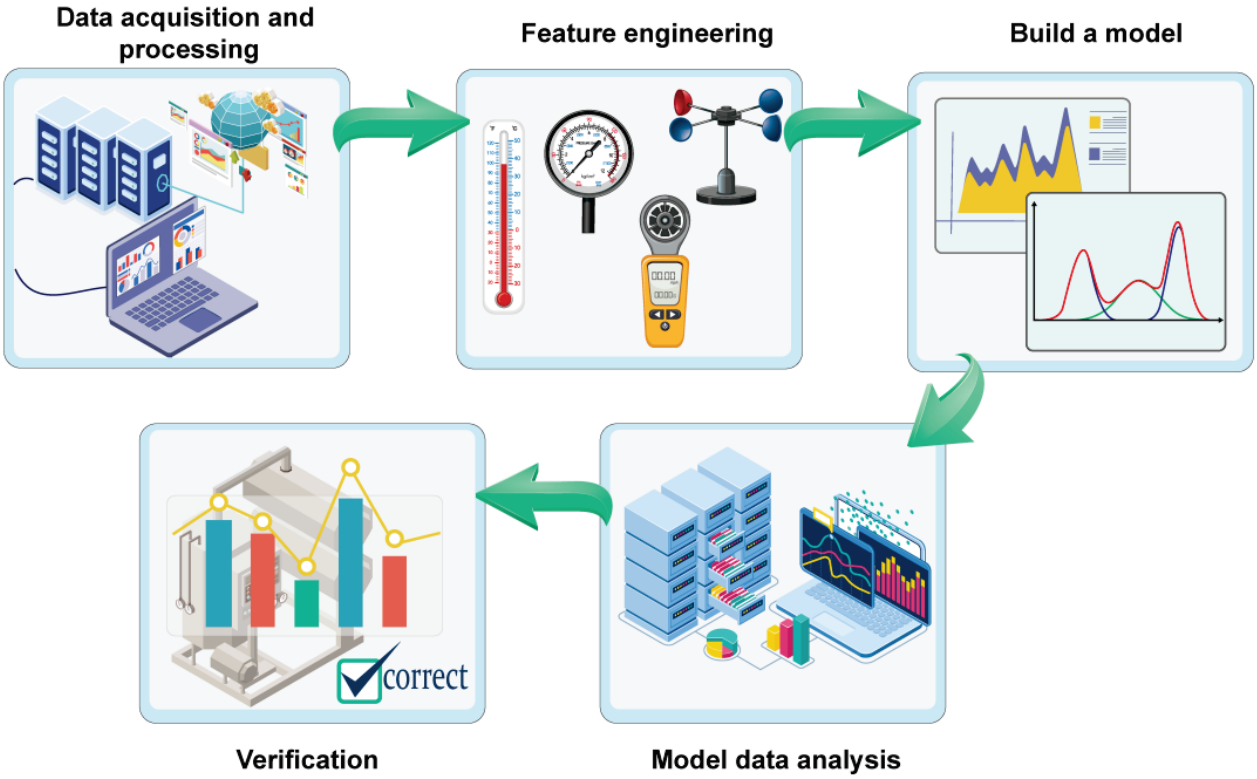

Figure 1. Machine learning-assisted CVD synthesis of a large-area MoS_2 workflow diagram.

2.1. Data Acquisition and Processing

To form a dataset, 200 sets of experimental conditions for CVD synthesis of MoS_2 were collected from the literature and laboratory (see Table S1 from the Supporting Information). The molybdenum-to-sulfur ratio, carrier gas flow rate, reaction temperature, reaction time and side-length dimensions of the synthesized triangular MoS_2 were recorded. Due to the different selection of samples, the collected data were preprocessed to remove some duplicate experimental conditions and results. Subsequently, 200 sets of data in the dataset were statistically analyzed, with the scatterplots of each characteristic variable and experimental results being shown in Figure 2. The 200 sets of experimental condition data in our dataset originated from different laboratories, and there might have been a few subtle differences in the experimental conditions. In our study, apart from the four characteristic parameters selected, other parameters were not the main factors affecting the experimental results. Rather, the other parameters were idealized and considered consistent during the experiment process.

The triangular MoS_2 edge lengths synthesized with CVD in the dataset ranged from 0.5 μm to 300 μm. Among them, those greater than 30 μm were defined as delimiting a large area [16,17] and accounted for 48% of the total. The area size of MoS_2 corresponds to different experimental conditions, and there is an urgent need for a machine learning model that can predict the generation area of MoS_2 based on the input of experimental conditions. In this study, the Gaussian regression model was used to fit the influence of each feature parameter on the experimental results to predict the area size of the obtained MoS_2.

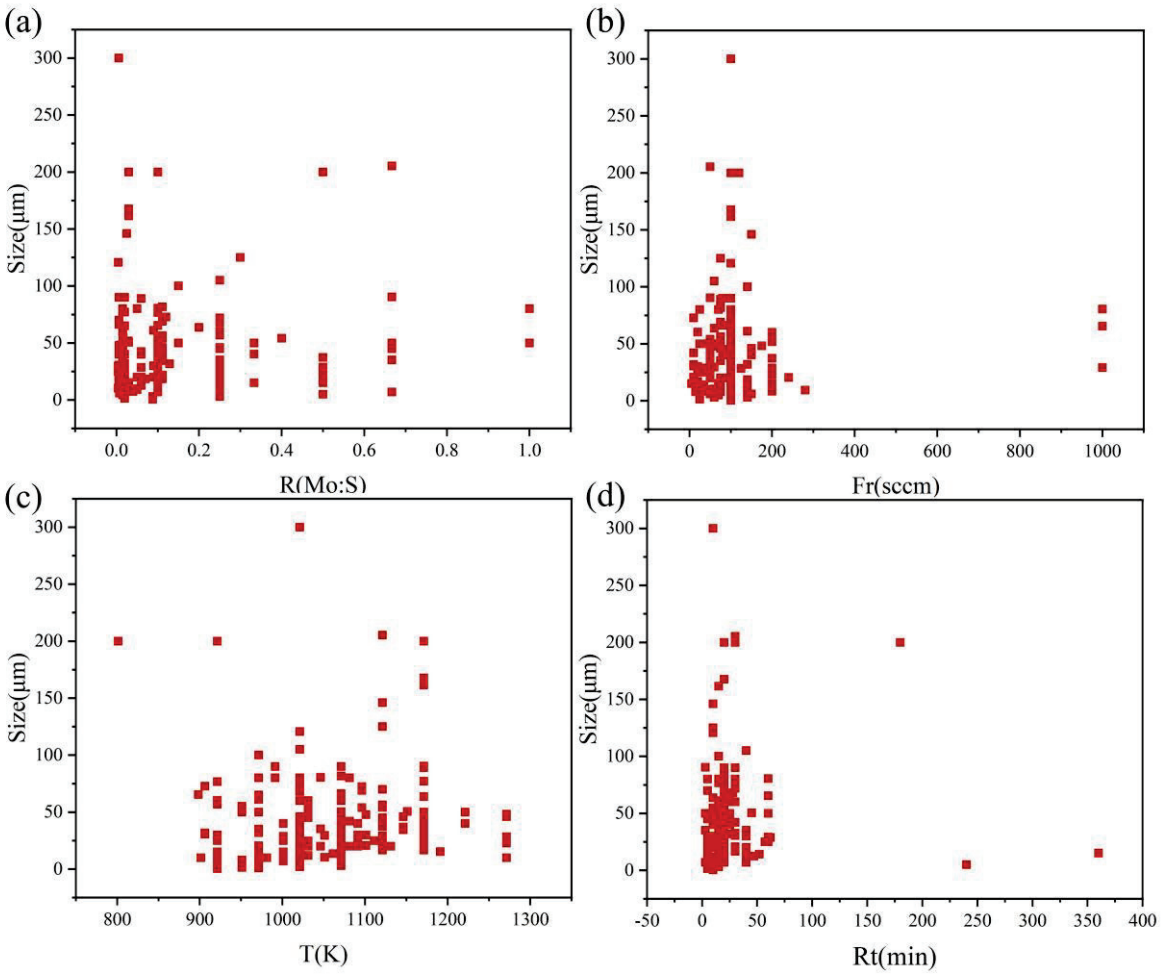

Figure 2. Scatter plots of each feature parameter and size in the dataset. (**a**) Molybdenum sulfur ratio, (**b**) carrier gas flow rate, (**c**) reaction temperature, (**d**) reaction time.

2.2. Feature Engineering

In order to reduce model computation time and make the fitting effect of the regression model better, it is necessary to select the feature data that are a completely decisive factor for the synthesized area of MoS_2. Four characteristic parameters, including the ratio of two precursors (molybdenum trioxide and sulfur, R), carrier gas flow rate (Fr), reaction temperature (T) and reaction time (Rt) were selected during the establishment of the model. The characteristics of the dataset for describing the potential relationship between the size of MoS_2 and the selected characteristic values are shown in Table 1; the distribution of each feature parameter data in the dataset is described through means and standard deviations. In machine learning, the Pearson correlation coefficient is a statistical data test used to reflect the degree of similarity between two variables. It can be used to determine whether the relationship between the extracted feature descriptors and categories is positive, negative or noncorrelated. The correlation among the four selected feature parameters is shown in Figure 3. Among them, the molybdenum-to-sulfur ratio was positively correlated with the reaction temperature and reaction time. In addition, the reaction time and the carrier gas velocity were also positively correlated. Among all the correlation coefficients, the maximum value was 0.21, indicating that the independence of the different variables was good and that there would be little influence exerted between them.

Table 1. Characteristics of the MoS_2 dataset prepared with CVD.

Notation	Feature	Unit	Mean	Standard Deviation
R(Mo:S)	Molybdenum-to-sulfur ratio		0.12	0.18
Fr	Gas flow rate	sccm	105.10	120.70
T	Reaction temperature	K	1045.36	82.41
Rt	Reaction time	min	22.39	33.15

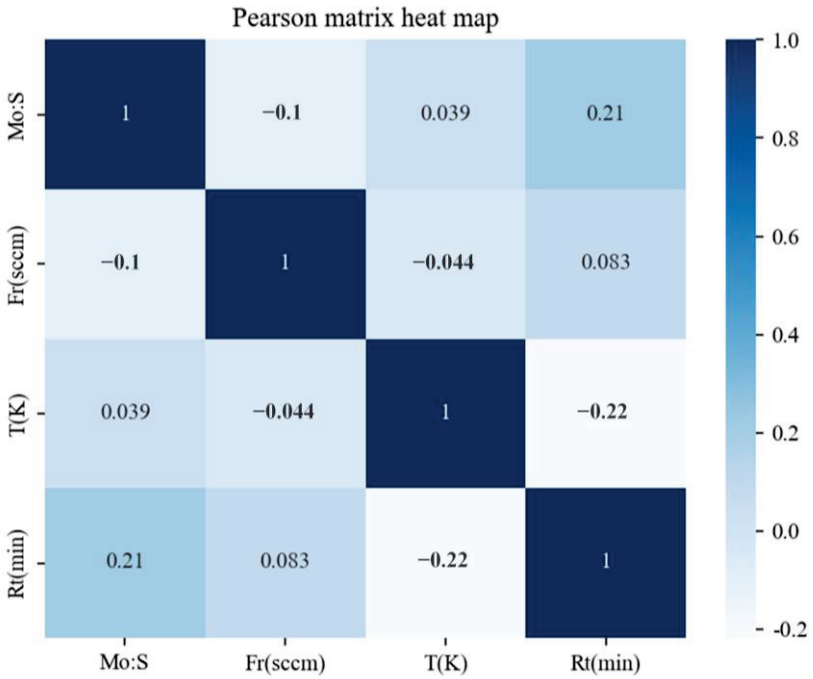

Figure 3. Pearson matrix heat map of the four characteristic parameters in CVD synthesis of MoS_2.

There are many experimental variables in the preparation of MoS_2. In addition to the above four characteristic parameters, there were other parameters that needed to be considered in the actual CVD preparation of the MoS_2 experiment, such as the heating rate during the reaction, potential addition of NaCl, boat configuration, and the pressure in the quartz tube. In the reaction process, NaCl can be added in order to promote the formation of a monolayer of molybdenum disulfide film and the increase of film area. Studies have shown that mixing metal oxides with salts can generate droplets or metal chloride oxides, which increase the mass flux and vapor pressure of the Mo source as well as the reaction and nucleation rate [18]. However, it does not affect the resulting molybdenum disulfide film. The boat configuration has a certain influence on the uniformity of the molybdenum disulfide film. It has been also found that the heating rate of the reaction is closely related to the pressure in the quartz boat during the reaction. If these two parameters are trained in learning, the reliability of the model will be reduced, which will affect the model evaluation index and prediction results. The environmental conditions of the laboratory, mainly those related to temperature and humidity, can also have a certain impact on the experimental results,. However, in the process of preparing molybdenum disulfide with CVD method, the whole experiment was carried out in a CVD furnace, and the synthesis of molybdenum disulfide was less affected by laboratory environmental conditions. Due to the large amount of literature exploring the influence of the four characteristic quantities on the prepared thin film area, no other characteristic parameters were selected to describe this experiment. Although these feature parameters were not selected to explore their impact on the experimental results, controlling the consistency of other variables during the experimental process could reduce the impact of the experimental results.

The molybdenum source commonly used for preparing MoS_2 is molybdenum trioxide powder, and the sulfur source is sulfur powder. The schematic diagram of the experimental boat is shown in Figure 4. The positions of the precursor molybdenum source and sulfur source are at the center of the quartz boat, and the substrate material is SiO_2. The carrier gas is the inert gas argon. The cooling method is natural cooling. By fixing the above parameters to reduce the parameters in the training process of the model, we could shorten the training time of machine learning.

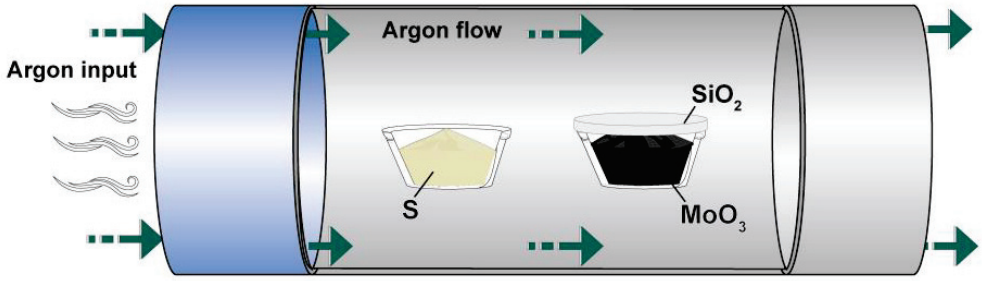

Figure 4. Schematic diagram of the MoS_2 experimental vessel prepared via CVD.

2.3. Model Establishment

Gaussian process regression (GP_R) is a regression model based on the Gaussian process. This model obtains a Gaussian distribution function by fitting the data to obtain accurate prediction results [19]. Gaussian process (GP) is a commonly used stochastic process model. In the field of machine learning, GP is a machine learning method developed on the basis of the Gaussian stochastic process and Bayesian learning theory. It is strictly anchored in statistical learning theory and has a good adaptability in dealing with complex problems, such as high dimensions, small samples, nonlinearity, etc. The Gaussian regression model has greater flexibility and prediction accuracy than does traditional regression, and it can adapt to different data distributions and model complexity with more accurate prediction results than can traditional regression (linear or quadratic). Therefore, the Gaussian regression model was deemed highly suitable for the data set collected. GP has also become a research hot spot in the field of machine learning and been successfully applied in many fields [20–24].

There is a complex correlation between the experimental results and the selected feature parameters, but the number of datasets obtained was relatively small. Hence, cross-validation was conducted on the established regression model to verify its performance [25]. The principle of this process is to divide the dataset into two parts: a training set and a test set. The model was trained through the training set, and the performance of the model was verified using the testing set. During the model training process, GridSearchCV, only applicable to small datasets, was used to automatically adjust the relevant parameters. This method is highly suitable for our dataset although it is more time-consuming [26,27]. Cross-validation can effectively evaluate model performance and avoid overfitting and underfitting problems. In terms of model performance evaluation, four indicators were selected to obtain the conditions for the best model, including goodness of fit (r^2), mean squared error (MSE), Pearson correlation coefficient and *p*-value of Pearson correlation coefficient [28]. Among these, goodness of fit (r^2) and mean-squared error (MSE) were used to evaluate the model training process. Pearson correlation coefficient and *p*-value of Pearson correlation coefficient were used to determine the correlation between feature parameters. Goodness of fit reflects the extent to which the model fits the data, with values ranging from 0 to 1: the closer to 1, the better the model fits the data. r^2 equal to 1 indicates that the model fits the data perfectly, while r^2 equal to 0 indicates that the model is unable to explain the variance of the data. Mean squared error (MSE) reflects the gap between the predicted and actual values of the model: the smaller the value, the better the prediction performance of the model. Pearson correlation coefficient is an indicator used to measure the degree of linear correlation between two variables, with values ranging from −1 to 1:

the closer to 1, the higher the positive correlation between the two variables; the closer to −1, the greater the negative correlation between the two independent variables; the closer to 0, the less linear the relationship between the two variables. The *p*-value of Pearson correlation coefficient is used to test whether the linear correlation between two variables is significant: the smaller the value, the more significant the linear correlation between the two variables.

3. Results and Discussion

3.1. Model Results and Analysis

In the established Gaussian regression model, a group of model conditions with the best evaluation index was selected to predict the area of MoS_2. Two performance indicators under six different iterations were processed and statistically analyzed, and the mean values of each evaluation indicator were obtained, as shown in Figure 5. Usually, the increase of the number of iterations in cross-validation will continuously improve the performance of the model, but setting the value of the number of iterations too large often leads to the overfitting of the model. Research indicates that r^2 continues to increase in iterations from 5 to 15 and then begins to decrease as the number of iterations continues to increase [29–31]. Moreover, when the number of iterations is 15, the MSE reaches its minimum value, indicating that the model has good prediction performance. In summary, it can be concluded that the optimal number of iterations is 15.

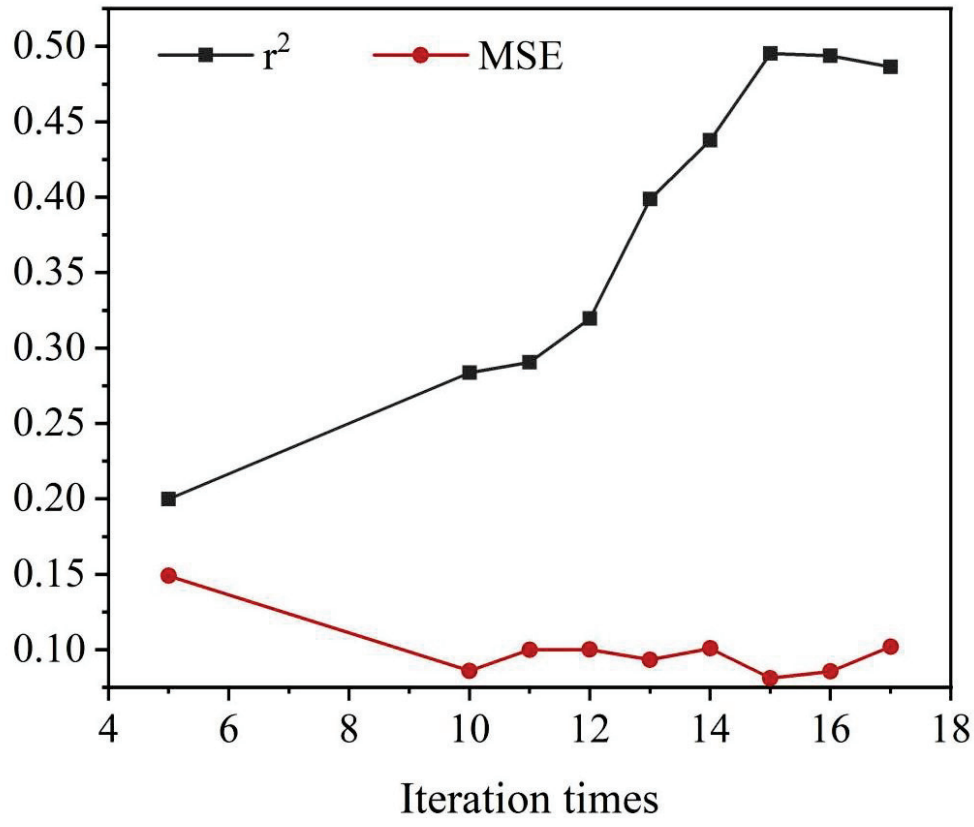

Figure 5. The curves of the evaluation indicators (r^2, MSE) in the Gaussian regression model with increasing iterations.

3.2. Optimization of Synthesis Conditions

Synthesis conditions play a crucial role in the preparation of molybdenum disulfide via CVD. However, in practical experiments, there are always cases where the reaction is incomplete, the reactants do not react sufficiently, or the concentration of the reactants is impure. The amount of reactants needed for the experiment is always more than the theoretical amount. Therefore, in the actual experiment, the experimenter should select the dosage

ratio of the two precursors most suitable for the preparation of molybdenum disulfide with CVD according to the experimental conditions. In addition to this, the reaction temperature (T) affects the growth rate of molybdenum disulfide. The temperature affects the rate of gasification of precursor S and the reaction rate of preparing molybdenum disulfide with CVD. Therefore, the reaction temperature should be considered. If the reaction temperature is too high, a series of problems will occur. Firstly, the evaporation rate of precursor S source is accelerated, which will lead to insufficient reaction of the molybdenum source. Secondly, it can also cause excessive internal pressure in the quartz tube and require a long time during the natural cooling process. Thirdly, this will have a certain impact on the service life of the experimental device. If the reaction temperature is too low, the evaporation of the S source and the flow rate of the carrier gas will decrease, which will result in a lower growth rate of molybdenum disulfide and a longer reaction time. Therefore, whether in the preparation of molybdenum disulfide with CVD in actual experiments or the conclusion obtained through machine learning model training data, the reasonable selection of carrier gas flow, molybdenum-to-sulfur ratio and reaction temperature during the reaction process is of great significance to the formation of molybdenum disulfide. Additionally, it can be stated that machine learning plays an important role in the analysis and selection of characteristic parameters in the preparation of molybdenum disulfide with controllable area in CVD.

In order to optimize the synthesized feature parameters, the SHAP (SHapley Additive exPlanations) library in the XGBoost model was used to extract the feature importance from the four selected feature parameters. SHAP is an explanatory technique used to explain the effect of each feature parameter on the output in the model [32]. Feature importance analysis provides an estimate of the predictive power of all the features used to train an ML model. It can be seen from Figure 6 that the characteristic parameter that has the greatest impact on the film area is the flow rate of the carrier gas (Fr), followed by the molybdenum sulfur ratio (R), with the reaction time (Rt) having the smallest impact.

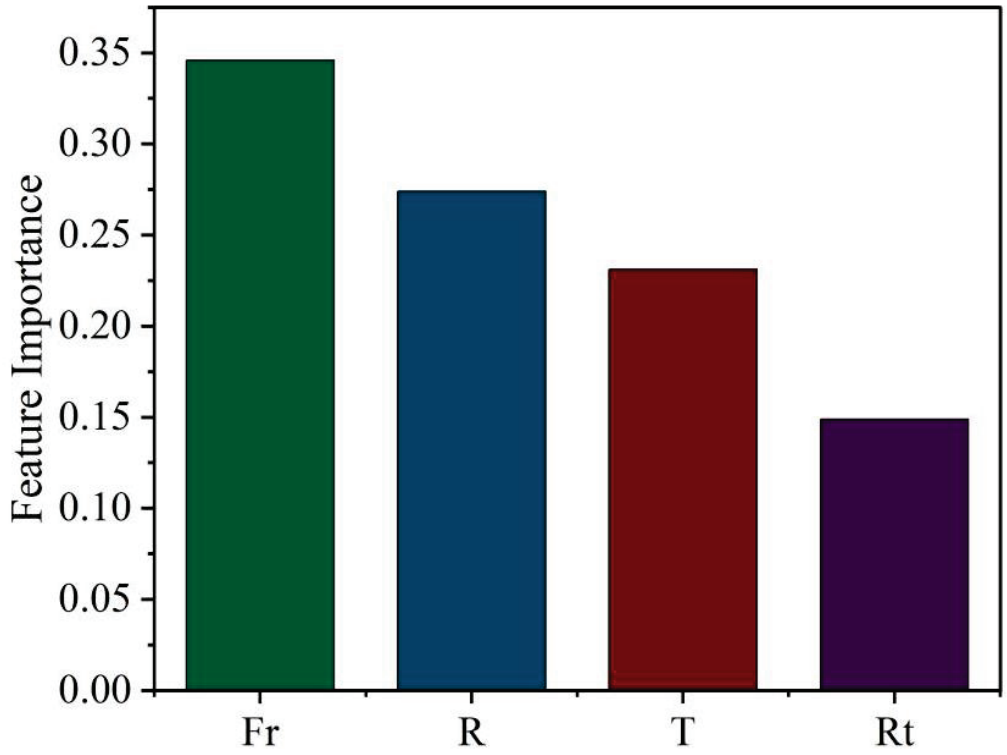

Figure 6. The importance of the features extracted from the SHAP library, which was learned from a sample of 200 datasets, with Fr and R being the two most important features.

With reference to a large number of literatures, a large area of MoS_2 was defined as a triangle with a size range greater than 30 μm, and further statistical analysis was conducted on the predicted area to determine the optimal experimental conditions. This model was used to predict the MoS_2 size of a dataset composed of 185,900 virtual experimental conditions data, 159,352 of which were located in a large area, accounting for 85.72%. Based on the prediction results, the corresponding molybdenum-to-sulfur ratio, carrier gas flow rate, reaction temperature and reaction time could be optimized. Therefore, the preparation conditions for large area MoS_2 were be optimized, as shown in Table 2.

Table 2. Optimization range of growth conditions for MoS_2 generated with CVD.

Growth Parameter	Min	Max
Molybdenum-to-sulfur ratio, R (Mo:S)	0.02	1
Gas flow rate, Fr (sccm)	25	200
Reaction temperature, T (K)	850	1200
Reaction time, Rt (min)	8	75

3.3. Model Verification

The area of MoS_2 predicted with machine learning might have contained a degree of deviation, so the model needed to be verified. Firstly, four sets of experimental conditions and results that were not used for model training were found from different literature sources. The model was validated using the prediction results of the model under the corresponding conditions, as shown in Table 3. The results from the literature were compared with the predicted results of the model. It was found that the relative errors were 3.19%, 4.40%, 0.68% and 0.67%, respectively. In addition, the experiments were conducted to further verify the reliability of the model. The SEM images of MoS_2 prepared under experimental conditions of R = 0.128, Fr = 175 sccm, T = 800 °C and Rt = 30 min, with a measured edge length of 43.571 μm, are shown in Figure 7a. Under this condition, the predicted edge length of the model was 42.302 μm. The relative error between the experiment and prediction was 2.91%. The SEM images of MoS_2 prepared under experimental conditions of R = 0.01, Fr = 100 sccm, T = 800 °C and Rt = 15 min, with a measured edge length of 35.869 μm, are shown in Figure 7b. The predicted edge length of the model was 37.975 μm. The relative error was 5.87%. In summary, both literature validation and experimental validation showed that the relative error did not exceed 6%, indicating high reliability of the predicted results. These results prove that the trained machine learning model can assist in the preparation of large-area molybdenum disulfide. To a certain extent, it provides practical guidance for the growth of molybdenum disulfide in combination with different growth parameters.

Table 3. Validation of the model with experimental conditions and results from the literature.

No.	R(Mo:S)	F_r(sccm)	T(K)	Rt (min)	Size from Literature (μm)	Predicted Size (μm)	Literature Source
1	0.05	50	1098.15	10	40.639	41.935	Senkić A et al. [33]
2	0.50	200	1123.15	15	39.252	40.980	Saenz G A L et al. [34]
3	0.02	10	923.15	10	37.975	38.235	Zhang X et al. [35]
4	0.02	50	1073.15	15	25.104	24.935	Yang S Y et al. [36]

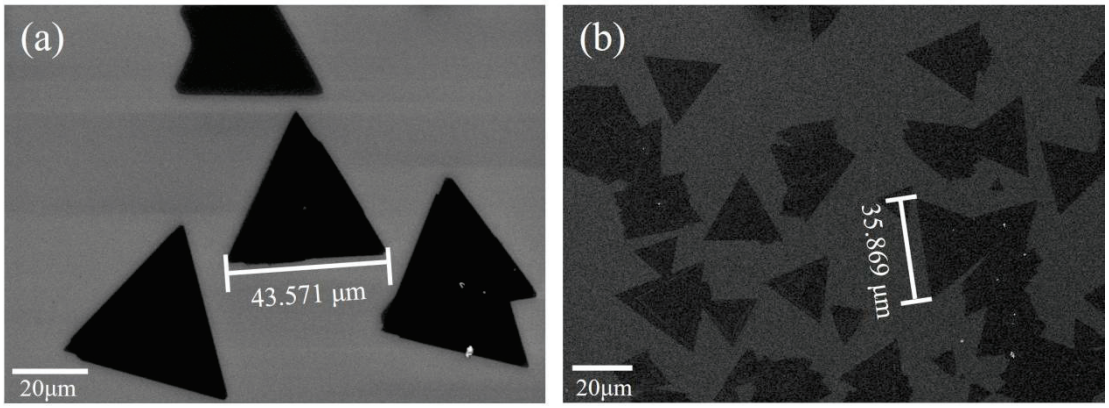

Figure 7. SEM images of MoS_2 prepared with CVD under different experimental conditions. (**a**) R = 0.128, Fr = 175 sccm, T = 800 °C, Rt = 30 min. (**b**) R = 0.01, Fr = 100 sccm, T = 800 °C, Rt = 15 min.

4. Conclusions

In this study, machine learning was used to examine the preparation of large-area MoS_2 materials via the Gaussian regression model. First, the model was applied to extract the feature importance in the dataset. Then, under the optimal model with 15 iterations, size prediction was performed on the simulated data that included 189,000 data sets. Furthermore, the growth conditions were optimized, and the optimal range of each growth condition was obtained. Finally, the model was validated. The results showed that the model could be used to predict the area obtained under experimental conditions in the literature, and the maximum difference between the literature results and the predicted results with a max relative error was 4.40%. Meanwhile, experimental verification was conducted on the predicted area of the model, with a max relative error of 5.87%. These results also indicate that machine learning has significant advantages in assisting in the preparation of large-area MoS_2 materials and provide an important foundation for the subsequent preparation of large area two-dimensional materials.

Supplementary Materials: The following supporting information can be downloaded at: https://www.mdpi.com/article/10.3390/nano13162283/s1, Table S1. Datasets from literatures and laboratories.

Author Contributions: Software, B.L. and L.Y.; Validation, M.L. and Y.C.; Formal analysis, G.H.; Investigation, J.W. and H.J.; Resources, L.W.; Writing—original draft, J.W. and H.J.; Writing—review & editing, H.J and P.T. All authors have read and agreed to the published version of the manuscript.

Funding: This research was funded by the National Natural Science Foundation of China (No. 51902276 and 62005234), the Natural Science Foundation of Hunan Province (No. 2019JJ50583, 2023JJ30585), the Scientific Research Fund of Hunan Provincial Education Department (No. 21B0111 and 21B0136) and the Hunan Provincial Innovation Foundation for Postgraduate (No. QL20220158).

Data Availability Statement: Data available on request.

Conflicts of Interest: The authors declare no conflict of interest.

References

1. Kumar, V.P.; Panda, D.K. Next generation 2D material molybdenum disulfide (MoS_2): Properties, applications and challenges. *ECS J. Solid State Sci. Technol.* **2022**, *11*, 033012. [CrossRef]
2. Ellis, J.K.; Lucero, M.J.; Scuseria, G.E. The indirect to direct band gap transition in multilayered MoS_2 as predicted by screened hybrid density functional theory. *Appl. Phys. Lett.* **2011**, *99*, 261908. [CrossRef]
3. Radisavljevic, B.; Radenovic, A.; Brivio, J.; Giacometti, V.; Kis, A. Single-layer MoS_2 Transistors. *Nat. Nanotechnol.* **2011**, *6*, 147–150. [CrossRef]
4. Hao, G.; Huang, Z.; Liu, Y.; Qi, X.; Ren, L.; Peng, X.; Yang, L.; Wei, X.; Zhong, J. Electrostatic properties of few-layer MoS_2 films. *AIP Adv.* **2013**, *3*, 042125. [CrossRef]

5. Sebastian, A.; Pendurthi, R.; Choudhury, T.H.; Redwing, J.M.; Das, S. Benchmarking monolayer MoS_2 and WS2 field-effect transistors. *Nat. Commun.* **2021**, *12*, 693. [CrossRef]
6. Wei, J.; Zhao, Z.; Lan, K.; Wang, Z.; Qin, G.; Chen, R. Highly sensitive detection of multiple proteins from single cells by MoS_2-FET biosensors. *Talanta* **2022**, *236*, 122839. [CrossRef]
7. Park, J.H.; Kim, D.; Shin, S.S.; Jo, Y.; Cho, J.-S.; Park, J.; Kim, T. Van der Waals heterojunction interface passivation using ZnS nanolayer and enhanced photovoltaic behavior of semitransparent ultrathin 2D-MoS_2/3D-chalcogenide solar cells. *Appl. Surf. Sci.* **2021**, *558*, 149844. [CrossRef]
8. Tian, J.; Chen, L.; Qiao, R.; Xiong, K.; Zhang, W.; Mao, Y.; Li, H.; Li, J. Photothermal-assist enhanced high-performance self-powered photodetector with bioinspired temperature-autoregulation by passive radiative balance. *Nano Energy* **2021**, *79*, 105435. [CrossRef]
9. Nikpay, M.A.; Mortazavi, S.Z.; Aghaei, M.; Elahi, S.M.; Reyhani, A. Prospect of single and coupled heterojunction solar cells based on n-MoS_2 and n-WS2. *Mater. Sci. Eng. B* **2021**, *274*, 115493. [CrossRef]
10. Lee, Y.-H.; Zhang, X.-Q.; Zhang, W.; Chang, M.-T.; Lin, C.-T.; Chang, K.-D.; Yu, Y.-C.; Wang, J.T.-W.; Chang, C.-S.; Li, L.-J.; et al. Synthesis of large-area MoS_2 atomic layers with chemical vapor deposition. *Adv. Mater.* **2012**, *24*, 2320–2325. [CrossRef] [PubMed]
11. Beckham, J.L.; Wyss, K.M.; Xie, Y.; McHugh, E.A.; Li, J.T.; Advincula, P.A.; Chen, W.; Lin, J.; Tour, J.M. Machine learning guided synthesis of flash graphene. *Adv. Mater.* **2022**, *34*, 2106506. [CrossRef]
12. Chen, Y.; Ji, H.; Lu, M.; Liu, B.; Zhao, Y.; Ou, Y.; Wang, Y.; Tao, J.; Zou, T.; Huang, Y.; et al. Machine learning guided hydrothermal synthesis of thermochromic VO_2 nanoparticles. *Ceram. Int.* 2023; *in press*. [CrossRef]
13. Chen, J.; Luo, J.B.; Hu, M.Y.; Zhou, J.; Huang, C.Z.; Liu, H. Controlled Synthesis of Multicolor Carbon Dots Assisted by Machine Learning. *Adv. Funct. Mater.* **2023**, *33*, 2210095. [CrossRef]
14. Lu, M.; Ji, H.; Zhao, Y.; Chen, Y.; Tao, J.; Ou, Y.; Wang, Y.; Huang, Y.; Wang, J.; Hao, G. Machine Learning-Assisted Synthesis of Two-Dimensional Materials. *ACS Appl. Mater. Interfaces* **2023**, *15*, 1871–1878. [CrossRef]
15. Tang, B.; Lu, Y.; Zhou, J.; Chouhan, T.; Wang, H.; Golani, P.; Xu, M.; Xu, Q.; Guan, C.; Liu, Z. Machine learning-guided synthesis of advanced inorganic materials. *Mater. Today* **2020**, *41*, 72–80. [CrossRef]
16. Jeon, J.; Jang, S.K.; Jeon, S.M.; Yoo, G.; Jang, Y.H.; Park, J.H.; Lee, S. Layer-controlled CVD growth of large-area two-dimensional MoS_2 films. *Nanoscale* **2015**, *7*, 1688–1695. [CrossRef]
17. Van Der Zande, A.M.; Huang, P.Y.; Chenet, D.A.; Berkelbach, T.C.; You, Y.; Lee, G.-H.; Heinz, T.F.; Reichman, D.R.; Muller, D.A.; Hone, J.C. Grains and grain boundaries in highly crystalline monolayer molybdenum disulphide. *Nat. Mater.* **2013**, *12*, 554–561. [CrossRef] [PubMed]
18. Zhou, J.; Lin, J.; Huang, X.; Zhou, Y.; Chen, Y.; Xia, J.; Wang, H.; Xie, Y.; Yu, H.; Lei, J.; et al. A library of atomically thin metal chalcogenides. *Nature* **2018**, *556*, 355–359. [CrossRef]
19. Kong, D.; Chen, Y.; Li, N. Gaussian process regression for tool wear prediction. *Mech. Syst. Signal Process.* **2018**, *104*, 556–574. [CrossRef]
20. Liu, K.; Hu, X.; Wei, Z.; Li, Y.; Jiang, Y. Modified Gaussian process regression models for cyclic capacity prediction of lithium-ion batteries. *IEEE Trans. Transp. Electrif.* **2019**, *5*, 1225–1236. [CrossRef]
21. Deringer, V.L.; Bartók, A.P.; Bernstein, N.; Wilkins, D.M.; Ceriotti, M.; Csányi, G. Gaussian process regression for materials and molecules. *Chem. Rev.* **2021**, *121*, 10073–10141. [CrossRef]
22. Tapia, G.; Elwany, A.H.; Sang, H. Prediction of porosity in metal-based additive manufacturing using spatial Gaussian process models. *Addit. Manuf.* **2016**, *12*, 282–290. [CrossRef]
23. Lin, C.; Li, T.; Chen, S.; Liu, X.; Lin, C.; Liang, S. Gaussian process regression-based forecasting model of dam deformation. *Neural Comput. Appl.* **2019**, *31*, 8503–8518. [CrossRef]
24. Chen, B.; Shen, L.; Zhang, H. Heteroscedastic sparse Gaussian process regression-based stochastic material model for plastic structural analysis. *Sci. Rep.* **2022**, *12*, 3017. [CrossRef] [PubMed]
25. Lu, H.J.; Zou, N.; Jacobs, R.; Afflerbach, B.; Lu, X.-G.; Morgan, D. Error assessment and optimal cross-validation approaches in machine learning applied to impurity diffusion. *Comput. Mater. Sci.* **2019**, *169*, 109075. [CrossRef]
26. Ahmad, G.N.; Fatima, H.; Ullah, S.; Saidi, A.S. Efficient medical diagnosis of human heart diseases using machine learning techniques with and without GridSearchCV. *IEEE Access* **2022**, *10*, 80151–80173. [CrossRef]
27. Alhakeem, Z.M.; Jebur, Y.M.; Henedy, S.N.; Imran, H.; Bernardo, L.F.A.; Hussein, H.M. Prediction of ecofriendly concrete compressive strength using gradient boosting regression tree combined with GridSearchCV hyperparameter-optimization techniques. *Materials* **2022**, *15*, 7432. [CrossRef] [PubMed]
28. Emmert-Streib, F.; Dehmer, M. Evaluation of regression models: Model assessment, model selection and generalization error. *Mach. Learn. Knowl. Extr.* **2019**, *1*, 521–551. [CrossRef]
29. Bassman Oftelie, L.; Rajak, P.; Kalia, R.K.; Nakano, A.; Sha, F.; Sun, J.; Singh, D.J.; Aykol, M.; Huck, P.; Persson, K.; et al. Active learning for accelerated design of layered materials. *NPJ Comput. Mater.* **2018**, *4*, 74. [CrossRef]
30. Solomou, A.; Zhao, G.; Boluki, S.; Joy, J.K.; Qian, X.; Karaman, I.; Arróyave, R.; Lagoudas, D.C. Multi-objective Bayesian materials discovery: Application on the discovery of precipitation strengthened NiTi shape memory alloys through micromechanical modeling. *Mater. Des.* **2018**, *160*, 810–827. [CrossRef]

31. Baird, S.G.; Liu, M.; Sparks, T.D. High-dimensional Bayesian optimization of 23 hyperparameters over 100 iterations for an attention-based network to predict materials property: A case study on CrabNet using Ax platform and SAASBO. *Comput. Mater. Sci.* **2022**, *211*, 111505. [CrossRef]
32. Silva, S.J.; Keller, C.A.; Hardin, J. Using an Explainable Machine Learning Approach to Characterize Earth System Model Errors: Application of SHAP Analysis to Modeling Lightning Flash Occurrence. *J. Adv. Model. Earth Syst.* **2022**, *14*, e2021MS002881. [CrossRef]
33. Senkić, A.; Bajo, J.; Supina, A.; Radatović, B.; Vujičić, N. Effects of CVD growth parameters on global and local optical properties of MoS_2 monolayers. *Mater. Chem. Phys.* **2023**, *296*, 127185. [CrossRef]
34. Saenz, G.A.L.; Biswas, C.; Yamaguchi, H.; Villarrubia, C.N.; Mohite, A.D.; Kaul, A.B. Effects of synthesis parameters on CVD molybdenum disulfide growth. *MRS Adv.* **2016**, *1*, 2291–2296. [CrossRef]
35. Zhang, X.; Zhao, H.B.; Zhang, Q.Z.; Wei, F. Controllable growth and morphology evolution of 2D MoS_2 via CVD method. *Chin. J. Rare Met.* **2020**, *44*, 1249.
36. Yang, S.Y.; Shim, G.W.; Seo, S.B.; Choi, S.Y. Effective shape-controlled growth of monolayer MoS_2 flakes by powder-based chemical vapor deposition. *Nano Res.* **2017**, *10*, 255–262. [CrossRef]

nanomaterials

MDPI

Article

Synthesis of Composites for the Removal of F^- Anions

Adriana Saldaña-Robles [1,*], Javier Antonio Arcibar-Orozco [2], Luz Rocío Guerrero-Mosqueda [1], César Eduardo Damián-Ascencio [3,*], Alfredo Marquez-Herrera [1], Miguel Corona [4], Armando Gallegos-Muñoz [3] and Sergio Cano-Andrade [3]

1 Department of Agricultural Engineering, University of Guanajuato, Ex Hacienda El Copal km 9, Irapuato 36500, Mexico; rocioguerrerogto@gmail.com (L.R.G.-M.); amarquez@ugto.mx (A.M.-H.)
2 Centro de Innovación Aplicada en Tecnología Competitiva, CIATEC, Omega 201, Industrial Delta, Leon 37545, Mexico; jarcibar@ciatec.mx
3 Department of Mechanical Engineering, Universidad de Guanajuato, Salamanca 36885, Mexico; gallegos@ugto.mx (A.G.-M.); sergio.cano@ugto.mx (S.C.-A.)
4 Mechanical Engineering and Management, Autonomous University of San Luis Potosi, COARA, San Luis Potosi 78000, Mexico; miguel.corona@uaslp.mx
* Correspondence: adriana.saldana@ugto.mx (A.S.-R.); cesar.damian@ugto.mx (C.E.D.-A.); Tel.: +52-462-624-1889 (A.S.-R.)

Abstract: This work presents the synthesis of amine and ferrihydrite functionalized graphene oxide for the removal of fluoride from water. The synthesis of the graphene oxide and the modified with amine groups is developed by following the modified Hummer's method. Fourier transform infrared spectrometry, X-ray, Raman spectroscopy, thermogravimetric analysis, surface charge distribution, specific surface area and porosity, adsorption isotherms, and the van't Hoff equation are used for the characterization of the synthesized materials. Results show that the addition of amines with ferrihydrite generates wrinkles on the surface layers, suggesting a successful incorporation of nitrogen onto the graphene oxide; and as a consequence, the adsorption capacity per unit area of the materials is increased.

Keywords: fluoride adsorption; graphene oxide composites; nitrogen groups; advanced materials

Citation: Saldaña-Robles, A.; Arcibar-Orozco, J.A.; Guerrero-Mosqueda, L.R.; Damian-Ascencio, C.E.; Marquez-Herrera, A.; Corona, M.; Gallegos-Muñoz, A.; Cano-Andrade, S. Synthesis of Composites for the Removal of F^- Anions. *Nanomaterials* **2023**, *13*, 2277. https://doi.org/10.3390/nano13162277

Academic Editor: George Z. Kyzas

Received: 3 June 2023
Revised: 20 June 2023
Accepted: 22 June 2023
Published: 8 August 2023

1. Introduction

The pollution of water bodies around the world represents an issue, mainly due to the presence of hazardous arsenic and fluoride [1–7]. This is especially hazardous for uses such as water drinking and irrigation in agriculture. Particularly, the presence of fluoride in groundwater is controlled by the mass exchange with the media and mineral composition of the soil [1,8,9].

The presence of fluoride in drinking water within the permissible limits, stablished by the World Health Organization (WHO), i.e., concentrations lower than 1.5 mg L^{-1}, can be beneficial for bone formation [10]. However, in concentrations higher than 1.5 mg L^{-1}, fluoride represents a threat to human health because it reduces the adsorption of calcium and phosphorous, causing dental fluorosis, neural degeneration, and brain damage, among other disorders [11–15]. Thus, there is a need to develop water treatment systems capable of efficiently remove this constituent from groundwater. Some treatments commonly used are precipitation/coagulation [1,13,14,16,17], electrocoagulation [14,18,19]), ion exchange [20,21], membrane processes [22,23], and adsorption processes [22,24,25]. Among these methodologies, adsorption technology is widely used for fluoride removal because its ease of operation, low cost, and high efficiency. Some adsorbents employed are based on innocuous metal oxides such as iron, zinc, aluminum, manganese, and carbon-based materials [12,13,15,18,25–27].

Graphene-based adsorbents are novel materials that have attracted much interest in recent years. The diversity of surface oxygenated groups in graphene oxide (GO)

makes them ideal for the attraction of adsorbates and the insertion of reactive functional groups [13,20,28,29]. Most of fluoride adsorption occurs through complexation reactions and electrostatic interactions [30]. Thus, if acid groups are present in the GO surface, the adsorption occurs between the metallic complexes in solution and dissociated groups, by electrostatic attraction (such as van der Waals forces) and/or ligand interchanges [31]. In order to improve the adsorptive capacities, different researchers focused on surface modifications for the incorporation of functional groups and other materials, such as metal oxides [3,13–15,29,32–35]. Particularly, iron oxides are widely used to modify the surface of the GO in order to increase the fluoride removal [12,15,29,33]. The efficiency of iron-oxides for removing fluoride depends on physical properties such as crystalline structure, morphology, specific surface area, and particle size. These properties can be modified in the synthesis process [33]. Huang et al. [22] reported that the defluorination mechanism involves the following two categories

$$MO_x + xH_2O \rightarrow M(OH)_{2x} \quad (1)$$

$$M(OH)_{2x} + yF^- \rightarrow M(OH)_{2x-y}F_y + yOH^- \quad (2)$$

$$MOH + HF \rightarrow MOHHF \quad (3)$$

$$MOHHF \rightarrow MF + H_2O \quad (4)$$

where M represents metals such as Zr, Mg, Fe, Al, etc.

The first category follows Equations (1) and (2), where hydrogen bonds hydroxy and fluoride ions. The second category follows Equations (3) and (4), where the Fe-doped species are typically hard Lewis acids and possess strong interactions with hard bases of fluoride due to a hydroxy transition. From the above reactions, it is observed that hydroxyl groups play a significant role during fluoride adsorption. Also, the incorporation of nitrogen in the GO surface is an interesting form of surface modification, with the potential of improving during chemical interactions with iron complexes composite formation.

Among nitrogen-based surface modifiers of GO, surfactants improve the adsorption capacity by increasing the surface charge and thus, favoring the electrostatic attraction of inorganic compounds contained in water [20,36–38]. Some authors reported that cationic surfactants with ammonium compounds increase the positive zeta potential of the adsorbent, whereas anionic surfactants favor the surface negative charge [39]. Arcibar et al. [40], reported that nitrogen incorporation into the GO matrix has the potential of improving the surface area of composites with iron oxyhydroxides, which is a consequence of a better distribution of iron hexaaquo complexes during nucleation. This effect improves the performance of the composites during the adsorption of surrogates of chemical warfare agents [40]. Also, Mahmudov et al. [41] reported that activated carbon can be functionalized with quaternary ammonium salts, improving the adsorption capacity of perchlorate.

Some composites including graphene oxides functionalized with ferric oxyhydroxide materials have been synthesized, such as composites of magnetic graphene nanoplaquets coated with nanoparticles of FeO-Fe_2O_3, graphene oxides with reduced Fe_3O_4 dispersible in water [42], and metal-organic frameworks (MOFs) [43]. The presence of nitrogenated groups has a basic character that promotes electrostatic attraction among the acid groups. This changes the thermodynamic environment, producing new materials characterized by a better dispersion of functional surface groups.

Another potential solution is Capacitive Deionization (CDI), a water desalination technology that has been the focus of recent studies due to its high ion selectivity, efficient water recovery, and low energy consumption. However, its industrial application has yet to be realized due to several limitations, including restricted electrosorption capacity, slow electrosorption rate, and poor cycling stability [44]. The photo-electric capacitive deionization (PECDI) technologies are presented as a novel variant of the CDI technologies, which takes advantage of photo-enhancement of ionic transport kinetics, which is enabled by the edge-enhanced vertical graphenes, obtaining higher adsorption capacities as well as

faster responses. However, this technology is still under investigation and its full potential and limitations are still to be understood [45].

To the best knowledge of the authors, only some materials based on graphene oxides as a matrix for ferric oxyhydroxides that has not been functionalized with amine groups have been studied [13,33]. The present work focuses on GO modified with nitrogen and ferrihydrite composites for the removal of fluoride from aqueous solutions. We study the impregnation of GO with nitrogen compounds, i.e., amines with different pK_a prior to iron nucleation. The goal is to determine if the addition of nitrogen moieties with different chemistry can improve the nucleation of iron during ferrihydrite formation and in this way, obtain advanced adsorbent materials.

2. Materials and Methods

2.1. Reagents

Graphite powder (99%) and sodium fluoride (NaF) (purity: 99.95%) were obtained from Sigma Aldrich. All chemical reactants were of analytical grade, such as sulfuric acid (H_2SO_4), nitric acid (HNO_3), potassium permanganate ($KMnO_4$), potassium hydroxide (KOH), sodium hydroxide (NaOH), hydrogen peroxide (H_2O_2, 30%), carbonyldiamine (CH_4N_2O), diphenylamine ($C_{12}H_{11}N$), ethylene glycol ($C_2H_6O_2$), ferric nitrate nonahydrate ($Fe(NO_3)_3{\cdot}9H_2O$), deionized water and TISAB II.

2.2. Experimental Set-Up

The synthesis of the GO composites functionalized with ferrihydrite/amine groups was developed in three steps:

Step 1: GO synthesis. The synthesis of the GO was carried out according to the modified Hummer's method [46], where 10 g of graphite powder was mixed with 230 mL of H_2SO_4 (98%). The mixture was stirred for 2 h into a cold bath. After this, 30 g of $KMnO_4$ were added to the mixture and it was stirred for 180 min and kept at a temperature below 20 °C until it reached 2 °C. Then, the mixture was aged at room temperature for 30 min. After that, 250 mL of deionized water was added slowly under a cold bath and stirred for 15 min. Subsequently, 1.4 L of deionized water was added, followed by 100 mL of H_2O_2 at 30%. The mixture was aged 12 h at room temperature. This mixture was washed several times with deionized water to obtain a pH of 3.03 approximately. Then, the mixture was centrifuged at 5000 rpm for 30 min, and the graphite oxide obtained was cooled to −20 °C for 15 days. Finally, the graphite oxide obtained was sonicated for 2 h to exfoliate it and obtain graphene oxide.

Step 2: Addition of amine groups. The addition of amine groups was developed following two methodologies. The former is carried out by modification with carbonyl diamine (urea) and the latter with diphenylamine. For both methods, 198 mL of deionized water was added to 1.2 g of GO, and the mixture was sonicated by 2 h in order to disperse GO into water. Then, either 3.6 g of carbonyl diamine or 3.6 g of diphenylamine were dissolved in 210 mL of ethylene glycol, added to the GO dispersion, and stirred at 140 rpm and 80 °C for 24 h. Finally, both modified mixtures were centrifuged at 400 rpm for 40 min, washed with water-ethylene glycol (1:1), and centrifuged several times until a pH of 7 was reached in the residual solution. These mixtures were filtered (Watman, 40) and dried at 80 °C for 15 h. The resultant materials were named GOU and GODA because of the addition of amine groups through the carbonyl diamine and diphenylamine, respectively.

Step 3: GOU and GODA decorated with ferrihydrite (FH) ($Fe_5HO_8{\cdot}\ 4H_2O$). First, 1 g of GOU (GODA) was dispersed into 165 mL of deionized water by sonication for 2 h. Then, 39.13 g of $Fe(NO_3)_3\ 9H_2O$ was added to the GOU (GODA) dispersion, 800 mL of deionized water was added, the mixture was stirred at 100 rpm, and then 0.1 M of KOH was dropped carefully until a pH of 7.6–8 is reached. After that, the mixture was centrifuged at 4500 rpm for 10 min. The product was dispersed in water and centrifuged several times in order to remove all unreacted residues. Finally, the products were dried in a convection oven at 60 °C for 24 h, and the resulting materials were named GOUFH and GODAFH.

3. Characterization

3.1. Fourier Transform Infrared Spectrometry

The Fourier transform infrared spectrometry (FT-IR) was obtained in a Thermo Scientific NICOLET IS10 in attenuated total reflectance (ATR) mode in order to characterize the functional groups. The spectrum was generated in the range of wave numbers between 4000 and 550 cm^{-1} with 32 scans and 4 cm^{-1} of resolution.

3.2. X-ray

The X-ray diffraction (XRD) was carried out in a Philips X'pert spectrometer with a 0.02° step at 30 mA and 40 kV between anglles of 10° and 90°. The X-ray analysis is developed with a $\kappa - \alpha$ X-ray like excitation source of 1486.6 eV. The analysis was developed in the range of 292–288 eV, and the spectra data is deconvoluted.

3.3. Raman Spectra Microscopy

The Raman spectra microscopy was carried out in a RENISHAW (In-Via), using a laser wavelength of 514 nm as excitation source, and a laser spot of 1 μm with a power at the sample below 10 mW. The exfoliation of graphitic oxide into GO monolayers was carried out through a SONIC VCX 750 model (20 kHz, 750 W) in a direct immersion oven of titanium.

3.4. Thermogravimetric Analysis

The thermogravimetric analysis (TGA) of the sample was carried out with a thermogravimetric differential scanning calorimetry analysis (TGA; NETZSCH, STA449F3), from room temperature to 800 °C, with a temperature increasing rate of 10 °C min^{-1} and 25 mL min^{-1} of air as heat carrier.

3.5. Surface Charge Distribution

The distribution of surface charge was obtained by adding 100 mg of the compound to 50 mL of NaCl 0.1 M electrolyte solution. The suspension was bubbled with N_2 by 2 h. Then, 0.1 M HCl was added to the suspension. After that, the suspension was titrated with NaOH in a 916 Ti-touch (Metrohom). Finally, the distribution of surface charge was obtained by determining the characterization of the surface of activated carbons in terms of their acidity constant contributions.

3.6. Specific Surface Area and Porosity

The specific surface area and porosity of the compounds were measured in a Micromeritics TriStar II Plus 2.03 equipment by N_2 adsorption at −196 °C, before the sample was degassed at 60 °C and a vacuum of 10^{-4} atm, for 2 h. The calculation of the specific surface area and pore volume was developed using the Brunauer-Emmet-Teller (BET) and Barret-Joiner-Halenda (BJH) relations, respectively.

3.7. Scanning Electron Microscopy

Materials were observed by Scanning Electron Microscopy (SEM) in a Helios microscope (FEI 600 NANOLAB) at an acceleration voltage of 8 keV, using secondary and backscattered electrons. Before the analysis, the samples were grinded in an agate mortar, then they were suspended in isopropanol. Finally, the samples were mounted in a SEM-pin.

3.8. Adsorption Isotherms

Step 1. The adsorption experimental study for the removal of fluoride ions was carried out at 25 °C and a pH of 4. First, 0.025 g of each synthesized material (GO, GOFH, GODA, GOU, GODAFH, GOUFH) as adsorbent was placed into an Erlenmeyer flask. Then, 20 mL of a fluoride solution at different initial concentration was added (0–10 m L^{-1}). The flask with the mixture was stirred at 160 rpm. The pH was adjusted with 0.1 M NaOH and HCl. Finally, the mixture was centrifugated at 4000 rpm for 15 min and the solution was collected

and analyzed by a fluoride ion selective electrode (Orion Star A214 Thermo Scientific). The adsorption capacity was adjusted using both, the Langmuir and Freundlich models. From these results, the better adsorbent was selected for further characterization.

Step 2. For the selected material, the adsorption experimental studies for the removal of fluoride ions were carried out at 25, 35, and 45 °C, and a pH of 4, 6, and 8. First, 0.025 g of the adsorbent was placed into an Erlenmeyer flask. Then 20 mL of a fluoride solution at different initial concentrations (0–10 mg L^{-1}) was added. These mixtures were shaken at 160 rpm, at different temperatures, and at different pHs. The pH was adjusted during the experiment with 0.1 M NaOH and HCl until the equilibrium was reached. Then, the mixtures were separated by centrifugation at 4000 rpm, for 15 min. Finally, the clear solutions were collected, and the fluoride residual concentration was analyzed. The adsorption capacity was adjusted to the Langmuir and Freundlich models.

The Langmuir model implies a monolayer capacity and is given as

$$q_e = \frac{q_L b C_e}{1 + bC_e} \tag{5}$$

where q_e is the equilibrium adsorption capacity, C_e is the equilibrium solute concentration, q_L is related to the maximum adsorption capacity, and b is related to the bonding energy of adsorption.

The Freundlich model, which represents heterogeneous adsorption, is given as

$$q_e = K_F C_e^{1/n} \tag{6}$$

where K_F is the adsorption equilibrium constant representative of the adsorption capacity, C_e is the equilibrium adsorption capacity, and n is the adsorption intensity.

3.9. The Van't Hoff Equation

Considering the relations between the Gibbs free energy and the equilibrium constant ($\Delta G^0 = \Delta H^0 - T\Delta S^0$ and $\Delta G^0 = -RT \ln K_d$), the van't Hoff equation is given as

$$\ln K_d = -\frac{\Delta H^0}{R}\left(\frac{1}{T}\right) + \frac{\Delta S^0}{R} \tag{7}$$

where T is the temperature in absolute units, R is the ideal gas constant and K_d is the equilibrium constant. The adsorption constant was determined from the data coming from the isotherm by the identification $K_d = b$, and in consequence K_d is dimensionless and its numerical value is equal to b [47]. The absolute value of ΔG^0 is associated to specific interactions. For instance, ΔG^0 around 4 kJ/mol is associated to a hydrophobic force whereas a value ranging from 4 to 10 kJ/mol is associated to Van der Waals forces.

4. Results and Discussion

4.1. Fourier Transform Infrared Spectrometry

Base material: The infrared curve for the synthesized GO contains a region between 3000–3600 cm^{-1} where a wide band is present, which corresponds to both adsorbed water and also bulk hydroxil groups. This water accumulation increases the inter-planar distances, producing a structure modification, and through exfoliation in the synthesis process for the GO material, it generates imperfections in the hexagonal lattice, such as vacancies. These imperfections generate an anchorage of the epoxy functional groups between the basal planes and carboxylic acid in the edge of the sheets [48,49].

Modified materials: A modification of the GO surface suggests the reduction of these functional groups, favoring the formation of bonds with the nitrogenated groups as well as the oxygen surface groups of iron. In the same way, it is possible to identify in GO the presence of carbonyl (C=O) at ~1730 cm^{-1}, carboxyle (COOH) at ~2360 cm^{-1}, epoxide at ~1201 cm^{-1}, and C−O groups at ~1034 cm^{-1}. The above-mentioned groups obtained in the GO fix its hydrophilic properties. These bands are in agreement with those of the

materials reported in the technical literature [46]. As is observed the bands at 1150 cm^{-1} and 1600 cm^{-1} reveal the presence of urea whereas the amine group can be attributed to the band at 3400 cm^{-1}.

The composites named GOFH, GODAFH, and GOUFH, prevailed in three regions which are shown in Figure 1. In the spectrum, it is observed the bands at ∼3150 cm^{-1} which represent the stretching of O−H bonds characterized by a wide band, are related to structural hydroxide and adsorbed H_2O. Also, the bands between 1650 and 1300 cm^{-1} belong to symmetric and asymmetric stretching of the C−O and the deformation of water at ∼1630 cm^{-1}. In addition, the stretching of Fe−O is shown in the bands at 980, 890, 617, and 565 cm^{-1}. However, the lower crystallinity of the ferrihydrite is a factor that affects the infrared spectrum, decreasing the resolution of the signals [50,51].

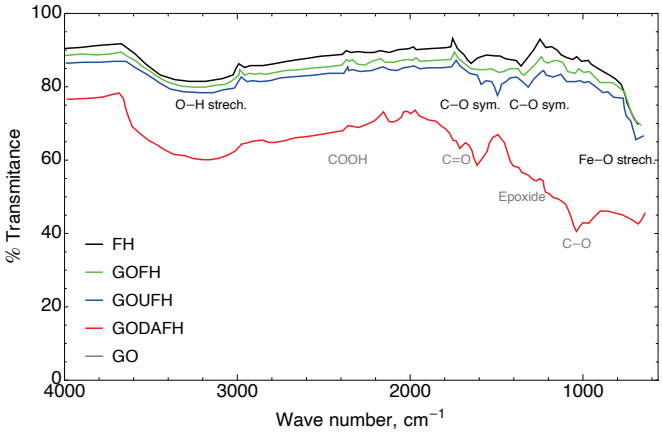

Figure 1. FT-IR of the FH (black), GOFH (green), GOUFH (blue), GODAFH (red), and GO (gray) materials.

Kuang et al. [33] synthesized GO impregnated with goethite and akageneite for the remotion of fluoride. They found that the synthesized materials have characteristic signals at ∼3300 cm^{-1} due to the stretching of structural hydroxile groups, at ∼1628 cm^{-1} due to C=O groups, at ∼1620 cm^{-1} due to vibrations of C=C bounds, at ∼1380 cm^{-1} due to carboxile groups, and at ∼1032 cm^{-1} due to the stretching of C−O. Also, the composite material GO/Goethite, shows a signal at ∼3340 cm^{-1} related to the stretching of hydroxile group of the goethite, confirming the presence of Fe−O with signals at 847 and 671 cm^{-1}. For the composite material GO/Akageneite the FT-IR shows signals at 588 and 466 cm^{-1}. These signals are in agreement with the signals shown in Figure 1, related with oxygenated groups for the GO and some signals related to stretching of Fe−O bounds in the range of 400–600 cm^{-1}.

4.2. X-ray Analysis

Figure 2 shows the X-ray diffractogram of the oxidized material synthesized by the modified Hummers method. In the GO, it is observed a characterized signal at an angle of 7° (2θ), which is related to the distance between layers of GO, and indicates the positive oxidation of graphene. An absence of a pronounced peak at 26.5° is also observed, suggesting that all the graphite has been converted into GO. This peak is observed for the modified materials only. The results obtained in the DRX analysis are in agreement with those reported in previous works and exhibit the transformation of graphite to graphene oxide [52,53].

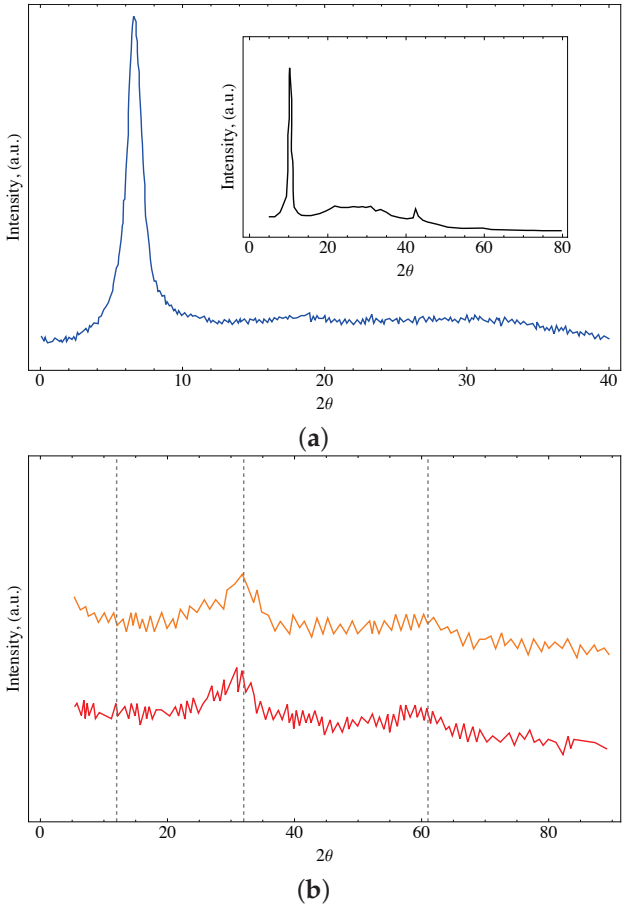

Figure 2. X-ray of the (**a**) GO where the insert shows the graphene oxide reported in [54] and (**b**) for the GOFH (orange line) and GOUFH (red line) materials.

It is also observed that the ferrihydrite diffractogram shows noise related to its lower degree of crystallinity. The most defined bands at 35 and 63 can be attributed to 2-line ferrihydrite. These results are in agreement with the reported in the literature [55,56]. In general, it is observed an amorphous compound with wide peaks related to both, a lower degree of crystallinity and a small size of crystals (see Figure 2). The identity of the ternary composite was confirmed in similar patterns for both GOFH and GOUFH materials, with the two characteristic bands centered at 35° and 63°. The small difference in the peaks observed at 23, 30, and 40° could be related to the presence of urea [57]. However, these differences are too small to be analyzed.

4.3. Raman Analysis

Raman spectroscopy is a non-destructive test useful to analyze the structure of materials with carbon content. The Raman analysis was carried out for the characterization of the graphene oxides synthesized in the present work, i.e., GO, GOUFH, and GODAFH, and is shown in Figure 3. The Raman test shows a characteristic peak at 1336, 1292, and 1331 cm^{-1} for the GO, GOUFH, and GODAFH materials, respectively. This band is known as the D band, which is an indicator of the presence of imperfections in the graphite crystalline structure, such as order, bound angle, vacancies, and lattice defects. Also, the bands observed at 1574 and 1567 cm^{-1} in GO and GODAFH materials, respectively, correspond to a dispersion of first order in the E2g modes. Both sets of bands have a similar intensity due to the strong oxidation produced by the modified Hummers method, which induces a structural disorder. Additionally, the small peaks at 2627 and 2673 cm^{-1} for the GOUFH and GOUFG materials are related to the resonance of the D band, which is absent in the GODAFH material. The double resonant modes in the Raman dispersion at the 2322 cm^{-1}

band for the GOUFH are still a matter of discussion; however, some authors [58–60] mention that these bands are related to a process of two phonons of the D and D′ type. This process involves the contribution of optic phonons (D) and acoustic longitudinal phonons (D′), which are usually known as G″ (or D+D′) modes.

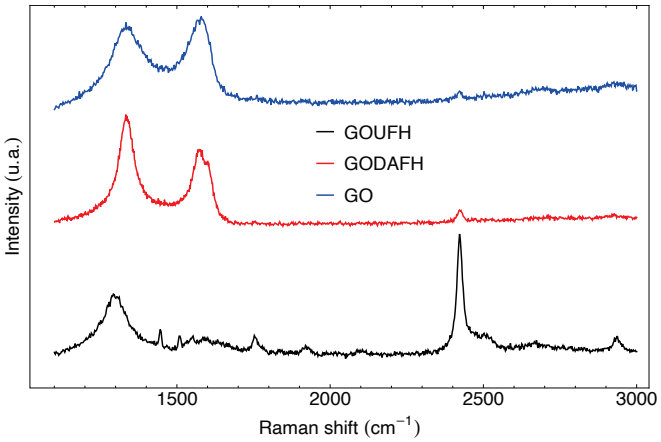

Figure 3. Raman spectroscopy of the GO (blue), GODAFH (red), and GOUFH (black).

4.4. Thermogravimetric Analysis

Figure 4 shows the TGA termograms of the GOUFH material. Figure 4a shows three weight loss stages. It is observed that the lower weight loss of 7.04% occurs from 32 °C to 100 °C, is related to either desorption or evaporation of water from dehydroxylation of hydrous mixed oxide and GO of the composite. This is in agreement with the results reported in the literature [15,16]. The weight loss of 13.08% from 100 to 400 °C is related to the decomposition of nitrogen groups in the GOUFH material. In addition, it is observed a weight loss of 2.81% from 400 to 500 °C. Thus, a total weight loss of 23.83% was observed. The high temperature required for the decomposition of the GOUFH, indicates that after the functionalization with amine groups, its thermal stability is increased.

To determine the nature of the DTGA profile, the rate of change of the weight loss with respect to time is considered, as is shown in Figure 4b. It is observed that the DT spectrum has two endothermic peaks at just before 48 °C and 395 °C, and two exothermic bands at around 222 °C and 310 °C.

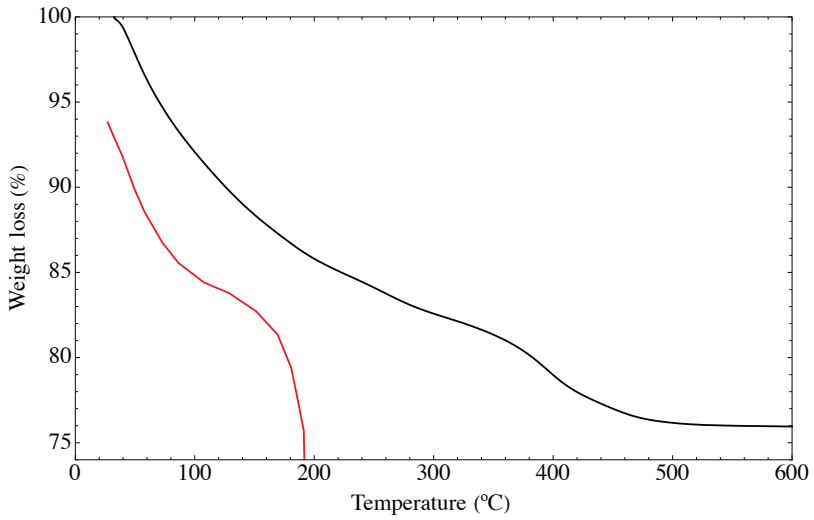

(**a**)

Figure 4. *Cont.*

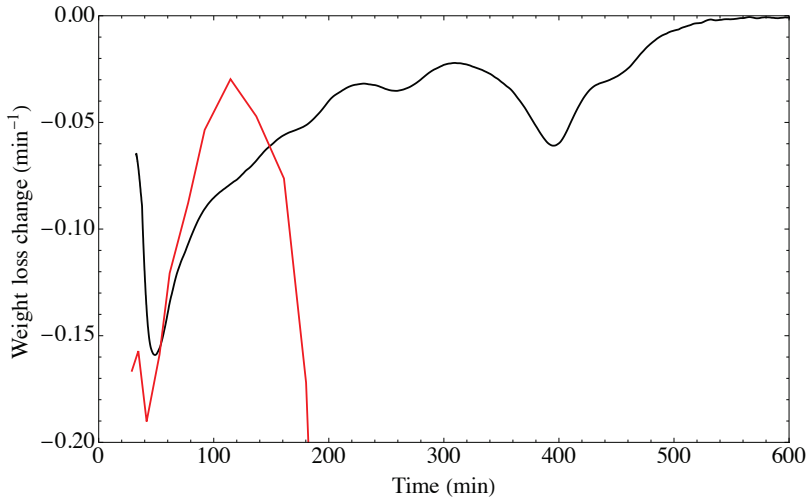

(**b**)

Figure 4. TGA spectra of GOUFH material (**a**) weight loss and (**b**) rate of change of the weight loss, the red line corresponds to the precursor materials and the black line to the GOUGFH material.

As is observed in Figure 4 the GO materials have lower thermal stability since it is completely degraded at temperatures of 190 °*C* whereas the modified material degrades at higher temperatures.

4.5. XPS Analysis

The functional groups on the adsorbent surface of GOUFH and GO were analyzed by the XPS technique. Figure 5a shows the XPS spectra for the GOUFH, which is the material with the best F^- adsorption capacity. In the deconvoluted spectra, C1s is observed because the spectrum of the sample contains three peaks at 284.2, 285.4, and 288.2 eV, corresponding to the carbonyl, epoxide/ether, and carboxyl functional groups, respectively. These results confirmed the presence of GO with a considerable oxidation degree [61]. A section of the XPS not deconvoluted is shown in the insert of Figure 5a. It is observed a peak of low intensity at 400 eV, is characteristic of N1s [62]. This N1s peak is related to the amine groups added during the modification of the GO surface. These results indicate that the GOUFH maintains its functionality even after the composite formation.

Figure 5b shows that the O1s region could be deconvoluted into three overlapped peaks at 531, 530, and 529 eV, corresponding to $Fe(OH)_3$, Fe(OH)O, and iron oxides in the lattice structure, respectively. These results are in agreement with those reported in the literature [16,33]. In addition, the GOUFH shows the formation and growth of iron oxide on its surface, as expected.

Figure 5c displays the C1s XPS spectra for the graphene oxide (GO) sample, which consists of three peaks at 283.3, 284.4, and 287.0 eV. These peaks correspond to the C−C, C−O, and C=O functional groups, respectively. Despite GO has the potential to exhibit six possible C1s components like graphene, the XPS spectrum of graphene oxide typically presents two main peaks, in contrast to the single peak displayed by graphene, as depicted in Figure 5a,c. These observations confirm the formation of GO [61,63,64].

Figure 5d exhibits the O1s XPS spectra for the graphene oxide (GO) sample, containing three peaks at 531.8, 532.4, and 532.9 eV. These peaks correlate with the C−OH, C−O, and C−C functional groups, respectively (3). It's significant to note that the O1s XPS spectra for the GOUFH material (Figure 5b) demonstrate lower binding energy than the O1s XPS spectra for the OG sample, as indicated in Figure 5c (dashed line, non-normalized curve).

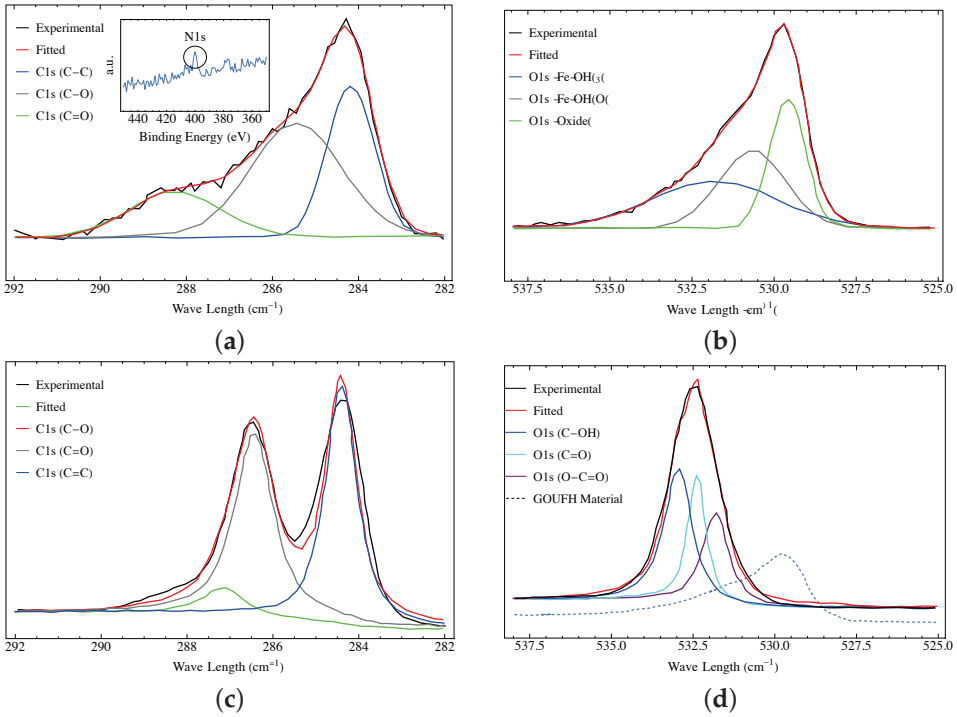

Figure 5. XPS spectra of the GOUFH material (**a**) C1s and (**b**) O1s, and for the precursor (**c**) C1s and (**d**) O1s.

4.6. Surface Charge Distribution

The charge distribution of the synthesized materials is shown in Figure 6 through the pH_{PZC} for the GODA, GOU, GODAFH, and GOUFH materials. As it is observed, the GODA and GOU materials have a pH_{PZC} of 5.8 and 7.2, respectively, whereas the GODAFH and GOUFH materials have a pH_{PZC} of 8.5 and 8.3, respectively. The difference between the first materials (GODA and GOU) with respect to the second materials (GODAFH and GOUFH) is due to the addition of ferric oxyhydroxides groups, which affect the surface charge density. Also, the surface charge of the GODAFH and GOUFH materials depends of the pH, because at a pH $<$ pH_{PZC}, the adsorbent materials have a positive surface charge, whereas at a pH $>$ pH_{PZC}, the adsorbent materials have a negative surface charge. Thus at a pH $<$ pH_{PZC}, the surface of the GODAFH and GOUFH materials is more suitable for the electrostatic attraction of F^-. This mechanism has already been described in the technical literature [33,65]. As is known, the charge distribution on the surface of the materials is related to the dissociation and deprotonation of surface groups. Thus, if the pH_{PZC} of the GODAFH and GOUFH materials is higher than the pH_{PZC} of ferrihydrite, the nucleation, and condensation of iron complexes on the GO surface are linked to a higher amount of hydroxyl groups of an acidic nature.

The pH_{PZC} obtained for each synthesized material was lower than 3 for the GO and around 9 for the FH material and around 8.6, 7.2, 5.8, 8.5, and 8.3 for the GOFH, GODA, GOU, GODAFH, and GOUFH respectively. As is known, the modification of GO with nitrogenated groups affects the surface charge of the adsorbent material [20,39]. Thus, the difference in the pH_{PZC} between the GOUFH and the GODAFH is related to the fact that the GOUFH is synthesized with a primary amine, where its basic character promotes a bigger electrostatic attraction with the cation acid groups, i.e., the hydroxyl groups of the ferric oxyhydroxides. On the other hand, the GODAFH material was synthesized with a secondary amine, which limits the electrostatic attraction with the acidic hydroxyl groups of the ferric oxyhydroxide. This is reflected in the specific surface area i.e., the GOUFH shows a bigger specific surface area than the GODAFH.

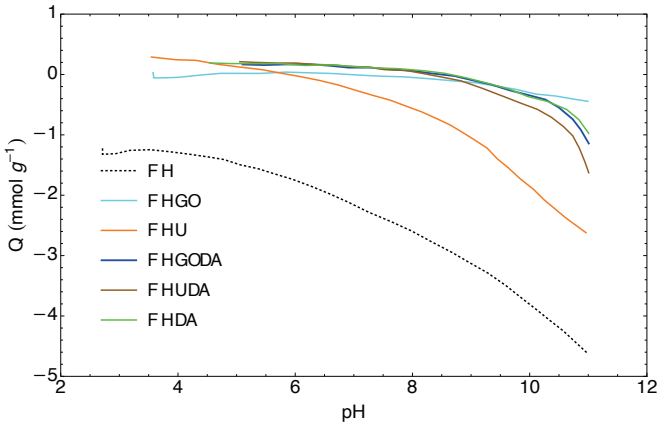

Figure 6. Charge distribution of the synthesized materials.

4.7. BET Analysis

The specific surface area is determined from the nitrogen adsorption isotherms, shown in Figure 7. The GO shows a specific surface area of 4 m^2 g^{-1} which is less than the surface area reported in the literature of 20–40 m^2 g^{-1} [46,66]. This discrepancy is due to the stiffness and beds of the laminar structure, which affects the laminar spacing of the GO, not allowing the nitrogen molecule to go into the laminar structure. On the other hand, after the modification of the GO surface with amine groups, the specific surface area obtained is 4 and 5 m^2 g^{-1} for the GOU and GODA materials, respectively. It is observed that these values did not represent a significant change with respect to that of GO.

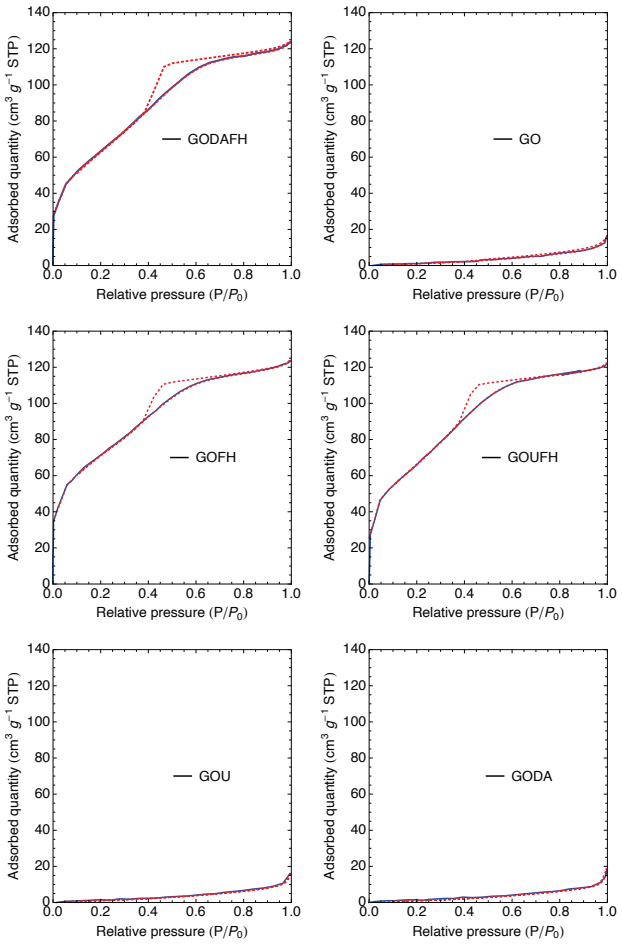

Figure 7. Nitrogen adsorption isotherms of the synthesized materials, The blue line represents the adsorption process, while the red dashed line indicates the adsorption-desorption process.

The composites modified with ferric oxy-hydroxides show a significative increase in the specific surface area, i.e., 247, 226, and 239 m^2 g^{-1} for the GOFH, GODAFH, and GOUFH materials, respectively. This increase in the specific surface area indicates a successful growth of iron oxides on the surface of the GO since iron oxyhydroxides are known to have a large surface when in an amorphous structure. This growth depends on different synthesis factors, such as the flow rate at which the ferric solution is added to the GO and the stirring rate. Also, these specific surface areas are in agreement with the values reported in the literature [67]. Table 1 shows the specific surface area and pore size distribution of the materials. It is observed that the GOUFH has a bigger specific surface area than the GODAFH. In the same manner, the pore diameter of the GOUFH is bigger than that of the GODAFH, suggesting a higher adsorption capacity for the GOUFH. This result is also in agreement with the reported in the technical literature [68].

Table 1. Specific surface area and pore size distribution.

Material	Specific Surface Area (m^2 g^{-1})	Volume (cm^3 g^{-1})	Pore Diameter (nm)
GO	4	0.015	5.594
GODA	4	0.012	5.826
GOU	5	0.012	5.668
GOFH	247	0.185	3.207
GODAFH	226	0.185	3.303
GOUFH	239	0.183	3.155

The pore size distribution of the synthesized materials is shown in Figure 8. This distribution is obtained using the Barrett–Joyner–Halenda (BJH) method, assuming that the pore filling due to condensation represents a well-defined interface in the pores. Both materials, GOUFH and GODAFH, show the maximum pore volume with pore diameters around 3.155 and 3.303 nm respectively. That is, narrow mesopores are present, which is in agreement with the reported in the literature, i.e., iron oxides have an average pore diameter between 3 and 4 nm [69]. Also, the GODAFH shows the highest pore volume, which has a shoulder at a pore width of 4 nm.

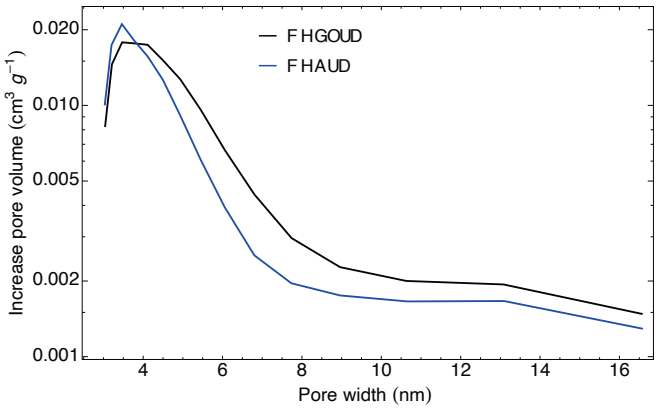

Figure 8. Pore size distribution obtained with the BJH method for the GOUFH (blue line) and the GODAFH (black line) materials.

4.8. SEM Analysis

SEM images of the materials are shown in Figure 9. It is observed that the GO morphology displays the distinctive sheet-like of graphene, which is corrugated by the effect of the oxygen groups. Interestingly, the GOU seems to have a more corrugated and folded surface. According to the GO model described by Szabó et al. [70], the corrugated carbon network has a ribbon-like arrangement linked by a periodically cleaved ribbon of

cyclohexane chairs. The slight tilting angle between the boundaries of the regions explains the wrinkling of the layers.

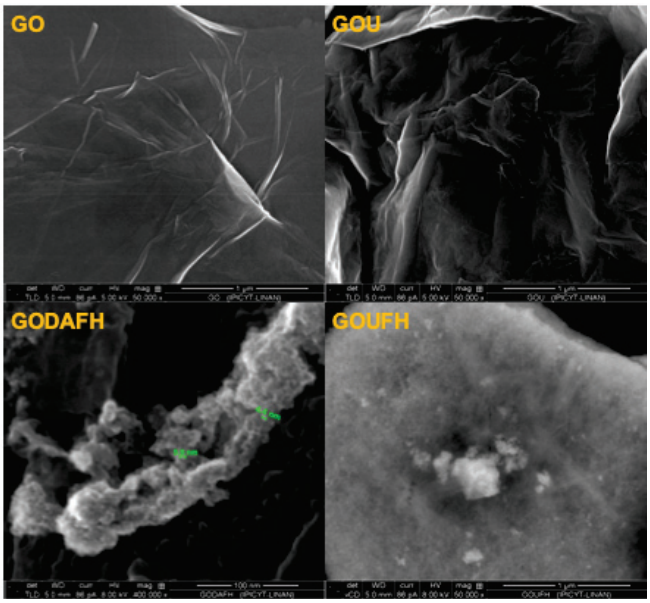

Figure 9. SEM images of the materials.

The successful incorporation of nitrogen, i.e., amines, on the GO allows an electrostatic attraction of OH-NH groups, causing a slight change in the torsion angle, and increasing the wrinkles on its surface. The GODAFH and GOUFH materials show the characteristic particles of ferrihydrite without a particular morphology. A fluffy cluster of particles seemed to be the result of the agglomeration of nanoparticles for the GODAFH material.

4.9. Adsorption Isotherms

Adsorption isotherms were developed to determine the fluoride adsorption capacity of the synthesized materials. Figure 10 shows the characterization of the interactions between F^- and the adsorbent materials, i.e., GO, GOU, GODA, GOFH, GOUFH, and GODAFH. The parameters used for the Langmuir and Freundlich models are given in Table 2. It is observed that the regression coefficient of the Freundlich model is bigger than that of the Langmuir model. This suggests an uneven distribution of the adsorption energy sites and a possible formation of adsorbate multilayers.

Table 2. Parameters of the Freundlich and Langmuir isotherms at a pH of 4 and a temperature of 25 °C for the synthesized materials.

	Freundlich			
Material	$\mathbf{K_F}$ **(mg g^{-1}) (L mg^{-1})$^{1/n}$**	**1/n**	**R^2**	**SE**
GO	0.919	0.979	0.99	0.031
GODA	0.539	0.959	0.99	0.078
GOU	0.574	0.915	0.99	0.053
GODAFH	9.345	0.576	0.99	0.304
GOUFH	10.033	0.575	0.99	0.327

Table 2. *Cont.*

	Langmuir			
Material	$\mathbf{q}_L$ **mg g^{-1}**	**b L mg^{-1}**	$\mathbf{R}^2$	**SE**
GO	2.007	32.705	0.98	0.035
GODA	1.002	35.290	0.98	0.119
GOU	1.014	45.411	0.98	0.118
GODAFH	9.405	3.524	0.98	0.223
GOUFH	9.706	4.176	0.97	0.493

It is observed, that the adsorption capacity of the GOUFH and GODAFH is considerably higher than that of the GO materials, which is due to the presence of ferrihydrite. This can be linked to the slight differences induced for the two methods for nitrogen incorporation on GO. The lack of fluoride capacity on the GO materials can be attributed to the negatively charged sites of acidic moieties that serve as repulsion sites of F^- ions. When considering a fluoride equilibrium concentration of 0.5 mg L^{-1}, the Freundlich constant capacity of the GO, GODA, and GOU, is 0.919, 0.539, and 0.574 (mg g^{-1}) (L mg^{-1})$^{1/n}$, respectively. At this same concentration, the Freundlich constant capacity of GODAFH and GOUFH is 9.345, and 10.033 (mg g^{-1}) (L mg^{-1})$^{1/n}$, respectively. When considering the adsorption capacity per surface area at an equilibrium concentration of 0.5 mg L^{-1}, the adsorption capacities were 0.0276 and 0.0281 mg m^{-2} for the GODAFH and GOUFH materials, respectively. These values represent a better surface area coverage than that of the GOFH material, i.e., 0.0293 mg m^{-2}. This suggests that an increase in the adsorption capacity is related to a better exposition of coordination sites when nitrogen is present. As discussed above, amine groups cause torsion of the graphene layers, allowing for the exposition of reactive groups during iron nucleation. Thus, the resultant material has a better exposition of iron exaaquo complexes and, as a consequence, a slightly higher adsorption capacity. This idea is strengthened when considering that the "n" parameter of the Freundlich model has a higher value for the composites containing nitrogen. For instance, the area changes as the surface is deformed due to the presence of functional groups. Considering the functional

$$A \propto \int_R d^2\sigma \sqrt{\det \gamma} \tag{8}$$

where $\det \gamma = \det P[g]$ is the determinant of the pullback of the metric which is obtained as $\gamma_{\alpha\beta} = \frac{\partial x^a}{\partial \sigma^\alpha} \frac{\partial x^b}{\partial \sigma^\beta} g_{ab}$, where sum over repeated indexes is understood, and the integration region R is determined by the boundaries of a selected region of the GO layers with characteristics lengths l_x and l_y which are greater to zero. In the absence of functional groups, the graphene layers are nearly flat and the metric describing the layers is approximately δ_{ab}. Thus, the surface area is proportional to

$$A_0 \propto \int_R d^2\sigma \tag{9}$$

This case implies that a flat 2D surface embedded in the Euclidean 3D space is considered. The pullback is trivial since $\det \gamma = 1$. Now, any deformation of the flat surface can be expressed as a deformation of the embedding coordinates, namely, the $x^i \in \{x, y\}$. Now with the deformation

$$x^i = x^i + f(x^i)\,, \tag{10}$$

thus, the A functional changes as follows

$$A' \propto A_0 + l_y|f(x)| + l_x|f(y)| + |f(x)f(y)|\,, \tag{11}$$

which implies that any deformation of the flat region R contains positive definite terms that increase the area of the surface. Thus, it is concluded that the wrinkles generated by the addition of functional groups always tend to increase the surface area and thus increasing the posible cites of adsorption.

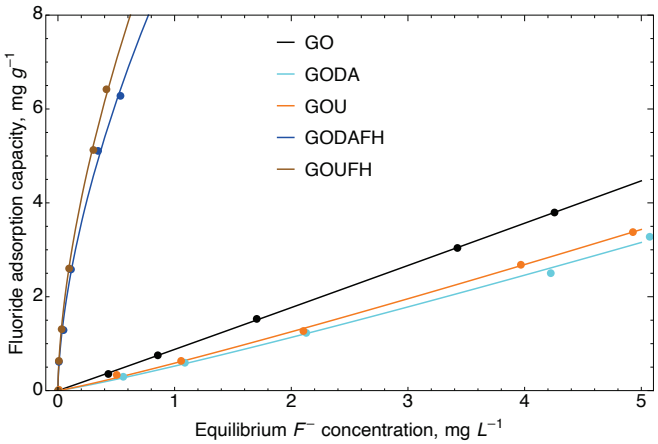

Figure 10. Adsorption isotherms of fluoride adsorption on the studied material at 25 °C and a pH 4.

The adsorption tests for the synthesized materials are obtained at a pH 4 because almost all the materials show a pH_{PZC} higher than 5.8. Thus, at a higher pH (see Figure 6), the surface of the materials is positively charged and the adsorption capacity is drastically reduced. This may be the reason that the GOUFH material displayed a bigger adsorption capacity than the GODAFH material. It is probably related with the presence of NH_2 groups contained in the urea, which triggers the formation of anchorage (for iron clusters) and adsorption sites, as opposed to the difenilamine which contains NH groups.

It is also observed that for the Freundlich model, the $1/n$ parameter obtained for the GO, GODA, and GOU materials is 0.979, 0.959, and 0.915, respectively. This suggests a lower homogeneity of adsorbed F^- for the GO materials. However, the composite materials functionalized with ferrihydrite displayed a higher adsorption capacity of F^-, i.e., with $1/n$ values of 0.747, 0.576, and 0.575 for the GOFH, GODAFH, and GOUFH respectively.

The GO material modified with urea and ferrihydrite, named GOUFH, shows a higher adsorption capacity than the other modified materials. Thus, it is used as a reference to test the adsorption properties at several conditions. The adsorption isotherms where obtained for the GOUFH material at a temperature of 25 °C, 35 °C, and 45 °C, and at a pH of 4, 6, and 8 (see Figure 11).

The experimental data obtained is predicted using both, the Freundlich and Langmuir models. The correlation coefficient, R^2, is used to compare the models. It is observed that both, the Freundlich and Langmuir models, predict well the experimental data. The parameters used in the models to predict the adsorption of F^- in the GOUFH material at the conditions established are given in Table 3.

The adsorption experiments were obtained at a pH smaller than the pH_{PZC}, which is about 8.3 (see Figure 6). It is observed that the GOUFH is capable to remove well the fluorides for a pH lower than 8. However at a pH of 8, the pH_{PZC} is quite close and the material is not able to adsorb F^-; as a consequence, the R^2 is decreased. This is caused by the addition of ferrihydrite as well as the nitrogenated groups contained in the urea deposited on the GO surface. Since the GOUFH is positively charged, it increases the electrostatic force between the fluoride and the surface of the material. It is also observed that the modified GO increases its adsorption capacity because of the presence of Fe, which has a high affinity with the F^- and, thus, increases the probability of adsorption.

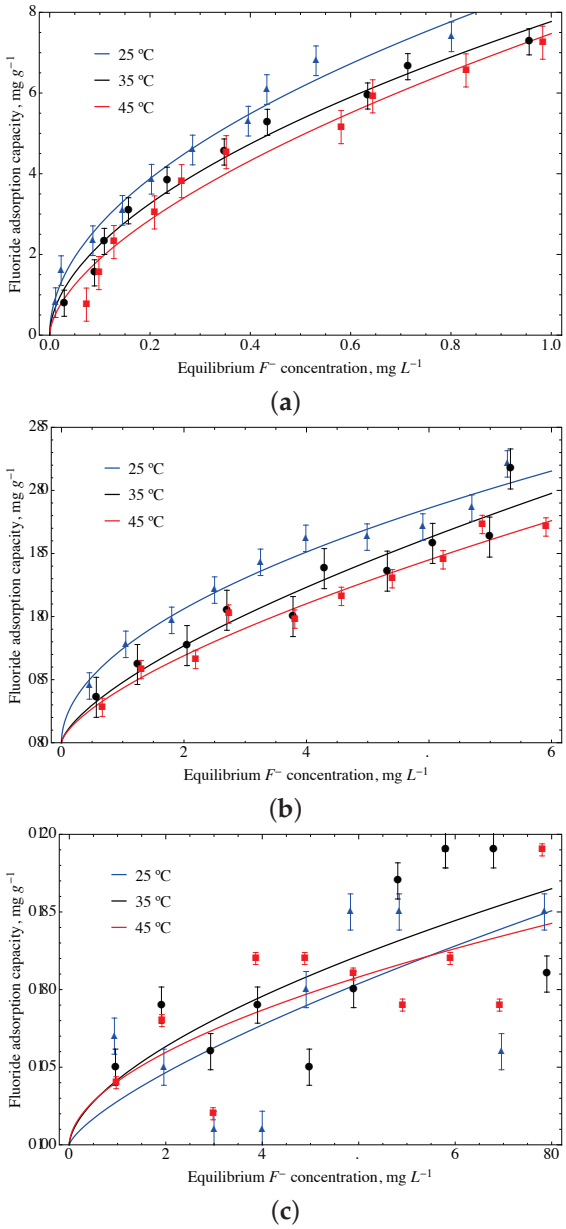

Figure 11. Adsorption isotherms obtained using the Freundlich model for the GOUFH material at a temperature of 25 °C, 35 °C and 45 °C, and at a pH of (**a**) 4, (**b**) 6, and (**c**) 8.

The adsorption isotherms for a pH 4 at a temperature of 35 °C and 45 °C show a better prediction using the Langmuir model with a q_L of 10.147 and 11.018 mg g^{-1}, respectively. On the other hand, the isotherm at a pH of 4 and a temperature of 25 °C shows the highest adsorption, and the Freundlich model shows a better prediction than the Langmuir model. The K_F of 8.697 mg g^{-1} and $1/n$ of 0.502 are related to a higher adsorption intensity. Thus, the modifications of the GO surface with oxihydroxides and amine groups from the urea suggest an increase in the active sites on the surface of the ternary material. As is expected, the pH of 4, which is below the pH_{PZC}, i.e., ∼8, allows increasing the adsorption capacity. This favors the protonated sites, increasing the F^- retained on the surface of the material.

In order to evaluate the accuracy of the predictions, standardized residuals (SR) were employed. Standardized residuals are defined as the ratio of the residuals over the estimated variance. In the present work, the SR ranges from −2.0 to 2.0 and is distributed randomly around the abscissa. This result suggests that there is no over or under-estimation of the overall prediction. Overall, the SR suggests that the model fits reasonably well with the measured values.

Table 3. Parameters used in the Freundlich and Langmuir models to predict the adsorption of F^- on the GOUFH material at a temperature of 25 °C, 35 °C and 45 °C, and a pH of 4, 6, and 8.

		Freundlich		
		pH = 4		
Temperature °C	K_F **(mg g^{-1}) (L mg^{-1})$^{1/n}$**	**1/*n***	R^2	**SE**
25	8.687	0.502	0.984	0.301
35	7.772	0.540	0.981	0.323
45	7.472	0.597	0.970	0.420
		pH = 6		
25	0.745	0.510	0.970	0.099
35	0.479	0.682	0.922	0.160
45	0.432	0.676	0.964	0.097
		pH = 8		
25	0.028	0.730	0.362	0.054
35	0.042	0.595	0.510	0.041
45	0.041	0.543	0.490	0.490
		Langmuir		
		pH = 4		
Temperature °C	q_L **(mg g^{-1})**	B **(L mg^{-1})**	R^2	**SE**
25	10.325	3.117	0.979	0.430
35	10.147	2.497	0.992	0.206
45	11.018	1.806	0.983	0.309
		pH = 6		
25	2.854	0.308	0.960	0.116
35	4.120	0.110	0.909	0.180
45	3.520	0.117	0.958	0.107
		pH = 8		
25	0.405	0.059	0.367	0.054
35	0.303	0.116	0.503	0.041
45	0.213	0.187	0.473	0.037

There exist materials based on nano-functionalized graphene oxide (GO) for fluoride removal. Some of these materials include GO/Al_2O_3 [71] with an adsorption capacity of 4.68 mg g^{-1}, and GO doped with zirconium with an adsorption capacity of 6.12 mg g^{-1} [72]. Another material, Zr-MCGO, reported an adsorption capacity of 8.84 mg g^{-1}[73]. These materials displayed lower adsorption capacities than the reported in the present work, which was around 11 mg g^{-1}. This increase in the adsorption capacity is due to the folds produced during the functionalization of the GO, which is reflected in an increase in surface area.

However, multi-functionalized materials with greater removal capacities have also been reported. These include the Zr-Chitosan membrane and GO with an adsorption capacity of 29.05 mg g^{-1}[14], FeOOH+Ac/GO with an adsorption capacity of 19.82 mg g^{-1} [33], $\alpha-$FeOOH/rGO with an adsorption capacity of 24.67 mg g^{-1}, and HIAGO with an adsorption capacity of 27.8 mg g^{-1} [15]. Also, MgO/$MgFe_2O_4$/GO [9] has an adsorption capacity of 34 mg g^{-1}. It should be noted that HIAGO, MgO/$MgFe_2O_4$/GO, as well as FeOOH+Ac/GO, has dual metal functionalization, which implies a greater number of functional groups on the surface, thereby increasing the adsorption capacity.

4.10. Effects of pH and Temperature

The results show that higher adsorption capacities are obtained at a pH of 4. This is related to the protonation of the surface below the pH_{PZC} as well as the natural effect of the electrostatic interactions. This suggests that, as the pH increases, a decrease in the adsorption capacity is obtained [74]. Thus, it is interesting to compare adsorption capacities close to the pH_{PZC} of the materials. At this point, the electrostatic interactions are decreased to zero, and the fluoride adsorption is driven by a different mechanism. The particular interaction can be due to ligand exchange reactions of the form

$$\equiv Fe - OH + F^- \rightarrow \equiv Fe - F + OH^- . \quad (12)$$

This process releases OH groups to the solution, leading to a change in the surface charge distribution, promoting electrostatic interactions and repulsions. Also, a considerable disruption of the adsorption isotherms is observed at a pH of 8. It is known that iron oxides are amphoteric; thus, they can be dissolved in acidic and basic media. It is possible that at this pH some of the iron nuclei, particularly those bonded with the graphene oxide surface, are dissolved, leading to a dissolution of the reactive material. Hence, the adsorption capacity is decreased. It is also important to mention that early studies on ferrihydrite have reported the formation of colloidal ferrihydrite, which is complicated to separate from dissolved Fe [75].

In summary, the maximum adsorption capacities were obtained at a temperature of 25 °C. It is also observed that the adsorption capacity decreases as the temperature increases. This suggests that an exothermic process is favored at low temperatures. This phenomenon is usually attributed to an increase in the internal energy of adsorbed molecules that overcome the adsorption energy.

4.11. The Van't Hoff Equation

In Figure 12 it is presented the regression analysis of the experimental data with the non-linear van't Hoff equation. As is observed the K_d constant has a non-linear dependence with $1/T$ at values of pH of 6 and 8, whereas it shows almost a linear dependence with $1/T$ for a pH of 4. Besides, it is observed a negative entropy change of entropy at pH of 4 and 6, i.e., $\Delta S^0 = -62.36$ kJ kmol^{-1} K^{-1} for a pH of 4 and $\Delta S^0 = -140.68$ kJ kmol^{-1} K^{-1} for a pH of 6. However, the entropy change was positive for values of pH of 8, i.e., $\Delta S^0 = 129.40$ kJ kmol^{-1} K^{-1} for a pH of 8. Thus, it is inferred that the adsorption sites are decreasing for pH of 4 and 6 whereas they are increasing at a pH of 8. In addition, the changes in enthalpy have a positive change for all the values of pH studied in the present work, suggesting exothermic reactions.

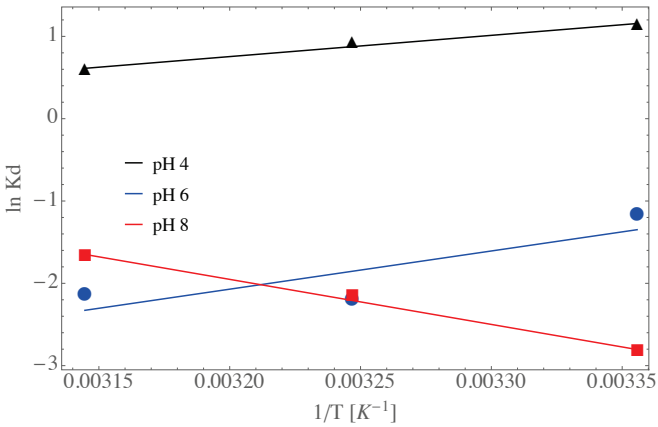

Figure 12. Linear van't Hoff prediction for the GOUFH material.

5. Conclusions

In the present work, amine-graphene oxide-ferrhydrite materials were sinthesized, and used as adsorbents of fluoride ions from an aqueous solution. The synthesis was developed following the modified Hummers method. The characterization of the material was carried out by means of Fourier transform infrared spectrometry, X-ray, Raman spectroscopy, thermogravimetric analysis, surface charge distribution, specific surface area and porosity, adsorption isotherms, and the van't Hoff equation.

The difractogram shows that the materials contain characteristic peaks, which confirms the material structure. Also, the addition of amines is corroborated by the increase of wrinkles on the surface layers of the modified materials, suggesting a successful incorporation of nitrogen into the graphene oxide. This causes an increase in the adsorption capacity per unit area of the materials. In addition, the SEM analysis confirms an amorphous surface of the materials, which is a characteristic of ferrihydrite particles. Thus, the incorporation of nitrogen into the GO matrix shows an improvement of the surface area due to the better distribution of iron hexaaquo complexes during the nucleation.

Besides, the presence of the nitrogenated groups shows a basic character, promoting the electrostatic attraction among the acid groups contained in cations, changing the thermodynamic environment, and giving room to new materials characterized by a better dispersion of functional groups on the surface.

The adsorption tests confirm that the materials modified with nitrogen increase their adsorptive capacities as well as the surface area. This can be related to a better exposition of coordination sites when nitrogen is present. Particularly, the GOUFH material, which is synthesized with a primary amine, shows the best F^- adsorption capacity, maintains its functionality even after the composite formation, shows the formation and growth of iron oxide on its surface, and shows a bigger specific surface area.

Finally, the Freundlich and Langmuir models, as well as the linear van't Hoff equation predict well the F^- adsorption capacity of the materials.

Author Contributions: Conceptualization, A.S.-R. and L.R.G.-M.; methodology, A.S.-R. and L.R.G.-M.; formal analysis, A.S.-R., L.R.G.-M., C.E.D.-A. and A.G.-M.; investigation, J.A.A.-O., M.C., C.E.D.-A. and A.S.-R.; resources, A.G.-M., A.S.-R. and C.E.D.-A. writing—original draft preparation, S.C.-A., A.S.-R. and C.E.D.-A.; writing—review, A.S.-R., J.A.A.-O. and S.C.-A., editing, all the authors; visualization, M.C. and A.M.-H.; supervision, A.S.-R. and J.A.A.-O.; project administration, C.E.D.-A. and A.S.-R. All authors have read and agreed to the published version of the manuscript.

Funding: This research was funded by the University of Guanajuato grant number CIIC 076/20221.

Institutional Review Board Statement: Not applicable.

Informed Consent Statement: Not applicable.

Data Availability Statement: Not aplicable

Acknowledgments: The authors gratefully acknowledge the financial support of the National Council of Science and Technology (CONACyT), Mexico, under its SNI program. This work was partially supported by the University of Guanajuato under grant no. DAIP-CIIC 076/2021.

Conflicts of Interest: The authors declare no conflict of interest. The funders had no role in the design of the study; in the collection, analyses, or interpretation of data; in the writing of the manuscript; or in the decision to publish the results.

References

1. Borgohain, X.; Boruah, A.; Sarma, G.K.; Rashid, M.H. Rapid and extremely high adsorption performance of porous MgO nanostructures for fluoride removal from water. *J. Mol. Liq.* **2020**, *305*, 112799. [CrossRef]
2. Chen, L.; Zhang, K.S.; He, J.Y.; Xu, W.H.; Huang, X.J.; Liu, J.H. Enhanced fluoride removal from water by sulfate-doped hydroxyapatite hierarchical hollow microspheres. *Chem. Eng. J.* **2016**, *285*, 616–624. [CrossRef]
3. Li, Y.; Zhang, P.; Du, Q.; Peng, X.; Liu, T.; Wang, Z.; Xia, Y.; Zhang, W.; Wang, K.; Zhu, H.; et al. Adsorption of fluoride from aqueous solution by graphene. *J. Colloid Interface Sci.* **2011**, *363*, 348–354. [CrossRef]

4. Sharma, D.; Singh, A.; Verma, K.; Paliwal, S.; Sharma, S.; Dwivedi, J. Fluoride: A review of pre-clinical and clinical studies. *Environ. Toxicol. Pharmacol.* **2017**, *56*, 297–313. [CrossRef] [PubMed]
5. Smedley, P.L.; Kinniburgh, D.G. A review of the source, behaviour and distribution of arsenic in natural waters. *Appl. Geochem.* **2002**, *17*, 517–568. [CrossRef]
6. Mandal, B.K.; Suzuki, K.T. Arsenic round the world: A review. *Talanta* **2002**, *58*, 201–235. [CrossRef]
7. Sharma, V.K.; Sohn, M. Aquatic arsenic: Toxicity, speciation, transformations, and remediation. *Environ. Int.* **2009**, *35*, 743–759. [CrossRef]
8. Dehbandi, R.; Moore, F.; Keshavarzi, B. Geochemical sources, hydrogeochemical behavior, and health risk assessment of fluoride in an endemic fluorosis area, central Iran. *Chemosphere* **2018**, *193*, 763–776. [CrossRef]
9. Sahoo, S.K.; Hota, G. Surface functionalization of GO with $MgO/MgFe_2O_4$ binary oxides: A novel magnetic nanoadsorbent for removal of fluoride ions. *J. Environ. Chem. Eng.* **2018**, *6*, 2918–2931. [CrossRef]
10. World Health Organization. *The World Health Report 2003: Shaping the Future*; World Health Organization: Geneva, Switzerland, 2003.
11. Murambasvina, G.; Mahamadi, C. Effective fluoride adsorption using water hyacinth beads doped with hydrous oxides of aluminium and iron. *Groundw. Sustain. Dev.* **2020**, *10*, 100302. [CrossRef]
12. Corral-Capulin, N.G.; Vilchis-Nestor, A.R.; Gutiérrez-Segura, E.; Solache-Ríos, M. Comparison of the removal behavior of fluoride by Fe^{3+} modified geomaterials from water. *Appl. Clay Sci.* **2019**, *173*, 19–28. [CrossRef]
13. He, J.; Cui, A.; Ni, F.; Deng, S.; Shen, F.; Yang, G. A novel 3D yttrium based-graphene oxide-sodium alginate hydrogel for remarkable adsorption of fluoride from water. *J. Colloid Interface Sci.* **2018**, *531*, 37–46. [CrossRef] [PubMed]
14. Zhang, J.; Chen, N.; Su, P.; Li, M.; Feng, C. Fluoride removal from aqueous solution by zirconium-chitosan/graphene oxide membrane. *React. Funct. Polym.* **2017**, *114*, 127–135. [CrossRef]
15. Kanrar, S.; Debnath, S.; De, P.; Parashar, K.; Pillay, K.; Sasikumar, P.; Ghosh, U.C. Preparation, characterization and evaluation of fluoride adsorption efficiency from water of iron-aluminium oxide-graphene oxide composite material. *Chem. Eng. J.* **2016**, *306*, 269–279. [CrossRef]
16. Gao, M.; Wang, W.; Yang, H.; Ye, B.C. Hydrothermal synthesis of hierarchical hollow hydroxyapatite microspheres with excellent fluoride adsorption property. *Microporous Mesoporous Mater.* **2019**, *289*, 109620. [CrossRef]
17. Shen, J.; Schäfer, A. Removal of fluoride and uranium by nanofiltration and reverse osmosis: A review. *Chemosphere* **2014**, *117*, 679–691. [CrossRef]
18. Mullick, A.; Neogi, S. Ultrasound assisted synthesis of Mg-Mn-Zr impregnated activated carbon for effective fluoride adsorption from water. *Ultrason. Sonochem.* **2019**, *50*, 126–137. [CrossRef]
19. Gwala, P.; Andey, S.; Mhaisalkar, V.; Labhasetwar, P.; Pimpalkar, S.; Kshirsagar, C. Lab scale study on electrocoagulation defluoridation process optimization along with aluminium leaching in the process and comparison with full scale plant operation. *Water Sci. Technol.* **2011**, *63*, 2788–2795. [CrossRef]
20. Chen, C.L.; Park, S.W.; Su, J.F.; Yu, Y.H.; Heo, J.e.; Kim, K.d.; Huang, C.P. The adsorption characteristics of fluoride on commercial activated carbon treated with quaternary ammonium salts (Quats). *Sci. Total Environ.* **2019**, *693*, 133605. [CrossRef]
21. Changmai, M.; Pasawan, M.; Purkait, M.K. A hybrid method for the removal of fluoride from drinking water: Parametric study and cost estimation. *Sep. Purif. Technol.* **2018**, *206*, 140–148. [CrossRef]
22. Huang, L.; Yang, Z.; He, Y.; Chai, L.; Yang, W.; Deng, H.; Wang, H.; Chen, Y.; Crittenden, J. Adsorption mechanism for removing different species of fluoride by designing of core-shell boehmite. *J. Hazard. Mater.* **2020**, *394*, 122555. [CrossRef] [PubMed]
23. Owusu-Agyeman, I.; Reinwald, M.; Jeihanipour, A.; Schäfer, A.I. Removal of fluoride and natural organic matter from natural tropical brackish waters by nanofiltration/reverse osmosis with varying water chemistry. *Chemosphere* **2019**, *217*, 47–58. [CrossRef] [PubMed]
24. Sarma, G.K.; Rashid, M.H. Synthesis of Mg/Al layered double hydroxides for adsorptive removal of fluoride from water: A mechanistic and kinetic study. *J. Chem. Eng. Data* **2018**, *63*, 2957–2965. [CrossRef]
25. Ye, Y.; Yang, J.; Jiang, W.; Kang, J.; Hu, Y.; Ngo, H.H.; Guo, W.; Liu, Y. Fluoride removal from water using a magnesia-pullulan composite in a continuous fixed-bed column. *J. Environ. Manag.* **2018**, *206*, 929–937. [CrossRef] [PubMed]
26. Xie, D.; Gu, Y.; Wang, H.; Wang, Y.; Qin, W.; Wang, G.; Zhang, H.; Zhang, Y. Enhanced fluoride removal by hierarchically porous carbon foam monolith with high loading of UiO-66. *J. Colloid Interface Sci.* **2019**, *542*, 269–280. [CrossRef]
27. Zhao, Z.; Geng, C.; Yang, C.; Cui, F.; Liang, Z. A novel flake-ball-like magnetic Fe_3O_4/γ-MnO_2 meso-porous nano-composite: Adsorption of fluorinion and effect of water chemistry. *Chemosphere* **2018**, *209*, 173–181. [CrossRef]
28. Heidarizad, M.; Şengör, S.S. Synthesis of graphene oxide/magnesium oxide nanocomposites with high-rate adsorption of methylene blue. *J. Mol. Liq.* **2016**, *224*, 607–617. [CrossRef]
29. Fang, Q.; Shen, Y.; Chen, B. Synthesis, decoration and properties of three-dimensional graphene-based macrostructures: A review. *Chem. Eng. J.* **2015**, *264*, 753–771. [CrossRef]
30. Sitko, R.; Turek, E.; Zawisza, B.; Malicka, E.; Talik, E.; Heimann, J.; Gagor, A.; Feist, B.; Wrzalik, R. Adsorption of divalent metal ions from aqueous solutions using graphene oxide. *Dalton Trans.* **2013**, *42*, 5682–5689. [CrossRef]
31. Zhao, G.; Li, J.; Ren, X.; Chen, C.; Wang, X. Few-layered graphene oxide nanosheets as superior sorbents for heavy metal ion pollution management. *Environ. Sci.Technol.* **2011**, *45*, 10454–10462. [CrossRef]

32. Wang, Q.; Chen, P.; Zeng, X.; Jiang, H.; Meng, F.; Li, X.; Wang, T.; Zeng, G.; Liu, L.; Shu, H.; et al. Synthesis of (ZrO_2-Al_2O_3)/GO nanocomposite by sonochemical method and the mechanism analysis of its high defluoridation. *J. Hazard. Mater.* **2020**, *381*, 120954. [CrossRef]
33. Kuang, L.; Liu, Y.; Fu, D.; Zhao, Y. FeOOH-graphene oxide nanocomposites for fluoride removal from water: Acetate mediated nano FeOOH growth and adsorption mechanism. *J. Colloid Interface Sci.* **2017**, *490*, 259–269. [CrossRef]
34. Mohan, S.; Kumar, V.; Singh, D.K.; Hasan, S.H. Synthesis and characterization of rGO/ZrO_2 nanocomposite for enhanced removal of fluoride from water: Kinetics, isotherm, and thermodynamic modeling and its adsorption mechanism. *RSC Adv.* **2016**, *6*, 87523–87538. [CrossRef]
35. Barathi, M.; Kumar, A.S.K.; Kumar, C.U.; Rajesh, N. Graphene oxide–aluminium oxyhydroxide interaction and its application for the effective adsorption of fluoride. *RSC Adv.* **2014**, *4*, 53711–53721. [CrossRef]
36. Mobarak, M.; Mohamed, E.A.; Selim, A.Q.; Sellaoui, L.; Lamine, A.B.; Erto, A.; Bonilla-Petriciolet, A.; Seliem, M.K. Surfactant–modified serpentine for fluoride and Cr(VI) adsorption in single and binary systems: Experimental studies and theoretical modeling. *Chem. Eng. J.* **2019**, *369*, 333–343. [CrossRef]
37. Mobarak, M.; Selim, A.Q.; Mohamed, E.A.; Seliem, M.K. Modification of organic matter-rich clay by a solution of cationic surfactant/H_2O_2: A new product for fluoride adsorption from solutions. *J. Clean. Prod.* **2018**, *192*, 712–721. [CrossRef]
38. Yıldız, N.; Gönülşen, R.; Koyuncu, H.; Çalımlı, A. Adsorption of benzoic acid and hydroquinone by organically modified bentonites. *Colloids Surfaces A Physicochem. Eng. Asp.* **2005**, *260*, 87–94. [CrossRef]
39. Başar, C.A.; Karagunduz, A.; Keskinler, B.; Cakici, A. Effect of presence of ions on surface characteristics of surfactant modified powdered activated carbon (PAC). *Appl. Surf. Sci.* **2003**, *218*, 170–175. [CrossRef]
40. Arcibar-Orozco, J.A.; Bandosz, T.J. Visible light enhanced removal of a sulfur mustard gas surrogate from a vapor phase on novel hydrous ferric oxide/graphite oxide composites. *J. Mater. Chem. A* **2015**, *3*, 220–231. [CrossRef]
41. Mahmudov, R.; Chen, C.; Huang, C.P. Functionalized activated carbon for the adsorptive removal of perchlorate from water solutions. *Front. Chem. Sci. Eng.* **2015**, *9*, 194–208. [CrossRef]
42. Peng, F.; Luo, T.; Qiu, L.; Yuan, Y. An easy method to synthesize graphene oxide–FeOOH composites and their potential application in water purification. *Mater. Res. Bull.* **2013**, *48*, 2180–2185. [CrossRef]
43. Ploychompoo, S.; Liang, Q.; Zhou, X.; Wei, C.; Luo, H. Fabrication of Zn-MOF-74/polyacrylamide coated with reduced graphene oxide (Zn-MOF-74/rGO/PAM) for As (III) removal. *Phys. E Low-Dimens. Syst. Nanostruct.* **2021**, *125*, 114377. [CrossRef]
44. Bo, Z.; Huang, Z.; Xu, C.; Chen, Y.; Wu, E.; Yan, J.; Cen, K.; Yang, H.; Ostrikov, K.K. Anion-kinetics-selective graphene anode and cation-energy-selective MXene cathode for high-performance capacitive deionization. *Energy Storage Mater.* **2022**, *50*, 395–406. [CrossRef]
45. Bo, Z.; Xu, C.; Huang, Z.; Chen, P.; Yan, G.; Yang, H.; Yan, J.; Cen, K.; Ostrikov, K.K. Photo-electric capacitive deionization enabled by solar-driven nano-ionics on the edges of plasma-made vertical graphenes. *Chem. Eng. J.* **2021**, *422*, 130156. [CrossRef]
46. Vazquez-Jaime, M.; Arcibar-Orozco, J.A.; Damian-Ascencio, C.E.; Saldana-Robles, A.L.; Martínez-Rosales, M.; Saldana-Robles, A.; Cano-Andrade, S. Effective removal of arsenic from an aqueous solution by ferrihydrite/goethite graphene oxide composites using the modified Hummers method. *J. Environ. Chem. Eng.* **2020**, *8*, 104416. [CrossRef]
47. Lenoble, V.; Deluchat, V.; Serpaud, B.; Bollinger, J.C. Arsenite oxidation and arsenate determination by the molybdene blue method. *Talanta* **2003**, *61*, 267–276. [CrossRef] [PubMed]
48. Acik, M.; Mattevi, C.; Gong, C.; Lee, G.; Cho, K.; Chhowalla, M.; Chabal, Y.J. The role of intercalated water in multilayered graphene oxide. *ACS Nano* **2010**, *4*, 5861–5868. [CrossRef] [PubMed]
49. Liu, X.; Zhang, H.; Ma, Y.; Wu, X.; Meng, L.; Guo, Y.; Yu, G.; Liu, Y. Graphene-coated silica as a highly efficient sorbent for residual organophosphorus pesticides in water. *J. Mater. Chem. A* **2013**, *1*, 1875–1884. [CrossRef]
50. Berrones, M.d.l.Á.; Lascano, L. Síntesis de nanopartículas de hematita por el método de precipitación controlada. *Rev. Politécnica Quito* **2009**, *30*, 91–99.
51. Villacís-García, M.; Ugalde-Arzate, M.; Vaca-Escobar, K.; Villalobos, M.; Zanella, R.; Martínez-Villegas, N. Laboratory synthesis of goethite and ferrihydrite of controlled particle sizes. *Boletín Soc. Geológica Mex.* **2015**, *67*, 433–446. [CrossRef]
52. An, W.; Zhang, Y.; Zhang, X.; Li, K.; Kang, Y.; Akhtar, S.; Sha, X.; Gao, L. Ocular toxicity of reduced graphene oxide or graphene oxide exposure in mouse eyes. *Exp. Eye Res.* **2018**, *174*, 59–69. [CrossRef]
53. Zahed, M.; Parsamehr, P.S.; Tofighy, M.A.; Mohammadi, T. Synthesis and functionalization of graphene oxide (GO) for salty water desalination as adsorbent. *Chem. Eng. Res. Des.* **2018**, *138*, 358–365. [CrossRef]
54. Guerrero-Contreras, J.; Caballero-Briones, F. Graphene oxide powders with different oxidation degree, prepared by synthesis variations of the Hummers method. *Mater. Chem. Phys.* **2015**, *153*, 209–220. [CrossRef]
55. Eggleton, R.A.; Fitzpatrick, R.W. New data and a revised structural model for ferrihydrite. *Clays Clay Miner.* **1988**, *36*, 111–124. [CrossRef]
56. Xiu, W.; Guo, H.; Zhou, X.; Wanty, R.B.; Kersten, M. Change of arsenite adsorption mechanism during aging of 2-line ferrihydrite in the absence of oxygen. *Appl. Geochem.* **2018**, *88*, 149–157. [CrossRef]
57. Cysewski, P.; Przybyłek, M.; Ziółkowska, D.; Mroczyńska, K. Exploring the cocrystallization potential of urea and benzamide. *J. Mol. Model.* **2016**, *22*, 103. [CrossRef] [PubMed]
58. Kawashima, Y.; Katagiri, G. Fundamentals, overtones, and combinations in the Raman spectrum of graphite. *Phys. Rev. B* **1995**, *52*, 10053. [CrossRef] [PubMed]

59. Tan, P.; An, L.; Liu, L.; Guo, Z.; Czerw, R.; Carroll, D.L.; Ajayan, P.M.; Zhang, N.; Guo, H. Probing the phonon dispersion relations of graphite from the double-resonance process of Stokes and anti-Stokes Raman scatterings in multiwalled carbon nanotubes. *Phys. Rev. B* **2002**, *66*, 245410. [CrossRef]
60. May, P.; Lazzeri, M.; Venezuela, P.; Herziger, F.; Callsen, G.; Reparaz, J.S.; Hoffmann, A.; Mauri, F.; Maultzsch, J. Signature of the two-dimensional phonon dispersion in graphene probed by double-resonant Raman scattering. *Phys. Rev. B* **2013**, *87*, 075402. [CrossRef]
61. Johra, F.T.; Lee, J.W.; Jung, W.G. Facile and safe graphene preparation on solution based platform. *J. Ind. Eng. Chem.* **2014**, *20*, 2883–2887. [CrossRef]
62. Jeyaseelan, A.; Ghfar, A.A.; Naushad, M.; Viswanathan, N. Design and synthesis of amine functionalized graphene oxide for enhanced fluoride removal. *J. Environ. Chem. Eng.* **2021**, *9*, 105384. [CrossRef]
63. Chen, X.; Wang, X.; Fang, D. A review on C1s XPS-spectra for some kinds of carbon materials. *Fullerenes Nanotub. Carbon Nanostruct.* **2020**, *28*, 1048–1058. [CrossRef]
64. Al-Gaashani, R.; Najjar, A.; Zakaria, Y.; Mansour, S.; Atieh, M. XPS and structural studies of high quality graphene oxide and reduced graphene oxide prepared by different chemical oxidation methods. *Ceram. Int.* **2019**, *45*, 14439–14448. [CrossRef]
65. Kumar, E.; Bhatnagar, A.; Ji, M.; Jung, W.; Lee, S.H.; Kim, S.J.; Lee, G.; Song, H.; Choi, J.Y.; Yang, J.S.; et al. Defluoridation from aqueous solutions by granular ferric hydroxide (GFH). *Water Res.* **2009**, *43*, 490–498. [CrossRef] [PubMed]
66. Li, X.; Li, S.; Bai, Q.; Sui, N.; Zhu, Z. Gold nanoclusters decorated amine-functionalized graphene oxide nanosheets for capture, oxidative stress, and photothermal destruction of bacteria. *Colloids Surfaces B Biointerfaces* **2020**, *196*, 111313. [CrossRef]
67. Lakshmipathiraj, P.; Narasimhan, B.R.V.; Prabhakar, S.; Raju, G.B. Adsorption of arsenate on synthetic goethite from aqueous solutions. *J. Hazard. Mater.* **2006**, *136*, 281–287. [CrossRef] [PubMed]
68. Hammad, M.; Fortugno, P.; Hardt, S.; Kim, C.; Salamon, S.; Schmidt, T.C.; Wende, H.; Schulz, C.; Wiggers, H. Large-scale synthesis of iron oxide/graphene hybrid materials as highly efficient photo-Fenton catalyst for water remediation. *Environ. Technol. Innov.* **2021**, *21*, 101239. [CrossRef]
69. Bumajdad, A.; Ali, S.; Mathew, A. Characterization of iron hydroxide/oxide nanoparticles prepared in microemulsions stabilized with cationic/non-ionic surfactant mixtures. *J. Colloid Interface Sci.* **2011**, *355*, 282–292. [CrossRef] [PubMed]
70. Szabó, T.; Berkesi, O.; Forgó, P.; Josepovits, K.; Sanakis, Y.; Petridis, D.; Dékány, I. Evolution of surface functional groups in a series of progressively oxidized graphite oxides. *Chem. Mater.* **2006**, *18*, 2740–2749.
71. Xu, N.; Li, S.; Li, W.; Liu, Z. Removal of fluoride by graphene oxide/alumina nanocomposite: Adsorbent preparation, characterization, adsorption performance and mechanisms. *ChemistrySelect* **2020**, *5*, 1818–1828. [CrossRef]
72. Prathibha, C.; Biswas, A.; Chunduri, L.A.; Reddy, S.K.; Loganathan, P.; Kalaruban, M.; Venkatarmaniah, K. Zr (IV) functionalized graphene oxide anchored sand as potential and economic adsorbent for fluoride removal from water. *Diam. Relat. Mater.* **2020**, *109*, 108081. [CrossRef]
73. Liu, M.; Zang, Z.; Zhang, S.; Ouyang, G.; Han, R. Enhanced fluoride adsorption from aqueous solution by zirconium (IV)-impregnated magnetic chitosan graphene oxide. *Int. J. Biol. Macromol.* **2021**, *182*, 1759–1768. [CrossRef] [PubMed]
74. Mourabet, M.; El Boujaady, H.; El Rhilassi, A.; Ramdane, H.; Bennani-Ziatni, M.; El Hamri, R.; Taitai, A. Defluoridation of water using Brushite: Equilibrium, kinetic and thermodynamic studies. *Desalination* **2011**, *278*, 1–9. [CrossRef]
75. Cornell, R.M.; Schwertmann, U. *The Iron Oxides: Structure, Properties, Reactions, Occurrences and Uses*; John Wiley & Sons: Hoboken, NJ, USA, 2003.

nanomaterials

MDPI

Article

Study on Oxygen Evolution Reaction of Ir Nanodendrites Supported on Antimony Tin Oxide

Yu-Chun Chiang [1,2,*], Zhi-Hui Pu [1] and Ziyi Wang [1]

[1] Department of Mechanical Engineering, Yuan Ze University, Taoyuan 320, Taiwan; s1080821@mail.yzu.edu.tw (Z.-H.P.); s1080857@mail.yzu.edu.tw (Z.W.)
[2] Fuel Cell Center, Yuan Ze University, Taoyuan 320, Taiwan
* Correspondence: ycchiang@saturn.yzu.edu.tw; Tel.: +886-3-4638800 (ext. 2476)

Abstract: In this study, the iridium nanodendrites (Ir NDs) and antimony tin oxide (ATO)-supported Ir NDs (Ir ND/ATO) were prepared by a surfactant-mediated method to investigate the effect of ATO support and evaluate the electrocatalytic activity for the oxygen evolution reaction (OER). The nano-branched Ir ND structures were successfully prepared alone or supported on ATO. The Ir NDs exhibited major diffraction peaks of the fcc Ir metal, though the Ir NDs consisted of metallic Ir as well as Ir oxides. Among the Ir ND samples, Ir ND2 showed the highest mass-based OER catalytic activity (116 mA/mg at 1.8 V), while it suffered from high degradation in activity after a long-term test. On the other hand, Ir ND2/ATO had OER activity of 798 mA/mg, and this activity remained >99% after 100 cycles of LSV and the charge transfer resistance increased by less than 3 ohm. The enhanced durability of the OER mass activities of Ir ND2/ATO catalysts over Ir NDs and Ir black could be attributed to the small crystallite size of Ir and the increase in the ratio of Ir (III) to Ir (IV), improving the interactions between the Ir NDs and the ATO support.

Keywords: iridium nanodendrites; antimony tin oxide; oxygen evolution reaction

Citation: Chiang, Y.-C.; Pu, Z.-H.; Wang, Z. Study on Oxygen Evolution Reaction of Ir Nanodendrites Supported on Antimony Tin Oxide. *Nanomaterials* **2023**, *13*, 2264. https://doi.org/10.3390/nano13152264

Academic Editor: Francesc Viñes Solana

Received: 14 July 2023
Revised: 1 August 2023
Accepted: 5 August 2023
Published: 7 August 2023

1. Introduction

Hydrogen is a clean and efficient energy carrier. When hydrogen is used in the replacement of fossil fuels, the immediate benefits include a reduction in emissions. Water electrolysis is well known as a practical way to produce hydrogen with high purity, which is green when the power is from renewable energy sources [1,2]. Compared to the conventional alkaline electrolysis, the proton exchange membrane water electrolysis (PEMWE) is an alternative and promising technique because of several advantages including high efficiency at high current densities, ease of maintenance, system compactness, and rapid response to startups and shutdowns [2–4]. However, the application of PEMWE is limited by the high cost and high loading of the anodic electrocatalysts. The high cost is associated with the use of high loadings of noble metals, where the high loadings are due to the sluggish kinetics of the oxygen evolution reaction (OER) [5]. Noble metals, such as iridium (Ir) and ruthenium (Ru) as well as their oxides (IrO_2 and RuO_2), are currently available electrocatalysts for the OER to provide high corrosion resistance and good catalytic activity [6–11]. Since noble metals are expensive and scarce, lowering the loading of the OER noble metal catalyst is necessary for the mass production of hydrogen based on this technology.

The most proposed reaction pathway for OER in acidic media is that of two H_2O molecules being oxidized into one oxygen molecule by releasing four H^+ ions and four electrons [11]. Since four electrons are transferred, the mechanisms comprise multistep adsorption–desorption reaction processes. The dissolution processes during the cycles with and without hydrous oxide buildup on an iridium metal electrode were suggested [12], and the mechanism of iridium dissolution triggered by OER was also proposed by Cherevko et al. [13]. Ru-based materials have high OER activity; however, they suffer

from rapid dissolution due to the formation of volatile tetroxide (RuO_4) in OER potential regions; thus, their durability issues must be addressed to ensure practical use [14,15]. In contrast, Ir-based materials possess compatible electrochemical activity and durability and are now the most widely used electrocatalysts for the OER in acid media [16,17].

An increase in the utilization of catalysts facilitates a decrease in the use of catalysts. One attractive strategy for addressing this challenge is to use a support material, which must possess a high surface area, a porous and interconnected structure, corrosion resistance, and high electrical conductivity [18]. The use of a high-surface-area support enables an increase in accessible surface area by decreasing the Ir particle size and increasing the surface-to-mass ratio of the catalyst [19,20]. Supported nanocatalysts were observed to be extremely active toward the OER because they possessed mixed Ir oxidation states and a high density of active sites [21]. Carbon materials are used as the support of the electrocatalysts in the applications of the proton exchange membrane fuel cell. However, carbon materials could not resist the high working potential and harshly acidic environment of water electrolysis. The resultant outcome is carbon corrosion, which results in the migration and agglomeration of the nanocatalysts and even detachment from the surface of the support. Therefore, several metal oxides have been studied as alternatives for carbon materials, such as TiO_2, SnO_2, doped metal oxides [10,22–24], etc.

Most of the metal oxides are semiconductors; thus, doping with hypovalent or hypervalent ions is a prerequisite to high electrical conductivity, but the change in the doping concentration causes severe ohmic losses [18]. Among them, antimony tin oxide (ATO) has attracted much attention because of its nanometer-size scales and relatively high electrical conductivity, compared with most metal oxides. The dispersion of Ir nanoparticles on ATO has been reported to improve the OER activity [10], where the uniform dispersion of Ir nanoparticles and large strong metal–support interaction (SMSI) led to high OER activity of Ir/ATO. It was observed that the introduction of vanadium into ATO support did not provide any more active sites but could change the porosity of the aerogel support and decrease the impurity content of the chlorine [22].

One IrO_2/ATO catalyst possessing a current density of 63 A/g Ir at an overpotential of 300 mV versus a reversible hydrogen electrode was reported [23], significantly exceeding a commercial TiO_2-supported IrO_2 catalyst under the same measurement conditions. Abbou et al. [18] found that the durability of electrochemical activity of IrOx/doped SnO_2 aerogels was controlled by the resistance to corrosion of the doping element, and by its concentration in the host SnO_2 matrix. Specifically, Sb-doped SnO_2 supports continuously dissolve while Ta-doped or Nb-doped SnO_2 supports with appropriate doping concentrations are stable under acidic OER conditions. This implied that a complex equilibrium relationship existed between SnO_2 and the doping element oxide.

Another approach is to tailor the structure and morphology of the catalysts. For instance, a nanoneedle network of iridium-containing oxides assembled into macroporous micro-scaled particles [9], nanoporous Ir nanosheets [25], a porous nano net cage of RuIrOx hollow particles [26,27], and amorphous Ir-atomic-cluster-deposited ultrathin IrO_2 nanoneedles [28] all had high catalytic activity for OER in comparison to a commercial IrO_2 nanoparticle catalyst. Claudel et al. [29] investigated the degradation mechanisms of OER electrocatalysts and showed that Ir (III) and Ir (V) were the best-performing Ir valences for the OER.

The highly branched structure of the Ir nanodendrites (Ir NDs) with a particle size of ~10 nm provides an increased active facet area that is available for OER in comparison to a commercial Ir catalyst, resulting in enhanced activity toward OER, though the formation of an anodic IrO_2 film on the surface of the Ir NDs was observed [30]. Oh et al. [5] found that Ir NDs supported on ATO were efficient and stable catalysts for water-splitting reactions. The Ir ND catalysts exhibited a kinetic water-splitting activity twofold larger than supported Ir nanoparticles and eightfold larger than commercial Ir blacks. The size of the nanodendrites was highly related to the reaction temperature; specifically, at a higher temperature, smaller particle sizes were produced by the burst-nucleation process [31].

The formation mechanism of Ir NDs was observed to be a time-dependent process, which suggested that Ir ions were first reduced to Ir^0 by the reducing agent. Subsequently, the size of the initially formed NPs started to increase as the reaction proceeded. Finally, the NPs self-aggregated, reducing the surface energy, and began to form highly branched dendritic nanostructures through an oriented-attachment formation mechanism [32,33]. Several Ir-based alloy NDs were also studied, including IrPt [34], IrCo [35], and IrW [36], and they usually behaved as bifunctional electrocatalysts.

In this study, the Ir NDs and Ir ND supported on antimony tin oxide (Ir ND/ATO) were prepared. Several material properties were characterized, and the electrocatalytic activity toward OER was evaluated. In addition, the long-term tests and resistance analysis were also investigated. According to the results of this study, ATO can be a good candidate as a support material, and Ir ND/ATO has been demonstrated to be an efficient and stable OER catalyst under a suitable concentration of Ir precursor.

2. Materials and Methods

2.1. Synthesis of Ir NDs and Ir ND/ATO

The Ir ND nanostructures were prepared by a surfactant-mediated method [5], where three Ir concentrations in the precursor solution were investigated. Firstly, 0.1 mmol dihydrogen hexachloroiridate (IV) hydrate (H2IrCl6·xH2O, 99%, Alfa Aesar) and 10 mmol tetradecyltrimethyl ammonium bromide (TTAB, 99%, Sigma) were dissolved in 75 mL deionized water, where iridium salt: TTAB = 1: 100 mol%, heating to 70 °C with vigorous stirring for 30 min to dissolve the Ir precursor. Then, 50 mg of sodium hydroxide (NaOH, 97%, Riedel-deHaën) was added to the mixture under vigorous stirring, and the color of the solution changed to clear blue. Next, 25 mL ice-cold sodium borohydride ($NaBH_4$, 98%, Aldrich) aqueous solution (150 mM) was added dropwise to the mixture under stirring. After that, mixing continued for 6 h at 70 °C, and the solution was cooled down to room temperature naturally. The products were collected by centrifugation and washed several times with ethanol–water mixtures (1:1 *v/v*). Then, the sample was dried at 80 °C in a vacuum oven and denoted as Ir ND1.

In order to determine the effect of the concentration of Ir precursor, in this study, the concentration of Ir precursor was 2- and 5-fold that of the Ir ND1, and all chemicals were also proportionally increased except for the amount of deionized water. The products of the Ir ND prepared with 2- and 5-fold concentrations were named Ir ND2 and Ir ND3. For the preparation of Ir ND/ATO, one commercial ATO (nanopowder, <50 nm, 47 m^2/g, Aldrich) was dispersed in deionized water (25 mL). This solution was added to the above-mentioned Ir-containing mixture with NaOH, and mixing continued for another 1 h. The following processes were the same as in the previous description.

2.2. Characterization of the Samples

Transmission electron microscopy (TEM) was employed to observe the morphology of the Ir NDs nanoparticles and Ir NDs deposited on the ATO support using a transmission electron microscope (Hitachi H-7100, Tokyo, Japan). The electrical conductivity (σ, S/cm) of the ATO was calculated using the equation: $\sigma = 1/(R_{sh}\ t)$ [37]. The results were obtained based on the average of ten conductivity measurements on a tablet of 13 mm in diameter. The sheet resistance (R_{sh}, Ω) of the tablet was measured using a four-point probe (source meter, Keithley 2401, Radiotek, New Taipei City, Taiwan). The thickness of the tablets (t, cm) was determined using a precise vernier caliper, where the resolution of the scale is 0.01 mm. The elemental compositions of Ir NDs and ATO-supported Ir NDs were acquired by energy dispersive X-ray spectroscopy (EDX), conducted with a QUANTAX Annular XFlash® QUAD FQ5060 (Bruker, Kanagawa, Japan). X-ray diffraction (XRD) was carried out using a powder diffractometer (Rigaku TTRAX III, Tokyo, Japan) equipped with Cu-Kα radiation (λ = 0.15418 nm) to determine the crystal structure. The XRD patterns were collected at a rate of 4°/min over 10–90° in 2θ mode. X-ray photoelectron spectroscopy (XPS) analysis was carried out using a spectrophotometer (PHI 5000 VersaProbe II, ULVAC-PHI,

Kanagawa, Japan). The spectrophotometer was equipped with an Al- Kα monochromatic source. The XPSPEAK software (version 4.1) was utilized for the deconvolution of the XPS spectra, which is a nonlinear least-squares curve-fitting program.

2.3. Electrochemical Activity Tests

Electrochemical characterization of the electrocatalysts was carried out using a CHI 6116E electrochemical analyzer (CH Instruments, Austin, Texas, USA). A common three-electrode setup and an electrolytic bath filled with 0.1 M $HClO_4$ aqueous solution were used to conduct the electrochemical experiments. A glassy carbon rotating disk electrode (RDE, Pine Research Instrument) of 0.5 cm in diameter with a thin layer of the catalyst ink was used as the working electrode. A saturated calomel electrode (SCE) and a platinum wire were used as the reference and counter electrodes, respectively. The catalyst inks, which consisted of 5 mg catalyst, 0.02 mL Nafion® ionomer (5 wt%, DuPont), 2.49 mL deionized water, and 2.49 mL isopropanol [5], were prepared by magnetic stirring for 48 h. Prior to the measurement, the working electrode was activated using a potential sweep between 0.5 and 1.5 V for 100 cycles at a scan rate of 0.1 V/s (a conditioning step). Then, the polarization curves of OER were measured using the linear sweep voltammetry (LSV) for 100 cycles at a scan rate of 0.005 V/s and 1600 rpm at 30 °C in N_2-saturated 0.1 M $HClO_4$ aqueous solution. Moreover, electrochemical impedance spectroscopy (EIS) was performed to determine the ohmic resistance. The EIS spectra of the samples were recorded at 1.8 V with an ac potential amplitude of 5 mA and a frequency range from 1 Hz to 10^5 Hz.

3. Results and Discussion

3.1. Physical and Chemical Properties of the Electrocatalysts

TEM images of the samples are shown in Figure 1. It can be seen that Ir NDs could be prepared by the self-assembly of tiny metal seeds using TTAB as an organic capping agent [5,30]. The strong reductant, $NaBH_4$, led to the rapid formation of tiny Ir seeds, and the Ir seeds were self-assembled into a dendritic structure through the guidance of TTAB [38]. Figure 1a shows a single Ir-ND1 composed of three-to-five branches in various directions. When the concentration of Ir precursor increased, the number or width of branches increased (Figure 1b,c). The size of each Ir ND was in the order of 5–15 nm. Figure 1d–e confirm that the Ir NDs could be dispersed uniformly on the surface of ATO supports through the in situ synthesis. In addition, the TEM image of one commercial Ir black (Figure 1f) was provided for comparison.

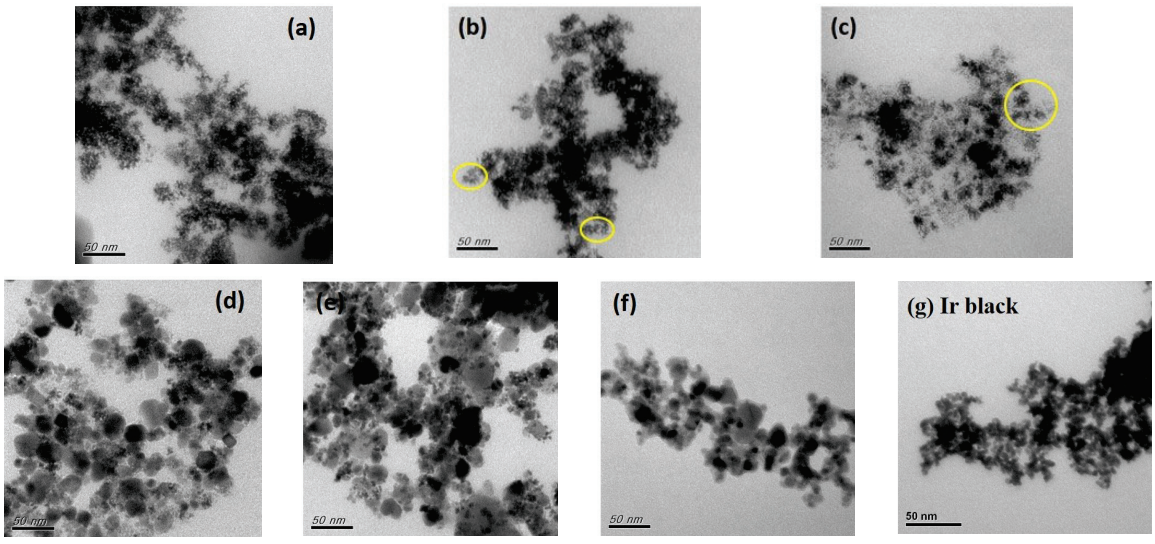

Figure 1. TEM images of the samples: (**a**) Ir ND1; (**b**) Ir ND2; (**c**) Ir ND3; (**d**) Ir ND1/ATO; (**e**) Ir ND2/ATO; (**f**) ATO; (**g**) Ir black (Premetek). The yellow circles show the number or width of branches increased as the concentration of Ir precursor increased.

The elemental compositions of the samples were investigated by EDX analysis, as shown in Table 1. For Ir NDs, the Ir content ranged from 88.1 to 95.5 wt.%, similar to that of Ir black (Premetek). For the ATO-supported Ir NDs, the Ir contents in Ir ND1/ATO and Ir ND2/ATO were 20.9 and 26.1 wt.%, respectively, close to the designed percent (20 wt.%). The Sb/(Sn + Sb) was 15% in ATO, while the ratios reduced when Ir NDs were incorporated onto the surface of ATO. It was expected that some Sb ions would be dissolved during the Ir ND deposition processes. The EDX spectrum of Ir ND2/ATO was used as an example, as shown in Figure 2a. The corresponding atomic percentages are also shown in Table 1.

Table 1. The elemental compositions of the samples from EDX analysis.

Sample	Elemental Composition							
	Weight Percentage (wt.%)				Atomic Percentage (at.%)			
	Ir	O	Sn	Sb	Ir	O	Sn	Sb
Ir ND1	88.8	11.2	—	—	39.8	60.2	—	—
Ir ND2	88.1	11.9	—	—	38.2	61.8	—	—
Ir ND3	95.5	4.5	—	—	63.63	36.37	—	—
Ir ND1/ATO	20.9	13.7	59.5	5.9	7.2	56.5	33.1	3.2
Ir ND2/ATO	26.1	14.6	56.4	2.9	8.7	59.0	30.7	1.6
Ir black (Premetek)	92.8	7.2	—	—	51.7	48.3	—	—
ATO	—	31.3	58.3	10.4	—	77.2	19.4	3.4

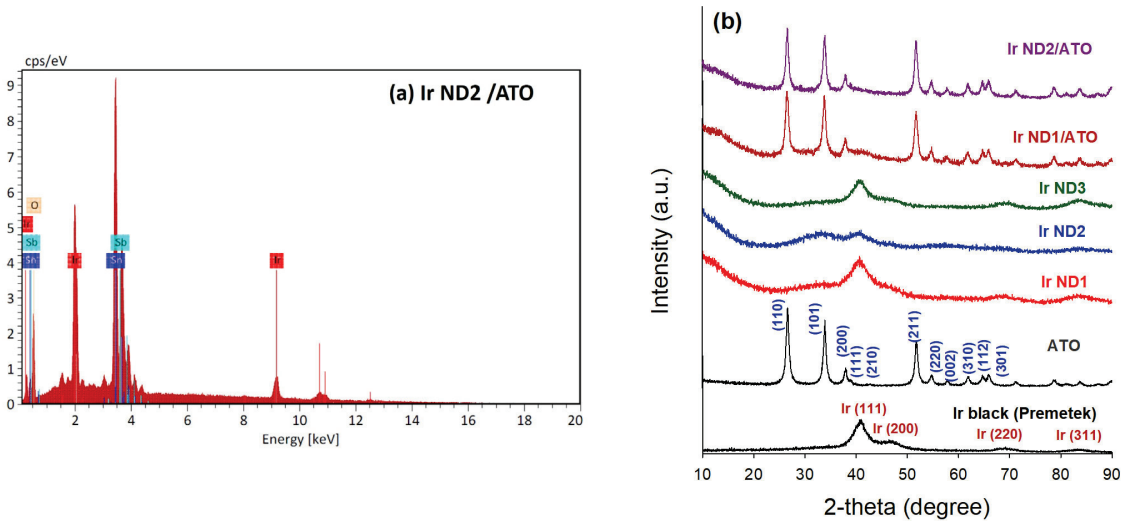

Figure 2. (**a**) EDX pattern of Ir ND2/ATO. (**b**) XRD patterns of all samples.

Figure 2b displays the XRD patterns of all samples. Four major peaks on the patterns of Ir NDs at 40.6, 47.3, 69.1, and 83.4° were assigned to diffractions from the (111), (200), (220) and (311) plans of the Ir metallic face-centered cubic (fcc) structure (JCPDS no. 87-0715), respectively. The XRD patterns of the branched Ir NDs suggested that the obtained nanostructures were primarily composed of pure Ir. For Ir ND2/ATO, the major diffraction peaks of metallic Ir were insignificant, indicating the formation of IrOx species on ATO. The crystallite size (d) of Ir nanoparticles was calculated from the Ir (111) peak according to Scherrer's equation [39], as shown below:

$$d = \frac{K\,\lambda}{\beta \cos\theta} \quad (1)$$

where K is the Scherrer's constant of 0.9 [40], λ is the X-ray wavelength of Cu-Kα, β is the full width at half maximum (FWHM) in radians, and θ is the Bragg angle in radians. The

crystallite sizes of Ir ND1, Ir ND2, Ir ND3, and Ir black (Premetek) were 2.28, 1.68, 2.86, and 3.42 nm, respectively.

The chemical states of the samples were investigated by XPS. Figure 3 displays the results of the curve fitting of high-resolution XPS Ir 4f peaks, which confirms the presence of metallic Ir (Ir^0), Ir (IV), and Ir (III) phases. The latter two may correspond to the molecular formulas $Ir(OH)_4$ and $Ir(OH)_3$ or IrOx [10]. The existence of Ir oxides may be due to the oxidation of the surface when exposed to air. Table 2 shows the fitting results of the XPS Ir 4f regions for the samples, in which the atomic ratios of Ir 4f were also displayed in the table. Three chemical states of Ir for all samples are illustrated in Figure 4, indicating that the atomic ratio of Ir^0 increased as the concentration of Ir precursor increased for unsupported Ir NDs, and Ir ND2 comprised the highest percent of Ir (IV). The phase distribution of Ir ND1 was similar to that of Ir (Premetek).

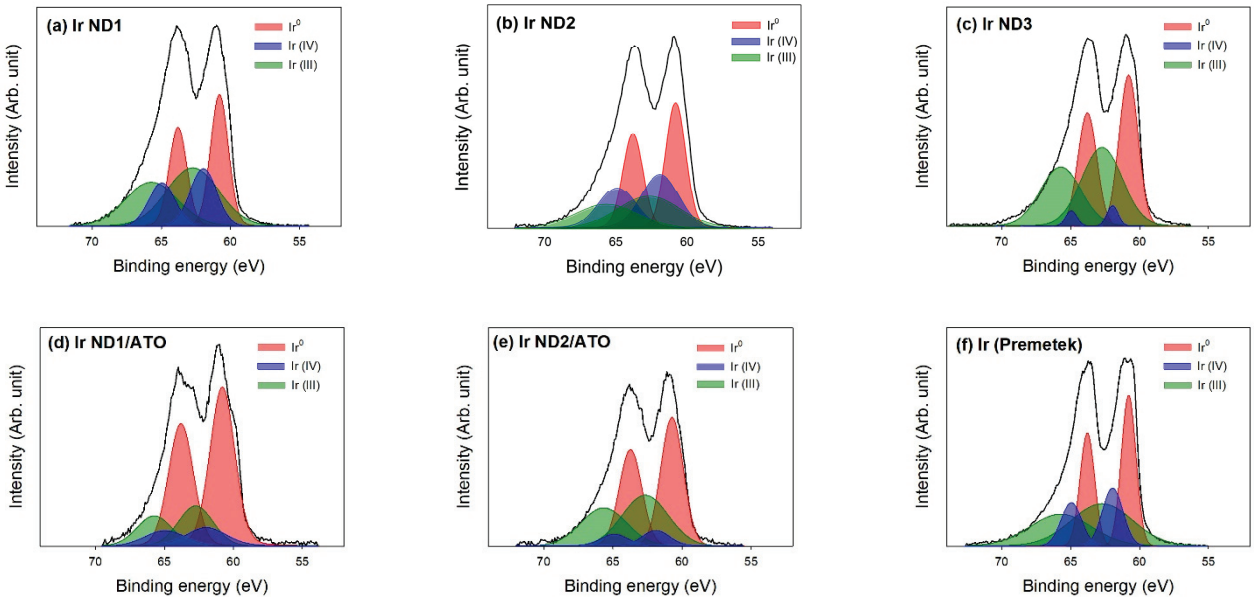

Figure 3. Curve fitting of high-resolution XPS Ir 4f spectra for the samples: (**a**) Ir ND1; (**b**) Ir ND2; (**c**) Ir ND3; (**d**) Ir ND1/ATO; (**e**) Ir ND2/ATO; (**f**) Ir black (Premetek).

Table 2. Results of fitting of the XPS Ir 4f region for the samples; values given in at.% of total intensity.

Sample	Ir 4f	Binding Energy (eV)					
		Ir^o		Ir (IV)		Ir (III)	
		60.8	63.8	61.9	64.9	62.7	65.7
Ir ND1	16.6	3.30	2.48	2.07	1.55	4.11	3.09
Ir ND2	26.1	5.90	4.43	4.47	3.35	4.54	3.41
Ir ND3	32.3	8.43	6.32	0.66	0.50	9.37	7.03
Ir ND1/ATO	5.51	2.07	1.55	0.40	0.30	0.68	0.51
Ir ND2/ATO	6.68	1.96	1.47	0.28	0.21	1.59	1.19
Ir black (Premetek)	37.4	7.90	5.92	4.26	3.20	9.21	6.91

For Ir ND/ATO samples, the percent of Ir^0 increased in comparison to unsupported Ir NDs, indicating that the deposition of Ir NDs on the surface of ATO contributed to the reduction in Ir precursor. In addition, Ir (III)/Ir (IV) was higher in Ir ND2/ATO than in Ir ND1/ATO, for which it was expected that Ir ND2/ATO might have better electrocatalytic activity [24,29].

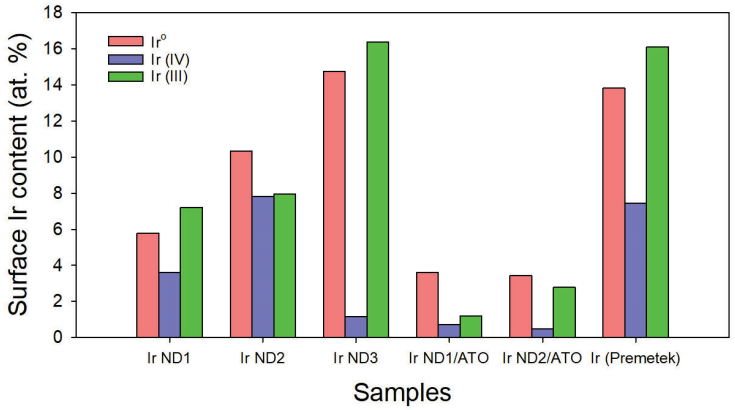

Figure 4. The different chemical states of surface Ir contents from XPS analysis for all samples.

Figure 5 shows the curve fitting of high-resolution XPS Sn 3d spectra and the atomic ratios are outlined in Table 3. The as-received ATO contained a small portion of Sn (II), though the majority was still Sn (IV). As seen from Figure 6, the XPS Sn 3d regions were only Sn (IV) for Ir ND/ATO, indicating that the oxidation of Sn (II) to form Sn(IV) promoted the reduction in Ir precursor.

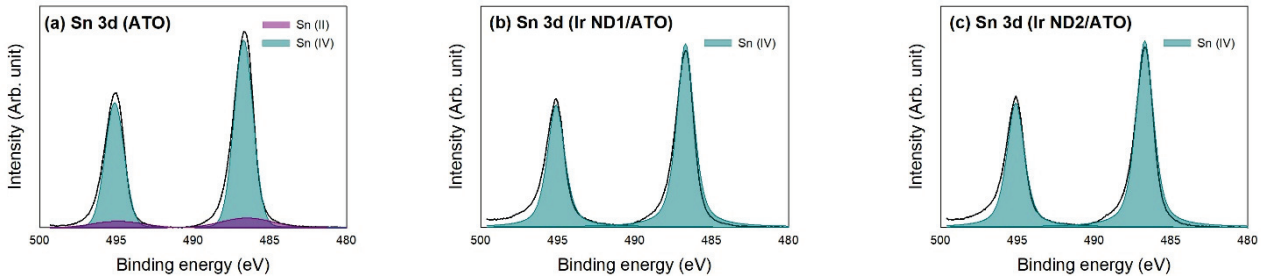

Figure 5. Curve fitting of high-resolution XPS Sn 3d spectra for the samples: (**a**) ATO; (**b**) Ir ND1/ATO; (**c**) Ir ND2/ATO.

Table 3. Results of fitting of the XPS Sn 3d region for the samples; values given in at.% of total intensity.

Sample	Sn 3d	Binding Energy (eV)			
		Sn (II)		Sn (IV)	
		486.5	494.91	486.7	495.11
ATO	23.3	1.71	1.14	12.27	8.18
Ir ND1/ATO	21.1	—	—	12.66	8.44
Ir ND2/ATO	23.32	—	—	13.99	9.33

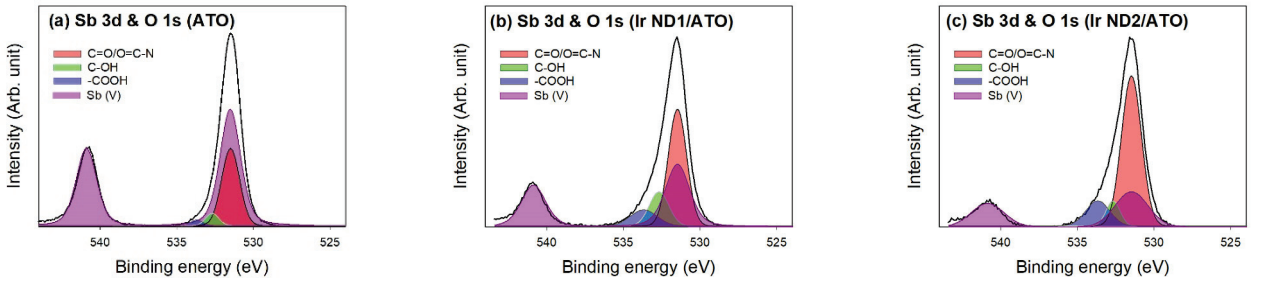

Figure 6. Curve fitting of high-resolution XPS Sb 3d and O 1s spectra for the samples: (**a**) ATO; (**b**) Ir ND1/ATO; (**c**) Ir ND2/ATO.

The overlapping of Sb $3d_{5/2}$ and O 1s regions renders the peak decomposition more complicated. Taking the area ratio of the Sb $3d_{3/2}$ peak to Sb $3d_{5/2}$ peak as 2 to 3, the peak decomposition could be accomplished [41], as shown in Figure 6 and Table 4. The oxidation state of Sb on ATO was Sb (V), corresponding to the molecular formula of Sb_2O_5/SnO_2. The deposition of Ir NDs was expected to lead to the dissolution of Sb ions in which the degree of loss was dependent on the Ir content. This implies that Sb was not stable in the alkaline environment during the synthesis process of Ir ND/ATO. However, the Sb amount on Ir ND1/ATO and Ir ND2/ATO remained 3 and 2.03 at.%, respectively. Consequently, the oxidation of Sn and Sb in ATO support suppressed the oxidation of Ir^0 and Ir (III).

Table 4. Results of fitting of the XPS Sb 3d and O 1s regions for the samples; values given in at.% of total intensity.

Sample	Sb3d	O1s	Binding Energy (eV)				
			Sb (V)		C=O	C-OH	-COOH
			531.5	540.88	531.5	532.7	533.7
ATO	10.9	65.8	6.54	4.36	56.80	6.38	2.62
Ir ND1/ATO	3	70.39	1.80	1.20	46.71	14.46	9.23
Ir ND2/ATO	2.03	67.97	1.22	0.81	51.69	6.02	10.25

3.2. Electrochemical Properties of the Electrocatalysts

The electrocatalytic activity for the OER of the catalysts was evaluated in acidic electrolytes using the LSV process. Figure 7a shows OER polarization curves of three unsupported Ir NDs, two Ir ND/ATO samples, and one commercial Ir nanoparticle. The mass-based activities at 1.8 V were 113 mA/mg for Ir ND1, 116 mA/mg for Ir ND2, and 106 mA/mg for Ir ND3. All performed slightly lower activity compared to the commercial Ir black (154 mA/mg). Since the catalytic activity of Ir NDs followed the order Ir ND2 > Ir ND1 > IrND3, the ATO-supported Ir NDs were only prepared for Ir ND1 and Ir ND2. The mass activities of ATO-supported Ir NDs at 1.8 V were 414 mA/mg for Ir ND1/ATO and 798 mA/mg for Ir ND2/ATO, significantly higher than unsupported Ir NDs. These excellent activities were attributed to the uniformly distributed intrinsically Ir nano-dendritic structure on the surface of ATO nanoparticles. The electrical conductivity of the ATO support was 0.026 ± 0.001 S/cm by the four-point probe method. The high electrical conductivity of the ATO support was expected to be another reason that the ATO-supported Ir NDs had good activity. The corresponding OER polarization curves (normalized to the geometric disk area) of the samples are shown in Figure 7b, and the optimal activities at 1.8 V for unsupported and ATO-supported Ir NDs occurred at Ir ND2 (0.0060 A/cm^2) and Ir ND2/ATO (0.0106 A/cm^2), respectively. The Ir-mass-based activity at 1.5, 1.65, and 1.8 V is also displayed in Figure 7c,d for comparison.

A comparison of the mass-based OER activities at 1.8 V on the polarization curves for the 1st and the 100th cycles of LSV is shown in Figure 8. The activity decay of the electrocatalysts increased in the order Ir ND2/ATO < Ir ND1/ATO < Ir ND3 < Ir ND1 < Ir black (Premetek) < Ir ND2. It is evident that the ATO-supported Ir NDs exhibited higher durability than Ir black and unsupported Ir NDs. Specifically, the activity decay of Ir ND2/ATO was only 0.8% after 100 cycles of LSV. The excellent durability of the electrocatalytic activity for Ir ND/ATO was primarily attributed to the in situ synthesis of Ir NDs on the surface of ATO nanoparticles, the uniform dispersion of Ir NDs on the surface of ATO, and good corrosion resistance of ATO in an acidic environment. It is anticipated that the metallic Ir would convert to hydrous Ir oxides upon potential cycling. In addition, strong metal–support interactions would change the electrochemical behavior of the hydrous Ir oxides [10].

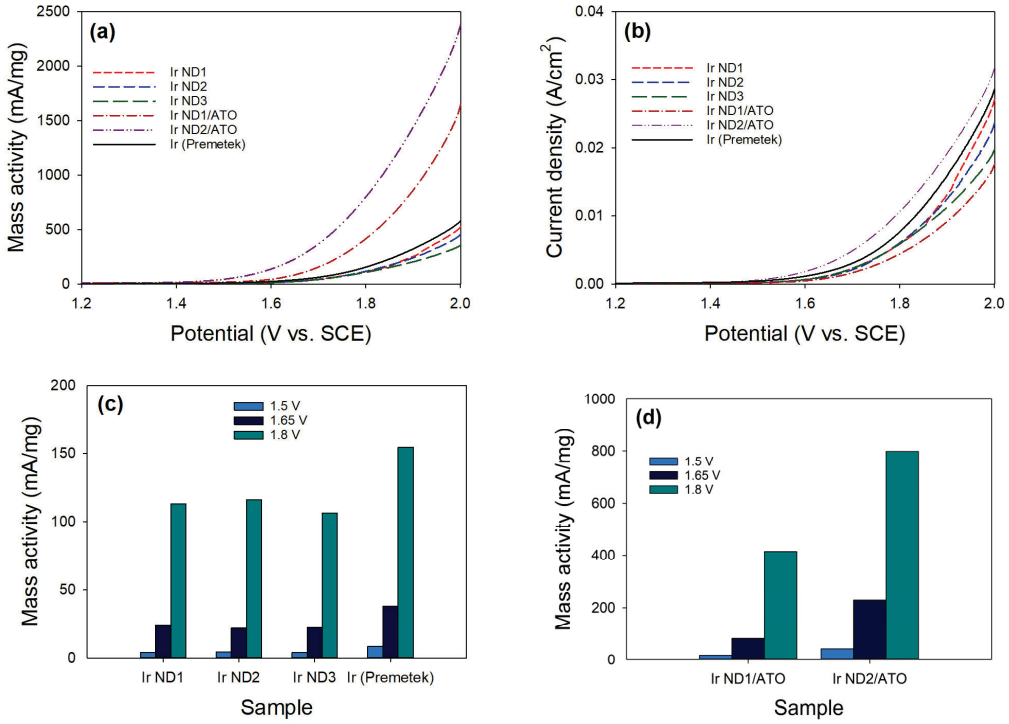

Figure 7. Electrocatalytic OER activity of the catalysts: (**a**) mass activity; (**b**) current density; the Ir-mass-based activity at 1.5, 1.65, and 1.8 V: (**c**) unsupported Ir; (**d**) Ir ND/ATO.

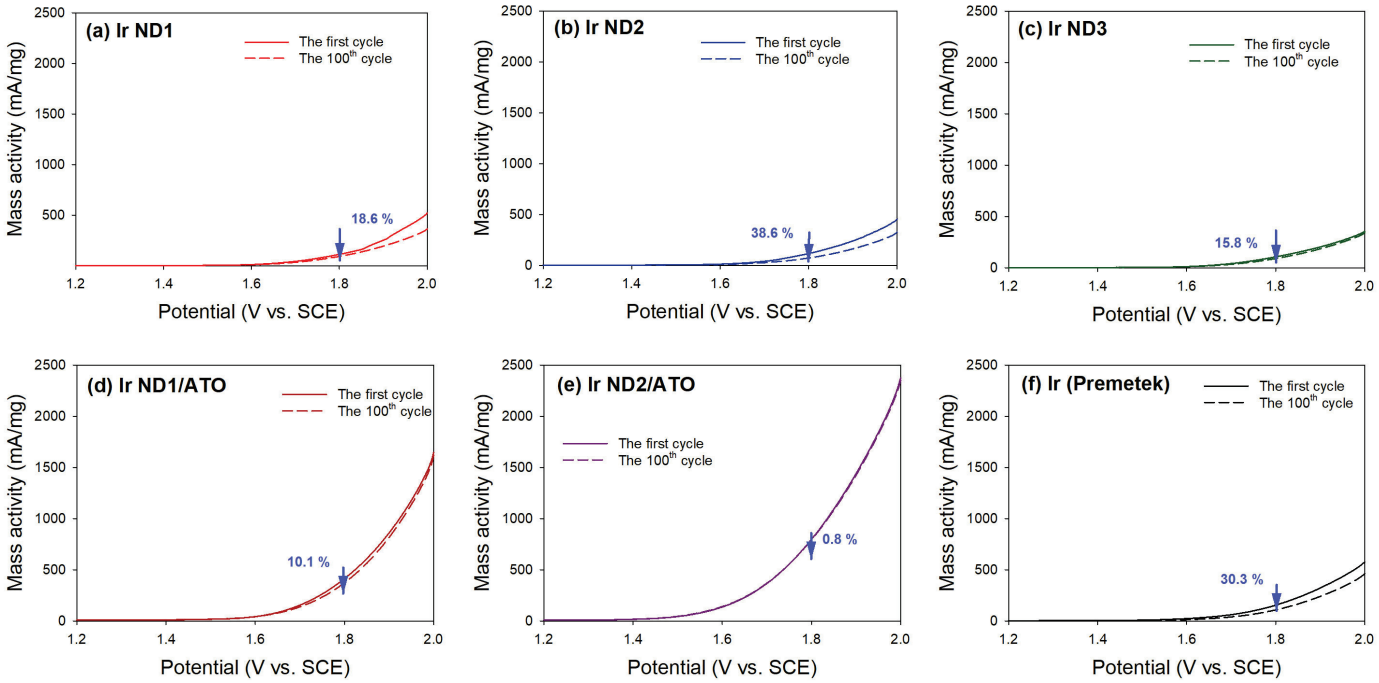

Figure 8. Degradation of electrocatalytic OER activity of the catalysts at 1.8 V: (**a**) Ir ND1; (**b**) Ir ND2; (**c**) Ir ND3; (**d**) Ir ND1/ATO; (**e**) Ir ND2/ATO; (**f**) Ir black (Premetek).

The EIS was used to investigate the internal resistances of the electrocatalysts, where the resistance was determined from the width of the semicircles in the *X*-axis. The Nyquist plots obtained from EIS data are shown in Figure 9. Before the LSV measurements, the Nyquist diagrams of Ir NDs only showed diffusion resistance in the electrolyte, about 20 ohm (Figure 9a–c). The charge transfer resistance occurring at the catalyst–electrolyte

interface was observed after 100 cycles of LSV, and the resistances of Ir ND1, Ir ND2, and Ir ND3 were approximately 193, 152, and 151 ohm, respectively. This was highly associated with the OER activity decay.

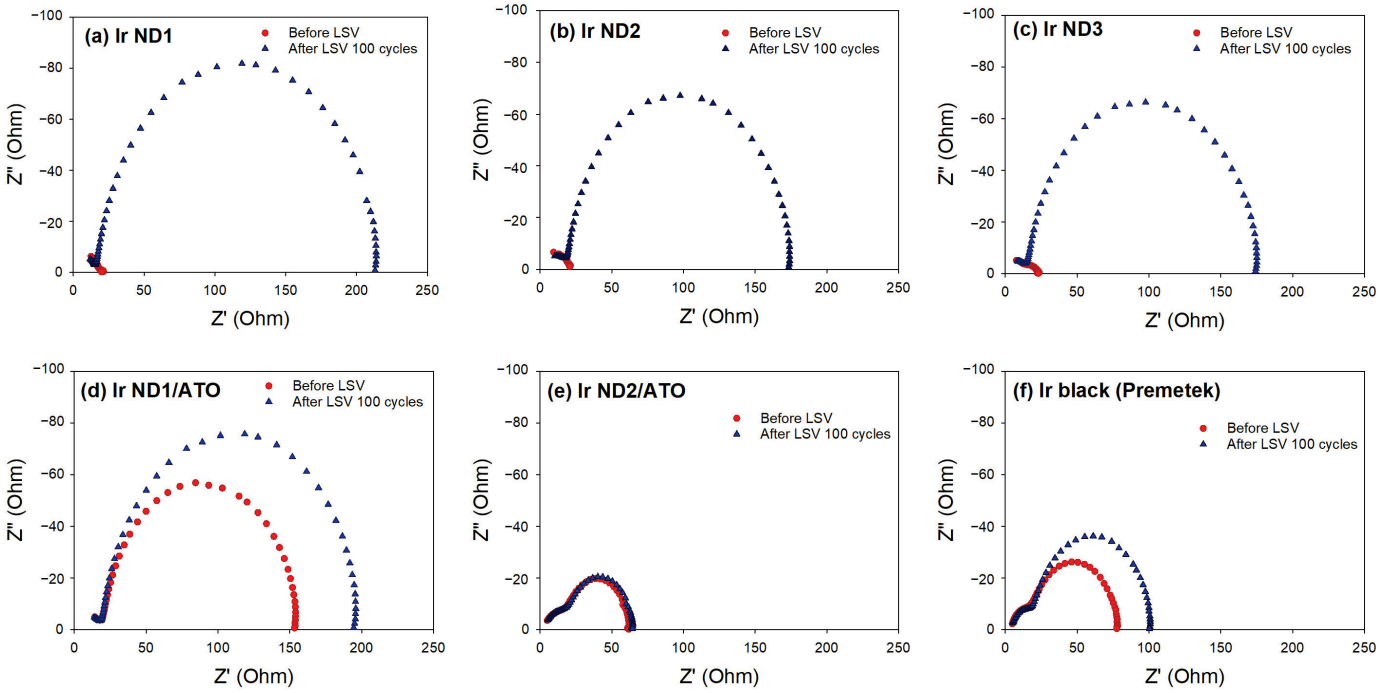

Figure 9. Nyquist plots of the catalysts: (**a**) Ir ND1; (**b**) Ir ND2; (**c**) Ir ND3; (**d**) Ir ND1/ATO; (**e**) Ir ND2/ATO; (**f**) Ir black (Premetek).

The ATO-supported Ir NDs displayed a different pattern. Except for the diffusion resistance, another semicircle occurred, indicating the resistance of ATO support, which was about 130 ohm for Ir ND1/ATO and 40 ohm Ir ND2/ATO. It is expected that the effect of ATO on the resistance depends on the interactions between Ir NDs and ATO. The interactions were stronger in Ir ND2/ATO; hence, the resistance from the ATO support was less significant. After 100 cycles of LSV, the resistances of the samples increased to about 170 and 43 ohm for Ir ND1/ATO and Ir ND2/ATO, respectively, which was also related to the activity decay.

4. Conclusions

The results showed that Ir NDs nanostructures were successfully prepared alone or supported on ATO nanoparticles, where the structures of nanodendrites were dependent on the Ir concentrations in the precursor solution. The XRD patterns of Ir NDs exhibited major diffraction peaks, which were indexed to the reflections of the fcc Ir metal. However, for Ir ND/ATO, the major diffraction peaks of metal Ir were insignificant, indicating the formation of IrOx species on ATO. The unsupported and ATO-supported Ir NDs consisted of metallic Ir as well as Ir oxides, which was supported by the results of XPS. Moreover, the oxidation of ATO stimulated the reduction in Ir during the synthesis processes. The mass-based OER catalytic activity at a potential of 1.8 V had the order Ir ND2/ATO (798 mA/mg) > Ir ND1/ATO (414 mA/mg) > Ir black (155 mA/mg) > Ir ND2 (116 mA/mg) > Ir ND1 (113 mA/mg) > Ir ND3 (106 mA/mg). After performing LSV of 100 cycles, the OER catalytic activity of Ir ND2/ATO remained at > 99% of activity, while Ir ND2 had only about 61.4% of the activity left, indicating that Ir NDs supported on ATO significantly improve the durability of the OER catalytic activity. This observation was also supported by the results of EIS, according to which the charge transfer resistance was the lowest on Ir ND2/ATO.

Author Contributions: Conceptualization, Y.-C.C.; methodology, Y.-C.C.; software, Z.W.; validation, Y.-C.C.; investigation, Z.-H.P.; resources, Y.-C.C.; data curation, Z.-H.P. and Z.W.; writing—original draft preparation, Y.-C.C.; writing—review and editing, Y.-C.C.; visualization, Y.-C.C.; supervision, Y.-C.C.; project administration, Y.-C.C.; funding acquisition, Y.-C.C. All authors have read and agreed to the published version of the manuscript.

Funding: This research was funded by the National Science and Technology Council, Taiwan, grant numbers MOST 111-2221-E-155-010- and NSTC 111-2622-E-155-009-.

Data Availability Statement: The data presented in this study are available on request from the corresponding author. The data are not publicly available due to privacy restrictions.

Acknowledgments: The authors would like to thank the Instrumentation Center at NTU for performing the TEM and EDX analyses; the Instrumentation Center at NTHU for performing the XRD and XPS analyses.

Conflicts of Interest: The authors declare no conflict of interest.

References

1. Barbir, F. PEM electrolysis for production of hydrogen from renewable energy sources. *Sol. Energy* **2005**, *78*, 661–669. [CrossRef]
2. Carmo, M.; Fritz, D.L.; Mergel, J.; Stolten, D. A comprehensive review on PEM water electrolysis. *Int. J. Hydrogen Energy* **2013**, *38*, 4901–4934. [CrossRef]
3. Nieminen, J.; Dincer, I.; Naterer, G. Comparative performance analysis of PEM and solid oxide steam electrolysers. *Int. J. Hydrogen Energy* **2010**, *35*, 10842–10850. [CrossRef]
4. Buttler, A.; Spliethoff, H. Current status of water electrolysis for energy storage, grid balancing and sector coupling via power-to-gas and power-to-liquids. *Renew. Sustain. Energy Rev.* **2018**, *82*, 2440–2454. [CrossRef]
5. Oh, H.S.; Nong, H.N.; Reier, T.; Gliech, M.; Strasser, P. Oxide-supported Ir nanodendrites with high activity and durability for the oxygen evolution reaction in acid PEM water electrolyzers. *Chem. Sci.* **2015**, *6*, 3321–3328. [CrossRef]
6. Siracusano, S.; Baglio, V.; Di Blasi, A.; Briguglio, N.; Stassi, A.; Ornelas, R.; Trifoni, E.; Antonucci, V.; Aricò, A.S. Electrochemical characterization of single cell and short stack PEM electrolyzers based on a nanosized IrO_2 anode electrocatalyst. *Int. J. Hydrogen Energy* **2010**, *35*, 5558–5568. [CrossRef]
7. Oh, J.G.; Lee, W.H.; Kim, H. The inhibition of electrochemical carbon corrosion in polymer electrolyte membrane fuel cells using iridium nanodendrites. *Int. J. Hydrogen Energy* **2012**, *37*, 2455–2461. [CrossRef]
8. Siracusano, S.; Van Dijk, N.; Payne-Johnson, E.; Baglio, V.; Aricò, A.S. Nanosized IrOx and IrRuOx electrocatalysts for the O_2 evolution reaction in PEM water electrolysers. *Appl. Catal. B-Environ.* **2015**, *164*, 488–495. [CrossRef]
9. Faustini, M.; Giraud, M.; Jones, D.; Rozière, J.; Dupont, M.; Porter, T.R.; Nowak, S.; Bahri, M.; Ersen, O.; Sanchez, C.; et al. Hierarchically structured ultraporous iridium-based materials: A novel catalyst architecture for proton exchange membrane water electrolyzers. *Adv. Energy Mater.* **2019**, *9*, 1802136. [CrossRef]
10. Hartig-Weiss, A.; Miller, M.; Beyer, H.; Schmitt, A.; Siebel, A.; Freiberg, A.T.S.; Gasteiger, H.A.; El-Sayed, H.A. Iridium oxide catalyst supported on antimony-doped tin oxide for high oxygen evolution reaction activity in acidic media. *ACS Appl. Nano Mater.* **2020**, *3*, 2185–2196. [CrossRef]
11. Song, H.J.; Yoon, H.; Ju, B.; Kim, D.W. Highly efficient perovskite-based electrocatalysts for water oxidation in acidic environments: A Mini Review. *Adv. Energy Mater.* **2021**, *11*, 2002428. [CrossRef]
12. Cherevko, S.; Geiger, S.; Kasian, O.; Mingers, A.; Mayrhofer, K.J.J. Oxygen evolution activity and stability of iridium in acidic media. Part 1.—Metallic iridium. *J. Electroanal. Chem.* **2016**, *773*, 69–78. [CrossRef]
13. Cherevko, S.; Geiger, S.; Kasian, O.; Mingers, A.; Mayrhofer, K.J.J. Oxygen evolution activity and stability of iridium in acidic media. Part 2.—Electrochemically grown hydrous iridium oxide. *J. Electroanal. Chem.* **2016**, *774*, 102–110. [CrossRef]
14. Roy, C.; Rao, R.R.; Stoerzinger, K.A.; Hwang, J.; Rossmeisl, J.; Chorkendorff, I.; Shao-Horn, Y.; Stephens, I.E.L. Trends in activity and dissolution on RuO_2 under oxygen evolution conditions: Particles versus well-defined extended surfaces. *ACS Energy Lett.* **2018**, *3*, 2045–2051. [CrossRef]
15. Chen, Z.; Duan, X.; Wei, W.; Wang, S.; Ni, B.J. Electrocatalysts for acidic oxygen evolution reaction: Achievements and perspectives. *Nano Energy* **2020**, *78*, 105392. [CrossRef]
16. Chen, Z.; Duan, X.; Wei, W.; Wang, S.; Ni, B.J. Iridium-based nanomaterials for electrochemical water splitting. *Nano Energy* **2020**, *78*, 105270. [CrossRef]
17. She, L.; Zhao, G.; Ma, T.; Chen, J.; Sun, W.; Pan, H. On the durability of iridium-based electrocatalysts toward the oxygen evolution reaction under acid environment. *Adv. Funct. Mater.* **2022**, *32*, 2108465. [CrossRef]
18. Abbou, S.; Chattot, R.; Martin, V.; Claudel, F.; Solà-Hernandez, L.; Beauger, C.; Dubau, L.; Maillard, F. Manipulating the corrosion resistance of SnO_2 aerogels through doping for efficient and durable oxygen evolution reaction electrocatalysis in acidic media. *ACS Catal.* **2020**, *10*, 7283–7294. [CrossRef]
19. Hayden, B.E. Particle size and support effects in electrocatalysis. *Acc. Chem. Res.* **2013**, *46*, 1858–1866. [CrossRef]

20. Puthiyapura, V.K.; Mamlouk, M.; Pasupathi, S.; Pollet, B.G.; Scott, K. Physical and electrochemical evaluation of ATO supported IrO_2 catalyst for proton exchange membrane water electrolyser. *J. Power Sources* **2014**, *269*, 451–460. [CrossRef]
21. Da Silva, C.D.F.; Claudel, F.; Martin, V.; Chattot, R.; Abbou, S.; Kumar, K.; Jiménez-Morales, I.; Cavaliere, S.; Jones, D.; Rozière, J.; et al. Oxygen evolution reaction activity and stability benchmarks for supported and unsupported IrOx electrocatalysts. *ACS Catal.* **2021**, *11*, 4107–4116. [CrossRef]
22. Wang, L.; Song, F.; Ozouf, G.; Geiger, D.; Morawietz, T.; Handl, M.; Gazdzicki, P.; Beauger, C.; Kaiser, U.; Hiesgen, R.; et al. Improving the activity and stability of Ir catalysts for PEM electrolyzer anodes by SnO_2: Sb aerogel supports: Does V addition play an active role in electrocatalysis? *J. Mater. Chem. A* **2017**, *5*, 3172–3178. [CrossRef]
23. Böhm, D.; Beetz, M.; Schuster, M.; Peters, K.; Hufnagel, A.G.; Döblinger, M.; Böller, B.; Bein, T.; Fattakhova-Rohlfing, D. Efficient OER catalyst with low Ir volume density obtained by homogeneous deposition of iridium oxide nanoparticles on macroporous antimony-doped tin oxide support. *Adv. Funct. Mater.* **2020**, *30*, 1906670. [CrossRef]
24. Kim, E.J.; Shin, J.; Bak, J.; Lee, S.J.; Kim, K.H.; Song, D.H.; Roh, J.H.; Lee, Y.; Kim, H.W.; Lee, K.S.; et al. Stabilizing role of Mo in TiO_2-MoO_x supported Ir catalyst toward oxygen evolution reaction. *Appl. Catal. B-Environ.* **2021**, *280*, 119433. [CrossRef]
25. Chatterjee, S.; Peng, X.; Intikhab, S.; Zeng, G.; Kariuki, N.N.; Myers, D.J.; Danilovic, N.; Snyder, J. Nanoporous iridium nanosheets for polymer electrolyte membrane electrolysis. *Adv. Energy Mater.* **2021**, *11*, 2101438. [CrossRef]
26. Zhuang, Z.; Wang, Y.; Xu, C.Q.; Liu, S.; Chen, C.; Peng, Q.; Zhuang, Z.; Xiao, H.; Pan, Y.; Lu, S.; et al. Three-dimensional open nano-netcage electrocatalysts for efficient pH-universal overall water splitting. *Nat. Commun.* **2019**, *10*, 4875. [CrossRef]
27. Wang, Y.Z.; Yang, M.; Ding, Y.M.; Li, N.W.; Yu, L. Recent advances in complex hollow electrocatalysts for water splitting. *Adv. Funct. Mater.* **2022**, *32*, 2108681. [CrossRef]
28. Lim, J.; Kang, G.; Lee, J.W.; Jeon, S.; Jeon, H.; Kang, P.W.; Lee, H. Amorphous Ir atomic clusters anchored on crystalline IrO_2 nanoneedles for proton exchange membrane water oxidation. *J. Power Sources* **2022**, *524*, 231069. [CrossRef]
29. Claudel, F.; Dubau, L.; Berthome, G.; Sola-Hernandez, L.; Beauger, C.; Piccolo, L.; Maillard, F. Degradation mechanisms of oxygen evolution reaction electrocatalysts: A combined identical-location transmission electron microscopy and X-ray photoelectron spectroscopy study. *ACS Catal.* **2019**, *9*, 4688–4698. [CrossRef]
30. Lee, W.H.; Kim, H. Oxidized iridium nanodendrites as catalysts for oxygen evolution reactions. *Catal. Commun.* **2011**, *12*, 408–411. [CrossRef]
31. Kim, C.; Oh, J.-G.; Kim, Y.-T.; Kim, H.; Lee, H. Platinum dendrites with controlled sizes for oxygen reduction reaction. *Electrochem. Commun.* **2010**, *12*, 1596–1599. [CrossRef]
32. Wang, C.; Xiao, G.J.; Sui, Y.M.; Yang, X.Y.; Liu, G.; Jia, M.J.; Han, W.; Liu, B.B.; Zou, B. Synthesis of dendritic iridium nanostructures based on the oriented attachment mechanism and their enhanced CO and ammonia catalytic activities. *Nanoscale* **2014**, *6*, 15059–15065. [CrossRef]
33. Chaudhari, N.K.; Joo, J.; Kwon, H.; Kim, B.; Kim, H.Y.; Joo, S.H.; Lee, K. Nanodendrites of platinum-group metals for electrocatalytic applications. *Nano Res.* **2018**, *11*, 6111–6140. [CrossRef]
34. Zhang, G.; Shao, Z.G.; Lu, W.; Li, G.; Liu, F.; Yi, B. One-pot synthesis of Ir@Pt nanodendrites as highly active bifunctional electrocatalysts for oxygen reduction and oxygen evolution in acidic medium. *Electrochem. Commun.* **2012**, *22*, 145–148. [CrossRef]
35. Fu, L.; Zeng, X.; Cheng, G.; Luo, W. IrCo nanodendrite as an efficient bifunctional electrocatalyst for overall water splitting under acidic conditions. *ACS Appl. Mater. Interfaces* **2018**, *10*, 24993–24998. [CrossRef] [PubMed]
36. Lv, F.; Feng, J.; Wang, K.; Dou, Z.; Zhang, W.; Zhou, J.; Yang, C.; Luo, M.; Yang, Y.; Li, Y.; et al. Iridium−tungsten alloy nanodendrites as pH-universal water-splitting electrocatalysts. *ACS Cent. Sci.* **2018**, *4*, 1244–1252. [CrossRef]
37. Fadil, Y.; Dinh, L.N.M.; Yap, M.O.Y.; Kuchel, R.P.; Yao, Y.; Omura, T.; Aregueta-Robles, U.A.; Song, N.; Huang, S.; Jasinski, F.; et al. Ambient-temperature waterborne polymer/rGO nanocomposite films: Effect of rGO distribution on electrical conductivity. *ACS Appl. Mater. Interfaces* **2019**, *11*, 48450–48458. [CrossRef]
38. Gu, J.; Zhang, Y.W.; Tao, F. Shape control of bimetallic nanocatalysts through well-designed colloidal chemistry approaches. *Chem. Soc. Rev.* **2012**, *41*, 8050–8065. [CrossRef]
39. Li, W.; Liang, C.; Zhou, W.; Qui, J.; Zhou, Z.; Sun, G.; Xin, Q. Preparation and characterization of multiwalled carbon nanotube-supported platinum for cathode catalysts of direct methanol fuel cells. *J. Phys. Chem. B* **2003**, *107*, 6292–6299. [CrossRef]
40. Kojima, Y.; Suzuki, K.I.; Fukumoto, K.; Sasaki, M.; Yamamoto, T.; Kawai, Y.; Hayashi, H. Hydrogen generation using sodium borohydride solution and metal catalyst coated on metal oxide. *Int. J. Hydrogen Energy* **2002**, *27*, 1029–1034. [CrossRef]
41. Jiménez-Morales, I.; Cavaliere, S.; Dupont, M.; Jones, D.; Roziere, J. On the stability of antimony doped tin oxide supports in proton exchange membrane fuel cell and water electrolysers. *Sustain. Energy Fuels* **2019**, *3*, 1526–1535. [CrossRef]

nanomaterials

MDPI

Article

Facile Preparation of $SrZr_{1-x}Ti_xO_3$ and $SrTi_{1-x}Zr_xO_3$ Fine Particles Assisted by Dehydration of Zr^{4+} and Ti^{4+} Gels under Hydrothermal Conditions

José Remigio Quiñones-Gurrola [1], Juan Carlos Rendón-Angeles [1,*], Zully Matamoros-Veloza [2], Jorge López-Cuevas [1], Roberto Pérez-Garibay [1] and Kazumichi Yanagisawa [3]

[1] Centre for Research and Advanced Studies of the National Polytechnic Institute, Saltillo Campus, Ramos Arizpe 25900, Mexico; jose.quinones@cinvestav.edu.mx (J.R.Q.-G.); jorge.lopez@cinvestav.edu.mx (J.L.-C.); roberto.perez@cinvestav.edu.mx (R.P.-G.)
[2] Tecnológico Nacional de México/(I.T. Saltillo), Technological Institute of Saltillo, Graduate Division, Saltillo 25280, Mexico; zully.mv2@saltillo.tecnm.mx
[3] Research Laboratory of Hydrothermal Chemistry, Faculty of Science, Kochi University, Kochi 780-8073, Japan; yanagi@kochi-u.ac.jp
* Correspondence: jcarlos.rendon@cinvestav.edu.mx; Tel.: +52-(844)-438-9600

Abstract: In recent decades, perovskite-type compounds ($ABB'O_3$) have been exhaustively studied due to their unique ferroelectric properties. In this work, a systematic study aiming to prepare fine particles in the binary system $SrZrO_3$–$SrTiO_3$ was conducted under hydrothermal conditions in a KOH (5 M) solution at 200 °C for 4 h under a constant stirring speed of 130 rpm. The precursors employed were $SrSO_4$ powder (<38 μm size) and coprecipitated hydrous gels of $Zr(OH)_4 \bullet 9.64\ H_2O$ (Zr-gel) and $Ti(OH)_4 \bullet 4.5H_2O$ (Ti-gel), which were mixed according to the stoichiometry of the $SrZr_{1-x}Ti_xO_3$ in the compositional range of $0.0 > x > 100.0$ mol% Ti^{4+}. The XRD results revealed the formation of two crystalline phases rich in Zr^{4+}, an orthorhombic structured $SrZr_{0.93}Ti_{0.07}O_3$ and a cubic structured $SrZr_{0.75}Ti_{0.25}O_3$ within the compositional range of 0.1–0.5 mol of Ti^{4+}. A cubic perovskite structured solid solution, $SrTi_{1-x}Zr_xO_3$, was preferentially formed within the compositional range of $0.5 > x > 0.1$ mol% Ti^{4+}. The $SrZrO_3$ and $SrZr_{0.93}Ti_{0.07}O_3$-rich phases had particle sizes averaging 3 μm with a cubic morphology. However, a remarkable reduction in the particle size occurred on solid solutions prepared with hydrous Ti-gel over contents of 15 mol% Ti^{4+} in the reaction media, resulting in the formation of nanosized particle agglomerates with a cuboidal shape self-assembled via a 3D hierarchical architecture, and the sizes of these particles varied in the range between 141.0 and 175.5 nm. The limited coarsening of the particles is discussed based on the Zr-gel and Ti-gel dehydration capability differences that occurred under hydrothermal processing.

Keywords: hydrothermal synthesis; gel dehydration; $SrZrO_3$–$SrTiO_3$; solid solution; crystallization; cubic structure; orthorhombic structure

Citation: Quiñones-Gurrola, J.R.; Rendón-Angeles, J.C.; Matamoros-Veloza, Z.; López-Cuevas, J.; Pérez-Garibay, R.; Yanagisawa, K. Facile Preparation of $SrZr_{1-x}Ti_xO_3$ and $SrTi_{1-x}Zr_xO_3$ Fine Particles Assisted by Dehydration of Zr^{4+} and Ti^{4+} Gels under Hydrothermal Conditions. *Nanomaterials* **2023**, *13*, 2195. https://doi.org/10.3390/nano13152195

Academic Editor: Meiwen Cao

Received: 6 July 2023
Revised: 20 July 2023
Accepted: 21 July 2023
Published: 28 July 2023

1. Introduction

Perovskite structured oxide compounds with an ABX_3 chemical formula have been investigated because of their broad practical applications and academic research interest. These are associated with their unique properties due to their relatively simple crystalline structure [1–3]. The cubic structural perovskite framework (*Pm3m*) comprises two linked coordination polyhedral networks, the BX_6 octahedra and AX_{12} cuboctahedra. Bonding between the BX_6 octahedra polyhedron and sites incorporating A cations occurs via corner sharing. Interestingly, the BX_6 octahedra exhibit volumetric variations, namely expansion, contraction, and tilt, to maintain non-ideal ionic size substitutions. Likewise, the local electronic instabilities can distort the octahedra or cause a slight cation shift from their unit cell structural positions. Perovskite structured materials allow ionic partial substitutions

and the formation of vacancies on their three structural atomic locations [3]. Therefore, this structure is remarkably flexible to locate various periodic table elements at both A and B sites, resulting in a wide range of properties. The most important are ferroelectricity, ferromagnetism and colossal magnetoresistance, piezoelectricity and multiferroicity [3,4]. B-site cation doping has been one of the major research subjects in developing new advanced perovskite materials; this site controls and tunes some of the most technologically attractive properties, such as electrical conductivity and magnetic order [5–8]. The tuning of these properties results from combining at least two elements, which maintain the cation structural ordering allowing to development of advanced new materials [3].

The perovskite binary system $SrTiO_3$–$SrZrO_3$, which has technological importance due to its dielectric properties [9], has attracted significant research interest for solid solution preparation via the B-site cation isomorphous substitution. The end members of this system, cubic $SrTiO_3$ (space group *Pm3m*) and orthorhombic $SrZrO_3$ (*Pbnm*) do not possess ferroelectric properties. However, the partial substitution of Zr^{4+} up to 5 mol% provided a remarkable increase in the dielectric breakdown strength (14.4 kV/mm), simultaneously maintaining the high dielectric constant (330) characteristic of $SrTiO_3$, which makes these materials suitable for technical applications as high voltage capacitors [9,10]. Likewise, the $SrTi_{1-x}Zr_xO_3$ microstructure mobility causes octahedral structural transitions, which consequently cause electronic changes, resulting in a peculiar ferroelastic switching behavior; this feature is essential for magnetic applications [11–13]. Similarly, the superlattice crystalline structures formed in $SrTi_{1-x}Zr_xO_3$ layered compounds achieve special BX_6 ordering that induces a two-dimensional tension mechanism, causing, at low temperatures, a ferroelectric Ti-rich solid solution (SS) Ti [13]. To some extent, the structural distortion somewhat might promote the proton motion [14]. Another potential technical application determined for ultrafine powders of $SrTi_{1-x}Zr_xO_3$ solid solutions SS include photoluminescence emission [15] and organic dye photocatalysts [16].

Various systematic studies have been focused on the SS-$SrTi_{1-x}Zr_xO_3$ preparation in the $0.0 \geq x \leq 0.5$ mol% Zr^{4+} compositional range by the conventional high-temperature solid-state reaction [1,4,6,8,10,11]. The powders were produced by mixing high-purity $SrCO_3$, TiO_2 and ZrO_2 powders, which were appropriately mixed in stoichiometric molar ratios to form a slurry with acetone. The powder mixtures were homogenized by vigorous grinding and then pressed. The pellets underwent calcination in a three-step heat treatment between 800 and 1400 °C for 24 to 96 h reaction intervals. However, the SS-$SrTi_{1-x}Zr_xO_3$ monodisperse nanoparticle formation was not feasible under the conventional ceramic processing route.

On the contrary, chemical solution processing techniques, namely sol-spray pyrolysis [5], low-temperature coprecipitation [7], and sol–gel [16], successfully achieved the preparation of $SrTi_{1-x}Zr_xO_3$ nanoparticles with accurate stoichiometric compositions, controlled morphology and monomodal particle size distributions that boosted their physical and chemical properties [5,7,16]. Furthermore, the hydrothermal technique has successfully prepared $SrTiO_3$ mesocrystals with nanoparticle sizes and controlled cubic morphology [17–19]. The systematic studies focused on the chemical reaction of a slurry media containing TiO_2 particles and $Sr(OH)_2$ hydrolyzed in a highly alkaline NaOH media (5–10 M) under hydrothermal conditions, resulting in the formation of the $SrTiO_3$ nanoparticles via two mechanisms, namely the topochemical transformation of the TiO_2 particles [17,18] and the conventional dissolution–precipitation process [19]. A different approach involving the employment of a mineral source as Sr^{2+} ($SrSO_4$) precursor and hydrous Ti-gel ($Ti(OH)_4 \bullet 4.5H_2O$) was also evaluated under hydrothermal conditions at 250 °C for 24 h in a KOH solution 5 M [20]. Under these conditions, the dissolution of the $SrSO_4$, coupled with the Ti-gel dehydration, established the chemical equilibrium for triggering the crystallization of monodispersed fine cubic-shaped $SrTiO_3$ crystals, which exhibited a monomodal particle size distribution. This process can reduce global production costs compared to the low-temperature chemical solution processing and the conventional hydrothermal technique, which uses pure Sr^{2+} chemical reagents produced from the celestite mineral.

A literature review suggests that further efforts must be made to investigate the feasibility of producing $SrZr_{1-x}Ti_xO_3$ or $SrTi_{1-x}Zr_xO_3$ solid solution via hydrothermal alkaline processing. Hence, this work systematically investigated the preparation of particles with different chemical compositions in the binary $SrZrO_3$-$SrTiO_3$ system in alkaline media (5 M KOH). The experiments were conducted at a standard temperature (200 °C), which is relatively low for rapidly dissolving the $SrSO_4$ particles, and seemingly vertical agitation might provide an adequate dispersion of the mineral particles and precursor gels in the alkaline solvent solution during the treatment. Particular emphasis was on determining the effect of the precursor gels (Zr-gel and Ti-gel) dehydration capability on the particle crystallization of both $SrZr_{1-x}Ti_xO_3$ and $SrTi_{1-x}Zr_xO_3$ (SS). A detailed analysis was made to determine the stability of the tetragonal structure in the compositional $2.5 \geq x \leq 50.0$ mol% of Ti^{4+} for the $SrZr_{1-x}Ti_xO_3$ samples. The nanoparticle size and morphological differences were correlated with the dehydration capability of the gels.

2. Materials and Methods

2.1. Materials and Preparation of Zr^{4+} and Ti^{4+} Precursor Gels

Reagent-grade zirconium IV ($ZrCl_4$) and titanium IV ($TiCl_4$) chlorides (Wako, Japan, 99.0% purity) were used for preparing the precursor gels. Initially, the transition metal precursor solutions were produced with a concentration of 0.43 M for $ZrCl_4$ and $TiCl_4$ with deionized water, following the procedure described elsewhere [20,21], respectively. A 500 mL liquor aliquot of each solution was poured into a glass beaker, and then the gels were precipitated by adding a volume of 150 mL of 5 M NaOH solution. Each gel was separated from the residual mother liquor by centrifugation. The thermogravimetry analysis determined the total weight loss of each gel, indicating that the chemical composition of the hydrous gels corresponds to $Zr(OH)_4 \bullet 9.64H_2O$ and $Ti(OH)_4 \bullet 4.5H_2O$, respectively. The $SrSO_4$ mineral (Celestite) crystals were previously grounded and pulverized to a particle size < 38 μm. The wet chemical analysis of the highly pure crystalline $SrSO_4$ (1 g) revealed that the mineral is constituted by 46.61 wt% Sr, 1.33 wt% Ba, and 52.05 wt% SO_4^{2-}, which correspond to 96.8 wt% $SrSO_4$ and 2.25 wt% $BaSO_4$, plus the following minor compounds were CaO (0.73 wt%), Fe_2O_3 (0.19 wt%), MnO (0.02 wt%) and Al_2O_3 (0.007 wt%). The alkaline reagent-grade chemical employed was KOH (Wako, Japan, 99.0% purity).

2.2. Hydrothermal Treatments

Experiments aimed to determine the feasibility of producing stable $SrZr_{1-x}Ti_xO_3$ and $SrTi_{1-x}Zr_xO_3$ and to elucidate the solid solution (SS) crystalline structural and microstructural features, which might vary due to transition metal gel dehydration process that occurs under alkaline stirring hydrothermal conditions. Other experimental parameters study, such as the reaction time and temperature, were avoided in the present study. Therefore, the synthesis of the solid solutions in the binary $SrZrO_3$–$SrTiO_3$ system proceeded in the entire compositional range. However, a particular emphasis took place on the molar content of $1.0 \geq x \leq 0.5$ of Zr^{4+} to investigate the tetragonal structure stability; this crystalline structure is predominant at temperatures lower than 400 °C [5,10]; thus, the compositions studied varied in a molar span of 2.5 mol% Zr^{4+}. A $SrSO_4$ powder sample (4.8 ± 0.05 g) was placed at the bottom of a Teflon test tube-type chamber (500 mL volume), the amount of each gel was calculated according to the chemical formulas mentioned in Section 2.1, and the stoichiometric Zr:Ti molar ratio 1-x:x, was then added. All the treatments were conducted at a constant volume (95 mL) of the 5 M KOH solution selected as a solvent media. The stainless-steel autoclave was sealed, and the vertical propel rotation set was at 130 rpm during the heating and soaking stages (Figure 1). The autoclave was then heated at a constant speed of 5 °C/min up to the standard temperature of 200 °C, which has been proposed as optimum in preliminary research kinetics studies focused on synthesizing $SrTiO_3$ [20] and $SrZrO_3$ [21] under similar hydrothermal conditions. The treatments were conducted at this temperature for 4 h. After treatment, the reaction products were separated

from the remaining mother liquor and ultrasonically washed several times with hot water. Then, the powders were dried at 80 °C overnight.

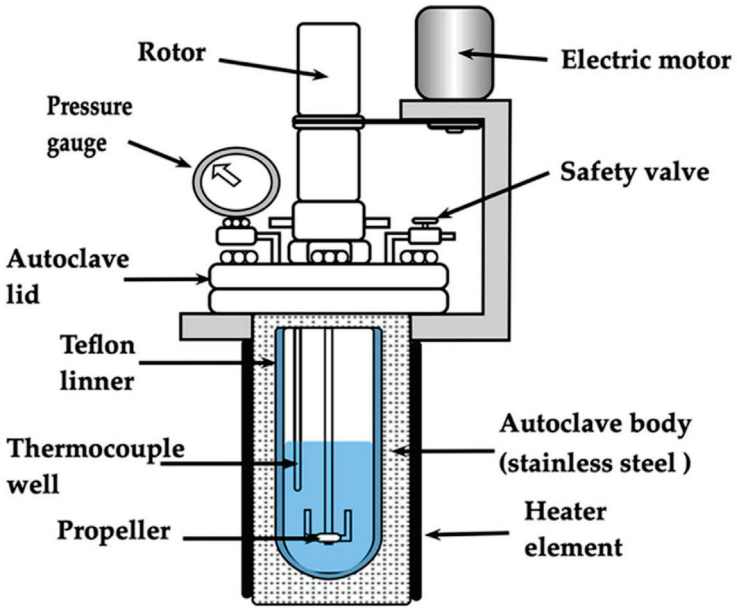

Figure 1. Scheme of the stainless-steel vessel accoupled with a vertical stirring propel and internal Teflon liner tube with a capacity of 500 mL.

2.3. Characterization

Powder X-ray diffraction (PXRD). The analyses were conducted in a Rigaku Ultima IV diffractometer operated at 40 kV and 20 mA, using Cu-Kα radiation (λ = 1.54056 Å). XRD analyses were collected in the 2θ range of 5–80° at a constant scanning speed of 20°/min with a 0.02° step. Rietveld refinement analyses were carried out on the PXRD patterns collected in the 2θ range of 15–130°, under standard conditions at a scanning speed of 0.01°/min and 0.002° step. The refinement calculations were performed using the TOPAS 4.2 software (Bruker AXS: Karlsruhe, Germany, 2009). The space group, and the atomic position (Wyckoff number and coordinates), correspond to the COD card No. 96-900-7150. All details associated with the Rietveld refinement analysis are in the Supplementary Supporting Information File (hereafter referred to as SSIF), Section S1 includes Tables S1 and S2 where the Wyckoff spatial coordinates are given.

Morphology and microstructural observation. The microstructural aspects of the produced particles were observed in a field emission scanning electron microscopy (JEOL JSM-7100F) equipped with a solid-state microprobe (EBSD, Bruker e-flash). Typical micrographs were observed with the microscope operated at 10 kV and a constant current of 69 μA. The particle size distribution was statistically determined from SEM images of 50 particles. Crystalline structural details of selected $SrZr_{1-x}Ti_xO_3$ particles were revealed using high-resolution transmission electron (HR-TEM, Philips Titan 300) operated at 200 kV.

Differential scanning calorimetry analysis (DSC). The DSC technique was applied to determine the thermal behavior of single Zr-gel and Ti-gel and some selected samples with varied Zr/Ti weight ratios. These analyses also revealed the differences in the dehydration behavior of the Zr/Ti raw gel mixtures. Simultaneously, the gel weight loss of selected samples was determined by thermal gravimetric analyses (TGA). These analyses were carried out using a Perkin Elmer Pyris Diamond TG/DSC apparatus in the temperature range from 30 to 1000 °C. The heating rate selected for the thermal evaluation was 10 °C/min; all the treatments were conducted using an air atmosphere.

3. Results

3.1. Thermal Stability of Gel Mixtures and Zr-Gel and Ti-Gel

Thermogravimetry and DSC analyses were conducted to evaluate the thermal stability and structural changes of single pasty Zr-gel, Ti-gel and some selected gels mixtures containing different Zr/Ti ratios. These analyses aimed to determine the total weight loss monitored in the air atmosphere within the 30–1000 °C temperature range. The change in the weight of the gels is portrayed in Figure 2a. In general, the gels selected exhibited a remarkable weight loss above 50 °C, without further weight variation above 150 °C. Interestingly, the Zr pure gel had the most significant weight loss of approximately 90.93 wt%; in comparison with that observed for the Ti pure (67.2 wt%) and Zr/Ti (75.5–80.0 wt%) gel samples. According to the total amount of water that Zr and Ti pure gels released during the heat treatment, their chemical formulas are $Zr(OH)_4 \bullet 9.64H_2O$ and $Ti(OH)_4 \bullet 4.5H_2O$, respectively.

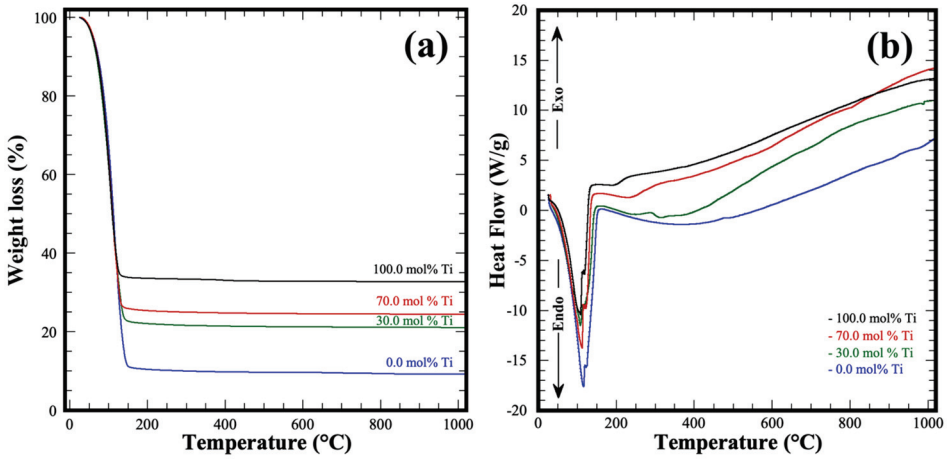

Figure 2. (**a**) Gels weight loss variation determined via TGA analyses, and (**b**) thermal behavior of the precursor Zr-Ti gels determined by DSC in air atmosphere up to 1000 °C.

Furthermore, the thermal behavior of all the Zr-Ti gels observed in the DSC curves (Figure 2b) revealed an endothermic event in the temperature range from 45–150 °C. This event is irrespective of the pasty gel chemical composition; therefore, this peak correlates with the water molecules' ultimate dehydration process. Above 200 °C, only a regular baseline variation was observed on all samples rather than the expected crystallization events associated with the oxide formation on all the gels. Moreover, the differences in the dehydration degree determined might alter the bulk concentration of the alkaline fluid used during the hydrothermal treatments conducted under the standard hydrothermal conditions of 200 °C for 4 h under stirring. This agrees with the differences in the crystal growth of the $SrZrO_3$ particles hydrothermally synthesized using a pasty Zr-gel and a previously dried amorphous $Zr(OH)_4{}^0$ reported elsewhere [21].

3.2. Structural Aspects of the Hydrothermal Synthesis of $SrZr_{1-x}Ti_xO_3$ and $SrTi_{1-x}Zr_xO_3$ SS

Figure 3 shows the typical XRD patterns of selected powders produced under hydrothermal conditions at 200 °C for 4 h under constant stirring (130 rpm), varying the content of Ti^{4+} in the mixture. Generally, the single-step chemical reaction between the $SrSO_4$ and the pasty gels is enhanced under stirring conditions, triggering the formation of a fine white powder, as confirmed in all treatments by naked-eye observations. When the Zr-gel was solely used as a precursor of the tetravalent metal perovskite, the peaks in the XRD pattern were indexed by those of the $SrZrO_3$ perovskite with orthorhombic structure (ICDD 70-0283 space group *Pbnm*, Figure 3a). On the contrary, at Ti^{4+} contents over 10.0 mol%, new peaks located at 2θ angles of 32.25°, 39.7°, 45.8° and 56.9° were determined in the PXRD pattern, as seen in Figure 3a. To determine the formation pathway of

the new compound, experiments were conducted with a Ti^{4+} compositional span variation of 2.5 mol% Ti^{4+}. The new phase was formed under alkaline hydrothermal conditions in the Ti^{4+} compositional range between 7.5 and 47.5 mol% Ti^{4+}, as depicted by the signal that appeared at 32.25° 2θ angle (see Figure 3b). It deserves emphasizing that this peak exhibited a gradual shift toward higher 2θ angles coupled with peak intensity increment. These crystalline structural features are likely due to the Ti^{4+} gradual incorporation into the crystalline structure, and its bulk content produced over 7.5 mol% Ti^{4+} contents in the reaction media. Simultaneously, the central peak corresponding to the orthorhombic structured $SrZrO_3$:Ti^{4+} (hereafter referred to as SS1) did not exhibit further compositional variations because it remained at a mean 2θ angle of 31.09°. Therefore, these results suggest that the chemical composition of this solid solution is $SrZr_{0.925}Ti_{0.075}O_3$. However, the content of this stable phase was proportionally reduced by increasing the Ti^{4+} amount, as indicated by the progressive reduction in the orthorhombic phase peaks in the PXRD pattern (Figure 3a). Above 50.0 mol% Ti^{4+} peaks corresponding to a new secondary phase (hereafter referred to as SS2) were obtained. Based on these structural results, we infer that the crystalline structure of the SS2 single-phase can be indexed with the cubic structured $SrTiO_3$ perovskite (space group *Pm3m*, ICDD card no. 40-1500) because it agrees with the peaks distribution of the $SrTiO_3$ single pattern. These results depict that the cubic perovskite SS2 crystalline phase is chemically stable under hydrothermal conditions in the compositional range of 7.5–100.0 mol% Ti^{4+}. In addition, the powder crystallized without contaminant by-products, namely $SrCO_3$, which is predominantly formed due to its low solubility in alkaline solutions [22]. Furthermore, a steady-state chemical reaction involving the solute saturation of the hydrothermal media is likely to proceed and trigger the simultaneous crystallization of both crystalline compounds under fluid stirring [23].

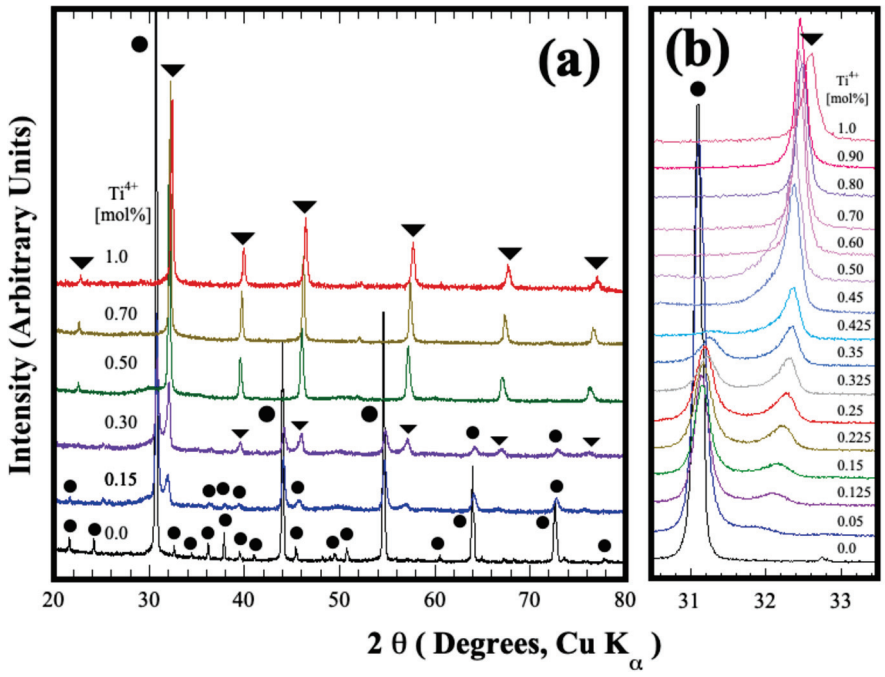

Figure 3. (**a**,**b**) X-ray diffraction patterns of the products obtained hydrothermally by treating celestite powders with various molar contents of pasty $Zr(OH)_4 \bullet 9.64H_2O$ and $Ti(OH)_4 \bullet 4.5H_2O$ gels, with a solvent (5 M KOH) volume filling ratio of 20% at 200 °C for 4 h. Perovskite single phases: (●) orthorhombic $SrZrO_3$, and (▼) cubic $SrTiO_3$.

The compositional variation suggested by the PXRD analyses was observed in the SS2 phase. Stoichiometric computation was carried out to determine the Ti^{4+} content incorporated in the cubic perovskite secondary SS2′ phase (new phase produced in the Ti^{4+} range of 7.5–47.5 mol%) and into the orthorhombic SS1; this procedure considered the nominal

Ti^{4+} molar content added as a raw material. Likewise, the fraction of each solid solution that constitutes the ultimate powder produced was calculated by the expression [(1-x)SS1 + xSS2′] = 1, which depicts the quantitative variation in the phase content revealed by the diffraction patterns of Figure 3b. The typical Rietveld refined plots that correlate the quantitative stoichiometric computation abovementioned are shown in Figure 4. Interestingly, a minimal variation in the residual difference was also revealed in those samples exhibiting the formation of SS1 and SS2 perovskite phases. These results show that the calculated Zr^{4+}:Ti^{4+} stoichiometric contents in the orthorhombic and cubic phases with *Pbnm* and *Pm3m* space groups highly fitted the atomic occupation in the Rietveld refinement algorithm. The algorithm ultimately computed the fraction content of each perovskite phase in the powder sample prepared with nominal molar Zr^{4+}:Ti^{4+} ratios of (a) 92.5:7.5 (b) 75.0:25.0 and (c) 62.5:37.5, as it can be seen in Figure 4. Additional results are shown in the refinement plots in Figure S1 and the unit cell lattices in Figure S2 in the SSIF. Furthermore, the structural crystalline refinement approach also considered other fitting parameters such as background, thermal isotropy, lattice parameters, scale factor, profile half-width, crystallite size and local strain; the details regarding the atomic Wyckoff elemental spatial distribution are given in the SSIF, which includes Table S3 (see the SSIF) that summarizes the results of the crystalline structural refinement. This approach was adequate to fit the structural differences of the reaction products obtained after the hydrothermal reaction, which is depicted by both the low mean values of the goodness-of-fit factor (GOF, mean χ^2 value of 3.48%) and R_{wp} = 3.26. It deserves to emphasize that the analyses confirmed that the orthorhombic and cubic crystalline perovskite particles were simultaneously formed under hydrothermal conditions employing the highly soluble $SrSO_4$ powder and the mixture of Zr^{4+} and Ti^{4+} gels.

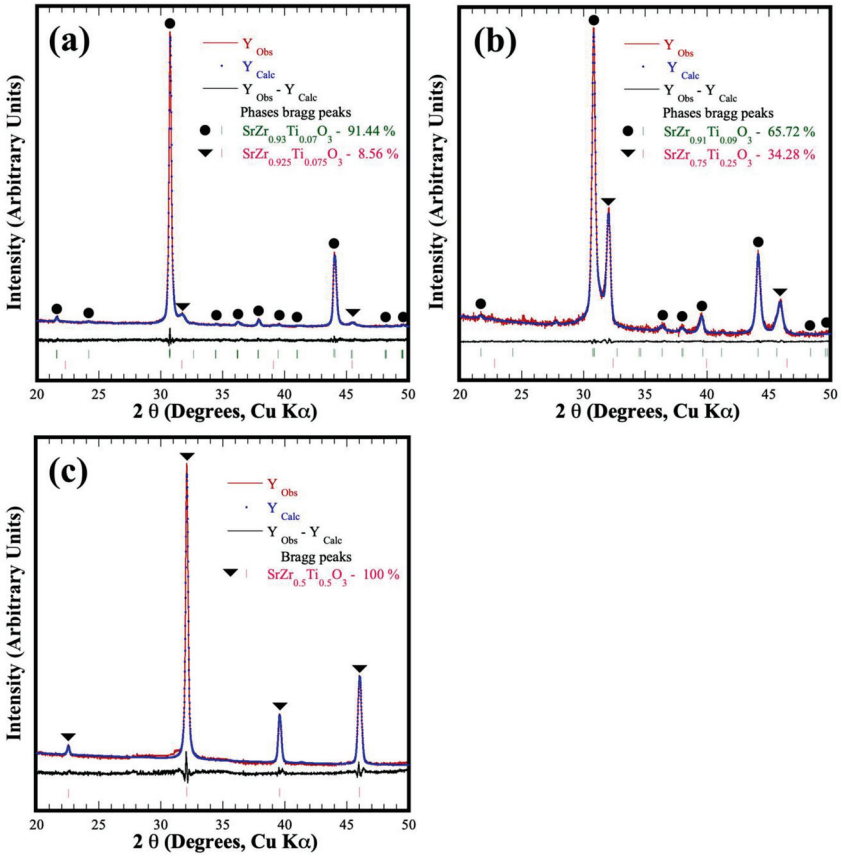

Figure 4. Rietveld refinement plots of products obtained hydrothermally using celestite powders mixed with different metal precursor gels in molar ratios of (**a**) 92.5:7.5, (**b**) 75.0:25.0 and (**c**) 62.5:37.5 mol% Zr^{4+}:Ti^{4+}, with a solvent (5 M KOH) volume filling ratio of 20% at 200 °C for 4 h. Perovskite single phases (●) orthorhombic and (▼) cubic.

The variation in the content of both orthorhombic and cubic structured solid solutions, which were hydrothermally produced within the whole compositional range of the binary system $SrZrO_3$-$SrTiO_3$; using a KOH 5 M solution, is portrayed in Figure 5a. Generally, the formation of the new cubic perovskite phase (SS2′) occurred in the compositional range between 7.5 mol% and 47.5 mol% Ti^{4+}. The quantitative analyses conducted on the nominal stoichiometric tetravalent metal compositions depict that the new cubic SS2′ phase reach in Zr^{4+} ($SrZr_{1-x}Ti_xO_3$) exhibited a marked increase in its content when the Ti^{4+} concentration increased progressively in the solvent fluid. Interestingly, the variation in the bulk content of this phase likely resembles a typical sigmoidal kinetic behavior. On the contrary, the residual content of the hydrothermally crystallized orthorhombic phase (SS1) powder proportionally decreased following a reverse sigmoidal behavior. The simultaneous crystallization of both perovskite phases is likely triggered under hydrothermal conditions because the continuous gel dehydration promotes a cooperative reaction steady state; thereby, a constant increase in the Ti^{4+} mass gradient provoked a rise in the cubic SS2′ single phase amount. This inference is supported by the fact that the Zr^{4+} atomic ratio in the SS2′ cubic phase exhibited a linear decrease, proportional to the rise of the Ti^{4+} content, as seen in Figure 5b.

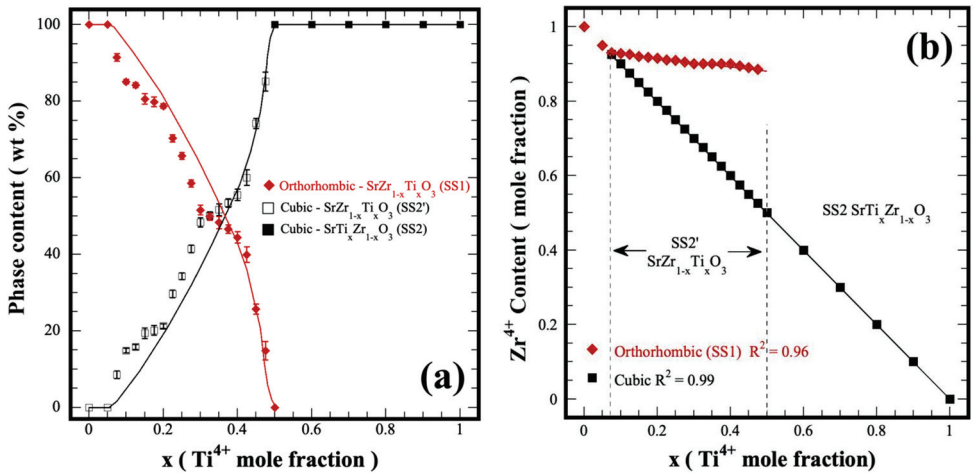

Figure 5. (**a**) Content variation in the hydrothermally prepared solid solutions SS1, SS2′ and SS2, and (**b**) change in the Zr^{4+} molar fraction in both the orthorhombic (SS1) and cubic (SS2′) in the compositional range of 7.5–47.5 mol% Ti^{4+} of the binary system $SrZrO_3$-$SrTiO_3$.

Furthermore, the orthorhombic SS1 phase had 4.0 mol % in Zr^{4+} reduction within the compositional range where both crystalline phases coexist in the binary system $SrZrO_3$-$SrTiO_3$. According to these compositional results, three chemical reaction equilibria drive the crystallization of chemically stable perovskite SS in the hydrothermal system studied. These are included in the Supplementary Supporting Information File. The chemical formulas of all the SS1, SS2′ and SS2 hydrothermally prepared are summarized in Table S3 in the SSI file, and the contents of the phases SS1 and SS2′ are also included.

Additionally, details on the crystalline unit cell, lattice parameters and volume cell, corresponding to the perovskite solid solutions, which were produced under hydrothermal conditions in a 5 M KOH solution at 200 °C for 4 h with a constant stirring speed of 130 rpm, are portrayed in the graphs in Figure 6. Generally, the lattice constants corresponding to the end members of the perovskite binary system $SrZrO_3$-$SrTiO_3$ are slightly higher in comparison with the values reported in Table S3 (see SSIF) for the same compounds. Meanwhile, a marked continuous decrease in "a_0", "b_0", and "c_0" parameters was determined in the orthorhombic solid solution (SS1, ●), with *Pbnm* space group, by increasing the Ti^{4+} content uptake in the resulting crystalline particles, as seen in Figure 6a. Likewise, the "a_0" lattice parameter corresponding to the new cubic SS2′ and SS2 (■) constituents (space group *Pm3m*) exhibited a linear decrease within the Ti^{4+} compositional variation,

which occurred within the ranges of 7.5 ≥ x ≤ 50.0 mol% Ti^{4+} and 50.0 ≥ x ≤ 100.0 mol% Ti^{4+}, as seen in Figure 6a. In both cases, the variation determined for lattice parameter values of either orthorhombic or cubic perovskite structures agree with the systematic peak displacement determined in the X-ray results shown in Figure 3. Interestingly, all the lattice constants calculated exhibited a linear variation, which is depicted by the mean data dispersion coefficient R^2 that varied between 0.912 and 0.987. This behavior indicates a linear dependence of the structural parameters occurred by incorporating Ti^{4+} content in the orthorhombic and cubic structured perovskite compound produced under hydrothermal conditions. Furthermore, the linear variation in the lattice parameters agrees with Vegard's law, despite two simultaneous perovskite-related compounds crystallizing within the compositional range of 7.5 ≥ x ≤ 50.0 Ti^{4+} mol%. Therefore, in the context of the chemical composition, the processing approach investigated is devoted to determining the chemical reaction pathway related to the formation of stable perovskite solid solution compounds in the binary system $SrZrO_3$-$SrTiO_3$; the results suggest that a steady-state single-step reaction is triggered under stirring hydrothermal condition, preferentially crystallize two solid solutions at the B site of the perovskite $SrZr_{1-x}TiO_3$ with orthorhombic and cubic structures. The reaction pathway is likely controlled by the tetravalent metal gel dehydration process inherent to the proposed system.

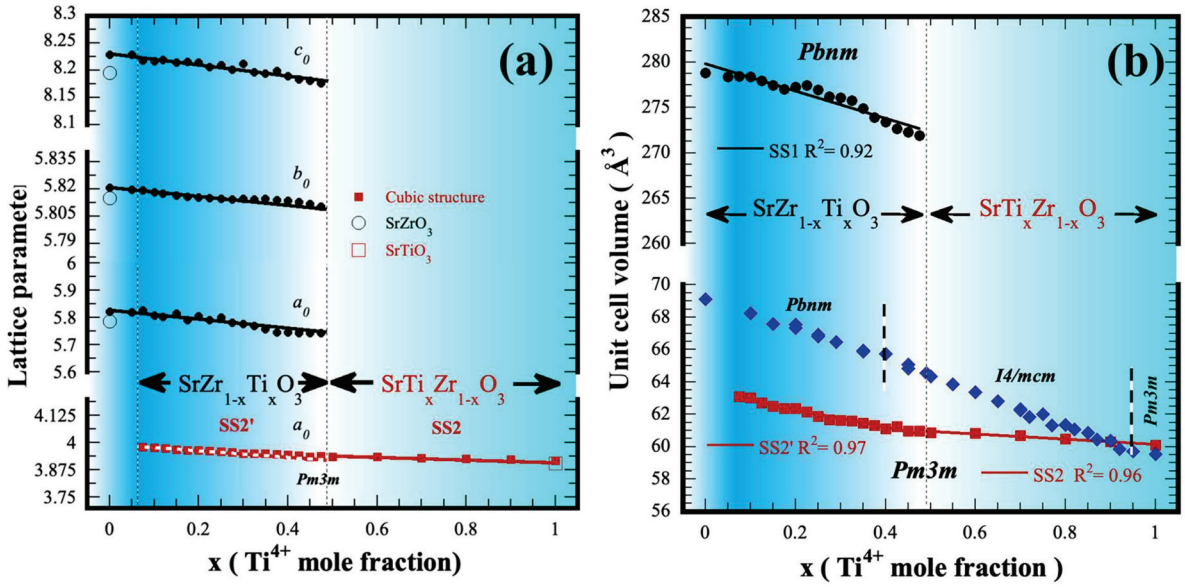

Figure 6. Variation in the crystalline structural parameters for the orthorhombic (SS1) and cubic (SS2′ and SS2) perovskite structured solid solutions prepared under hydrothermal conditions at 200 °C for 4 h with stirring at 130 rpm. (**a**) Unit cell lattice parameters and (**b**) unit cell volume. ♦ Unit cell values of $SrZr_{1-x}Ti_xO_3$ and $SrTi_{1-x}Zr_xO_3$ solid solutions produced at a high temperature within the entire compositional range of the binary system $SrZrO_3$–$SrTiO_3$; data taken from [8].

In addition, a similar trend was observed for the lattice constants variation for the unit cell volume of the perovskite solid solutions. These values are portrayed in the plot shown in Figure 6b, and this plot also includes the unit cell volume values calculated for the $SrTi_xZr_{1-x}O_3$ (solid ♦ symbol) solid solutions prepared at 1400 °C for 96 h [8]; these data were included for comparison purposes. Some data are likely similar to those determined in our case, namely at Ti^{4+} contents above ≤90.0 mol%. The authors demonstrate that the formation of stable solid solution preferentially occurs within the entire compositional range of the system $SrZrO_3$-$SrTiO_3$, as depicted by the data plotted in Figure 6b. Exhaustive crystalline structural analyses conducted by neutron and synchrotron diffraction confirmed the dependence of the SS´s composition with the crystalline structural transformations, which leads to obtaining orthorhombic, tetragonal and cubic structures stable at specific Ti^{4+} contents incorporated into the SS $SrTi_xZr_{1-x}O_3$. Superlattice reflections revealed near

2θ = 33 and 41° (021 and 122/212 Miller indexes) corresponding to the orthorhombic structure were detected up to 40.0 mol% Ti^{4+}; above this content, tetragonal structure predominates as sole phase produced at high temperature, the new reflection at 2θ ≈ 40° (121) confirmed the formation of $SrTi_xZr_{1-x}O_3$ SS that belongs to this structure, which predominates at the highest Ti^{4+} content of 90.0 mol% at low temperature [8].

Interestingly, the PXRD analyses conducted on the hydrothermally prepared specimens with Ti^{4+} contents between 7.5 mol% and 90.0 mol% did not reveal the superlattice peaks associated with the perovskite tetragonal structure, despite the observation of a similar variation trend on the unit cell volume of both reaction products with orthorhombic and cubic structures prepared here, compared with the continuous solid solutions obtained via solid-state reaction at high temperature [8]. We infer from these results that the Ti-gel dehydration yield plays an essential role in achieving a steady-state chemical reaction, which enhances a specific solute supersaturation stage that causes the simultaneous crystallization of both phases. This process proceeds faster than the solid-state reaction producing a broad compositional series of solid solutions in the system $SrZrO_3$–$SrTiO_3$ [8].

On the other hand, according to the crystalline structural results calculated by Rietveld refinement given in Table S3 of the SSIF, the minor structural differences revealed on the unit cell parameters in both perovskite compounds (orthorhombic and cubic) are caused by the variation in the Sr-O, Ti-O and Zr-O bond lengths. A systematic increase in the Ti-O bond length proportionally occurred by decreasing the Ti^{4+} content incorporated into the octahedral BO_6 site in the cubic structured SS2, in the compositional range of $7.5 \leq x \leq 90$ mol% Ti^{4+}. Similarly, the Sr-O bond length is considerably affected, reaching a maximum value of 2.822 Å, which is remarkably more extensive than that for the cubic structured $SrTiO_3$ single phase (2.769 (1) Å, as seen in Table S3). From these results, we surmise that this structural phenomenon maintains the cubic structured solid solution thermodynamically stable at low contents of Ti^{4+} below 50.0 mol%. This inference is supported by the fact that under solid-state reaction conditions, a series of intermediate tetragonal structured solid solutions were successfully formed in a shorter range of Ti^{4+} ($40.0 \leq x \leq 90.0$ mol% Ti^{4+}). It deserves to emphasize that the tetragonal structure remains stable because it corresponds to the primitive cell of the orthorhombic structured perovskite. Therefore, this structural transformation is favored by a slight structural tilt in the BO_6 octahedra caused by the Ti^{4+} partial incorporation. This structural transformation is markedly provoked under solid-state reaction conditions at high temperatures [8]. Another factor that might cause the predominant formation of the SS2 solutions with cubic structure and their structural variations is associated with the processing conditions (reaction temperature and stirring speed), as suggested elsewhere [21]. This inference is likely supported by the marked differences determined for the lattice strain caused in the unit cell by partially incorporating Ti^{4+} in the cubic SS2′ SS. Large lattice strain values were calculated from the Rietveld refinements for the SS2′ SS prepared with Ti^{4+} contents between 7.5 and 50 mol% and are shown in Table S3 of the Supplementary Supporting Information File.

3.3. Particle Morphology Variation for the Hydrothermally Synthesized $SrZr_{1-x}Ti_xO_3$ and $SrTi_{1-x}Zr_xO_3$ (SS)

Recently, the morphological habit features for $SrZrO_3$ particles were elucidated; the hydrothermal treatments conducted without stirring in an alkaline media (5 M KOH) using the same reaction precursors resulted in the crystallization of micron-sized (averaging 10 μm) $SrZrO_3$ particles with cuboidal morphology [21]. On the contrary, our results depicted that continuous stirring (130 rpm) of the hydrothermal media remarkably improved the size reduction in the cuboidal-like $SrZrO_3$ particles, which were produced free of reaction by-products, namely $SrCO_3$, at 200 °C for 4 h. The monodispersed $SrZrO_3$ particles had a unimodal particle size distribution with an average size of 3.8 μm, as seen in the inlet graph of Figure 7a. Under these conditions, the continuous agitation caused a homogeneous distribution of solute dissolved in the alkaline solvent.

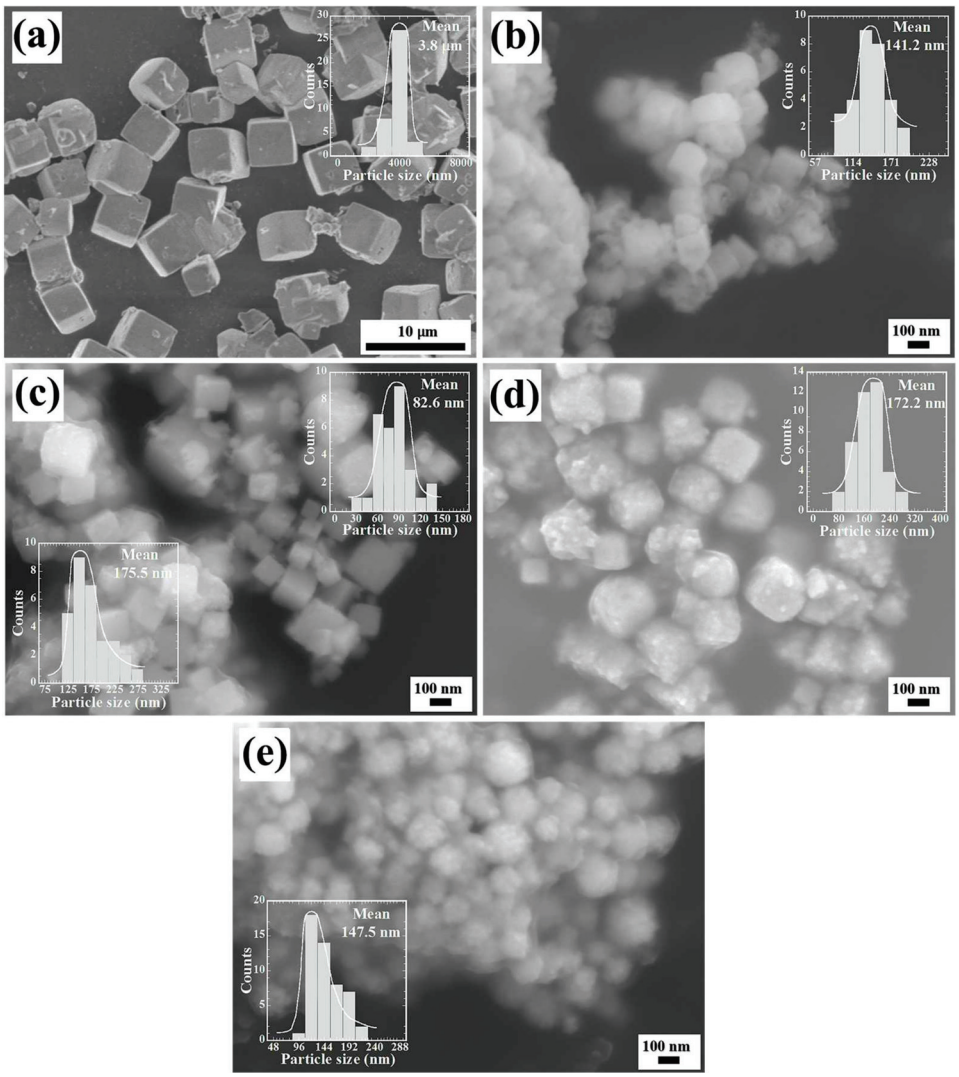

Figure 7. FE-SEM micrographs of the particles of the $SrZr_{1-x}Ti_xO_3$ and $SrTi_{1-x}Zr_xO_3$ solid solutions, obtained under dynamic hydrothermal conditions at 200 °C in a reaction medium of 5 M KOH for a reaction time of 4 h, using $SrSO_4$ and different ratios of Zr and Ti gels ($Zr(OH)_4 \bullet 9.64H_2O$, $Ti(OH)_4 \bullet 4.5H_2O$). (**a**) $SrZrO_3$, (**b**) 5.0 mol% Ti^{4+}, (**c**) 30.0 mol% Ti^{4+}, (**d**) 50.0 mol% Ti and (**e**) $SrTiO_3$.

On the contrary, a marked particle reduction occurred on the perovskite particles produced when the Ti^{4+} pasty gel was stoichiometrically introduced into the reaction system. Above Ti^{4+} contents of 5.0 mol%, the single phase $SrZr_{0.95}Ti_{0.05}O_3$ powders exhibited a mean particle size of 141.2 nm. The morphology resembling cuboidal-shaped particles forming some irregularly shaped agglomerates, Figure 7b. Furthermore, the formation of a noticeable number of fine meso-crystals (average size 82.6 nm) with a pseudocuboidal shape were formed together with a large amount of cubic-like shaped large particles having an average size of 175.5 nm, Figure 7c. It deserves to emphasize that these particles were formed using the content of 30 mol% Ti^{4+}, and the FE-SEM observation agrees with the PXRD results which revealed the coexistence of two $SrZr_{1-x}Ti_xO_3$ solutions with different Ti^{4+} content (Figure 3a). Likewise, the difference on the $Zr_{(L\alpha)}$ and $Ti_{(K\alpha)}$ peak intensities between the fine sized pseudocuboidal and large cubic-like particles confirmed the variation on the bulk chemical composition of the SS1 and SS2′ (as seen in Figure S3b in SSIF). Based on the Rietveld refinement analyses, their chemical formulas correspond to $SrZr_{0.9}Ti_{0.1}O_3$ and $SrZr_{0.70}Ti_{0.3}O_3$, respectively.

The pseudocubic meso-crystals were formed preferentially under hydrothermal stirring conditions with Ti^{4+} contents over 50 mol%. Generally, the new pseudocubic-shaped

meso-crystals were monodispersed and exhibited a unimodal size distribution with an average size of 172.2 nm. Furthermore, the single-phase $SrZr_{0.5}Ti_{0.5}O_3$ (SS2) cubic structured meso-crystals were likely formed from tiny particles self-assembled via a 3D hierarchical architecture; this assumption was inferred from the roughness surface of the meso-crystals shown in Figure 7d. Additionally, the FE-SEM observations conducted on the hydrothermally produced single phase $SrTiO_3$ meso-crystals (see Figure 7e), allowed to infer that these meso-crystals underwent a crystallization process analogous to that observed on samples containing low contents of Ti^{4+} up to 50.0 mol%. Thus, the meso-crystals solely prepared with $Ti(OH)_4{}^0$ gel had a slight reduction in their particle size, which averaged 147.5 nm. According to the experimental results, it can be inferred that the chemical compositional variation in the crystalline phases produced (SS1, SS2′ and SS2) and the particle coarsening differences are strongly dependent on the $Ti(OH)_4{}^0$ gel content variation in the hydrothermal treatments conducted under vigorous agitation. Details of the crystallization mechanism and its correlation with the precursor gels ($Zr(OH)_4{}^0$ and $Ti(OH)_4{}^0$) are discussed in the following Section 3.4.

3.4. Crystallization of $SrZr_{1-x}Ti_xO_3$ and $SrTi_{1-x}Zr_xO_3$ Meso-Crystals under Alkaline Hydrothermal Conditions

HR-TEM observations and compositional EDS analyses systematically investigated the crystallization process for both $SrZr_{1-x}Ti_xO_3$ and $SrTi_{1-x}Zr_xO_3$ promoted under hydrothermal treatment conducted with vigorous fluid agitation, according to the differences in morphology revealed by the FE-SEM analyses (Figure 7, and Figure S4 in the SSI), the growth process of the meso-crystals depends on the $Ti(OH)_4{}^0$ gel. This inference is supported by the remarkable reduction in either Zr^{4+} rich orthorhombic or cubic structured particles preferentially formed on the hydrothermal treatments conducted with compositional variations between 7.5 mol and 50.0 mol% of Ti^{4+}. Indeed, some of the present authors reported the differences in the chemical reactivity of metal transition hydroxide gels in the alkaline hydrothermal media [20,21]. It deserves to emphasize that the crystallization of cuboidal-shaped $SrZrO_3$ particles rapidly occurred using powders of $SrSO_4$ and $Zr(OH)_4{}^0$ dried gel in a 5 M KOH solution at 240 °C for 24 h, in comparison with an analogous reaction system employing a $Zr(OH)_4{}^0$ coprecipitated gel. The pasty hydroxide gel undergoes a dehydration process that markedly hinders the $SrSO_4$ dissolution; consequently, the bulk solute saturation proceeded slowly, triggering the nucleation of flower-shaped $SrZrO_3$ crystals. These crystals grew epitaxially along the [111] direction, resulting in large particles (mean size of 60 μm) for reaction intervals of 96 h [21].

By these results, we infer that the vigorous fluid agitation accelerated the $SrSO_4$ dissolution and the pasty $Zr(OH)_4{}^0$ gel dehydration, consequently triggering a rapid solute supersaturation within 4 h at a relatively low temperature of 200 °C, which rapidly provoked the crystallization of $SrZrO_3$ cuboidal-shaped monodispersed crystals. The structural details determined by the TEM diffraction spot image indicated that the hydrothermally prepared $SrZrO_3$ crystals are single crystals in nature (Figure 8a). In contrast, the HR-TEM images depicted their high crystallinity, as confirmed by the 2D finger lattice atomic distribution. Interestingly, the observation conducted at the crystal edge in areas exhibiting $SrZrO_3$ fine particles grown on the surface indicated that the micron-sized $SrZrO_3$ single crystals grew epitaxially along the direction of the plane (112) that, corresponding to the lattice plane distance of 2.895 Å of the orthorhombic structure (card ICDD 70-0283). However, the dissolution-crystallization mechanism provoked the SS1 and SS2 perovskite structured particles, irrespective of the $Ti(OH)_4{\bullet}4.5H_2O$ gel content. Likewise, the reactivity of the $Zr(OH)_4{}^0$ precursor gel seemingly proceeded faster when compared with the sample prepared solely with $Zr(OH)_4{\bullet}9.64H_2O$. The bulk alkalinity of the solvent fluid remains high when the Ti^{4+} concentration varies because the alkalinity reduction caused by the large water content released by the $Zr(OH)_4{\bullet}9.64H_2O$ dissolution is progressively hindered. Therefore, a specific reaction steady-state reaction is reached, triggering an accelerated solute supersaturation state that results in a fast crystallization of orthorhombic (SS1) and

cubic (SS2′), or solely the SS2 meso-crystals. Consequently, the primary crystal growth is hindered, as revealed by the HR-TEM micrographs of the single-phase $SrZr_{0.5}Ti_{0.5}O_3$ and $SrTiO_3$ fine particles shown in Figures 8b and 8c, respectively. These images also revealed features regarding the self-assembly process for primary anhedral nanosized crystals (20–45 nm), which proceeds along the {011} crystallographic planes of the cubic structure. We surmise that their surface facets favor the fine crystals assembly with (011) indexes, seemingly exhibiting low surface energy, allowing them to coalesce rapidly.

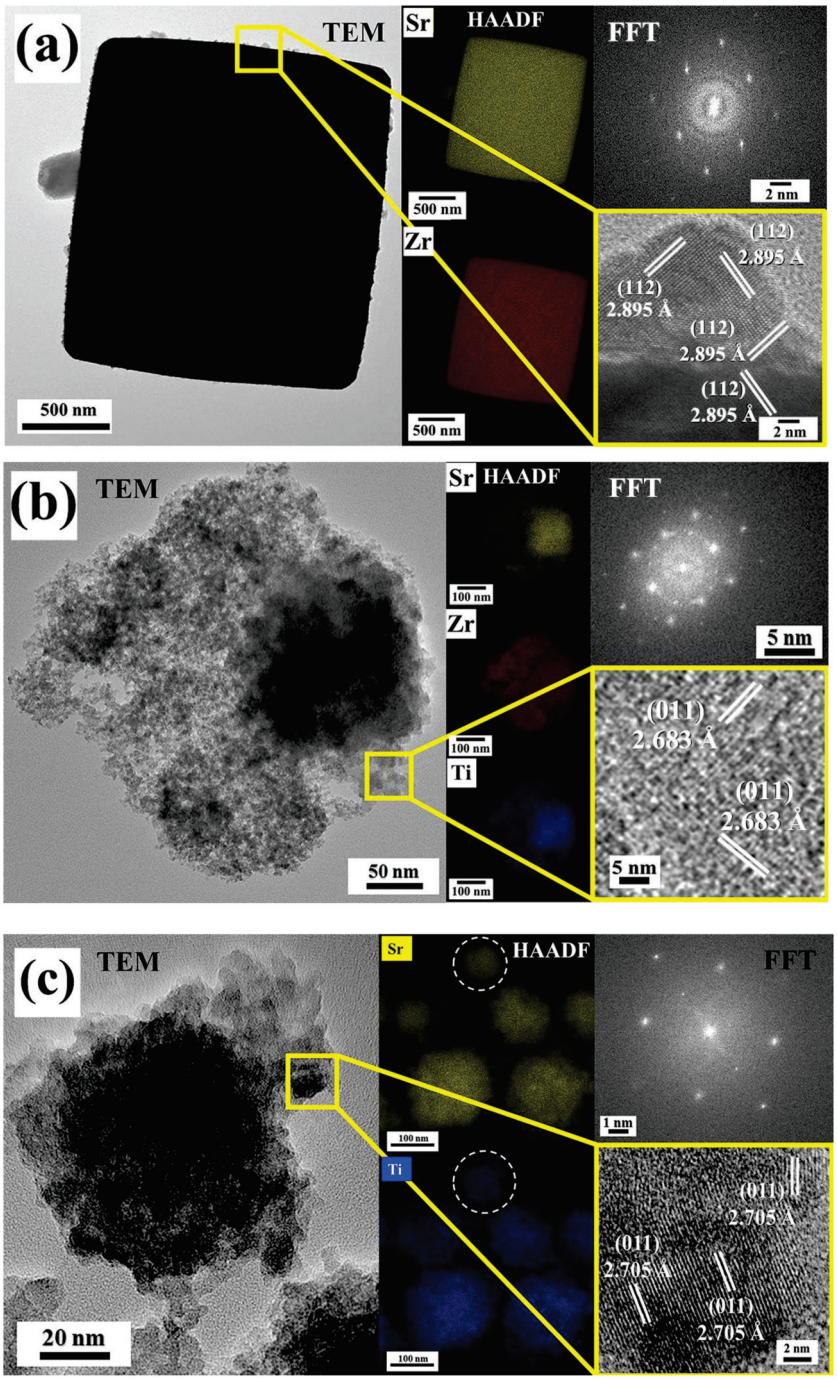

Figure 8. TEM micrographs of the SS $SrZr_{1-x}Ti_xO_3$ and $SrTi_{1-x}Zr_xO_3$ particles, obtained under hydrothermal conditions at 200 °C in a 5 M KOH for 4 h. The images correspond to single-phase samples of (**a**) $SrZrO_3$, (**b**) $SrZr_{0.5}Ti_{0.5}O_3$ and (**c**) $SrTiO_3$.

Consequently, the 3D hierarchical assembly produces highly crystalline agglomerates with pseudocubic morphology. This inference is supported by 2D finger lattice atomic distribution images and FFT diffraction patterns, as shown in Figure 8b,c. These results revealed that the single-phase cubic structured $SrZr_{0.5}Ti_{0.5}O_3$ and $SrTiO_3$ primary crystals grew along (011) planes and subsequently coalesced to form the nanosized (140–175 nm) meso-crystals agglomerates, which exhibited single crystal areas as revealed by the FFT diffraction patterns. Interestingly, the 3D assembly process irrespectively proceeded by varying the Ti^{4+} content in the 7.5–100 mol% range. According to these results, we inferred that under hydrothermal conditions, the continuous vigorous stirring of the alkaline fluid triggered a homogeneous dispersion of the raw precursors ($SrSO_4$ powder and the mixture of the pasty gel species), yielding a controlled dissolution-crystallization reaction carried out in a single step to synthesize various perovskite solid solution in the binary system $SrZrO_3$–$SrTiO_3$. Indeed, the proposed soft chemistry process is faster than that even conducted under highly alkaline 5 M NaOH fluid to produce $SrZrO_3$ without stirring under hydrothermal conditions [21].

4. Conclusions

A systematic investigation directed toward synthesizing powders with various Zr^{4+} and Ti^{4+} ions contents was satisfactorily conducted via a single-step reaction under hydrothermal conditions. The particles of $SrZr_{1-x}Ti_xO_3$ and $SrTi_{1-x}Zr_xO_3$ solid solutions rapidly crystallized at 200 °C for 4 h after the dissolution of low-grade $SrSO_4$ mineral coupled with the mixture of hydrous Zr^{4+} and Ti^{4+} gels. A dependence on the stability of either crystalline orthorhombic or cubic structured phases occurred on the processed particles against the content of Ti^{4+}. The synthesis of the solid solutions was boosted by the vigorous stirring of the alkaline 5 M KOH media, which triggered a massive dissolution–crystallization mechanism of ionic species under alkaline hydrothermal conditions. However, the solvent alkalinity was affected by the $Zr(OH)_4 \bullet 9.64H_2O$ dehydration causing a specific steady-state equilibrium for triggering the solute saturation that achieved simultaneous SS1 and SS2′ fine particle crystallization in the range between 7.5 and 47.5 mol% Ti^{4+}.

The rapid dehydration of the Ti-gel in the reaction system reduced the mesocrystals size for the orthorhombic (SS1) and cubic (SS2′) structured solid solutions, resulting in pseudocubic-shaped mesocrystals with sizes varying between 141.0 and 175.5 nm. These mesocrystals were produced via a 3D hierarchical self-assembly process of fine crystals (10.0 nm to 20.0 nm), which occurs along the crystallographic planes {011}, leading to the pseudocubic-shaped agglomerate formation. According to the present results, research must be focused on the electrical and ferroelectric properties of specific chemical compositions for potential industrial application. The soft chemistry hydrothermal processing proposed here might be employed for synthesizing other inorganic perovskite binary systems to tailor solid solutions with enhanced functional properties.

Supplementary Materials: The following supporting information can be downloaded at: https://www.mdpi.com/article/10.3390/nano13152195/s1, Figure S1: Selected Rietveld refinement plots of powder samples prepared at 200 °C for 4 h with 5 M KOH stirred at 130 rpm, using different Ti4+-gel contents of (a) 0.0, (b) 30.0, (c) 50.0, (d) 80.0 and (e) 100.0 mol% Ti, respectively; Figure S2: Estimated unit cell lattices corresponding to the orthorhombic (a,b) and cubic (c,d) structured solid solutions prepared with different contents of Ti4+, (a) 0.05 mol%, (b,c) 30.0 mol% and (d) 50.0 mol%. The proportional Ti4+ content in each solution is represented in the Zr4+ locations (spatial Wyckoff positions 4c and 4a). The unit cell lattices were plotted using the CIF data file from the Rietveld refinements and the VESTA 3 software (K. Momma and F. Izumi, "VESTA 3 for three-dimensional visualisation of crystal, volumetric and morphology data", J. Appl. Crystallogr., 44, (2011) 1272–1276. These structures do not represent the real atomic distribution; a superlattice is suggested to be formed to include the stoichiometric amount of the dopant Ti4+ in either orthorhombic or cubic structures.; Figure S3: FE-SEM micrographs of particles of the solid solutions $SrZr_{1-x}Ti_xO_3$ and $SrTi_{1-x}Zr_xO_3$, obtained under hydrothermal conditions at 200 °C for 4 h, using a reaction medium of 5 M KOH and SrSO4 with different contents of Ti gel ($Ti(OH)4 \bullet 4.5H_2O$), (a) 0.0, (b) 10.0, (c) 15.0,

(d) 20.0, (e) 25.0, (f) 30.0, (g) 40.0, (h) 50.0, (i) 75.0 and (j) 100.0 %mol Ti4+; Figure S4: FE-SEM images, mapping of metal elements and EDX spectra of particles corresponding to the solid solutions $SrZr_{1-x}Ti_xO_3$ and $SrTi_{1-x}Zr_xO_3$, obtained under alkaline hydrothermal conditions at 200 °C for 4 h, using a 5 M KOH solution, SrSO4 and different contents of Ti-gel ($Ti(OH)4\bullet 4.5H_2O$), (a) 15.0, (b) 30.0 and (c) 50.0 %mol Ti.; Table S1: Strontium titanate cubic structure atomic coordinates associated with the Pm3m, 221, space group. These were used to carry out the Rietveld refinements by TOPAS 4.2 software; spatial locations were reported in the CIF file ICDD card no. 40–1500; Table S2: Strontium zirconate orthorhombic structure atomic coordinates (space group Pbnm, 62) were used for Rietveld refinements by TOPAS 4.2 software; spatial locations were reported in CIF file ICDD card no. 70-0283; Table S3: Summary of experiments conducted to prepare powders of $SrZr_{1-x}Ti_xO_3$ and $SrTi_{1-x}Zr_xO_3$ under hydrothermal conditions at 200 °C for 4 h.

Author Contributions: Conceptualization, J.C.R.-A.; methodology and experiments J.C.R.-A. and Z.M.-V.; data analyses, J.R.Q.-G. and Z.M.-V.; writing—original draft preparation, J.C.R.-A. and J.L.-C.; writing—review and editing, J.C.R.-A., J.L.-C. and R.P.-G.; supervision, J.C.R.-A. and J.L.-C.; funding acquisition, J.C.R.-A. and K.Y. All authors have read and agreed to the published version of the manuscript.

Funding: A part of this research was supported by the federal research budget, C-3000-2019, of the NPI Centre for Research and Advanced Studies.

Data Availability Statement: The data supporting this study's findings are available from the corresponding author upon reasonable request.

Acknowledgments: J.C.R.-A.; Z.M.-V., J.L.-C. and R.P.-G. are indebted to CONACYT-SNI. J.R.Q.-G is indebted to the PhD scholarship from CONACYT. Many thanks are also given to Miguel Angel Aguilar-González and Felipe de Jesus Marquez-Torres at the Center for Research and Advanced Studies for the NPI for their assistance on the FE-SEM and HR-TEM observations, respectively.

Conflicts of Interest: The authors declare no conflict of interest.

References

1. Bera, J.; Rout, S.K. $SrTiO_3$–$SrZrO_3$ solid solution: Phase formation kinetics and mechanism through solid-oxide reaction. *Mater. Res. Bull.* **2005**, *40*, 1187–1193. [CrossRef]
2. Vasala, S.; Karppinen, M. $A_2B'B''O_6$ perovskites: A review. *Prog. Solid State Chem.* **2015**, *43*, 1–36. [CrossRef]
3. Benedek, N.A.; Fennie, C.J. Why are there so few perovskite ferroelectrics? *J. Phys. Chem. C.* **2013**, *117*, 13339–13349. [CrossRef]
4. McKnight, R.E.A.; Kennedy, B.J.; Zhou, Q.; Carpenter, M.A. Elastic anomalies associated with transformation sequences in perovskites: II. The strontium zirconate–titanate $Sr(Zr,Ti)O_3$ solid solution series. *J. Phys. Condens. Matter.* **2009**, *21*, 015902. [CrossRef]
5. Yang, Y.; Luo, S.; Dong, F.; Ding, Y.; Li, X. Synthesis of High-Phase Purity $SrTi_{1-x}Zr_xO_3$ Ceramics by Sol-Spray Pyrolysis Method. *Mater. Manuf. Processe.* **2015**, *30*, 585–590. [CrossRef]
6. Parida, S.; Rout, S.K.; Gupta, N.; Gupta, V.R. Solubility limits and microwave dielectric properties of $Ca(Zr_xTi_{1-x})O_3$ solid solution. *J. Alloys Compd.* **2013**, *546*, 216–223. [CrossRef]
7. Chen, C.; Wei, Y.; Chen, D.; Jiao, X. $SrTi_{1-x}Zr_xO_3$ uniform particles: Low-temperature synthesis, characterisation and sintered properties. *J. Mater. Process. Technol.* **2008**, *205*, 432–438. [CrossRef]
8. Wong, T.K.-Y.; Kennedy, B.J.; Howard, C.J.; Hunter, B.A.; Vogt, T. Crystal structures and phase transitions in the $SrTiO_3$-$SrZrO_3$ solid solution. *J. Solid State Chem.* **2001**, *156*, 255–263. [CrossRef]
9. Shende, R.V.; Krueger, D.S.; Rossetti, G.A.; Lombardo, S.J. Strontium zirconate and strontium titanate ceramics for high-voltage applications: Synthesis, processing, and dielectric properties. *J. Am. Ceram. Soc.* **2001**, *84*, 1648–1650. [CrossRef]
10. Wu, Z.; Cao, M.; Yu, H.; Yao, Z.; Luo, D.; Liu, H. The microstructures and dielectric properties of $xSrZrO_3$–$_{(1-x)}SrTiO_3$ ceramics. *J. Electroceram.* **2008**, *21*, 210–213. [CrossRef]
11. Zhang, Z.; Koppensteiner, J.; Schranz, W.; Carpenter, M.A. Anelastic loss behaviour of mobile microstructures in $SrZr_{1-x}Ti_xO_3$ perovskites. *J. Phys. Condens. Matter.* **2010**, *22*, 295401. [CrossRef]
12. Christen, H.M.; Knauss, L.A.; Harshavardhan, K.S. Field-dependent dielectric permittivity of paraelectric superlattice structures. *Mater. Sci. Eng. B.* **1998**, *56*, 200–203. [CrossRef]
13. Yugami, H.; Iguchi, F.; Naito, H. Structural properties of $SrCeO_3$/$SrZrO_3$ proton conducting superlattices. *Solid State Ionics* **2000**, *136–137*, 203–207. [CrossRef]
14. Longo, V.M.; Cavalcante, L.S.; Costa, M.G.S.; Moreira, M.L.; De Figueiredo, A.T.; Andrés, J.; Varela, J.A.; Longo, E. First principles calculations on the origin of violet-blue and green light photoluminescence emission in $SrZrO_3$ and $SrTiO_3$ perovskites. *Theor. Chem. Acc.* **2009**, *124*, 385–394. [CrossRef]

15. Celik, G.; Cabuk, S. First-principles study of electronic structure and optical properties of Sr(Ti,Zr)O_3. *Cent. Eur. J. Phys.* **2013**, *11*, 387–393. [CrossRef]
16. Khunrattanaphon, P.; Chavadej, S.; Sreethawong, T. Synthesis and application of novel mesoporous-assembled $SrTi_xZr_{1-x}O_3$-based nanocrystal photocatalysts for azo dye degradation. *Chem. Eng. J.* **2011**, *170*, 292–307. [CrossRef]
17. Kalyani, V.; Vasile, B.S.; Ianculescu, A.; Buscaglia, M.T.; Buscaglia, V.; Nanni, P. Hydrothermal synthesis of $SrTiO_3$ mesocrystals: Single crystal to mesocrystal transformation induced by topochemical reactions. *Cryst. Growth Des.* **2012**, *12*, 4450–4456. [CrossRef]
18. Huang, S.T.; Lee, W.W.; Chang, J.L.; Huang, W.S.; Chou, S.Y.; Chen, C.C. Hydrothermal synthesis of $SrTiO_3$ nanocubes: Characterisation, photocatalytic activities, and degradation pathway. *J. Taiwan Inst. Chem. Eng.* **2014**, *45*, 1927–1936. [CrossRef]
19. Kalyani, V.; Vasile, B.S.; Ianculescu, A.; Testino, A.; Carino, A.; Buscaglia, M.T.; Buscaglia, V.; Nanni, P. Hydrothermal synthesis of $SrTiO_3$: Role of interfaces. *Cryst. Growth Des.* **2015**, *15*, 5712–5725. [CrossRef]
20. Rangel-Hernandez, Y.M.; Rendón-Angeles, J.C.; Matamoros-Veloza, Z.; Pech-Canul, M.I.; Diaz-de la Torre, S.; Yanagisawa, K. One-step synthesis of fine $SrTiO_3$ particles using $SrSO_4$ ore under alkaline hydrothermal conditions. *Chem. Eng. J.* **2009**, *155*, 483–492. [CrossRef]
21. Quiñones-Gurrola, J.R.; Rendón-Angeles, J.C.; Matamoros-Veloza, Z.; Rodríguez-Galicia, J.L.; Yanagisawa, K. Rapid one-step preparation of $SrZrO_3$ using Zr^{4+} gel and $SrSO_4$ ore under alkaline hydrothermal conditions. *Bol. Soc. Esp. Cerám. Vidr.* **2023**, *in press*. [CrossRef]
22. Mourão, H.A.J.L.; Lopes, O.F.; Ribeiro, C.; Mastelaro, V.R. Rapid hydrothermal synthesis and pH-dependent photocatalysis of strontium titanate microspheres. *Mater. Sci. Semicond. Process.* **2015**, *30*, 651–657. [CrossRef]
23. Rendón-Angeles, J.C.; Matamoros-Veloza, Z.; Gonzalez, L.A.; López-Cuevas, J.; Ueda, T.; Yanagisawa, K.; Hernández-Calderón, I.; Garcia-Rocha, M. Rapid hydrothermal synthesis of $SrMo_{1-x}W_xO_4$ powders: Structure and luminescence characterization. *Adv. Powder Technol.* **2017**, *28*, 629–640. [CrossRef]

nanomaterials

MDPI

Article

In Situ Ultra-Small- and Small-Angle X-ray Scattering Study of ZnO Nanoparticle Formation and Growth through Chemical Bath Deposition in the Presence of Polyvinylpyrrolidone

Karina Abitaev [1], Petia Atanasova [2], Joachim Bill [2], Natalie Preisig [1], Ivan Kuzmenko [3], Jan Ilavsky [3], Yun Liu [4] and Thomas Sottmann [1,*]

[1] Institute of Physical Chemistry, University of Stuttgart, 70569 Stuttgart, Germany; karina.abitaev@ipc.uni-stuttgart.de (K.A.); natalie.preisig@ipc.uni-stuttgart.de (N.P.)
[2] Institute for Materials Science, University of Stuttgart, 70569 Stuttgart, Germany; atanasova@imw.uni-stuttgart.de (P.A.); bill@imw.uni-stuttgart.de (J.B.)
[3] X-ray Science Division, Advanced Photon Source, Argonne National Laboratory, Argonne, IL 60439, USA; kuzmenko@anl.gov (I.K.); ilavsky@anl.gov (J.I.)
[4] National Institute of Standards and Technology Center for Neutron Research, Gaithersburg, MD 20899, USA; yun.liu@nist.gov
* Correspondence: thomas.sottmann@ipc.uni-stuttgart.de

Abstract: ZnO inverse opals combine the outstanding properties of the semiconductor ZnO with the high surface area of the open-porous framework, making them valuable photonic and catalysis support materials. One route to produce inverse opals is to mineralize the voids of close-packed polymer nanoparticle templates by chemical bath deposition (CBD) using a ZnO precursor solution, followed by template removal. To ensure synthesis control, the formation and growth of ZnO nanoparticles in a precursor solution containing the organic additive polyvinylpyrrolidone (PVP) was investigated by in situ ultra-small- and small-angle X-ray scattering (USAXS/SAXS). Before that, we studied the precursor solution by in-house SAXS at T = 25 °C, revealing the presence of a PVP network with semiflexible chain behavior. Heating the precursor solution to 58 °C or 63 °C initiates the formation of small ZnO nanoparticles that cluster together, as shown by complementary transmission electron microscopy images (TEM) taken after synthesis. The underlying kinetics of this process could be deciphered by quantitatively analyzing the USAXS/SAXS data considering the scattering contributions of particles, clusters, and the PVP network. A nearly quantitative description of both the nucleation and growth period could be achieved using the two-step Finke–Watzky model with slow, continuous nucleation followed by autocatalytic growth.

Keywords: chemical bath deposition; ZnO; USAXS; SAXS; polyvinylpyrrolidone; PVP; particle formation; kinetics

Citation: Abitaev, K.; Atanasova, P.; Bill, J.; Preisig, N.; Kuzmenko, I.; Ilavsky, J.; Liu, Y.; Sottmann, T. In Situ Ultra-Small- and Small-Angle X-ray Scattering Study of ZnO Nanoparticle Formation and Growth through Chemical Bath Deposition in the Presence of Polyvinylpyrrolidone. *Nanomaterials* **2023**, *13*, 2180. https://doi.org/10.3390/nano13152180

Academic Editor: Meiwen Cao

Received: 7 July 2023
Revised: 20 July 2023
Accepted: 21 July 2023
Published: 26 July 2023

1. Introduction

The field of artificial, structured organic–inorganic hybrid materials has received enormous attention in the last few decades given the major contributions in numerous fields such as coatings, catalysis, sensors, and electronics [1–3]. In terms of fabrication, one straightforward approach is the use of organic templates, including carbon nanotubes [4,5], polymers [6,7], or even biological objects such as viruses [8,9], on which an inorganic matrix is deposited in situ. To preserve the delicate template structure, mild deposition conditions are necessary. Next to the frequently used sol–gel procedure [6,10,11], chemical bath deposition (CBD) has been proven beneficial, in particular for the synthesis of nanostructured hybrid materials with a finely tuned thickness of the deposited inorganic phase on the organic template. In CBD, an (organic) template is mineralized while being immersed in a precursor solution at moderate temperatures, typically below 100 °C [12]. Additives such as polymers [13] or small molecules like amino acids [14] may be present

and used as a structure-directing agent to precisely control the growth of the solid with respect to size, morphology, and crystallinity. Such control is achieved by the ability of the additives to stabilize the dissolved ions, direct and restrict the particle growth, and prevent nanoparticle agglomeration by steric and/or electrostatic interactions. Using this approach, dense and smooth thin films and nanostructured hybrid materials of metal chalcogenides like CdS [15–17], TiO_2 [18–20], and ZnO [21–23] were fabricated through organic templates. Among them, the transparent semiconductor ZnO is of particular interest as it covers a vast range of applications from optoelectronics [24,25] to gas sensors [26,27] and lasing devices [28,29], etc.

Applying a well-established CBD route and using various organic templates such as self-assembled monolayers [30–33], polymers [32,34], polymer foams [35], DNA [36], and viruses [37–40], ZnO hybrid materials were prepared from a methanolic ZnO precursor solution in the presence of polyvinylpyrrolidone (PVP). In addition, close-packed assemblies of polymer nanoparticles were mineralized by applying the same approach, followed by the removal of the particles to produce ZnO inverse opals [41,42]. They are a promising candidate for photonic applications [43,44] or as catalyst solid supports in heterogeneous catalysis [45], combining the ordered porous structure with the favorable electrical and optical properties of ZnO. First insights into the role of PVP on the deposition rate, mechanism, and film morphology of ZnO films obtained applying this CBD approach were given in the studies of Lipowsky et al. [30,31,33]. It was found that in the absence of PVP, the immediate precipitation of micron-sized ZnO particles takes place, whereas intermediate PVP volume fractions ($0.06 < \phi_{PVP} < 0.14$) are required for the successful preparation of thin, homogeneous nanocrystalline ZnO films. It was also shown that the deposition of ZnO occurs via a transient amorphous phase in which needle-like particles containing both zinc and PVP are formed [33], similar to the well-known formation of intermediate amorphous phases in biomineralization and bioinspired mineralization processes [46,47].

A powerful technique for the in situ study of the structural evolution during nanoparticle synthesis is time-resolved small-angle X-ray scattering (SAXS), which can be complemented by ex situ imaging techniques such as transmission electron microscopy (TEM). As far as ZnO formation via the sol–gel method is concerned, Caetano et al. investigated the nucleation and growth of ZnO nanoparticles synthesized through an additive-free sol–gel process via time-resolved tandem SAXS/UV-Vis and X-ray adsorption fine structure (XAFS) experiments [48–50]. These studies revealed that ZnO nuclei formed by supersaturation-induced nucleation are subject to the so-called oriented attachment growth [51,52], where particles aggregate by coalescence. In the late stages, Ostwald ripening [53,54] with dissolution and reprecipitation processes dominates. Analogies were found by Herbst et al. during the thermolysis of Zn-oleate precursors, verified by in situ SAXS/WAXS/UV-Vis measurements [55]. In their study, a classical homogeneous nucleation and growth model was applied to describe the process of ZnO nanoparticle synthesis. A nonclassical growth behavior where both diffusion- and surface-control occur was observed when the PVP-mediated solvothermal synthesis of ZnO nanorods was studied by ex situ SAXS and TEM [56].

In this study, we use time-resolved USAXS and SAXS for the in situ investigation of the role of the organic additive PVP during the formation and growth of individual ZnO nanoparticles and ZnO clusters in a methanolic precursor solution applying the above-mentioned CBD method. As found in previous studies, this method requires a relatively high volume fraction of PVP ($\phi_{PVP} = 7.1 \times 10^{-2}$); therefore, its scattering contribution must be considered when analyzing the scattering data. Accordingly, the first part of this work deals with the study of the polymer structure in the precursor solution before initiating the synthesis of ZnO particles by heating. In the second part, we clarified the ZnO particle formation performed at two temperatures, i.e., 58 °C and 63 °C, via time-resolved synchrotron USAXS measurements. Form factor modeling and model-independent invariant analyses of the recorded USAXS data allowed us to not only describe the data quantitatively but also to unravel the ZnO nanoparticle formation mechanism.

2. Materials and Methods

2.1. Synthesis of ZnO Nanoparticles

ZnO nanoparticles were synthesized following an established procedure [35,41,42]. Briefly, three methanolic stock solutions of zinc acetate dihydrate ($ZnAc_2 \times 2\ H_2O$) (37.4 mM, Sigma-Aldrich, St. Louis, MO, USA), tetraethylammonium hydroxide (TEAOH) (79.0 mM, Sigma-Aldrich), and polyvinylpyrrolidone (PVP) (25.7 mM) (Sigma-Aldrich, M_w = 10,000 g/mol (10 k), Lot # BCBJ4889V) were used to prepare the precursor solution. While the stock solutions can be stored for a longer period of time, the precursor solution was prepared freshly before use to avoid unwanted ZnO formation. Equal volumes of the $ZnAc_2$ and PVP stock solution were mixed, followed by dropwise addition (1 mL/min) of the same volume of the TEAOH stock solution under continuous stirring. Thus, a precursor solution with a volume ratio of 1:1:1 of the stock solutions and final concentrations of [PVP] = 8.6 mM, [Zn^{2+}] = 12.5 mM, and [TEAOH] = 26.3 mM was obtained. For the synthesis of ZnO particles, the precursor solution was heated to T = 58 °C and 63 °C, respectively.

2.2. Characterization

2.2.1. In-House Small-Angle X-ray Scattering

Room temperature studies of the precursor solution were performed on a SAXSess instrument from Anton Paar (Graz, Austria). The instrument was equipped with a Cu K_α X-ray source (λ = 1.54 Å) operated in line collimation mode. Samples were filled into a quartz capillary flow cell and data were collected at 25 °C using imaging plates from Fujifilm (Greenwood, SC, USA), which were read by a cyclone scanner from PerkinElmer (Covina, CA, USA). One-dimensional corrected and reduced scattering profiles $I(q)$ as a function of the absolute value of the scattering vector q, with $q = 4\pi/\lambda \sin(\theta/2)$, where θ is the scattering angle, were obtained using Anton Paar's SAXSquant 2D and 1D software, including the subtraction of the dark current and the empty cell scattering. To normalize the data to an absolute scale, water was used as a secondary calibration standard [57]. The scattering data were analyzed using SasView version 5.0.4, with slit-smearing accounted for in the fit model. Alternatively, the slit-smeared data were desmeared using SAXSquant 2.0.

2.2.2. Ultra-Small- and Small-Angle Synchrotron X-ray Scattering

USAXS and SAXS data were collected at the 9-ID-C beamline at the Advanced Photon Source at Argonne National Laboratory (Argonne, IL, USA) [58,59]. A combined q range between 3.7×10^{-4} Å^{-1} and 1.7 Å^{-1} was covered using an X-ray energy of 21 keV (λ = 0.5895 Å) and an X-ray flux of about 5×10^{12} photons mm^{-2} s^{-1}. To study the time-dependent growth of the ZnO particles, the precursor solution was filled into an NMR tube (Wilmad-LabGlass^{TM}, WG-1000-4, inner diameter 4 mm), which was placed in a thermostated home-built cell holder. USAXS scattering data were recorded starting at T = 25 °C, followed by rapid heating (1 K/s) to T = 58 °C and 63 °C, respectively, with collection times of 100 s each. Before and after the time-resolved USAXS measurements, SAXS patterns were acquired with collection times of 20 s.

The slit-smeared USAXS data were reduced for instrumental background and empty cell scattering, normalized to absolute scale, and desmeared using the instrument data reduction software package Indra for Igor Pro 9.0. For the SAXS data and to combine the USAXS and SAXS data, Nika [60] and Irena [61] were used, respectively. The scattering data were analyzed using SasView version 5.0.4, with the slit-smearing accounted for in the fit model.

2.2.3. Transmission Electron Microscopy

For particle visualization, TEM images were collected on a EM10 from Zeiss (Jena, Germany) operated at 60 kV. Each nanoparticle solution was diluted in methanol at room temperature. A small drop of the diluted sample was placed on a TEM copper grid covered with a thin holey carbon film. The drop was then gently blotted to remove the excess

sample. After the solvent had completely evaporated, the dry grid containing the particles was transferred to the microscope. A 1 k × 1 k CCD camera was used to record the TEM images, which were analyzed using the software *ImageJ* to evaluate the size of at least 100 ZnO particles and clusters, respectively, based on which the mean radii $R_{ZnO,i,TEM}$ and the standard deviations $\sigma_{i,TEM}$ were determined using a Gaussian size distribution function.

3. Results and Discussion

In the following, we first describe the structural investigation of PVP in the methanolic ZnO precursor solution by in-house SAXS and USAXS/SAXS. We then discuss the time-resolved synchrotron USAXS measurements performed to determine the kinetic processes of ZnO particle formation and growth in situ. We show that a quantitative analysis of all scattering data is possible when considering the scattering contributions of the previously determined stabilizing polymer structure and two ZnO species, i.e., ZnO nanoparticles and their clusters. In the last part, we use the determined time evolution of the size and volume fraction of ZnO particle clusters to study the kinetics using the two-step Finke–Watzky model [62–65].

3.1. PVP Structure in the Precursor Solution

The chemical bath deposition (CBD) of ZnO nanoparticles studied in this work is based on the thermally induced hydrolysis of the zinc precursor zinc acetate ($ZnAc_2$) in a methanolic solution under basic conditions adjusted by the organic base tetraethylammonium hydroxide (TEAOH). Furthermore, the ion-stabilizing and structure-directing agent PVP (10 k) is added at a volume fraction of $\phi_{PVP} = 7.1 \times 10^{-2}$. As a prerequisite for the comprehensive investigation of the ZnO particle formation by USAXS/SAXS, the contribution of all components to the total scattering should be clarified first. Therefore, we started with the investigation of the PVP structure in methanol before and after the addition of the respective components as well as the PVP structure in the final composition of the precursor solution by SAXS at 25 °C.

In Figure 1a, the recorded slit-smeared SAXS intensities $I(q)$ were plotted as a function of the scattering vector q using a double-logarithmic representation. The scattering curve of PVP in pure methanol $\phi_{PVP} = 7.1 \times 10^{-2}$ (8.6 mM) (■) shows a Guinier region at low q with almost constant scattering intensity. As q increases, a power law decay is observed until a minimum is reached at $q \approx 1$ Å^{-1}, followed by the intermolecular C-C chain interaction peak [66] at $q \approx 1.5$ Å^{-1}. Similar behavior was found when 12.5 mM $ZnAc_2$ (▼) or 26.3 mM TEAOH (●) were added while keeping the polymer amount constant at $\phi_{PVP} = 7.1 \times 10^{-2}$. However, for the final composition of the precursor solution (▲), instead of a Guinier region for $q < 0.1$ Å^{-1}, a power law decay with $I(q) \approx q^{-1.4}$ can be seen. Thus, the presence of both $ZnAc_2$ and TEAOH results in a significantly different structure of the polymer.

In general, the recorded scattering curves provide information about the polymer structure on different-length scales: the Guinier region gives the overall dimension of the polymer, i.e., its radius of gyration R_g(PVP), while the exponent m of the power law decay is related to the polymer–solvent interactions [67,68]. Furthermore, the correlation length ξ, quantifying the end-to-end distance of a coil or the mesh size, i.e., the mean diameter of a cavity within the polymer network [69], respectively, can be extracted.

To determine R_g(PVP) and the exponent m of the power law decay, the scattering curves, except for the final composition, were analyzed according to the polymers with excluded volume effects model [67,68]:

$$I(q)_{poly} = I_0 \left[\frac{m}{U^{\frac{m}{2}}} \gamma\left(\frac{m}{2}, U\right) - \frac{m}{U^m} \gamma(m, U) \right], \quad (1)$$

where I_0 corresponds to the forward scattering intensity, γ is the incomplete gamma function, and the parameter U is defined by

$$U = \frac{q^2 {R_g}^2 (2/m+1)(2/m+2)}{6}. \quad (2)$$

Since $I(q)_{\text{poly}}$ does not account for large q features such as the intermolecular C-C chain interaction peak [66], Equation (1) was combined with a Gaussian $I(q)_G$, which finally leads to the following expression:

$$I(q) = I(q)_{\text{poly}} + I(q)_G = I(q)_{\text{poly}} + G \cdot \exp\left(\frac{1}{2}(q - q_G)^2 / {\sigma_G}^2\right). \quad (3)$$

Herein, G is the scaling factor for the Gaussian with the maximum peak position at q_G, and the peak width σ_G. Note that the solid lines in Figure 1a correspond to the final fit following Equation (3), while in Figure 1b, the final fit as well as the respective contributions of Equation (3) are shown exemplarily for the scattering pattern of PVP in methanol ( ).

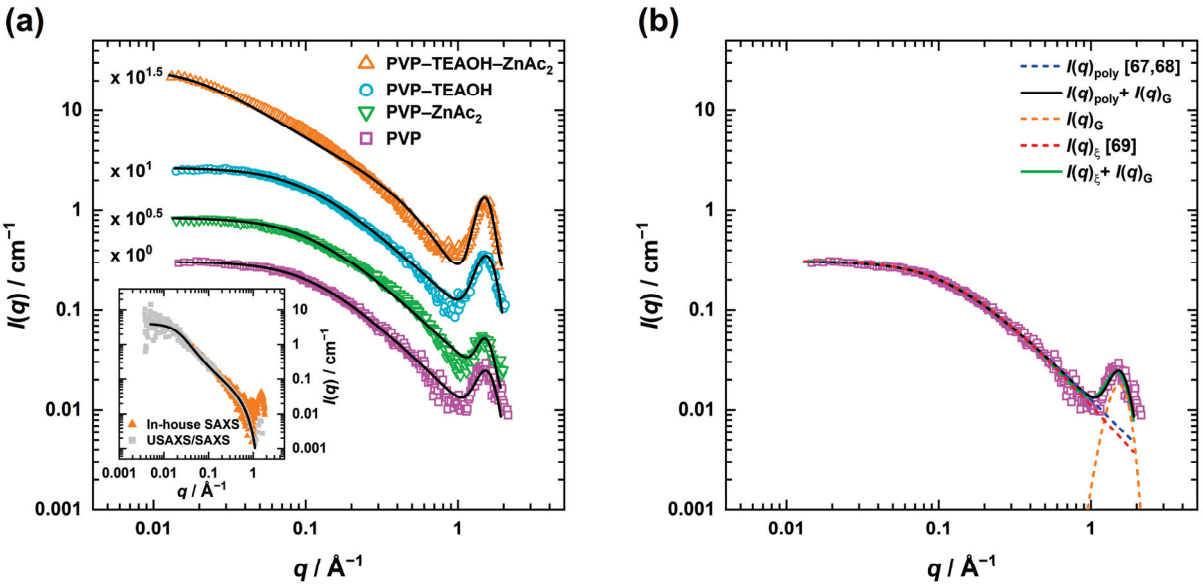

Figure 1. (**a**) Slit-smeared SAXS profiles of PVP at $\phi_{\text{PVP}} = 7.1 \times 10^{-2}$ in methanol with the respective compounds and the final composition (TEAOH = 26.3 mM, $ZnAc_2$ = 12.5 mM), measured at T = 25 °C. The scattering curves were described using the polymers with excluded volume effects model [67,68], and for the final composition, the flexible cylinder model [70,71] combined with a Gaussian, respectively (solid lines). To help the reader distinguish between the scattering curves, they are displaced by an arbitrary factor. Inset: Comparison of desmeared in-house SAXS and USAXS/SAXS data for the final composition with the flexible cylinder fit. (**b**) Applied fit models (Equations (3) and (4)) and their respective scattering contributions are shown for PVP in methanol.

The correlation length ξ was obtained, separately, by applying the correlation length model [69] $I(q)_\xi$, which was again combined with a Gaussian:

$$I(q) = I(q)_\xi + I(q)_G = \frac{A}{q^{m'}} + \frac{C}{1 + (q\xi)^b} + I(q)_G \quad (4)$$

where the first term accounts for the scattering of large-scale polymer clusters, and the second term for the polymer chains. A and C are scaling parameters and m' and b are the exponent of the power law decay($'$ denotes for small q's) and the Lorentzian exponent, respectively. In cases where the low q power law decay was absent, the first term was

neglected ($A = 0$). Also, for Equation (4), the respective contributions, together with the final fit, are shown exemplarily for PVP in methanol (■) in Figure 1b.

Applying Equations (3) and (4) and taking the slit-smearing into account, it was possible to describe the scattering curves quantitatively. The best-fit parameters are compiled in Tables S1 and S2 in the Supplementary Materials, while the corresponding Guinier radius R_g(PVP), the exponent m of the power law decay at high $q's$, and the correlation length ξ_{PVP} are summarized in Table 1. Following the analysis of the scattering data of PVP in methanol (■) with Equation (3) revealed a high q power law decay exponent of $m \approx 1.5$, suggesting that the polymer chains are no longer in an ideal ($m = 2$) or swollen ($m = 5/3$) state but already approach a rod-like state ($m = 1$) [68,72]. A similar behavior was found by Sapir et al. [73] once the overlap concentration c^* of PVP-10k in D_2O ($\phi_{PVP} \sim 4.8 \times 10^{-2}$) was exceeded and the semidilute polymer regime began. This regime refers to a state in which the polymer forms a network with overlapping and entangled chains. When PVP was studied at lower volume fractions ($\phi_{PVP} = 1.0$, 2.0, and 4.0×10^{-2}) in methanol, shown in the Supplementary Materials Figures S1 and S2 and Tables S3 and S4, ideal chain behavior was observed exclusively for the lowest PVP volume fraction $\phi_{PVP} = 1.0 \times 10^{-2}$. At $\phi_{PVP} = 2.0 \times 10^{-2}$, the exponent of the power law decay drops steeply and then slowly decreases with increasing PVP amount, while R_g(PVP) decreases continuously. Furthermore, the change of the scaling dependency of the correlation length, observed between $\phi_{PVP} = 4.0$ and 7.1×10^{-2}, confirms that the PVP concentration in the methanolic precursor solution can be assigned to the semidilute regime [74].

The analysis of the scattering data from the methanolic PVP solution ($\phi_{PVP} = 7.1 \times 10^{-2}$) in which $ZnAc_2$ (▼) or TEAOH (●) was added revealed a slight increase in R_g(PVP) (see Table 1) while the decrease in the exponent of the power law decayindicates that the polymer becomes more rod-like [72]. Though PVP is a nonionic polymer, the pyrrolidone head group is polar and interacts with the ions of the ZnO precursor and the organic base [33,75]. Their accumulation along the polymer chains, leading to repulsion of the segments within the polymer chain, can explain why the polymer chain becomes slightly stiffer and more swollen compared to the ion-free solution. This effect is slightly more pronounced with TEAOH, whose concentration is more than twice of $ZnAc_2$.

Table 1. Parameters obtained from the analysis of SAXS data from PVP in methanol at $\phi_{PVP} = 7.1 \times 10^{-2}$ before and after adding 12.5 mM $ZnAc_2$ and 26.3 mM TEAOH, respectively, as well as the final composition. While the polymer with excluded volume model [67,68] provided the radius of gyration R_g(PVP) and the high q power law exponent m, the exponent of the power law decay at low q m' and the correlation length ξ_{PVP} were obtained through the correlation length model [69].

Sample	R_g(PVP)/nm	m	m'	ξ_{PVP}/nm
PVP	1.5 ± 0.1	1.52 ± 0.01	-	1.1 ± 0.1
PVP–$ZnAc_2$	1.7 ± 0.1	1.46 ± 0.01	-	1.1 ± 0.1
PVP–TEAOH	1.8 ± 0.1	1.45 ± 0.01	-	1.3 ± 0.1
PVP–TEAOH–$ZnAc_2$	6.3 ± 0.3 [a]	-	1.55 ± 0.01	2.9 ± 0.2

[a] obtained by the Guinier analysis.

Discussing the scattering data of the precursor solution (▲) (where both $ZnAc_2$ and TEAOH are present) in more detail, the power law decay ($I(q) \approx q^{-1.4}$) recorded in the low q limit of the in-house SAXS instrument provides little information on the global structure and size of the polymer. This information can be obtained by extending the q-range towards much smaller values using the USAXS/SAXS setup at the 9-ID-C beamline at the Advanced Photon Source at the Argonne National Laboratory [58,59]. The inset in Figure 1 shows a good agreement between the desmeared in-house (▲) and USAXS/SAXS (■) data. In addition, the combination of the data clearly shows the transition of the power law into a Guinier region at $q < 0.01$ Å^{-1}. Utilizing Guinier's approximation for low q ($\ln I(q) \approx \ln I_0 - ({R_g}^2/3)\, q^2$), we obtained R_g(PVP) = 6.3 ± 0.3 nm, which corresponds to a fourfold increase compared to R_g(PVP) in pure methanol and in solutions containing only $ZnAc_2$ or TEAOH. This significant change in the PVP structure

caused by the increased ion concentration due to the presence of both ZnO precursor and base is most likely related to a stronger repulsion of the segments within the polymer chain, leading to a further increase in the chain stiffness. This hypothesis is supported by the increase in mesh size determined from the analysis at medium q's to ξ_{PVP} = 2.9 ± 0.2 nm. Moreover, $ZnAc_2$ might start to hydrolyze even at 25 °C, changing its chain flexibility so that the first particle nuclei could have formed within the PVP. However, this reaction is significantly accelerated only by increasing the temperature.

For the quantitative analysis of the precursor solution data, we used the flexible cylinder model for single semiflexible polymer chains [70,71], which has already been applied to the scattering of aqueous PVP-40 k and -360 k solutions [76], combined with a Gaussian to describe the intermolecular C-C chain interaction peak [66] at high q. Accordingly, the scattering intensity was modeled by

$$I(q) = I(q)_{\text{flexC}} + I(q)_{\text{G}} = \phi_{\text{PVP}} \Delta\rho^2 V_{\text{C}} S(q, L, b) P(q, R_{\text{C}}) + I(q)_{\text{G}} \quad (5)$$

where ϕ_{PVP} is the volume fraction of PVP, $\Delta\rho^2$ is the square of the scattering length density difference between PVP ($\rho_{PVP} = 11.0 \times 10^{-6}$ Å^{-2}) and methanol ($\rho_{MeOH} = 7.5 \times 10^{-6}$ Å^{-2}), V_C is the volume of the cylinder and $S(q, L, b)$ is the scattering of a polymer chain with excluded volume effects with the contour length L, the Kuhn length b, a measure of the local stiffness, and the circular cross section $P(q, R_C)$ of a cylinder with the radius R_C. The comprehensive mathematical expression of $S(q, L, b)$ can be found in the work of Chen et al. [71], while $P(q, R_C)$ is given by the first-order Bessel function J_1 with $P(q, R_C) = \left(\frac{2J_1(qR_C)}{qR_C}\right)^2$.

As can be seen in Figure 1, this model is able to describe the smeared and desmeared (inset) scattering data of the precursor solution, almost quantitatively, yielding a contour length of L = 80 ± 1 nm, a Kuhn length of b = 3.3 ± 0.3 nm, and a cross-section radius of R_C = 0.27 ± 0.01 nm. b and R_C are in the same range, as already reported for PVP-40 k and -360 k in dilute aqueous solutions (b = 3.0 ± 0.2 nm and $R_C \approx 0.1$ nm [76]) as well as for PVP-2 k to -2200 k in 0.1 M aqueous NaAc solution ($b \approx 1.7 - 2.4$ nm and R_C = 0.25 ± 0.01 nm [77]). Estimating the radius of gyration from the contour and Kuhn length with ${R_g}^2 \approx Lb/6$ [78], we obtain R_g(PVP) = 6.5 ± 0.4 nm, in good agreement with the Guinier analysis. Note that in the region around $q \sim 0.1$ Å, the modeled scattering curve shows a stronger curvature than the recorded data. This small but systematic difference is most likely related to polymer–polymer interactions, which are neglected in the applied model [70].

The shape- and size-independent invariant analysis of the desmeared USAXS/SAXS data ($q < 1$ Å^{-1}), which are on absolute scale, has shown that the scattering length density difference $\Delta\rho$ had to be increased from $\Delta\rho = \rho_{PVP} - \rho_{MeOH} = 3.5 \times 10^{-6}$ Å^{-2} to $\Delta\rho = 5.6 \times 10^{-6}$ Å^{-2} in order to obtain the experimental PVP volume fraction. The same increase in contrast factor was also obtained from the analysis of desmeared in-house SAXS data as well as of additional SAXS data recorded at the ID02 beamline at the European Synchrotron Radiation Facility (ESRF) in Grenoble, France [79]. The higher X-ray scattering contrast might be related to ion association along the polymer chain as well as additional specific volume effects, which both increase the scattering length density of the polymer.

In summary, due to the relatively high volume fraction of PVP, the initial state of the precursor solution is characterized by the scattering of a PVP network. Ions are distributed along and within the cavities of the PVP network, where they interact with the pyrrolidone moiety of the polymer, leading to a semiflexible polymer chain behavior.

3.2. In Situ Study of ZnO Particle Formation and Growth

Having studied the initial state of the precursor solution at 25 °C, we then focused on elucidating the formation of ZnO particles induced by heating. Typically, the reaction is carried out at 60 °C, as $ZnAc_2$ hydrolyzation and mass transport during the ZnO formation are accelerated at this temperature. Herein we chose to study the ZnO kinetics

at T = 58 °C and 63 °C. The reason for that is the significantly slower deposition below 50 °C, as confirmed in preliminary studies, while the upper limitation for the reaction temperature is given by the boiling point of methanol at 65 °C. Figure 2 shows the time-dependent slit-smeared USAXS curves starting from 25 °C (t = 0 min) followed by rapid heating to T = 58 °C (a) or 63 °C (b).

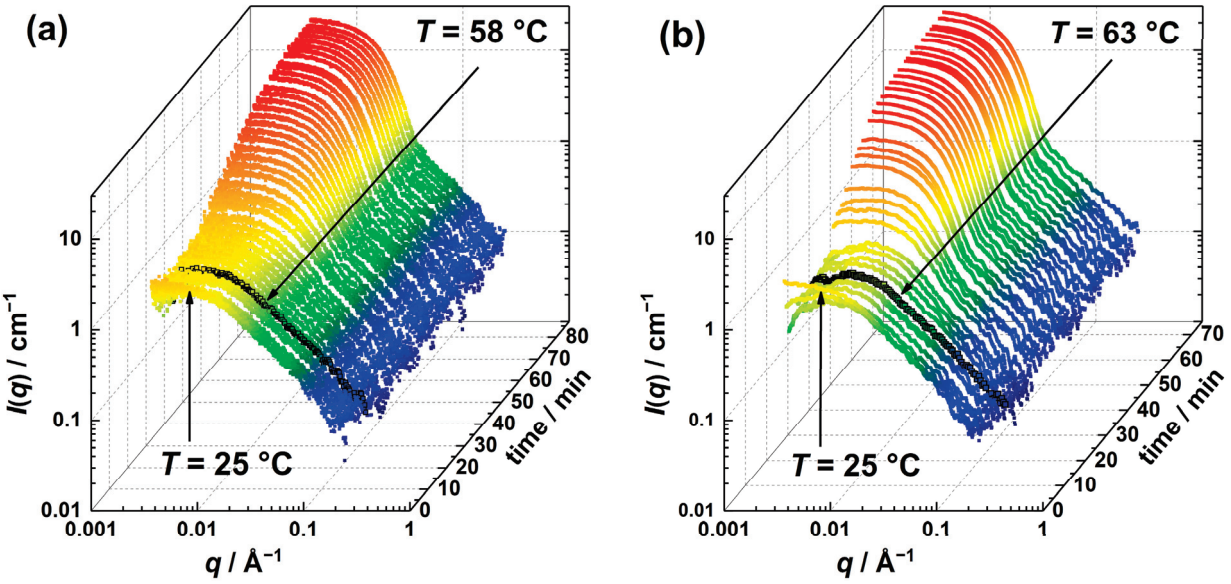

Figure 2. Scattering intensity colored stack-plot of slit-smeared USAXS curves during the ZnO particle formation at T = 58 °C (**a**) and T = 63 °C (**b**). The initial scattering curve at T = 25 °C and the curve at which the target temperature was reached are marked with arrows.

During heating and temperature equilibration the precursor solution to T = 58 °C (Figure 2a), which took about 10 min, the scattering curves are dominated by the scattering of the polymer network with the above-mentioned features of a Guinier region at low q, followed by a power law decay. The slight decrease in the intensity at low q might relate to the heating with an inhomogeneous temperature distribution inside the solution. Potential over subtraction of solvent scattering, which was measured at T = 58 °C, might be another explanation for this decrease.

Subsequently, for reaction times t > 13 min, the scattering intensities at low q increase continuously, which can be attributed to the form factor contribution of newly formed ZnO species, while above $q \geq 0.1$ Å^{-1}, the scattering is dominated by the PVP scattering. As the reaction progresses, the form factor minimum becomes increasingly apparent and shifts to lower q values, suggesting the growth of the ZnO species. Finally, the increase in the low q scattering intensity levels off, indicating that the precursor $ZnAc_2$ has been consumed; therefore, the data acquisition was stopped after 87 min. Contrary to what Lipowsky et al. [33] have seen when ZnO films are formed in the presence of PVP via CBD, no additional contribution of needle-like species with a length scale between 20 and 50 nm was observed in the scattering curves.

A similar behavior of the scattering curves can be seen during the formation of ZnO particles at T = 63 °C in Figure 2b. Compared to the formation at 58 °C, the decrease in the forward scattering observed in the curves recorded at the early stages of the process is even more pronounced, most likely due to over subtraction of the background, measured at the higher final temperature. The earlier appearance of the form factor signature and the earlier leveling off of the increase in forward scattering after 75 min clearly indicate that the reaction is faster at higher temperatures. This can be explained by the enhanced mass transport with increasing temperature, which accelerates the formation of ZnO.

A comparison of the first (t = 0 min, T = 25 °C) and the last (t = 87 min, T = 58 °C) time-resolved USAXS/SAXS scattering curves are shown by means of the ZnO particles' formation at

T = 58 °C (Figure 3, left). This comparison highlights the presence of the additional form factor contribution ($q \leq 0.08$ Å^{-1}) in the scattering curve recorded at the process end (t = 87 min). A closer look also reveals a weak shoulder around q~0.15 Å^{-1}. One exemplary image of complementary TEM studies taken from a separately prepared solution after an analogous heating procedure starting from 25 °C to 58 °C is shown in the center of Figure 3. Therein, two species are visible: smaller ones with a radius of $R_{\mathrm{ZnO,TEM}}$ = 1.3 ± 0.7 nm as well as agglomerates of those with an average radius of $R_{\mathrm{ZnO\text{-}cluster,TEM}}$ = 8.5 ± 1.4 nm. We will refer to the smaller particles as individual ZnO particles and to the larger ones as clusters of ZnO particles. Strikingly, the diameter of the individual ZnO particles is only slightly smaller than the mesh size within the PVP network ($\xi_{\mathrm{PVP}} \approx 2.9$ nm), indicating initial growth of the ZnO particles in the network cavities before cluster formation occurs. Furthermore, the average cluster radius is only slightly larger than the Guinier radius of PVP in the precursor solution with R_g(PVP) = 6.3 ± 0.3 nm.

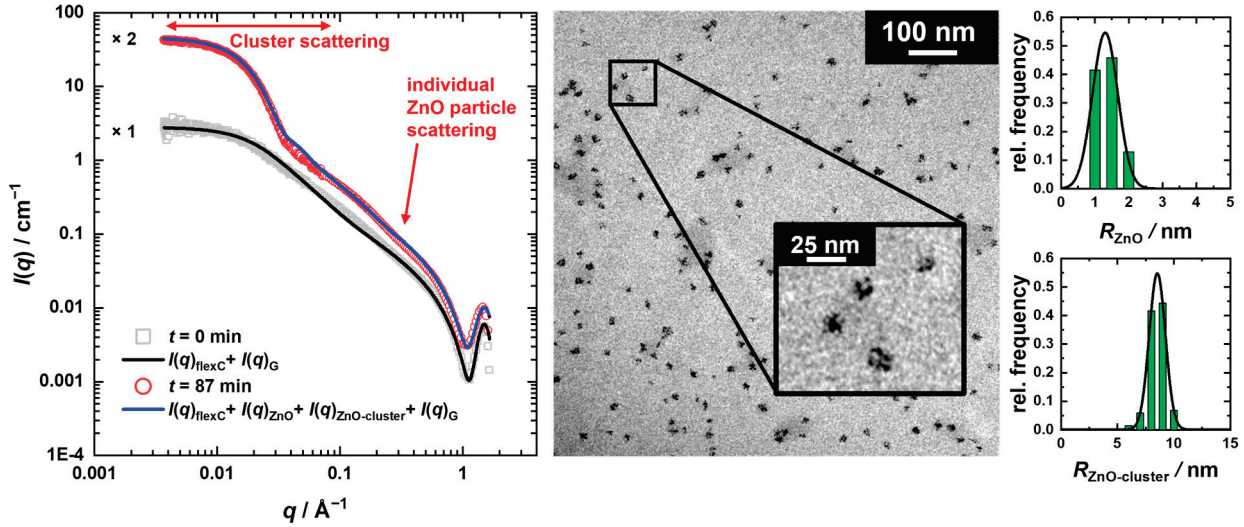

Figure 3. Left: Slit-smeared USAXS/SAXS curves measured before heating (t = 0 min, T = 25 °C) and after the reaction was stopped (t = 87 min, T = 58 °C), displaced by an arbitrary factor. To model the final scattering curve, the flexible cylinder model [70,71] used for t = 0 min was additively combined with two polydisperse spherical form factors [80] for the scattering contributions of the ZnO particles and their clusters, as well as with a Gaussian. Right: TEM image taken after the ZnO synthesis at T = 58 °C with the corresponding volume-weighted size distribution of the ZnO particles and clusters, described by a Gaussian size distribution, respectively.

Comparing the final cluster radius obtained from the USAXS/SAXS scattering curve analysis ($R_{\mathrm{ZnO\text{-}cluster,f}}$ = 10.5 ± 1.9 nm) to TEM, one may assume that the clustered particles are surrounded by a PVP layer that is not visible in the TEM, similar to what has been demonstrated for silica-polymethyl methacrylate (PMMA) nanocomposites by SANS [81]. Since we were not able to study such a layer independently with SANS, we used a simple approach for the quantitative analysis of the time-resolved USAXS/SAXS data. In this approach, the scattering contribution of the PVP network described by the flexible cylinder model [70,71] $I(q)_{\mathrm{flexC}}$ was additively combined with the scattering contributions of the individual ZnO particles $I(q)_{\mathrm{ZnO}}$ and their clusters $I(q)_{\mathrm{ZnO\text{-}cluster}}$, each modeled by the form factor of polydisperse spheres [80], as well as a Gaussian $I(q)_{\mathrm{G}}$ for the intermolecular C-C chain interaction peak [66] at high q. Thus, the total intensity is given by

$$I(q) = I(q)_{\mathrm{flexC}} + I(q)_{\mathrm{ZnO}} + I(q)_{\mathrm{ZnO-cluster}} + I(q)_{\mathrm{G}} + I_{\mathrm{background}} \quad (6)$$

where

$$I(q)_{\mathrm{ZnO,i}} = \phi_{\mathrm{ZnO,i}} V_{\mathrm{ZnO,i}} \Delta\rho^2 \int P(q, R_{\mathrm{ZnO,i}}) f(R_{\mathrm{ZnO,i}}, R_{\mathrm{ZnO,i,f}}, \sigma_{\mathrm{i}}) dR \quad (7)$$

with $\phi_{ZnO,i}$ and $V_{ZnO,i}$ being the volume fractions and average volumes of particles and particle clusters, respectively. $\Delta\rho^2$ is the scattering length density difference between ZnO (ρ_{ZnO} = 44.8 × 10^{-6} Å^{-2}) and methanol (ρ_{MeOH} = 7.5 × 10^{-6} Å^{-2}) and $P(q,R_{ZnO,i})$ = $\left(\frac{3J_1(qR_{ZnO,i})}{qR_{ZnO,i}}\right)^2$ the form factor of a sphere with the radius $R_{ZnO,i}$. To account for size distribution effects, the form factor was convoluted with a Gaussian size distribution functions $f(R_{ZnO,i}, R_{ZnO,i,f}, \sigma_i)$ which yields the mean radius $R_{ZnO,i,f}$ and the width σ_i.

Using this approach, we were able to describe the recorded time-resolved scattering curves almost quantitatively, as shown in the left panel of Figure 3. In this regard, the solid line for t = 0 min corresponds to the final fit following Equation (5), with a PVP chain contour length of L = 80 ± 1 nm, a Kuhn length of b = 3.3 ± 0.3 nm, and a cross-section radius of R_C = 0.27 ± 0.01 nm. For the solid line at t = 87 min (T = 58 °C), Equation (6) was used. Here, the previously determined characteristics of the PVP chains with a slightly adjusted Kuhn length of b = 4.0 ± 0.3 nm were applied, while the polydispersity $p_i = \sigma_i / R_{ZnO,i0}$ = 0.18 of both the ZnO particles and clusters was kept constant. Hence, the analysis of the USAXS/SAXS curve measured after the termination of the reaction yields average radii of $R_{ZnO,f}$ = 1.5 ± 0.3 nm and $R_{ZnO\text{-}cluster,f}$ = 10.5 ± 1.9 nm for the individual ZnO particles and their clusters, respectively. While the size of the individual ZnO particles matches that from the TEM images within the measurement error, the size of the clusters is slightly larger, most probably due to a surrounding PVP layer, as discussed before. The respective contributions of Equation (6) to the final fit are shown in Figure S3 in the Supplementary Materials.

Also, for the ZnO formation performed at T = 63 °C, starting from T = 25 °C, the final ZnO particle and cluster size obtained from TEM images ($R_{ZnO,TEM}$ = 1.7 ± 0.5 nm, $R_{ZnO\text{-}cluster,TEM}$ = 9.7 ± 1.9 nm), shown exemplarily in Figure S4 in the Supplementary Materials, are in good accordance with that from USAXS/SAXS ($R_{ZnO,f}$ = 1.5 ± 0.3 nm, $R_{ZnO\text{-}cluster,f}$ = 11.8 ± 2.1 nm). Comparing the size of the clusters obtained from CBD at the two different temperatures, the temperature increase leads to slightly larger ZnO clusters, which is related to accelerated kinetics at higher temperatures. Hereby, a higher number of individual ZnO particles might be formed, which are subsequently consumed faster by the formation of the clusters.

Figure 4 shows selected time-resolved USAXS scattering curves recorded at T = 58 °C (Figure 4a) and T = 63 °C (Figure 4b), which are almost quantitatively described by the combination of the flexible cylinder model [70,71] and the two spherical form factor contributions [80]. It should be noted that for t < 13 min, we could not obtain any information about the ZnO formation due to the dominance of the PVP scattering contribution.

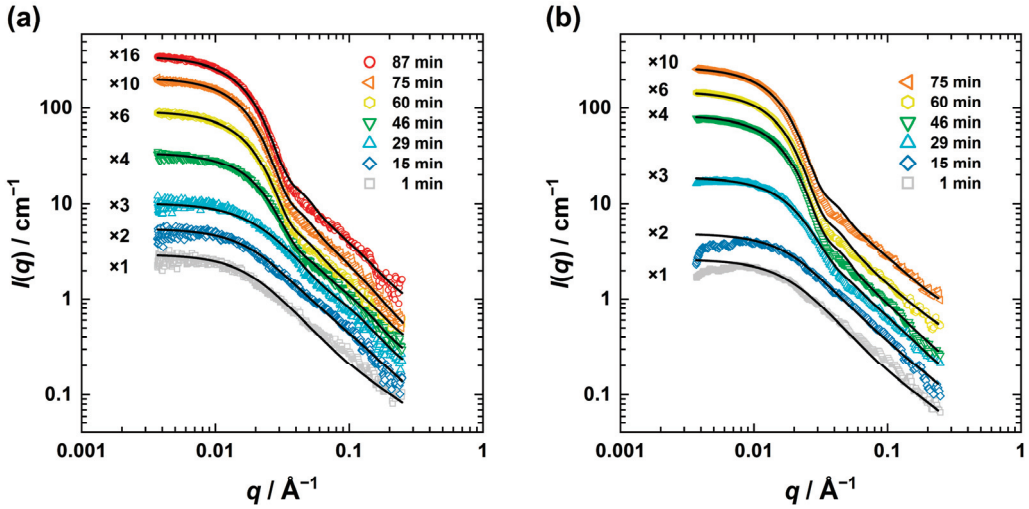

Figure 4. Selected slit-smeared USAXS curves measured during the ZnO particle formation at T = 58 °C (**a**) and T = 63 °C (**b**) at different times described by a combination of the flexible cylinder model [70,71] with two sphere form factor contributions [80].

The results of the quantitative analysis of the scattering data according to Equation (6), with the free fitting parameters being the mean radii from the ZnO particles, $R_{ZnO,f}$, and that from the clusters $R_{ZnO,cluster,f}$ as well as their volume fractions ϕ_{ZnO} and $\phi_{ZnO\text{-}cluster}$, are shown in Figures 5 and 6. While Figure 5 shows the radius (R) and $R^3(t)$ of the ZnO nanoparticles and ZnO clusters as a function of time for T = 58 °C and T = 63 °C, the time evolution of the respective volume fraction for T = 58 °C is shown in Figure 6.

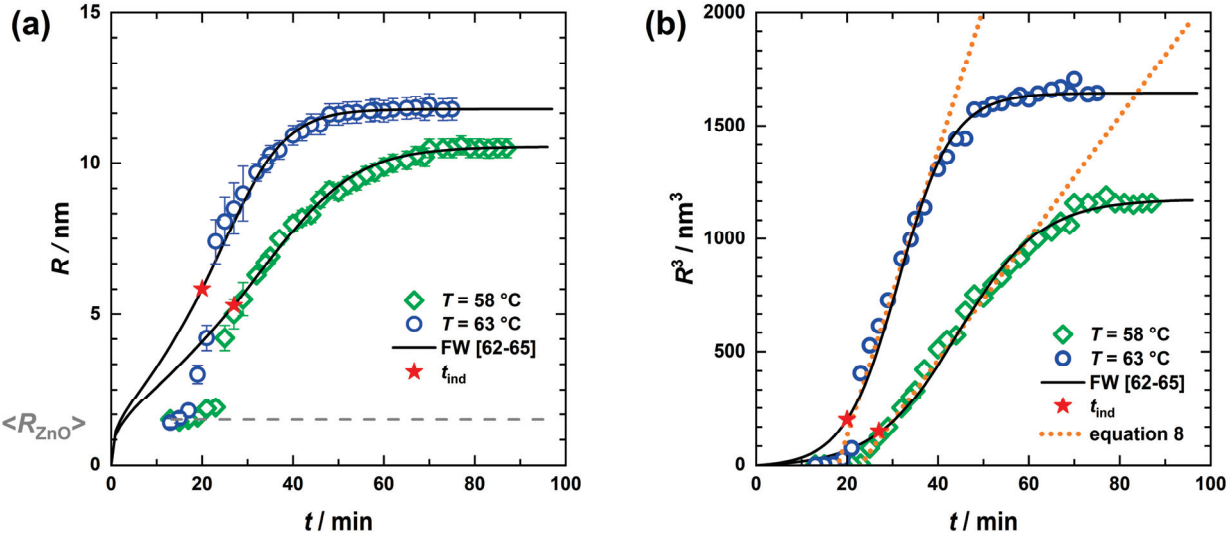

Figure 5. Time evolution of ZnO cluster radii at T = 58 °C (◇) and T = 63 °C (○) with ZnO nanoparticles (dashed line) held constant (**a**) obtained from the USAXS curve analysis, as well as the corresponding cube of radii (**b**). A phenomenological approach can describe the growth period (dotted lines), yet to fit the nucleation and growth phase the Finke–Watzky model [62–65] (solid lines) is more suitable and also provides the induction time t_{ind} (red stars).

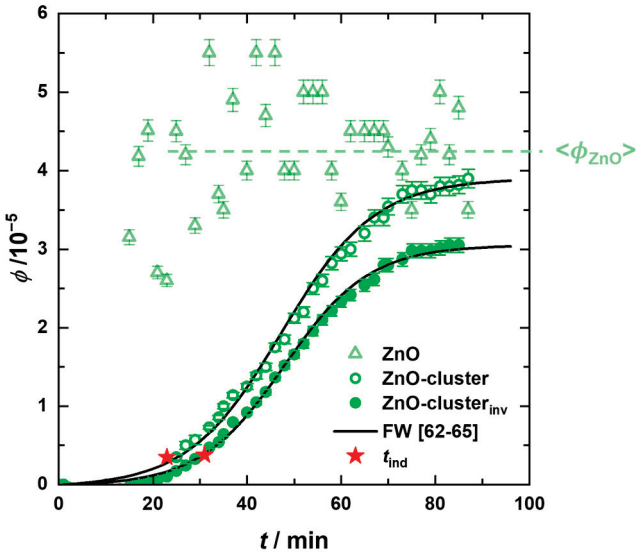

Figure 6. Volume fractions of the ZnO nanoparticles $\phi_{ZnO}(t)_{I(q)}$ and the clusters $\phi_{ZnO\text{-}cluster}(t)_{I(q)}$ determined from the fitted USAXS curves at T = 58 °C, together with the cluster volume fractions obtained from the invariant analysis $\phi_{ZnO\text{-}cluster,inv}(t)$ as a function of time. The solid lines correspond to the Finke–Watzky modelling [62–65] which also yields the induction time t_{ind} (red stars).

As can be seen in Figure 5a, the size of the formed ZnO species for T = 58 °C remains almost constant during a short period (~between t = 13 and 18 min). Thereafter, cluster growth occurs, where the average size of these clusters initially increases rapidly before

slowly approaching the final size due to the consumption of zinc precursor. Performing the reaction at T = 63 °C, a similar but steeper growth profile was obtained, during which the clusters are consistently larger. For comparison, the ZnO particle size appeared to remain constant and was kept fixed at $R_{ZnO,f}$ = 1.5 ± 0.3 nm (dashed line in Figure 5a).

Interestingly, when plotting ${R^3}_{ZnO\text{-}cluster,f}$ as a function of time, as shown in Figure 5b, a linear increase starting from t~20 min is observed, which levels off to a plateau. The former region can be associated with the growth phase of the ZnO clusters by agglomeration of individual ZnO particles. Thus, a reasonable description of the growth phase is given by

$$R(t)^3 = k(t_{cluster}) + {R_{ZnO,f}}^3 \quad (8)$$

with k being the temperature-dependent growth rate constant, and $t_{cluster}$ being the time after which clusters start to grow $t_{cluster} = t - t_{cluster,0}$ and $R_{ZnO,f}$ the individual ZnO nanoparticle radius. The analysis of ${R^3}_{ZnO\text{-}cluster,f}(t)$ with Equation (8) (dotted lines in Figure 5b) yielded $k(T = 58\ ^\circ C) = 0.44 \pm 0.01\ nm^3/s$ with $t_{cluster,0}$ (T = 58 °C) = 23 min and $k(T = 63\ ^\circ C) = 1.05 \pm 0.01\ nm^3/s$ with $t_{cluster,0}$ (T = 63 °C) = 18 min. For comparison, much smaller rate constants in the order of ~10^{-3} nm^3/s were found for the formation of ZnO particles in propanol, without the addition of a polymer such as PVP [82,83].

The large growth rates obtained here can be explained by the occurrence of depletion forces [84,85], as observed during ZnS particle formation in the presence of PVP, where cluster growth via depletion forces appeared as soon as the particle surface was too crowded by PVP [86].

While large parts of the ZnO cluster growth phase can reasonably be described by this power law approach, neither the nucleation phase nor the growth deceleration can be described. Furthermore, the occurrence of depletion forces is not considered in this model. Thus, to describe the sigmoidal time evolution of R^3(t), the two-step Finke–Watzky (FW) model was used. In this model slow, continuous nucleation $\left(A \xrightarrow{k_1} B\right)$ is followed by autocatalytic growth $\left(A + B \xrightarrow{k_2} 2B\right)$ with the nucleation (k_1) and growth (k_2) constants [62–64]. Here, the cube of the radius as a function of time is given by [65]

$$t \geq t_{ind} \qquad R(t)^3_{FW} = R_f^3 \cdot \left(1 - \frac{k_1 + k_2 \cdot [A]_0}{k_2 \cdot [A]_0 + k_1\ e^{(k_1 + k_2 \cdot [A]_0)t}}\right) \quad (9)$$

where R_f corresponds to the final cluster size, and $[A]_0$ to the starting concentration of Zn^{2+}. The induction time, here related to the time after which agglomeration of the ZnO particles into clusters is accelerated, is defined by the intersection of the initial and maximal slope and can be determined according to [65]:

$$t_{ind} = \frac{k_1 + k_2 \cdot [A]_0}{\left(k_1 - k_2 \cdot [A]_0\right)^2} \cdot ln\left(\frac{k_2 \cdot [A]_0}{k_1}\right) + \frac{2}{k_1 - k_2 \cdot [A]_0}. \quad (10)$$

Furthermore, the ratio of the growth to nucleation rate constant $S = \frac{k_2}{k_1}$ (M^{-1}) is a measure of kinetic control, indicating whether nucleation of new particles or growth of the existing clusters is preferred. Thus, larger S values yield narrow size distributions. In addition, larger ratios were shown to be related to larger clusters [87]. Note that the two-step FW model can be extended to include bimolecular aggregation ($B + B \rightarrow C$) [88] and autocatalytic agglomeration ($B + C \rightarrow 1.5\ C$) [89,90]. However, this was not performed here to keep the number of free-fitting parameters at a minimum.

As can be seen from the solid lines in Figure 5, the FW model provides a quantitative description of the time evolution of the ZnO cluster size for $t \geq t_{ind}$. The systematic mismatch of the model at $t < t_{ind}$ could be due, on one hand, to a nucleation rate that is not constant during the heating process but increases strongly. On the other hand, the spherical form factor used in the analysis of the scattering data represents only an

approximation, especially for clusters consisting of a few ZnO particles. The obtained parameters, summarized in Table 2, reflect what was already evident from the USAXS data: the induction time shortens from t_{ind} = 27 min at T = 58 °C to t_{ind} = 20 min for T = 63 °C, while the growth rate constant k_2 increases considerably by a factor of 50% at higher temperatures to $k_2[A]_0 = 0.17\ s^{-1}$. The nucleation rate, however, does not change. Consequently, the ratio of the growth-to-nucleation rate constant S is higher for T = 63 °C, which also confirms the previously mentioned assumption of a faster growth rate for higher temperatures.

Table 2. Values for the nucleation rate k_1 and growth rate constant $k_2[A]_0$ determined from the two-step Finke–Watzky model [62–65] together with the induction time t_{ind} and the ratio of the rate constants S obtained from the size evolution profile $R^3(t)_{FW}$ and the volume fractions from the invariant analysis $\phi_{ZnO\text{-}cluster,\ inv}(t)_{FW}$. We estimate the relative errors to be about 10%.

	$R^3(t)_{FW}$				$\phi_{ZnO\text{-}cluster,\ inv}(t)_{FW}$			
	k_1/s^{-1}	$k_2[A]_0/s^{-1}$	t_{ind}/min	S/M^{-1}	k_1/s^{-1}	$k_2[A]_0/s^{-1}$	t_{ind}/min	S/M^{-1}
58 °C	8.0×10^{-4}	0.11	27	141	5.5×10^{-4}	0.11	31	200
63 °C	8.0×10^{-4}	0.17	20	213	5.0×10^{-4}	0.17	23	340

The FW model assumes continuous nucleation of ZnO particles. This can be indeed observed in the volume fraction profile of the ZnO particles (▲) for T = 58 °C in Figure 6, where an initial increase is followed by reaching an almost constant value, while the volume fraction of the cluster (○) follows a sigmoidal profile. These results suggest that new ZnO particles are formed continuously throughout the reaction, feeding the clusters, which in turn grow simultaneously. Hence, at intermediate times, an equilibrium is established between ZnO particles' formation and consumption.

Since R^3 is proportional to the volume fraction, Equation (9) can also be used to model $\phi_{ZnO\text{-}cluster}(t)_{I(q)}$ (○) (see solid line in Figure 6), yielding nearly identical values for the FW parameters as compared to the $R^3(t)$-data with $k_1(T = 58\ °C) = 8.5 \times 10^{-4}$ 1/s, $k_2[A]_0$ (T = 58 °C) = 0.11 1/s with $t_{ind}(T = 58\ °C)$ = 29 min.

In a complementary approach, we determined the volume fraction of ZnO clusters $\phi_{ZnO\text{-}cluster}$ from the shape- and size-independent scattering invariant Q of the time-resolved desmeared USAXS scattering curves for $q \leq 0.04\ Å^{-1}$. It should be noted that the invariant was only determined in the low q-part, since on the one hand, the scattering in the large q-part is dominated by the scattering of PVP, and on the other hand, the USAXS data are noisy in this range. To account only for the scattering of the ZnO clusters, the scattering invariant determined for t = 1 min was subtracted from all other data, resulting in a reduced invariant Q^*, according to

$$Q^* = Q(t) - Q(t = 1\ \text{min}) = \int_0^{0.04 Å^{-1}} q^2 I(q) dq = 2\pi^2 (\Delta\rho)^2 \phi_{ZnO-cluster}(1 - \phi_{ZnO-cluster}) \quad (11)$$

where $\Delta\rho^2 = |\rho_{ZnO} - \rho_{MeOH}|^2$. In Figure 6, the obtained cluster volume fraction $\phi_{ZnO\text{-}cluster,inv}(t)$ (●) for T = 58 °C is plotted as a function of time. Comparing the cluster volume fractions obtained from the model analysis of the USAXS data and the invariant, i.e., $\phi_{ZnO\text{-}cluster,I(q)}$ and $\phi_{ZnO\text{-}cluster,inv}$, slightly lower values are found for the latter, which might be a consequence of the finite q-range used for the invariant determination as well as the approximation of spherical clusters with compact packing of ZnO particles and a homogeneous scattering length density distribution.

The profiles of the cluster volume fraction $\phi_{ZnO\text{-}cluster,inv}(t)$ were also described using the FW model (in Figure S5 of the Supplementary Materials, the profiles obtained for T = 58 °C and T = 63 °C are shown for comparison). A comparison of the parameters (Table 2) obtained from the analysis of the $R^3(t)$-data and $\phi_{ZnO\text{-}cluster,inv}(t)$-data, respectively, reveal the same growth rate constants k_2 and induction times t_{ind}, which are similar within the measurement uncertainty. The smaller value of the nucleation rate constant for the

$\phi_{\text{ZnO-cluster,inv}}(t)$-data might also be a consequence of the finite q-range used for the invariant determination. Consequently, larger S-values in the analysis of the $\phi_{\text{ZnO-cluster,inv}}(t)$-data are obtained.

To conclude the in situ study of ZnO particle formation and growth, we found that shortly after heating the precursor solution, ZnO nanoparticles of the order of $R_{\text{ZnO}} \approx 1.5$ nm are initially formed, followed by the formation of clusters. An increase in the reaction temperature from 58 °C to 63 °C resulted in the acceleration of the reaction and the formation of larger clusters. From the time evolution of the cube of radius, a linear relationship is apparent at intermediate times. Depletion forces caused by the high volume fraction of PVP might explain the relatively high growth rate. A quantitative description of the time evolution of the ZnO nanoparticle cluster radius, the corresponding cube of the radius, as well as the volume fraction, could be achieved by the Finke–Watzky model [62–65] with slow, continuous nucleation of individual ZnO particles followed by autocatalytic growth of the clusters, as illustrated in Figure 7. From the analysis of the kinetic data, the higher ratio of growth to nucleation rate explains that slightly larger clusters are formed at the higher temperature of 63 °C.

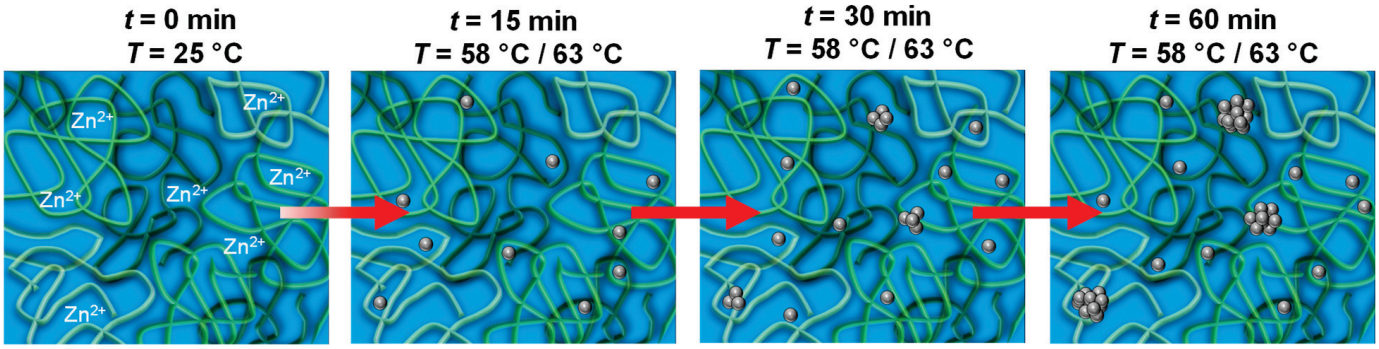

Figure 7. Schematic illustration of the ZnO formation through CBD starting from a methanolic ZnO precursor solution. The organic additive PVP (green strings) forms an entangled network in which the zinc ions are homogeneously distributed. Upon heating, ZnO particles (grey spheres) are continuously formed, which eventually aggregate into clusters.

4. Conclusions

A crucial step for the synthesis of metal oxide inverse opals is the mineralization of the voids of a close-packed polymer nanoparticle templates via the chemical bath deposition (CBD) process. Intrigued by the vision of tuning the size and shape of ZnO particles, we aimed to gain more insight into the particle formation in an additive containing precursor solution by in situ time-resolved ultra-small- and small-angle X-ray scattering (USAXS/SAXS).

First, we used in-house SAXS and USAXS/SAXS to study the structure of polyvinylpyrrolidone (PVP) applied as structure directing agent for the ZnO formation in the methanolic precursor solution at $T = 25$ °C. We found that at the volume fraction of $\phi_{\text{PVP}} = 7.1 \times 10^{-2}$ used in the CBD process, the polymer forms a network of entangled chains in which ions of the ZnO precursor salt and the organic base are distributed, causing the polymer chains to adopt a semiflexible behavior.

We then followed the ZnO formation using in situ USAXS/SAXS by heating the precursors solution from $T = 25$ °C to $T = 58$ °C and 63 °C, respectively. A significant increase in the intensity of the forward scattering and the formation of an additional weak shoulder was observed after 13 min, both of which occur more rapidly at $T = 63$ °C. The origin of the two scattering contributions was clarified from post-synthesis TEM images, which clearly showed the presence of two ZnO species: ZnO nanoparticles with a radius of $R_{\text{ZnO,TEM}} = 1.5 \pm 0.5$ nm and clusters of these with $R_{\text{ZnO-cluster,TEM}} = 8.5 \pm 1.4$ nm and $R_{\text{ZnO-cluster,TEM}} = 9.7 \pm 1.9$ nm at $T = 58$ °C and 63 °C, respectively. Through this additional information, we were able to quantitatively analyze the time-resolved USAXS/SAXS data

by additively combining the scattering contribution of the PVP network with the scattering contributions of the individual ZnO particles and their clusters. This analysis revealed that the radius of the formed individual ZnO particles ($R_{ZnO,f}$ = 1.5 ± 0.3 nm) remains constant over time for both temperatures, while the radius of the particle clusters increases from the induction time onwards to $R_{ZnO\text{-}cluster,f}$ = 10.5 ± 1.9 nm at T = 58 °C and, $R_{ZnO\text{-}cluster,f}$ = 11.8 ± 2.1 nm at T = 63 °C, with $R^3(t)$ following a sigmoidal profile.

From the linear relationship of $R^3(t)$ at intermediate times, relatively large rate cluster growth constants were determined, which might indicate PVP-induced depletion forces. Finally, using the Finke–Watzky two-step model, we were able to quantitatively describe the ZnO formation with slow, continuous nucleation of individual ZnO particles followed by autocatalytic growth of the clusters. A faster growth rate of the clusters compared to the nucleation of new ZnO particles was observed at higher temperatures, which thus explains the formation of larger clusters at 63 °C.

The determination of the kinetics of ZnO formation, synthesized by CBD using a methanolic solution and PVP as a stabilizing and structuring agent, will provide us with valuable insights into the understanding of ZnO deposition in the voids of densely packed polymer nanoparticle templates, where both surface and confinement effects are expected.

Supplementary Materials: The following supporting information can be downloaded at https://www.mdpi.com/article/10.3390/nano13152180/s1: SAXS fitting parameters of PVP in methanol at $\phi_{PVP} = 7.1 \times 10^{-2}$ before and after adding 12.5 mM $ZnAc_2$ and 26.3 mM TEAOH obtained with the polymer with excluded volume model (Table S1) or the correlation length model (Table S2) combined with a Gaussian, respectively; Figure S1: Slit-smeared SAXS curves of PVP in methanol at various volume fractions ϕ; SAXS fitting parameters from PVP in methanol at ϕ_{PVP} = 1.0, 2.0, 4.0, and 7.1×10^{-2} obtained with the polymer with excluded volume model (Table S3) and the correlation length model (Table S4) combined with a Gaussian, respectively. Figure S2: Obtained fitting parameters for PVP in methanol at various volume fractions ϕ_{PVP}; Figure S3: Final fit for the scattering curve of the precursor solution after heating to T = 58 °C for t = 87 min with the respective scattering contributions. Figure S4: TEM image taken after the ZnO synthesis for T = 63 °C with the corresponding volume-weighted size distribution of the ZnO particles and clusters, described by a Gaussian size distribution, respectively. Figure S5: Time evolution of the volume fraction $\phi_{ZnO\text{-}cluster,inv}$ of ZnO particle clusters determined from the invariant analysis ($\phi_{invariant}$) of the USAXS curves up to $q \leq 0.04$ Å^{-1}. The profiles were described by the two-step Finke–Watzky model (solid lines) from which the induction time t_{ind} (stars) were calculated.

Author Contributions: Conceptualization, K.A. and T.S.; validation, K.A. and N.P.; formal analysis, K.A.; investigation, K.A., N.P., I.K. and J.I.; resources, P.A.; data curation, K.A. and T.S.; writing—original draft preparation, K.A.; writing—review and editing, K.A., P.A., J.B., Y.L., J.I. and T.S.; visualization, K.A.; supervision, Y.L. and T.S.; project administration, T.S.; funding acquisition, T.S. All authors have read and agreed to the published version of the manuscript.

Funding: Funded by the Deutsche Forschungsgemeinschaft (DFG, German Research Foundation)—Project-ID 358283783—SFB 1333/2 2022.

Institutional Review Board Statement: Not applicable.

Informed Consent Statement: Not applicable.

Data Availability Statement: The data presented in this study are available on request from the corresponding author.

Acknowledgments: K.A. would like to acknowledge the SFB 1333 for the generous financial support during her research stay at the group of Y.L., as well as the National Institute of Standards and Technology (NIST) and the NIST Center for Neutron Research (NCNR). Preliminary SAXS experiments were performed on beamline ID02 at the European Synchrotron Radiation Facility (ESRF), Grenoble, France. K.A. and T.S. are grateful to Theyencheri Narayanan and Lauren Matthews at the ESRF for providing assistance in using the beam-line ID02 and for the fruitful discussion on optimizing the experimental conditions and solvent scattering subtraction. This research, furthermore, used resources of the Advanced Photon Source, a U.S. Department of Energy (DOE) Office of Science user facility operated for the DOE Office of Science by Argonne National Laboratory under Contract

No. DE-AC02-06CH11357. Y.L. acknowledges the support by the Center for High Resolution Neutron Scattering, a partnership between the National Institute of Standards and Technology and the National Science Foundation under Agreement No. DMR-2010792.

Conflicts of Interest: The authors declare no conflict of interest. The funders had no role in the design of the study, in the collection, analyses, or interpretation of data; in the writing of the manuscript; and in the decision to publish the results. Certain commercial equipment, instruments, or materials (or suppliers, or software, ...) are identified in this paper to foster understanding. Such identification does not imply recommendation or endorsement by the National Institute of Standards and Technology, nor does it imply that the materials or equipment identified are necessarily the best available for the purpose.

References

1. Sanchez, C.; Belleville, P.; Popall, M.; Nicole, L. Applications of advanced hybrid organic–inorganic nanomaterials: From laboratory to market. *Chem. Soc. Rev.* **2011**, *40*, 696–753. [CrossRef]
2. Sanchez, C.; Julián, B.; Belleville, P.; Popall, M. Applications of hybrid organic–inorganic nanocomposites. *J. Mater. Chem.* **2005**, *15*, 3559–3592. [CrossRef]
3. Mir, S.H.; Nagahara, L.A.; Thundat, T.; Mokarian-Tabari, P.; Furukawa, H.; Khosla, A. Review—Organic-Inorganic Hybrid Functional Materials: An Integrated Platform for Applied Technologies. *J. Electrochem. Soc.* **2018**, *165*, B3137–B3156. [CrossRef]
4. Eder, D. Carbon Nanotube−Inorganic Hybrids. *Chem. Rev.* **2010**, *110*, 1348–1385. [CrossRef]
5. Khan, F.S.A.; Mubarak, N.M.; Khalid, M.; Khan, M.M.; Tan, Y.H.; Walvekar, R.; Abdullah, E.C.; Karri, R.R.; Rahman, M.E. Comprehensive review on carbon nanotubes embedded in different metal and polymer matrix: Fabrications and applications. *Crit. Rev. Solid State Mater. Sci.* **2021**, *47*, 837–864. [CrossRef]
6. Zou, H.; Wu, S.; Shen, J. Polymer/Silica Nanocomposites: Preparation, Characterization, Properties, and Applications. *Chem. Rev.* **2008**, *108*, 3893–3957. [CrossRef]
7. Adnan, M.M.; Dalod, A.R.M.; Balci, M.H.; Glaum, J.; Einarsrud, M.-A. In Situ Synthesis of Hybrid Inorganic–Polymer Nanocomposites. *Polymers* **2018**, *10*, 1129. [CrossRef] [PubMed]
8. Shenton, W.; Douglas, T.; Young, M.; Stubbs, G.; Mann, S. Inorganic-Organic Nanotube Composites from Template Mineralization of Tobacco Mosaic Virus. *Adv. Mater.* **1999**, *11*, 253–256. [CrossRef]
9. Lee, S.-Y.; Lim, J.-S.; Harris, M.T. Synthesis and application of virus-based hybrid nanomaterials. *Biotechnol. Bioeng.* **2012**, *109*, 16–30. [CrossRef]
10. Caruso, R.A.; Antonietti, M. Sol−Gel Nanocoating: An Approach to the Preparation of Structured Materials. *Chem. Mater.* **2001**, *13*, 3272–3282. [CrossRef]
11. Lei, Q.; Guo, J.; Kong, F.; Cao, J.; Wang, L.; Zhu, W.; Brinker, C.J. Bioinspired Cell Silicification: From Extracellular to Intracellular. *J. Am. Chem. Soc.* **2021**, *143*, 6305–6322. [CrossRef] [PubMed]
12. Parikh, H.; de Guire, M.R. Recent progress in the synthesis of oxide films from liquid solutions. *J. Ceram. Soc. Jpn.* **2009**, *117*, 228–235. [CrossRef]
13. Koczkur, K.M.; Mourdikoudis, S.; Polavarapu, L.; Skrabalak, S.E. Polyvinylpyrrolidone (PVP) in nanoparticle synthesis. *Dalton Trans.* **2015**, *44*, 17883–17905. [CrossRef]
14. Carreón-Moncada, I.; González, L.; Rodríguez-Galicia, J.; Rendón-Angeles, J. Chemical deposition of CdS films by an ammonia-free process with amino acids as complexing agents. *Thin Solid Film.* **2016**, *599*, 166–173. [CrossRef]
15. Enríquez, J.P.; Mathew, X. Influence of the thickness on structural, optical and electrical properties of chemical bath deposited CdS thin films. *Sol. Energy Mater. Sol. Cells* **2003**, *76*, 313–322. [CrossRef]
16. Lee, J.-H. Structural and optical properties of CdS thin films on organic substrates for flexible solar cell applications. *J. Electroceramics* **2006**, *17*, 1103–1108. [CrossRef]
17. Preda, N.; Enculescu, M.; Gherendi, F.; Matei, E.; Toimil-Molares, M.; Enculescu, I. Synthesis of CdS nanostructures using template-assisted ammonia-free chemical bath deposition. *J. Phys. Chem. Solids* **2012**, *73*, 1082–1089. [CrossRef]
18. Shimizu, K.; Imai, H.; Hirashima, H.; Tsukuma, K. Low-temperature synthesis of anatase thin films on glass and organic substrates by direct deposition from aqueous solutions. *Thin Solid Film.* **1999**, *351*, 220–224. [CrossRef]
19. Santhiya, D.; Burghard, Z.; Greiner, C.; Jeurgens, L.P.H.; Subkowski, T.; Bill, J. Bioinspired Deposition of TiO_2 Thin Films Induced by Hydrophobins. *Langmuir* **2010**, *26*, 6494–6502. [CrossRef]
20. Dussan, A.; Bohórquez, A.; Quiroz, H.P. Effect of annealing process in TiO_2 thin films: Structural, morphological, and optical properties. *Appl. Surf. Sci.* **2017**, *424*, 111–114. [CrossRef]
21. O'Brien, P.; Saeed, T.; Knowles, J. Speciation and the nature of ZnO thin films from chemical bath deposition. *J. Mater. Chem.* **1996**, *6*, 1135–1139. [CrossRef]
22. Tseng, Y.-H.; Lin, H.-Y.; Liu, M.-H.; Chen, Y.-F.; Mou, C.-Y. Biomimetic Synthesis of Nacrelike Faceted Mesocrystals of ZnO−Gelatin Composite. *J. Phys. Chem. C* **2009**, *113*, 18053–18061. [CrossRef]
23. Shi, Z.; Walker, A.V. Chemical Bath Deposition of ZnO on Functionalized Self-Assembled Monolayers: Selective Deposition and Control of Deposit Morphology. *Langmuir* **2015**, *31*, 1421–1428. [CrossRef] [PubMed]

24. Fortunato, E.; Barquinha, P.; Pimentel, A.; Gonçalves, A.; Marques, A.; Pereira, L.; Martins, R. Recent advances in ZnO transparent thin film transistors. *Thin Solid Film.* **2005**, *487*, 205–211. [CrossRef]
25. Gordillo, G.; Pena, J. Development of system to grow ZnO films by plasma assisted reactive evaporation with improved thickness homogeneity for using in solar cells. *J. Mater. Res. Technol.* **2022**, *19*, 1191–1202. [CrossRef]
26. Zhang, S.; Li, H.; Wang, X.; Liu, Y.; Dai, J.; Chen, C. Highly Integrated In Situ Photoenergy Gas Sensor with Deep Ultraviolet LED. *ACS Omega* **2020**, *5*, 9985–9990. [CrossRef] [PubMed]
27. Ahn, M.-W.; Park, K.-S.; Heo, J.-H.; Park, J.-G.; Kim, D.-W.; Choi, K.J.; Lee, J.-H.; Hong, S.-H. Gas sensing properties of defect-controlled ZnO-nanowire gas sensor. *Appl. Phys. Lett.* **2008**, *93*, 263103. [CrossRef]
28. Ryu, Y.R.; Lubguban, J.A.; Lee, T.S.; White, H.W.; Jeong, T.S.; Youn, C.J.; Kim, B.J. Excitonic ultraviolet lasing in ZnO-based light emitting devices. *Appl. Phys. Lett.* **2007**, *90*, 131115. [CrossRef]
29. Dong, H.; Zhou, B.; Li, J.; Zhan, J.; Zhang, L. Ultraviolet lasing behavior in ZnO optical microcavities. *J. Mater.* **2017**, *3*, 255–266. [CrossRef]
30. Lipowsky, P.; Jia, S.; Hoffmann, R.C.; Jin-Phillipp, N.Y.; Bill, J.; Rühle, M. Thin film formation by oriented attachment of polymer-capped nanocrystalline ZnO. *Int. J. Mater. Res.* **2006**, *97*, 607–613. [CrossRef]
31. Lipowsky, P.; Hoffmann, R.C.; Welzel, U.; Bill, J.; Aldinger, F. Site-Selective Deposition of Nanostructured ZnO Thin Films from Solutions Containing Polyvinylpyrrolidone. *Adv. Funct. Mater.* **2007**, *17*, 2151–2159. [CrossRef]
32. Lipowsky, P.; Burghard, Ž.; Jeurgens, L.P.H.; Bill, J.; Aldinger, F. Laminates of zinc oxide and poly(amino acid) layers with enhanced mechanical performance. *Nanotechnology* **2007**, *18*, 345707. [CrossRef]
33. Lipowsky, P.; Hedin, N.; Bill, J.; Hoffmann, R.C.; Ahniyaz, A.; Aldinger, F.; Bergström, L. Controlling the Assembly of Nanocrystalline ZnO Films by a Transient Amorphous Phase in Solution. *J. Phys. Chem. C* **2008**, *112*, 5373–5383. [CrossRef]
34. Lipowsky, P.; Hirscher, M.; Hoffmann, R.C.; Bill, J.; Aldinger, F. Zinc oxide microcapsules obtained via a bio-inspired approach. *Nanotechnology* **2007**, *18*, 165603. [CrossRef]
35. Qawasmi, Y.; Atanasova, P.; Jahnke, T.; Burghard, Z.; Müller, A.; Grassberger, L.; Strey, R.; Bill, J.; Sottmann, T. Synthesis of nanoporous organic/inorganic hybrid materials with adjustable pore size. *Colloid Polym. Sci.* **2018**, *296*, 1805–1816. [CrossRef]
36. Atanasova, P.; Weitz, R.T.; Gerstel, P.; Srot, V.; Kopold, P.; van Aken, P.A.; Burghard, M.; Bill, J. DNA-templated synthesis of ZnO thin layers and nanowires. *Nanotechnology* **2009**, *20*, 365302. [CrossRef] [PubMed]
37. Atanasova, P.; Rothenstein, D.; Schneider, J.J.; Hoffmann, R.C.; Dilfer, S.; Eiben, S.; Wege, C.; Jeske, H.; Bill, J. Virus-Templated Synthesis of ZnO Nanostructures and Formation of Field-Effect Transistors. *Adv. Mater.* **2011**, *23*, 4918–4922. [CrossRef]
38. Atanasova, P.; Stitz, N.; Sanctis, S.; Maurer, J.H.M.; Hoffmann, R.C.; Eiben, S.; Jeske, H.; Schneider, J.J.; Bill, J. Genetically Improved Monolayer-Forming Tobacco Mosaic Viruses to Generate Nanostructured Semiconducting Bio/Inorganic Hybrids. *Langmuir* **2015**, *31*, 3897–3903. [CrossRef]
39. Stitz, N.; Eiben, S.; Atanasova, P.; Domingo, N.; Leineweber, A.; Burghard, Z.; Bill, J. Piezoelectric Templates—New Views on Biomineralization and Biomimetics. *Sci. Rep.* **2016**, *6*, 26518. [CrossRef]
40. Atanasova, P.; Hoffmann, R.C.; Stitz, N.; Sanctis, S.; Burghard, Z.; Bill, J.; Schneider, J.J.; Eiben, S. Engineered nanostructured virus/ZnO hybrid materials with dedicated functional properties. *Bioinspired Biomim. Nanobiomaterials* **2019**, *8*, 2–15. [CrossRef]
41. Abitaev, K.; Qawasmi, Y.; Atanasova, P.; Dargel, C.; Bill, J.; Hellweg, T.; Sottmann, T. Adjustable polystyrene nanoparticle templates for the production of mesoporous foams and ZnO inverse opals. *Colloid Polym. Sci.* **2021**, *299*, 243–258. [CrossRef]
42. Kousik, S.R.; Sipp, D.; Abitaev, K.; Li, Y.; Sottmann, T.; Koynov, K.; Atanasova, P. From Macro to Mesoporous ZnO Inverse Opals: Synthesis, Characterization and Tracer Diffusion Properties. *Nanomaterials* **2021**, *11*, 196. [CrossRef]
43. Lin, X.; Chen, M. Fabrication and Photo-Detecting Performance of 2D ZnO Inverse Opal Films. *Appl. Sci.* **2016**, *6*, 259. [CrossRef]
44. Kiyomi, Y.; Shiraiwa, N.; Nakazawa, T.; Fukawa, A.; Oshio, K.; Takase, K.; Ito, T.; Shingubara, S.; Shimizu, T. Fabrication and UV photoresponse of ordered ZnO nanonets using monolayer colloidal crystal template. *Micro Nano Eng.* **2022**, *16*, 100160. [CrossRef]
45. Li, Q.; Yang, C. Facile fabrication of Ag_3PO_4 supported on ZnO inverse opals for enhancement of solar-driven photocatalysis. *Mater. Lett.* **2017**, *199*, 168–171. [CrossRef]
46. Meldrum, F.C.; Cölfen, H. Controlling Mineral Morphologies and Structures in Biological and Synthetic Systems. *Chem. Rev.* **2008**, *108*, 4332–4432. [CrossRef] [PubMed]
47. Rieger, J.; Kellermeier, M.; Nicoleau, L. Die Bildung von Nanopartikeln und Nanostrukturen—$CaCO_3$, Zement und Polymere aus Sicht der Industrie. *Angew. Chem.* **2014**, *126*, 12586–12603. [CrossRef]
48. Caetano, B.L.; Santilli, C.V.; Pulcinelli, S.H.; Briois, V. SAXS and UV–Vis combined to Quick-XAFS monitoring of ZnO nanoparticles formation and growth. *Phase Transit.* **2011**, *84*, 714–725. [CrossRef]
49. Caetano, B.L.; Santilli, C.V.; Meneau, F.; Briois, V.; Pulcinelli, S.H. In Situ and Simultaneous UV−vis/SAXS and UV−vis/XAFS Time-Resolved Monitoring of ZnO Quantum Dots Formation and Growth. *J. Phys. Chem. C* **2011**, *115*, 4404–4412. [CrossRef]
50. Caetano, B.L.; Briois, V.; Pulcinelli, S.H.; Meneau, F.; Santilli, C.V. Revisiting the ZnO Q-dot Formation Toward an Integrated Growth Model: From Coupled Time Resolved UV–Vis/SAXS/XAS Data to Multivariate Analysis. *J. Phys. Chem. C* **2017**, *121*, 886–895. [CrossRef]
51. Penn, R.L.; Banfield, J.F. Imperfect Oriented Attachment: Dislocation Generation in Defect-Free Nanocrystals. *Science* **1998**, *281*, 969–971. [CrossRef]
52. Ribeiro, C.; Lee, E.J.H.; Longo, E.; Leite, E.R. A Kinetic Model to Describe Nanocrystal Growth by the Oriented Attachment Mechanism. *ChemPhysChem* **2005**, *6*, 690–696. [CrossRef] [PubMed]

53. Lifshitz, I.; Slyozov, V. The kinetics of precipitation from supersaturated solid solutions. *J. Phys. Chem. Solids* **1961**, *19*, 35–50. [CrossRef]
54. Wagner, C. Theorie der Alterung von Niederschlägen durch Umlösen (Ostwald-Reifung). *Z. Electrochem.* **1961**, *65*, 581–591. [CrossRef]
55. Herbst, M.; Hofmann, E.; Förster, S. Nucleation and Growth Kinetics of ZnO Nanoparticles Studied by in Situ Microfluidic SAXS/WAXS/UV–Vis Experiments. *Langmuir* **2019**, *35*, 11702–11709. [CrossRef] [PubMed]
56. Biswas, K.; Das, B.; Rao, C.N.R. Growth Kinetics of ZnO Nanorods: Capping-Dependent Mechanism and Other Interesting Features. *J. Phys. Chem. C* **2008**, *112*, 2404–2411. [CrossRef]
57. Orthaber, D.; Bergmann, A.; Glatter, O. SAXS experiments on absolute scale with Kratky systems using water as a secondary standard. *J. Appl. Crystallogr.* **2000**, *33*, 218–225. [CrossRef]
58. Ilavsky, J.; Jemian, P.R.; Allen, A.J.; Zhang, F.; Levine, L.E.; Long, G.G. Ultra-small-angle X-ray scattering at the Advanced Photon Source. *J. Appl. Crystallogr.* **2009**, *42*, 469–479. [CrossRef]
59. Ilavsky, J.; Zhang, F.; Andrews, R.N.; Kuzmenko, I.; Jemian, P.R.; Levine, L.E.; Allen, A.J. Development of combined microstructure and structure characterization facility for in situ and *operando* studies at the Advanced Photon Source. *J. Appl. Crystallogr.* **2018**, *51*, 867–882. [CrossRef]
60. Ilavsky, J. Nika: Software for two-dimensional data reduction. *J. Appl. Crystallogr.* **2012**, *45*, 324–328. [CrossRef]
61. Ilavsky, J.; Jemian, P.R. Irena: Tool suite for modeling and analysis of small-angle scattering. *J. Appl. Crystallogr.* **2009**, *42*, 347–353. [CrossRef]
62. Watzky, M.A.; Finke, R.G. Transition Metal Nanocluster Formation Kinetic and Mechanistic Studies. A New Mechanism When Hydrogen Is the Reductant: Slow, Continuous Nucleation and Fast Autocatalytic Surface Growth. *J. Am. Chem. Soc.* **1997**, *119*, 10382–10400. [CrossRef]
63. Finney, E.E.; Finke, R.G. Nanocluster nucleation and growth kinetic and mechanistic studies: A review emphasizing transition-metal nanoclusters. *J. Colloid Interface Sci.* **2008**, *317*, 351–374. [CrossRef]
64. Finney, E.E.; Finke, R.G. Is There a Minimal Chemical Mechanism Underlying Classical Avrami-Erofe'ev Treatments of Phase-Transformation Kinetic Data? *Chem. Mater.* **2009**, *21*, 4692–4705. [CrossRef]
65. Bentea, L.; Watzky, M.A.; Finke, R.G. Sigmoidal Nucleation and Growth Curves Across Nature Fit by the Finke–Watzky Model of Slow Continuous Nucleation and Autocatalytic Growth: Explicit Formulas for the Lag and Growth Times Plus Other Key Insights. *J. Phys. Chem. C* **2017**, *121*, 5302–5312. [CrossRef]
66. Timaeva, O.; Pashkin, I.; Mulakov, S.; Kuzmicheva, G.; Konarev, P.; Terekhova, R.; Sadovskaya, N.; Czakkel, O.; Prevost, S. Synthesis and physico-chemical properties of poly(N-vinyl pyrrolidone)-based hydrogels with titania nanoparticles. *J. Mater. Sci.* **2020**, *55*, 3005–3021. [CrossRef]
67. Benoit, H. The diffusion of light by polymers dissolved in a good solvent. *Comptes Rendus* **1957**, *245*, 2244–2247.
68. Hammouda, B. SANS from homogeneous polymer mixtures: A unified overview. In *Polymer Characteristics*; Springer: Berlin/Heidelberg, Germany, 1993; pp. 87–133.
69. Hammouda, B.; Ho, D.L.; Kline, S. Insight into Clustering in Poly(ethylene oxide) Solutions. *Macromolecules* **2004**, *37*, 6932–6937. [CrossRef]
70. Pedersen, J.S.; Schurtenberger, P. Scattering Functions of Semiflexible Polymers with and without Excluded Volume Effects. *Macromolecules* **1996**, *29*, 7602–7612. [CrossRef]
71. Chen, W.-R.; Butler, P.D.; Magid, L.J. Incorporating Intermicellar Interactions in the Fitting of SANS Data from Cationic Wormlike Micelles. *Langmuir* **2006**, *22*, 6539–6548. [CrossRef]
72. Porod, G. Die Röntgenkleinwinkelstreuung von dichtgepackten kolloiden Systemen. *Kolloid Zeit.* **1951**, *124*, 83–114. [CrossRef]
73. Sapir, L.; Stanley, C.B.; Harries, D. Properties of Polyvinylpyrrolidone in a Deep Eutectic Solvent. *J. Phys. Chem. A* **2016**, *120*, 3253–3259. [CrossRef] [PubMed]
74. Hamada, F.; Kinugasa, S.; Hayashi, H.; Nakajima, A. Small-angle x-ray scattering from semidilute polymer solutions. I. Polystyrene in toluene. *Macromolecules* **1985**, *18*, 2290–2294. [CrossRef]
75. Distaso, M.; Taylor, R.N.K.; Taccardi, N.; Wasserscheid, P.; Peukert, W. Influence of the Counterion on the Synthesis of ZnO Mesocrystals under Solvothermal Conditions. *Chem.-A Eur. J.* **2011**, *17*, 2923–2930. [CrossRef] [PubMed]
76. Knappe, P.; Bienert, R.; Weidner, S.; Thünemann, A.F. Characterization of poly(N-vinyl-2-pyrrolidone)s with broad size distributions. *Polymer* **2010**, *51*, 1723–1727. [CrossRef]
77. Pavlov, G.M.; Panarin, E.F.; Korneeva, E.V.; Kurochkin, C.V.; Baikov, V.E.; Ushakova, V.N. Hydrodynamic properties of poly(1-vinyl-2-pyrrolidone) molecules in dilute solution. *Makromol. Chem.* **1990**, *191*, 2889–2899. [CrossRef]
78. Benoit, H.; Doty, P. Light Scattering from Non-Gaussian Chains. *J. Phys. Chem.* **1953**, *57*, 958–963. [CrossRef]
79. Narayanan, T.; Sztucki, M.; Van Vaerenbergh, P.; Léonardon, J.; Gorini, J.; Claustre, L.; Sever, F.; Morse, J.; Boesecke, P. A multipurpose instrument for time-resolved ultra-small-angle and coherent X-ray scattering. *J. Appl. Crystallogr.* **2018**, *51*, 1511–1524. [CrossRef]
80. Guinier, A.; Fournet, G. *Small-Angle Scattering of X-rays*; John Wiley & Sons: New York, NY, USA, 1955.
81. Jouault, N.; Crawford, M.K.; Chi, C.; Smalley, R.J.; Wood, B.; Jestin, J.; Melnichenko, Y.B.; He, L.; Guise, W.E.; Kumar, S.K. Polymer Chain Behavior in Polymer Nanocomposites with Attractive Interactions. *ACS Macro Lett.* **2016**, *5*, 523–527. [CrossRef]
82. Wong, E.M.; Bonevich, J.E.; Searson, P.C. Growth Kinetics of Nanocrystalline ZnO Particles from Colloidal Suspensions. *J. Phys. Chem. B* **1998**, *102*, 7770–7775. [CrossRef]

83. Hu, Z.; Santos, J.F.H.; Oskam, G.; Searson, P.C. Influence of the reactant concentrations on the synthesis of ZnO nanoparticles. *J. Colloid Interface Sci.* **2005**, *288*, 313–316. [CrossRef]
84. Asakura, S.; Oosawa, F. On Interaction between Two Bodies Immersed in a Solution of Macromolecules. *J. Chem. Phys.* **1954**, *22*, 1255–1256. [CrossRef]
85. Asakura, S.; Oosawa, F. Interaction between particles suspended in solutions of macromolecules. *J. Polym. Sci.* **1958**, *33*, 183–192. [CrossRef]
86. Ghosh, G.; Naskar, M.K.; Patra, A.; Chatterjee, M. Synthesis and characterization of PVP-encapsulated ZnS nanoparticles. *Opt. Mater.* **2006**, *28*, 1047–1053. [CrossRef]
87. Watzky, M.A.; Finke, R.G. Nanocluster Size-Control and "Magic Number" Investigations. Experimental Tests of the "Living-Metal Polymer" Concept and of Mechanism-Based Size-Control Predictions Leading to the Syntheses of Iridium(0) Nanoclusters Centering about Four Sequential Magic Numbers. *Chem. Mater.* **1997**, *9*, 3083–3095. [CrossRef]
88. Hornstein, B.J.; Finke, R.G. Transition-Metal Nanocluster Kinetic and Mechanistic Studies Emphasizing Nanocluster Agglomeration: Demonstration of a Kinetic Method That Allows Monitoring of All Three Phases of Nanocluster Formation and Aging. *Chem. Mater.* **2004**, *16*, 139–150. [CrossRef]
89. Besson, C.; Finney, E.E.; Finke, R.G. A Mechanism for Transition-Metal Nanoparticle Self-Assembly. *J. Am. Chem. Soc.* **2005**, *127*, 8179–8184. [CrossRef] [PubMed]
90. Besson, C.; Finney, E.E.; Finke, R.G. Nanocluster Nucleation, Growth, and Then Agglomeration Kinetic and Mechanistic Studies: A More General, Four-Step Mechanism Involving Double Autocatalysis. *Chem. Mater.* **2005**, *17*, 4925–4938. [CrossRef]

nanomaterials

MDPI

Article

Enhanced Degradation of Methyl Orange and Trichloroethylene with PNIPAm-PMMA-Fe/Pd-Functionalized Hollow Fiber Membranes

Rollie Mills, Cameron Tvrdik, Andrew Lin and Dibakar Bhattacharyya *

Department of Chemical and Materials Engineering, University of Kentucky, Lexington, KY 40508, USA; rolliegmills@uky.edu (R.M.); cameron.tvrdik@uky.edu (C.T.); andrew.lin@uky.edu (A.L.)
* Correspondence: db@uky.edu; Tel.: +1-(859)-312-7790

Abstract: Trichloroethylene (TCE) is a prominent groundwater pollutant due to its stability, widespread contamination, and negative health effects upon human exposure; thus, an immense need exists for enhanced environmental remediation techniques. Temperature-responsive domains and catalyst incorporation in membrane domains bring significant advantages for toxic organic decontamination. In this study, hollow fiber membranes (HFMs) were functionalized with stimuli-responsive poly-N-isopropylacrylamide (PNIPAm), poly-methyl methacrylate (PMMA), and catalytic zero-valent iron/palladium (Fe/Pd) for heightened reductive degradation of such pollutants, utilizing methyl orange (MO) as a model compound. By utilizing PNIPAm's transition from hydrophilic to hydrophobic expression above the LCST of 32 °C, increased pollutant diffusion and adsorption to the catalyst active sites were achieved. PNIPAm-PMMA hydrogels exhibited 11.5× and 10.8× higher equilibrium adsorption values for MO and TCE, respectively, when transitioning from 23 °C to 40 °C. With dip-coated PNIPAm-PMMA-functionalized HFMs (weight gain: ~15%) containing Fe/Pd nanoparticles (d_p~34.8 nm), surface area-normalized rate constants for batch degradation were determined, resulting in a 30% and 420% increase in degradation efficiency above 32 °C for MO and TCE, respectively, due to enhanced sorption on the hydrophobic PNIPAm domain. Overall, with functionalized membranes containing superior surface area-to-volume ratios and enhanced sorption sites, efficient treatment of high-volume contaminated water can be achieved.

Keywords: hollow fiber membrane; methyl orange; trichloroethylene; thermoresponsive; PNIPAm; bimetallic catalysts; water detoxification; zero-valent iron

Citation: Mills, R.; Tvrdik, C.; Lin, A.; Bhattacharyya, D. Enhanced Degradation of Methyl Orange and Trichloroethylene with PNIPAm-PMMA-Fe/Pd-Functionalized Hollow Fiber Membranes. *Nanomaterials* **2023**, *13*, 2041. https://doi.org/10.3390/nano13142041

Academic Editor: Meiwen Cao

Received: 6 June 2023
Revised: 5 July 2023
Accepted: 7 July 2023
Published: 10 July 2023

1. Introduction

Volatile organic compounds (VOCs), such as trichloroethylene (TCE) and tetrachloroethylene (PCE), are a wide category of compounds utilized in various industrial processes, such as paint, degreasing solvent, and metal machinery cleaning [1,2], and have caused various contamination issues in groundwater and other water resources. Due to their high volatility, these compounds also pose indoor air contamination concerns. As previously mentioned, trichloroethylene is a well-known VOC with a Henry's Law constant of 0.10 mol/(kg·bar) [3] and has become a pollutant of focus in recent years due to its prevalent nature (it does not naturally break down in the environment), widespread use, and emerging health concerns. Upon human exposure, TCE has been shown to be highly carcinogenic as well as damaging one's immune system, central nervous system, liver, kidneys, and developing fetuses [4–6]. Humans are typically exposed to TCE via ingestion of contaminated water or inhalation of generated vapor. TCE reaches human resources through improper waste disposal, industrial site spills, landfill dumping of contaminated products, and subsequent leaching into the surrounding soil/water sources [2]. Due to these aspects of TCE, the need for impactful environmental remediation techniques to

capture and degrade such pollutants into less toxic compounds is immense and developing technologies is vital to improving both short-term and long-term health benefits.

There are many methods currently being tested for environmental remediation to combat TCE pollution and reduce human exposure to contaminated water. The capture of TCE has been achieved with several materials, such as activated carbon, biochar, and polymeric materials [7–10]. In various groundwater treatment sites, TCE is often removed by membrane air-stripping (MAS) in packed columns, followed by vapor adsorption by activated carbon. TCE adsorption, though, is limited by several factors, such as (1) the ability to regenerate the adsorption sites (proven difficult without a costly high-temperature process) [8] and (2) subsequent processing, as the captured TCE is still harmful to humans and the materials still need further treatment.

Alternatively, degrading TCE is becoming an appealing option as the pollutant is being detoxified. Destruction via incineration is an effective method of disposal, but it can be costly with the high temperature needed as well as dangerous with the production of other toxic products [11]. TCE degradation has also been achieved with microorganisms under aerobic conditions [12], but is limited by reaction time (>48 h for 60% degradation). A method with promising efficiency and scalability for volatile pollution degradation is utilizing zero-valent iron (ZVI) and palladium (Pd) nanoparticles, which can dechlorinate polychlorinated contaminants via the reductive pathway [13–15]. Briefly, ZVI acts as an electron source that generates hydrogen gas from the surrounding water. This hydrogen gas is utilized by the hydro-dechlorination catalyst (Pd) to produce highly reactive hydrogen radicals that dechlorinate the pollutant. It is important to note that this system is limited by the presence of oxygen in the system, as it can oxidize ZVI and eliminate its ability to generate the hydrogen gas necessary for the catalyst. Compared to free particles in a solution, the immobilization of such Fe/Pd particles into a membrane matrix has been favorable due to high particle loading, high-volume convective flow treatment options, reduction of magnetic particle aggregation, and long-term particle stability with reduced oxidation of ZVI [16].

Our group has reported success in functionalizing optimal membranes for reactive nanoparticle immobilization [17–20]. Base microfiltration (MF) and ultrafiltration (UF) commercial membranes, such as polyvinylidene fluoride (PVDF), have favorable chemical and mechanical stability and have been commonly used in a variety of water/air treatment applications. The surface and pores of these membranes are functionalized through different modification methods (dip coating, layer-by-layer assembly, surface grafting) with a pH/ionic-responsive polymer, such as poly (acrylic acid) (PAA) or poly (methyl methacrylate) (PMMA) [13,19,21]. This incorporates new properties in the membrane, as these polymers are responsive to the surrounding pH levels and certain functional groups deionize at high pH environments (above the pKa value, which is ~4.5 for PMMA). While the change in ionization can generate electrostatic interactions, which control the effective pore diameter of the membrane and the polymer's transition between a coil and globule phase, this functionalization's primary purpose is the immobilization of catalytic metal ions and subsequent reduction to nanosized particles. By controlling the protonation of the $COOCH_3$ group of PMMA, Fe can be incorporated into the system via ion exchange. The immobilized iron can then be reduced to ZVI using a reducing agent, such as sodium borohydride, and subsequently doped with Pd for a bimetallic catalytic system [18,20].

The interaction between chlorinated organics and the catalytic sites of these membranes, though, has been proven to be hindered by mass transfer limitations [18]. The diffusion of the contaminant to the active site, as well as the overall catalytic activity, can be increased by utilizing the enhanced hydrophobic interactions of poly (N-isopropylacrylamide) (PNIPAm), a thermoresponsive polymer that can transition from hydrophilic (coil-like polymer structure) to hydrophobic (globule-like structure) properties at its lower critical solution temperature (LCST) of ~32 °C [22]. This response is due to different preferences for hydrogen bond interactions between the polymer functional groups, which are more favorable

with water (causing hydrogel swelling) and the polymer itself (causing deswelling via water expulsion) below the LCST and above the LCST, respectively [17].

In flat sheet membranes, Saad et al. showed that functionalizing the surface and pores of a PMMA-Fe/Pd-PVDF400 membrane with PNIPAm increased the dechlorination rate of polychlorinated biphenyl (PCB-1) by 35% above the LCST [18]. This system also subsequently increased the amount of treatment volume allowed by the functionalized membrane as the effective membrane permeability increased above the LCST due to PNIPAm's phase transition from coil to globule structure. However, the effects of incorporating PNIPAm into Fe/Pd catalytic membranes for the common pollutants TCE and MO degradation (Figure 1) have not been previously reported in the literature. Furthermore, membrane studies with catalytic and thermoresponsive properties have been limited to flat sheet membranes. Systems with scalability potential (high surface area to volume ratio) and increased flux capabilities (larger water treatment per unit time), such as hollow fiber membranes (HFM) [23], have also not been previously investigated, indicating potential for significant advances in the field of catalytic membrane remediation. HFM systems have shown immense promise for the incorporation of catalytic and magnetic materials, such as osmium NPs in polypropylene (PP) HFMs [24], manganese oxide in PTFE HFMs [25], and magnetic particles impregnated in PP HFMs [26].

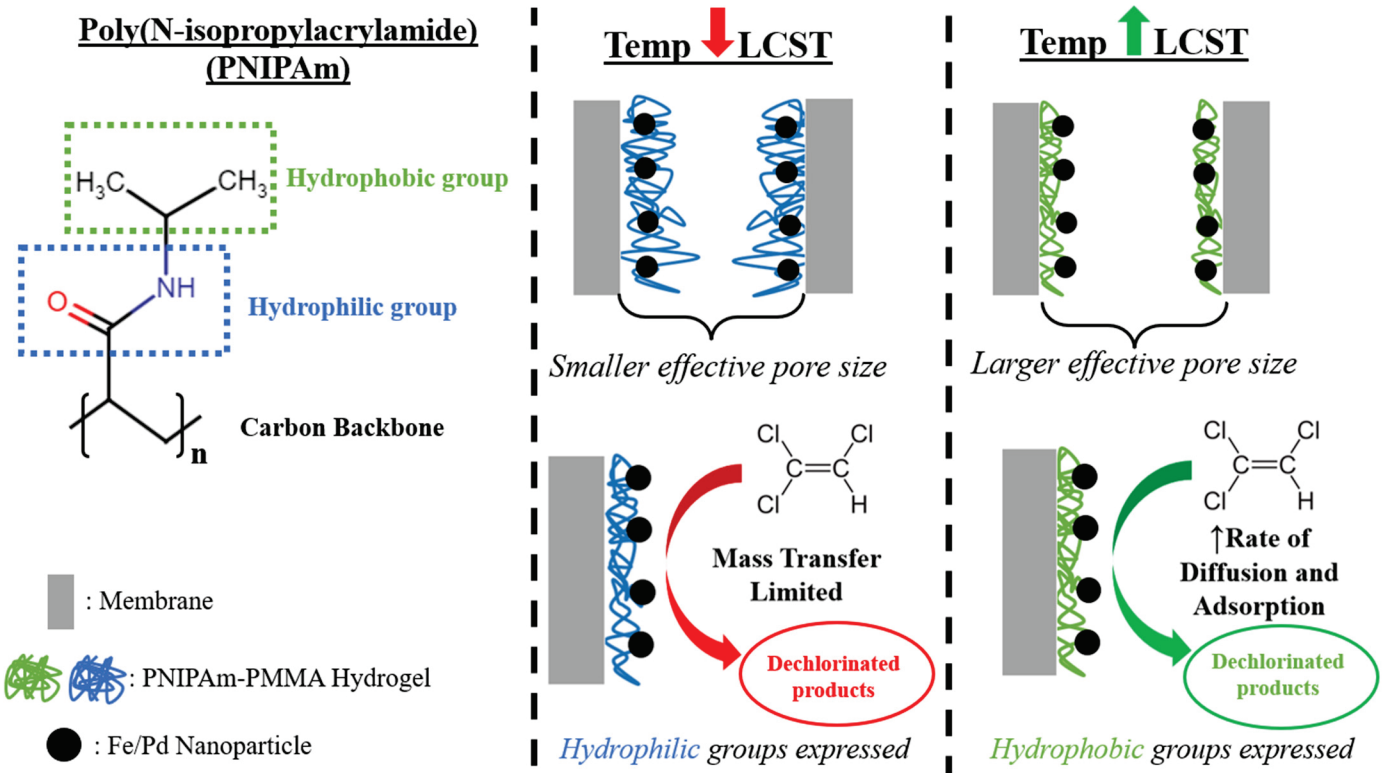

Figure 1. Effect of incorporating PNIPAm into PMMA-Fe/Pd-functionalized membrane systems' ability to degrade TCE. In this case, TCE is shown as an example of a contaminant, but similar trends with non-chlorinated contaminants, such as methyl orange, can be observed.

Furthermore, TCE is a challenging pollutant for experimentation in the solution phase due to its high volatility and harmful vapor. Azo dyes, such as methyl orange (MO), have been commonly used as model compounds for such pollutants [27,28], as they (1) have a high stability (due to aromaticity) [29], (2) have azo bonds that are easily detected using ultraviolet-visible spectrophotometry (UV-Vis), and (3) are degraded by catalytic nanoparticle systems, thus activity tests can be performed. It is important to note that methyl orange itself is considered a prominent pollutant, with approximately 70,000 tons of dye waste released into water sources every year [30] and certain negative health effects,

such as being a contact allergen, an endocrine disruptor, and a possible carcinogen [31,32]. As previously mentioned, the effect of enhancing the degradation of MO with the presence of PNIPAm in a Fe/Pd bimetallic system has not been previously reported.

In this work, the feasibility of integrating PNIPAm into Fe/Pd-PMMA-functionalized hollow fiber membrane systems (with a higher surface area to volume ratio than flat sheet membranes [33]), as well as other flat sheet microfiltration membranes with larger catalyst loading capacities than previously tested, was investigated. PMMA is utilized as the ionic-responsive polymer in this study, it provides scale-up advantages with its considerably lower vapor pressure than PAA [18]. MO has shown usage for initial activity experimentation; thus, MO and TCE degradation by these functionalized materials above and below the LCST of PNIPAm were explored in batch mode. In addition, initial testing was performed to establish that TCE volatilization by hydrophobic HFMs (followed by carbon adsorption) could be an energy-efficient alternative to traditional packed bed stripping. Ultimately, the novelty of this work stems from (1) the functionalization/synthesis of PNIPAm into HFMs, (2) the efficacy of utilizing PNIPAm's hydrophobic properties (above LCST) in catalytic membranes for previously untested contaminants (such as an azo dye and TCE), and (3) the utilization of hydrophobic HFMs for VOC stripping from groundwater sources.

2. Materials and Methods

2.1. Materials

Hydrophilized PVDF400 and PVDF650 membranes were provided by Solecta Membranes (Oceanside, CA, USA). The hollow fiber membranes (Tribore, 3M, and Lifestraw) were obtained from START Center Singapore (Cleantech One, Singapore), Quantum Flow Technologies (Charlotte, NC, USA), and Vestergaard (Baltimore, MD, USA), respectively. Sodium borohydride (99%, CAS: 16940-66-2), methyl methacrylate (99%, 80-62-6), and N-isopropylacrylamide (2210-25-5) were obtained from Fisher Scientific (Waltham, MA, USA). Iron(III) chloride hexahydrate (10025-77-1) and iron(II) chloride tetrahydrate (13478-10-9) were obtained from Alfa Aesar (Tewksbury, MA, USA). Sodium chloride, hydrochloric acid, ethanol, sodium hydroxide, and methyl orange (547-58-0) were obtained from VWR (Atlanta, GA, USA). Ammonium persulfate (APS, 98% purity, 7727-54-0) was obtained from Acros Organics (NJ, USA). Potassium tetrachloropalladate(II) was obtained from Strem Chemicals (Newburyport, MA, USA, CAS: 10025-98-6). Trichloroethylene (79-01-6) and N,N′-methylenebisacrylamide (110-26-9) were obtained from Sigma Aldrich (St. Louis, MO, USA). Deionized ultrafiltered (DIUF) water was obtained from a PURELAB Flex 3 filtration system (4–18 MΩ). Deoxygenated water was obtained by bubbling nitrogen gas in DIUF water for 30 min.

2.2. Hydrogel and Nanoparticle Synthesis

PNIPAm/PMMA hydrogels were created via temperature-initiated free radical polymerization. A polymerization solution was made by adding 13.5 g of NIPAm monomer to 100 mL of DIW. The DIW was bubbled with nitrogen gas for 30 min prior to mixture to ensure minimal oxygen presence. MMA and bisacrylamide cross-linkers were added in a 90 (NIPAm):5:5 molar ratio, respectively, and then 2 mol% of APS was added (relative to NIPAm monomer). The solution was then poured into glass vials (with headspace for hydrogel growth) and left in a vacuum oven for 2 h at 70 °C. Hydrogels were then rinsed with DIW (to remove unreacted monomers) and stored in a cold room (2 °C).

Fe/Pd nanoparticles suspended in solution (without membrane matrix) were synthesized by bubbling 35 mL of DIW with N_2 gas for 30 min. A total of 15 mL ethanol was added to the solution to obtain a 100 mL solution. A total of 0.284 g of iron(III) chloride hexahydrate was then added to the 50 mL solution (0.035 M) using a mechanical stirrer at 100 rpm. A total of 50 mL of a sodium borohydride solution (0.14 M) was added into the beaker drop wise (5 mL per min) to convert Fe^{3+} to Fe^0 with cooling packs to prevent temperature rise. This reaction was allowed to occur for 60 min. Then the formed ZVI particles in solution were sealed and sonicated for 5–10 min to allow for the maximum

surface area available for Pd interaction. The sonicated solution was then combined with 50 mL of a 5 mol% K_2PdCl_4 solution and mixed on an orbital shaker at 300 rpm for 30 min. The formed Fe/Pd particles were subsequently rinsed with ethanol and then stored in an ethanol solution with minimal headspace. Note that mechanical stirring was utilized throughout this process, as the ZVI would stick onto magnetic stirring bars, and, when possible, the solutions were in closed containers to minimize oxidation of the iron particles.

2.3. Hydrogel Functionalization of Membranes

For functionalization of membranes with PNIPAm and PMMA, a polymerization solution was created, similar to the free hydrogel polymerization method. Briefly, NIPAm (6 g, 13 wt %), MMA monomer, and bisacrylamide cross-linker were added to 50 mL of DIW (deoxygenated) at a molar ratio of 90:5:5, respectively. After the addition of 1 mol% APS, the membranes were soaked in the polymerization solution for 5–10 min. After soaking, the membranes were then placed between two Teflon plates and heated for 2 h in a vacuum oven at 70 °C. Membranes were then rinsed with DIW (to remove unreacted monomers) and stored in a cold room (2 °C).

The weight gains of the membranes were determined using the dry weights of the membrane before and after polymerization, calculated using the following equation:

$$Weight\ Gain\ (\%) = 100 * \frac{m_{final} - m_{initial}}{m_{initial}} \quad (1)$$

where $m_{initial}$ and m_{final} are the dry membrane weights before and after functionalization with polymer. Post-functionalization and DIW rinsing, the membranes were left in a fume hood for 24 h to dry before weighing.

2.4. Fe/Pd Nanoparticle Functionalization of Membrane

Bimetallic Fe/Pd synthesis and immobilization into the membrane matrix were performed via an ion-exchange method previously reported [18,34], summarized in Figure 2. Briefly, functionalized membranes were soaked in a 70 mM NaCl solution (pH 10–11.5) overnight (12–24 h) to increase the membrane's ion-exchange affinity with Fe^{2+}. The significantly basic pH (above the pKa of PMMA) utilizes the pH response of PMMA, thus allowing the carboxyl functional groups of PMMA to chelate with sodium ions and release H^+. This exchange can be confirmed by a decrease in pH from the release of hydrogen ions. After this exchange, membranes were soaked in a 36 mM $FeCl_2{\cdot}4H_2O$ solution at 100 rpm for 30 min to ensure ion exchange in the polymer matrix between sodium and iron ions. The membranes were then soaked in a reduction solution (25 mM $NaBH_4$ with deoxygenated DIW) for 30 min to reduce the immobilized Fe^{2+} to Fe^0. Then the membrane was shaken in a 3 mol% $Pd(OAc)_2$ solution (10:90 molar ratio of DIW and ethanol to avoid oxidation) at 100 rpm for 30 min for palladium deposition on the iron NPs. The resulting functionalized membranes are washed with ethanol and stored in ethanol with minimal headspace to avoid oxidation of the ZVI NPs.

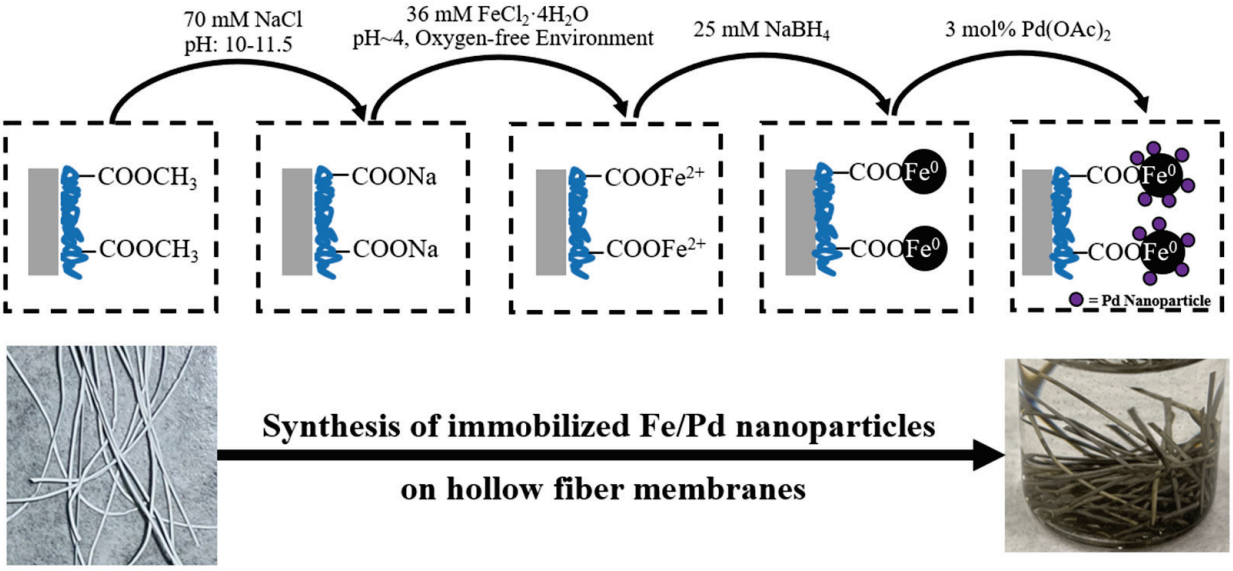

Figure 2. Method summary for ZVI/Pd nanoparticle synthesis and immobilization into a polymer/hydrogel matrix. The depicted HFMs are Lifestraw membranes.

2.5. Responsive Flux Studies of Functionalized Membranes

To examine the permeability of the flat sheet membranes, the membranes were placed in a glass dead-end stirred filtration cell from Millipore. The feed side of the cell was filled with DIUF water and pressurized with ultra-high purity nitrogen gas to create a pressure differential for fluid flow across the membrane. The membrane was compacted at ~1.5 bar until the water flux through the membrane did not change with time. After compaction occurred, the pressure was varied from 0 to 2 bar, and the permeate water volume over specific time intervals was measured at each set pressure. Steady-state flow was achieved before measurements and triplicate samples were taken. Using a linear correlation between the number of liters of water passed per m^2 of membrane surface per hour versus the pressure difference, the permeability of the tested membrane was determined using the following equation:

$$Membrane\ Permeability = \frac{Q}{A \times \Delta P} \quad (2)$$

where Q (L/hour) is volumetric flowrate, A is membrane area (m^2), and ΔP is pressure drop across the membrane (bar).

To examine the temperature-responsive nature of the PNIPAm-PMMA-functionalized flat sheet membranes, a heating coil was wrapped around the filtration cell, and a temperature probe was placed inside the cell (as close to the membrane as possible). The permeability of the membrane was measured at different temperature levels. Once the desired temperature was reached, 5 min were allowed to pass before sample measurement, ensuring the thermoresponse and phase transition of PNIPAm.

To examine the pH-responsive nature of the PNIPAm-PMMA-functionalized flat sheet membranes, the membrane permeability was measured with solutions of different pH levels. The pH of the DIUF water was controlled using hydrochloric acid and sodium hydroxide. Five minutes were allowed to pass before sample measurement to ensure the phase transition response of PMMA.

2.6. Temperature-Responsive MO and TCE Adsorption/Desorption of Hydrogels

PNIPAm/PMMA hydrogels (1.7 g) were placed in glass vials with ~100 mg/L and ~90 mg/L of MO and TCE, respectively, and shaken at 200 rpm for roughly 24 h (until equilibrium was reached) in an incubated shaker with temperature control. The MO sample was then diluted (1 mL of sample in 50 mL of DIW with 0.1 NaOH for pH adjustment) to reach absorbance values under 1, thus still following the Beer–Lambert Law. pH was

also measured and adjusted if necessary to ensure all UV-Vis measurements for MO were taken at the same pH. UV-Vis measurements were conducted using a UV-6300PC (VWR International, Leuven, Belgium).

Alternatively, the TCE sample was extracted in hexane, 1 µL of the extracted solvent was taken, and it was then diluted 100:1 during GCMS injection. Specifically, for the adsorption study, the incubator was set at 40 °C, which, as previously mentioned, allowed for adsorption to reach equilibrium. After adsorption equilibrium and measurement of concentration (2–3 mL for UV-Vis), the hydrogel was then placed into DIW and shaken again for ~24 h at 23 °C to reach desorption equilibrium. As the hydrogel was in a swollen state below PNIPAm's LCST, the samples were centrifuged at 2000 rpm for 5 min to separate the hydrogel from the water, and then the separated DIW (with desorbed contaminant) was measured based on the previously mentioned steps.

2.7. MO/TCE Degradation via Fe/Pd NPs and Catalytic Functionalized HFMs

For MO degradation using Fe/Pd NPs (free in solution), 0.1 g of bimetallic nanoparticles (ZVI with ~5–10% Pd) was added to 20 mL of a deoxygenated MO solution (3 mg/L), and samples were shaken at 100 rpm below and above the LCST in an incubated shaker. For obtaining a sample at time *t*, the nanoparticles were isolated from the surrounding solution via a heavy-duty magnet (as the Fe/Pd NPs are magnetic), and then 2–3 mL of the sample was removed. MO concentration was analyzed using UV-Vis at a wavelength of 464 nm.

For MO degradation using catalytic functionalized HFMs, 20 mL MO solutions of 5 mg/L were created with deoxygenated water. Roughly 0.15 g of functionalized membranes (cut to 4 cm fiber length) were added to each solution and shaken for 60 min total at 200 rpm. At each timepoint, 2 mL was placed in a cuvette, analyzed via UV-Vis, and then added back into the solution to keep the solution volume consistent across experiments. An incubator shaker was utilized to control the temperature of the samples below and above PNIPAm's LCST.

For TCE degradation using catalytic functionalized HFMs, 42 mL TCE solutions of ~0.4 mg/L were created with minimal headspace. Roughly 0.44 g of functionalized 3M membranes were added to each solution and shaken for 90 min total at 200 rpm, taking 1 mL samples at the following timepoints: 0 min, 5 min, 15 min, 30 min, 60 min, and 90 min. Septa vial caps were utilized, along with a volumetric needle, for taking samples, ensuring minimal TCE was lost due to volatility. An incubator shaker was utilized to control the temperature of the samples below and above PNIPAm's LCST. A control without membranes was utilized to normalize TCE concentrations based on lost vapor during sampling. A total of 1 mL of hexane was added to the 1 mL samples taken and shaken at 200 rpm for 30 min for solvent extraction. The 1 mL of hexane (now containing TCE) is then separated from the water for analysis. Triplicate measurements were analyzed using an Agilent (Santa Clara, CA, USA) GCMS system (8890 for GC, 5977C for mass selective detector). Note that the TCE concentration was determined from a calibration curve with known TCE standards (Figure S1). The identification of TCE in experimental samples was confirmed using the gas chromatograph (Figure S2a) and the National Institute of Standards and Technology (NIST) library search with the sample's mass spectrum (Figure S2b).

2.8. Membrane-Air Stripping (MAS)

Membrane-air stripping capabilities for TCE were evaluated using a 3M polypropylene hollow fiber membrane module in a recirculating vacuum membrane distillation apparatus. The hollow fiber module contained approximately 5000 4.9 inch fibers. Initial 200 mL TCE (3.7 mg/L) and DIW mixtures were prepared. One sample was covered as a control (for TCE loss due to volatility), and the other sample was used in the recirculation loop. The solution was pumped through the hollow fiber module at 50 mL/min using a peristaltic pump. Inlet, outlet, and flask temperatures were measured, as well as inlet gauge pressure and shell vacuum pressure. The shell side pressure of the hollow fiber module was reduced

using a scroll vacuum pump with a water-chilled Liebig condenser operating at 1–2 °C in line to collect some vapors. The solution was circulated through the hollow fiber module for 30 min, and samples were collected from the recirculated flask, control flask, and condensed liquid.

2.9. Gas Chromatography-Mass Spectroscopy (GCMS)

An Agilent GCMS system (8890 for GC, 5977C for mass selective detector) was utilized for the analysis of semi-volatile compounds, such as trichloroethylene. High-purity hexane (CAS: 110-54-3, from Millipore Sigma) was obtained and used as the injection solvent. A high-purity (>98%) TCE standard (CAS: 79-01-6, from Millipore Sigma) was utilized to create external standards for a calibration curve, ranging from 0 (blank control) to 10 mg/L of TCE. Solvent extraction of TCE samples was required prior to GCMS analysis. A total of 10 mL of the sample (solution of DIW, TCE, and subsequent formed products if reaction occurred) was placed into a vial with 10 mL of hexane with minimum headspace and shaken at 200 rpm for 1 h to allow for TCE extraction into the hexane solvent. Control runs were conducted at each experiment to obtain an extraction percent, which was then utilized for normalizing the corresponding resulting data. After allowing the two solvents to separate, a syringe was utilized to extract 2 mL of the hexane solvent (now containing TCE) and placed into 2 mL septa-sealed vials. During analysis, 1 μL of the sample (with 2 sample pumps) is injected into the injection port with a 0.2 μL air gap in the syringe. Three washes with hexane were conducted before and after each sample injection to prevent contamination. The oven temperature was set to 250 °C. A solvent delay of 3.2 min was utilized for observing clear TCE peaks. The limit of detection was found to be under 1 μg/L for TCE.

3. Results and Discussion

3.1. Membrane Functionalization and Nanoparticle Synthesis

3.1.1. Membranes Characteristics

In this study, several flat sheet and hollow fiber membranes were initially investigated for their functionalization and remediation potential. Variation of different membrane characteristics (structure, hydrophobicity, and pore size) was necessary to investigate the scalability of the polymer and NP functionalization processes. Commercial hydrophilized PVDF400 and PVDF650 membranes were utilized for flat sheet testing with a volumetric water permeability, measured in liters per m^2 per hour (LMH), found to be 969.4 ± 175.7 and 2557.3 ± 468.3 LMH/bar, respectively (Figure S3). Both membranes contain an asymmetric structure, meaning the pore size varies with membrane thickness (thin PVDF separating layer on an open polyester backing support, highlighted in Figure S4). Commercial hydrophobic PVDF (Tribore-HFM), hydrophobic polypropylene (3M-HFM), and hydrophilized polyether sulfone (Lifestraw-HFM) were utilized for HFM testing. The characteristics of the membranes functionalized in this study are highlighted in Table 1, including material, mean pore size, porosity, and thickness. It is important to note that HFMs will typically have different pore sizes depending on the surface side. The shell side is the outer surface layer of the membrane, while the lumen side is the inner surface (Figure S5).

Table 1. Membrane characteristics of flat sheet and hollow fiber membranes utilized in this study.

	PVDF400-Flat Sheet	PVDF650-Flat Sheet	Tribore-HFM	3M-HFM	Lifestraw-HFM
Material	Hydrophilized polyvinylidene fluoride (PVDF)	Hydrophilized polyvinylidene fluoride (PVDF)	Hydrophobic polyvinylidene fluoride (PVDF) *1	Hydrophobic polypropylene (PP) *1	Hydrophilized polyether sulfone (hPES) *1
Mean pore size	40.6 nm, with the largest being 300–400 nm (SEM)	62.2 nm, with the largest being 300–400 nm (SEM)	1153 nm	40 nm (manufacturer)	200 nm (manufacturer)
Thickness	178 ± 13 µm	178 ± 13 µm	412.6 ± 106.2 µm *1	41.8 ± 2.2 µm	85.5 ± 3.5 µm
Bulk porosity	46% *2	47%	24% *1	24% *1 or 40% (manufacturer)	45% *1
Shell surface mean pore size	Not applicable	Not applicable	57 ± 35 nm *1	42 ± 17 nm *1	140 ± 87 nm *1
Lumen surface mean pore size	Not applicable	Not applicable	1346 ± 1086 *1	46 ± 27 nm *1	748 ± 896 nm *1
Tortuosity	Not measured	Not measured	3.1692 *1	Not measured	Not measured

*1 Data obtained from Baldridge et al. [35]. *2 Data obtained from a prior study (Mills et al.) [36].

3.1.2. PNIPAm-PMMA Functionalization of Membranes

PNIPAm is a temperature-responsive polymer that can undergo a conformation change at its LCST (~32 °C). Above the LCST, the isopropyl groups of PNIPAm initially dehydrate, with a subsequent backbone collapse. This leads to the hydrophilic amide groups preferring to hydrogen bond with each other rather than the surrounding water, thus transitioning to a globule-like hydrogel state and releasing previously bound water [37,38]. Quantification of this transition has been conducted previously in our group with swelling studies below and above the LCST with PNIPAm-PMMA hydrogel systems [18]. The purpose of PNIPAm functionalization of the membrane surface and pores is to control membrane pore size (and thus permeability), as well as have the capability to regulate primarily hydrophilic or hydrophobic properties of the membrane system. The purpose of PMMA functionalization, in addition to pH responsiveness to membrane pores and surfaces, is for Fe/Pd NP immobilization into the membrane matrix via ion exchange, which does not allow for the significant release of metals during remediation processes (Wan et al. reported less than 2% leaching in similar systems [39]). This mitigates one of the main concerns with this technology, which is the release of iron and palladium into treated water. Furthermore, pH-responsive polymer functionalization has been known to increase the antifouling properties of the membrane due to the control of surface charge via the pH of the surrounding solution [40,41]. It is important to note that this functionalization method is transferable to other membrane materials. The process does not utilize covalent attachment between the hydrogel and membrane surface; thus, a variety of membrane materials can be utilized. Long-term stability of membrane functionalization with hydrogel can be a concern due to the hydrogel not being chemically attached to the membrane. Many studies, such as one by Chiao et al. [42], have proven that ionic-responsive polymers, such as PAA and PMMA, can be covalently grafted onto polymeric membranes to increase system stability. There are certain trade-offs for implementing this method, though, such as higher functionalization costs and more complex methods, which can decrease the scalability of the resulting systems.

All five membranes in this study were functionalized with PMMA and PNIPAm polymers via a free hydrogel polymerization method. The degree of functionalization was initially quantified by weight gain percent before and after the polymerization process, utilizing Equation (1) (Figure 3). Further confirmation of PNIPAm and PMMA presence was obtained using FTIR (Figure S6 and Supplementary Materials: Section C), where the PNIPAm-PMMA's -NH_3 group (~1540 cm^{-1}) and -C=O group (~1650 cm^{-1}) were identified on the functionalized PNIPAm-PMMA-3M HFM.

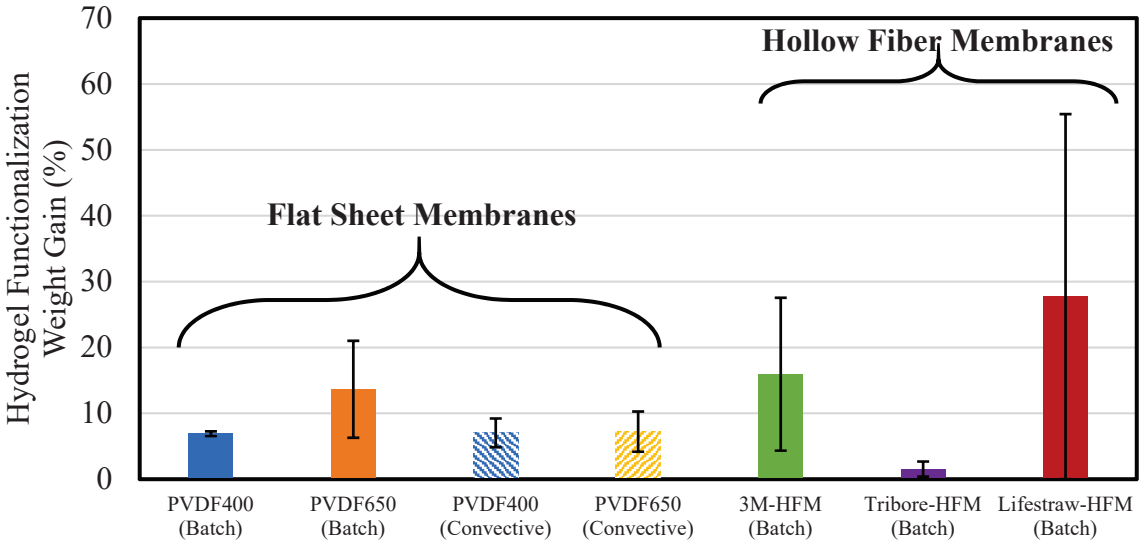

Figure 3. Hydrogel functionalization weight gains of membrane systems. Batch functionalization indicates only the soaking of membrane in polymerization solution, while convective indicates both soaking and convective flow with polymerization solution. Error bars represent the standard deviation of triplicate experiments.

With average weight gains above 15%, HFMs displayed a higher affinity (on average) than flat sheet membranes, due to HFMs' higher specific surface area per gram of membrane [43]. The Lifestraw exhibited the highest average weight gain (27.7%), which can be explained due to the hydrophilization of the polyether sulfone. In this surface/pore coating process, hydrophilic membranes allow for greater coating with the polymerization solution. Alternatively, hydrophobic membranes have low coating affinity. Due to their hydrophobic nature, the Tribore and 3M membranes yielded lower functionalization weights than the hydrophilized Lifestraw, with 1.4% and 15.9%, respectively. There was a significant difference between the two hydrophobic HFMs, though, which indicated that specific surface area and hydrophobicity could not be the sole factors affecting weight gain. Membrane materials (polypropylene and PVDF) could largely affect this process. Overall, these findings indicate that further investigation could be beneficial regarding the effect of membrane variables on the membranes' hydrogel functionalization capabilities as well as the affinity of the functionalization material (i.e., PMMA) for certain chemical bonds of the membrane material (C-H versus C-F).

3.1.3. Fe/Pd Synthesis and Immobilization into the Membrane System

After PNIPAm and PMMA functionalization, immobilization, and synthesis of Fe/Pd NPs in the membrane matrix were conducted. As mentioned in the "Materials and Methods" section, the first step involved soaking the membranes in a basic solution (below the pKa of PMMA) with 70 mM NaCl to allow for an ion exchange between hydrogen and sodium (Figure 4a). Due to the release of hydrogen ions, this process decreased the overall pH of the soaking solution (Figure 4b), indicating successful PMMA functionalization, ion exchange, and membrane pH responsiveness. The pH of the 3M and Lifestraw HFMs dropped the most (from roughly 10 to 3) due to their highest average weight gain. Alternatively, the flat sheet membranes with a lower weight gain showed a less significant pH drop (from roughly 10 to 7), and the Tribore, with the lowest weight gain, showed a miniscule pH drop (from 11 to 10). Overall, this pH drop was proportional to the functionalization weight exhibited by each membrane (Figure 4c), up to a solution pH of roughly 2–3, where the released hydrogen ions do not significantly decrease the pH further. This data indicated that, up to a weight gain of roughly 0.1 g of polymer, a linear trend between membrane functionalization weight and pH drop can be developed. It is important to note that

error bars for these figures represent triplicate measurements and that unfunctionalized membranes do not produce a pH drop over 24 h.

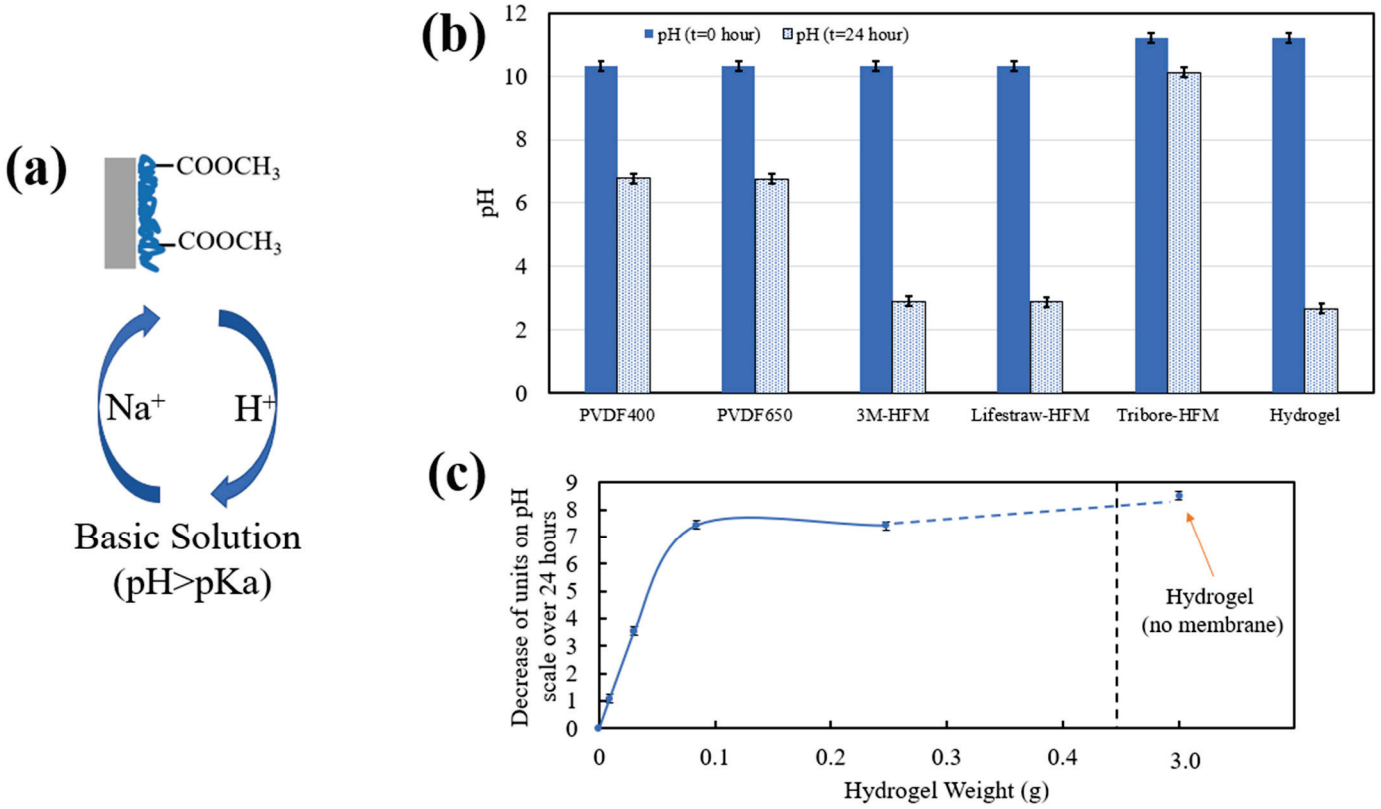

Figure 4. pH-responsive nature of PNIPAm-PMMA hydrogel and functionalized membranes. (**a**) Visual representation of ion exchange for the first step of Fe/Pd immobilization into the hydrogel/membrane domain. (**b**) pH change of solution before and after soaking PNIPAm-PMMA-functionalized membranes for 24 h. A total of 3 g of PNIPAm-PMMA hydrogel was utilized as a reference. The initial pH was set at 10–11. Error bars represent triplicate measurements. (**c**) Correlation of membrane functionalization weight and release of hydrogen ions quantified as decrease of units on the pH scale over 24 h of membrane/hydrogel soaking. Error bars represent triplicate measurements.

3.1.4. Functionalized Membrane Characterization via SEM and EDX

After the initial ion exchange step, a second exchange occurred with Fe^{2+} (confirmed with ICP, Supplementary Materials: Section C) and then reduction to ZVI with subsequent immobilization of palladium onto the NPs. After functionalization studies, PVDF650 was selected as the flat sheet membrane of focus in this study due to its larger pore size and permeability than PVDF400 (previously mentioned in Figure S3), which can result in greater NP loading and daily water treatment volume. The 3M system was selected as the HFM of focus in this study due to its high functionalization weight and release of hydrogen ions, confirming significant PMMA presence, as well as its hydrophobicity for TCE stripping potential via MAS. While the Lifestraw HFM system had a greater weight gain than that of the 3M, the 3M fibers are held together by perpendicular microfibers (Figure S7), which increases the structural integrity of the fibrous system and is more appealing for commercial and scalable modules. Additionally, the Lifestraw functionalization (~20 nm surface pore size post-functionalization) showed a much larger inconsistency during functionalization (large error bars) than that of the 3M, making the latter a more consistent functionalization material. It is important to note that, to the group's knowledge, this is the first reported case of HFM functionalization with both catalytic NPs and the thermoresponsive polymer

PNIPAm, incorporating both adsorptive and degradative properties for highly efficient water remediation in a hollow fiber system.

The Fe/Pd-PNIPAm-PMMA-functionalized membrane systems of focus were characterized using SEM imaging to investigate surface/pore morphology as well as Fe/Pd NP presence (Figure 5), which were found to have an average particle diameter of 33.6 nm and 34.8 nm for PVDF650 and 3M HFM, respectively (Figure S8). Note that the NPs observed on the surface were confirmed to be Fe/Pd nanoparticles via EDX analysis, with respective peaks for both Fe and Pd.

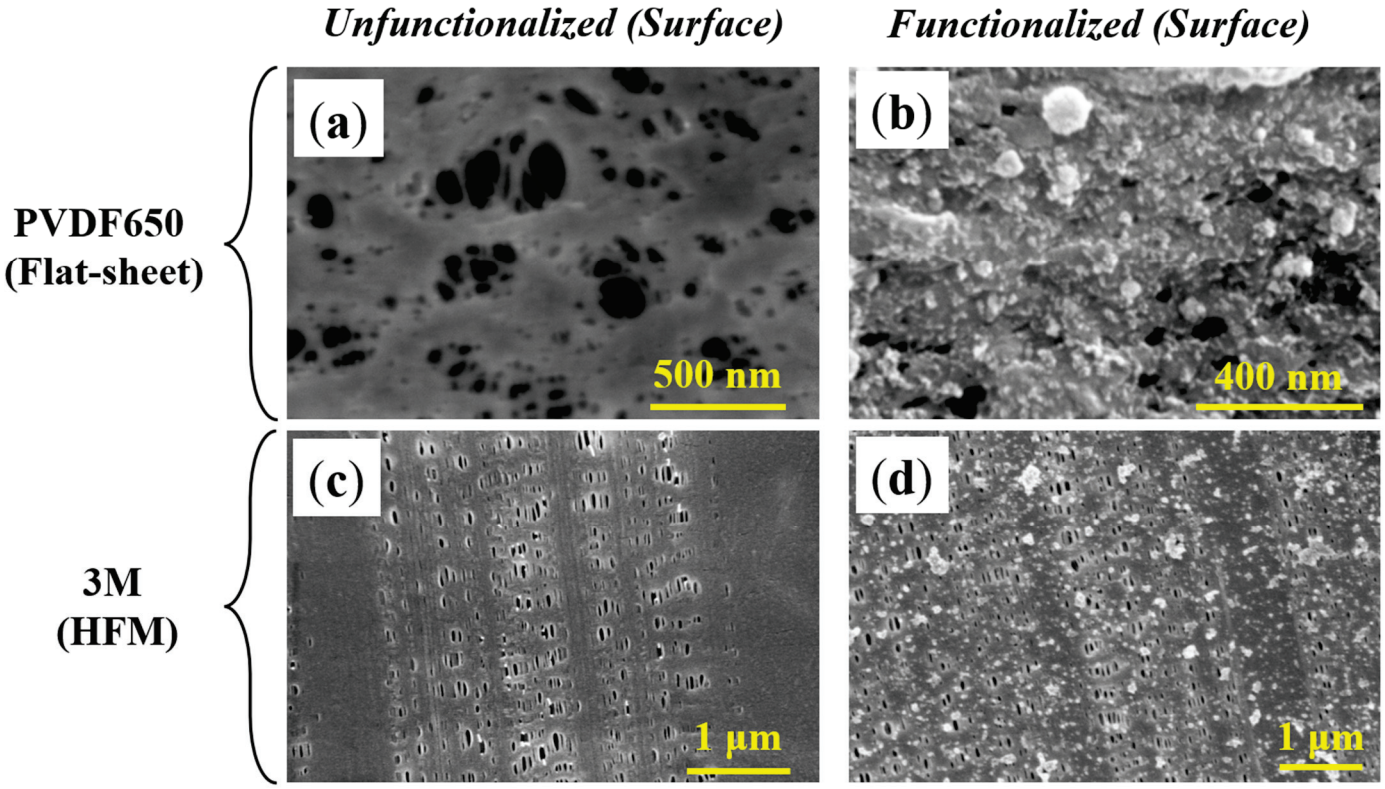

Figure 5. SEM analysis of flat sheet and hollow fiber membranes. Imaging of (**a**) an unfunctionalized PVDF650 surface, (**b**) a PVDF650 surface functionalized with PNIPAm, PMMA, and Fe/Pd NPs, (**c**) an unfunctionalized 3M HFM surface, and (**d**) a 3M HFM surface functionalized with PNIPAm, PMMA, and Fe/Pd NPs.

The surface imaging of the PVDF650 membrane showed significant pore functionalization, as the surface pores are less frequent and smaller in diameter post-functionalization (Figure 5a,b). This phenomenon was also confirmed experimentally, as the PNIPAm, PMMA, and Fe/Pd functionalization of the PVDF650 membrane decreased the water permeability from around 2500 LMH/bar to about 824 LMH/bar, indicating significant functionalization of the membrane pores. Due to the complexity of HFM modules that can support water filtration pressures, flux data for HFMs before and after functionalization, as well as temperature/pH response, was not investigated, which is a limitation of this current work. A significant reduction of membrane permeability is not expected for the 3M HFM, though, as the pores do not show significant interference post-functionalization (Figure 5c,d). This difference can be explained by the hydrophobic nature of the 3M fibers (compared to the hydrophilic PVDF650). After investigation of the 3M membrane pores (cross-section) using SEM and ion milling, no NPs were found throughout the pores (Figure S9), which indicates that the majority of functionalization occurred on the shell surface of the 3M membrane and only minimally, if any, in the pores and lumen side. Due to this observation, the recommended direction for convective filtration with the catalytic membranes in this study is shell-to-lumen flow. It is important to note, though, that other

sections of HFMs can be functionalized as well, such as lumen-side functionalization with NPs in a packed-bed-style format [44]. Additionally, with ImageJ, the average diameter of Fe/Pd NPs was found to be 33.6 nm and 34.8 nm, respectively, for the PVDF650 and 3M membranes (Figure S9), which is similar to previous membrane-bound Fe/Pd studies [18]. Note that the previous numbers are mean values, and larger particles (diameter: 100–200 nm) were also observed.

Free Fe/Pd NPs (in solution) were also synthesized for initial activity tests. Briefly, the initial oxidized iron solution was reduced via sodium borohydride, where ZVI NP formation occurred (Figure S10). An initial check of this step was conducted visually with a color change from orange/brown to black, which corresponds with Fe^{3+} and ZVI, respectively, in the literature. Further confirmation was obtained with magnetic testing. Unlike Fe^{3+}, the formed ZVI nanoparticles displayed paramagnetic properties [45], as shown in Figure S10. After ZVI formation, a palladium acetate solution (3 mol%) was then added for palladium reduction (from ZVI) and subsequent deposition onto the NP surface. It is important to note that our group has previously reported X-ray diffraction (XRD) characterization of ZVI NPs prepared utilizing the same synthesis methodology. This analysis confirmed the formation of zero-valent NP via the peak for body-centered cubic (BCC) Fe^0 (Figure S11) [46].

The resulting Fe/Pd particles were characterized using TEM and EELS (Figure S12), where the zero-valent iron core was observed with a thin oxygen layer surrounding it. EELS analysis confirmed bimetallic NP formation (not separate Fe and Pd NPs), as a clear Fe core region with Pd coating was observed, which agrees with TEM/EELS analysis in the literature [47]. It is important to note that the formation of Pd NPs had to occur on the ZVI NP surface (thus forming a bimetallic system), as the Pd must be reduced by the ZVI for Pd NP formation ($Fe^0 + Pd^{2+} \rightarrow Fe^{3+} + Pd^0$) with subsequent deposit on the iron NP surface [47].

Using EELS, the weight percent composition of a single NP was found to be 12.11%, 80.11%, and 7.77% for oxygen, iron, and palladium, respectively (Table S1), further confirming bimetallic NP synthesis. Additionally, the synthesized particles had an average size of 36 nm (Figure S13). Note that NPs formed in membrane systems have a lower average size than those formed unbound in solution, due to the prevention of NP agglomeration (from PMMA charge groups).

3.2. Temperature and pH Response of Functionalized Materials

In this study, unbound hydrogels were synthesized using the polymerization solution, consisting of MMA and bisacrylamide cross-linker in a 90 (NIPAm):5:5 molar ratio, respectively, with an overall APS molar percentage of 8%. It is important to note that the degree to which the hydrogel can swell and respond to external stimuli is dependent on the degree of polymer cross-linking and monomer concentration, which can be controlled by the molar ratio of the cross-linker. The swelling capacity of the hydrogels can be described as:

$$S = \frac{d_{swollen}}{d_{unswollen}} \tag{3}$$

where S is the swelling capacity, described as the ratio of the apparent hydrogel diameter in the swollen state (below LCST) to that in the unswollen state (above LCST). Swelling capacity was found to be approximately 10.3 and 3.4 for 3 mol% and 10 mol% crosslinkers in prior studies [18], respectively, which indicates the inverse relationship between swelling capacity and crosslinking concentration in the polymerization solution. This also indicates that, as the degree of crosslinking increases, the responsive nature of the hydrogel subsequently decreases, as the hydrogel does not have the flexibility to swell/shrink.

Temperature-responsive adsorption of TCE onto hydrogels has been reported by Xiao et al. with 80:10:10 NIPAm:AA:poly (ethylene glycol) 600 dimethacrylate molar ratios, resulting in almost twice as much adsorption of TCE onto PNIPAm-poly (acrylic acid) hydrogels above than below the LCST [48]. The thermoresponsive adsorption/desorption

properties of hydrogels that substitute poly (acrylic acid) with PMMA have not been previously investigated with MO or TCE compounds. In this study, free PNIPAm-PMMA hydrogels were utilized for initial responsive experimentation before membrane testing. Equilibrium adsorption isotherm studies were conducted with hydrogel samples in batch solutions of MO and TCE to determine the equilibrium adsorption (Q_e) of contaminants onto the responsive hydrogel below and above the LCST of PNIPAM. Note that the molar concentrations of TCE and MO are not equal; thus, comparisons were simply made for the investigation of responsive LCST behavior. Initially, Q_e was determined to be 0.044 ± 0.003 mg of MO per gram of hydrogel sample at 23 °C. Above the LCST, though, at 40 °C, the value for Q_e dramatically increased to 0.504 ± 0.101 mg/g, indicating a 11.5× increase in adsorptive capabilities (Figure 6a,b). For TCE, Q_e was determined to be 0.156 ± 0.046 mg of TCE per gram of hydrogel sample at 23 °C. Above the LCST (40 °C), the value for Q_e increased to 1.692 ± 0.383 mg/g, indicating a 10.8× increase in adsorptive capabilities (Figure 6b). This increase can be attributed to the dehydration of the PNIPAm chains, which resulted in increased exhibition of hydrophobic properties/groups and greater interaction between the PNIPAm and the hydrophobic sections of the pollutants. It is important to note that PMMA itself is temperature-responsive [49], but it is assumed to have negligible effects on the system due to the low molar ratio of MMA to NIPAm. Despite this, drastically larger Q_e were observed at higher temperatures, indicating that hydrogel hydrophilicity was primarily controlled by the responsive PNIPAm chains and that their dehydrating isopropyl groups dominated the more hydrophilic PMMA groups. Additionally, note that the molar concentrations of TCE and MO are not equal; thus, comparisons were simply made to prove responsive LCST behavior.

Additionally, the same hydrogels (utilized in 40 °C MO adsorption in Figure 6b) were returned to temperatures below the LCST over a total of two temperature swing cycles and shaken for ~24 h until equilibrium. In these cycles, minimal desorption was observed, with less than 20% of adsorbed MO released back into the surrounding solution (Figure 6c). The low desorption could be attributed to the strong hydrophobic interactions remaining, the entanglement of the pollutant in the polymer chains, and the bulky size of MO (327.33 g/mol) hindering the mass transfer, compared to the smaller contaminant PCB-1 (188.7 g/mol) that had a higher desorption capacity in previous studies [17,18]. Overall, the efficacy of implementing PNIPAm for increased interaction between the active site and the contaminants MO and TCE above the LCST was shown, as well as the thermoresponsive nature of the hydrogel itself.

The pH responsiveness of the functionalized membrane samples was shown prior to the Fe/Pd immobilization process with the release of hydrogen ions and subsequent pH drop in a solution with a pH > pKa value of PMMA. This response validated the presence of carboxylic groups in the hydrogel domain of the membrane system. Temperature responsiveness, as well as additional pH responsiveness, was shown in the flat sheet PVDF650 membrane with water flux changes at different temperatures and pH levels (Figure 6d). During the transition from below to above the LCST of PNIPAm, the permeability of the functionalized PVDF650 membrane increased by approximately 14%, 22%, and 37% for pH levels of 3.0, 6.8, and 10.5, respectively. These changes indicate the thermoresponsive nature of membranes with functionalization. It is important to note that these flux values were obtained after undertaking viscosity corrections with respect to temperature; thus, flux changes below and above the LCST were solely due to the swelling/shrinking of the PNIPAm chains, respectively. Furthermore, below the pKa of PMMA, the PMMA chains are in a collapsed state, which restricts the responsive nature of the PNIPAm chains. This is seen in the sample at a pH of 3.0 (below the pKa), which had the lowest increase in flux transitioning above the LCST. Overall, these differences indicate the successful pH-responsiveness of the membrane after functionalization.

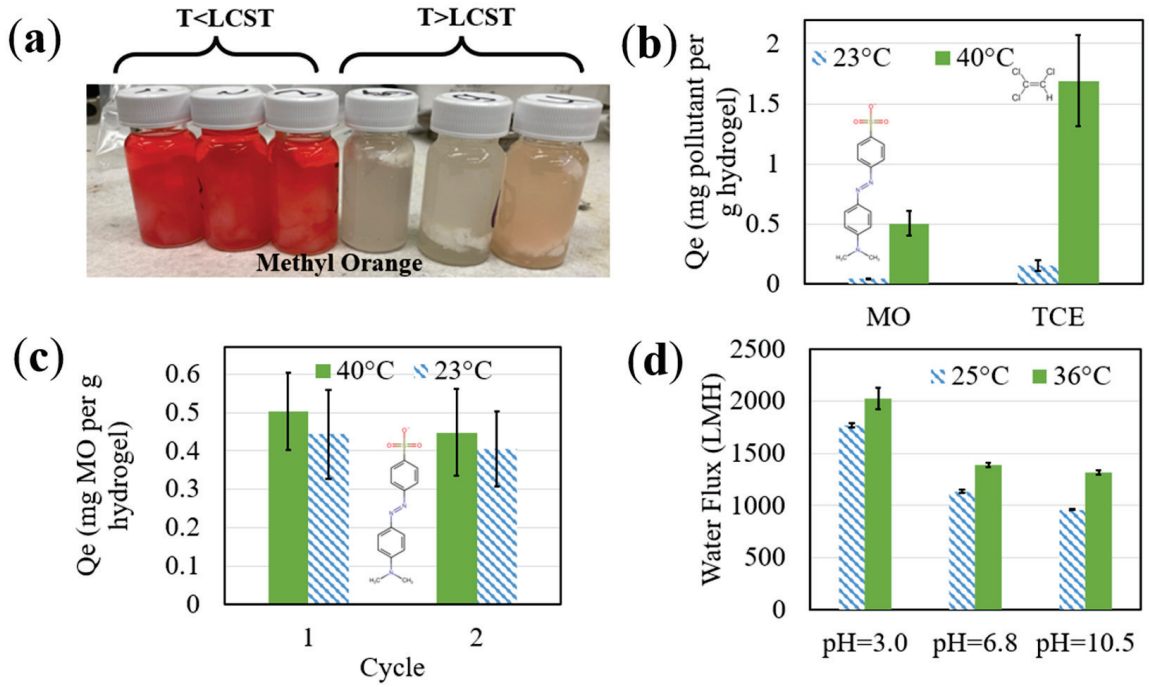

Figure 6. Methyl orange adsorption interactions with PNIPAm/PMMA hydrogel and flux studies of PNIPAm/PMMA-functionalized flat sheet membranes. (**a**) MO (indicated by a red color) solution with PNIPAm-PMMA hydrogel below and above the LCST of PNIPAm. Adsorption of (**b**) MO and TCE onto PNIPAm-PMMA hydrogels below and above the LCST at a pH of 7–8, as well as (**c**) two temperature swing cycles with desorption below the LCST at a pH of 7–8. Note that the 40 °C of cycle 1 corresponds to the same hydrogels as the 40 °C samples from (**b**). Green bars represent experimentation at 40 °C, and blue-lined bars represent experimentation at 23 °C. The initial concentrations of MO and TCE were ~100 mg/L and 93 mg/L, respectively, and the weight of the hydrogels utilized was approximately 1.7 g. Error bars represent triplicate samples, except for TCE data, which represents duplicates. (**d**) Volumetric water flux changes of a PNIPAm-PMMA-PVDF650 flat sheet membrane in response to variation in temperature and pH. Green bars represent experimentation at 36 °C, and blue-lined bars represent experimentation at 25 °C. Note that these flux values are corrected for changes in viscosity with respect to changes in temperature. Water flux is measured at 1.4 bar with an unfunctionalized membrane flux of 3580 LMH. Error bars represent triplicate samples.

3.3. Pollutant Degradation with Responsive Catalytic Membranes

3.3.1. Steps of the Reductive Degradation Pathway with Corresponding Models

The degradation of TCE with ZVI systems is typically modeled using pseudo-zero-order or first-order reaction rate kinetics with high and low concentrations of TCE, respectively [50]. In this study, the concentrations of pollutants are relatively low, so the following pseudo-first-order (PFO) reaction rate relationship was utilized for degradation modeling:

$$-\frac{dC}{dt} = C \times k_{obs} = C \times (k_{sa}\rho_m a_s) \quad (4)$$

where k_{obs} is the observed reaction rate constant (1/min), ρ_m is the iron loading density (g/L), a_s is the nanoparticle surface area to mass ratio (m^2/g), and k_{sa} is the bimetallic nanoparticle surface area-normalized reaction rate constant (L/m^2/h). It is important to note that PFO rates have certain limitations, as several assumptions are made: (1) negligible mass transfer resistance between the liquid and solid boundary layer, (2) irreversible degradation of TCE, DCE, and other intermediates, (3) TCE adsorbed onto the NP surface dechlorinates before product desorption can occur, (4) all reactions are isothermal, (5) no competitive effects between pollutant and product species, and (6) products in gas form

(i.e., ethylene) are present only in headspace and not in solution (due to low aqueous solubility) [51].

To create a more accurate mode, the specific phases of this pathway must be considered. The degradation of TCE via Fe/Pd NPs occurs through several steps, summarized in Figure 7a. Initially, the ZVI is oxidated (converting to Fe^{2+} or Fe^{3+}), which releases electrons. Through a hydrogen evolution reaction, these electrons produce hydrogen gas from the surrounding H_2O in addition to hydroxide (OH^-). H_2 gas is then adsorbed onto the surface of the Pd^0, along with the contaminant TCE, where hydrogen radicals are produced. These hydrogen radicals then hydrodechlorinate the TCE contaminants to DCE, ethylene, and eventually ethane (C_2H_6).

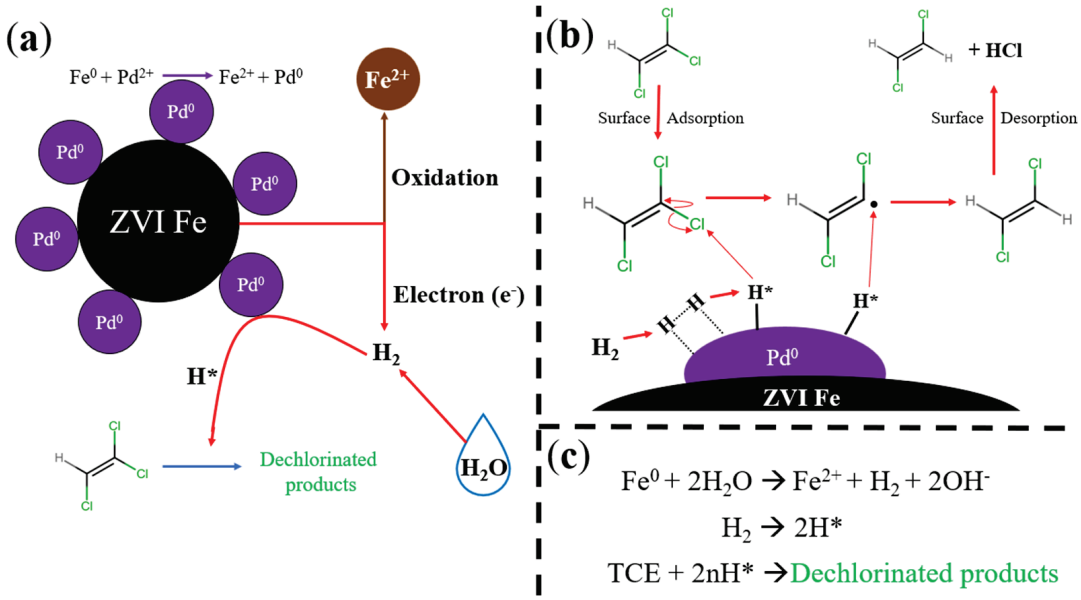

Figure 7. Schematic detailing degradation of TCE via Fe/Pd NPs. This schematic contains (**a**) an overview of the processes with a detailed explanation of hydrogen gas generation from iron corrosion, (**b**) the multi-step process of the TCE contaminant, including adsorption, degradation, and desorption, and (**c**) simplified stoichiometric reaction steps for the overall process. The "*" symbol represents a radical.

Several mathematical models have been used for the degradation of TCE via Fe/Pd NPs in batch mode. Summarized in Figure 7b in simplistic terms, there are three main steps to this process that the model can include [51]:

(1) Mass transfer of TCE (C_2HCl_3) from the bulk solution to the surface of the catalyst site and subsequent surface adsorption, forming a di-σ-bonded species from the intermediate (π-bonded):

$$C_2HCl_3 + S\ (active\ site) \underset{k_{1a}}{\overset{k_{-1a}}{\rightleftharpoons}} C_2HCl_3 - S$$

$$C_2HCl_3 - S + S \rightarrow C_2HCl_3 * -S_2;$$

(2) Hydrodechlorination of TCE on the active sites of the NPs with DCE as a product and eventually ethane:

$$\frac{5}{2}Fe^0 + 5H_2O + 5Pd \rightarrow \frac{5}{2}Fe^{2+} + 5OH^- + 5Pd - H$$

$$\frac{3}{2}Fe^0 \rightarrow \frac{3}{2}Fe^{2+} + 3e^-$$

$$C_2HCl_3 * -S_2 + 5Pd - H + 3e^- \rightarrow C_2H_6 * -S_2 + 5Pd + 3Cl^-;$$

(3) Generated products desorb from the catalyst surface and transport into the surrounding bulk solution:

$$C_2H_6 * -S_2 \rightarrow C_2H_6 + S_2.$$

In the second step, note that the hydrogen generation originates from the oxidation of the ZVI but is a short-lived product and is not included as an individual step. Overall, this pathway, along with the basic overall reaction steps in Figure 7c, is a simplified version of the complete process and can be affected by several other factors. For example, the degradation of TCE produces several compounds that can compete for active sites on the NP surface if their concentration is high enough [50].

Alternatively, for methyl orange, Fe/Pd NPs facilitate the cleavage of the azo bond (-N=N-) to -NH groups [52]. This azo bond has a significant absorption peak around 464 nm; thus, degradation and NP activity can be easily quantified by analyzing the reduction of absorption at this peak using UV-Vis (calibration curve available as Figure S14). It is important to note that the desorption step of MO is slower than that of TCE, meaning that significant adsorption of MO onto the NP surface occurs [53], which is a limitation of utilizing MO as a model compound.

3.3.2. Effect of Temperature on MO Degradation via Fe/Pd Nanoparticles

Bulk diffusion plays a significant role in the degradation process of MO and TCE via Fe/Pd immobilized in membrane systems and can be modeled using the Wilke–Chang model or the Stokes–Einstein equation. The Stokes–Einstein equation is described as follows:

$$D_s = \frac{k_B T}{6\pi\mu r_{part}} \quad (5)$$

where D_s is the bulk diffusion coefficient, k_B is the Boltzmann's constant, T is the temperature (K), r_{part} is the solute molecular radius, and μ is the dynamic viscosity of the solvent. Utilizing the Stokes–Einstein equation, the bulk diffusion coefficients from 5 to 50 °C have been calculated for MO, TCE, and polychlorinated biphenyl (PCB-1, used in prior studies [18]) in a water solvent in Figure S15. In summary, the bulk diffusion coefficients of MO and TCE at 25 °C were found to be 5.5×10^{-11} and 9.1×10^{-10} m^2/s, respectively, while at 40 °C, they were found to be 7.8×10^{-11} and 1.3×10^{-9} m^2/s, respectively. This proves that diffusion itself will increase with system temperature elevation. Additionally, it is important to note that the larger diffusion coefficient of TCE compared to MO can be explained by TCE's smaller molecular size, which decreases resistance to mass transfer.

The activity of Fe/Pd NPs free in solution at both 22.5 °C and 50 °C was initially tested with MO to verify the activity of the nanoparticles, the validity of MO as a model pollutant, the fit of a PFO model, and investigate particle fouling with the pollutant. For pollutant sampling, the nanoparticles (with paramagnetic properties) were briefly separated from the surrounding solution via a strong magnet. MO concentration was then analyzed using UV-Vis at a wavelength of 464 nm, representing the N=N bond that was reduced upon the Fe/Pd reaction (Figure 8a).

As expected, more rapid degradation of MO occurred at 50 °C than at 22.5 °C (Figure 8b), which can be explained by the increased MO diffusivity at the higher temperature (Stokes–Einstein equation). Oxidation of ZVI as well as NP fouling via adsorbed MO (and subsequent products after reduction) can be observed as the degradation process begins to deviate from first-order kinetics after approximately 25 min of reaction time. Low desorption rates (7%) have been reported by Arshadi et al. with MO and metal nanoparticles, which can be attributed to the formation of a strong metal-dye complex [54]. Additionally, there is a small initial delay in degradation activity, which can be explained by the transport limitations of MO through the oxygen layer surrounding the NPs as well as the H_2O interacting with the Fe core and subsequent hydrogen generation.

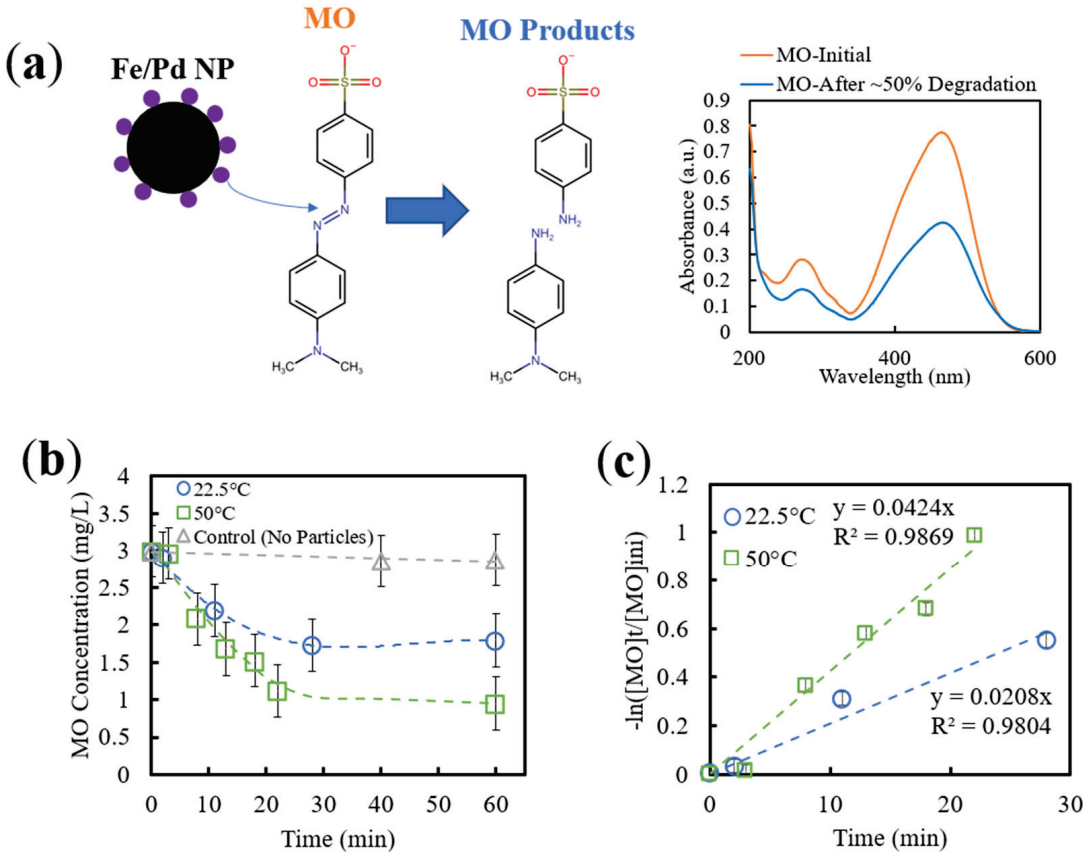

Figure 8. MO degradation with Fe/Pd NPs in a solution. (**a**) Schematic of interaction between Fe/Pd NP and MO, as well as an example of UV-Vis absorbance spectrum before and after degradation from NPs (initial concentration: ~10 mg/L MO). (**b**) MO degradation of Fe/Pd NPs at different temperatures with respect to reaction time. A total of 0.1 g Fe (~10% Pd) in 20 mL vials was used with a MO concentration of 3 mg/L and a pH of 6.8. Samples were shaken at 100 rpm. Error bars indicate triplicate measurements. (**c**) Pseudo-first-order model of MO degradation via Fe/Pd NPs in solution at two different temperatures. Error bars indicate triplicate measurements.

The experimental data was fitted to a pseudo-first-order model to quantify reactivity and obtain reaction rate kinetics (Figure 8c). Utilizing data until degradation stopped (20–30 min of reaction time), the observed reaction rate (k_{obs}) was determined from the slope of the linear fit to be 0.0208 and 0.0424 min^{-1} for 22.5 °C and 50 °C, respectively (Table 2). A more accurate representation of reaction rate can be obtained by calculating the surface area-normalized reaction rate constants (k_{sa}), as it normalizes the constants with respect to NP loading and surface area (average obtained from TEM imaging). It is important to note that the values for loading and surface area of NPs can vary significantly depending on membrane weight gain after hydrogel functionalization (available sites of Fe ion exchange and immobilization) and formed NP size (surface area ratio compared to mass of NP). Using Equation (4), k_{sa} was calculated to be 0.0118 and 0.0240 L/m^2/hour for 22.5 °C and 50 °C, respectively, indicating a ~two-fold increase in reaction rate constants from this temperature increase. To eliminate the effect of temperature on the model values, these constants can be normalized with respect to temperature using the Arrhenius equation:

$$\ln \frac{k_2}{k_1} = \frac{-E_a}{R}\left(\frac{1}{T_2} - \frac{1}{T_1}\right) \quad (6)$$

where R is the gas constant, T is the temperature (K), and E_a is the activation energy (kJ/mol). After normalization with respect to 22.0 °C, the k_{sa} values were roughly equal (Table 2), indicating that there were no other forces affecting the reactivity at different

temperatures besides changes in contaminant diffusion. Overall, MO was confirmed to be an appropriate model for Fe/Pd NP systems, and the effect of temperature on diffusivity was investigated with appropriate kinetic models, yet a possible limitation of utilizing MO as a model compound was found (low MO desorption from the NP surface).

Table 2. Observed and surface area-normalized reaction rate constants (k_{obs} and k_{sa}) of batch-mode MO degradation via Fe/Pd NPs in solution. The average diameter of NPs utilized for calculations was 36 nm on average.

T (°C)	k_{obs} (1/min)	ρ_m (g/L)	a_s (m^2/g)	k_{sa} (LMH)	Temperature-Normalized k_{sa} (LMH) *
22.5 °C	0.0208	5	21.2	0.0118	0.0118
50 °C	0.0424	5	21.2	0.0240	0.0108

* Normalized with respect to 22.0 °C using the Arrhenius equation and an activation energy of ~23 kJ/mol from the ZVI system of Shih et al. [55].

3.3.3. Thermo-Responsive Degradation of MO via Catalytic Membranes

The Stokes–Einstein model is appropriate for batch NP experiments, but with catalytic NPs imbedded into a membrane/hydrogel matrix, the diffusion rate will be significantly lower due to the crosslinked hydrogel matrix and membrane material. Yang et al. developed a model that can be fitted to the obtained data for contaminant diffusion in the presence of a catalytic membrane [56]:

$$\frac{C_{TCE}}{C_{TCE,initial}} = \left(\frac{DH}{l}\right)\left(\frac{A}{V}\right)\left(t - \frac{l^2}{6D}\right) \quad (7)$$

where D is the diffusion coefficient (m^2/s), H is the partition coefficient, A is the membrane area (m^2), V is the permeate solution volume (m^3), and t is the time (s). Using Equation (7), the diffusion coefficient can be derived from the slope and intercept. It is important to note that, as previously mentioned, several literature sources have found this catalytic process to be diffusion-limited [39,57,58], which is the motivation for PNIPAm incorporation. Significant differences in diffusion coefficients have been reported for PNIPAm-functionalized membranes in the literature, as 6.6×10^{-11} and 8.7×10^{-11} m^2/s at 25 and 35 °C, respectively, for PCB-1 [18], showing the validity of Yang et al.'s model and the PNIPAm functionalization.

Similar to diffusion modeling, though, the previous equations are not adapted for responsive membranes. The residence time (Equation (8)) within the membrane varies depending on the temperature and permeate flow rates (which are pressure-dependent) of an Fe/Pd-PNIPAm-membrane as the void fraction (membrane volume multiplied by surface porosity) changes above and below the LCST (due to polymer swelling/shrinking). Wan et al. derived a model to determine the pseudo-first-order reaction constants of such membranes using the following two equations [46].

$$\tau = V_{void}/(J_w A) \quad (8)$$

$$\overline{C}_{final} = \overline{C}_{initial}\frac{\tau^2}{4}\left[{k_{obs}}^2\left(\int_{k_{obs}\tau/2}^{\infty}\frac{e^{-t}}{t}dt\right) + e^{-k_{obs}\tau/2}\left(\frac{4}{\tau^2} - \frac{2k_{obs}}{\tau}\right)\right] \quad (9)$$

where V_{void} is the membrane void fraction, $\overline{C}_{final}$ is the final contaminant concentration, $\overline{C}_{initial}$ is the initial contaminant concentration, and τ is the residence time (s).

It is important to note that these models are not without their limitations. Foo et al. present a comprehensive review of different adsorption isotherm systems [59]. Langmuir and Freundlich adsorption isotherms are typically used for such TCE adsorption reactions, with assumptions regarding monolayer vs. double layer adsorption. Furthermore, as previously mentioned, convective flow for HFMs is a current limitation of this work, but

previously shown models could theoretically be applied to HFM flow to compare diffusion coefficient changes across the LCST.

The temperature-responsive presence of PNIPAm on the functionalized HFMs containing Fe/Pd NPs was tested with MO in batch mode. The membranes were cut to 4 cm fiber length and shaken for 60 min total in a ~5 mg/L MO solution. An incubator shaker was utilized to control the temperature of the samples below and above PNIPAm's LCST. Note that the tested membranes had a NP loading of 5.9 mg iron per g of membrane, determined from ICP, with approximately 3 mol% of Pd.

Similar to free NPs, a more significant MO degradation versus time was observed at a higher temperature of 40 °C (Figure 9a). Note that control absorbance values (from shaking HFM without MO presence, ranging from 0.01 to 0.1) were subtracted from measured values to ensure the change in absorbance was due to MO degradation and not the release of unbound NPs. When fitted to a PFO model, though, a significant deviation occurred (Figure 9b) from a linear fit. This is most likely due to the low desorption rates of MO from the catalytic NPs (as previously mentioned), lower mass transfer rates overall through membrane systems (as opposed to free catalysts in solution), as well as the oxidation of ZVI throughout the duration of experimentation (Figure 9c). This could be an indication of a limitation of the pseudo-models for describing complicated reaction processes. Furthermore, functionalized membranes were characterized with SEM after 90 min of MO degradation, showing significant surface fouling and some loss of iron NP structure (Figure 9d), indicating limitations for long-term MO treatment.

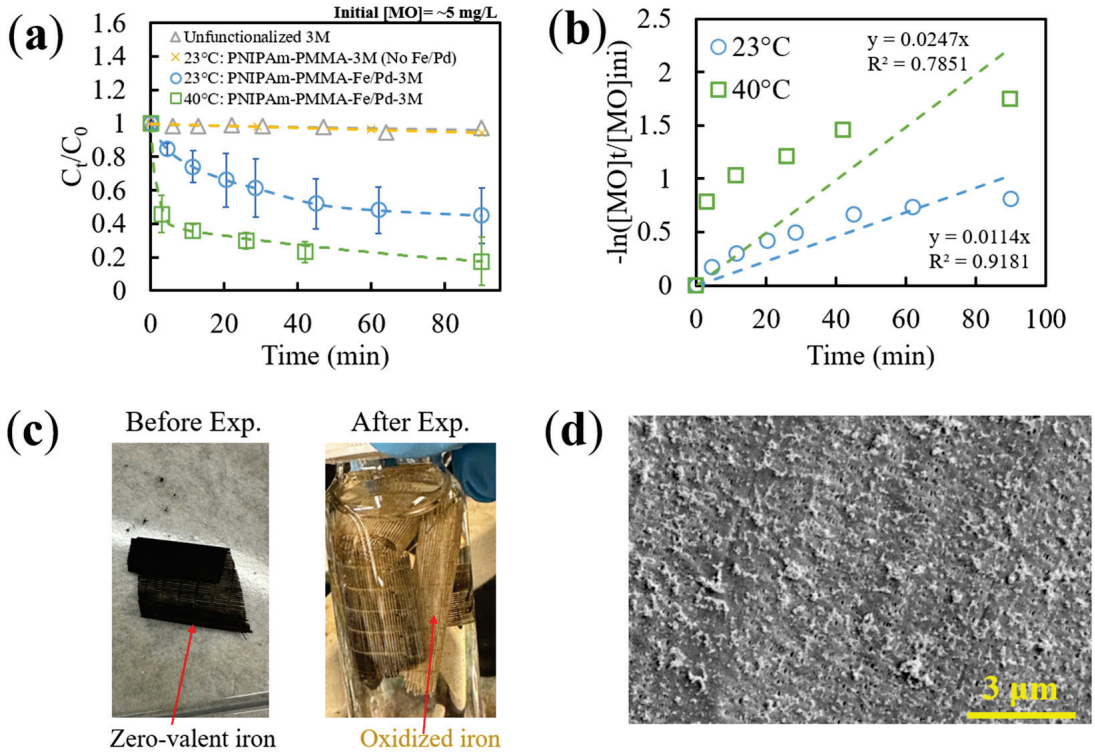

Figure 9. Degradation of MO via PNIPAm-PMMA-functionalized 3M HFMs with 5.9 mg iron per g of membrane and approximately 3 mol% of Pd. (**a**) MO degradation by PNIPAm-PMMA-functionalized 3M HFMs below and above the LCST of PNIPAm in batch mode. Concentration values were normalized based on membrane weight (150–170 mg). Error bars represent triplicate samples. Samples were shaken at 200 rpm, and the solution pH was roughly 6.5. Non-degraded MO was analyzed at a wavelength of 464 nm using UV-Vis. (**b**) Pseudo-first-order fit of MO degradation data by functionalized HFMs. Error bars represent triplicate samples. (**c**) Image of 3M membrane before and after experimentation, indicating significant oxidation of iron (from black to brown color). (**d**) SEM image of functionalized membrane after 90 min of MO degradation.

It is important to note that oxidation of the ZVI NPs is a current limitation of this technology, as conversion from ZVI (black-colored membrane) to Fe^{2+} (brown-colored membrane) depletes the electron-donating source. This can lead to a loss of long-term activity, leading to the need for regeneration of the ZVI or the introduction of dilute hydrogen gas. Even though NPs in this study are immobilized in a hydrogel matrix, thus offering some protection from oxidation, the color change in Figure 9c does indicate a certain degree of oxidation. For similar membrane systems, our group has reported less than 20% Fe/Pd initial activity after four degradation cycles over a 3 month period in water [16]. One promising method for overcoming this limitation is the reduction of Fe^{2+} via green tea extract instead of sodium borohydride. This method has been shown to maintain at least 85% of Fe/Pd initial activity in membranes after 3 months of periodic activity testing [16] and could be implemented in future HFM studies.

In this work, an initial Fe/Pd stability test was performed by storing the NPs in DIW with different dissolved oxygen (DO) concentrations (~0 ppm and 5.5 ppm). After 24 h of storage, the samples were analyzed using TEM and EELS (Figure S16). The sample with minimal DO levels showed a prominent iron core with a small oxidative shell surrounding it, indicating no noticeable difference from the initial sample (Figure S12). Alternatively, the 5.5 ppm DO sample showed loss of the iron core with significant NP oxidation as well as the formation of iron oxide sheets, thus displaying a leading example of the long-term oxidative limitations of these systems.

Furthermore, the MO concentration did not decrease for both controls (unfunctionalized HFM and PNIPAm-PMMA-3M without NPs). This indicated that the decrease in MO during experimentation with NP-functionalized membranes can be primarily attributed to catalytic degradation and not adsorption onto the membrane system. Additionally, the initial delay observed in the free NP samples was not apparent in this system, which could be due to the PNIPAm in the system overcoming the previously mentioned mass transfer limitations. Overall, though, it is important to note that, to the group's knowledge, this is one of the first reported demonstrations of enhancing MO degradation with the presence of PNIPAm in a Fe/Pd bimetallic system. These findings bring significant advances to the remediation field by increasing the range of effective contaminants that these thermoresponsive membrane systems can treat in groundwater sources.

For direct comparison with free NPs as well as with TCE degradation, approximate observed reaction rate constants were obtained from the slope of the linear PFO model fit for these functionalized membranes. When correcting the observed constants with respect to temperature, surface-area-normalized constants were found to be 0.6247 and 0.8147 LMH for 23 °C and 40 °C, respectively (Table 3), which are comparable to previous studies with similar catalytic HFM systems [60]. This 30% increase in reaction rate constants can be attributed to the PNIPAm's phase transition above LCST (expressing hydrophobic domains), leading to lower mass transfer limitations during remediation. It is important to note that, in comparison to the free NPs, the membrane-bound system had significantly higher k_{sa} values (after particle loading normalization), which further indicates the benefit of the hydrogel domain incorporation and subsequent increased adsorptive properties for degradation efficiency. Overall, the efficacy of utilizing PNIPAm's phase transition to increase the degradation capabilities of catalytic HFM systems was validated, showing promising advances for scalable environmental remediation devices.

Table 3. Observed and surface area-normalized reaction rate constants (k_{obs} and k_{sa}) of batch-mode MO degradation via Fe/Pd-PNIPAm-PMMA-functionalized HFMs in solution. The average diameter of NPs utilized for calculations was 34.8 nm on average.

T (°C)	k_{obs} (1/min)	ρ_m (g/L)	a_s (m^2/g)	k_{sa} (LMH)	Temperature-Normalized k_{sa} (LMH) *
23 °C	0.0114	0.05	21.9	0.6247	0.6247
40 °C	0.0247	0.05	21.9	1.3534	0.8147

* Normalized with respect to 23.0 °C using the Arrhenius equation and an activation energy of ~23 kJ/mol from the ZVI system of Shih et al. [55].

3.3.4. Thermoresponsive TCE Degradation via Catalytic Membranes

After initial testing with the model compound MO, batch degradation of TCE below and above PNIPAm's LCST was conducted with PNIPAm-PMMA-functionalized HFMs containing Fe/Pd NPs (in vials with minimal to no headspace). Septa vial caps were utilized, along with a volumetric needle, for taking samples, ensuring minimal TCE was lost due to volatility. Additionally, an incubator shaker was utilized to control the temperature of the samples below and above PNIPAm's LCST. A control without membranes was also utilized to normalize TCE concentrations based on maximum lost vapor during sampling.

Below the LCST (23 °C), roughly 65% of TCE was degraded within 90 min of reaction time, while above the LCST (40 °C), 96% degradation was observed within the first 30 min (Figure 10a). Similar to MO, the primary reduction in TCE concentration was assumed to occur primarily due to catalytic degradation. A preliminary experiment utilizing PNIPAm-PMMA-3M membranes (similar weight to experimental) with oxidized NPs (thus inactive) showed a small decrease (<5%) in TCE concentration (5 mg/L) over 90 min of shaking. Degradation of TCE was further confirmed to be occurring via analysis of the MS spectrum of the contaminated solution at t = 0 min and t = 30 min (Figure S17), indicating a higher chloroethylene signal (~57.0 m/z) at t = 30 min, compared to DCE and TCE (~95 and 130 m/z, respectively), than that of the initial sample at t = 0 min.

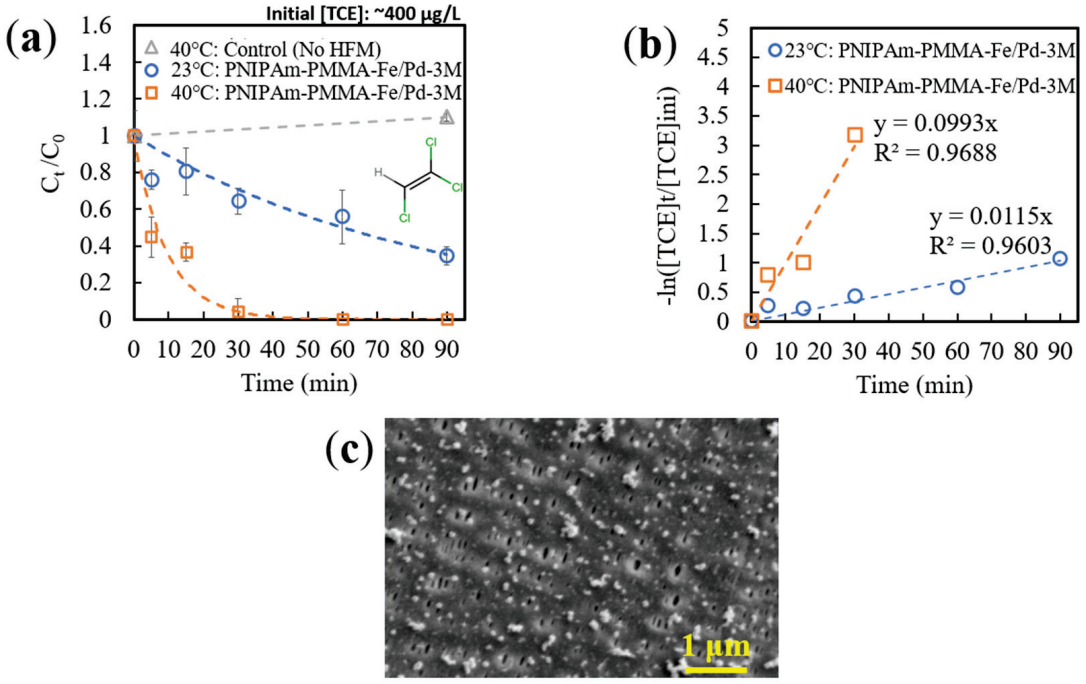

Figure 10. TCE degradation with functionalized membrane systems with 5.9 mg iron per g of membrane and approximately 3 mol% of Pd. (**a**) TCE degradation by PNIPAm-PMMA-functionalized 3M HFMs below and above the LCST of PNIPAm in batch mode. Each vial contained roughly 4.3–4.6 g of HFM with minimal headspace. Error bars represent triplicate measurements. Samples were shaken at 200 rpm, and the solution pH was roughly 6.5. Zero values indicate TCE concentrations less than the limit of detection (<1 µg/L TCE). (**b**) Pseudo-first-order fit of TCE degradation data by functionalized HFMs. Near-zero values under the limit of detection (<1 µg/L TCE) were not included in the PFO fit for 40 °C samples. (**c**) SEM image of functionalized membrane after 90 min of TCE degradation.

Furthermore, this data was fitted to a PFO model (Figure 10b), yielding observed reaction rate constants of 0.0115 and 0.0993 min^{-1} at 23 °C and 40 °C, respectively. Unlike with MO, TCE degradation from these reactive membranes exhibited a stronger fit to the PFO model ($R^2 > 0.96$), indicating the validity of the model for demonstrating this process.

Additionally, it is important to note that the TCE concentration utilized in these experiments was 0.5 mg/L. While technologies to remediate highly contaminated water (>5 mg/L TCE) are important, systems that can remediate trace-contaminated sources (0.1–1 mg/L TCE) to be under the maximum contaminant level (MCL) of TCE (5 μg/L) [61] are vital to ensuring the long-term health of the effected communities by eliminating chronic TCE exposure. With an analytic limit of detection of 1 μg/L, the ability of the catalytic HFM systems in this research to reach below the MCL was observed above PNIPAm's LCST.

The observed constants were corrected with respect to temperature; thus, the resulting surface-area-normalized constants were found to be 0.5251 and 2.7293 LMH for 23 °C and 40 °C, respectively (Table 4). This 420% increase (after temperature correction) can be attributed to PNIPAm's expressed hydrophobic domains above the LCST and overall higher rates of mass transfer between the contaminant and active site. This difference between MO and TCE degradation increases above the LCST (30% and 420%, respectively) and can most likely be attributed to the difference in molecule size. The significantly higher bulk diffusion coefficient of TCE previously mentioned (Figure S15) can also be attributed, indicating high desorption rates of degradation products from the NP surface and lower mass transfer limitations overall for TCE compared to MO. This difference also indicates the limitations of utilizing MO to model catalytic systems with the intended application of TCE remediation. Additionally, it is important to note that the functionalized membrane was found to be relatively unchanged (compared to t = 0 min) via SEM analysis after 90 min of TCE degradation (Figure 10c). Unlike the membrane after MO degradation, this sample showed little surface fouling, with the observed spherical NPs remaining prominent, indicating this system's potential for long-term TCE remediation.

Table 4. Observed and surface area-normalized reaction rate constants (k_{obs} and k_{sa}) of batch-mode TCE degradation via Fe/Pd-PNIPAm-PMMA-functionalized HFMs in solution. The average diameter of NPs utilized for calculations was 34.8 nm on average.

T (°C)	k_{obs} (1/min)	ρ_m (g/L)	a_s (m^2/g)	k_{sa} (LMH)	Temperature-Normalized k_{sa} (LMH) *
23 °C	0.0115	0.06	21.9	0.5251	0.5251
40 °C	0.0993	0.06	21.9	4.5342	2.7293

* Normalized with respect to 22.0 °C using the Arrhenius equation and an activation energy of ~23 kJ/mol from the ZVI system of Shih et al. [55].

Overall, incorporating PNIPAm hydrogels into catalytic HFMs shows valid advances in increasing the TCE degradation capabilities of such systems, which have not been previously reported in the literature, leading to more effective remediation techniques at environmentally relevant contaminant concentrations.

It is important to note that further methods can be utilized to optimize water remediation from TCE and other VOCs. While hydrophilic membranes offer lower operating pressures for convective water flow through traditional filtration, this work implemented this functionalization process on a primarily hydrophobic HFM. The main benefit of the membrane hydrophobicity is the ability to utilize membrane air-stripping (MAS) [62,63], which has been proven to be effective for TCE stripping (in vapor form) from liquid water sources with polypropylene HFMs [64]. A preliminary experiment was conducted with a full-sized 3M-HFM module for TCE stripping from a 200 mL solution (initial [TCE] = 3.7 ± 0.2 mg/L), utilizing a MAS set-up (Figure S18). While the control solution only dropped to 3.4 ± 0.1 mg/L TCE, the MAS solution dropped to below the limit of detection (<1 μg/L TCE) after 60 min of recycle flow, indicating that the 3M HFM's hydrophobicity allowed for TCE to be stripped out of the contaminated solution in vapor form. By combining MAS and Fe/Pd-functionalized HFMs, even higher degradation efficiencies could be achieved, as degrading TCE in a vapor form can allow for lower mass transfer limitations between the contaminant and active site, while the water vapor can maintain adequate hydration for ZVI's hydrogen gas generation. This process can also separate TCE from other natural organics (present in real groundwater) that could inhibit/foul the catalyst surface or act as

active site competition. In this work, functionalization of the lumen side is not a significant concern, as primary degradation is desired to occur while TCE is in vapor form (present in pores and the shell side). Overall, the selection of membrane material in this work allows for potential MAS applications to achieve higher environmental remediation efficiencies in the long-term.

4. Conclusions

This research investigated the integration of the temperature-responsive polymer, PNIPAm, into Fe/Pd-PMMA-functionalized hollow fiber membranes, establishing a significant step towards the scalability of these systems. Temperature-responsive functionalization of HFMs was achieved, a synthesis aspect that has not been previously reported in the literature. After functionalization, the dip-coated flat sheet and HFMs showed weight gains of roughly 9% and 15%, respectively, indicating significant retention of stimuli-responsive hydrogel. Due to enhanced hydrophobic interactions between the hydrogel matrix and the pollutant (expressed at $T > LCST_{PNIPAm}$), degradation increases of 30% and 420% for azo dyes (methyl orange) and VOCs (trichloroethylene), respectively, were observed with the developed HFM in batch mode, overcoming previously-reported mass transfer limitations that occur when integrating such catalysts into polymer-membrane matrixes. These findings signified significant novelties in the remediation field, as the range of contaminants that such membrane systems can treat in groundwater sources has been expanded to MO and TCE, both previously unreported in the literature with these thermoresponsive systems. Furthermore, the resulting degradation data was modeled using a pseudo-first-order model, obtaining surface-area and temperature-corrected reaction rate constants of 0.6247 and 0.5251 at 23 °C and 0.8147 and 2.7293 at 40 °C for methyl orange and TCE, respectively. Overall, the implementation of catalytic and temperature-responsive functionalizations into hollow fiber membrane systems with superior surface area per packing volume provided novel advances to the field of membrane-based water remediation. This work demonstrated the capabilities of developing temperature-responsive membrane modules that can result in treating larger volumes of contaminated water per unit time than current established filtration methods.

In future work, the effect of natural organic presence can be quantified in relation to degradation efficiency over long periods of treatment time, thus simulating more realistic remediation scenarios. The ability of catalytic hollow fiber membranes to degrade VOCs in a convective mode can be further studied as well, which could prove its efficacy in at-home water treatment modules with low replacement needs. Additionally, a grafting method could be established for attaching the polymer/catalyst system to the membrane domain, furthering the long-term stability and low metal leaching of the resulting filter.

Supplementary Materials: The following supporting information can be downloaded at: https://www.mdpi.com/article/10.3390/nano13142041/s1, Section A. Figure S1: Calibration curve of known TCE concentration (after 100:1 injection dilution) versus the area under the measured peak via GCMS analysis. Hexane (GCMS grade) was utilized as the solvent; Figure S2: GCMS analysis of TCE standards. (a) Total ion chromatograph (TIC) of 1 mg/L TCE solution (after 100:1 injection dilution) and (b) MS spectrum results (counts vs. mass-to-charge) for TCE peak displayed; Figure S3: Volumetric water flux versus applied pressure of flat sheet PVDF400 and PVDF650 commercial membranes; Figure S4: Full-thickness cross-section SEM image of an asymmetric PVDF400 membrane; Figure S5: SEM of cross-section 3M-HFM with corresponding schematic of hollow fiber membrane structure, shell side, and lumen side; Figure S6: FTIR of unfunctionalized and functionalized membrane samples; Figure S7: SEM image of microfibers holding together 3M-HFM; Figure S8: Fe/Pd particle size of functionalized (a) PVDF650 and (b) 3M-HFM; Figure S9: Cross-section SEM image of cross-section pores of 3M-HFM functionalized with Fe/Pd bimetallic nanoparticles, PNIPAm, and PMMA; Figure S10: Schematic of Fe/Pd NP synthesis in solution; Figure S11: An XRD diffractogram of (a) freshly made metallic iron (Fe^0) particles, (b) freshly made palladium particles, (c) palladium coated iron particles, (d) deliberately oxidized Fe/Pd particles, (e) regenerated Fe/Pd particles, and (f) Fe_2O_3 particles [46]; Figure S12: TEM, EDX, EELS analysis of Fe/Pd NPs free in solution; Figure S13: Size

distribution of Fe/Pd NPs free in solution; Figure S14: Calibration curve of MO standards, analyzed using UV-Vis; Figure S15: Calculated bulk diffusion coefficients for MO, TCE, and PCB-1 water contaminants in a water solvent, with respect to temperature; Figure S16: TEM and EEL analysis of Fe/Pd NPs stored in DIW solutions with different dissolved oxygen (DO) concentrations over a 24 h period; Figure S17: GCMS analysis of contaminant solution during PNIPAm/PMMA-Fe/Pd-functionalized HFM experimentation above the LCST of PNIPAm; Figure S18: Schematic of MAS set-up utilized for TCE stripping; Section B. Table S1: EELS analysis of Fe/Pd nanoparticle. Section C. Supplementary Methods.

Author Contributions: Conceptualization, R.M. and D.B.; methodology, R.M., C.T., A.L. and D.B.; formal analysis, R.M., C.T., A.L. and D.B.; investigation, R.M., C.T., A.L. and D.B.; resources, R.M., C.T., A.L. and D.B.; data curation, R.M., C.T., A.L. and D.B.; writing—original draft preparation, R.M., C.T., A.L. and D.B.; writing—review and editing, R.M., C.T., A.L. and D.B.; visualization, R.M. and D.B.; supervision, D.B.; project administration, D.B.; funding acquisition, R.M. and D.B. All authors have read and agreed to the published version of the manuscript.

Funding: This research was funded by the National Institute of Environmental Health Sciences-Superfund Research Program (NIEHS-SRP) Grant P42ES007380. Rollie Mills is funded by the National Science Foundation (NSF)-Graduate Research Fellowship Program (GRFP).

Data Availability Statement: The data that support the findings of this study are available from the corresponding author upon reasonable request.

Acknowledgments: The authors acknowledge Solecta Membranes (Oceanside, CA, USA) for providing large-sheet commercial PVDF400 and PVDF650 membranes, as well as Kevin Baldridge, Francisco Leniz, Ben Weaver, Ronald Vogler, and Matthew Bernard for technical discussions. The authors also acknowledge Zachary Hilt for providing analytical instrumentation (FTIR) and Nico Briot at the Electron Microscopy Center (University of Kentucky) for SEM/TEM/EDX instrumentation.

Conflicts of Interest: The authors declare no conflict of interest.

References

1. Jo, W.-K.; Park, K.-H. Heterogeneous photocatalysis of aromatic and chlorinated volatile organic compounds (VOCs) for non-occupational indoor air application. *Chemosphere* **2004**, *57*, 555–565. [CrossRef] [PubMed]
2. Wu, C.; Schaum, J. Exposure assessment of trichloroethylene. *Environ. Health Perspect.* **2000**, *108*, 359–363. [CrossRef] [PubMed]
3. Gossett, J.M. Measurement of Henry's law constants for C1 and C2 chlorinated hydrocarbons. *Environ. Sci. Technol.* **1987**, *21*, 202–208. [CrossRef]
4. Chiu, W.A.; Jinot, J.; Scott, C.S.; Makris, S.L.; Cooper, G.S.; Dzubow, R.C.; Bale, A.S.; Evans, M.V.; Guyton, K.Z.; Keshava, N.; et al. Human health effects of trichloroethylene: Key findings and scientific issues. *Environ. Health Perspect.* **2013**, *121*, 303–311. [CrossRef]
5. Karami, S.; Lan, Q.; Rothman, N.; Stewart, P.A.; Lee, K.-M.; Vermeulen, R.; Moore, L.E. Occupational trichloroethylene exposure and kidney cancer risk: A meta-analysis. *Occup. Environ. Med.* **2012**, *69*, 858–867. [CrossRef]
6. Vermeulen, R.; Zhang, L.; Spierenburg, A.; Tang, X.; Bonventre, J.V.; Reiss, B.; Shen, M.; Smith, M.T.; Qiu, C.; Ge, Y.; et al. Elevated urinary levels of kidney injury molecule-1 among Chinese factory workers exposed to trichloroethylene. *Carcinogenesis* **2012**, *33*, 1538–1541. [CrossRef] [PubMed]
7. Liu, Y.; Sohi, S.P.; Liu, S.; Guan, J.; Zhou, J.; Chen, J. Adsorption and reductive degradation of Cr(VI) and TCE by a simply synthesized zero valent iron magnetic biochar. *J. Environ. Manag.* **2019**, *235*, 276–281. [CrossRef] [PubMed]
8. Nakano, Y.; Hua, L.Q.; Nishijima, W.; Shoto, E.; Okada, M. Biodegradation of trichloroethylene (TCE) adsorbed on granular activated carbon (GAC). *Water Res.* **2000**, *34*, 4139–4142. [CrossRef]
9. Liu, P.; Long, C.; Li, Q.; Qian, H.; Li, A.; Zhang, Q. Adsorption of trichloroethylene and benzene vapors onto hypercrosslinked polymeric resin. *J. Hazard. Mater.* **2009**, *166*, 46–51. [CrossRef]
10. Erto, A.; Andreozzi, R.; Lancia, A.; Musmarra, D. Factors affecting the adsorption of trichloroethylene onto activated carbons. *Appl. Surf. Sci.* **2010**, *256*, 5237–5242. [CrossRef]
11. Blankenship, A.; Chang, D.P.Y.; Jones, A.D.; Kelly, P.B.; Kennedy, I.M.; Matsumura, F.; Pasek, R.; Yang, G. Toxic combustion by-products from the incineration of chlorinated hydrocarbons and plastics. *Chemosphere* **1994**, *28*, 183–196. [CrossRef]
12. Li, Y.; Li, B.; Wang, C.P.; Fan, J.Z.; Sun, H.W. Aerobic degradation of trichloroethylene by co-metabolism using phenol and gasoline as growth substrates. *Int. J. Mol. Sci.* **2014**, *15*, 9134–9148. [CrossRef] [PubMed]
13. Kim, H.; Hong, H.J.; Jung, J.; Kim, S.H.; Yang, J.W. Degradation of trichloroethylene (TCE) by nanoscale zero-valent iron (nZVI) immobilized in alginate bead. *J. Hazard. Mater.* **2010**, *176*, 1038–1043. [CrossRef] [PubMed]
14. Cheng, S.F.; Wu, S.-C. The Enhancement Methods for the Degradation of TCE by Zero-valent Metals. *Chemosphere* **2000**, *41*, 1263–1270. [CrossRef] [PubMed]

15. Wang, T.; Su, J.; Jin, X.; Chen, Z.; Megharaj, M.; Naidu, R. Functional clay supported bimetallic nZVI/Pd nanoparticles used for removal of methyl orange from aqueous solution. *J. Hazard. Mater.* **2013**, *262*, 819–825. [CrossRef] [PubMed]
16. Smuleac, V.; Varma, R.; Sikdar, S.; Bhattacharyya, D. Green synthesis of Fe and Fe/Pd bimetallic nanoparticles in membranes for reductive degradation of chlorinated organics. *J. Membr. Sci.* **2011**, *379*, 131–137. [CrossRef]
17. Saad, A.; Mills, R.; Wan, H.; Mottaleb, M.A.; Ormsbee, L.; Bhattacharyya, D. Thermo-responsive adsorption-desorption of perfluoroorganics from water using PNIPAm hydrogels and pore functionalized membranes. *J. Memb. Sci.* **2020**, *599*, 117821. [CrossRef]
18. Saad, A.; Mills, R.; Wan, H.; Ormsbee, L.; Bhattacharyya, D. Thermoresponsive PNIPAm–PMMA-Functionalized PVDF Membranes with Reactive Fe–Pd Nanoparticles for PCB Degradation. *Ind. Eng. Chem. Res.* **2020**, *59*, 16614–16625. [CrossRef]
19. Xiao, L.; Davenport, D.M.; Ormsbee, L.; Bhattacharyya, D. Polymerization and Functionalization of Membrane Pores for Water Related Applications. *Ind. Eng. Chem. Res.* **2015**, *54*, 4174–4182. [CrossRef]
20. Lewis, S.; Smuleac, V.; Montague, A.; Bachas, L.; Bhattacharyya, D. Iron-Functionalized Membranes for Nanoparticle Synthesis and Reactions. *Sep. Sci. Technol.* **2009**, *44*, 3289–3311. [CrossRef]
21. Madaeni, S.S.; Zinadini, S.; Vatanpour, V. A new approach to improve antifouling property of PVDF membrane using in situ polymerization of PAA functionalized TiO2 nanoparticles. *J. Membr. Sci.* **2011**, *380*, 155–162. [CrossRef]
22. Jain, K.; Vedarajan, R.; Watanabe, M.; Ishikiriyama, M.; Matsumi, N. Tunable LCST behavior of poly(N-isopropylacrylamide/ionic liquid) copolymers. *Polym. Chem.* **2015**, *6*, 6819–6825. [CrossRef]
23. Krzeminski, P.; Gil, J.A.; van Nieuwenhuijzen, A.F.; van der Graaf, J.H.J.M.; van Lier, J.B. Flat sheet or hollow fibre—comparison of full-scale membrane bio-reactor configurations. *Desalination Water Treat.* **2012**, *42*, 100–106. [CrossRef]
24. Albu, P.C.; Ferencz, A.; Al-Ani, H.N.A.; Tanczos, S.-K.; Oprea, O.; Grosu, V.-A.; Nechifor, G.; Bungău, S.G.; Grosu, A.R.; Goran, A.; et al. Osmium Recovery as Membrane Nanomaterials through 10–Undecenoic Acid Reduction Method. *Membranes* **2022**, *12*, 51. [CrossRef]
25. Wang, Y.; Hu, D.; Zhang, Z.; Yao, J.; Militky, J.; Wiener, J.; Zhu, G.; Zhang, G. Fabrication of Manganese Oxide/PTFE Hollow Fiber Membrane and Its Catalytic Degradation of Phenol. *Materials* **2021**, *14*, 3651. [CrossRef]
26. Nechifor, A.C.; Goran, A.; Grosu, V.-A.; Bungău, C.; Albu, P.C.; Grosu, A.R.; Oprea, O.; Păncescu, F.M.; Nechifor, G. Improving the Performance of Composite Hollow Fiber Membranes with Magnetic Field Generated Convection Application on pH Correction. *Membranes* **2021**, *11*, 445. [CrossRef]
27. Al-Qaradawi, S.; Salman, S.R. Photocatalytic degradation of methyl orange as a model compound. *J. Photochem. Photobiol. A Chem.* **2002**, *148*, 161–168. [CrossRef]
28. Channei, D.; Inceesungvorn, B.; Wetchakun, N.; Ukritnukun, S.; Nattestad, A.; Chen, J.; Phanichphant, S. Photocatalytic degradation of methyl orange by CeO2 and Fe-doped CeO2 films under visible light irradiation. *Sci. Rep.* **2014**, *4*, 5757. [CrossRef]
29. Naik, A.P.; Mittal, H.; Wadi, V.S.; Sane, L.; Raj, A.; Alhassan, S.M.; Al Alili, A.; Bhosale, S.V.; Morajkar, P.P. Super porous TiO2 photocatalyst: Tailoring the agglomerate porosity into robust structural mesoporosity with enhanced surface area for efficient remediation of azo dye polluted waste water. *J. Environ. Manag.* **2020**, *258*, 110029. [CrossRef]
30. Wang, J.; Qin, L.; Lin, J.; Zhu, J.; Zhang, Y.; Liu, J.; Van der Bruggen, B. Enzymatic construction of antibacterial ultrathin membranes for dyes removal. *Chem. Eng. J.* **2017**, *323*, 56–63. [CrossRef]
31. Chung, K.T. Azo dyes and human health: A review. *J. Env. Sci. Health C Environ. Carcinog. Ecotoxicol. Rev.* **2016**, *34*, 233–261. [CrossRef] [PubMed]
32. Seshadri, S.; Bishop, P.L.; Agha, A.M. Anaerobic/aerobic treatment of selected azo dyes in wastewater. *Waste Manag.* **1994**, *14*, 127–137. [CrossRef]
33. Hou, Y.; Mi, K.; Sun, L.; Zhou, K.; Wang, L.; Zhang, L.; Liu, Z.; Huang, L. The Application of Hollow Fiber Cartridge in Biomedicine. *Pharmaceutics* **2022**, *14*, 1485. [CrossRef] [PubMed]
34. Gui, M.; Ormsbee, L.E.; Bhattacharyya, D. Reactive Functionalized Membranes for Polychlorinated Biphenyl Degradation. *Ind. Eng. Chem. Res.* **2013**, *52*, 10430–10440. [CrossRef]
35. Baldridge, K.C.; Edmonds, K.; Dziubla, T.; Hilt, J.Z.; Dutch, R.E.; Bhattacharyya, D. Demonstration of Hollow Fiber Membrane-Based Enclosed Space Air Remediation for Capture of an Aerosolized Synthetic SARS-CoV-2 Mimic and Pseudovirus Particles. *ACS EST Eng.* **2022**, *2*, 251–262. [CrossRef]
36. Mills, R.; Vogler, R.J.; Bernard, M.; Concolino, J.; Hersh, L.B.; Wei, Y.; Hastings, J.T.; Dziubla, T.; Baldridge, K.C.; Bhattacharyya, D. Aerosol capture and coronavirus spike protein deactivation by enzyme functionalized antiviral membranes. *Commun. Mater.* **2022**, *3*, 34. [CrossRef]
37. Wu, T.-Y.; Zrimsek, A.B.; Bykov, S.V.; Jakubek, R.S.; Asher, S.A. Hydrophobic Collapse Initiates the Poly(N-isopropylacrylamide) Volume Phase Transition Reaction Coordinate. *J. Phys. Chem. B* **2018**, *122*, 3008–3014. [CrossRef]
38. Sun, S.; Hu, J.; Tang, H.; Wu, P. Chain Collapse and Revival Thermodynamics of Poly(N-isopropylacrylamide) Hydrogel. *J. Phys. Chem. B* **2010**, *114*, 9761–9770. [CrossRef]
39. Wan, H.; Islam, M.S.; Briot, N.J.; Schnobrich, M.; Pacholik, L.; Ormsbee, L.; Bhattacharyya, D. Pd/Fe nanoparticle integrated PMAA-PVDF membranes for chloro-organic remediation from synthetic and site groundwater. *J. Membr. Sci.* **2020**, *594*, 117454. [CrossRef]

40. Sathya, S.; Murthy, P.S.; Das, A.; Gomathi Sankar, G.; Venkatnarayanan, S.; Pandian, R.; Sathyaseelan, V.S.; Pandiyan, V.; Doble, M.; Venugopalan, V.P. Marine antifouling property of PMMA nanocomposite films: Results of laboratory and field assessment. *Int. Biodeterior. Biodegrad.* **2016**, *114*, 57–66. [CrossRef]
41. Mills, R.; Baldridge, K.C.; Bernard, M.; Bhattacharyya, D. Recent advances in responsive membrane functionalization approaches and applications. *Sep. Sci. Technol.* **2022**, *58*, 1202–1236. [CrossRef]
42. Chiao, Y.-H.; Chen, S.-T.; Yap Ang, M.B.M.; Patra, T.; Castilla-Casadiego, D.A.; Fan, R.; Almodovar, J.; Hung, W.-S.; Wickramasinghe, S.R. High-Performance Polyacrylic Acid-Grafted PVDF Nanofiltration Membrane with Good Antifouling Property for the Textile Industry. *Polymers* **2020**, *12*, 2443. [CrossRef] [PubMed]
43. Huang, F.Y.C.; Arning, A. Performance Comparison between Polyvinylidene Fluoride and Polytetrafluoroethylene Hollow Fiber Membranes for Direct Contact Membrane Distillation. *Membranes* **2019**, *9*, 52. [CrossRef] [PubMed]
44. Jin, B.; Li, S.; Liang, X. High-Performance Catalytic Four-Channel Hollow Fibers with Highly Dispersed Nickel Nanoparticles Prepared by Atomic Layer Deposition for Dry Reforming of Methane. *Ind. Eng. Chem. Res.* **2022**, *61*, 10377–10386. [CrossRef]
45. Kim, D.H.; Kim, J.; Choi, W. Effect of magnetic field on the zero valent iron induced oxidation reaction. *J. Hazard. Mater.* **2011**, *192*, 928–931. [CrossRef]
46. Wan, H.; Briot, N.J.; Saad, A.; Ormsbee, L.; Bhattacharyya, D. Pore Functionalized PVDF Membranes with In-Situ Synthesized Metal Nanoparticles: Material Characterization, and Toxic Organic Degradation. *J. Memb. Sci.* **2017**, *530*, 147–157. [CrossRef]
47. Xu, J.; Bhattacharyya, D. Modeling of Fe/Pd Nanoparticle-Based Functionalized Membrane Reactor for PCB Dechlorination at Room Temperature. *J. Phys. Chem. C Nanomater. Interfaces* **2008**, *112*, 9133–9144. [CrossRef]
48. Xiao, L.; Isner, A.B.; Hilt, J.Z.; Bhattacharyya, D. Temperature responsive hydrogel with reactive nanoparticles. *J. Appl. Polym. Sci.* **2013**, *128*, 1804–1814. [CrossRef]
49. Sinek, A.; Kupczak, M.; Mielańczyk, A.; Lemanowicz, M.; Yusa, S.I.; Neugebauer, D.; Gierczycki, A. Temperature and pH-Dependent Response of Poly(Acrylic Acid) and Poly(Acrylic Acid-co-Methyl Acrylate) in Highly Concentrated Potassium Chloride Aqueous Solutions. *Polymers* **2020**, *12*, 486. [CrossRef]
50. Schäfer, D.; Köber, R.; Dahmke, A. Competing TCE and cis-DCE degradation kinetics by zero-valent iron—Experimental results and numerical simulation. *J. Contam. Hydrol.* **2003**, *65*, 183–202. [CrossRef]
51. Tee, Y.-H.; Bachas, L.; Bhattacharyya, D. Degradation of Trichloroethylene by Iron-Based Bimetallic Nanoparticles. *J. Phys. Chem. C* **2009**, *113*, 9454–9464. [CrossRef] [PubMed]
52. Kubendiran, H.; Hui, D.; Pulimi, M.; Chandrasekaran, N.; Murthy, P.S.; Mukherjee, A. Removal of methyl orange from aqueous solution using SRB supported Bio-Pd/Fe NPs. *Environ. Nanotechnol. Monit. Manag.* **2021**, *16*, 100561. [CrossRef]
53. Ravikumar, K.V.G.; Santhosh, S.; Sudakaran, S.V.; Nancharaiah, Y.V.; Mrudula, P.; Chandrasekaran, N.; Mukherjee, A. Biogenic nano zero valent iron (Bio-nZVI) anaerobic granules for textile dye removal. *J. Environ. Chem. Eng.* **2018**, *6*, 1683–1689. [CrossRef]
54. Arshadi, M.; SalimiVahid, F.; Salvacion, J.W.L.; Soleymanzadeh, M. Adsorption studies of methyl orange on an immobilized Mn-nanoparticle: Kinetic and thermodynamic. *RSC Adv.* **2014**, *4*, 16005–16017. [CrossRef]
55. Shih, Y.-h.; Tso, C.-P.; Tung, L.-Y. Rapid degradation of methyl orange with nanoscale zerovalent iron particles. *Sustain. Environ. Res.* **2010**, *20*, 137–143.
56. Yang, C.; Nuxoll, E.E.; Cussler, E.L. Reactive barrier films. *AIChE J.* **2001**, *47*, 295–302. [CrossRef]
57. Xu, J.; Bhattacharyya, D. Fe/Pd Nanoparticle Immobilization in Microfiltration Membrane Pores: Synthesis, Characterization, and Application in the Dechlorination of Polychlorinated Biphenyls. *Ind. Eng. Chem. Res.* **2007**, *46*, 2348–2359. [CrossRef]
58. Fang, X.; Li, J.; Ren, B.; Huang, Y.; Wang, D.; Liao, Z.; Li, Q.; Wang, L.; Dionysiou, D.D. Polymeric ultrafiltration membrane with in situ formed nano-silver within the inner pores for simultaneous separation and catalysis. *J. Membr. Sci.* **2019**, *579*, 190–198. [CrossRef]
59. Foo, K.Y.; Hameed, B.H. Insights into the modeling of adsorption isotherm systems. *Chem. Eng. J.* **2010**, *156*, 2–10. [CrossRef]
60. Hernández, S.; Lei, S.; Rong, W.; Ormsbee, L.; Bhattacharyya, D. Functionalization of flat sheet and hollow fiber microfiltration membranes for water applications. *ACS Sustain. Chem. Eng.* **2016**, *4*, 907–918. [CrossRef]
61. Niño de Guzmán, G.T.; Hapeman, C.J.; Millner, P.D.; Torrents, A.; Jackson, D.; Kjellerup, B.V. Using adaptive management to guide multiple partners in TCE remediation using a permeable reactive barrier. *Environ. Res. Commun.* **2019**, *1*, 075001. [CrossRef]
62. Khan, M.A.; Lipscomb, G.; Lin, A.; Baldridge, K.C.; Petersen, E.M.; Steele, J.; Abney, M.B.; Bhattacharyya, D. Performance evaluation and model of spacesuit cooling by hydrophobic hollow fiber-membrane based water evaporation through pores. *J. Membr. Sci.* **2023**, *673*, 121497. [CrossRef]
63. Mahmud, H.; Kumar, A.; Narbaitz, R.M.; Matsuura, T. Membrane Air Stripping: A Process for Removal of Organics from Aqueous Solutions. *Sep. Sci. Technol.* **1998**, *33*, 2241–2255. [CrossRef]
64. He, J.; Arnold, R.G.; Sáez, A.E.; Betterton, E.A.; Ela, W.P. Removal of Aqueous Phase Trichloroethylene Using Membrane Air Stripping Contactors. *J. Environ. Eng.* **2004**, *130*, 1232–1241. [CrossRef]

nanomaterials

MDPI

Article

Bimetallic AgPt Nanoalloys as an Electrocatalyst for Ethanol Oxidation Reaction: Synthesis, Structural Analysis, and Electro-Catalytic Activity

Fabian Mares-Briones [1], América Higareda [2], Jose Luis Lopez-Miranda [1], Rubén Mendoza-Cruz [3] and Rodrigo Esparza [1,*]

[1] Centro de Física Aplicada y Tecnología Avanzada, Universidad Nacional Autónoma de México, Boulevard Juriquilla 3001, Santiago de Querétaro 76230, Qro., Mexico; fabianmares@gmail.com (F.M.-B.); lopezfim@gmail.com (J.L.L.-M.)
[2] Unidad de Energía Renovable, Centro de Investigación Científica de Yucatán A.C., Carretera Sierra Papacal-Chuburná Puerto, Km 5, Sierra Papacal, Mérida 97302, Yuc., Mexico; ame_libert.16@hotmail.com
[3] Instituto de Investigaciones en Materiales, Universidad Nacional Autónoma de México, Circuito Exterior S/N, Circuito de la Investigación Científica, C.U., Ciudad de México 04510, CDMX, Mexico; rmendoza@materiales.unam.mx
* Correspondence: resparza@fata.unam.mx; Tel.: +52-442-192-6128 (ext. 136)

Abstract: In the present work, the chemical synthesis of AgPt nanoalloys is reported by the polyol method using polyvinylpyrrolidone (PVP) as a surfactant and a heterogeneous nucleation approach. Nanoparticles with different atomic compositions of the Ag and Pt elements (1:1 and 1:3) were synthesized by adjusting the molar ratios of the precursors. The physicochemical and microstructural characterization was initially performed using the UV-Vis technique to determine the presence of nanoparticles in suspension. Then, the morphology, size, and atomic structure were determined using XRD, SEM, and HAADF-STEM techniques, confirming the formation of a well-defined crystalline structure and homogeneous nanoalloy with an average particle size of less than 10 nm. Finally, the cyclic voltammetry technique evaluated the electrochemical activity of bimetallic AgPt nanoparticles supported on Vulcan XC-72 carbon for the ethanol oxidation reaction in an alkaline medium. Chronoamperometry and accelerated electrochemical degradation tests were performed to determine their stability and long-term durability. The synthesized AgPt (1:3)/C electrocatalyst presented significative catalytic activity and superior durability due to the introduction of Ag that weakens the chemisorption of the carbonaceous species. Thus, it could be an attractive candidate for cost-effective ethanol oxidation compared to commercial Pt/C.

Keywords: AgPt nanoparticles; nanoalloy; structural characterization; electrocatalysis; ethanol oxidation reaction

Citation: Mares-Briones, F.; Higareda, A.; Lopez-Miranda, J.L.; Mendoza-Cruz, R.; Esparza, R. Bimetallic AgPt Nanoalloys as an Electrocatalyst for Ethanol Oxidation Reaction: Synthesis, Structural Analysis, and Electro-Catalytic Activity. *Nanomaterials* **2023**, *13*, 1396. https://doi.org/10.3390/nano13081396

Academic Editor: Francesc Viñes Solana

Received: 24 March 2023
Revised: 12 April 2023
Accepted: 13 April 2023
Published: 18 April 2023

1. Introduction

The use of alcohols as fuels in electrochemical cells has increased over the last decade due to their potential application in self-sustainable energy production with minimal environmental impact [1–4]. In addition, liquid fuels are safer and more convenient for storage and transportation than compressed hydrogen. Furthermore, for their high efficiency, fast refueling, and low outgassing, direct ethanol fuel cells (DEFCs) are considered future portable power conversion devices [5–9]. Platinum (Pt) is one of the most important noble metals for manufacturing electrocatalysts used in DEFCs [10]. However, its commercialization is limited by its high cost and decreased oxidation potential due to the ethanol crossover effect (ECO), electrocatalyst poisoning by chemisorbed intermediate species during transport, and oxidation of ethanol through the membrane, which results in the obtaining mixed potentials for the ethanol oxidation (EOR) and oxygen reduction (ORR) reactions, with a significant loss of their performance [11–14].

In recent years, particular attention has been paid to designing cost-effective electrocatalysts with excellent resistance to carbonaceous intermediate species poisoning without compromising the high catalytic activity of EOR [15,16]. Furthermore, implementing heterogeneous Pt-based nanostructures in nanoalloys form with controlled size and morphology has improved suppression in the adsorption of poisonous species to monometallic Pt [17]. Due to the above, several noble metals (Rh, Pd, Au, Ni, Ru), as oxophilic components with relatively stable and considerable reactivity, have been used to form Pt nanoalloys, facilitating the formation of oxygen species at lower potentials to effectively oxidize intermediate species through the Langmuir–Hinshelwood mechanism and improve electrocatalyst stability [18–21].

Moreover, silver (Ag) has been proposed as a functional and beneficial element with high chemical stability. It has an electronic structure and an atomic radius similar to that of Pt, fulfilling the conditions for forming substitutional solid solution rules; furthermore, their implementation in forming bimetallic nanostructures can modify the electronic valence bands, minimizing activation energies and developing new interfaces promoting electronic exchange between elements.

The AgPt alloy during the ethanol oxidation reaction can simultaneously promote the oxidation of intermediates through the activation of the surface sites of Pt to reduce its poisoning by CO-like species due to weak surface adsorption originating from introducing Ag atoms to the system [22–25]. Therefore, the modification in the stoichiometric composition will affect the local elemental arrangement, affecting the electronic structure of the superficial sites of Pt and modifying its stability and catalytic activity. In addition, control of the size and morphology during the synthesis of the alloy can result in an increase in the surface area of the material and a preferential atomic arrangement, improving, in the same way, its catalytic performance [26].

Based on the considerations described above, this study presents the development of AgPt electrocatalysts using an easy and flexible synthesis method based on the polyol technique to obtain alloyed nanoparticles with a controlled size and morphology. In addition, by varying the molar ratio of the precursors, the relationship between the composition and its catalytic behavior toward the ethanol oxidation reaction was studied. Electrochemical measurements confirmed that AgPt nanoparticles with different molar ratios exhibit an enhanced electrocatalytic performance compared to commercial Pt/C, having the highest performance, with AgPt (1:3)/C showing better catalytic activity and stability.

2. Materials and Methods

2.1. Materials

AgPt bimetallic nanoalloys, as well as pure Ag-seeds, were synthesized using silver nitrate ($AgNO_3$, 99.99%) and potassium tetrachloroplatinate (II) (K_2PtCl_4, 99.99%) as metal precursors. All nanoparticles (NPs) were synthesized using ethylene glycol (EG 99.8%), as a reducer agent and stabilized with poly(N-vinylpyrrolidone) (PVP, M = 40,000 g mol^{-1}). Reagent-grade acetone and isopropyl alcohol were used to carry out nanoparticle washing. For the electrochemical tests, solutions of potassium hydroxide (KOH, $\geq$85%) in deionized water (Milli-Q, 18 MΩ·cm) were used as an alkaline medium, and reagent-grade ethanol (CH_3CH_2OH, $\geq$99.5%). For the electrochemical inks, a solution of Nafion® 117 perfluorinated resin (5% in water), and isopropyl alcohol ($(CH_3)_2CHOH$, 99.5%). Commercial platinum on Vulcan XC-72 carbon (20 wt% of filler, PRD.0.ZQ5.10000029756, Figure S1) was used as a reference sample. All chemicals were purchased from Sigma-Aldrich (Sigma-Aldrich, St. Louis, MO, USA).

2.2. Synthesis Procedures

The AgPt bimetallic nanoalloys were prepared using the seed-mediated growth polyol method. Ag seeds were first synthesized by adding 2 mL of $AgNO_3$ (20 mM) and 4 mL of PVP (50 mM) into ten aliquots every 2.5 min to 10 mL of EG previously heated at 160 °C under magnetic stirring and maintaining the reaction for 1 h [27]. Subsequently, to

synthesize the nanoalloys AgPt (1:1), 0.5 mL of Ag seeds were dispersed in 5 mL of EG at 160 °C. Then, 1 mL of $AgNO_3$ (50 mM) and 2 mL of PVP (50 mM) were added to the dispersed Ag seed solution in 10 aliquots every 2.5 min under magnetic stirring. Finally, 1 mL of metal precursor K_2PtCl (50 mM) and 2 mL of PVP (50 mM) were added to the solution using a procedure similar to that mentioned above by aliquots, ending the reaction with a residence time of 1h at 160 °C under magnetic stirring and a last heating ramp at 190 °C for 15 min. A similar procedure was used to synthesize the AgPt nanoalloys (1:3), modifying only the volumes of the precursor agents K_2PtCl_4 to 3 mL and twice the surfactant agent PVP (6 mL). The resulting nanoalloys were washed four times; the sample was diluted with acetone on every wash and centrifugated at 5000 rpm for 5 min. The supernatant was subsequently removed, and the sample was redispersed by ultrasound using isopropyl alcohol. Next, electrocatalysts were prepared by dispersing a known amount of AgPt NPs solution with 32 mg of Vulcan XC-72 carbon by ultrasonic (UP200Ht, 200 W, 26 kHz) for 5 min; the amount of the NPs was calculated to be 20 wt% of the total metal phase.

2.3. Structural Characterization

The post-synthesized AgPt NPs were investigated using a UV-Vis spectrophotometer Metash UV6000 (Shanghai Metash Instruments Co., Shanghai, China) in the 200–800 nm range. The structural characterization was performed with a Rigaku Ultima IV diffractometer (Rigaku Co., Tokyo, Japan) using the powder XRD technique in a 2θ range from 30° to 90° at room temperature. The Hitachi SU8230 cold-field emission scanning electron microscope CFE-SEM (Hitachi High-Tech Co., Tokyo, Japan) and Jeol JEM-ARM200F scanning transmission electron microscope TEM/STEM (JEOL Ltd., Tokyo, Japan) were used to analyze the structural, morphological, and chemical properties.

2.4. Electrochemical Characterization

The electrochemical measurements were performed on a BioLogic VSP potentiostat (Biologic, Seyssinet-Pariset, France) coupled with a standard electrochemical cell in a three-electrode configuration: a Hg/HgO electrode filled with NaOH (1.0 M) solution and a graphite bar, used as a reference and counter electrode, respectively, and a working electrode prepared by depositing 6 µL of catalytic ink on a glassy carbon BASi electrode (3 mm in diameter). The suspension consisted of 1 mg of the corresponding electrocatalyst, 70 µL of isopropyl alcohol, and 7 µL of Nafion®117 (Sigma-Aldrich, St. Louis, MO, USA) perfluorinated resin solution (5 wt%) dispersed by ultrasound for 15 min.

At least three different electrochemical profiles were carried out by cyclic voltammetry (CV) in a potential window of −0.80 to 0.85 V vs. NHE at a scan rate of 50 mVs^{-1} to inquire into the oxidation-reduction processes. The electrochemically active surface area (*ECSA*) was calculated using Equation (1), and the respective experimental errors were obtained.

$$ECSA\left(cm^2\ mg^{-1}\right) = \frac{Q\ (mC)}{Q^o(mC\ cm^{-2}) * M_{Pt\ or\ Ag}(mg)} \quad (1)$$

where Q is the electric charge corresponding to the integrated hydrogen adsorption/desorption region after subtracting the double-layer capacitive current for pure Pt/C, and AgPt/C bimetallic surface or the oxide reduction peak for pure Ag/C, Q^o corresponds to the specific charge, 0.21 mC $cm^{-2}{}_{Pt}$ is used for one-electron transfer reaction of Pt and 0.40 mC $cm^{-2}{}_{Ag}$ [28] to convert the formation of one monolayer of $AgOH/Ag_2O$ to the surface area of Ag.

Electrochemical tests were performed to evaluate the ethanol oxidation reaction (EOR) using an aqueous solution of 1.0 M ethanol plus 0.3 M KOH as a supporting electrolyte, unless otherwise indicated. The catalytic performance was evaluated by CV at a scan rate of 20 mVs^{-1} and a potential window of −0.85 and 0.65 V vs. NHE for the AgPt/C system. In addition, the stability and CO-like tolerance were researched by chronoamperometry (CA) measurements for the ethanol oxidation process during 3600 s in the half-peak potential

(Ep/2). Afterward, two potential cycles in a fresh electrolyte solution were recorded from the lower potential limit toward the anodic direction for the oxidative desorption of the intermediated species. In addition, cyclic stability toward the EOR to inquire about the long-term durability of the electrocatalysts was performed through an accelerated electrochemical degradation test that consisted of 2500 sweeps of cyclic potential in the same range of potential at a scan rate of 100 mVs^{-1}.

Before each electrochemical measurement was performed, the adequate aqueous solution was deaerated by bubbling nitrogen-purging for at least 10 min. After that, all electrochemical tests were carried out at room temperature. The potential was reported with respect to a normal hydrogen electrode (NHE).

3. Results

The crystallographic nature of the synthesized bimetallic nanoparticles (BNPs) was characterized using the X-ray diffraction (XRD) technique. Typical XRD patterns of the AgPt alloy BNPs are shown in Figure 1. All XRD patterns showed three broad diffraction peaks that were assigned to (111), (200), and (220) reflections indexed with the face-centered cubic (fcc) crystal structure with an Fm-3m space group. No other diffraction peaks were observed in the second phase. These three peaks were observed at different 2θ compared to pure Ag (JCPDS 04-0783) and Pt (JCPDS 04-0802) structures. The XRD patterns displayed diffraction peak shifts linear to higher 2θ as the amount of Pt increased in the AgPt BNPs. This indicated that AgPt (1:3) had a higher composition of Pt than AgPt (1:1). Therefore, the results suggest that the AgPt BNPs are uniformly alloyed. The miscibility of an alloy was determined according to the Hume–Rothery rules [29], which indicate that the alloy is preferred when the crystal structure, atomic radii, valence, and electronegativity of the two elements are similar; therefore, Ag and Pt are capable of forming AgPt alloys. Furthermore, the corresponding phase diagram of the elements confirmed that the Ag-Pt system formed miscible heterogeneous alloys with atomic contents rich in Pt for the concentrations used in this study (1:1 and 1:3) [30]. Likewise, according to theoretical and experimental studies, the miscibility and diffusion improve with a decrease in particle size [31]. However, in some bimetallic nanosystems, it is also necessary to include the surface energy of the elements to determine their miscibility [32]. Vegard's law can be an indication of miscible binary alloys that form solid solution (Equation (2)) [33]:

$$a = a_2\left(1 + \frac{a_1 - a_2}{a_2} \times x_1\right) \tag{2}$$

where a is the calculated lattice parameter of AgPt BNPs, a_1 and a_2 are lattice parameters of two corresponding pure metals, Ag (0.4086 nm) and Pt (0.3923 nm), respectively, and x_1 is the atomic fraction of component 1 (0.5 for AgPt (1:1), and 0.25 for AgPt (1:3)). The experimental lattice parameter was calculated from the Rietveld refinement, obtaining 0.3996 nm and 0.3965 nm for AgPt (1:1) and AgPt (1:3), respectively. According to Vegard's law, the average calculated atomic composition was $Ag_{45}Pt_{55}$, and $Ag_{26}Pt_{74}$, these values were corroborated by energy dispersive X-ray spectroscopy (EDX) analysis. The average crystallite size was determined based on the broad peak of the (111) plane using Scherrer's formula (Equation (3)) [34]:

$$t = \frac{0.9\lambda}{\beta\cos\theta} \tag{3}$$

where t is the crystallite size, 0.9 is a shape factor that is an attribute of the equipment, λ is the X-ray wavelength (0.154 nm), β is the full width at half maximum intensity, and θ is the Bragg angle. The crystallite size values of the AgPt BNPs increased when the Pt content increased, from 6 nm to 10 nm for AgPt (1:1) and AgPt (1:3), respectively.

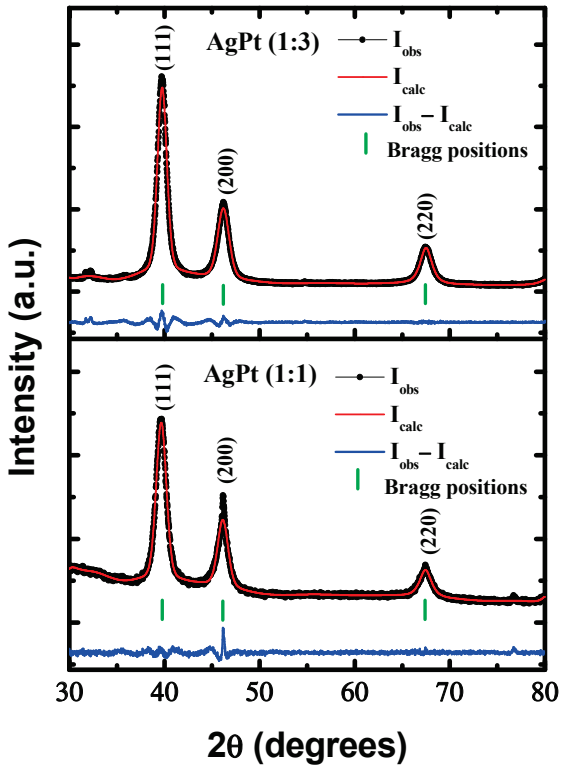

Figure 1. XRD patterns obtained from AgPt bimetallic nanoparticles with different atomic ratios.

Figure 2a shows the results of the analysis using UV-Vis spectroscopy. Several metal nanoparticles showed the surface plasmon surface (SPR) phenomenon. For Ag, this signal was between 350 and 600 nm, the position of which depended on the size and morphology of the nanoparticles [35,36]. An intense absorption band located at 401 nm was observed in the spectrum corresponding to the Ag seeds. According to some reports, this position indicates the presence of small particles [37,38].

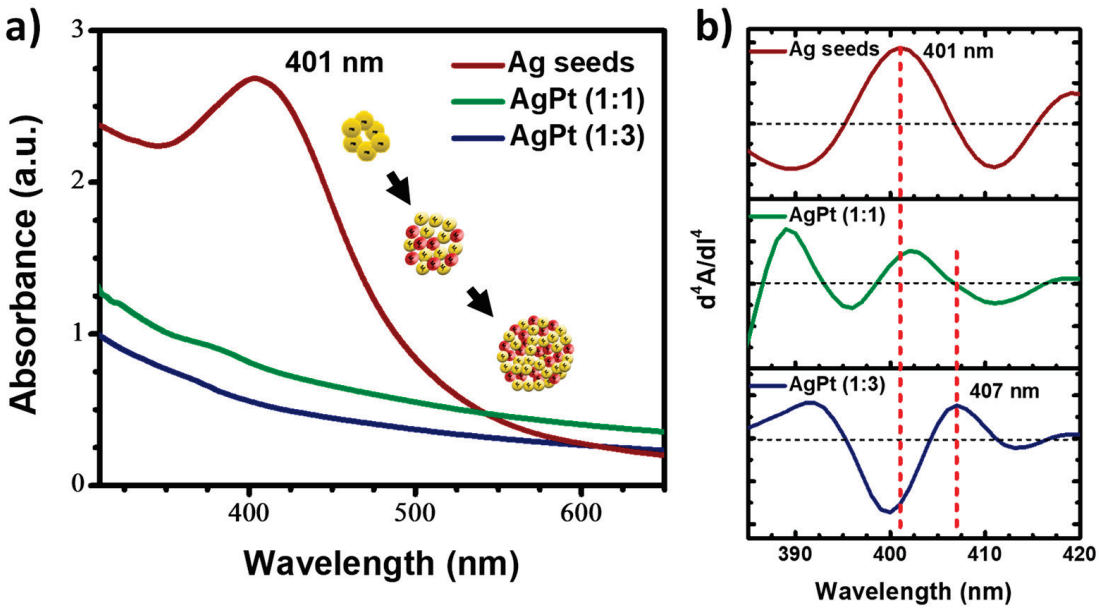

Figure 2. (**a**) UV-Vis absorption spectra and (**b**) fourth-derivative absorption spectra of the obtained Ag seeds, AgPt (1:1), and AgPt (1:3) BNPs.

On the other hand, the spectrum corresponding to the AgPt (1:1) bimetallic nanoparticles showed a significant decrease in the signal corresponding to the Ag seeds. This decrease was more evident when the Pt concentration increased, as observed in the spectrum corresponding to the AgPt (1:3) sample. This behavior is because Pt does not show the SPR phenomenon in the UV-Vis spectrum. Therefore, the alteration of the shape and intensity of the band located at 407 nm depended on the combination of Pt with Ag seed leads. Sometimes, the Ag absorption band was shifted, wider, or disappeared completely [39]. Some very weak signals can be distinguished in the spectra shown in the figure. However, it was not possible to determine whether they corresponded to Ag. Therefore, the derivation process was used to corroborate the type of synthesized nanoparticles, specifically the fourth derivative with which absorption bands masked by other signals were distinguished. Figure 2b shows the results of the fourth derivative. As can be seen, in the graph corresponding to the Ag seeds, the same signal was observed in the UV-Vis spectrum at 401 nm. The graph of the AgPt (1:1) sample showed a signal at 406 nm due to the low concentration of Pt, without altering the position of Ag. Finally, the graph of AgPt (1:3) showed a signal at 407 nm, indicating the presence of Ag on the surface of the nanoparticles. The movement of the signal was attributed to the size increase by adding Ag and Pt atoms to the Ag seeds. All considerations mentioned above suggest the synthesis of bimetallic nanoalloys. Concerning the catalytic properties, the formation of AgPt nanoalloys in different atomic compositions can significantly modify the geometric factor and electron ligand effects, defining the number of atoms oriented in preferential directions and modifying the electron density distribution by the formation of missing links, thereby improving the selectivity and stability of the nanoalloy for specific catalytic reactions [40,41].

Aberration-corrected scanning transmission electron microscopy (STEM) was utilized for the detailed characterization of the AgPt BNPs. STEM is an invaluable tool for the characterization of nanostructures, mainly using the high-angle annular dark field (HAADF) detector, which is associated with the atomic number (Z) of the atoms on the specimen. The contrast in this imaging technique is strongly dependent on the chemical composition (Z-contrast). Therefore, HAADF-STEM allows easy identification of the elements present in the sample, elemental composition, and crystal information at an atomic scale. However, in this particular case, it was difficult to distinguish Ag and Pt as individual atomic columns by Z-contrast in the image because the atoms were randomly distributed, forming an alloy in contrast with the ordered alloys, where it was possible to distinguish individual atomic columns by Z-contrast in the images [42]. Figure 3a shows an HAADF-STEM image of the AgPt (1:3) BNP. From the image, d-spacings of 0.2299 and 0.1991 nm were obtained, which corresponded to (111) and (020) planes and were directly revealed in the atomic HAADF-STEM image. Meanwhile, the corresponding fast Fourier transform (FFT) reflects the fcc structure along the [101] zone axis (Figure 3b). It is clear that a well-defined truncated octahedron shape, enclosed by the {111} and {100} facets, appeared in the HAADF-STEM image. The geometry of the BNP was in accordance with the projection of a truncated octahedron model along the same direction (Figure 3c). The truncated octahedral shape is a highly symmetric structure enclosed by six {100} and eight {111} crystallographic surfaces. The surface energy density of {111} planes is the most stable, followed by {100} planes, and the other planes are relatively unstable [43]. Due to the catalytic reaction that occurs on the surface of the electrocatalyst, it is important to synthesize nanoparticles with the most stable planes [44]. A recent theoretical study reported that the exposed {111} crystal planes help C–C bond cleavage during ethanol oxidation, resulting in a higher fuel utilization [45].

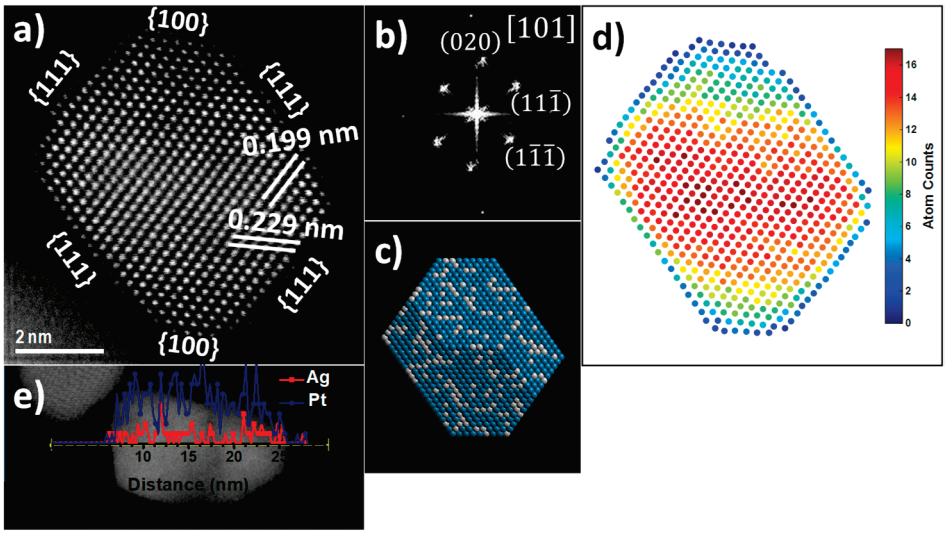

Figure 3. (**a**) HAADF-STEM image of AgPt (1:3) BNP along the [101] zone axis, (**b**) FFT pattern, (**c**) truncated octahedron model along the same direction, (**d**) atom counts, and (**e**) Ag and Pt elemental profiles along the line across the BNPs.

The statistics-based atom-counting method has been applied to the atomic resolution image by using the StatSTEM program [46]. The statistics-based method relies on the total intensity of scattered electrons for each projected atomic column. The number of atoms in each projected atomic column is shown in Figure 3d, where the elements Ag and Pt distribution are presented randomly on its surface to form an alloy in a 1:3 relation with a total count of 6932 atoms, indicating the approximated atom composition for these size nanoparticles. The 2D thermal diagram corresponding to the thickness of the nanoparticle indicates that the entire perimeter has approximately 4 to 6 atoms; subsequently, a step of 10 and 12 atoms is generated until reaching the center of the particle with a thickness of 16 atoms according to the intensity bar. From these results, the physicochemical behavior of the nanoalloy for heterogeneous catalysis reactions can be discussed.

The energy dispersive X-ray spectroscopy (EDX)-STEM technique was applied to investigate the elemental distribution compositional line profiles on the AgPt (1:3) BNPs. The distributions of Ag and Pt are shown in Figure 3e, which reveals the homogeneous distribution of Ag and Pt elements across the entire BNP, showing the formation of the AgPt alloy structure.

The size and distribution of AgPt BNPs were determined by cold field emission scanning electron microscopy (SEM/STEM). Figure S2 shows the low-magnification BF-STEM images obtained from the AgPt (1:1) and AgPt (1:3) BNPs. The average particle sizes were 6.3 nm and 10.4 nm, respectively. The increase in particle size was directly related to the increase in the volume of the precursor salts used during the synthesis procedure. Figure 4a,c shows the SEM images of AgPt (1:1) and AgPt (1:3) BNPs supported on Vulcan XC-72 carbon, which was beneficial to increasing electrical conductivity and reducing the charge of the metallic phase simultaneously. In addition, the proper dispersion of nanoparticles acts as an interconnected path for the flow of electrons during electrochemical evaluations. In addition, the exposed Ag atoms on the surface may significantly enhance the electrical conductivity of the bimetallic surface, improving electron transport, an essential step in electrocatalysis [47]. Both samples show a homogeneous distribution and adequate concentration of nanoparticles on the support material without aggregation, indicating the effectiveness of the synthesis method for obtaining dispersed bimetallic nanoparticles and a good sample preparation for further analysis.

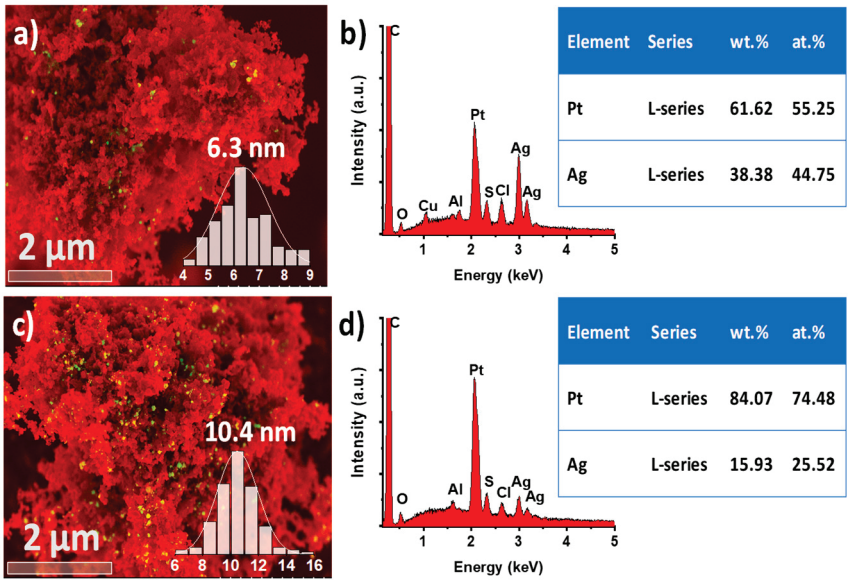

Figure 4. SEM image with its corresponding EDX analysis of (**a**) and (**b**) AgPt (1:1), and (**c**) and (**d**) AgPt (1:3) BNPs.

Figure 4b,d shows the EDX-SEM analysis of AgPt (1:1) and AgPt (1:3) BNPs, respectively. The spectra showed the presence of Ag, Pt, and C from the samples, Cu and Al from the holder samples, and low detection of the Cl element from the remainder of the precursor salts used. From the EDX analysis, elementary information and atomic (at%) and weight (wt%) percentages were easily obtained. In addition, the analysis revealed that the AgPt BNPs maintained the elemental ratio of (1:1) and (1:3). These results agree with the ratios of the starting precursor salts and those obtained by XRD, UV-Vis, and STEM techniques.

Prior to analyzing the catalytic activity toward the ethanol oxidation reaction (EOR) on the as-prepared AgPt/C electrocatalysts, cyclic voltammetry (CV) curves were performed in 0.3 M KOH solution as an alkaline electrolyte in the absence of ethanol at a scan rate of 50 mVs^{-1}, to gather information on the electrode surface behavior. The electrochemical profiles were recorded over a potential window of −0.80 to 0.85 V vs. NHE to include the processes of oxidation/reduction of both metal components.

Figure 5a displays the CV curves for AgPt (1:1)/C and AgPt (1:3)/C electrocatalysts, together with their monometallic counterparts (Ag/C and Pt/C). The Pt/C electrocatalyst showed a well-known electrochemical profile. The hydrogen desorption (H_{des}) peaks were at a lower potential. Beyond the double-layer capacitive current, the Pt-oxide region was observed at around −0.05 V vs. NHE; these anodic processes occurred in the forward scan. The expected reduction of surface oxide from −0.05 to −0.50 V vs. NHE and the adsorption of hydrogen (H_{ads}) at about −0.68 V vs. NHE occurred in the backward scan. For the Ag/C electrocatalyst, H_{ads}/H_{des} peaks were not observed due to its electron configuration. This element had a weak hydrogen chemisorption ability, the same as Au and Cu (group 11 of the periodic table). However, when the forward potential scan reached 0.15 V vs. NHE, the first stage of formation of silver oxides started [48–50]. Two oxidation regions (Ox_1 and Ox_2) were observed. The Ox_1 zone between 0.15 V vs. NHE and 0.60 V vs. NHE was due to Ag (I) oxide formation, a multi-stage process; thus, more than one signal was noticed. According to the present literature, Ag_2O (or AgOH) monolayers originate first and then, through nucleation and a 3D growth mechanism, Ag_2O multilayers. The Ox_2 region was due to the subsequent oxidation of Ag_2O to AgO and the direct oxidation of Ag to Ag (II) oxide through a two-electron process, which co-occurred simultaneously in the same potential range between 0.70 V vs. NHE and 0.85 V vs. NHE. Surprisingly, a small anodic peak (*Ox_3) was observed at 0.66 V vs. NHE when reversing the potential scan direction. It has been associated with an autocatalytic process in which Ag (I) oxide is

converted to Ag (II) oxide [48]. This means that the surface forms AgO multilayers through a non-stoichiometric oxidation process and is a mixed oxide. In addition, the reduction of the silver oxides takes place. The two cathodic peaks (R_2 and R_1) were conjugated with the oxidation signals, which were verified to progressively increase the anodic reverse potential limit. Figure 5b shows the relationship between the anodic and cathodic peaks of AgPt (1:1)/C. Thus, for all Ag-based samples, the cathodic peaks corresponded to the reduction of AgO to Ag_2O (R_2) and Ag_2O to Ag (R_1).

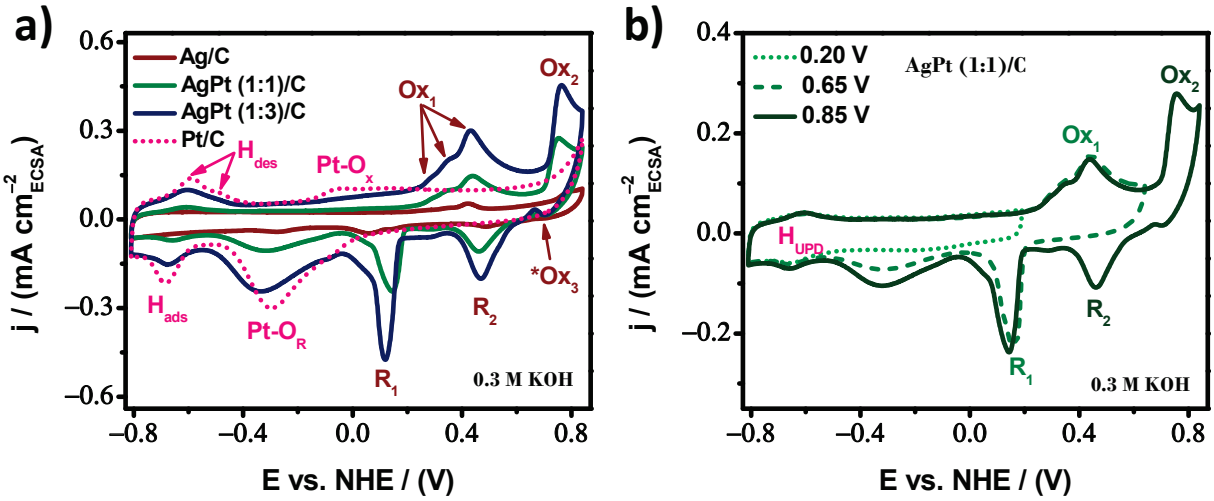

Figure 5. Cyclic voltammograms profiles in 0.3 M KOH solution at 50 mVs^{-1}; (**a**) for AgPt/C system, and (**b**) at the different anodic potential limits for AgPt (1:1)/C.

All oxidation/reduction processes of pure Pt and Ag were present in the bimetallic electrocatalysts. In essence, these electrochemical reactions occurred at or near the catalyst surface, suggesting that both metals are electrochemically accessible regardless of the elemental composition. They were dispersed on the surface of the BNPs, supporting the presence of an alloy structure. In addition, from Figure 5a, a negative shift in the Pt oxide reduction peak may be observed on both AgPt surfaces; consequently, the bimetallic surface transforms more oxygen species because they require less energy than pure Pt/C. As a complement to the analysis, Figure 5b displays an increase in the current density of the Pt oxide reduction peak. The hydrogen underpotential deposition (H_{UPD}) region did not change as the reverse potential limit increased. This behavior supports the synergy between the Ag and Pt elements. Thus, the generation and reduction of more Pt oxides were favored when the oxidation of Ag was achieved.

The electrochemical active surface area (ECSA) was determined using CV curves similar to a powerful surface-sensitive technique. For pure Pt and AgPt bimetallic surface, the ECSA was determined on the charge associated with the Pt-H_{UPD} region, which is based on the adsorption/desorption of H atoms. Meanwhile, for pure Ag, the ECSA was determined by the coulomb charge of the redox reaction of the surface metal. This is the interaction between the surface atoms and oxygenated species, so the reduction peak of one monolayer of metal oxides was integrated. The resulting ECSA values are shown in Table 1. AgPt (1:3)/C presented an ECSA of 19.43 $m^2\ g^{-1}$, which was higher than AgPt (1:1)/C (15.50 $m^2\ g^{-1}$). Although the AgPt (1:3) BNPs had a larger size, the lower ECSA to AgPt (1:1)/C was attributed to introducing more Ag atoms on the surface, which was inactive toward the H_{UPD} and may have partially blocked the Pt sites. This represents a challenge for the surface modification strategy, tailoring the local electronic structure to boost the EOR catalytic performance but not represent a significative sacrifice of the ECSA [51].

Table 1. Electrochemically active surface area, mass activity, and specific activity of the different electrocatalysts.

Electrocatalyst	ECSA m^2/g	MA A/mg	SA mA/cm^2
AgPt (1:1)/C	15.4 ± 0.3	0.29	1.86
AgPt (1:3)/C	19.5 ± 0.3	0.62	3.19
Pt/C	14.5 ± 0.2	0.16	1.15
Ag/C	11.1 ± 0.1	-	-

The catalytic response in the presence of ethanol was explored by CV curves performed in 1.0 M ethanol solution in alkaline media (0.3 M KOH) at a scan rate of 20 mVs^{-1}. The Ag surface failed to interact actively with ethanol molecules. Since it was catalytically inactive for ethanol oxidation, the current density was normalized by the Pt charge to obtain the mass activity (MA), which mainly reflects the cost efficiency between similar electrocatalysts, considering that all atoms of the particle were active sites. Figure 6a displays the catalytic behavior toward the EOR of AgPt (1:1)/C and AgPt (1:3)/C electrocatalysts, along with commercial Pt/C as a reference. The current density of the forward peak indicates the maximum reaction rate; thus, it was a principal parameter for insight into catalytic properties. The AgPt (1:3)/C presented an enhanced MA of 0.62 A mg^{-1} and for AgPt (1:1)/C of 0.29 A mg^{-1}, while the commercial Pt/C was 0.16 A mg^{-1}. This result indicates an MA for AgPt (1:3)/C of 3.9-fold higher than the commercial Pt/C results. This confirms that alloying with a lower-cost metal in an adequate composition is an effective approach to achieve superior mass activity and thus cost-effective bimetallic electrocatalysts, using an engineering perspective to develop electrochemical devices. However, to evaluate the intrinsic electrochemical performance of the catalyst surface, the specific activity (SA) was obtained, and the corresponding CV curves are shown in Figure 6b. The AgPt (1:3)/C presented an enhanced SA of 3.19 mA cm^{-2} and for AgPt (1:1)/C of 1.86 mA cm^{-2}, while the commercial Pt/C was 1.15 mA cm^{-2}. This result indicates a SA for AgPt (1:3)/C of 2.8-fold higher than commercial Pt/C. The MA and SA are also present in Figure 6c for better visualization and are reported in Table 1. Likewise, we noticed new properties, such as the AgPt (1:3)/C electrocatalyst presenting an onset potential with more negative values than the rest of the materials. The dashed line in Figure 6d indicates that AgPt (1:3)/C reaches a SA of 0.1 mA cm^{-2}, 160 mV earlier than the commercial Pt/C, indicating a lower energy barrier of the reaction, so the EOR was more facile on the AgPt (1:3)/C surface.

A review of the literature supports the advancement of AgPt (1:3)/C compared to other transition metals as a co-catalyst element toward the EOR. For example, the forward peak current density of the octahedral $Pt_{2.3}Ni/C$ with an average size of 10 nm displayed an SA of 1.46 mA cm^{-2}, and the authors explained that the improved catalytic performance implies the octahedral shape and alloying effect [52]. In other work, PtAg porous nanotubes with delicate 3D porous wall structures showed a specific current density of 1.97 mA cm^{-2} [45]. The previous materials showed lower performance than the AgPt (1:3)/C prepared in this work. With a similar current density, the ethanol oxidation performance of the ultrathin PtRu NWs/C was 3.78 mA cm^{-2} [53]. Additionally, the working group evaluated the PdPt/C electrocatalyst, showing an SA of 3.27 mA cm^{-2} [54]; however, Ru and Pd are expensive noble metals. Therefore, the AgPt (1:3)/C electrocatalyst has competitive performance toward the OER with the advantage of being a cost-effective material. More information about comparing the catalytic activity of ethanol oxidation using Pt-based materials is shown in Table S1.

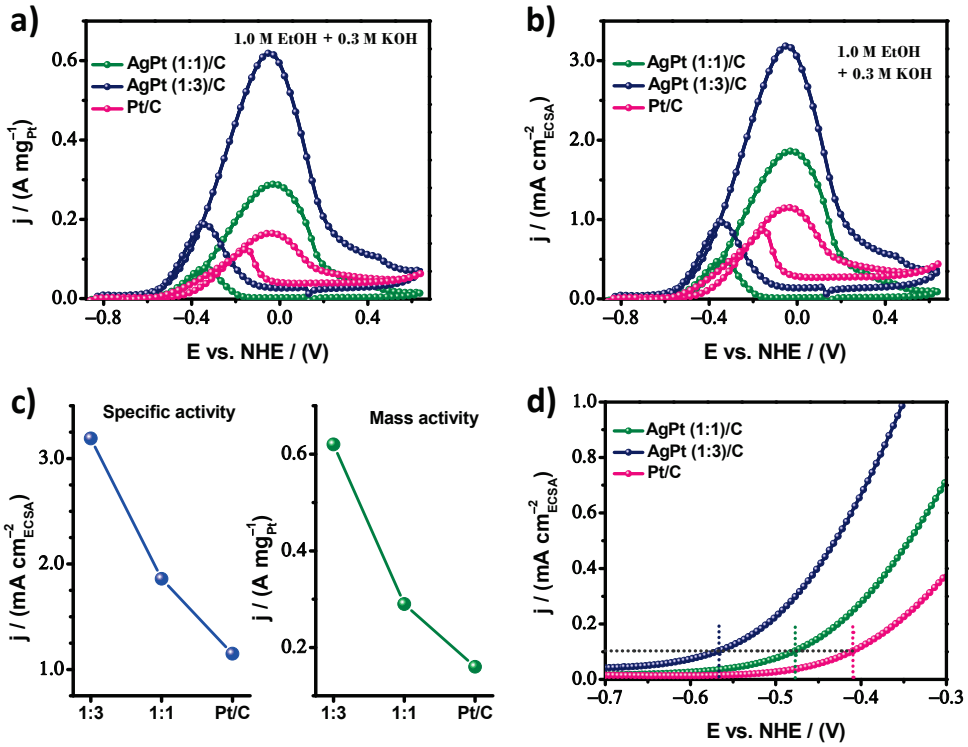

Figure 6. Cyclic voltammograms in 0.3 M KOH + 1.0 M ethanol solution at 20 mV s^{-1} normalized for (**a**) mass activity (MA), (**b**) specific activity (SA), (**c**) mass activity (MA) and specific activity (SA) at the maximum point of the reaction rate, and (**d**) close-up of the initial region of the ethanol oxidation for AgPt (1:1)/C, AgPt (1:3)/C, and Pt/C electrocatalysts.

As is customary, the stability of the electrocatalysts was investigated using chronoamperometry (CA) measurements under alkaline conditions. Figure 7a indicates the highest catalytic activity maintained on AgPt (1:3)/C after anodic polarization at −0.25 V (vs. Hg/HgO) for 3600 s. One point of interest was at 360 s (6.5 min). Both bimetallic electrocatalysts exhibited the same EOR oxidation current density, showing 37% retention of catalytic activity compared to 24% for commercial Pt/C. However, 14.8%, 9.6%, and 2.5% of the initial performance was sustained on AgPt (1:3)/C, AgPt (1:1)/C, and commercial Pt/C at the end of the CA test, respectively. During the electrocatalytic process, intermediate species, such as CO-like species, were generated, most likely due to the oxidation mechanism on Pt surfaces [45]. Adsorption of CO on the active site of the catalytic surface generates CO coverage that easily poisons the electrocatalyst. CO-like binds strongly to the active surface, causing a decrease in catalytic stability. More and more active sites are blocked as the reaction progresses if the electrocatalyst cannot perform the oxidative desorption of the CO-like species in a timely manner, resulting in a rate of decrease in current density. Therefore, presenting a higher current density implies a high number of active sites (higher ECSA) and a balance of binding energies between ethanol molecules and oxygenated adsorbed species (OH_{ads} and CO_{ads}) to observe reasonable EOR activity. Consequently, the OH_{ads} species can proceed from the H_2O adsorbed on the active site, which gives rise to the formation of OH^- species. According to the volcano plot, Ag binds weakly to oxygen species. Meanwhile, the strength of Pt is strong [55]. Combining both metals in a suitable elemental arrangement could tune the O-binding for the EOR through an ensemble effect, where specific group arrangements of atoms on the surface are needed to act as active sites, so that both metals interact in synergy, promoting faster kinetics.

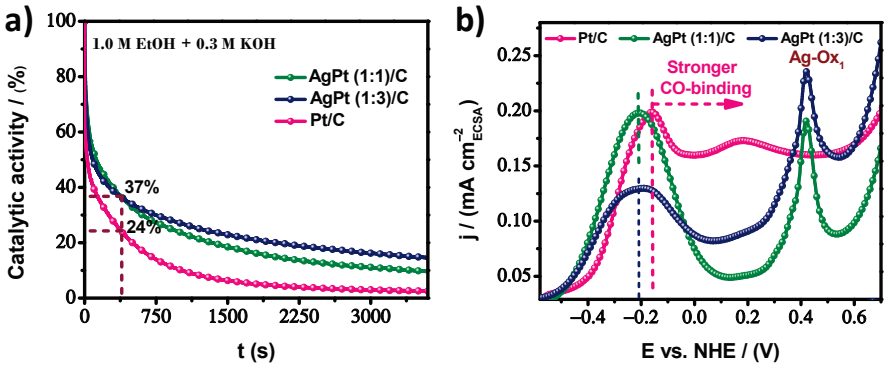

Figure 7. (**a**) Residual catalytic activity based on chronoamperometry (CA) measurement at −0.25 V vs. Hg/HgO for ethanol oxidation reaction in alkaline media and (**b**) close-up on cyclic voltammograms curves in the anodic scan for AgPt (1:1)/C, AgPt (1:3)/C, and commercial Pt/C electrocatalysts.

To verify the tolerance to poisonous species, following the CA test, with enough time to observe a stable state in the electrocatalytic response, a couple of voltammetry cycles were performed in a fresh alkaline solution for the same potential window and from a lower potential limit toward the anodic direction are displayed in Figure S3. It is assumed that the visualization of additional peaks or regions is due to the presence of active species that remained adsorbed on the electrode throughout the stability test. In this case, the effect of carbonaceous intermediates may be reflected in surface poisoning and correlated with the resulting stability test. Thus, the superior stability of AgPt (1:3)/C can be seen in Figure 7b, where a close-up of the anodic scan of the CV curves of Figure S3 is displayed to analyze the oxidative desorption of carbonous species on the different electrocatalysts. The main peak potential on AgPt (1:3)/C and AgPt (1:1)/C at −0.21 V vs. NHE was more negative than the value for Pt/C (−0.16 V vs. NHE); this indicates that the removal of CO-like species is more facile on the bimetallic surface, which is caused by the weaker CO adsorption strength due to the possible change in the electronic structure by the incorporation of Ag atoms into the Pt structure. However, the cover layer was higher on AgPt (1:1)/C. Therefore, the highest residual EOR activity on AgPt (1:3)/C may have arisen from the lower accumulation of intermediate carbonaceous species, such as CO, due to its higher ECSA and more effective oxidation step for such species. In addition, a prominent and broad CO-like oxidation region on Pt/C might correspond to the two types of CO_{ads} species due to its binding energy, which is stronger than AgPt/C samples. In the second cycle, the CO oxidation region is not observed; thus, a standard CV curve is observed for all materials (Figure S3).

As a strategy, this analysis supports the introduction of a smaller amount of foreign metal, such as Ag, on the active surface. Ag has a beneficial effect on the catalytic performance of the system due to the electrochemical behavior of these alloys, depending on their synthesis conditions. A successful modification of the surface composition can tune the electrocatalytic properties of the electrocatalyst by creating a high number of active sites (high ECSA) and optimizing the adsorption of intermediates. In this case, AgPt (1:3)/C present the highest Pt content; this ensures sufficient active surface sites, and the small portion of Ag does not sacrifice the ECSA. Instead, it shows a local change in the electronic structure that boosts the EOR through weakened Pt-intermediate bonding strength, such as Pt-CO, to ease the removal of the catalytic surface. Therefore, Ag plays an essential role in adjusting the inherent adsorption energies of the new catalytic surface.

Long-term stability testing is crucial for using electrocatalysts in fuel cells. In this sense, accelerated electrochemical degradation tests were performed on AgPt (1:3)/C to show the best catalytic performance and commercial Pt/C as a control electrocatalyst. The electrocatalysts were evaluated during 2500 potential scan cycles at a scan of 100 mVs^{-1} toward the EOR in alkaline media. Figure 8a shows the retention of the catalytic activity for the evaluated cycles (initial, 250, 500, 1000, and 2500), obtained from the forward peak of the CV curves recorded at 20 mVs^{-1} for ethanol oxidation. AgPt (1:3)/C displays

a lower degradation rate than Pt/C. Thus, the catalytic activity at the end of the test of 2.49 mA cm^{-2} for AgPt (1:3)/C and 0.63 mA cm^{-2} for commercial Pt/C (Figure 8b) corresponds to a loss of catalytic activity over initial values of 22% and 45%, respectively. Therefore, higher cyclic stability was confirmed for AgPt (1:3)/C, which suggests that the combination of two elements that are complementary due to their H- and O-binding energy. Ag is weak compared to Pt, which is strong, originates a new surface, and through a synergic effect, can express a balance in the adsorption energies, accomplishing the design of electrocatalysts with high catalytic activity and durability, simultaneously.

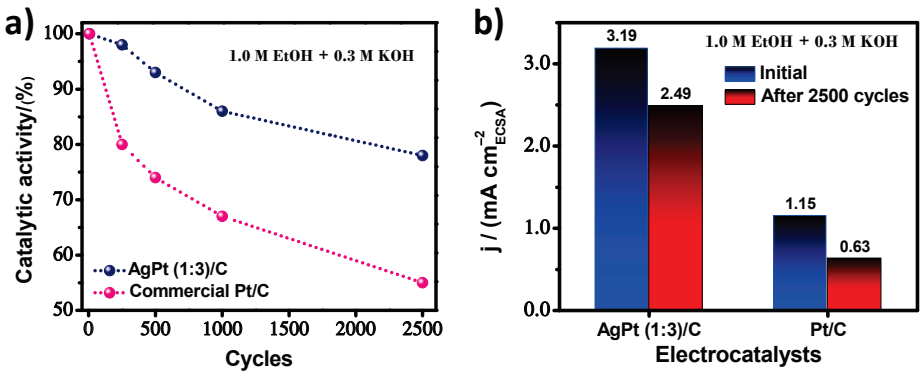

Figure 8. (**a**) Evaluation of the percentage of catalytic activity as a function of the number of cycles during the accelerated electrochemical degradation test, and (**b**) comparison of the initial and final catalytic activity for AgPt (1:3)/C and commercial Pt/C electrocatalysts.

4. Conclusions

In the present work, a chemical synthesis methodology based on the polyol method was successfully developed to obtain AgPt BNPs in different atomic compositions (1:1 and 1:3). The XRD technique determined that the AgPt BNPs present an fcc crystalline structure in an alloy-type configuration. Through the UV-Vis technique, the changes in the optoelectronic properties of the nanoalloys produced by the incorporation of Ag and Pt atoms into the Ag growth seeds were determined. The extinction of the SPR band characteristic of Ag seeds was defined with the increase in the atomic percentage of Pt, confirming the formation of AgPt nanoalloys. SEM and HAADF-STEM determined the particle size, morphology, and distribution of the nanoalloys, obtaining an average particle size of 6 and 10 nm for the ratios 1:1 and 1:3, respectively. The nanoparticles in both systems presented a good distribution along the support material (Vulcan XC-72 carbon). On the other hand, the particles exhibited a truncated octahedral morphology with exposed {100} and {111} surface planes related to highly stable surface energy densities and selectivity for specific catalytic reactions. The synergistic interaction between Ag and Pt was studied as an electrocatalyst for ethanol oxidation, verifying that the ratio between Pt and Ag significantly affected the electrocatalytic performance, although pure Ag has no activity toward the EOR. AgPt (1:3)/C presented a new catalytic surface exhibiting a MA/SA 3.9/2.8 times higher than the commercial Pt/C, as well as superior CO-like tolerance and the best stability. Alloying Pt with Ag is an attractive strategy for designing cost-effective electrocatalysts. Therefore, AgPt (1:3)/C has the competitive potential of being used as an electrode material for fuel cell applications.

Supplementary Materials: The following supporting information can be downloaded at: https://www.mdpi.com/article/10.3390/nano13081396/s1, Figure S1. A low magnification SEM-SE micrograph of Pt/C commercial electrocatalyst purchased from Sigma-Aldrich; Figure S2. Low magnification BF-STEM micrographs of (a) AgPt (1:1) and (b) AgPt (1:3) BNPs; Figure S3: Cyclic voltammograms in alkaline media recorded consecutively after chronoamperometry (CA) measurements for Pt/C, AgPt (1:1)/C, and AgPt (1:3)/C electrocatalysts; Table S1. Comparison of the catalytic

activity of ethanol oxidation using Pt-based materials. References [45,53,54,56–58] are cited in the Supplementary Materials.

Author Contributions: Conceptualization, F.M.-B., A.H. and J.L.L.-M.; Methodology, F.M.-B. and A.H.; Validation, R.M.-C. and J.L.L.-M.; Formal analysis, F.M.-B. and R.E.; Investigation, F.M.-B. and R.E.; Writing—original draft preparation, F.M.-B., A.H. and R.E.; Writing—review and editing, R.E.; Visualization, R.M.-C. and R.E.; Funding acquisition, R.E. All authors have read and agreed to the published version of the manuscript.

Funding: This research was funded by PAPIIT-DGAPA under grant number IN105821.

Data Availability Statement: Not applicable.

Acknowledgments: F. Mares-Briones acknowledges CONACYT for the postdoctoral research fellowship. R. Mendoza-Cruz acknowledges to PAPIIT-DGAPA grant number IA-106623. The authors want to acknowledge the Laboratorio Nacional de Caracterización de Materiales (LaNCaM) at the CFATA-UNAM and Laboratorio Universitario de Microscopía Electrónica (LUME) at IIM-UNAM.

Conflicts of Interest: The authors declare no conflict of interest.

References

1. Santasalo-Aarnio, A.; Tuomi, S.; Jalkanen, K.; Kontturi, K.; Kallio, T. The correlation of electrochemical and fuel cell results for alcohol oxidation in acidic and alkaline media. *Electrochim. Acta* **2013**, *87*, 730–738. [CrossRef]
2. Li, Y.S.; Zhao, T.S.; Liang, Z.X. Performance of alkaline electrolyte-membrane-based direct ethanol fuel cells. *J. Power Sources* **2009**, *187*, 387–392. [CrossRef]
3. Zhang, J.; Balakrishnan, P.; Chang, Z.; Sun, P.; Su, H.; Xing, L.; Xu, Q. Boosting the performance of alkaline direct ethanol fuel cell with low-pd-loading nickel foam electrode via mixed acid-etching. *Int. J. Hydrogen Energy* **2022**, *47*, 9672–9679. [CrossRef]
4. Lamy, C.; Lima, A.; LeRhun, V.; Delime, F.; Coutanceau, C.; Léger, J.-M. Recent advances in the development of direct alcohol fuel cells (dafc). *J. Power Sources* **2002**, *105*, 283–296. [CrossRef]
5. Gao, F.; Zhang, Y.; Zou, B.; Jiang, F.; Li, Z.; Du, Y. Facile synthesis of low-dimensional pdpt nanocrystals for high-performance electrooxidation of C 2 alcohols. *J. Colloid Interface Sci.* **2022**, *610*, 271–279. [CrossRef] [PubMed]
6. Luo, S.; Zhang, L.; Liao, Y.; Li, L.; Yang, Q.; Wu, X.; Wu, X.; He, D.; He, C.; Chen, W. A tensile-strained Pt–Rh single-atom alloy remarkably boosts ethanol oxidation. *Adv. Mater.* **2021**, *33*, 2008508. [CrossRef] [PubMed]
7. Maniam, K.K.; Chetty, R.; Thimmappa, R.; Paul, S. Progress in the development of electrodeposited catalysts for direct liquid fuel cell applications. *Appl. Sci.* **2022**, *12*, 501. [CrossRef]
8. Elsaid, K.; Abdelfatah, S.; Elabsir, A.M.A.; Hassiba, R.J.; Ghouri, Z.K.; Vechot, L. Direct alcohol fuel cells: Assessment of the fuel's safety and health aspects. *Int. J. Hydrogen Energy* **2021**, *46*, 30658–30668. [CrossRef]
9. Yu, Z.-Y.; Huang, R.; Liu, J.; Luo, C.-X.; Wang, C.-Y.; Song, Q.-T.; Xiao, C.; Yin, S.-H.; Xu, B.-B.; Sun, S.-G. Pdpt concave nanocubes directly electrodeposited on carbon paper as high active and durable catalysts for formic acid and ethanol oxidation. *Electrochim. Acta* **2020**, *354*, 136654. [CrossRef]
10. Figueiredo, M.C.; Solla-Gullón, J.; Vidal-Iglesias, F.J.; Nisula, M.; Feliu, J.M.; Kallio, T. Carbon-supported shape-controlled pt nanoparticle electrocatalysts for direct alcohol fuel cells. *Electrochem. Commun.* **2015**, *55*, 47–50. [CrossRef]
11. Wala, M.; Simka, W. Effect of anode material on electrochemical oxidation of low molecular weight alcohols—A review. *Molecules* **2021**, *26*, 2144. [CrossRef] [PubMed]
12. Lima, C.C.; Fonseca, W.S.; Colmati, F.; Ribeiro, L.K.; Franca, M.C.; Longo, E.; Garcia, M.A.S.; Tanaka, A.A. Enhancing the methanol tolerance of ultrasmall platinum nanoparticles and manganese oxide onto carbon for direct methanol fuel cell: The importance of the synthesis procedure. *Electrochim. Acta* **2020**, *363*, 137256. [CrossRef]
13. Altarawneh, R.M. Overview on the vital step toward addressing platinum catalyst poisoning mechanisms in acid media of direct ethanol fuel cells (defcs). *Energy Fuels* **2021**, *35*, 11594–11612. [CrossRef]
14. Song, S.; Zhou, W.; Tian, J.; Cai, R.; Sun, G.; Xin, Q.; Kontou, S.; Tsiakaras, P. Ethanol crossover phenomena and its influence on the performance of defc. *J. Power Sources* **2005**, *145*, 266–271. [CrossRef]
15. Jayabal, S.; Saranya, G.; Geng, D.; Lin, L.-Y.; Meng, X. Insight into the correlation of Pt–support interactions with electrocatalytic activity and durability in fuel cells. *J. Mater. Chem. A* **2020**, *8*, 9420–9446. [CrossRef]
16. Ren, X.; Lv, Q.; Liu, L.; Liu, B.; Wang, Y.; Liu, A.; Wu, G. Current progress of Pt and Pt-based electrocatalysts used for fuel cells. *Sustain. Energy Fuels* **2020**, *4*, 15–30. [CrossRef]
17. Liu, D.; Yang, N.; Zeng, Q.; Liu, H.; Chen, D.; Cui, P.; Xu, L.; Hu, C.; Yang, J. Core-shell Ag–Pt nanoparticles: A versatile platform for the synthesis of heterogeneous nanostructures towards catalyzing electrochemical reactions. *Chin. Chem. Lett.* **2021**, *32*, 3288–3297. [CrossRef]
18. Borghei, M.; Lehtonen, J.; Liu, L.; Rojas, O.J. Advanced biomass-derived electrocatalysts for the oxygen reduction reaction. *Adv. Mater.* **2018**, *30*, 1703691. [CrossRef]

19. Pham, H.Q.; Huynh, T.T.; Nguyen, S.T.; Dang, N.N.; Bach, L.G. Superior CO-tolerance and stability toward alcohol electro-oxidation reaction of 1d-bimetallic platinum-cobalt nanowires on tungsten-modified anatase TiO_2 nanostructure. *Fuel* **2020**, *276*, 118078. [CrossRef]
20. Yang, G.; Zhang, Q.; Yu, H.; Peng, F. Platinum-based ternary catalysts for the electrooxidation of ethanol. *Particuology* **2021**, *58*, 169–186. [CrossRef]
21. Li, C.; Yamauchi, Y. Facile solution synthesis of Ag@ Pt core–shell nanoparticles with dendritic Pt shells. *Phys. Chem. Chem. Phys.* **2013**, *15*, 3490–3496. [CrossRef] [PubMed]
22. Ehsani, A.; Heidari, A.; Asgari, R. Electrocatalytic oxidation of ethanol on the surface of graphene based nanocomposites: An introduction and review to it in recent studies. *Chem. Rec.* **2019**, *19*, 2341–2360. [CrossRef] [PubMed]
23. Bordley, J.A.; El-Sayed, M.A. Enhanced electrocatalytic activity toward the oxygen reduction reaction through alloy formation: Platinum–silver alloy nanocages. *J. Phys. Chem. C* **2016**, *120*, 14643–14651. [CrossRef]
24. Zhang, E.; Ma, F.; Liu, J.; Sun, J.; Chen, W.; Rong, H.; Zhu, X.; Liu, J.; Xu, M.; Zhuang, Z. Porous platinum–silver bimetallic alloys: Surface composition and strain tunability toward enhanced electrocatalysis. *Nanoscale* **2018**, *10*, 21703–21711. [CrossRef]
25. Fu, X.; Wan, C.; Zhang, A.; Zhao, Z.; Huyan, H.; Pan, X.; Du, S.; Duan, X.; Huang, Y. Pt_3Ag alloy wavy nanowires as highly effective electrocatalysts for ethanol oxidation reaction. *Nano Res.* **2020**, *13*, 1472–1478. [CrossRef]
26. Li, J.; Rong, H.; Tong, X.; Wang, P.; Chen, T.; Wang, Z. Platinum–silver alloyed octahedral nanocrystals as electrocatalyst for methanol oxidation reaction. *J. Colloid Interface Sci.* **2018**, *513*, 251–257. [CrossRef]
27. Higareda, A.; Kumar-Krishnan, S.; García-Ruiz, A.F.; Maya-Cornejo, J.; Lopez-Miranda, J.L.; Bahena, D.; Rosas, G.; Pérez, R.; Esparza, R. Synthesis of Au@Pt core—Shell nanoparticles as efficient electrocatalyst for methanol electro-oxidation. *Nanomaterials* **2019**, *9*, 1644. [CrossRef]
28. Wei, C.; Sun, S.; Mandler, D.; Wang, X.; Qiao, S.Z.; Xu, Z.J. Approaches for measuring the surface areas of metal oxide electrocatalysts for determining their intrinsic electrocatalytic activity. *Chem. Soc. Rev.* **2019**, *48*, 2518–2534. [CrossRef]
29. Hume-Rothery, W. The structure of metals and alloys. *Indian J. Phys.* **1969**, *11*, 74.
30. Goodwin, F.; Guruswamy, S.; Kainer, K.U.; Kammer, C.; Knabl, W.; Koethe, A.; Leichtfried, G.; Schlamp, G.; Stickler, R.; Warlimont, H. Metals. In *Springer Handbook of Condensed Matter and Materials Data*; Martienssen, W., Warlimont, H., Eds.; Springer: Berlin/Heidelberg, Germany, 2005; pp. 161–430.
31. Wisniewska, J.; Ziolek, M. Formation of Pt–Ag alloy on different silicas—Surface properties and catalytic activity in oxidation of methanol. *RSC Adv.* **2017**, *7*, 9534–9544. [CrossRef]
32. Guisbiers, G.; Mendoza-Cruz, R.N.; Bazán-Díaz, L.; Velázquez-Salazar, J.J.S.; Mendoza-Perez, R.; Robledo-Torres, J.A.; Rodriguez-Lopez, J.-L.; Montejano-Carrizales, J.M.; Whetten, R.L.; José-Yacamán, M. Electrum, the gold–silver alloy, from the bulk scale to the nanoscale: Synthesis, properties, and segregation rules. *ACS Nano* **2016**, *10*, 188–198. [CrossRef] [PubMed]
33. Peng, Z.; Yang, H. Ag–pt alloy nanoparticles with the compositions in the miscibility gap. *J. Solid State Chem.* **2008**, *181*, 1546–1551. [CrossRef]
34. Cullity, B.D. *Elements of X-ray Diffraction*; Addison-Wesley Publishing: Boston, MA, USA, 1956.
35. Rodrigues, J.F.B.; Junior, E.P.S.; Oliveira, K.S.; Wellen, M.R.R.; Simões, S.S.; Fook, M.V.L. Multivariate model based on uv-vis spectroscopy and regression in partial least squares for determination of diameter and polydispersity of silver nanoparticles in colloidal suspensions. *J. Nanomater.* **2020**, *2020*, 1279862. [CrossRef]
36. Saeb, A.T.M.; Alshammari, A.S.; Al-Brahim, H.; Al-Rubeaan, K.A. Production of silver nanoparticles with strong and stable antimicrobial activity against highly pathogenic and multidrug resistant bacteria. *Sci. World J.* **2014**, *2014*, 704708. [CrossRef]
37. Szerencsés, B.; Igaz, N.; Tóbiás, Á.; Prucsi, Z.; Rónavári, A.; Bélteky, P.; Madarász, D.; Papp, C.; Makra, I.; Vágvölgyi, C.; et al. Size-dependent activity of silver nanoparticles on the morphological switch and biofilm formation of opportunistic pathogenic yeasts. *BMC Microbiol.* **2020**, *20*, 176. [CrossRef]
38. Mukherji, S.; Bharti, S.; Shukla, G.; Mukherji, S. Synthesis and characterization of size- and shape-controlled silver nanoparticles. *Phys. Sci. Rev.* **2019**, *4*, 20170082. [CrossRef]
39. Pal, A. Gold–platinum alloy nanoparticles through water-in-oil microemulsion. *J. Nanostruct. Chem.* **2015**, *5*, 65–69. [CrossRef]
40. Guczi, L. Mechanism of reactions on multimetallic catalysts. *J. Mol. Catal.* **1984**, *25*, 13–29. [CrossRef]
41. Deng, L.; Deng, H.; Xiao, S.; Tang, J.; Hu, W. Morphology, dimension, and composition dependence of thermodynamically preferred atomic arrangements in ag–pt nanoalloys. *Faraday Discuss.* **2013**, *162*, 293–306. [CrossRef]
42. Pennycook, S.J. The impact of stem aberration correction on materials science. *Ultramicroscopy* **2017**, *180*, 22–33. [CrossRef]
43. Zhang, J.-M.; Ma, F.; Xu, K.-W. Calculation of the surface energy of fcc metals with modified embedded-atom method. *Chin. Phys.* **2004**, *13*, 1082. [CrossRef]
44. Xia, T.; Liu, J.; Wang, S.; Wang, C.; Sun, Y.; Gu, L.; Wang, R. Enhanced catalytic activities of nipt truncated octahedral nanoparticles toward ethylene glycol oxidation and oxygen reduction in alkaline electrolyte. *ACS Appl. Mater. Interfaces* **2016**, *8*, 10841–10849. [CrossRef] [PubMed]
45. Gu, X.; Wang, C.; Yang, L.; Yang, C. 3D porous ptag nanotubes for ethanol electro-oxidation. *J. Nanosci. Nanotechnol.* **2017**, *17*, 2843–2847. [CrossRef] [PubMed]
46. De Backer, A.; Van den Bos, K.; Van den Broek, W.; Sijbers, J.; Van Aert, S. Statstem: An efficient approach for accurate and precise model-based quantification of atomic resolution electron microscopy images. *Ultramicroscopy* **2016**, *171*, 104–116. [CrossRef] [PubMed]

47. Zhao, X.; Zhang, H.; Yan, Y.; Cao, J.; Li, X.; Zhou, S.; Peng, Z.; Zeng, J. Engineering the electrical conductivity of lamellar silver-doped cobalt (ii) selenide nanobelts for enhanced oxygen evolution. *Angew. Chem.* **2017**, *129*, 334–338. [CrossRef]
48. García-Morales, N.G.; García-Cerda, L.A.; Puente-Urbina, B.A.; Blanco-Jerez, L.M.; Antaño-López, R.; Castañeda-Zaldivar, F. Electrochemical glucose oxidation using glassy carbon electrodes modified with au-ag nanoparticles: Influence of ag content. *J. Nanomater.* **2015**, *2015*, 295314. [CrossRef]
49. Abd El Rehim, S.S.; Hassan, H.H.; Ibrahim, M.A.; Amin, M.A. Electrochemical behaviour of a silver electrode in naoh solutions. *Monatsh. Chem.* **1998**, *129*, 1103–1117. [CrossRef]
50. Hazzazi, O.A.; Zaky, A.M.; Amin, M.A.; Abd El Rehim, S.S. Passivation and cl induced depassivation of Cu-Ag alloys in borate buffer solutions. *Int. J. Electrochem. Sci* **2008**, *3*, 489–508.
51. Li, M.; Duanmu, K.; Wan, C.; Cheng, T.; Zhang, L.; Dai, S.; Chen, W.; Zhao, Z.; Li, P.; Fei, H.; et al. Single-atom tailoring of platinum nanocatalysts for high-performance multifunctional electrocatalysis. *Nat. Catal.* **2019**, *2*, 495–503. [CrossRef]
52. Sulaiman, J.E.; Zhu, S.; Xing, Z.; Chang, Q.; Shao, M. Pt–Ni octahedra as electrocatalysts for the ethanol electro-oxidation reaction. *ACS Catal.* **2017**, *7*, 5134–5141. [CrossRef]
53. Yin, K.; Chao, Y.; Zeng, L.; Li, M.; Liu, F.; Guo, S.; Li, H. Ultrathin ptru nanowires as efficient and stable electrocatalyst for liquid fuel oxidation reactions. *Energy Mater. Adv.* **2022**, *2022*, 9871842. [CrossRef]
54. Higareda, A.; Mares-Briones, F.; Rosas, G.; Pérez, R.; Esparza, R. Enhanced durability of pdpt/c electrocatalyst during the ethanol oxidation reaction in alkaline media. *J. Solid State Electrochem.* **2022**, *26*, 2143–2151. [CrossRef]
55. Vasileff, A.; Xu, C.; Jiao, Y.; Zheng, Y.; Qiao, S.-Z. Surface and interface engineering in copper-based bimetallic materials for selective CO_2 electroreduction. *Chem* **2018**, *4*, 1809–1831. [CrossRef]
56. Liu, D.; Huang, H.-Z.; Zhu, Z.; Li, J.; Chen, L.-W.; Jing, X.-T.; Yin, A.-X. Promoting the electrocatalytic ethanol oxidation activity of pt by alloying with cu. *Catalysts* **2022**, *12*, 1562. [CrossRef]
57. Jadali, S.; Kamyabi, M.A.; Solla-Gullón, J.; Herrero, E. Effect of pd on the electrocatalytic activity of pt towards oxidation of ethanol in alkaline solutions. *Appl. Sci.* **2021**, *11*, 1315. [CrossRef]
58. Duan, J.-J.; Feng, J.-J.; Zhang, L.; Yuan, J.; Zhang, Q.-L.; Wang, A.-J. Facile one-pot aqueous fabrication of interconnected ultrathin ptpbpd nanowires as advanced electrocatalysts for ethanol oxidation and oxygen reduction reactions. *Int. J. Hydrogen* **2019**, *44*, 27455–27464. [CrossRef]

nanomaterials

MDPI

Article

Nitrogen-Doped Graphene Oxide as Efficient Metal-Free Electrocatalyst in PEM Fuel Cells

Adriana Marinoiu [1,*], Mircea Raceanu [1,2], Elena Carcadea [1] and Mihai Varlam [1]

[1] ICSI Energy Department, National Research and Development Institute for Cryogenic and Isotopic Technologies, 240050 Ramnicu Valcea, Romania
[2] Doctoral School, University Politehnica of Bucharest, 060042 Bucharest, Romania
* Correspondence: adriana.marinoiu@icsi.ro

Abstract: Nitrogen-doped graphene is currently recognized as one of the most promising catalysts for the oxygen reduction reaction (ORR). It has been demonstrated to act as a metal-free electrode with good electrocatalytic activity and long-term operation stability, excellent for the ORR in proton exchange membrane fuel cells (PEMFCs). As a consequence, intensive research has been dedicated to the investigation of this catalyst through varying the methodologies for the synthesis, characterization, and technologies improvement. A simple, scalable, single-step synthesis method for nitrogen-doped graphene oxide preparation was adopted in this paper. The physical and chemical properties of various materials obtained from different precursors have been evaluated and compared, leading to the conclusion that ammonia allows for a higher resulting nitrogen concentration, due to its high vapor pressure, which facilitates the functionalization reaction of graphene oxide. Electrochemical measurements indicated that the presence of nitrogen-doped oxide can effectively enhance the electrocatalytic activity and stability for ORR, making it a viable candidate for practical application as a PEMFC cathode electrode.

Keywords: electrocatalyst; nitrogen-doped graphene oxide; metal-free; long-term operation stability; oxygen reduction reaction; proton-exchange membrane fuel cells

Citation: Marinoiu, A.; Raceanu, M.; Carcadea, E.; Varlam, M. Nitrogen-Doped Graphene Oxide as Efficient Metal-Free Electrocatalyst in PEM Fuel Cells. *Nanomaterials* **2023**, *13*, 1233. https://doi.org/10.3390/nano13071233

Academic Editor: Meiwen Cao

Received: 2 March 2023
Revised: 27 March 2023
Accepted: 28 March 2023
Published: 30 March 2023

1. Introduction

It is a common belief that nowadays we are witnessing an extremely exciting progress for the fuel cells (FCs), mainly due to the recognition of hydrogen as an attractive energy storage technology [1]. One promising solution represents the proton exchange membrane fuel cell (PEMFC) technology, which can definitely become a sustainable and clean electricity source. Light vehicles or stationary applications are just a few examples of applications where low temperature fuel cells can be successfully used.

However, the cost and durability of PEMFCs are still the main hindrances disfavoring the full commercialization on a large scale. The durability decreases mainly due to the degradation of FC components, the most important being the electrodes. It is known that the degradation rate at the cathode-side is higher than that of the anode side and substantially affects the outcomes of the PEMFC.

In addition, the key contributors to FC degradation are the following: the carbon support corrosion, loss of catalytic surface area, and deterioration of the membrane electrode assembly. The specific operation conditions inevitably generates a slow kinetic of the oxygen reduction reaction (ORR) at the cathode. The cathode degradation is the most significant, thus the development of a highly durable cathode has become a subject of great interest. The commonly used catalyst in PEMFC is platinum (Pt) due to its good catalytic activity. However, the limited abundance, high cost of Pt, as well as the stability and resistance to corrosion in the operating environment involved considerable efforts to identify some alternatives for Pt catalyst, but without diminishing the electrochemical performances.

The research strategy to obtain a high-performance and less expensive ORR catalyst consisted in two main approaches. The first direction was to diminish the metal catalyst loading by improving the platinum's utilization grade by (i) alloying Pt with less expensive transitional metals (Fe, Ni, Co, so on) or (ii) considering different support material for the deposition of noble metal particle, such as various types of carbon (graphene-based materials, carbon nanotubes). The second direction was to use the platinum group metals (PGMs) and the PGM-free materials. The actual state-of-the-art (SoA) research indicates that addressing a durable performance metal-free catalyst for oxygen reduction reaction (ORR) could significantly influence the widespread commercialization of PEMFC-based applications such as hybrid vehicles [2–5].

On the other hand, the most effective use of catalyst is possible only by considering a good material with high specific surface area, which can supply as many binding sites, where the catalyst nanoparticles could be anchored. Extended efforts were dedicated to various carbon nanomaterials such graphene-based materials, carbon nanofibers, or nanotubes, as support for anchoring the catalyst nanoparticles. Through innovative nanomaterials, graphene-based materials have stood out as a remarkable support in catalysis, by considering the high specific surface area, electrical conductivity, and interesting mechanical and chemical stability in the specific PEMFC operating conditions. Among graphene materials, graphene oxide (GO) has received remarkable attention as a valuable class of graphene derivatives, due to its chemical stability, high conductivity, and ability to form chemical bonds easily [6–9].

Recent research has shown that the introduction of heteroatoms into the carbon lattice could significantly improve surface properties, mainly by optimizing the electronic charge distribution. Thus, doping with p and n type elements (N, B, O, P, S) could be an efficient way to modify the electrical, chemical, or physical properties of GO. Through the different heteroatoms evaluated for functionalization/doping, the nitrogen has received a significant interest, especially due to the fact that it possesses the same atomic size as carbon, having one more electron than carbon. Thus, the electronic distribution of carbon atoms is disturbed when nitrogen is introduced into the graphene array.

Up to now, the nitrogen-doped graphene oxide (N/GO) represents one of the promising non-platinum catalysts mainly due to the advantages of low cost and high catalytic performance to reduce/replace the expensive Pt-based catalysts in various electrochemical devices [10–12]. Nitrogen doping disrupts the ideal sp^2 hybridization of carbon atoms and significantly changes the chemical reactivity and electronic properties of GO [13–15]. In particular, N/GO has been extensively investigated as a promising catalyst for the oxygen reduction reaction (ORR), especially due to improved electronic properties in the electron transfer reactions.

Significant progress has been noted with respect to the evaluation of non-PGM materials considering the development and improvement of innovative carbon structures, like nitrogen-doped carbon. Recently, the N/GO was demonstrated to act as metal-free electrode with a better electrocatalytic activity, long-term operation stability for oxygen reduction via a four-electron pathway in PEM fuel cells. Even the exact catalytic mechanism is still under debate, N/GO catalyst has demonstrated remarkable results for ORR and a high stability for FCs. Moreover, it has been noted that N/GO catalysts provided a catalytic activity comparable to that offered by Pt-based catalysts [15,16].

Thus, many papers were dedicated to the investigation of this catalyst through the methodologies for the synthesis, characterization, and technologies improvement [17–23].

Investigations about different chemical, physical, and mechano-chemical preparation procedures were discussed based on the features of N/GO catalysts, in particular regarding the nitrogen content. The literature presents various published papers for the synthesis of N/GO. Various substances, such as ammonia, urea, ammonium salts, and organic salts have been investigated as precursors of N. Until recently, N-doped graphene was prepared by using one of the techniques presented below: chemical vapor decomposition (CVD), the discharge of a graphite electrode in the presence of pyridine vapor, thermal exfoliation of

graphite oxide with NH_3, plasma nitrogen treatment of graphene, thermal decomposition, and solvothermal pathway [24].

The chemical vapor deposition (CVD) is the classic route to prepare the doped-graphene or N/GO catalysts for industrial and lab scale. However, this method involves several important disadvantages, namely: introduction of metal impurities (e.g., from Cu or Ni support) in the final doped graphene; using of gaseous ammonia as nitrogen source is a very toxic process, thus the additional costs are necessary to meet the special safety treatments. In this context, a metal-free route is recommended to be developed for the preparation of N/GO materials [15,25,26].

The CVD process synthesized N/GO directly on copper foil substrate, using urea, boric acid, and polystyrene as precursors containing carbon and nitrogen. Modifying the concentration of precursors, the nitrogen-doped concentration can be adjusted from 0.9% to 4.8%. It was noted that different types of nitrogen could be obtained. Graphene doped with about 2.1% indicated that N bond configuration was predominated by pyridine N. However, for graphene doped with 4.8%, the final product consists of 60.2% N-pyridine content and 39.8% N-pyrrole content. These results specified that the characteristics of N/GO could be optimized and controlled by modifying the degree of doping [27]. However, the state-of-the-art nitrogen doping level in N/GO involving the CVD process is between 3 wt.% to 8 wt.% [16,28].

The heat treatment method was involved to prepare N/GO by using a solid carbon source (e.g., graphene oxide), a nitrogen source (e.g., melamine), and a high temperature during the heat treatment (between 500–1000 °C). Apart from the obvious disadvantage of the high temperatures, it should be mentioned that it is necessary to use argon gas to secure the environment in which the carbon nitride polymer is produced. Moreover, it is very difficult to control the final nitrogen content at the different temperatures used during the process, which really hinders the large-scale development [23,29].

To date, N/GOs have been predominantly synthesized by various methods of thermal treatment. A catalyst-free synthesis method has been developed for the preparation of N/GO by heat treatment of graphite oxide with melamine (as a nitrogen source). The method included three steps: (i) the melamine molecules were adsorbed on pre-synthesized graphene oxide (GO); (ii) the melamine was converted to carbon nitride at elevated temperatures (above 500 °C); (iii) in the end, once the oxygen groups are removed from the graphene nanoparticles at high temperatures, the N atoms could dope the network. The concentration of doped nitrogen can be optimized by modifying the mass ratio between GO and melamine or by varying the temperature. The highest nitrogen content was 10 wt.% corresponding to a ratio GO to melamine of 1:5 (calculated as mass ratio) obtained at 700 °C. N/GO was prepared by thermal hardening of GO in an ammonia atmosphere. Oxygen-containing groups on the GO surface have been shown to be fundamental for C-N bond obtaining during the reaction with GO and NH_3. It is important to note that the biggest N content of 5 wt.% has been obtained at temperature of 500 °C.

Latterly, a synthesis method in gaseous phase with graphene substrate has been performed by considering the plasma process. The nitrogen atoms can partially replace carbon atoms from graphene structure by using the N_2 or NH_3 plasma treatment [29]. Gas annealing method is similar with the previous method in respect to the heat treatment. The method uses a solid carbon source (e.g., graphene oxide, carbon black) and nitrogen source (e.g., ammonia) and a high temperature. The main disadvantage of this route is the huge amount of inert gas used for many hours in the tubular furnace to secure the obtained N/GO from the air [30].

Even the reaction occurs as a low time-consuming method (up to 1 h), however the plasma treatment during the reaction involves some special instrumental requirements for nitrogen plasma generating, namely a high power and pressure, thus not favoring the scaling of the process at commercial scale [31].

The percentage of N atoms introduced in the GO structure could be controlled in the domain of 0.11–1.35 wt.%, especially by optimizing the exposure time. Taking into account

this aspect, the use of plasma protocol not only led to the including of N into the graphene network, but to increasing the oxygen content too, from approx. 15 wt.% in the case of graphene, up to approx. 27 wt.% in N/GO. A step-by-step approach was attempted to reduce GO and to introduce nitrogen in GO network at the same time at room temperature, by involving of plasma treatment in an atmosphere of a H_2 and NH_3 gas mixture. Through this chemical process, the highest nitrogen concentration of about 5.8 wt.% can be obtained, but the process still remains at the small scale [27–32].

The nanoscale high-energy wet ball milling derives from the previous method and results in minimal contamination, but involves more difficult operating conditions, thus the method is difficult to scale-up commercially.

A series of solvothermal and hydrothermal treatments for the preparation of N/GO have been developed in the presence of cyanuric chloride ($N_3C_3Cl_3$), Li_3N, and CCl_4 at 350 °C, for 6 h [32].

According to the SoA approaches for producing of N/GO, the conventional chemical methods such as CVD or thermal treatment have been considered more or less standard for the preparation of N/GO-based materials. The main disadvantages of the mentioned processes are mentioned: the preparation methods involved require multiple operating activities and sophisticated equipment, making the processes unattractive to be transposed to a larger production scale. Other disadvantages are harsh conditions requiring elevated temperatures for thermal decomposition and high pressure or supercritical conditions. Furthermore, these processes result in poorer quality graphene materials (many structural defects). The preparing of N/GO using a simple synthesis method is still a topical issue in this context.

The current study introduces an original protocol based on a low time-consuming method to obtain N/GO, considering a commercial graphene oxide, different nitrogen precursors (ammonia, urea, nitric acid) and different reducing agents.

2. Experimental

The nitrogen-doped graphene oxide (N/GO) samples were obtained starting from commercial graphene oxide by a one-step reaction process, under mild reaction conditions in the microwave field (60–80 °C, 800 W). The obtained materials were analyzed by different compositional, morphological, and structural characterization techniques and various electrochemical methods.

2.1. Materials

Graphene oxide powder (medium reduced GO, product no.2.1-M) was supplied by Abalonix Norway. Ammonia (25 wt.%) was purchased from Chimreactiv Romania; urea (98 wt.%), nitric acid (65 wt.%), ethanol and ethylene glycol were acquired from Alfa Aesar; Sharlau delivered synthetic grade sodium borohydride.

2.2. Catalyst Preparation

An amount of 250 mg of graphene oxide (GO) powder was well dispersed in demineralized water and then in 100 mL of reduction agent solution (ethylene glycol EG, sodium borohydride BH_4Na, ethanol Et), using both an ultrasonic bath and an ultrasonicator as well. Ammonia solution was added to the GO dispersion and sonicated again. The resulting mixture was placed in a microwave reactor (MARS 6 One touch oven, EMC) for 15 min under the following reaction conditions: reaction temperature 60–80 °C, microwave power 800 W. The reaction mixture, containing a polar liquid, absorbs microwave energy very quickly. Thus, the temperature in the suspension mass increases rapidly, causing the reaction of the sample in a short time. The reaction product was removed separately, washed well with deionized water and finally lyophilized. The obtained product (N/GO_A) in powder form was perfectly dispersible in deionized water (ultrasonic bath, 15 min) and could be dried and redispersed, being suitable for catalytic material.

A second route to obtain the nitrogen-based graphene oxide is presented. An aqueous solution based on urea (2.43 wt.%) was used as a nitrogen source, completely non-toxic and non-flammable. Nitrogen-doped graphene was prepared using a simple chemical method, described below. An amount of 250 mg of graphene oxide (GO) powder was well dispersed in demineralized water and then in ethanol solution, using both an ultrasonic bath and an ultrasonicator. The urea solution (2.5 g urea 98 wt.%, 100 mL deionized water) was introduced in the GO-based dispersion, and then ultrasonicated again. The obtained mixture was introduced into the microwave reactor, under the mentioned reaction conditions (reaction temperature 60–80 °C, microwave power 800 W, reaction time 15 min). The reaction product was separated, washed thoroughly with deionized water and finally dried by lyophilization. N/GO_U powder was obtained, as a product also perfectly dispersible in water.

A third example of nitrogen-based graphene oxide is presented. A dispersion of GO (250 mg powder in 100 mL demineralized water) was added to 100 mL of reduction agent solution (sodium borohydride BH_4Na), using both ultrasonic bath and ultrasonicator. Nitric acid solution was added to the GO-based dispersion and sonicated again. The resulting mixture was inserted into a cell made of Teflon of the MARS 6 One touch reactor. The reaction conditions were mentioned above. The product obtained was separated by ultracentrifugation, washed with deionized water and finally subjected to lyophilization. The final powder-like N/GO_N product was evaluated as a catalytic material.

2.3. Characterization Methods

X-ray photoelectron spectroscopy was carried out by the X-ray photoelectron spectrometer (PHI-5000 VersaProbe, PHI-Ulvac/Physical Electronics, Chigasaki, Japan). XPS measurements were obtained using the monochromatic Al Kα radiation (1486.7 eV). The photoelectrons were collected under an angle of 45°. The elemental qualitative analysis was determined by recording the broad spectra and then identifying various chemical bindings on the surface; finally, the deconvolutions of high resolution spectra were performed. XPS curves were interpreted from the PHI-MultiPak software. The atomic concentrations of the various chemical elements were calculated, considering the sensitivity factors for the elements identified on the surface, thus achieving a quantitative elemental analysis. The specific surface area measurements of graphene doped with nitrogen (powder) were performed using the Autosorb IQ Quantachrome equipment by the Brunauer–Emmett–Teller (BET) method. The nitrogen adsorption and desorption isotherms were measured at 77 K, and the specific surface area was calculated. The porosity analysis, the pore volume as well as the pore radius were estimated by considering the Barret–Joyner–Halenda method (BJH). Before the actual adsorption measurements, the prepared graphene-based materials were degassed at 393 K, time for 10 h. The elemental analysis was involved for a rapid and accurate analysis of solid materials to provide the C, H, N, and O concentrations. The TGA-DSC STA 449 Jupiter Simultaneous Thermal Analyzer (TG-DSC) with operating range between 25–1650 °C and controlled argon atmosphere was used to perform the simultaneous analyses of thermogravimetric mass loss (TG) and differential scanning calorimetry (DSC). For the quantification of carbon, nitrogen, and hydrogen, the combustion method at 950 °C was used, while the pyrolysis process at 1050 °C was carried out for oxygen calculation. The gas was separated by using the SM5A column (molecular sieve) and also detected by the TCD. The IR spectra (KBr pellets form) were collected on a Bruker Tensor 37 spectrometer in the range 4000–400 cm^{-1}.

Electrode Preparation and Electrochemical Measurements

The ex situ electrochemical analysis was performed by using the VersaSCAN electrochemical workstation (Princeton Applied Research) through the following electrochemical methods: the cyclic voltammetry (CV) and electrochemical impedance spectroscopy (EIS). CV measurements were mainly carried out to evaluate the electrochemical response of prepared N/GOs in term of stability. Therefore, a catalytic ink was prepared by making a suspension of the obtained N/GOs samples in C_3H_7OH (Alfa Aesar, Haverhill, MA, USA),

deionized water and 5 wt.% Nafion solution (Aldrich, St. Louis, MO, USA) and then sonication for 3 h. The working electrode (WE, 5 mm diameter, 0.196 cm^2) was carefully polished with 0.3 and 0.05 mm alumina slurry, respectively, and then ultrasonicated in ethanol and deionized water several times to obtain an almost perfect mirror-like surface. The electrode was obtained through deposition on pretreated WE of 5 μL from the as prepared catalytic ink, then the electrode was dried in an oven (at about 40 °C for 15 min). After evaporation of the solvent, the deposited catalyst was covered with 5 mL Nafion solution (0.5 wt.% in ethanol) to fix the catalyst on the surface. The prepared electrodes were allowed to dry in air. The conventional three electrodes electrochemical system (Ag/AgCl electrode and platinum wire as the reference and counter electrode, respectively) was used. The electrolyte was 0.1 M KOH. The CV potential was evaluated between −0.8 V to 0.3 V, using various voltage scan rates (25, 50, 75 and 100 mV s^{-1}). EIS measurements were evaluated in the frequency domain of 0.01 Hz to 100 kHz (in alternating AC voltage of 10 mV).

The in situ electrochemical analysis was performed by using the home-made FC workstation, composed by: DS electronic load, bubble-type humidifiers. The single FC was operated at 0.6 V for 1 h for MEA conditioning. A test cell hardware and compression set designed from Fraunhofer ISE for Baltic Fuel Cells GmbH (Karlsruhe, Germany) was used for compression with a pneumatic cylinder. The compression force (1.2 N mm^{-2}) was exclusively on the active area (50 × 50 mm) and not on the seals (no seals on the CCM, but a radial seal on the compression cylinder). The clamping pressure was controlled by a pneumatic cylinder so that the cell compression was independent of the GDL thickness, a ball joint leads to a homogeneous compression. To reduce boundary effects, the GDL overlaps the CCM area. The temperature sensor was placed in the cooling field, liquid cooling being applied. Copper parts were used for good heat conduction, but to avoid corrosion problems, these parts are gold plated. The geometry of the flow channels grooved in the bipolar plates was serpentine type for both. The humidified gases were introduced at 60–70 °C in countercurrent—flow pressure (atmospheric and applied back pressure of 1 bar). Gas flow rates (H_2 fed to anode, air to cathode, and N_2 as carrier) were fixed by using flow controllers. A control system based on NI c-RIO hardware was involved to control the workstation. The fuel cell was operated at 0.6 V for 1 h for membrane electrode assembly conditioning.

3. Results and Discussion

A successful synthesis protocol based on microwave method is proposed in this paper to prepare nitrogen-doped graphene oxides (N/GOs). This was confirmed and validated by using a chemical, physical, and electrochemical investigation. The electrocatalytic characteristics of the prepared N/GOs samples are directly connected to the chemical structure, mainly to the elemental composition and also to the chemical bonding. The experimental conditions influenced the nitrogen doping ratio, mainly by nitrogen precursors, both organic and inorganic compounds.

The nitrogen doping could be usually attained through rather severe chemical methods, such as CVD of nitrogen-containing precursors, high-temperature ammonia treatment with GO or solvothermal process of GO with nitrogen containing atoms, followed by annealing at elevated temperatures.

This study explores the challenge to obtain N/GOs under mild reaction conditions, in a microwave (MW) field, starting from different nitrogen precursors. The protocol could be a challenge for controlling the doping level, when different types of nitrogen centers were going to be inserted into the graphene network. Ammonia was used as a first nitrogen source, this precursor being well known in N1 chemistry. The ammonia molecule has a pyramidal-trigonal structure, with tetrahedral surfaces, which have a nitrogen atom with a free pair of electrons in the corner. Ammonia has an amphoteric character and contains a large amount of nitrogen (82% by mass) and a bifunctional structure. Urea (also called carbonic acid diamide) is the organic compound with the molecular formula $CO(NH_2)_2$, frequently used in organic reactions, due to its high N content. Nitric acid is the primary

reagent used for nitration typically in an organic molecule and was the third nitrogen precursor in this study.

The chemical composition of the prepared samples was investigated primarily by the elemental analysis using the combustion method (for C, H, N) and the pyrolysis method (for O). The results indicated the presence of all mentioned elements and the chemical composition is provided in Tables 1 and 2.

Table 1. Nitrogen-doped graphene oxide obtained by using the microwave method; comparison of N doping ratio based on experimental condition (inorganic N precursors: ammonia and nitric acid).

Sample N/Gr	Ammonia (mL)	Nitric Acid (mL)	Reduction Agent	T (°C)	C % (wt.)	N % (wt.)	H % (wt.)	O % (wt.)
1	**44**	**-**	**EG**	**80**	**78.98**	**7.52**	**0.94**	**12.56**
2	40	-	EG	80	79.35	6.96	0.98	12.71
3	36	-	EG	80	80.6	6.68	0.93	11.79
4	44	-	EG	60	82.41	5.2	1.16	11.23
5	40	-	EG	60	81.99	4.82	1.28	11.91
6	36	-	EG	60	82.58	4.18	1.26	11.98
7	44	-	BH_4Na	80	81.31	5.56	1.07	12.06
8	40	-	BH_4Na	80	80.87	5.45	1.12	12.56
9	36	-	BH_4Na	80	80.99	5.41	1.18	12.42
10	44	-	BH_4Na	60	82.57	5.09	0.96	11.38
11	40	-	BH_4Na	60	82.59	4.62	1.22	11.57
12	36	-	BH_4Na	60	82.71	4.21	1.36	11.72
13	44	-	Et	80	80.16	5.63	1.16	13.05
14	40	-	Et	80	79.92	5.58	1.24	13.26
15	36	-	Et	80	79.94	5.29	1.28	13.49
16	44	-	Et	60	80.42	4.65	1.19	13.74
17	40	-	Et	60	80.44	4.43	1.21	13.92
18	36	-	Et	60	80.59	4.16	1.23	14.02
19	**-**	**44**	**BH_4Na**	**80**	**82.12**	**2.68**	**1.57**	**13.63**
20	-	40	BH_4Na	80	82.55	2.44	1.73	13.28
21	-	36	BH_4Na	80	81.77	2.23	1.78	14.22
22	-	44	BH_4Na	60	81.51	1.98	1.83	14.68
23	-	40	BH_4Na	60	81.73	1.81	1.87	14.59
24	-	36	BH_4Na	60	81.96	1.33	1.93	14.78

Even the presence of nitrogen in all obtained materials was noted, however the difference of nitrogen content was generated by different precursors as well as various reduction agents. This indicated that the highest concentrations of nitrogen were obtained when ammonia and urea were used as precursors. An important conclusion derives from the fact that, even if the functionalization of graphene oxide during microwave process does not require a high pressure or a high temperature, still the heating temperature could be one of the factors that significantly influences the nitrogen content in synthesized catalysts.

The physical and chemical properties of the materials obtained from different precursors (such as ammonia, urea and nitric acid) were evaluated and compared. It was found that ammonia allows for a higher concentration of nitrogen, probably due to its high vapor pressure which facilitates the reaction of GO functionalization during microwave. Thus, it has been shown that the microwave can grind easily and even break the bulk solid powder to chop particles. The microwave reaction occurs in a liquid environment, so the phenomena of mechanical breakage and cavitation-related effect and shock waves are limited. This type of mechanism acts in process intensification to increase the reaction rates or production yields due to its direct (mechanical, thermal, and chemical) and secondary effects, including turbulence, mechanical vibration, macroscopic heating, emulsification, and dispersion [33].

Table 2. Nitrogen-doped graphene oxide materials obtained by using the microwave method; comparison of N doping ratio based on experimental condition (organic nitrogen precursor: urea).

Sample N/Gr	Urea (g)	Reduction Agent	T (C)	C % (wt)	N % (wt)	H % (wt.)	O % (wt.)
1	**3**	**EG**	**80**	**82.57**	**3.89**	**1.25**	**12.29**
2	2.5	EG	80	82.42	3.63	1.28	12.67
3	2	EG	80	82.18	3.59	1.31	12.92
4	3	EG	60	81.84	3.71	1.27	13.18
5	2.5	EG	60	81.73	3.62	1.29	13.36
6	2	EG	60	81.71	3.38	1.32	13.59
7	3	BH_4Na	80	81.95	2.25	1.38	14.42
8	2.5	BH_4Na	80	82.40	1.93	1.39	14.28
9	2	BH_4Na	80	82.19	1.76	1.42	14.63
10	3	BH_4Na	60	81.95	1.84	1.49	14.72
11	2.5	BH_4Na	60	81.88	1.72	1.52	14.88
12	2	BH_4Na	60	81.94	1.54	1.56	14.96
13	3	Et	80	83.61	3.06	1.26	12.07
14	2.5	Et	80	83.39	2.95	1.29	12.37
15	2	Et	80	83.51	2.74	1.33	12.42
16	3	Et	60	83.40	2.91	1.41	12.28
17	2.5	Et	60	83.32	2.77	1.46	12.45
18	2	Et	60	83.46	2.56	1.47	12.51

One material from each group was selected, namely the material with the highest nitrogen concentration, and their physico–chemical and electrochemical characterizations will be presented below. The samples were encoded: N/GO_A obtained from ammonia as nitrogen precursor, N/GO_U obtained from urea as nitrogen precursor, N/GO_N obtained from nitric acid.

Figure 1a,b reveals the SEM micrographs of the bare graphene oxide and prepared nitrogen-doped graphene oxide samples. The SEM micrographs of the bare graphene oxide in Figure 1a reveals the wavy, corrugated, and wrinkled morphology. However, Figure 1a (left and middle) appears to have fewer similarities. Particularly, Figure 1a (left) does not seem to match any of the figures in Figure 2. This implies that not all features of the basic structure remain intact in the nitrogen-doped graphene oxide. Figure 2b has an actual resemblance only to the pattern of Figure 1a (right): the highest match for N/GO_N and the least for N/GO_A. This means that the higher content of N%, in fact, changes the morphology of the basic structure of GO.

Fourier transform infrared spectroscopy (FT-IR) was involved to investigate the functional groups on the surface of the prepared N/GOs. FT-IR spectra shown in Figure 2 indicate mainly, the evidence of oxygen containing functional groups in all samples. The main characteristic bands were assigned: intense peaks at approx. 1572 cm^{-1} were assigned to the skeletal vibrations from non-oxidized graphitic domains from aromatic regions of GO; small peaks at around 1725 cm^{-1} correspond to C=O stretching and indicates the fact that this bond almost disappeared after microwave treatment. According to the literature, the identification of chemisorbed nitrogen on the GO surface is hindered by its spectral similarity to epoxy oxygen, which usually exists in the graphene lattice, particularly for materials obtained by reduction of GO. Thus, the graphene sp^2 configuration could restrain the graphitic N confinement because the nitrogen atom has almost the same atomic radius as the carbon atom. The identification is even more complicated since numerous feasible overlapping vibrational modes exist in the 1150−1600 cm^{-1} domain. However, a sharp peak at approx. 1300 cm^{-1} was clearly identified in the spectrum of N/GO synthesized through the pyrolysis of GO and urea, when the authors hypothesized that N was chemisorbed on the carbon nanotubes walls and assigned these peaks to C−N and N−CH_3 vibrations and pyridinic-N configuration [34]. In general, the pyridinic N bonds with two

C atoms at the edges or defects of graphene and could contribute with one *p* electron to the π system.

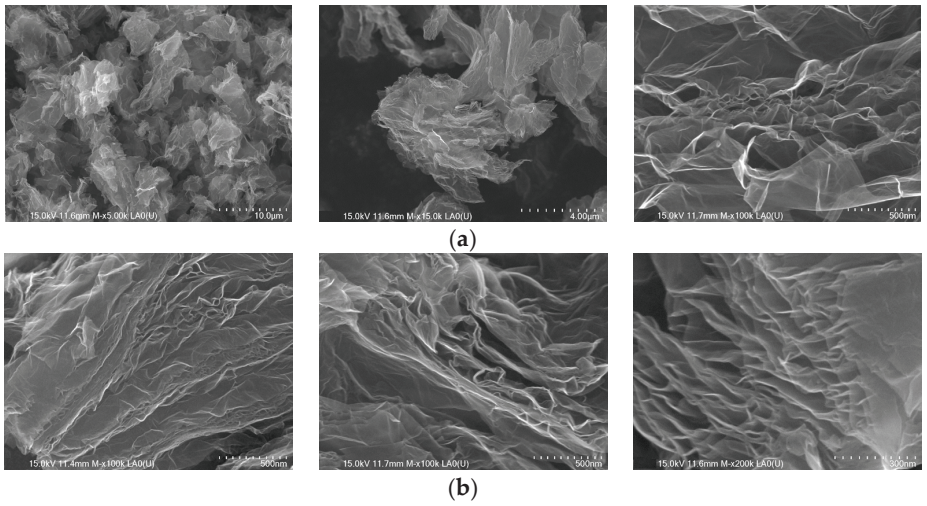

Figure 1. (**a**) SEM images of graphene oxide (GO); (**b**) SEM images of nitrogen-doped graphene oxide materials prepared by using different nitrogen precursors: N/GO_A (left)—from ammonia; N/GO_U (middle)—from urea, and N/GO_N (right)—from nitric acid.

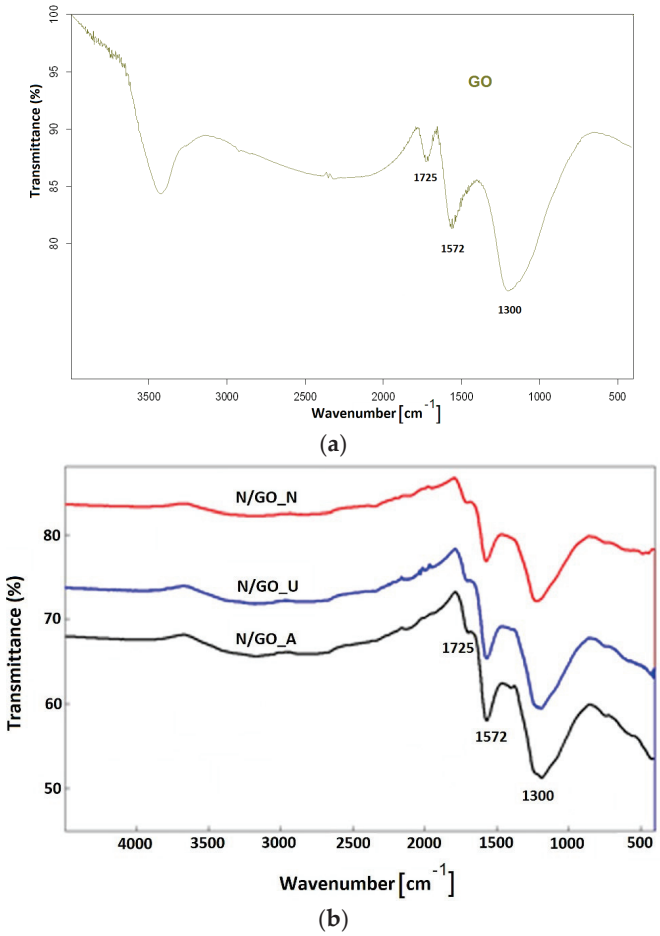

Figure 2. FT−IR spectra of: (**a**) GO and (**b**) Nitrogen-doped graphene oxide materials prepared by using different nitrogen precursors: N/GO_A from ammonia; N/GO_U from urea, and N/GO_N from nitric acid.

However, IR spectroscopy is not appropriate to distinguish between the different valence states of nitrogen in N/GO, mainly because the specific vibrations of nitrogen in N/GO materials are coupled with additional vibrations of carbon atoms coming from some symmetry changes induced by the doping process [34].

Regarding the prepared N/GOs, it is important to note the preservation of some oxygen functionalities from the initial GO structure namely the carboxyl group, which increase the conductivity of the doped material, providing an advantage for the application as electrodes for energy storage devices.

In contrast to the FTIR method, the X-ray photoelectron spectroscopy (XPS) represents the most appropriate spectroscopic method to remark and highlight between the different nitrogen bonds in graphene-based materials, especially since the various forms of N provide significantly different binding energies. The elemental composition of N/GOs was achieved by XPS measurements. The qualitative analysis of the chemical elements linked to the GO surface was investigated after obtaining the broad spectra, and the identification of various types of chemical bonds formed on the surface during the chemical reaction, was achieved by deconvolution of the high-resolution spectra of the existing chemical elements.

The XPS was the technique used to investigate the surface composition of prepared materials. The results of X-ray photoelectron spectroscopy measurements, with reference to the non-doped graphene oxide (GO) and to nitrogen-doped graphene oxides, starting from different nitrogen precursors, are presented in Figures 3–6. The XPS survey spectra of the prepared materials outlines three major peaks assigned to Carbon (C1s), Nitrogen (N1s), and Oxygen (O1s). The C1s peak indicates an intense peak at 284.5 eV, which correspond to sp^2 carbon hybridization and carbon atoms single or double bonded to the nitrogen atoms or oxygen. The C1s scan was deconvoluted in three major components located at approx. 284.3, 285.2 and 288.2 eV, assigned to C-C/C=C, C-O/C=O, and C-N/O-C=O bonding [35]. The peak from 284.5 eV was assigned to the graphitic carbon, showing that the most part of the carbon atoms were settled in conjugated honeycomb lattice. The C1s spectra indicated that the N-functionalized carbon where the nitrogen atoms were bonded within C through a graphitic matrix. The high-resolution N1s spectra were deconvoluted into three components: pyrrolic nitrogen (399.2 eV), graphitic nitrogen (399.7 eV), and pyridinic nitrogen (401.6 eV). These components were similar to those described for nitrogen-doped graphene in [35,36]. The O1s oxygen peaks look broad as a result of the doping process, indicating the existence of various chemical states for oxygen. Moreover, the oxygen functionalities for O1s were identified as carbonyl oxygen (531.4 eV), by using the deconvolution of the peaks corresponding to non-carbonyl oxygen atoms from esters (532.5 eV), and oxygen atoms from carboxylic functionality (531.7 eV) [14,37]. The O 1s peak relative to the corresponding C 1s peak observed for nitrogen-doped graphene indicates a stronger O_2 adsorption, which could be an additional advantage as an ORR electrode for PEM fuel cells.

The presence of large amounts of nitrogen and oxygen atoms on the graphene oxide surface together with the high porosity as will see from BET measurements could provide the necessary adsorption sites for the electrochemical response. Thus, a high amount of N doped in a carbon-based structure could offer the advantage of improving the catalytic and electrochemical properties. The elemental composition of the surface was carried out. The nitrogen content was determined by high resolution XPS measurements and the composition profiles are presented in Table 3.

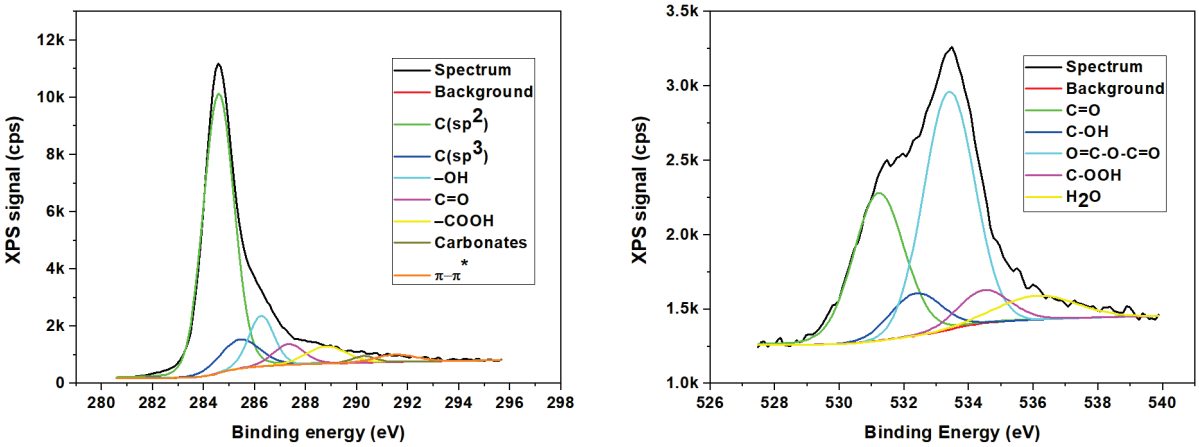

Figure 3. XPS high resolution spectra for non-doped graphene oxide (GO); (**a**) Carbon (C1s); (**b**) Oxygen (O1s).

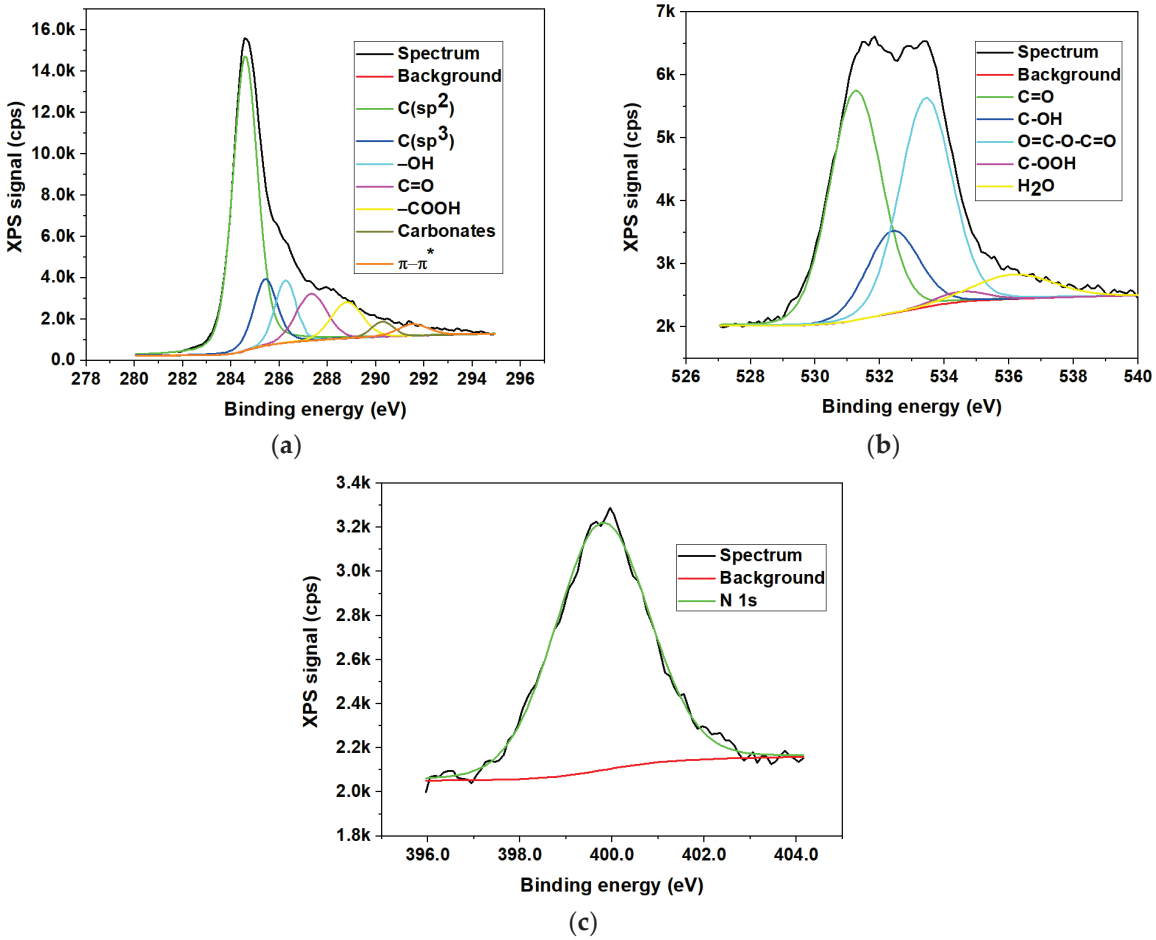

Figure 4. XPS high resolution spectra for nitrogen-doped graphene oxide synthesized using ammonia (N/GO_A); (**a**) Carbon (C1s); (**b**) Oxygen (O1s); (**c**) Nitrogen N1s.

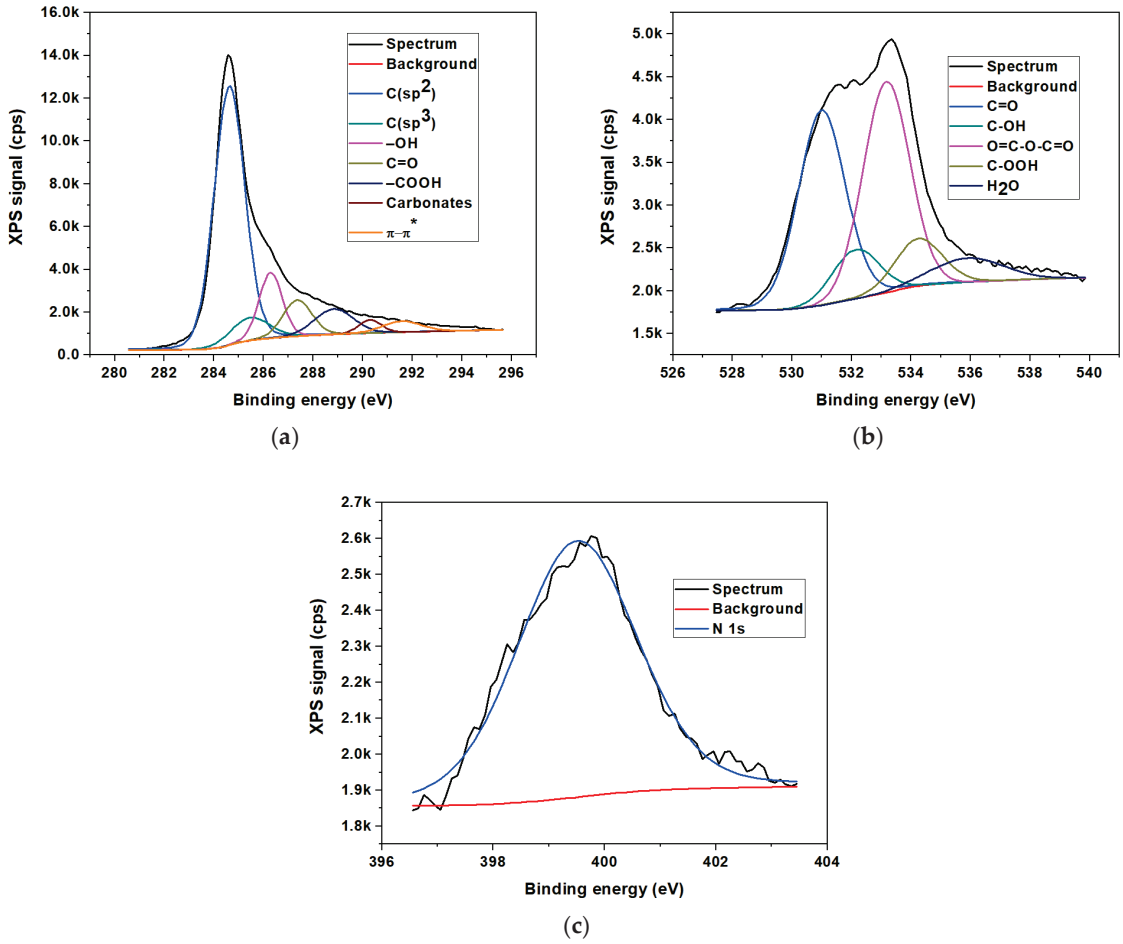

Figure 5. XPS high resolution spectra for nitrogen-doped graphene oxide synthesized using urea (N/GO_U); (**a**) Carbon (C1s); (**b**) Oxygen (O1s); (**c**) Nitrogen N1s.

The atomic concentrations of the chemical elements were determined from the areas of the peaks, taking into account the sensitivity factors of the analyzed elements, thus performing the quantitative elemental analysis. The concentration of nitrogen dopant incorporated into the final samples, according to the peak areas, indicated atomic percentages of 6.7 wt.%, 3.5 wt.%, and 2.2 wt.%, respectively, for the sample N/GO_A, N/GO_U, and N/GO_N. It can be noted the high degree of doping obtained in mild reaction conditions, the highest being for the sample obtained from ammonia as precursor.

Surface area and pore size are factors of most interest in processes involving gas or liquid interacting surfaces. An important characteristic of porous materials is the specific surface area of the materials, commonly calculated from the BET equation. The porous materials having a high specific surface area could offer more active sites and favor the kinetics and transport properties. The nitrogen adsorption and desorption curves were analyzed to estimate the specific surface area. The N_2 adsorption–desorption isotherms were analyzed and their shapes correspond to type IV in compliance to the IUPAC classification. The vertical gas adsorption in the low-pressure range (up to $P/P_0 = 0.02$), as well as the appearance of a pronounced hysteresis loop between $P/P_0 = 0.4$ and $P/P_0 = 1.0$ are the results of the coexistence of both micropores but also mesopores. The calculated BET area and the estimated textural properties for pore volume and pore radius are shown in Table 4.

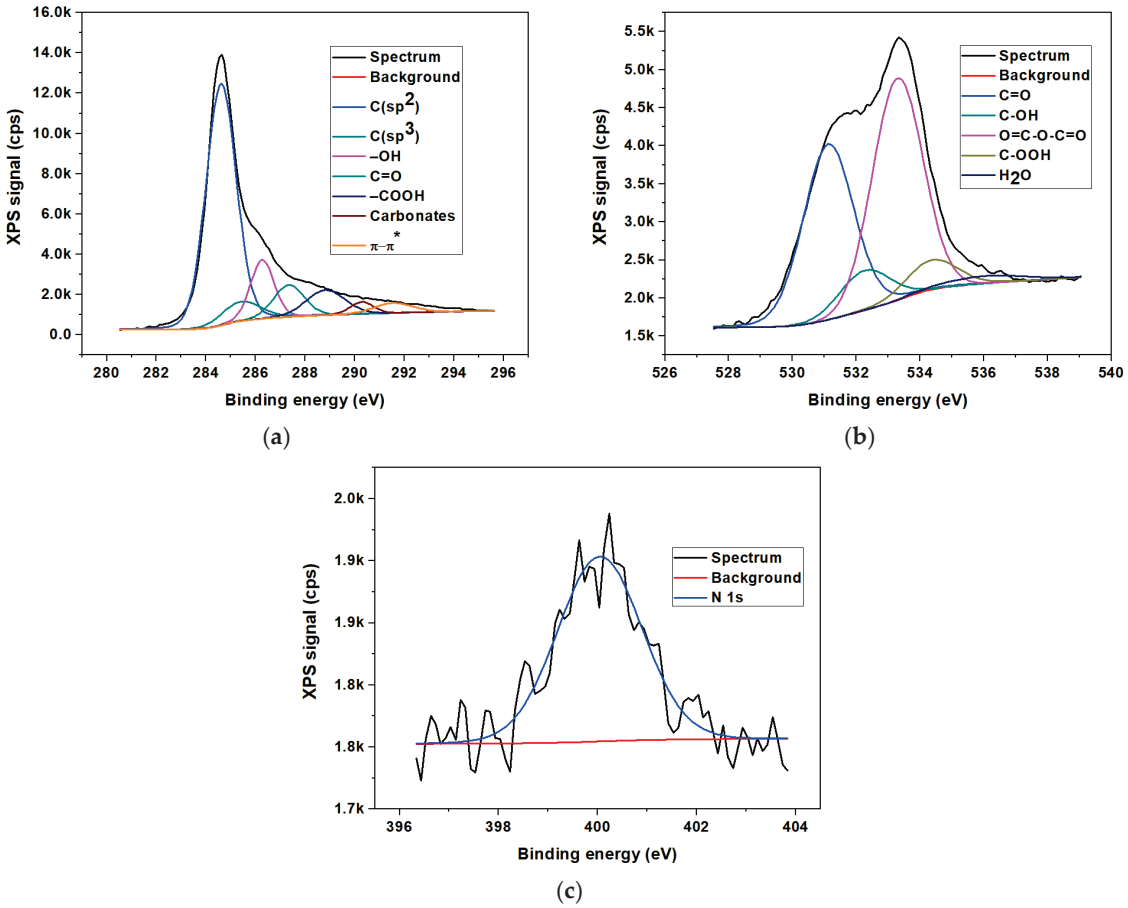

Figure 6. XPS high resolution spectra for nitrogen-doped graphene oxide synthesized using nitric acid (N/GO_N); (**a**) Carbon (C1s); (**b**) Oxygen (O1s); (**c**) Nitrogen N1s.

Table 3. XPS quantitative analysis—composition profile.

Element	GO	
	Weight%	**Atomic%**
C1s	82.9	86.61
O1s	17.09	13.39
	N/GO_A	
Element	**Weight%**	**Atomic%**
C1s	76.93	80.96
O1s	15.64	12.34
N1s	7.42	6.7
	N/GO_U	
Element	**Weight%**	**Atomic%**
C1s	79.73	83.62
O1s	16.47	12.88
N1s	3.8	3.5
	N/GO_N	
Element	**Weight%**	**Atomic%**
C1s	80.29	84.22
O1s	17.26	13.58
N1s	2.44	2.2

Table 4. Textural properties of nitrogen-doped graphene oxides.

Samples	S_{BET} (m^2 g^{-1})	BJH Pore Volume (cm^3 g^{-1})	BJH Pore Radius (A)
GO	421	1.629	19.691
N/GO_A	67	0.196	19.644
N/GO_U	83	0.268	19.675
N/GO_N	117	0.355	19.678

It was found that the specific area was smaller than the estimated surface area for the original GO material (421 m^2 g^{-1}), according to [38,39]. The BET values obtained for analyzed materials indicated that the chemical doping process during microwave has caused a decreasing of the specific surface area. The pore volume was diminished in comparison to that of the original GO structure. This indicated that some mesopores have been partially clogged due to the doping process. Thus, slightly lower values were calculated for prepared N/GO, as presented in Table 4.

The nitrogen adsorption–desorption isotherms (Figures 7–9) for these materials can be classified as representative for Type IV isotherms. These curves indicated well-defined H3 hysteresis loops which usually are accompanied by the capillary condensation. The difference between the specific surfaces were caused by the doping effect during the microwave process.

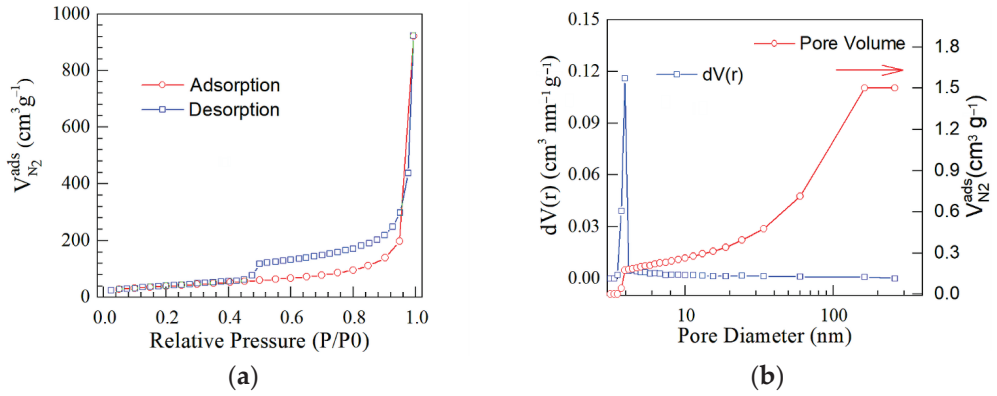

Figure 7. (**a**) N_2 adsorption–desorption isotherms; and (**b**) BJH curves corresponding to N/GO_A.

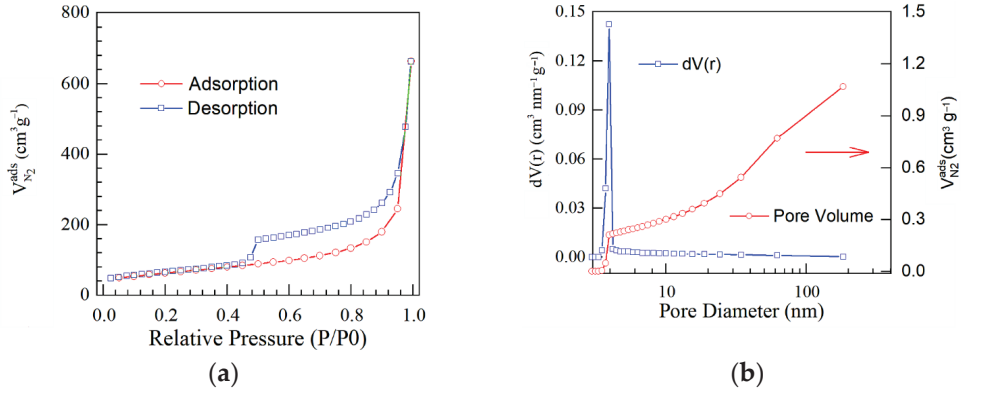

Figure 8. (**a**) N_2 adsorption–desorption isotherms and (**b**) BJH curves corresponding to N/GO_U.

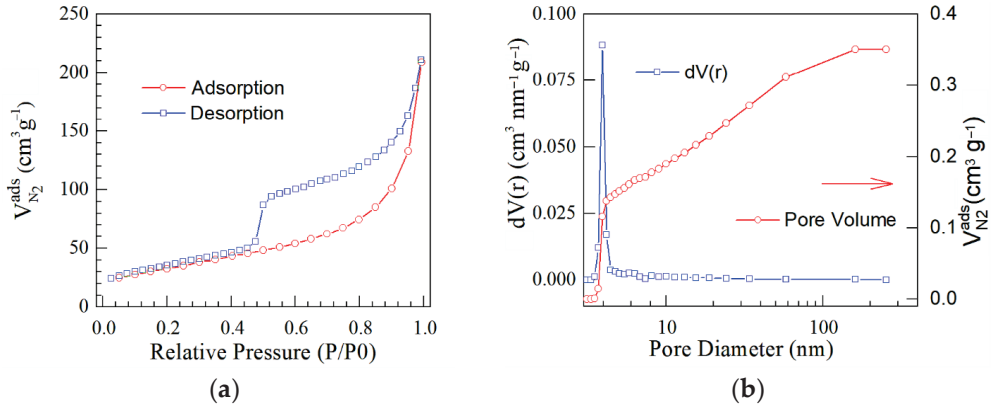

Figure 9. (**a**) N_2 adsorption–desorption isotherms and (**b**) BJH curves corresponding to N/GO_N.

The difference noted for the calculated specific surface area (S_{BET}) could be correlated with nitrogen content of each sample. Thus, the S_{BET} for N/GO_A and N/GO_N was estimated at 67 m^2 g^{-1} and 117 m^2 g^{-1}, respectively, while the nitrogen content was 7.42 wt.% and 2.44 wt.% These results indicated that the lowest S_{BET} corresponds to the highest nitrogen content, possibly due to the obtaining of a chemically more doped graphene oxide during the microwave reaction. It was found that the lowest specific surface area corresponds to the GO doped in the presence of ammonia. The hysteresis type indicates the presence of the micro and mesoporous structure in the N/GOs layers with plate-like slit-shaped pores. The pore size distribution calculated by BJH method considering the desorption branch displays a unimodal peak centered at 7 nm. The BJH pore-size distribution method pointed out the dominant role of mesoporosity, which contributed to approx. 65.8% of the total pore volume, while the microporosity contributed to approx. 33.2%. The remaining approx. 1% of the total pore volume was caused by macroporosity.

Thermogravimetric analysis (TGA) was employed to investigate the thermal stability of the prepared nanocomposites. The synthesized nitrogen-doped graphene exhibited similar curves with good thermal stability. TGA weight loss curves of prepared samples are presented in Figure 10. It was observed that the obtained thermograms show different temperature ranges for the thermal decomposition: an important mass loss in the decomposition range of 150–300 °C, emphasizing the efficient removal of oxygen functional groups during the chemical process in the microwave field; a continuous mass loss from 300–600 °C, possibly due to the loss of sp^2 carbon atoms in a hexagonal structure that occurs between the decomposition temperatures of 320 and 650 °C [40], which is associated with the elimination of certain functionalities specified by FTIR analysis. It is important to note that the drop in the 20–150 °C domain, especially for the sample N/GO_A is certainly due to the high nitrogen content, and is consistent with the elemental analysis in Table 1. Analysis of the thermal stability of N/GOs could be related to the nitrogen bonding configuration (nitrogen functionalities indicated by XPS analysis) in a graphene network, indicating that the pyridinic-N configuration is mostly dominant, instead of graphitic N [41]. According to this reference, the pyridinic-N configuration is mostly dominant at lower doping temperatures. This is precisely the case of the temperature used in actual experimental studies of N/GO preparation, as the working temperature was 60–80 °C during microwave reaction. However, this aspect may indicate that the nitrogen content is related to the process temperature in the microwave field, as well as to the degree of doping. Thus, we can understand that it would be possible to provoke and induce a configured and selective doping with nitrogen atoms, which is a major breakthrough in optimizing and tuning the physicochemical properties of nitrogen-doped graphene materials.

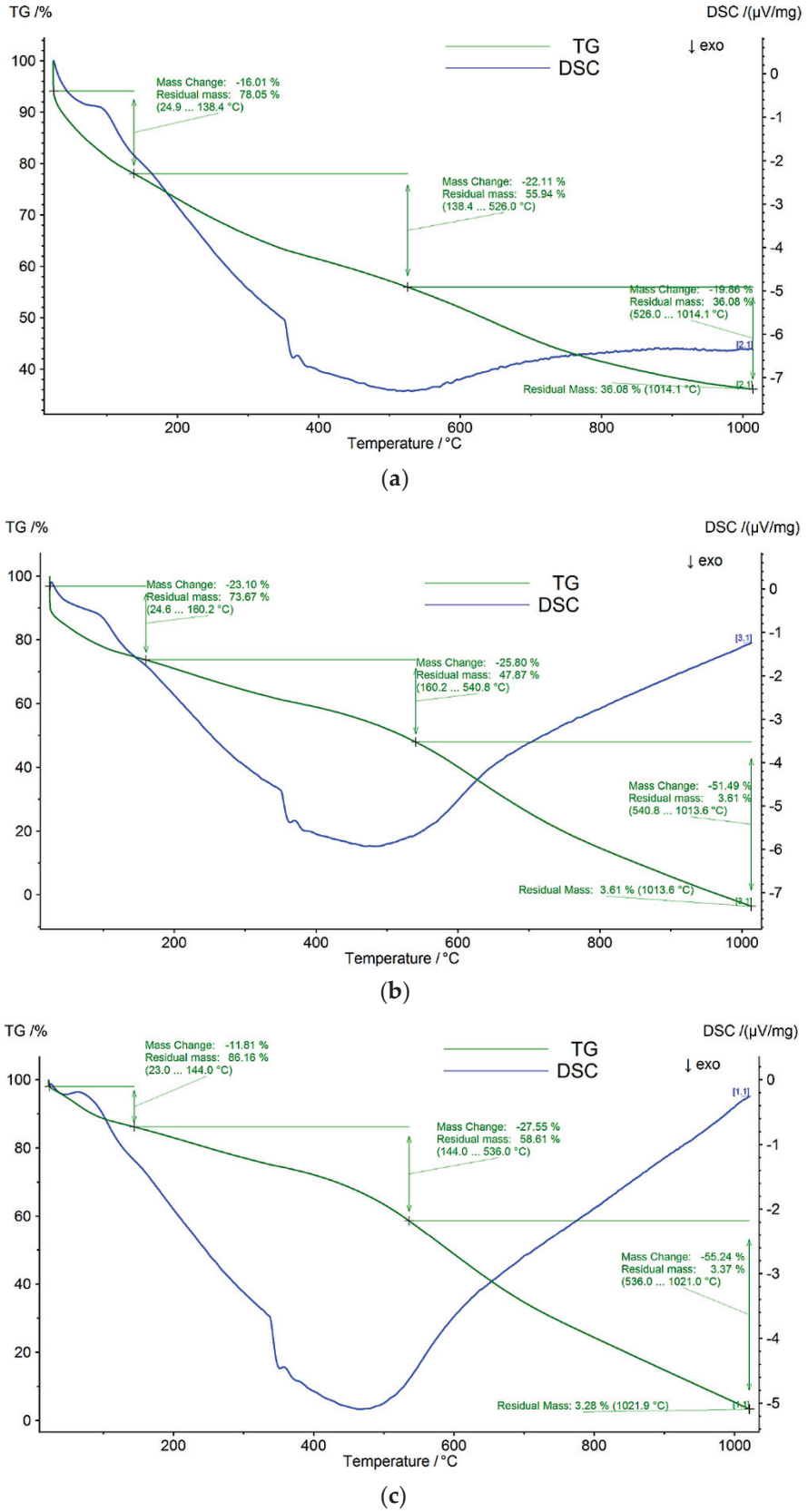

Figure 10. Thermogravimetric analysis (TGA) and differential scanning calorimetry (DSC) measurements of nitrogen-doped graphene oxides. (**a**) TGA and DSC curves corresponding to N/GO_A. (**b**) TGA and DSC curves corresponding to N/GO_U. (**c**) TGA and DSC curves corresponding to N/GO_N.

According to the literature, the nitrogen-doped graphene could provide a comparable electrocatalytic activity for the oxygen reduction reaction, and a higher durability and selectivity than the classic expensive Pt-based catalysts. These electrochemical performances were usually related to the nitrogen functional groups, as well as to the specific properties of graphene.

This highly doped nitrogen-doped graphene could exhibit electrochemical activity towards oxygen reduction in alkaline medium providing an affordable industrial alternative to currently used noble metal-based catalyst, such as Pt, Pd [42,43]. Alkaline electrolytes have notable importance in FCs research. Among alkaline electrolytes, the aqueous solution of KOH is of particular interest in PEMFCs operation. Similar to acidic electrolytes, the high ionic conductivity of alkaline electrolytes improves the performance of FCs by engaging functional groups attached to electrode material (e.g., –COOH group in graphene, nitrogen-doped carbon) and electrolyte ions. According to the accepted four-electron associative mechanism for oxygen reduction reaction referring to the nitrogen-doped graphene in alkaline solution, the intermediate OH (ads) is formed from O (ads) with the addition of H_2O and one electron. It was presumed that the OH (ads) could be attached to the catalytic core as well to the active site through a chemical bond. Thus, the ORR active sites can be determined from the presence of intermediate OH (ads). It is known that the −OH-attached pyridinic nitrogen after the electrochemical reaction suggests that pyridinic N acts an important role in the ORR process and the nearby C atoms represent the main active site, according to existing theoretical and experimental studies [12,43]. Thus, the neighbor C atoms of pyridinic N influence the atomic charges which affect the ORR: the absorption of the intermediate products, the formation of a C–O bond, and the disassociation of an O–O bond.

In order to investigate the electrocatalytic activities of the N/GO, different electrochemical measurements were involved in two stages: the initial measurement (beginning of life BoL) and the final measurement corresponding to the moment when the activity was diminished with 10% (end of life EoL). The catalytic activity for ORR was studied for the samples with the highest nitrogen content by CV carried out in a 0.1 M KOH solution. Before each test, the solution was saturated with oxygen.

The use of various scan rates is a proper methodology in terms of identification of oxidation and reduction peaks. Figure 11 shows the comparison of the voltametric cycles of N/GO_A and N/GO_U at different scan rates. Slight shifts in peak potentials were observed with increasing scan rate indicating some kinetic limitations. Reduction peaks were determined around of +0.15 and +0.2 V for N/GO_A and 0.05 and 0.15 V for N/GO_U, respectively. Peaks identified for oxidation were determined around of −0.25 and +0.2 V for N/GO_A and around of 0.25 V for N/GO_U, respectively. Anodic peak currents were plotted against square root of scan rate, as shown in Figure 11. The linearity of plots (R^2 = 0.99216; R^2 = 0.99064) confirmed that the mass diffusion-controlled electron transfer in all cases.

The most positive ORR peak potential and the highest peak current of N/GO_A towards N/GO_U must be discussed considering the difference of nitrogen content from compared samples. As reported, this content could cause distinct electrochemical properties, because during N doping, some C atoms are replaced, but some defects also appear leading to the structural distortions of GO [44].

Doped nitrogen atoms into the graphenic structure act as electron acceptor sites. The electron-accepting ability of the nitrogen atom can convert the next-neighbor carbon as positive, leading to a redistribution of spin density and charge density in the vicinity of N atoms. These properties influence the oxygen absorption and electrochemical reactions for ORR. As demonstrated, the atomic spin density and charge transfer cause electrocatalytic capacity for ORR.

The composition-dependent ORR activity is influenced by graphitic N and pyridinic N, considered to be responsible for the ORR. The spin and charge density was calculated for the charge transfer and was found that the carbon atoms with charge transfer higher

than 0.15 can be used as active sites. A calculation regarding the percentage of C atoms with larger charge density (over 0.15) as function of N content in graphene, indicated that the active sites of C atoms increase linearly as the N content in graphene grows and the maximum value of charge transfer also increase with the N content from 0.16 for 8% [44]. Thus, the sample N/GO_A with the nitrogen content of 7.2% have more catalytic reactive sites than N/GO_U and leads to a relatively better catalytic capability for ORR, which is consistent with our experimental observations.

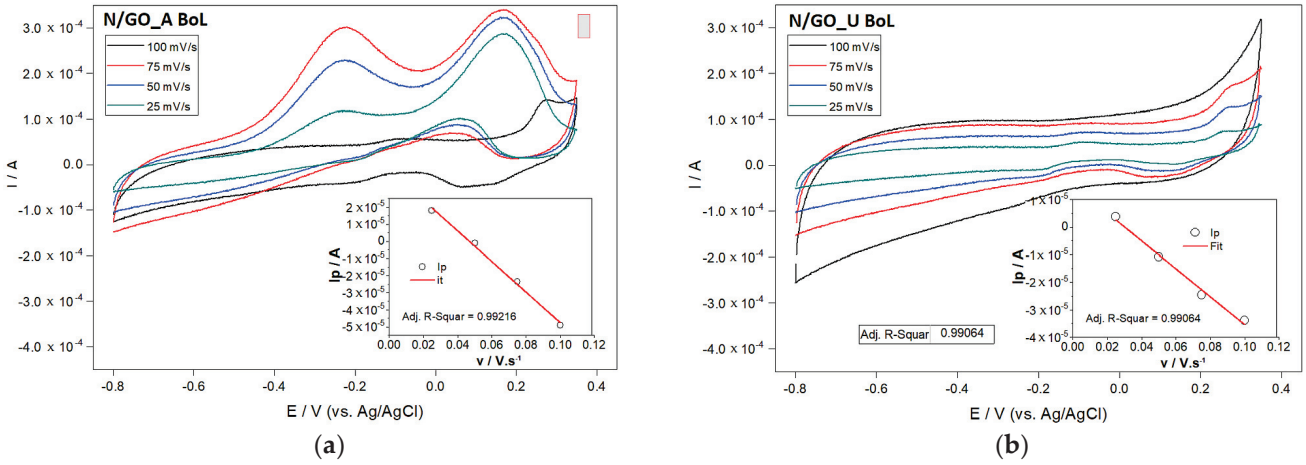

Figure 11. Cyclic voltamograms at different scan rates for N/GO_A (**a**) and N/GO_U (**b**) for BoL. Right bottom insert plot of the dependency of oxidation peak current on the square root of the rate.

Figure 11 shows the CV of oxygen reduction as a large cathodic peak current, demonstrating the activity of the both samples at the beginning of life moment. Both nitrogen-doped graphene showed a good onset potential, being known the fact that the onset potential indicates the catalytic activity of the catalysts. N-doping of graphene leads to the significant improvement of its functional characteristic in particular the electrocatalytic activity in oxygen reduction reaction (ORR), which is current-forming process in fuel cells. Well-defined cathode peaks were obtained for different scan rate. The electrochemical properties might be attributed to the introduction of defects and nitrogen-containing groups at the electrode surface, which could accelerate the charge transfer rate across electrode and ions solution interface. The comparison between N/GO_A and N/GO_U indicates the highest current for N/GO_A sample. It is quite clear that the oxidation peak and reduction current corresponding to the N/GO_A electrode are noticeably higher than those of the N/GO_U electrode, indicating that the first sample significantly improves the electrochemical kinetics of the redox reaction in air-saturated 0.1 M KOH electrolyte.

The long-term stability of the prepared samples was evaluated by chronoamperometry. The experiments were performed at a fixed potential of 0.2 V in the saturated KOH solution for 1000 min at the room temperature and the obtained data are presented in Figure 12. Both catalysts indicated a constant current decay. The current decreased more slowly for the N/GO_A electrode than for the N/GO_U electrode, indicating probably a less accumulation of adsorbed poisoning species.

The investigation using CV analysis after the stability test was taken into account in order to evaluate the electrochemical activity of the depleted catalyst. The end-of-life results are presented in Figure 13. Here the linear variation of the peak current with the square root of the scan rate for both N/GO catalysts is depicted in the insets.

The smallest peak potential difference (ΔEsep) was observed for the N/GO_A (Figure 13). Consequently, both the electrochemical activities and the reversibility were more efficient, probably due to the improved electrochemical properties, which could be attributed to the introduction of defects and nitrogen-containing groups at the electrode surface, accelerating the charge transfer rate across solution interface.

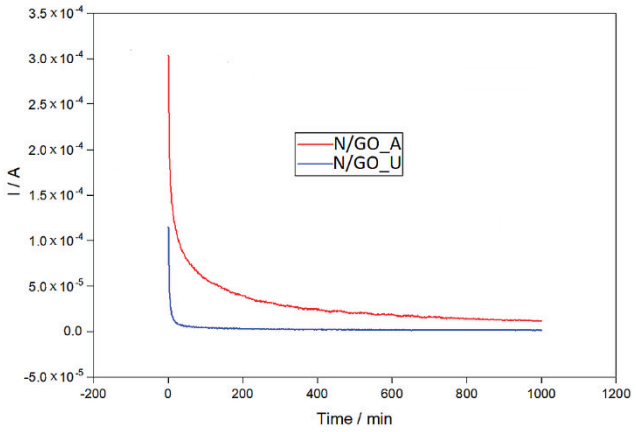

Figure 12. Chronoamperometric curves of different catalysts synthesized in the present work in 0.1 M KOH electrolyte at a constant potential of 0.3 V for 1000 min.

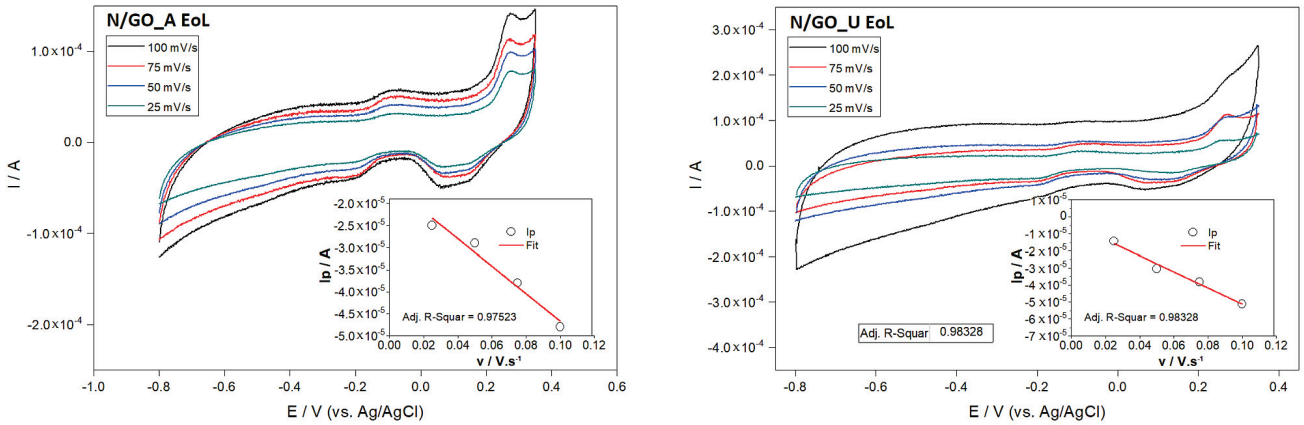

(**a**) (**b**)

Figure 13. Cyclic voltamograms at different scan rates for N/GO_A (**a**) and N/GO_U (**b**) for EoL. Right bottom insert plot of the dependency of the oxidation peak current on the square root of rate.

To investigate the electrochemical performance of the proposed N/GO electrode, the electrical impedance spectroscopy (EIS) was carried out at open-circuit potential. The Nyquist plot is presented in Figure 14. It was observed that the obtained curves include a linear part in the frequency between 0.01 Hz and 10 kHz, which suggests a mass transfer process. Moreover, these are an indication that both charge transfer and mass diffusion play an important role in the redox reaction. This behavior may be because the lone pair electron caused by the doped nitrogen improves the electrical conductivity of the electrode and reduces the electrochemical polarization during the redox reaction.

Performance in the PEMFC represents the key viability test for graphene-based PGM-free catalysts, due to the fact that the catalyst must facilitate the gas and proton transport through the cathode thickness and with graphene microstructure to the active sites, which are properties not provided by ex situ measurements.

Based on the structural characterization presented above, one of the prepared N/GOs (catalyst with the highest nitrogen concentration) was tested under practical fuel cell operation conditions, using a single FC with an active area of 25 cm^2. A set of PEMFC measurements were carried out to analyze the cathode performance, following the common benchmarking practice. After achieving steady-state operating conditions, the polarization curve was evaluated. The experiments were performed in potentiostatic mode and a predefined protocol was applied.

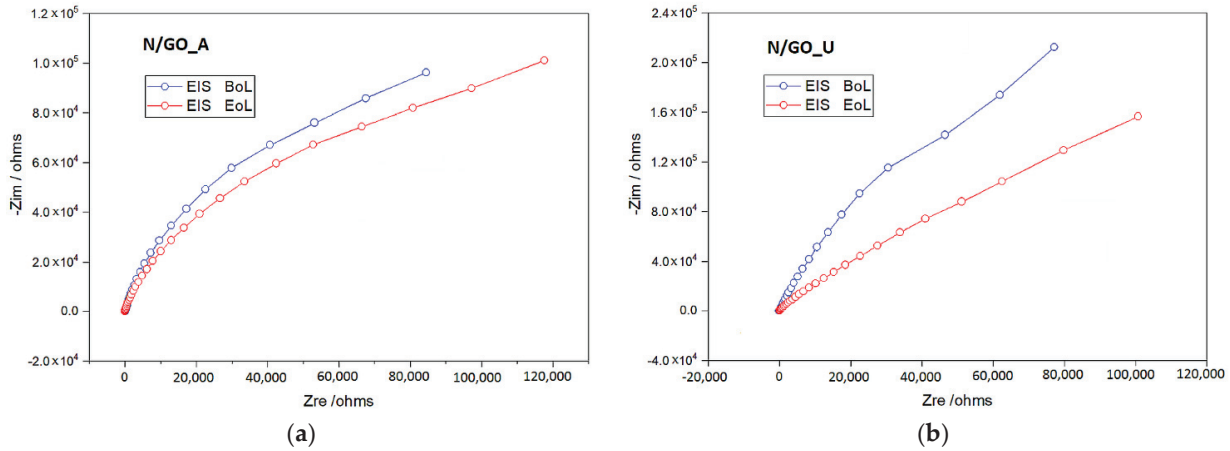

Figure 14. Nyquist plots of the catalysts N/GO_A (**a**) and N/GO_U (**b**).

Thus, using an N/GO_A -based membrane electrode assembly (MEA), with the highest power density achieved at 0.5 V was 343 mW cm^{-2} (720 mA cm^{-2}) and current density achieved at 0.7 V was 315 mA cm^{-2}.

The performance tests were carried out in potentiostatic mode by sweeping the voltage from OCV to the final voltage of 0.476 V with 8 mV s^{-1}. The test parameters were the following: temperature in the range of 61–62 °C, atmospheric pressure at the anode/cathode, stoichiometry 1.2 and 2.5 at anode and cathode, respectively. The following were monitored: the produced current, the flow rates of reactants and the dew point temperature.

A cyclic load profile has been proposed in order to investigate the electrocatalyst activity, as shown in Figure 15. A stress parameter was considered, in respect to the fuel cell sweeping voltage, varying between OCV and 0.476 V to accentuate the degradation of the fuel cell. The reported current density at 0.7 V in these operation conditions is comparable or even higher than state-of-the-art results related to PGM-free PEMFC [45–47].

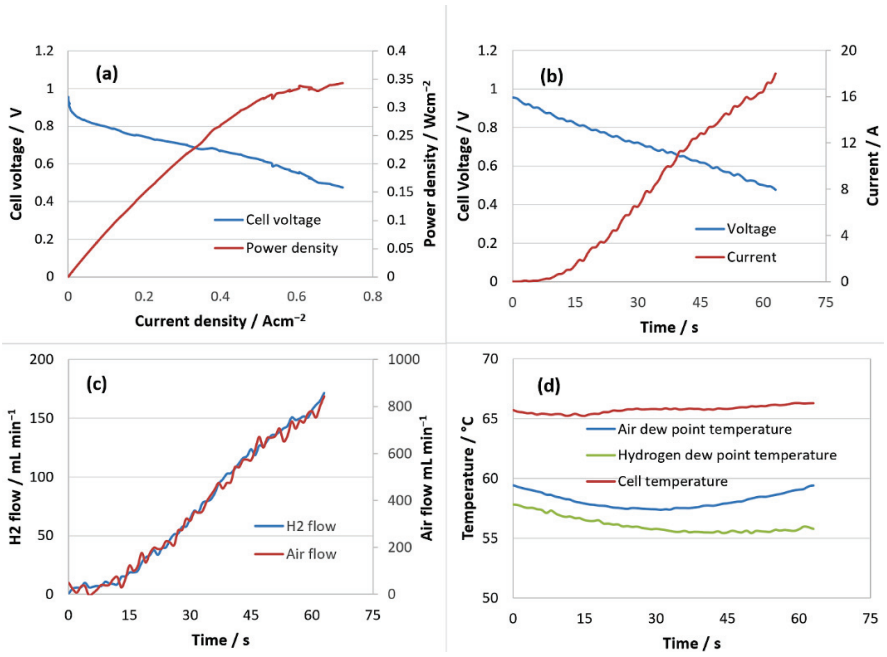

Figure 15. PEMFC performance using N/GO_A -based MEA. (**a**) Polarization and power density curves; (**b**) current variation profile depending on voltage; (**c**) flow rates consumed; (**d**) profiles: temperature of the PEMFC with MEA based on nitrogen doped graphene, and dew points of the reactants.

The above results demonstrate good performance of PEMFC using N/GO-based MEA. N/GO could be a promising candidate for practical application in cathode electrode under single FC working conditions. The presence of N/GO can effectively enhance the electrocatalytic stability for ORR. In this regard, N contributes as spacer between interconnected 3D porous structure avoiding the GO sheets restacking, favoring the transportation of reactants and product and also could provide many accessible active sites with electrocatalytic stability.

4. Conclusions

N/GO catalyst emerges as one of the promising non-PGM catalysts with the advantages of low cost and high ORR catalytic performance to replace expensive PGM catalysts in electrochemical systems. This work introduces a novel process for preparing of nitrogen-doped graphene by using microwave treatment under ambient conditions, as simple, effective, faster and economical protocol. The physical and chemical properties of the materials obtained from different precursors (ammonia, urea and nitric acid) were evaluated and compared and it was found that ammonia allows to obtain a higher concentration of nitrogen, due to its high vapor pressure which facilitates the functionalization reaction of GO during microwave. N/GO was obtained with the highest nitrogen concentration of 7 wt%, a high specific surface and a high porosity which gives the potential as catalytic material. The BET evaluation suggests that the doping process led to a slight decrease in the specific surface, but the pore volume was quite well preserved compared to the original graphene structure. This paper indicates that nitrogen-doped graphene with a high dopant level could be prepared by starting from a commercially accessible material—graphene oxide, as raw material, through an optimized designed process for chemical synthesis under the microwave field. It is believed that this approach can bring many possibilities in tailoring the chemical properties. Moreover, this route could be a step in the development of other types of non-metallic graphene-based catalysts by using MW. Furthermore, considering this cost-effective strategy, it is expected to broaden N/GO beyond fuel cell application.

Author Contributions: Conceptualization, A.M. and M.R.; methodology, A.M.; software, M.R.; validation, M.V.; formal analysis, E.C.; investigation, A.M.; resources, M.V.; data curation, M.R.; writing—original draft preparation, A.M.; writing—review and editing, A.M. and E.C. All authors have read and agreed to the published version of the manuscript.

Funding: This work was carried out through the Nucleus Program, financed by the Ministry of Education and Research, Romania, project no. PN 23 15 01 03; project number PN-III-P2-2.1-PED2021-0840 PED 695/2022, and Subprogram 1.1. Institutional performance-Projects to finance excellence in RDI, Contract No. 19PFE/30.12.2021.

Data Availability Statement: The authors confirm that the data supporting the findings of this study are available within the article. Raw data that support the findings of this study are available from the corresponding author, upon reasonable request.

Acknowledgments: The authors wish to thank to our colleagues: Felicia Bucura, Anca Zaharioiu and Marius Constantinescu for the elemental analysis; Elena Marin and Elena Georgescu for their valuable help in the synthesis procedure.

Conflicts of Interest: The authors declare no conflict of interest.

References

1. Chuanyu, S.; Huan, Z. Review of the Development of First-Generation Redox Flow Batteries: Iron-Chromium System. *ChemSusChem* **2022**, *15*, 202101798.
2. Ma, R.; Lin, G.; Zhou, Y.; Liu, Q.; Zhang, T.; Shan, G. A review of oxygen reduction mechanisms for metal-free carbon-based electrocatalysts. *Npj Comput. Mater.* **2019**, *5*, 78. [CrossRef]
3. Sui, S.; Wang, X.; Zhou, X.; Su, Y.; Riffat, S.; Liu, C. A comprehensive review of Pt electrocatalysts for the oxygen reduction reaction: Nanostructure, activity, mechanism, and carbon support in PEM fuel cells. *J. Mater. Chem. A* **2017**, *5*, 1808–1825. [CrossRef]

4. Chandran, P.; Ghosh, A.; Ramaprabhu, S. High-performance Platinum-free oxygen reduction reaction and hydrogen oxidation reaction catalyst in polymer electrolyte membrane fuel cell. *Sci. Rep.* **2018**, *8*, 3591. [CrossRef] [PubMed]
5. Kiani, M.; Tian, X.Q.; Zhang, W. Non-precious metal electrocatalysts design for oxygen reduction reaction in polymer electrolyte membrane fuel cells: Recent advances, challenges and future perspectives. *Coord. Chem. Rev.* **2021**, *441*, 213954. [CrossRef]
6. Marinoiu, A.; Carcadea, E.; Sacca, A.; Carbone, A.; Sisu, C.; Dogaru, A.; Raceanu, M.; Varlam, M. One-step synthesis of graphene supported platinum nanoparticles as electrocatalyst for PEM fuel cells. *Int. J. Hydrogen Energy* **2020**, *46*, 12242–12253. [CrossRef]
7. Marinoiu, A.; Andrulevicius, M.; Tamuleviciene, A.; Tamulevicius, T.; Raceanu, M.; Varlam, M. Synthesis of well dispersed gold nanoparticles on reduced graphene oxide and application in PEM fuel cells. *Appl. Surf. Sci.* **2020**, *504*, 44511. [CrossRef]
8. Marinoiu, A.; Raceanu, M.; Carcadea, E.; Varlam, M.; Balan, D.; Ion-Ebrasu, D. Iodine-doped graphene for enhanced electrocatalytic oxygen reduction reaction in proton exchange membrane fuel cell applications. *J. Electrochem. Energy Convers. Storage* **2017**, *14*, 031001. [CrossRef]
9. Marinoiu, A.; Gatto, I.; Raceanu, M.; Varlam, M.; Moise, C.; Pantazi, A. Low cost iodine doped graphene for fuel cell electrodes. *Int. J. Hydrogen Energy* **2017**, *42*, 26877–26888. [CrossRef]
10. Sathiskumar, C.; Ramakrishnan, S.; Vinothkannan, M.; Rhan Kim, A.; Karthikeyan, S.; Yoo, D.J. Nitrogen-Doped Porous Carbon Derived from Biomass Used as Trifunctional Electrocatalyst toward Oxygen Reduction, Oxygen Evolution and Hydrogen Evolution Reactions. *Nanomaterials* **2020**, *10*, 76. [CrossRef]
11. Logeshwaran, N.; Panneerselvam, I.R.; Ramakrishnan, S.; Kumar, R.S.; Kim, A.R.; Wang, Y.; Yoo, D.J. Quasihexagonal Platinum Nanodendrites Decorated over CoS_2-N-Doped Reduced Graphene Oxide for Electro-Oxidation of C1-, C2-, and C3-Type Alcohols. *Adv. Sci.* **2022**, *9*, 2105344. [CrossRef] [PubMed]
12. Natarajan, L.; Shanmugam, R.; Selvaraj, S.; Mohanraj, V.; Rhan, K.; Sivaprakash, S.; Dhinesh, B.V.; Purushothaman, V.; Jr-Hau, H.; Dong, J.Y. An efficient and durable trifunctional electrocatalyst for zinc–air batteries driven overall water splitting. *Appl. Catal. B Environ.* **2021**, *297*, 120405.
13. Lu, Z.J.; Bao, S.J.; Gou, Y.T.; Cai, C.J.; Ji, C.C.; Xu, M.W. Nitrogen-doped reduced-graphene oxide as an efficient metal-free electrocatalyst for oxygen reduction in fuel cells. *RSC Adv.* **2013**, *3*, 3990–3995. [CrossRef]
14. Qu, L.; Liu, Y.; Baek, J.B.; Dai, L. Nitrogen-Doped Graphene as Efficient Metal-Free Electrocatalyst for Oxygen Reduction in Fuel Cells. *ACS Nano* **2010**, *4*, 1321–1326. [CrossRef]
15. Wei, Q.; Tong, X.; Zhang, G.; Qiao, J.; Gong, Q.; Sun, S. Nitrogen-Doped Carbon Nanotube and Graphene Materials for Oxygen Reduction Reactions. *Catalysts* **2015**, *5*, 1574–1602. [CrossRef]
16. Wang, H.; Maiyalagan, T.; Wang, X. Review on Recent Progress in Nitrogen-Doped Graphene: Synthesis, Characterization, and Its Potential Applications. *ACS Catalysts* **2012**, *2*, 781–794. [CrossRef]
17. Zhuang, S.; Nunna, B.B.; Mandal, D.; Lee, E.S. A review of nitrogen-doped graphene catalysts for proton exchange membrane fuel cells-synthesis, characterization, and improvement. *Nano-Struct. Nano-Objects* **2018**, *15*, 140–152. [CrossRef]
18. Lu, Y.F.; Lo, S.T.; Lin, J.C.; Zhang, W.; Lu, J.Y.; Liu, F.H. Nitrogen-Doped Graphene Sheets Grown by Chemical Vapor Deposition: Synthesis and Influence of Nitrogen Impurities on Carrier Transport. *ACS Nano* **2013**, *7*, 6522–6532. [CrossRef]
19. Li, X.; Wang, H.; Robinson, J.T.; Sanchez, H.; Diankov, G.; Dai, H. Simultaneous Nitrogen Doping and Reduction of Graphene Oxide. *J. Am. Chem. Soc.* **2009**, *131*, 15939–15944. [CrossRef]
20. Jeon, I.Y.; Choi, H.J.; Ju, M.J.; Choi, I.T.; Lim, K.; Ko, J. Direct nitrogen fixation at the edges of graphene nanoplatelets as efficient electrocatalysts for energy conversion. *Sci. Rep.* **2013**, *3*, 2260. [CrossRef]
21. Zhuang, S.; Lee, E.S.; Lei, L.; Nunna, B.B.; Kuang, L.; Zhang, W. Synthesis of nitrogen-doped graphene catalyst by high-energy wet ball milling for electrochemical systems. *Int. J. Energy Res.* **2016**, *40*, 2136–2149. [CrossRef]
22. Zhuang, S.; Nunna, B.B.; Boscoboinik, J.A.; Lee, E.S. Nitrogen-doped graphene catalysts: High energy wet ball milling synthesis and characterizations of functional groups and particle size variation with time and speed. *Int. J. Energy Res.* **2017**, *41*, 2535–2554. [CrossRef]
23. Parvez, K.; Yang, S.; Hernandez, Y.; Winter, A.; Turchanin, A.; Feng, X. Nitrogen-Doped Graphene and Its Iron-Based Composite as Efficient Electrocatalysts for Oxygen Reduction Reaction. *ACS Nano* **2012**, *6*, 9541–9550. [CrossRef] [PubMed]
24. Kumar, M.P.; Raju, M.M.; Arunchander, A.; Selvaraj, S.; Kalita, G.; Narayanan, T.N. Nitrogen Doped Graphene as Metal Free Electrocatalyst for Efficient Oxygen Reduction Reaction in Alkaline Media and Its Application in Anion Exchange Membrane Fuel Cells. *J. Electrochem. Soc.* **2016**, *163*, 848–855. [CrossRef]
25. Wang, Z.; Jia, R.; Zheng, J.; Zhao, J.; Li, L.; Song, J. Nitrogen-Promoted Self-Assembly of N-Doped Carbon Nanotubes and Their Intrinsic Catalysis for Oxygen Reduction in Fuel Cells. *ACS Nano* **2011**, *5*, 1677–1684. [CrossRef]
26. Sasikala, S.P.; Huang, K.; Giroire, B.; Prabhakaran, P.; Henry, L.; Penicaud, A. Simultaneous Graphite Exfoliation and N Doping in Supercritical Ammonia. *ACS Appl. Mater. Interfaces* **2016**, *8*, 30964–30971. [CrossRef]
27. Wu, T.; Shen, H.; Sun, L.; Cheng, B.; Liu, B.; Shen, J. Nitrogen and boron doped monolayer graphene by chemical vapor deposition using polystyrene, urea and boric acid. *New J. Chem.* **2012**, *36*, 1385–1391. [CrossRef]
28. Chen, Z.; Higgins, D.; Yu, A.; Zhang, L.; Zhang, J. A review on non-precious metal electrocatalysts for PEM fuel cells. *Energy Environ. Sci.* **2011**, *4*, 3167–3192. [CrossRef]
29. Sheng, Z.H.; Shao, L.; Chen, J.J.; Bao, W.J.; Wang, F.B.; Xia, X.H. Catalyst-free synthesis of nitrogen-doped graphene via thermal annealing graphite oxide with melamine and its excellent electrocatalysis. *ACS Nano* **2011**, *5*, 4350–4358. [CrossRef]

30. Maddi, C.; Bourquard, F.; Barnier, V.; Avila, J.; Asensio, M.C.; Tite, T. Nano-Architecture of nitrogen-doped graphene films synthesized from a solid CN source. *Sci. Rep.* **2018**, *8*, 3247. [CrossRef]
31. Rybin, M.; Pereyaslavtsev, A.; Vasilieva, T.; Myasnikov, V.; Sokolov, I.; Pavlova, A.; Obraztsova, E.; Khomich, A.; Ralcenko, V.; Obraztsova, E. Efficient nitrogen doping of graphene by plasma treatment. *Carbon N. Y.* **2016**, *96*, 196–202. [CrossRef]
32. Geng, D.; Ding, N.; Andy Hor, T.S.; Liu, Z.; Sun, X.; Zong, Y. Potential of metal-free "graphene alloy" as electrocatalysts for oxygen reduction reaction. *J. Mater. Chem. A* **2015**, *3*, 1795–1810. [CrossRef]
33. Mingming; Sun, C.; Zhang, G.; Coutier-Delgosha, O.; Fan, D. Combined suppression effects on hydrodynamic cavitation performance in Venturi-type reactor for process intensification. *Ultrason. Sonochemistry* **2022**, *86*, 106035. [CrossRef] [PubMed]
34. Lazar, P.; Mach, R.; Otyepka, M. Spectroscopic Fingerprints of Graphitic, Pyrrolic, Pyridinic, and Chemisorbed Nitrogen in N-Doped Graphene. *J. Phys. Chem. C* **2019**, *123*, 10695–10702. [CrossRef]
35. Ariharan, A.; Viswanathan, B.; Nandhakumar, V. Nitrogen doped graphene as potential material for hydrogen storage. *Graphene* **2017**, *6*, 41–60. [CrossRef]
36. Ayiania, M.; Smith, M.; Hensley, A.; Scudiero, L. Deconvoluting the XPS spectra for nitrogen-doped chars: An analysis from first principles. *Carbon* **2020**, *162*, 528–544. [CrossRef]
37. Qazzazie, D.; Beckert, M.; Mulhaupt, R.; Yurchenco, O.; Urban, G. Modified graphene as electrocatalyst towards oxygen reduction reaction for fuel cells. *J. Phys.: Conf. Ser.* **2014**, *557*, 012009. [CrossRef]
38. Marinoiu, A.; Raceanu, M.; Carcadea, E.; Varlam, M. Iodine-doped graphene—Catalyst layer in PEM fuel cells. *Appl. Surf. Sci.* **2018**, *456*, 238–245. [CrossRef]
39. Marinoiu, A.; Raceanu, M.; Carcadea, E.; Andrulevicius, M.; Tamuleviciene, A.; Tamulevicius, T.; Capris, C.; Varlam, M. Efficient method to obtain Platinum–Cobalt supported on graphene oxide and electrocatalyst development. *Int. J. Hydrogen Energy* **2020**, *45*, 26226–26237. [CrossRef]
40. Ngidi, N.P.S.; Ollengo, M.; Nyamori, V. Effect of doping temperatures and nitrogen precursors on the physical, optical and electrical conductivity properties of nitrogen-doped reduced graphene oxide. *Materials* **2019**, *12*, 3376. [CrossRef]
41. Kumar, A.; Ganguly, A.; Papakonstantinou, P. Thermal stability study of nitrogen functionalities in a graphene network. *J. Phys. Condens. Matter.* **2012**, *24*, 235501–235506. [CrossRef] [PubMed]
42. Dumont, J.H.; Martinez, U.; Artyushkova, K.; Purdy, G.M. Nitrogen-doped graphene oxide electrocatalysts for the oxygen reduction reaction. *ACS Appl. Nano Mater* **2019**, *2*, 1675–1682. [CrossRef]
43. Ma, F.X.; Wang, J.; Wang, F.B.; Xia, X.H. The room temperature electrochemical synthesis of N- doped graphene and its electrocatalytic activity for oxygen reduction. *Chem. Commun.* **2015**, *51*, 1198–1201. [CrossRef]
44. Zhang, Y.; Ge, J.; Wang, L.; Wang, D.; Ding, F.; Tao, X.; Chen, W. Manageable N-doped Graphene for High Performance Oxygen Reduction Reaction. *Sci. Rep.* **2013**, *3*, 2771. [CrossRef] [PubMed]
45. Tan, X.Y.Z.; Lu, H.L.; Bruce, C.C.; Daniel, G.; Shi, Z.Q.; Shaoming, H.Y.C. Observation of Active Sites for Oxygen Reduction Reaction on Nitrogen-Doped Multilayer Graphene. *ACS Nano* **2014**, *8*, 6856–6862.
46. Dmitry, B.; Sander, H.; Navaneethan, M.; Marthe, B.; Magnus, R. Nitrogen-doped carbon nanofiber catalyst for ORR in PEM fuel cell stack: Performance, durability and market application aspects. *Int. J. Hydrogen Energy* **2016**, *41*, 17616–17630.
47. Niyazi, O.; Ayse, B.Y. Effect of nitrogen doping amount on the activity of commercial electrocatalyst used in PEM fuel cells. *NanoEra* **2022**, *2*, 5–9.

nanomaterials

MDPI

Communication

Hydrophilic Surface Modification of Amorphous Hydrogenated Carbon Nanocomposite Films via Atmospheric Oxygen Plasma Treatment

Algirdas Lazauskas *, Mindaugas Andrulevičius, Brigita Abakevičienė, Dalius Jucius, Viktoras Grigaliūnas, Asta Guobienėand Šarūnas Meškinis

Institute of Materials Science, Kaunas University of Technology, K. Baršausko 59, LT51423 Kaunas, Lithuania
* Correspondence: algirdas.lazauskas@ktu.edu; Tel.: +370-671-73375

Abstract: Herein we investigated hydrophilic surface modification of SiO_x containing amorphous hydrogenated carbon nanocomposite films (DLC:SiO_x) via the use of atmospheric oxygen plasma treatment. The modified films exhibited effective hydrophilic properties with complete surface wetting. More detailed water droplet contact angle (CA) measurements revealed that oxygen plasma treated DLC:SiO_x films maintained good wetting properties with CA of up to 28 $\pm$ 1° after 20 days of aging in ambient air at room temperature. This treatment process also increased surface root mean square roughness from 0.27 nm to 1.26 nm. Analysis of the surface chemical states suggested that the hydrophilic behavior of DLC:SiO_x treated with oxygen plasma is attributed to surface enrichment with C–O–C, SiO_2, and Si–Si chemical bonds as well as significant removal of hydrophobic Si–CH_x functional groups. The latter functional groups are prone to restoration and are mainly responsible for the increase in CA with aging. Possible applications of the modified DLC:SiO_x nanocomposite films could include biocompatible coatings for biomedical applications, antifogging coatings for optical components, and protective coatings to prevent against corrosion and wear.

Keywords: oxygen plasma; hydrophilic; wetting; surface modification; DLC; DLC:SiO_x

Citation: Lazauskas, A.; Andrulevičius, M.; Abakevičienė, B.; Jucius, D.; Grigaliūnas, V.; Guobienė, A.; Meškinis, Š. Hydrophilic Surface Modification of Amorphous Hydrogenated Carbon Nanocomposite Films via Atmospheric Oxygen Plasma Treatment. *Nanomaterials* **2023**, *13*, 1108. https://doi.org/10.3390/nano13061108

Academic Editors: Meiwen Cao and Antonios Kelarakis

Received: 22 February 2023
Revised: 13 March 2023
Accepted: 18 March 2023
Published: 20 March 2023

1. Introduction

Diamond-like carbon (DLC) films are a class of materials that exhibit unique properties, including high hardness [1], low friction [2,3], and excellent chemical resistance [4]. These properties make DLC films attractive for a wide range of applications, such as protective coatings for medical implants [5–7], wear-resistant coatings for mechanical components [8,9], and anti-reflective coatings for optical devices [10,11].

The wetting properties of DLC films, or the ability of a liquid to spread over the surface and form a uniform and stable contact angle is a very important factor in determining the performance and suitability of DLC films for specific applications. Good wetting properties can enhance the functionality of DLC films in various applications, such as in medical implants, where wetting properties play a crucial role in controlling the interaction between the implant and the surrounding biological fluids [12]. DLC films with good wetting properties can exhibit improved performance in specific applications, such as in optical devices, where a uniform and stable contact angle can help reduce reflections and increase optical transmission. Furthermore, hydrophilic DLC films can be effectively utilized in environments that involve liquids or high humidity [13]. Good wetting properties can improve the adhesion between DLC films and other materials, which is important in applications such as tribological coatings and protective [14,15].

The surface energy of DLC films is an important parameter that determines their wetting and adhesion characteristics [16]. One approach to tailor the surface energy of DLC films is through the use of plasma treatment. This treatment can be easily applied and does not require hazardous chemicals or specialized equipment, making it a cost-effective and scalable method. Plasma treatment involves exposing the DLC film to gas plasma,

which results in the formation/recombination of functional groups on the surface of the film. These functional groups can alter the surface energy of the DLC film and improve its wetting and adhesion properties. For example, oxygen plasma treatment has been reported to be an effective method to increase hydrophilicity as well as hemocompatibility of DLC films [17,18]. The formation of oxygen-related functional groups on the surface of the film after exposure to oxygen plasmas is mainly responsible for the increase in the hydrophilic character and surface energy of DLC [19,20].

Another strategy to improve wetting properties of DLC is through the use of hybrid films. Hybrid films are composed of DLC and other materials, such as metallic or organic compounds, which can affect the surface energy of the film. By carefully selecting the composition of the hybrid film, it is possible to achieve desired surface energy levels for specific applications, such as anti-fog coatings on automobile windshields, and biocoatings on contact lenses [21,22].

In addition to plasma treatments and hybrid films, the surface wetting properties of DLC films can be also tailored through other methods, e.g., chemical (piranha treatments [23]), photochemical (UV light and 30% hydrogen peroxide), ion implantation [24] and laser treatment [25]. These methods can also introduce functional groups onto the surface of the DLC film and modify its wetting characteristics. However, chemical treatment methods can be hazardous due to the highly reactive nature of the chemicals involved, which can pose safety concerns. Moreover, chemical modification methods may result in uncontrolled etching of the DLC film, leading to a reduced film thickness and surface roughness, which can negatively affect the DLC film properties. The photochemical method may not be effective for thicker films, and the process may require longer exposure times to achieve desired surface modification. Moreover, photochemical treatment may cause damage to the DLC film structure, leading to reduced film quality. Ion implantation and laser treatment can be expensive and require specialized equipment, which may not be easily accessible. Furthermore, these treatments may cause localized damage to the film and may not be effective for modifying the entire surface uniformly.

One specific type of DLC film—SiO_x containing amorphous hydrogenated carbon nanocomposite film (DLC:SiO_x), which is widely known for its high-hardness (10–20 GPa), low wear rate (10^{-5}–10^{-8} mm^3 N^{-1} m^{-1}) and friction coefficient (0.02–0.2), as well as low internal stresses (<1 GPa) and high optical transmittance (~80–85%) in the visible spectrum [11,26–28]. However, very little is known about the surface modification of DLC:SiO_x films with plasma techniques. Herein, we attempt to contribute to this topic by investigating how the wetting properties of DLC:SiO_x films are affected upon the atmospheric oxygen plasma treatment. We established the possible correlations between the oxygen plasma treatment and the changes it introduces to the surface of the DLC:SiO_x film via the use of water droplet contact angle (CA) measurements, X-ray photoelectron spectroscopy (XPS), and atomic force microscopy (AFM). It was found that atmospheric oxygen plasma treatment of the DLC:SiO_x film modifies its surface to be effectively hydrophilic. The wetting properties of DLC:SiO_x film deteriorate to some extent with aging in ambient air at room temperature.

2. Materials and Methods

A commercial high-grade extra clear float glass Pilkington Microwhite^{TM} (Sheet Glass Co., Tokyo, Japan) was used as a substrate material. Hexamethyldisiloxane (HMDSO) of analytical grade (≥99%, Sigma-Aldrich, Saint Louis, MO, USA) was used as a source of hydrocarbons, silicon, and oxygen for synthesis of DLC:SiO_x films. Deionized (DI) water with a resistivity higher than 18.2 MΩ/cm at 25 °C was used for CA measurements, and was obtained from a Direct-Q® 3 UV water purification system (Merck KGaA, Darmstadt, Germany).

The Hall-type closed drift ion beam source operating at a constant energy of 800 eV and a current density of 100 μA/cm^2 was used for deposition of DLC:SiO_x films at room temperature. The base pressure and work pressure in the vacuum chamber were 2×10^{-4} Pa

and 2×10^{-2} Pa, respectively. Hydrogen gas (H_2) was used for transportation of HMDSO vapor into the vacuum chamber. Simplified schematic illustrating experimental setup for DLC:SiO_x deposition is shown in Scheme 1.

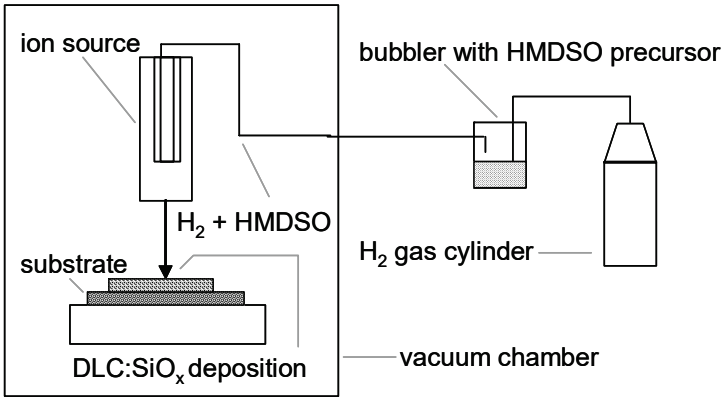

Scheme 1. Simplified schematic illustrating experimental setup for DLC:SiO_x deposition.

Control tests with monocrystalline Si(1 0 0) (UniversityWafer Inc., Boston, MA, USA) substrates were performed in order to determine deposition rate of DLC:SiO_x for H_2 gas. The thickness of DLC:SiO_x on Si(1 0 0) was determined using a laser ellipsometer Gaertner L-115 (Gaertner Scientific Corporation, Skokie, IL, USA) equipped with a He–Ne laser (wavelength of 632.8 nm). Film thickness of ~100 nm was chosen for the deposition of DLC:SiO_x on glass substrates.

The radio frequency capacitive plasma unit Plasma-600T (JSC Kvartz, Kuvasay, Uzbekistan) operating at a frequency of 13.56 MHz and power of 0.3 W/cm^2 was used for surface modification of as-deposited DLC:SiO_x films. The atmospheric oxygen plasma treatment time was varied in the range of 1–5 min.

CA measurements were performed at room temperature using the sessile drop method. The size of the DI droplets was 5 μL, the wetting angles were recorded after 10 min for all samples. CA were determined using an active contour method based on B-spline snakes (active contours) [29]. The CA is reported as an average of five measurements at different places on the surface of each sample.

AFM experiments were performed with NanoWizardIII microscope (JPK Instruments, Bruker Nano GmbH, Berlin, Germany) equipped with V-shaped silicon cantilever (spring constant of 3 N/m, tip curvature radius of 10.0 nm and the cone angle of 20°) operating in contact mode at room temperature. Data processing was carried out using a SurfaceXplorer and JPKSPM Data Processing software (Version spm-4.3.13, JPK Instruments, Bruker Nano GmbH).

The XPS measurements were performed employing XSAM800 spectrometer (Kratos Analytical Ltd., Manchester, United Kingdom). The non-monochromatized Al Kα radiation (hν = 1486.6 eV) was used for XPS spectra acquisition. The base pressure in the analytical chamber was lower than 8×10^{-8} Pa. The energy scale of the system was calibrated according to Au 4f7/2, Cu 2p3/2 and Ag 3d5/2 peak positions, respectively. The C 1s, O 1s, and Si 2p spectra were acquired at the 20 eV pass energy (0.1 eV energy step), and the analyzer was in the fixed analyzer transmission (FAT) mode. Spectra were fitted using a sum of Lorentzian–Gaussian (ratio of 30:70) functions and symmetrical peak shape; while for graphitic carbon asymmetrical peak shape and 70:30 ratio was used.

3. Results and Discussion

Figure 1 shows typical water droplet profile images of DLC:SiO_x films before and after oxygen plasma treatment for 3 min, as well as the plasma treated DLC:SiO_x film, which was aged for 20 days in ambient air at room temperature. The as-deposited DLC:SiO_x film exhibited water CA of 82 ± 1°, which is very close to the hydrophobic surface. After

oxygen plasma treatment for 3 min, the surface of the DLC:SiO_x film was modified to be effectively hydrophilic with complete spreading of water droplet (CA < 2°) on the surface. In [17], DLC films deposited using benzene and diluted silane as the precursor gases were subjected to plasma treatment using various gases such as N_2, O_2, H_2, and CF_4. They found that oxygen plasma treated films exhibited the lowest water CA of 13.4 ± 1.3° as compared to other plasma gases. In contrast, our result is significantly better. Further, we assessed the wetting stability of DLC:SiO_x. The water CA on the surface of the DLC:SiO_x film, which was modified using oxygen plasma treatment increased up to 28 ± 1°, still maintaining good hydrophilic properties after 20 days of aging. It was also found that the oxygen plasma treatment time variation (i.e., 1–5 min) of as-deposited DLC:SiO_x films had little effect on the hydrophilic surface modification as in all cases total surface wetting was observed (Figure 1d), whereas the lowest CA was determined for the 3 min oxygen plasma treated DLC:SiO_x films (CA 28 ± 1°) after 20 days of aging (Figure 1d). In Figure 1e, CA measurements indicated that during the first 10 days of aging, the oxygen plasma-treated DLC:SiO_x film rapidly loses its hydrophilic properties to some extent, after which stabilization is reached with CA ~28 ± 1° for the remaining 10 days of aging. S. Narayan et al. investigated oxygen plasma treatment effect on the wetting properties of DLC coatings deposited using plasma enhanced chemical vapor deposition (PECVD) technique [30]. They observed that hydrophilic properties of oxygen plasma treated DLC coatings rapidly deteriorate within 8 days of aging. Afterwards, better stability of CA with aging time was observed. However, CA values of >40° were reported for oxygen plasma treated DLC coatings in all cases after 10 days of aging.

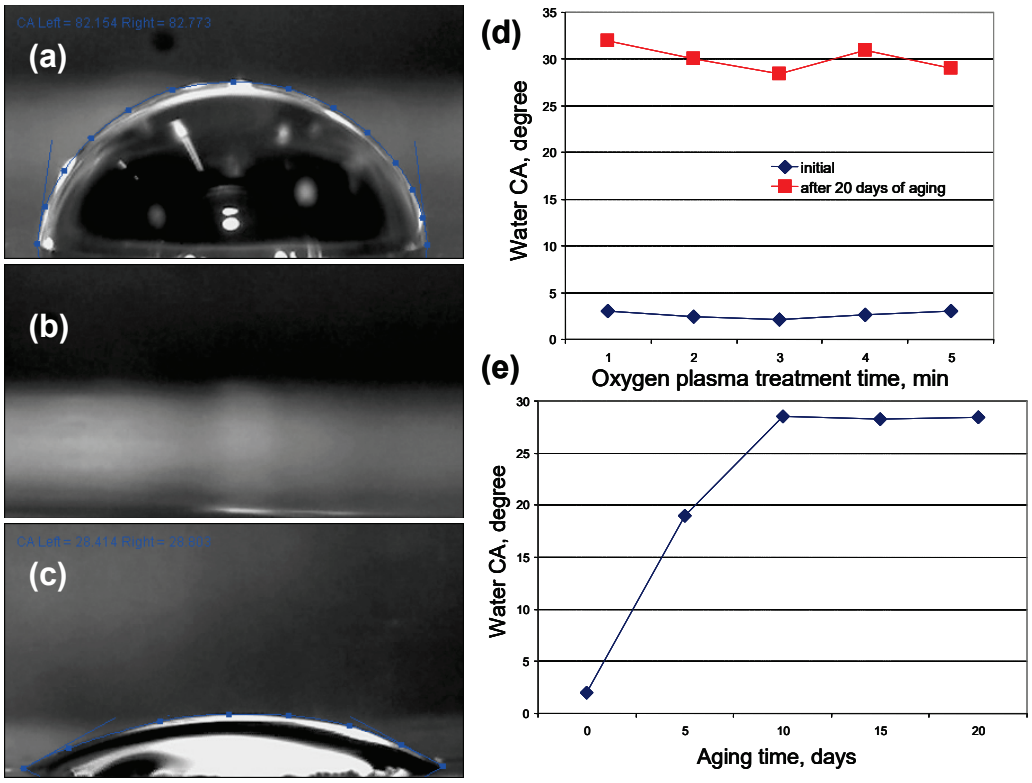

Figure 1. Water droplet profile images of DLC:SiO_x (**a**) as-deposited, (**b**) 3 min oxygen plasma treated and (**c**) oxygen plasma and aged for 20 days; (**d**) water CA as a function of oxygen plasma treatment time of as-deposited and after aging for 20 days; (**e**) water CA as a function of aging time.

Figure 2 shows characteristic AFM 2D topographical images of the as-deposited and 3 min oxygen plasma treated DLC:SiO_x films acquired over 2.0 × 2.0 μm^2 area in air using contact mode. The topography of the as-deposited DLC:SiO_x surface exhibits a random

distribution of surface mounds having different angle orientations to each other, without a preferred direction. A mean height of the surface structures (Z_{mean}) was determined to be 0.7 nm. The root mean square roughness (R_q) was found to be 0.27 nm. The as-deposited DLC:SiO_x film surface is dominated by the valleys with skewness (R_{sk}) value of −0.11 and has a platykurtoic distribution (i.e., relatively few high peaks and low valleys) of surface morphological features with kurtosis (R_{ku}) value of 2.7. In contrast, 3 min oxygen plasma treated DLC:SiO_x film surface exhibited higher R_q value of 1.26 nm with Z_{mean} value of 3.23 nm, and followed similar distribution of surface morphological features with R_{sk} and R_{ku} values of −0.11 and 2.46, respectively. In [31,32] surface morphological analysis was performed for as-deposited and oxygen plasma treated DLC films. Their results also indicated an increase in surface roughness after surface modification with oxygen plasma. This increase in surface roughness was attributed to oxygen ion bombardment during the treatment process. In our case, oxygen plasma treated DLC:SiO_x film maintained very low surface roughness, and therefore it is suggested that this change had negligible effect on the wetting properties.

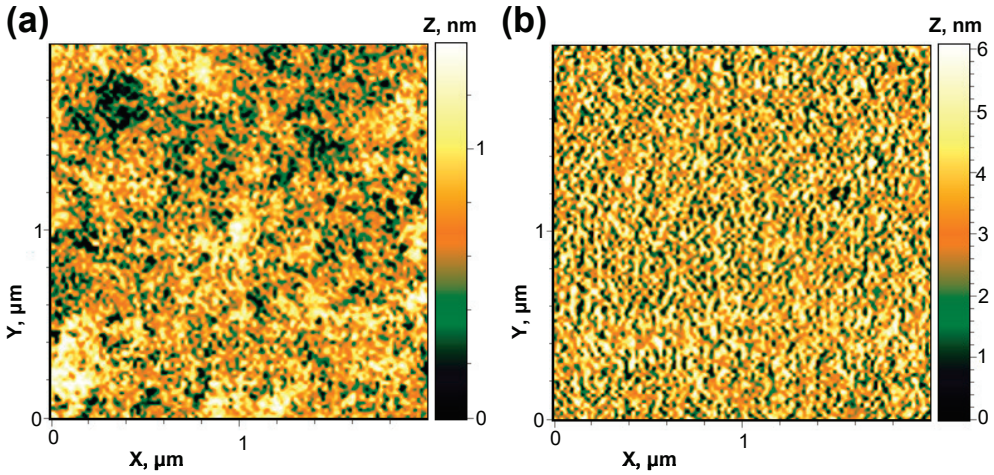

Figure 2. AFM surface topography of (**a**) as-deposited and (**b**) 3 min oxygen plasma treated DLC:SiO_x films.

The effect of oxygen plasma surface hydrophilic modification on the chemical states of DLC:SiO_x was investigated employing XPS. The deconvoluted high-resolution XPS spectra in the O 1s, C 1s and Si 2p regions of the as-deposited, oxygen plasma treated and 20 days aged DLC:SiO_x films are shown in Figure 3. The deconvoluted components of DLC:SiO_x films in the XPS O 1s spectra where assigned to C=O (531.2 eV), C–O (532.6 eV), C–O–C/SiO_x (533.1 eV) and O–H (534 eV) chemical bonds [33–37]. It can be seen that after oxygen plasma treatment the concentration of hydrophilic C–O–C functional groups on the surface of DLC:SiO_x increased considerably, remained stable after 20 days of aging. The deconvoluted component originating from C–O bonds decreased after oxygen plasma treatment and also remained stable after 20 days of aging. High-resolution XPS spectra in the C 1s region were deconvoluted into four components, respectively. A high intensity peak at 285 eV represents carbon in sp^3 hybridization, and it overlaps with C–H and Si–CH_x chemical bonds [38]. A low intensity peak at 284.1 eV was assigned to carbon sp^2 hybridization. The position and asymmetric shape of this component is typical for graphitic carbon [39,40]. Lower intensity peaks at higher binding energies could be assigned to O–C=O and C=O chemical bonds. No considerable changes were observed in C 1s region for oxygen plasma treated DLC:SiO_x films. The aging of the DLC:SiO_x films resulted in further oxidation in ambient air, which is indicated by slight increase of C=O component as well as recombination of sp^2 carbon into other functional groups. Two deconvoluted components of as-deposited DLC:SiO_x film in the XPS Si 2p spectrum were assigned to Si–CH_x (102.5 eV) and SiO_x (101.1 eV) chemical bonds [38,41]. Two additional components appeared at 104 eV and 99.8 eV after oxygen plasma treatment of DLC:SiO_x, assigned

to the SiO_2 and Si–Si chemical bonds, respectively [41]. After oxygen plasma treatment the concentration of hydrophobic Si–CH_x functional groups on the surface of DLC:SiO_x decreased significantly, and slightly increased after 20 days of aging, which is in good agreement with CA measurement results. The restoration of Si–CH_x chemical bonds is mainly responsible for CA increase with aging of DLC:SiO_x film. The appearance of SiO_2 and Si–Si chemical bonds for oxygen plasma treated DLC:SiO_x films also significantly contributed to the effective hydrophilic properties of the surface [21]. The concentration of these functional groups on the surface of oxygen plasma treated DLC:SiO_x film remained relatively stable after 20 days of aging.

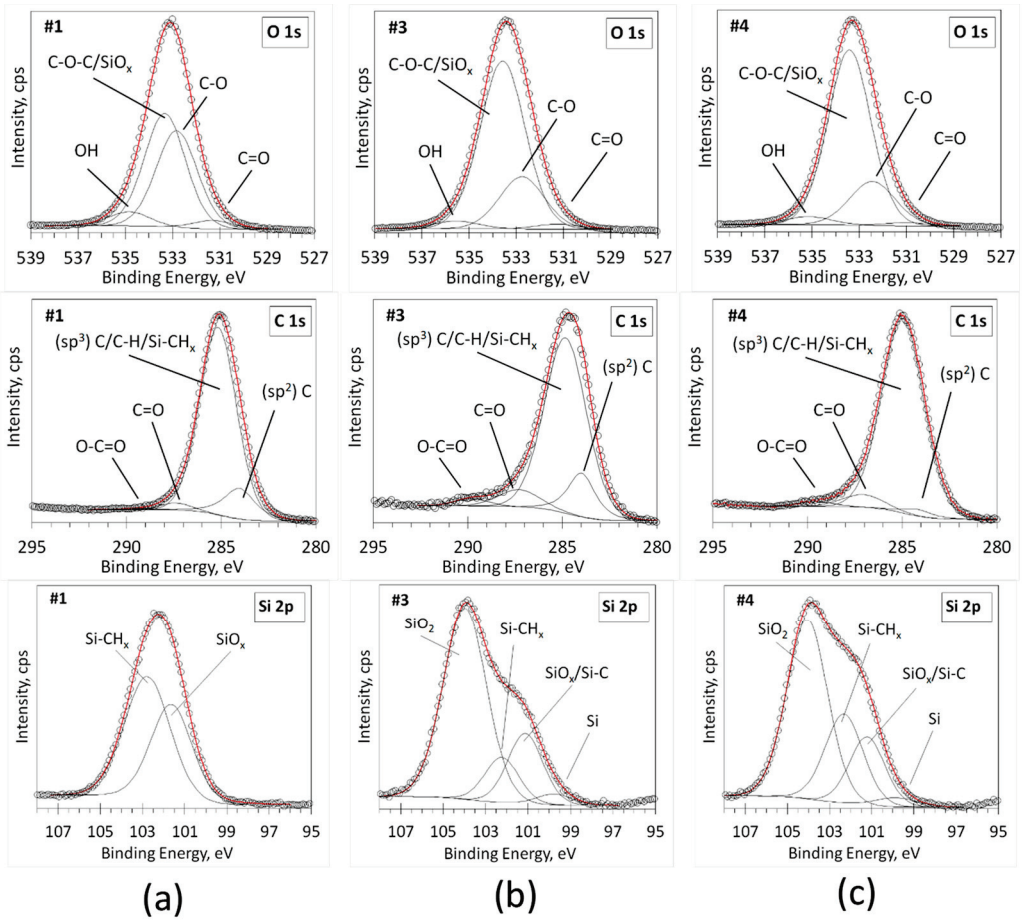

Figure 3. High-resolution deconvoluted XPS spectra in O 1s, C 1s and Si 2p regions of DLC:SiO_x (**a**) as-deposited, (**b**) 3 min oxygen plasma treated and (**c**) oxygen plasma treated and aged for 20 days.

Based on the findings of this study, several future directions are of the main importance:

- Investigation of the long-term stability of hydrophilic properties of the oxygen plasma treated DLC:SiO_x films under various environmental conditions, such as humidity, temperature, and exposure to different chemicals.
- Study of the underlying mechanisms of the restoration of hydrophobic Si-CH_x functional groups and the ways to prevent or delay this process, enhancing the long-term stability of the hydrophilic properties of the DLC:SiO_x films.
- Investigation of the effect of the hydrophilic DLC:SiO_x films on the adhesion, proliferation, and differentiation of various cell types to explore their potential applications in tissue engineering and regenerative medicine.

4. Conclusions

Atmospheric oxygen plasma treatment was used to modify DLC:SiO_x film wetting properties. The surface of the DLC:SiO_x film was modified to be effectively hydrophilic with complete spreading of water droplet (CA < 2°) on the surface. The CA increased up to $28 \pm 1°$ after 20 days of aging in ambient air at room temperature, still maintaining good hydrophilic properties. AFM analysis indicated that the root mean square roughness of the film increased from 0.27 nm to 1.26 nm after oxygen plasma treatment. XPS investigation revealed that the highly hydrophilic characteristics of the oxygen plasma treated DLC:SiO_x is attributed to surface enrichment with C–O–C, SiO_2 and Si–Si chemical bonds as well as significant removal of hydrophobic Si–CH_x functional groups. During aging process of DLC:SiO_x film the Si–CH_x functional groups tend to restore to some extent negatively affecting the wetting properties. The modified DLC:SiO_x nanocomposite films should be tested in various applications, such as biocompatible coatings for medical purposes, anti-fog coatings for optical components, and protective coatings to prevent corrosion and wear.

Author Contributions: Conceptualization, A.L., Š.M. and V.G.; investigation, A.L., Š.M., M.A., B.A., D.J., V.G. and A.G.; writing—original draft preparation, A.L.; writing—review and editing, A.L., M.A., D.J. and Š.M.; visualization, A.L., B.A. and M.A.; project administration, Š.M.; funding acquisition, Š.M. All authors have read and agreed to the published version of the manuscript.

Funding: This research has received funding from European Regional Development Fund (project No. 01.2.2-LMT-K-718-03-0058) under grant agreement with the Research Council of Lithuania (LMTLT).

Data Availability Statement: Not applicable.

Acknowledgments: A special thanks goes to V. Kopustinskas for technical assistance.

Conflicts of Interest: The authors declare that they have no known competing financial interests or personal relationships that could have appeared to influence the work reported in this paper.

References

1. Ohtake, N.; Hiratsuka, M.; Kanda, K.; Akasaka, H.; Tsujioka, M.; Hirakuri, K.; Hirata, A.; Ohana, T.; Inaba, H.; Kano, M. Properties and classification of diamond-like carbon films. *Materials* **2021**, *14*, 315. [CrossRef] [PubMed]
2. Liu, Y.; Jiang, Y.; Sun, J.; Wang, L.; Liu, Y.; Chen, L.; Zhang, B.; Qian, L. Durable superlubricity of hydrogenated diamond-like carbon film against different friction pairs depending on their interfacial interaction. *Appl. Surf. Sci.* **2021**, *560*, 150023. [CrossRef]
3. Liu, Y.; Chen, L.; Jiang, B.; Liu, Y.; Zhang, B.; Xiao, C.; Zhang, J.; Qian, L. Origin of low friction in hydrogenated diamond-like carbon films due to graphene nanoscroll formation depending on sliding mode: Unidirection and reciprocation. *Carbon* **2021**, *173*, 696–704. [CrossRef]
4. Nagai, T.; Hiratsuka, M.; Alanazi, A.; Nakamori, H.; Hirakuri, K. Anticorrosion of DLC coating in acid solutions. *Appl. Surf. Sci.* **2021**, *552*, 149373. [CrossRef]
5. Wachesk, C.; Seabra, S.; Dos Santos, T.; Trava-Airoldi, V.; Lobo, A.; Marciano, F. In vivo biocompatibility of diamond-like carbon films containing TiO2 nanoparticles for biomedical applications. *J. Mater. Sci. Mater. Med.* **2021**, *32*, 117. [CrossRef]
6. Yonezawa, K.; Kawaguchi, M.; Kaneuji, A.; Ichiseki, T.; Iinuma, Y.; Kawamura, K.; Shintani, K.; Oda, S.; Taki, M.; Kawahara, N. Evaluation of antibacterial and cytotoxic properties of a fluorinated diamond-like carbon coating for the development of antibacterial medical implants. *Antibiotics* **2020**, *9*, 495. [CrossRef] [PubMed]
7. Toyonaga, M.; Hasebe, T.; Maegawa, S.; Matsumoto, T.; Hotta, A.; Suzuki, T. The property of adhesion and biocompatibility of silicon and fluorine doped diamond-like carbon films. *Diamond Relat. Mater.* **2021**, *119*, 108558. [CrossRef]
8. Zhai, W.; Bai, L.; Zhou, R.; Fan, X.; Kang, G.; Liu, Y.; Zhou, K. Recent progress on wear-resistant materials: Designs, properties, and applications. *Adv. Sci.* **2021**, *8*, 2003739. [CrossRef]
9. Yamaki, T.; Osawa, T.; Matsuo, M.; Akasaka, H.; Tanaka, S.; Kikuchi, M.; Hirata, Y.; Ohtake, N.; Yamamoto, H. Wear Resistant DLC Coatings for Soft Metallic Materials. In Proceedings of the International Conference on Leading Edge Manufacturing/Materials and Processing, Online, 3 September 2020; American Society of Mechanical Engineers: New York, NY, USA, 2020. V001T08A015.
10. Song, J.-S.; Park, Y.S.; Kim, N.-H. Hydrophobic anti-reflective coating of plasma-enhanced chemical vapor deposited diamond-like carbon thin films with various thicknesses for dye-sensitized solar cells. *Appl. Sci.* **2021**, *11*, 358. [CrossRef]
11. Grenadyorov, A.; Solovyev, A.; Oskomov, K.; Oskirko, V.; Semenov, V. Thermal stability of anti-reflective and protective aC: H: SiOx coating for infrared optics. *Appl. Surf. Sci.* **2020**, *510*, 145433. [CrossRef]
12. Love, C.; Cook, R.B.; Harvey, T.; Dearnley, P.; Wood, R. Diamond like carbon coatings for potential application in biological implants—A review. *Tribol. Int.* **2013**, *63*, 141–150. [CrossRef]

13. Nagashima, S.; Hasebe, T.; Kamijo, A.; Yoshimoto, Y.; Hotta, A.; Morita, H.; Terada, H.; Tanaka, M.; Takahashi, K.; Suzuki, T. Effect of oxygen plasma treatment on non-thrombogenicity of diamond-like carbon films. *Diamond Relat. Mater.* **2010**, *19*, 861–865. [CrossRef]
14. Anil, M.; Ahmed, S.F.; Yi, J.W.; Moon, M.-W.; Lee, K.-R.; chan Kim, Y.; Seok, H.K.; Han, S.H. Tribological performance of hydrophilic diamond-like carbon coatings on Ti–6Al–4V in biological environment. *Diamond Relat. Mater.* **2010**, *19*, 300–304. [CrossRef]
15. Meškinis, Š.; Kopustinskas, V.; Šlapikas, K.; Tamulevičius, S.; Guobiene, A.; Gudaitis, R.; Grigaliūnas, V. Ion beam synthesis of the diamond like carbon films for nanoimprint lithography applications. *Thin Solid Films* **2006**, *515*, 636–639. [CrossRef]
16. Rahman, S.M.; Song, J.; Yeo, C.-D. Computational study on surface energy of amorphous DLC with respect to hybridization state of carbon and potential functions. *Diamond Relat. Mater.* **2019**, *95*, 127–134. [CrossRef]
17. Roy, R.K.; Choi, H.-W.; Park, S.-J.; Lee, K.-R. Surface energy of the plasma treated Si incorporated diamond-like carbon films. *Diamond Relat. Mater.* **2007**, *16*, 1732–1738. [CrossRef]
18. Marciano, F.; Bonetti, L.; Da-Silva, N.; Corat, E.; Trava-Airoldi, V. Wettability and antibacterial activity of modified diamond-like carbon films. *Appl. Surf. Sci.* **2009**, *255*, 8377–8382. [CrossRef]
19. López-Santos, C.; Yubero, F.; Cotrino, J.; González-Elipe, A. Lateral and in-depth distribution of functional groups on diamond-like carbon after oxygen plasma treatments. *Diamond Relat. Mater.* **2011**, *20*, 49–56. [CrossRef]
20. Siow, K.S.; Britcher, L.; Kumar, S.; Griesser, H.J. Plasma methods for the generation of chemically reactive surfaces for biomolecule immobilization and cell colonization—A review. *Plasma Process. Polym.* **2006**, *3*, 392–418. [CrossRef]
21. Yi, J.W.; Moon, M.-W.; Ahmed, S.F.; Kim, H.; Cha, T.-G.; Kim, H.-Y.; Kim, S.-S.; Lee, K.-R. Long-lasting hydrophilicity on nanostructured Si-incorporated diamond-like carbon films. *Langmuir* **2010**, *26*, 17203–17209. [CrossRef]
22. Sun, L.; Guo, P.; Li, X.; Wang, A. Comparative study on structure and wetting properties of diamond-like carbon films by W and Cu doping. *Diamond Relat. Mater.* **2017**, *73*, 278–284. [CrossRef]
23. Wang, J.; Zhang, K.; Wang, F.; Zheng, W. Improving frictional properties of DLC films by surface energy manipulation. *RSC Adv.* **2018**, *8*, 11388–11394. [CrossRef] [PubMed]
24. Ma, G.; Gong, S.; Lin, G.; Zhang, L.; Sun, G. A study of structure and properties of Ti-doped DLC film by reactive magnetron sputtering with ion implantation. *Appl. Surf. Sci.* **2012**, *258*, 3045–3050. [CrossRef]
25. Chen, L.; Minakawa, A.; Mizutani, M.; Kuriyagawa, T. Study of laser-induced periodic surface structures on different coatings exhibit super hydrophilicity and reduce friction. *Precis. Eng.* **2022**, *78*, 215–232. [CrossRef]
26. Jedrzejczak, A.; Kolodziejczyk, L.; Szymanski, W.; Piwonski, I.; Cichomski, M.; Kisielewska, A.; Dudek, M.; Batory, D. Friction and wear of aC: H: SiOx coatings in combination with AISI 316L and ZrO2 counterbodies. *Tribol. Int.* **2017**, *112*, 155–162. [CrossRef]
27. Koshigan, K.; Mangolini, F.; McClimon, J.; Vacher, B.; Bec, S.; Carpick, R.; Fontaine, J. Understanding the hydrogen and oxygen gas pressure dependence of the tribological properties of silicon oxide–doped hydrogenated amorphous carbon coatings. *Carbon* **2015**, *93*, 851–860. [CrossRef]
28. Batory, D.; Jedrzejczak, A.; Szymanski, W.; Niedzielski, P.; Fijalkowski, M.; Louda, P.; Kotela, I.; Hromadka, M.; Musil, J. Mechanical characterization of aC: H: SiOx coatings synthesized using radio-frequency plasma-assisted chemical vapor deposition method. *Thin Solid Films* **2015**, *590*, 299–305. [CrossRef]
29. Stalder, A.F.; Kulik, G.; Sage, D.; Barbieri, L.; Hoffmann, P. A snake-based approach to accurate determination of both contact points and contact angles. *Colloids Surf. A Physicochem. Eng. Asp.* **2006**, *286*, 92–103. [CrossRef]
30. Bachmann, S.; Schulze, M.; Morasch, J.; Hesse, S.; Hussein, L.; Krell, L.; Schnagl, J.; Stark, R.W.; Narayan, S. Aging of oxygen and hydrogen plasma discharge treated aC: H and ta-C coatings. *Appl. Surf. Sci.* **2016**, *371*, 613–623. [CrossRef]
31. Yun, D.Y.; Choi, W.S.; Park, Y.S.; Hong, B. Effect of H2 and O2 plasma etching treatment on the surface of diamond-like carbon thin film. *Appl. Surf. Sci.* **2008**, *254*, 7925–7928. [CrossRef]
32. Marciano, F.; Marcuzzo, J.; Bonetti, L.; Corat, E.; Trava-Airoldi, V. Use of near atmospheric pressure and low pressure techniques to modification DLC film surface. *Surf. Coat. Technol.* **2009**, *204*, 64–68. [CrossRef]
33. Sun, P.; Wang, Y.; Liu, H.; Wang, K.; Wu, D.; Xu, Z.; Zhu, H. Structure evolution of graphene oxide during thermally driven phase transformation: Is the oxygen content really preserved? *PLoS ONE* **2014**, *9*, e111908. [CrossRef]
34. Bokare, A.; Nordlund, D.; Melendrez, C.; Robinson, R.; Keles, O.; Wolcott, A.; Erogbogbo, F. Surface functionality and formation mechanisms of carbon and graphene quantum dots. *Diamond Relat. Mater.* **2020**, *110*, 108101. [CrossRef]
35. Kerber, S.; Bruckner, J.; Wozniak, K.; Seal, S.; Hardcastle, S.; Barr, T. The nature of hydrogen in X-ray photoelectron spectroscopy: General patterns from hydroxides to hydrogen bonding. *J. Vac. Sci. Technol. A Vac. Surf. Film.* **1996**, *14*, 1314–1320. [CrossRef]
36. Shen, Z.; Xia, Y.; Zhao, C.; Ding, Y.; Fan, P.; Li, J. Mechanical Property Evolution Model of Polyimide Film by Far Ultraviolet Irradiation. *J. Phys. Conf. Ser.* **2020**, *1637*, 012040. [CrossRef]
37. Milošev, I.; Jovanović, Ž.; Bajat, J.; Jančić-Heinemann, R.; Mišković-Stanković, V. Surface analysis and electrochemical behavior of aluminum pretreated by vinyltriethoxysilane films in mild NaCl solution. *J. Electrochem. Soc.* **2012**, *159*, C303. [CrossRef]
38. Hegemann, D.; Brunner, H.; Oehr, C. Plasma treatment of polymers to generate stable, hydrophobic surfaces. *Plasmas Polym.* **2001**, *6*, 221–235. [CrossRef]
39. Kaare, K.T.; Yu, E.; Volperts, A.; Dobele, G.; Zhurinsh, A.; Dyck, A.; Niaura, G.; Tamasauskaite-Tamasiunaite, L.; Norkus, E.; Andrulevičius, M. Highly active wood-derived nitrogen-doped carbon catalyst for the oxygen reduction reaction. *ACS Omega* **2020**, *5*, 23578–23587. [CrossRef]

40. Kaare, K.; Yu, E.; Käämbre, T.; Volperts, A.; Dobele, G.; Zhurinsh, A.; Niaura, G.; TamasauskaiteTamasiunaite, L.; Norkus, E.; Kruusenberg, I. Biomass-derived graphene-like catalyst material for oxygen reduction reaction. *ChemNanoMat* **2021**, *7*, 307–313. [CrossRef]
41. NIST X-ray Photoelectron Spectroscopy Database. *NIST Standard Reference Database Number 20*; National Institute of Standards and Technology: Gaithersburg, MD, USA, 2000; p. 20899.

nanomaterials

MDPI

Article

Ag Catalysts Supported on CeO_2, MnO_2 and $CeMnO_x$ Mixed Oxides for Selective Catalytic Reduction of NO by C_3H_6

Eleonora La Greca [1], Tamara S. Kharlamova [2], Maria V. Grabchenko [2], Luca Consentino [1], Daria Yu Savenko [2], Giuseppe Pantaleo [1], Lidiya S. Kibis [3], Olga A. Stonkus [3], Olga V. Vodyankina [2,*] and Leonarda Francesca Liotta [1,*]

[1] Institute for the Study of Nanostructured Materials (ISMN), (Italian) National Research Council (CNR), Via Ugo La Malfa 153, 90146 Palermo, Italy
[2] Laboratory of Catalytic Research, Tomsk State University, Lenin Ave. 36, 634050 Tomsk, Russia
[3] Boreskov Institute of Catalysis SB RAS, Lavrentiev Ave. 5, 630090 Novosibirsk, Russia
* Correspondence: vodyankina_o@mail.ru (O.V.V.); leonardafrancesca.liotta@cnr.it (L.F.L.)

Abstract: In the present study CeO_2, MnO_2 and $CeMnO_x$ mixed oxide (with molar ratio Ce/Mn = 1) were prepared by sol-gel method using citric acid as a chelating agent and calcined at 500 °C. The silver catalysts (1 wt.% Ag) over the obtained supports were synthesized by the incipient wetness impregnation method with $[Ag(NH_3)_2]NO_3$ aqueous solution. The selective catalytic reduction of NO by C_3H_6 was investigated in a fixed-bed quartz reactor using a reaction mixture composed of 1000 ppm NO, 3600 ppm C_3H_6, 10 vol.% O_2, 2.9 vol.% H_2 and He as a balance gas, at WHSV of 25,000 mL g^{-1} h^{-1}.The physical-chemical properties of the as-prepared catalysts were studied by several characterization techniques, such as X-ray fluorescence analysis, nitrogen adsorption/desorption, X-ray analysis, Raman spectroscopy, transmission electron microscopy with analysis of the surface composition by X-ray energy dispersive spectroscopy and X-ray photo-electron spectroscopy. Silver oxidation state and its distribution on the catalysts surface as well as the support microstructure are the main factors determining the low temperature activity in NO selective catalytic reduction. The most active $Ag/CeMnO_x$ catalyst (NO conversion at 300 °C is 44% and N_2 selectivity is ~90%) is characterized by the presence of the fluorite-type phase with high dispersion and distortion. The characteristic "patchwork" domain microstructure of the mixed oxide along with the presence of dispersed $Ag^+/Ag_n^{\delta+}$ species improve the low-temperature catalyst of NO reduction by C_3H_6 performance compared to Ag/CeO_2 and Ag/MnO_x systems.

Keywords: Ag^+; $CeMnO_x$; C_3H_6-SCR of NO; oxide microstructure; HRTEM; Raman; XPS

Citation: La Greca, E.; Kharlamova, T.S.; Grabchenko, M.V.; Consentino, L.; Savenko, D.Y.; Pantaleo, G.; Kibis, L.S.; Stonkus, O.A.; Vodyankina, O.V.; Liotta, L.F. Ag Catalysts Supported on CeO_2, MnO_2 and $CeMnO_x$ Mixed Oxides for Selective Catalytic Reduction of NO by C_3H_6. *Nanomaterials* **2023**, *13*, 873. https://doi.org/10.3390/nano13050873

Academic Editors: Antonio Guerrero-Ruiz and Meiwen Cao

Received: 1 February 2023
Revised: 23 February 2023
Accepted: 25 February 2023
Published: 26 February 2023

1. Introduction

Currently, internal combustion engines (ICEs), including diesel engines, are the most widely used due to their high efficiency and reliability [1]. However, the main disadvantage of the ICEs is the emission of exhaust gases that pose a serious threat to both the environment (increasing ozone concentration in the atmosphere and producing acid rains) and the human health as they are rich in particulates and nitrogen oxides (NO, NO_2 and N_2O) [2].

In recent years, several methods have been applied to reduce NO_x emissions. For this purpose, selective catalytic reduction (SCR) with hydrocarbons or alcohols (HC- or HCO-SCR, respectively) has proved to be interesting for their high efficiency and low cost [3–5]. The main advantage of such reaction is the use of gas mixtures with similar composition as the exhaust fumes; in this way, the HC and NO_x can be simultaneously abated without feeding additional reducing agents [6]. Furthermore, this process can be a useful alternative to commercial processes utilizing NH_3 or urea as reducing agents [7], which are the dominant technologies for NO_x removing from mobile (vehicles and marine engines) and stationary sources [8]. Nevertheless, the toxicity of concentrated ammonia, the

fact that urea must be temporarily stored on board, thus requiring additional infrastructures for supply and use (additional urea tank to be filled periodically), the costs of ammonia plants and ammonia slip, which can produce additional pollution [5,9], constitute the main obstacles that prevent the large use of such systems.

Numerous catalysts such as zeolites, noble metals and metal oxides have been studied for NO_x HC-SCR. The limited use of zeolite-based catalysts is due to hydrothermal deactivation and high-temperature activity limiting their real applications [10]. From the pioneer study by Miyadera [11], based on the performance efficiency of Ag/Al_2O_3, which showed high NO conversion in HC-SCR with various light hydrocarbons, the silver-based catalysts are extensively studied as promising candidates for practical use $DeNO_x$ systems, because they exhibit a high efficiency comparable to that of commercial catalysts applied in NH_3-SCR, especially at temperatures above 300 °C; moreover, they have a moderate resistance to water and SO_2 [12–14]. An advantage linked to the preferable use of Ag compared to Pt group metals is a lower oxidation activity of HC/HCO that limits the oxidation of hydrocarbons or oxygenates in simultaneous total combustion during the NO_x SCR. Previous studies showed that the catalytic properties of silver-alumina catalysts were related to the Ag loading on the support [15,16]. For low loadings, the Ag exists mainly in the form of Ag^+ or $Ag^{\delta+}$, while the catalysts with higher Ag content usually contain more Ag^0 nanoparticles. Another important aspect is the influence of Ag loading on the catalytic activity. In fact, isolated silver cations (Ag^+) and oxidized silver clusters ($Ag_n{}^{\delta+}$) are proposed to be the active species in the NO-SCR reaction, while metallic silver clusters (Ag^0) are responsible for the nonselective oxidation of hydrocarbons [16]. However, the practical application of Ag-based catalysts is limited by the low activity at temperatures in the range of 150–300 °C.

Among various supports used for NO_x SCR, CeO_2 and manganese oxides have attracted wide attention as they feature excellent low-temperature activity [17–19]. The high efficiency of CeO_2-based catalysts is due to the excellent Lewis surface acidity, redox properties and high oxygen storage capacity [20,21]. The Mn-based oxides are promising for application at low temperatures due to high NO conversion and good N_2 selectivity in the NO SCR by NH_3 [22,23]. Moreover, the $Mn\text{-}WO_3/TiO_2$ catalysts represent a valid alternative in the NH_3-SCR of NO to the typical $V_2O_5\text{-}WO_3/TiO_2$ commercial systems [24]. According to the available literature data, the Ag catalysts supported on Ce and Ce-based mixed oxides (Ce-Mn, Ce-Zr, Ce-Ti, etc.) are appealing as catalytic materials for NH_3 NO_x SCR in exhausts emitted by diesel engines of vehicles and ships in compliance with the EURO VI and IMO 2020 regulations [14,18,25,26]. However, such catalytic systems remain poorly understood for CH-SCR. Recently, Ag/CeZr catalysts have been shown to be very promising for NO_x HC-SCR [27], which increases interest in considering other Ce-based mixed oxides for NO_x HC-SCR.

This work is focused on the synthesis and detailed characterization of powder catalysts based on silver as an active phase supported on Ce, Mn and Ce-Mn reducible oxides and study of their activity in selective catalytic NO_x reduction with propylene. To synthesize the oxide supports, the citrate sol-gel method was chosen, while an impregnation of the prepared supports with $[Ag(NH_3)_2]NO_3$ followed by calcination in air was used to prepare the Ag catalysts. The citrate sol-gel method allowed preparing the ultrafine oxide materials and ensured good homogeneity through mixing of the initial components at the molecular level in solution [28,29]. This synthesis method allows obtaining the supports with the required elemental and phase composition, optimal specific surface area and pore size distribution, structural and textural characteristics [30,31]. In turn, the use of $[Ag(NH_3)_2]NO_3$ as a silver precursor to prepare the Ag catalysts was expected to ensure a strong interaction between the Ag precursor and support resulting in stabilization of silver cations (Ag^+) and/or oxidized silver clusters ($Ag_n{}^{\delta+}$) as active species on the catalyst surface [13,32]. The obtained catalysts were characterized by such methods as X-ray fluorescence (XRF) analysis, N_2 adsorption/desorption, Raman spectroscopy, transmission electron microscopy with analysis of the surface composition by X-ray energy dispersive

spectroscopy (TEM/EDX) and X-ray photo-electron spectroscopy (XPS) and were studied in the NO SCR with C_3H_6 cofeeding H_2 in the reaction mixture. For comparison, the catalytic activity in terms of NO conversion and selectivity towards N_2 was also investigated for the supports only.

2. Materials and Methods

2.1. Preparation of the Supports

The individual CeO_2, MnO_x and binary CeO_2–MnO_x (with a molar ratio of Ce/Mn = 1) oxide supports were synthesized by sol–gel citrate method. Analytical grade $Ce(NO_3)_3 \cdot 6H_2O$ and $Mn(NO_3)_2 \cdot 6H_2O$ salts (Unihim, St. Petersburg, Russia) were used as Ce and Mn precursors, respectively, and citric acid $C_6H_8O_7 \cdot H_2O$ (Khimprom, Kemerovo, Russia) was employed as a chelating agent. All reagents were used directly without any further purification. The colloidal solutions to synthesize the supports were prepared in a 500 mL ceramic tank using a heated magnetic stirrer. For this, the required volume of solutions of the corresponding metal precursors was rapidly added to a citric acid solution at a vigorous stirring with the molar ratio $C_6H_8O_7 \cdot H_2O$/(Me) = 1.2 (pH of solution was ~1–2) followed by heating up to 70 °C at a constant stirring. The above colloidal solutions were hold at 70 °C at a constant stirring for 2 h followed by the gel formation. To age the gel and additionally evaporate water, the resulting gel was placed in a drying oven overnight at 80 °C. The resulting gel was additionally dried at 120 °C (a heating rate was 10 deg/min) for 5 h and then calcined at 500 °C for 3 h with a linear heating rate up to a maximum set temperature of 5 °C/min. The synthesized samples were labelled as follows: CeO_2, MnO_x and $CeMnO_x$.

2.2. Preparation of Supported Ag Catalysts

Based on the obtained supports, a series of Ag catalysts with a fixed silver content (1 wt.%) was prepared by incipient wetness impregnation using an aqueous solution of ammonium silver complex $[Ag(NH_3)_2]NO_3$ as an Ag precursor. The wetness of the support was determined by adding drop by drop a known volume of water solution. The volume and concentration of the impregnating solution for each support were fixed taking into account its wetness and weight to ensure 1 wt.% of Ag in the final catalyst. The samples impregnated were dried at 70 °C and then calcined at 500 °C for 2 h. The obtained catalysts were designated as follows: Ag/CeO_2, Ag/MnO_x and $Ag/CeMnO_x$.

2.3. Aging of Supported Ag Catalysts

Samples were aged thermally. Sample powders were heated in air to 650 °C at a heating rate of 10°/min, calcined at 650 °C for 12 h, and then cooled to room temperature.

2.4. Characterization

The prepared samples were studied by several characterization methods, including X-ray fluorescence analysis (XRF), nitrogen adsorption/desorption at −196 °C, X-ray analysis (XRD), Raman spectroscopy, transmission electron microscopy (TEM) with analysis of the surface composition by X-ray energy dispersive spectroscopy (EDX) and X-ray photoelectron spectroscopy (XPS).

2.4.1. X-ray Fluorescence Analysis

The chemical composition of the samples was analyzed using the XRF-1800 sequential X-ray fluorescence spectrometer (Shimadzu, Tokyo, Japan).

2.4.2. Low-Temperature Nitrogen Adsorption/Desorption

The specific surface area, total pore volume and average pore diameter were determined from the low-temperature nitrogen adsorption/desorption (at −196 °C) using the TriStar II 3020 specific analyzer (Micromeritics, Norcross, GA, USA). Prior to experiments, all samples were degassed at 200 °C in a vacuum (10^{-2} Torr) for 2 h using the laboratory degassing station VacPrep Degasser (Micromeritics). The specific surface area was determined

by the Brunauer-Emmett-Teller (BET) method; the pore volume and pore size distributions were determined by the Barrett-Joyner-Halenda (BJH) method using the desorption branch of the adsorption-desorption isotherm.

2.4.3. XRD

The XRD patterns for the samples were recorded by the X-ray diffractometer XRD-7000 (Shimadzu) with monochromatic CuKα radiation (1.54 Å) in the angle range of 10–70° 2θ and a scanning rate of 0.02 °/s. The data were obtained using the Bragg-Brentano geometry. Crystalline Si (a = 5.4309 Å, λ = 1.540562 Å) was used as an external standard to calibrate the diffractometer. The phase composition was analyzed using the PDF-2 database (Release 2012 RDB). To refine the lattice parameters and determine the crystalline size, the POWDER CELL 2.4 full profile analysis program was used.

2.4.4. Raman Spectroscopy

Raman spectra were obtained on the InVia spectrometer (Renishaw, UK) equipped with the DM 2500M microscope (Leica, Germany) with a 50× objective. For excitation, the lasers with wavelengths of 532 and 785 nm and a power of 100 mW were used; the spectral resolution was 2 and 1 cm^{-1}, respectively. To prevent changes in the samples, only 5% of the full laser power and a 50% beam defocusing were applied.

2.4.5. TEM and EDX

Transmission electron microscopy (TEM) data were obtained using the double aberration-corrected (Thermo Fisher Scientific Themis Z, Netherlands) electron microscope operated at 200 kV. Images in Scanning-TEM (STEM) mode were taken using the high-angle annular dark field (HAADF) detector. The local composition of the samples was studied using the Thermo Fisher Scientific Super-X EDX spectrometer. The samples for the TEM study were dispersed ultrasonically and deposited on copper grids covered with a holey carbon film.

2.4.6. XPS

The samples were analyzed by X-ray photoelectron spectroscopy (XPS) using the photoelectron spectrometer ES 300 (Kratos Analytical, UK). Mg Kα (hν = 1256.6 eV) and Al Kα (hν = 1486.6 eV) X-ray sources were employed to acquire photoelectron spectra. To perform XPS analysis, the samples were fixed on a sample holder using a scotch-tape. The core-level spectra, namely, Ag3d, O1s, C1s, Ce3d, Mn2p, Mn3s, and Auger spectra for silver Ag MNN were acquired to estimate the quantitative composition of the samples surface as well as to analyze the oxidation state of the elements. The C1s line of the residual amorphous carbon species with a binding energy E_b(C1s) = 285.1 eV was used as an internal standard to calibrate the spectra. Such a calibration procedure gave the E_b value of the U‴ component of the Ce3d spectrum as E_b(U‴) = 916.7 eV being consistent with the literature data for ceria-based catalysts. The spectra were analyzed after Shirley background subtraction. The Ce3d, Mn2p, and Mn3s spectra were fitted with a combination of Gaussian and Lorentzian functions. The XPS-Calc program [33,34] was used for spectra processing. Atomic ratios were calculated using the area of the corresponding peaks with the consideration of the atomic sensitivity factor for each element [35].

2.5. Activity Tests in C_3H_6-SCR of NO

All the C_3H_6-SCR tests were performed in a fixed-bed continuous-flow U quartz reactor with an inner diameter of 12 mm. The feed gas consisting of 1000 ppm NO + 3600 ppm C_3H_6 + 2.9 vol.% H_2 + 10 vol.% O_2 in He was flowed over the catalyst (120 mg) at a rate of 50 mL·min^{-1} equivalent to a weight hourly space velocity (WHSV) of 25,000 mL g^{-1} h^{-1}. To study the effect of hydrogen presence, catalytic tests without it, where also carried out. To this purpose the feed gas consisting of 1000 ppm NO + 3600 ppm C_3H_6 + 10 vol.% O_2 in He was used. The conversion values were measured as a function of temperature from 100 °C to 500 °C with a heating rate of 5 °C/min, holding 40 min at each temperature that

was increased by steps of 50 °C. The inlet and outlet gas compositions were analyzed by mass quadrupole spectrometer (ThermostarTM, Balzers, Liechstenstein) and by ABB detectors, infrared (Limas 11) for NO, N_2O, NO_2, paramagnetic (Magnos 206) for O_2, and UV (Uras 14) for CO and CO_2 detection.

The NO conversion, selectivity to N_2 and N_2 yield were calculated according to procedures described in Refs. [9,12]:

$$NO \text{ conversion } (\%) : \frac{[NO]_{in} - [NO]_{out}}{[NO]_{in}} \times 100;$$

$$\text{Selectivity to } N_2 \ (\%) : 1 - \frac{[NO_2]_{out} + 2[N_2O]_{out}}{[NO]_{in} - [NO]_{out}} \times 100;$$

$$N_2 \text{ yield } (\%) : \frac{[NO]_{in} - [NO]_{out} - 2[N_2O]_{out} - [NO_2]_{out}}{[NO]_{in}} \times 100.$$

3. Results and Discussion

3.1. Chemical Composition and Textural Characteristics of the Samples

Table 1 shows the XFR data for the prepared Ag catalysts. The composition of the supports is consistent with those of the catalysts and is not presented in the table. According to the data obtained, there is a good consistency between the real and nominal chemical compositions.

Table 1. Bulk and surface sample composition according to X-ray fluorescence spectroscopy (XRF) and X-ray photoelectron spectroscopy (XPS) data.

Sample	Content, wt.%				Atomic Ratio, XRF/XPS		
	Ag	Ce	Mn	Ce/Mn	Ag/Ce	Ag/Mn	Ag/(Ce+Mn)
Ag/CeO_2	1.0	80.6	-	-	0.016/0.019	-	-
$Ag/CeMnO_x$	1.2	58.4	20.4	1.1/1.2	0.027/0.027	0.030/0.033	0.014/0.015
Ag/MnO_x	1.3	-	72.7	-	-	0.009/0.022	-

Figure 1 shows nitrogen adsorption-desorption isotherms and pore size distributions for CeO_2, MnO_x and $CeMnO_x$ supports and the corresponding Ag catalysts. Table 2 lists the values of specific surface area and total pore volume. For all samples, the adsorption–desorption isotherms belong to type IV according to the IUPAC classification [36]. The observed hysteresis loops of type H_2 indicate the presence of mesopores with a complex structure in the samples. For the CeO_2 and $CeMnO_x$ samples, wide hysteresis loops are observed in the relative pressure range of 0.45–1.0 corresponding to a rather narrow pore size distribution in the range of 2–10 nm. For the MnO_x sample, a narrow hysteresis loop is observed in the relative pressure range of 0.82–1.0, which corresponds to a wide pore size distribution in the range of 4–200 nm with a maximum at ~30 nm. The CeO_2 and $CeMnO_x$ supports are characterized by the relatively high specific surface area (40 and 51 m^2/g, respectively) and total pore volume (0.140 and 0.222 cm^3/g, respectively), while the MnO_x sample shows relatively low specific surface area (14 m^2/g) and total pore volume (0.115 cm^3/g).

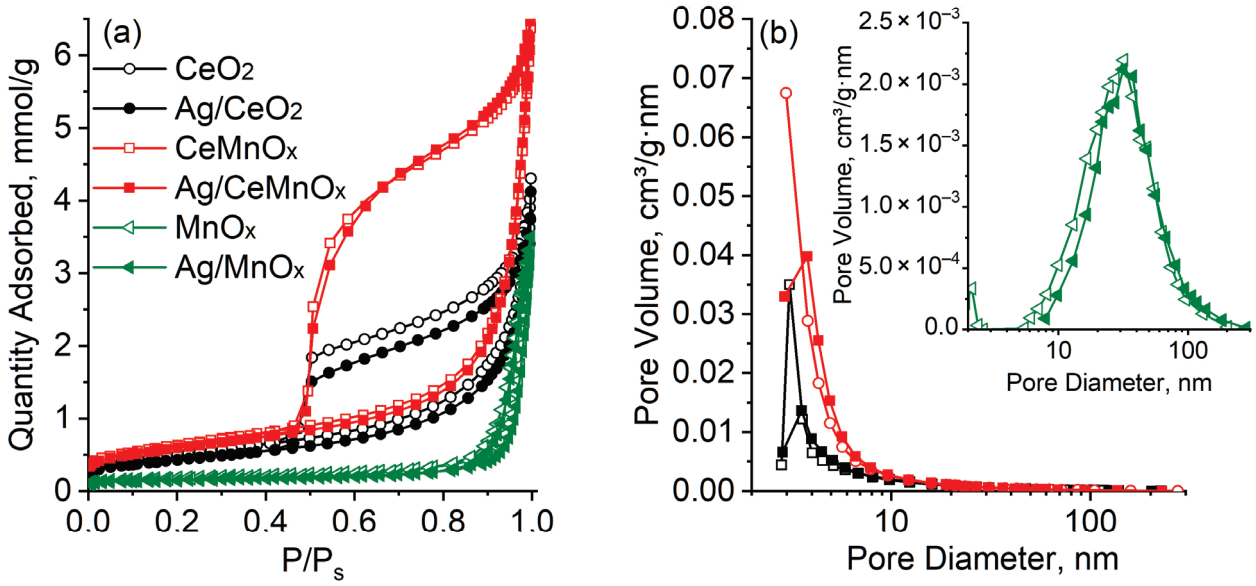

Figure 1. Adsorption-desorption isotherms (**a**) and pore size distribution (**b**) for oxide supports and Ag/oxide catalysts.

Table 2. Specific surface area (SSA) and total pore volume (V), phase composition, and characteristics of the crystalline phases revealed (space group (S.G.), symmetry, lattice parameters (*a*, *c*), and mean crystallite size (D_{XRD})) for oxide supports and Ag/oxide catalysts.

Sample	SSA, m^2/g	V, cm^3/g	Phase Composition		Structural Parameters				D_{XRD}, nm
			Phase	wt.%	S.G.	Symmetry	*a*, Å	*c*, Å	
CeO_2	40	0.14	fluorite	100	Fm-3m	cubic	5.405	-	13
Ag/CeO_2	34	0.13	fluorite	100	Fm-3m	cubic	5.405	-	15
MnO_x	14	0.12	Mn_2O_3	25	Ia-3	cubic	9.402	-	61
			Mn_3O_4	75	I41/amd	tetragonal	5.758	9.457	33
Ag/MnO_x	12	0.12	Mn_2O_3	76	Ia-3	cubic	9.403	-	52
			Mn_3O_4	24	I41/amd	tetragonal	5.755	9.466	n.a.
$CeMnO_x$	51	0.22	fluorite	100	Fm-3m	cubic	5.406	-	7
$Ag/CeMnO_x$	47	0.22	fluorite	100	Fm-3m	cubic	5.413	-	7

The Ag introduction does not significantly affect the isotherms and pore size distributions in the corresponding samples (Figure 1). The observed decrease in the specific surface area with a slight change in the total pore volume is apparently due to the support sintering according to the mechanism of surface diffusion during the calcination step. In general, the changes observed in the textural characteristics of the Ag/oxide catalysts indicate a uniform distribution of Ag introduced into the porous space of the supports.

3.2. Phase Composition and Structural Characteristics of Samples

The phase composition and structural features of the CeO_2, MnO_x and $CeMnO_x$ supports, and the corresponding Ag catalysts were studied by XRD, Raman spectroscopy with laser excitation wavelengths of 532 and 785 nm, and TEM. Figure 2 shows the XRD patterns for the samples studied. Table 2 presents the phase composition of the samples and the characteristics of the crystalline phases revealed during the XRD data analysis. Figure 3 shows the Raman spectra for the samples at two different laser excitation wavelengths; the use of various laser excitations provides wide information due to the resonance effect of Raman scattering [37,38]. Figures 4–6 display the high-resolution TEM (HRTEM) images and high resolution EDX mapping for Ag supported catalysts.

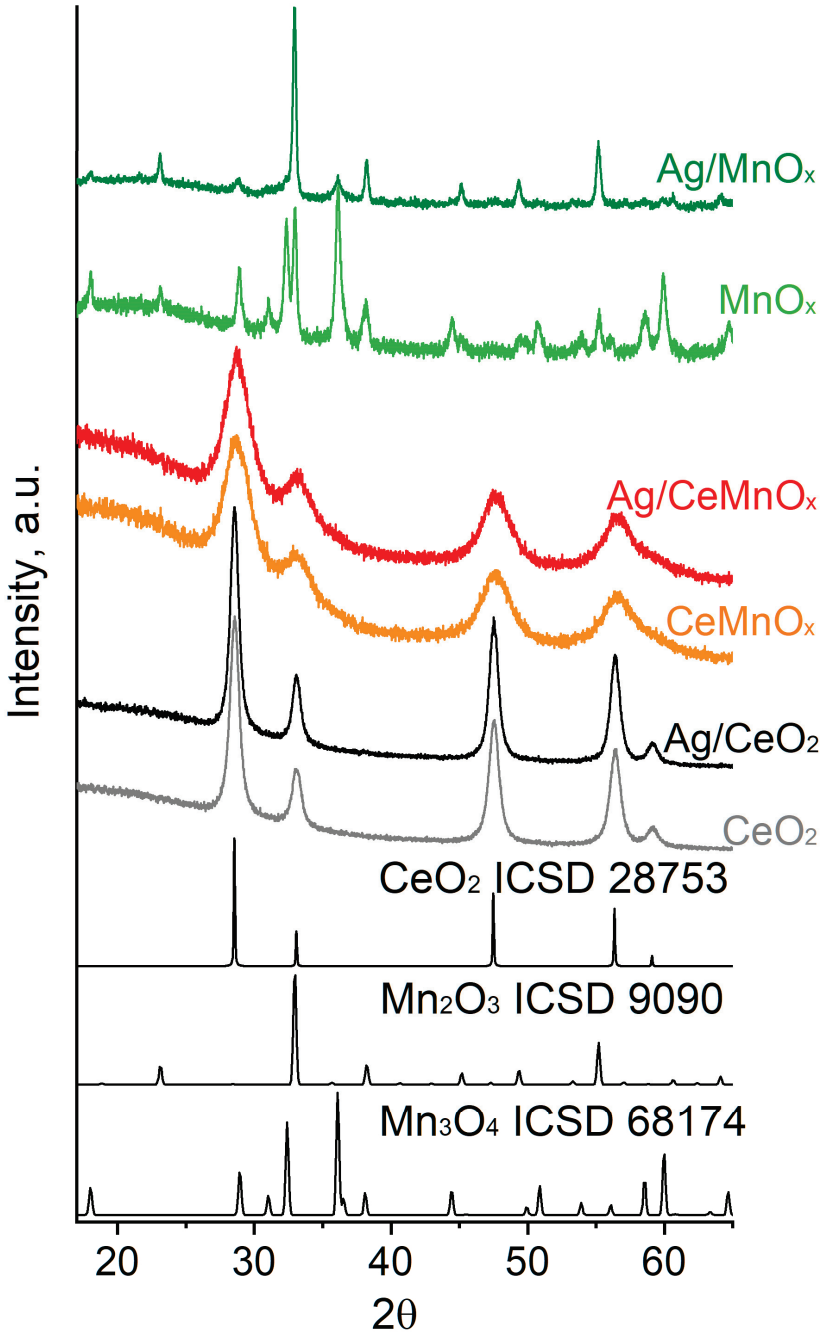

Figure 2. XRD patterns for oxide supports and Ag catalysts on the basis thereof.

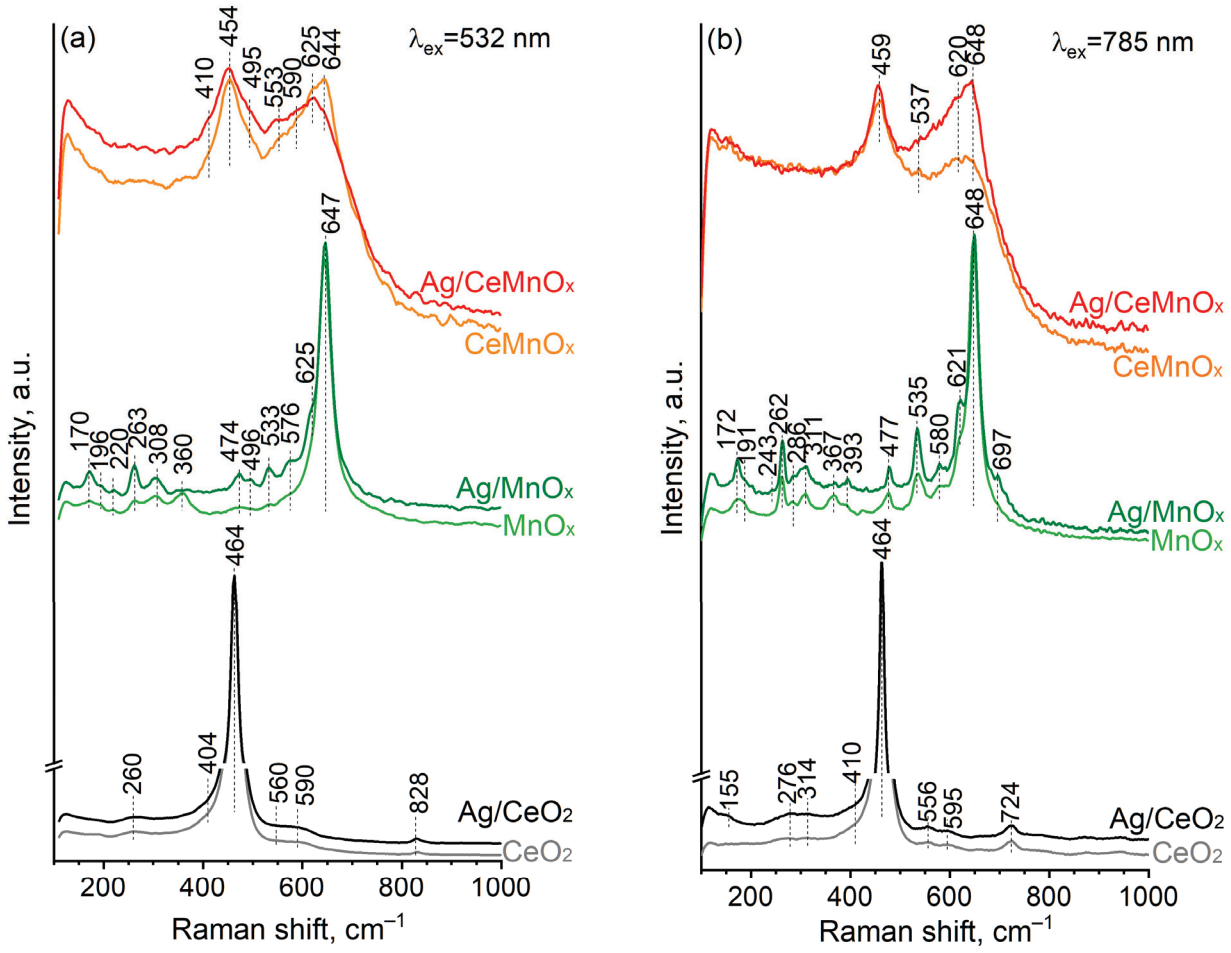

Figure 3. Raman spectra obtained under (**a**) 532 nm and (**b**) 785 nm lasers for oxide supports and Ag catalysts on the basis thereof.

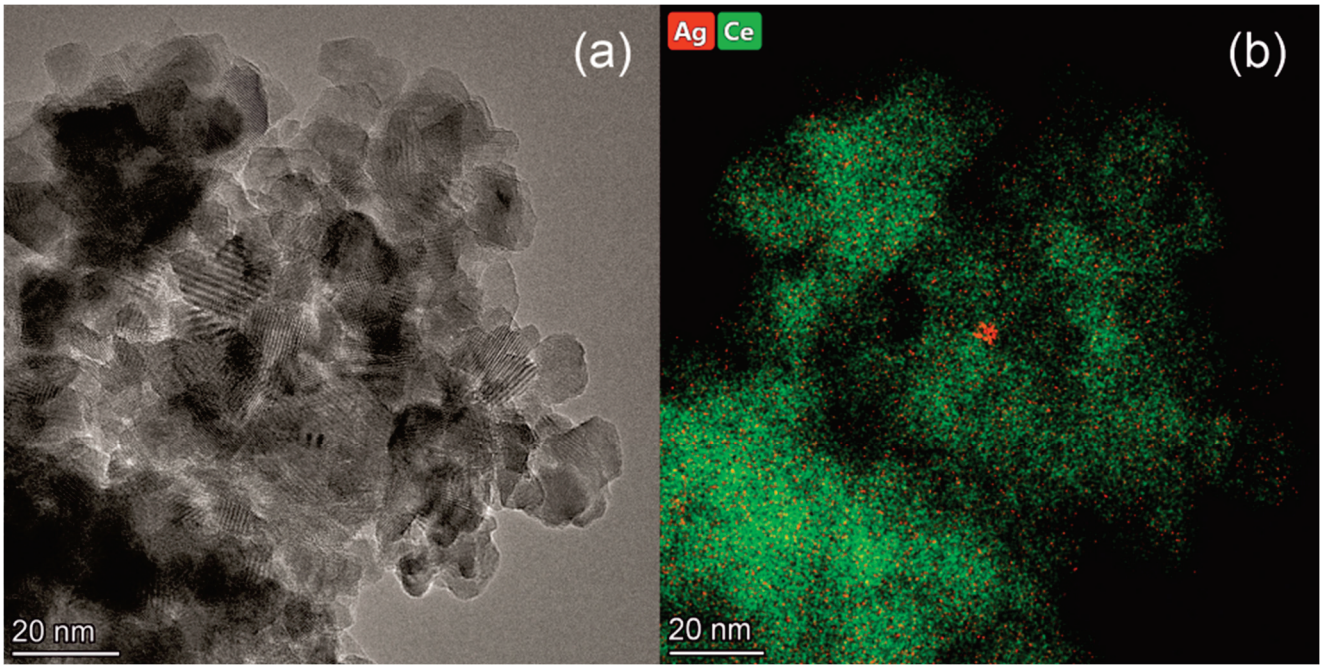

Figure 4. HRTEM image (**a**) and high resolution EDX mapping (**b**) for the Ag/CeO_2 sample.

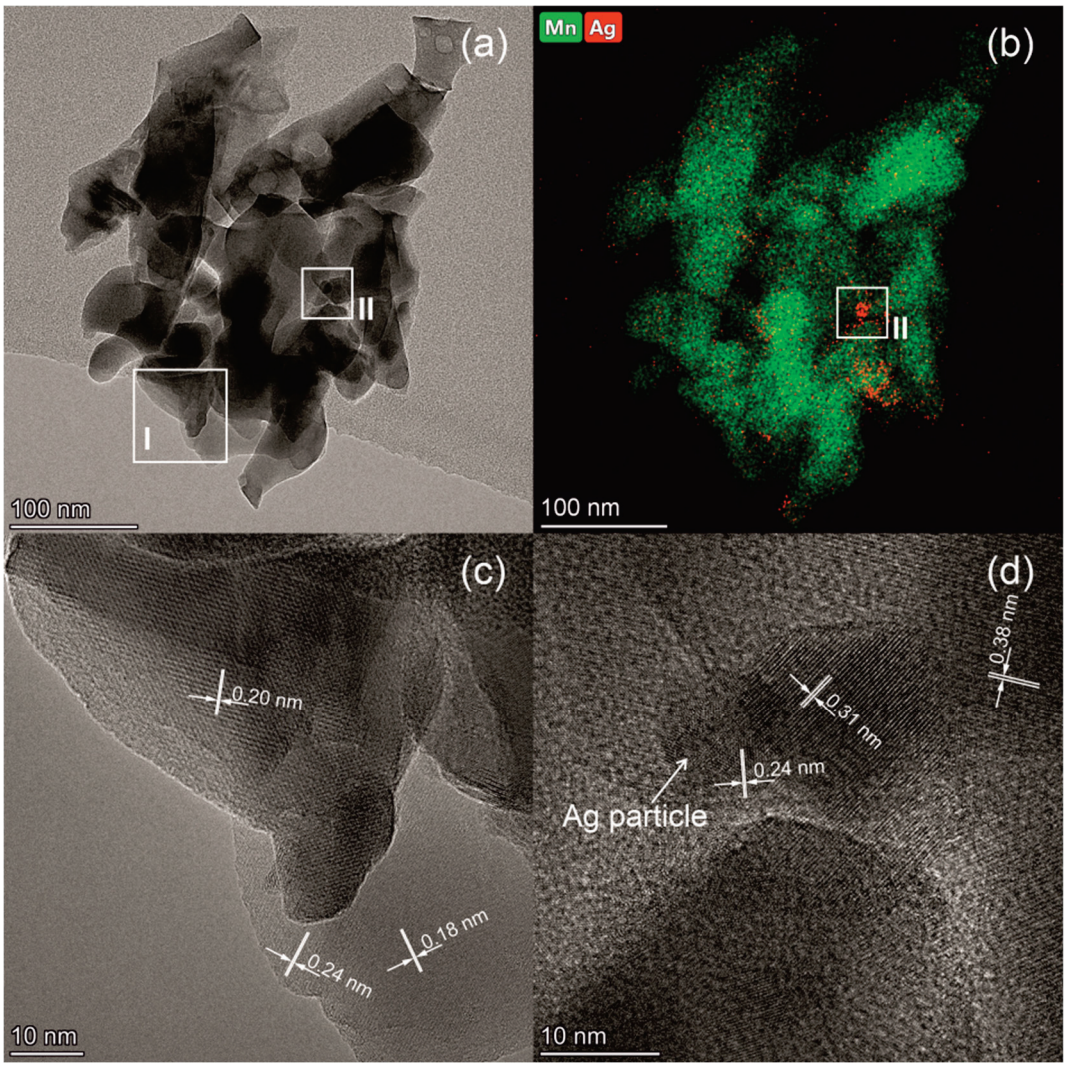

Figure 5. TEM (**a**), high resolution EDX mapping (**b**), and HRTEM of indicated regions I (**c**) and II (**d**) for the Ag/MnO_x sample.

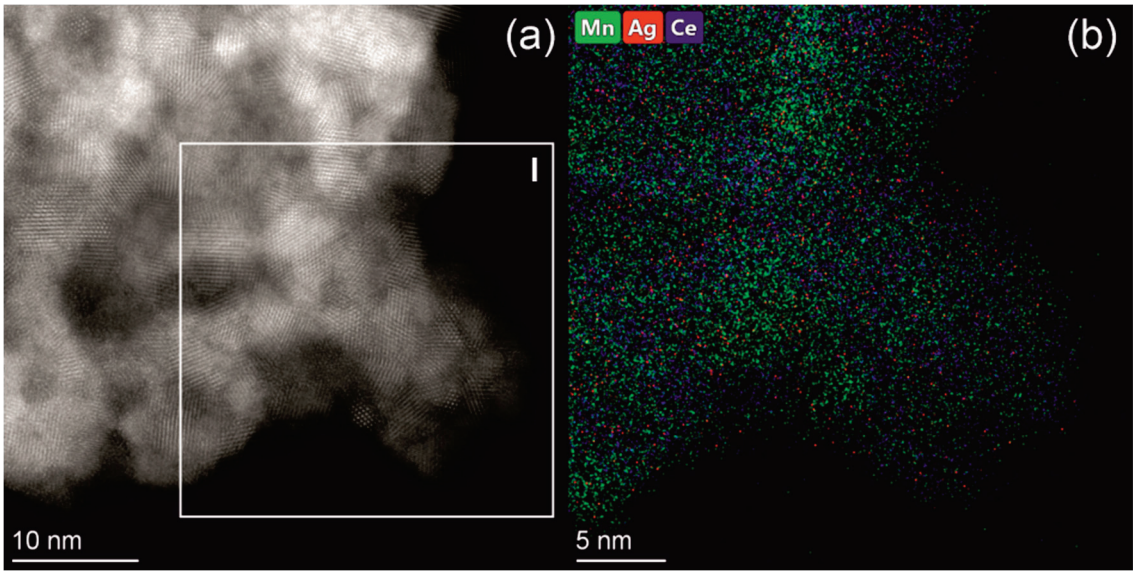

Figure 6. HRTEM image (**a**) and high resolution EDX mapping (**b**) taken from the indicated region I for the $Ag/CeMnO_x$ sample.

3.2.1. CeO_2 and Ag/CeO_2 Samples

According to the XRD data, the CeO_2 sample has a cubic fluorite-type phase with the lattice parameter *a* of 5.405 Å and the average XRD crystallite size of 13 nm. The formation of fluorite-type ceria is confirmed by Raman spectroscopy, with the structural defects being additionally indicated. Specifically, Raman spectrum for the CeO_2 support obtained under 532 nm laser contains the bands at 260, 404, 464, 560, 590 and 828 cm^{-1} (Figure 3a), while the one obtained under 785 nm laser is characterized by the bands at 276, 314, 410, 464, 556, 595, and 724 cm^{-1} (Figure 3b). The intense band at 464 cm^{-1} is attributed to the F2g band associated with the Ce–O stretching vibration in the [CeO_8] cubic subcell of ceria, and the weak bands located at 256–260, 404–410, and 590–595 cm^{-1} are referred to overtones [39]. The band at ~560 cm^{-1} is associated with the Ce^{3+} located in the immediate vicinity of the oxygen defect [39], the band at ~314 cm^{-1} is attributed to the displacement of oxygen atoms from the ideal positions of the fluorite lattice [38], and the band at 828 cm^{-1} is attributed to the surface peroxide O_2^{2-} species [39,40]. The presence of these bands indicates a defective structure of cerium oxide obtained by the citrate method.

For Ag/CeO_2 sample, no additional Ag-based phases were revealed by XRD, which is caused by the low Ag content as well as high dispersion of such phases. The lattice parameter *a* of the fluorite-type phase remains unchanged (5.405 Å), and the average crystallite size is 15 nm. These results are additionally confirmed by the HRTEM data (Figure 4) indicating the ceria crystallites of ~5 to 20 nm in size for the Ag/CeO_2 catalyst. According to the high resolution EDX analysis, silver is evenly distributed over the sample, however, in some places silver is concentrated as oxide species, which is reduced under the electron beam. The Raman spectroscopy does not reveal a significant effect of the Ag deposition on the ceria structure in the Ag/CeO_2 sample. Thus, a specific absorption below 200 cm^{-1} due to the Ag–O–Ce bond vibrations additionally appears in the spectra for the sample (Figure 3), while other bands remain intact.

3.2.2. MnO_x and Ag/MnO_x Samples

According to the XRD results, the MnO_x sample is characterized by the presence of two crystalline phases, namely, the tetragonal Mn_3O_4 and the cubic Mn_2O_3 in amounts of ~75 wt.% and ~25 wt.%, respectively (Figure 2, Table 2). The oxide phase crystallites formed in the MnO_x sample are noticeably larger than in the case of the CeO_2 sample. The Mn_2O_3 phase is rather well crystallized and characterized by the average XRD crystallite size of 61 nm. The Mn_3O_4 phase is less ordered and more dispersed, with the average crystallite size being 33 nm. The Raman spectroscopy data confirm the formation of Mn_3O_4 and Mn_2O_3 oxides and additionally reveal the presence of some MnO oxide in the MnO_x sample. Thus, the Raman spectrum for the MnO_x support obtained under 532 nm laser (Figure 3a) is characterized by an intense band at 647 cm^{-1} and weak bands at 263, 308, 360 and ~480 cm^{-1} characteristic of Mn_3O_4 with the spinel structure [41–44]. The intense band at 647 cm^{-1} is attributed to the A1g mode of the Mn–O stretching vibration for Mn^{2+} ions in tetrahedral coordination, and the weak bands at 263, 308, and 360 cm^{-1} are attributed to the Eg, A1g, B2g, and Eg modes, respectively [42]. The spectrum also contains week bands in the ranges of 150–240 cm^{-1} and 500–600 cm^{-1}, which are caused by other manganese oxide phases, i.e., Mn_2O_3 and Mn_5O_8. These phases are more reliably distinguished in the spectrum obtained under 785 nm laser (Figure 3b) due to the resonance effect of Raman scattering resulting in the presence of well-defined bands at 170, 262, 393, 477, 535 and 580 cm^{-1} attributed to Mn_5O_8 modes [45], and the bands at 191, 311 and 621sh cm^{-1} attributed to Mn_2O_3 [43,46,47], with those at 286, 367, and 648 cm^{-1} being assigned to Mn_3O_4 with a spinel structure [42,44]. The amount of the Mn_5O_8 phase seems to be negligible and is determined by Raman spectroscopy due to the high extinction coefficient.

Signs n.a. means not available due to the correct determination of a full width at half maximum is impossible.

The Ag introduction is accompanied by the increase in the relative Mn_2O_3 content up to 76 wt.% and the decrease in that of Mn_3O_4 up to 24 wt.% in the Ag/MnO_x sample

according to the XRD results. Besides, the Ag introduction results in the appearance of well-defined bands at 196, 308 and 625sh cm^{-1} attributed to Mn_2O_3 and at 170, 263, 533 and 576 cm^{-1} attributed to MnO in the spectrum for the Ag/MnO_x sample obtained under 532 nm laser (Figure 3a). In the spectrum obtained under 785 nm laser (Figure 3b), the relative intensities of the bands of Mn_2O_3 and MnO increase, with the additional bands assigned to Mn_2O_3 being distinguished at 191, 393, and 697 cm^{-1}, which is consistent with the increase in the Mn_2O_3 content in the sample according to the XRD data. The average XRD crystallite size for the main Mn_2O_3 phase is 52 nm, which is consistent with the presence of Mn_2O_3 particles revealed by TEM in the Ag/MnO_x sample (Figure 5), with their size varying from 20 to 100 nm. Besides, according to high resolution EDX mapping, the silver distribution in the sample is less uniform than for the CeO_2 sample. The mapping shows areas depleted (0.15–0.59 wt.%) and enriched (3–36 wt.%) with silver.

Some areas enriched with silver correspond to Ag particles (Figure 5, region II), however, most other areas enriched with silver correspond to oxidized silver species (Figure S1) in accordance with the XPS data (see Section 3.3 for details).

3.2.3. $CeMnO_x$ and $Ag/CeMnO_x$ Samples

The XRD data for the $CeMnO_x$ sample indicate the presence of only cubic phase with the fluorite structure, while individual phases of manganese oxides (MnO_2, Mn_2O_3, Mn_3O_4, or MnO) are not found. According to the XRD data, the average crystallite size of the fluorite-type phase is 7 nm in the $CeMnO_x$ sample, which is almost two times smaller than in the CeO_2 sample. At the same time, the parameter *a* of the fluorite phase of 5.406 Å indicates the presence of CeO_2 phase rather than the $Ce_{1-x}Mn_xO_2$ solid solution with the fluorite structure, which should be characterized by a noticeable compression of the crystal lattice due to the substitution of Ce^{4+}/Ce^{3+} ions by smaller Mn^{4+}/Mn^{3+} ions [48,49]. This finding was confirmed by the Raman spectroscopy and TEM data. The Raman spectra for $CeMnO_x$ sample contain two intense broad bands with maxima at 454 and 644 cm^{-1} in the case of 532 nm laser and at 459 and 647 cm^{-1} in the case of 785 nm laser. In both cases, absorption below 400 cm^{-1} is additionally observed as well as the additional shoulder peaks at 495, 410, 537, 553, 590, and 620–625 cm^{-1} can be distinguished. The indicated bands are caused by the individual CeO_2 and Mn_3O_4/Mn_2O_3 oxides. Such finding is consistent with the formation of undoped CeO_2 according to the XRD data analysis. A strong broadening of the bands suggests a high dispersion and/or distortion of the oxide phases presented in the $CeMnO_x$ sample in consistency with the HRTEM results indicating the formation a "patchwork" domain microstructure with rather small crystallite with sizes from 1.5 to 3 nm enriched by either Mn or Ce (Figure 6). The Mn/Ce atomic ratio is ~3/1 in some domains and ~1/2 in other domains. The interplanar spaces of ~0.33 and ~0.28 nm are primarily observed for both domain types that are typical for CeO_2 fluorite-type (JCPDS 34–0394) and cubic α-Mn_2O_3 bixbyite structures (JCPDS 41–1442), with the latter being the oxygen-deficient fluorite-related structure.

The Ag introduction does not affect the crystallite size of fluorite phase and does not lead to the appearance of additional crystalline phases in the $Ag/CeMnO_x$ sample. At the same time, the Ag introduction leads to a slight increase in the parameter *a* of the fluorite-type structure up to 5.413 Å in the Ag/CeMn sample (Table 2). This finding can be attributed to the formation of Ce^{3+} ions characterized by larger ionic radius (i.r.) (i.r. = 1.28 Å for CN = 8) than for Ce^{4+} ions (i.r. = 0.97 Å for CN = 8 [32]). The latter can result from the "bulk oxygen pump out" effect caused by the reverse spillover of oxygen from CeO_2 to Ag [50,51]. The Raman spectroscopy data reveal that the Ag introduction results in some changes in the range of 500–700 cm^{-1}, which confirms the Ce^{3+} formation in ceria (appearance of the band at ~553 cm^{-1} assigned to the defect-induced D1 mode) as well as indicates the change in the relative content of Mn_3O_4/Mn_2O_3 manganese oxides in the $Ag/CeMnO_x$ sample. According to the high resolution EDX mapping, silver is rather evenly distributed throughout the sample, with the XPS data indicating the primarily formation of Ag^+ ions dispersed on the surface or subsurface of the oxide support matrix

(see Section 3.3 for details). In some parts, isolated silver nanoparticles are observed (Figure S2).

Therefore, the use of the citrate method to prepare the $CeMnO_x$ support provides the formation of fluorite-type oxide nanocomposite with the "patchwork" nanodomain microstructure. This is caused by a good homogeneity achieved through mixing of the initial components at the molecular level in the gel formed, with the limited solubility of cerium and manganese oxides resulting in the system disintegration under thermal treatment in air to form nanodomains enriched with either Mn or Ce.

3.3. Surface Composition of the SUPPORTEd Ag Catalysts

The surface composition of the Ag catalysts was additionally studied by XPS. Table 3 shows atomic ratios of the elements on the sample surfaces. According to the XPS data, the Ce/Mn as well as Ag/Ce, Ag/Mn, and Ag/(Ce+Mn) atomic ratios on the surface of the $Ag/CeMnO_x$ sample correspond to the nominal ones according to XRF data. This indicates the uniform distribution of Ce, Mn and Ag in the sample, which is consistent with the oxide support microstructure formed by the 1.5–3 nm nanodomains enriched with either Mn or Ce and even Ag distribution over the sample revealed by HRTEM and EDX. For the Ag/CeO_2 sample, the Ag/Ce surface atomic ratio is also rather close to the nominal one, but the Ag/Mn surface atomic ratio for the Ag/MnO_x sample is significantly lower than the nominal value. The observed deviation of the surface Ag content is associated with the formation of rather large silver oxide particles (10–50 nm) in the samples (Figure S2).

Table 3. The binding energy $E_b(Ag3d_{5/2})$, kinetic energy of the $AgM_4N_{4.5}N_{4.5}$ peak, and modified Auger parameter; AgMNN and Ag3d peak area ratio for all samples.

Sample	$Ag3d_{5/2}$, eV	$AgM_4N_{4.5}N_{4.5}$, eV	α′, eV	AgMNN/Ag3d
Ag/Ce	368.0	355.5	723.5	0.76
Ag/Mn	368.1	356.7	724.8	0.64
Ag/CeMn	367.6	356.1	723.7	0.57

3.3.1. Oxidation States of Cerium and Manganese

Figure 7 shows the Ce3d spectra for Ag/CeO_2 and $Ag/CeMnO_x$ samples. Based on the literature data [52], the Ce 3d spectra were fitted with several peaks corresponding to Ce^{4+} (V, V″,V‴ and U, U″, U‴ peaks) and Ce^{3+} (V_0,V′ and U_0,U′ peaks) species. The relative fraction of Ce^{3+} species calculated as a ratio of the V_0,V′ and U_0,U′ peak areas to the one of the overall Ce3d peak was ~10% for both samples.

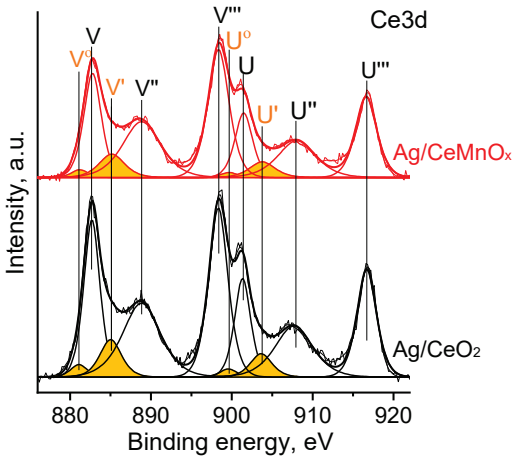

Figure 7. Ce3d spectra for Ag/CeO_2, $Ag/CeMnO_x$. The V_0,V′ and U_0,U′ peaks corresponding to Ce^{3+} species are marked in orange color.

To correctly interpret the manganese charging state, the Mn2p and Mn3s spectra were analyzed (Figure 8). The $Mn2p_{3/2}$ peak maximum is characterized by $E_b(Mn2p_{3/2})$ = 641.4 eV. Such E_b is often observed for Mn_2O_3 and Mn_3O_4 oxides [53,54]. Analysis of the splitting between the $Mn2p_{1/2}$ peak maximum and shake-up satellite gives ΔE_{sat} = 10.3 eV. Such ΔE_{sat} value also indicates the formation of Mn_2O_3 and Mn_3O_4 oxides [55]. Analysis of the multiplet splitting of the Mn3s spectra was also used to identify the Mn oxidation state. For Ag/Mn and $Ag/CeMnO_x$ samples, the ΔE is ~5.4–5.6 eV (Figure 8b). According to the literature data, such Mn3s multiplet splitting is typical for Mn_2O_3 and Mn_3O_4 oxides [53–55]. Thus, analysis of the Mn2p and Mn3s core-level spectra indicates the preferential formation of Mn^{3+} species in the composition of Mn_2O_3 and/or Mn_3O_4 oxides.

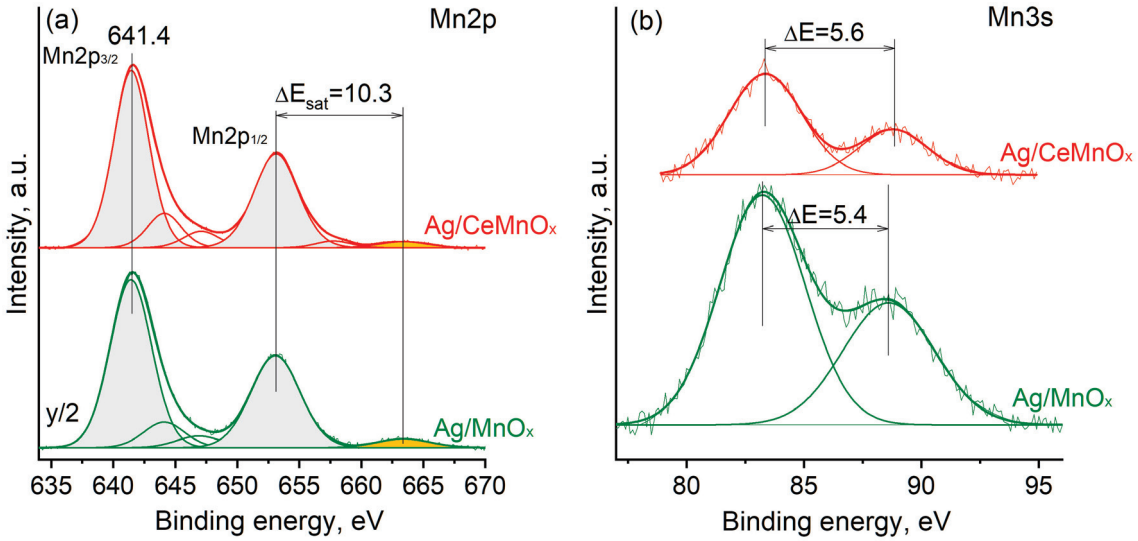

Figure 8. Mn2p (**a**) and Mn3s (**b**) spectra for Ag/MnO_x and $Ag/CeMnO_x$. To facilitate the comparison, the intensity of the Mn2p spectrum for the Ag/Mn sample was reduced 2 times.

3.3.2. Oxidation State of Silver

To analyze the Ag oxidation state in the samples, the core-level Ag3d spectra and Auger spectra AgMNN were collected (Figure 9). The Ag3d spectra for all samples can be fitted with one Ag3d spin-orbit doublet peak with a binding energy of the $Ag3d_{5/2}$ peak $E_b(Ag3d_{5/2})$ being in the range of 367.6–368.1 eV. The $E_b(Ag3d_{5/2})$ = 367.6 eV is usually considered characteristic of the oxidized silver species, while the $E_b(Ag3d_{5/2})$ values of ~368.0 and 368.1 eV are related to the metallic silver species [56,57]. However, it is known that the exact $E_b(Ag3d_{5/2})$ value is rather sensitive to the size of the silver particles, their interaction with the support and possible charging effects. To get reliable data on the oxidation state of silver in the samples, the modified Auger parameter (α′) calculated as a sum of the binding energy of $Ag3d_{5/2}$ peak and the kinetic energy of $M_4N_{4,5}N_{4,5}$ Auger peak were considered. Figure 7b shows the corresponding Auger spectra. Analysis of the α′ values (Table 3) indicates that in the Ag/MnO_x sample, silver exists in the oxidized state similar to the one in Ag_2O species [56,57]. Ag/CeO_2 and $Ag/CeMnO_x$ samples are characterized by the lower α′ value. Such α′ value was detected for the Ag^+ ions in the composition of inorganic salts [33,57]. Thus, the formation of Ag^+ ions dispersed on the surface or in the subsurface region of the oxide support matrix can be proposed. The ratio of the AgMNN and Ag3d peak areas is rather similar for all samples. Slightly higher AgMNN/Ag3d value for the Ag/CeO_2 sample might indicate higher degree of surface localization of the silver species.

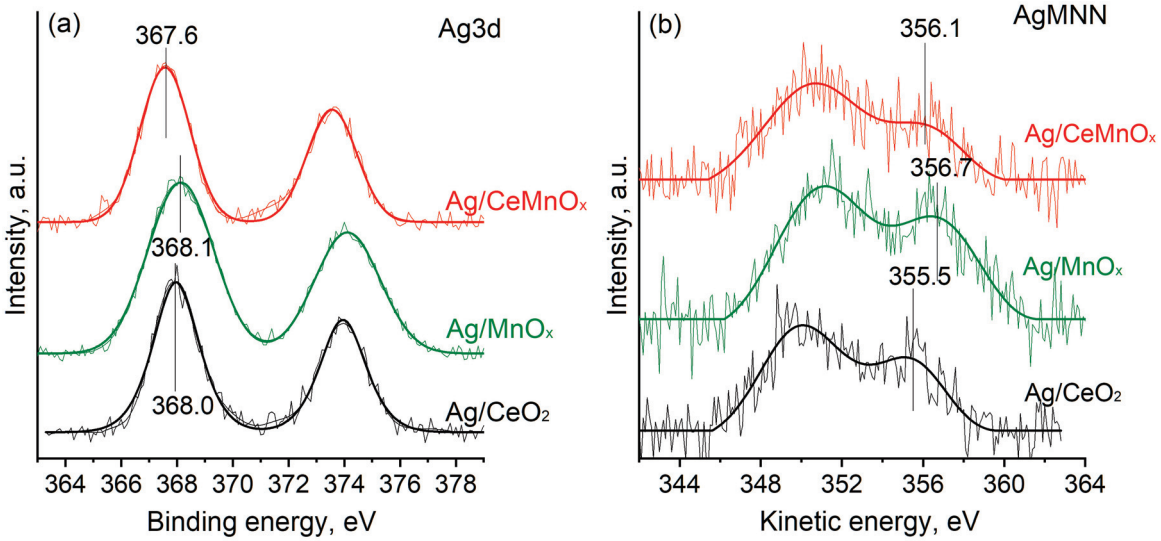

Figure 9. Ag3d (**a**) and AgMNN (**b**) spectra for Ag/CeO_2, Ag/MnO_x, and $Ag/CeMnO_x$.

3.4. Catalytic Performance

The obtained catalysts and the related support oxides were investigated in the NO SCR with C_3H_6 in the temperature range from 100 to 500 °C using H_2 2.9 vol.% as a reductant in the reaction mixture. All the figures herein reported are related to catalytic tests carried out in presence of hydrogen in the reaction mixture, unless differently specified.

Figure 10 shows the results of HC-SCR with propene over the Ag supported catalysts. The NO conversion over these catalysts declined in as follows: $Ag/CeMnO_x$ (44%) > Ag/MnO_x (37%) > Ag/CeO_2 (28%).

In the C_3H_6-SCR process, the $Ag/CeMnO_x$ catalyst shows a sharp increase in NO_x conversion from 250 °C, reaching maximum NO_x conversion of 44% at 300 °C, and it is much active as compared to the Ag/MnO_x and Ag/CeO_2 catalysts (Figure 10a). Subsequently, the NO_x conversion gradually decreases at 350 °C. This indicates that the combination of Ce and Mn oxides plays an important role in improving the HC-SCR activity at low temperatures. Figure 10b,c show the selectivity to N_2 and N_2 yield in C_3H_6-SCR: the Ag/MnO_x catalyst exhibits the highest selectivity to N_2 in the whole temperature range (250–500 °C) reaching values around 97–98% between 300–500 °C, while the N_2 yield that was close to 35%, at 300–350 °C, decreases with increasing temperature (>350 °C) indicating that undesired products such as N_2O are formed faster at higher temperatures. $Ag/CeMnO_x$ shows similar trend to Ag/MnO_x as for the N_2 selectivity at 250–300 °C, achieving values close to 90%. However, it suffered a fast decline of N_2 yield at $T \geq 350$ °C. Ag/CeO_2 is the worst catalyst in terms of NO conversion and selectivity to N_2.

In the temperature range of 175–500 °C, a high contribution due to the C_3H_6 oxidation is observed for all the catalysts, with more than 80% of conversion being achieved at 175 °C for the $Ag/CeMnO_x$. By comparing the NO and C_3H_6 conversion curves, it emerged that the propene oxidation by the oxygen present in the reaction mixture occurs alongside the C_3H_6-SCR of NO and above 350 °C (when the NO conversion declines) becomes the main reaction.

For comparison reasons, the C_3H_6-SCR of NO was also investigated for the CeO_2, MnO_x and $CeMnO_x$ supports (Figure 11).

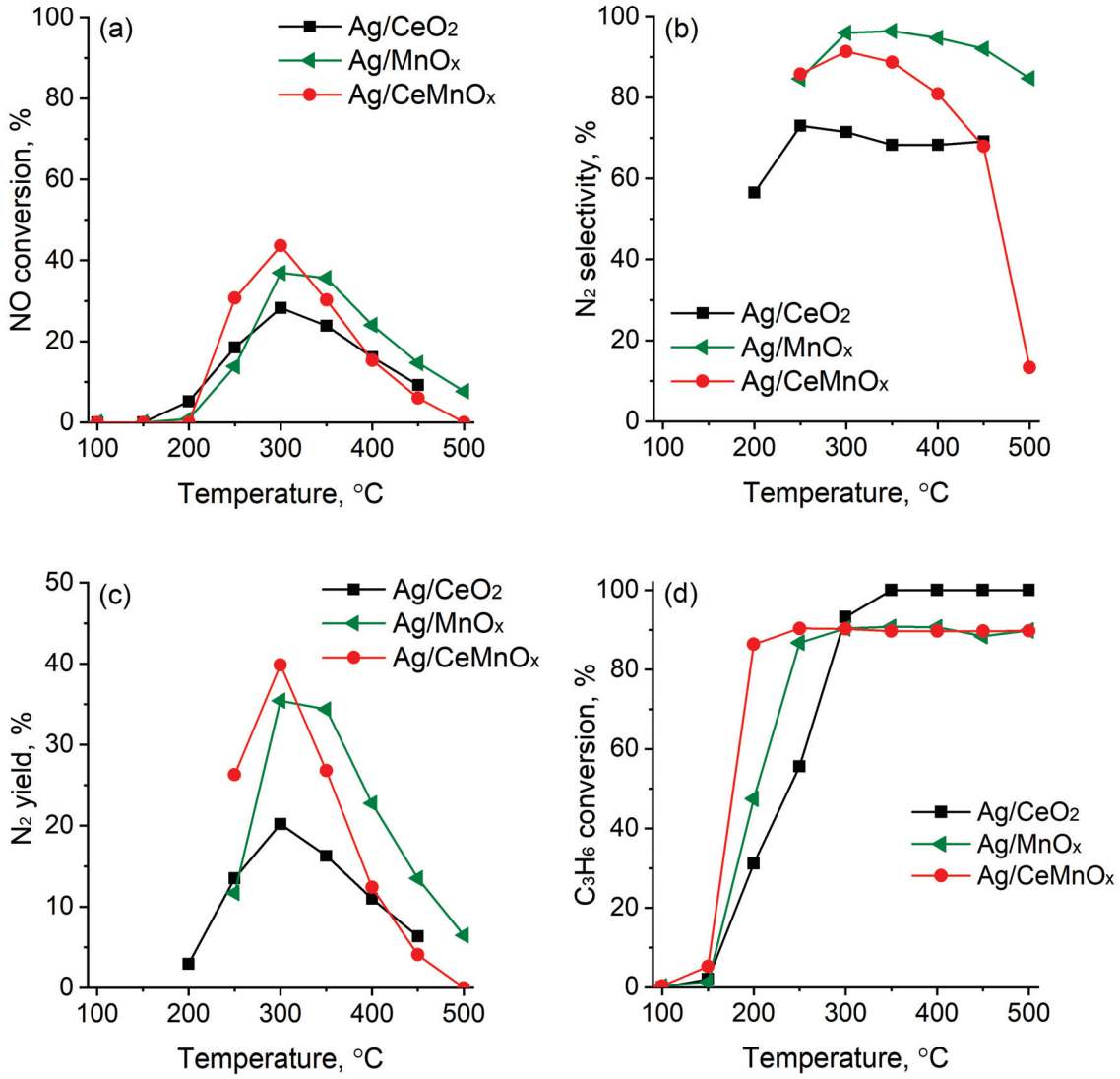

Figure 10. NO_x conversion (**a**), selectivity to N_2 (**b**), N_2 yield (**c**), and C_3H_6 conversion (**d**) over Ag/MnO_x, Ag/CeO_2 and $Ag/CeMnO_x$ catalysts.

According to the results, $CeMnO_x$ was the most active among the investigated oxides, although the NO conversion is relatively low in the absence of Ag particles, as can be seen in Figure 11a. The values registered for CeO_2 and MnO_x are even lower than those for $CeMnO_x$. A similar trend was observed as far as N_2 selectivity and yield. Therefore, the results imply that Ag loading significantly improves the NO SCR.

Figures 10d and 11d show the C_3H_6 conversion curves in C_3H_6-SCR at different temperatures for the samples studied. For the $CeMnO_x$ and MnO_x samples, the C_3H_6 conversion steadily increases between 150 and 200 °C reaching 100% at 250–300 °C (Figure 11d). For CeO_2 a sharp increase occurs at 300–400 °C and a total C_3H_6 conversion is achieved only at 500 °C. Conversely, as above mentioned, the silver catalysts exhibit higher activity than the corresponding supports reaching ~100% conversion at 250–350 °C (Figure 10d). It is worth noting that in all cases, for Ag catalysts and the supports, CO_2 was the main product detected by the C_3H_6 oxidation with negligible amounts of CO (less than 1–2%), according to the carbon mass balance. However, we cannot exclude that secondary products, such as acetic acid (see below Scheme 1), can be formed on the catalyst surface and they are fast oxidized to CO_2.

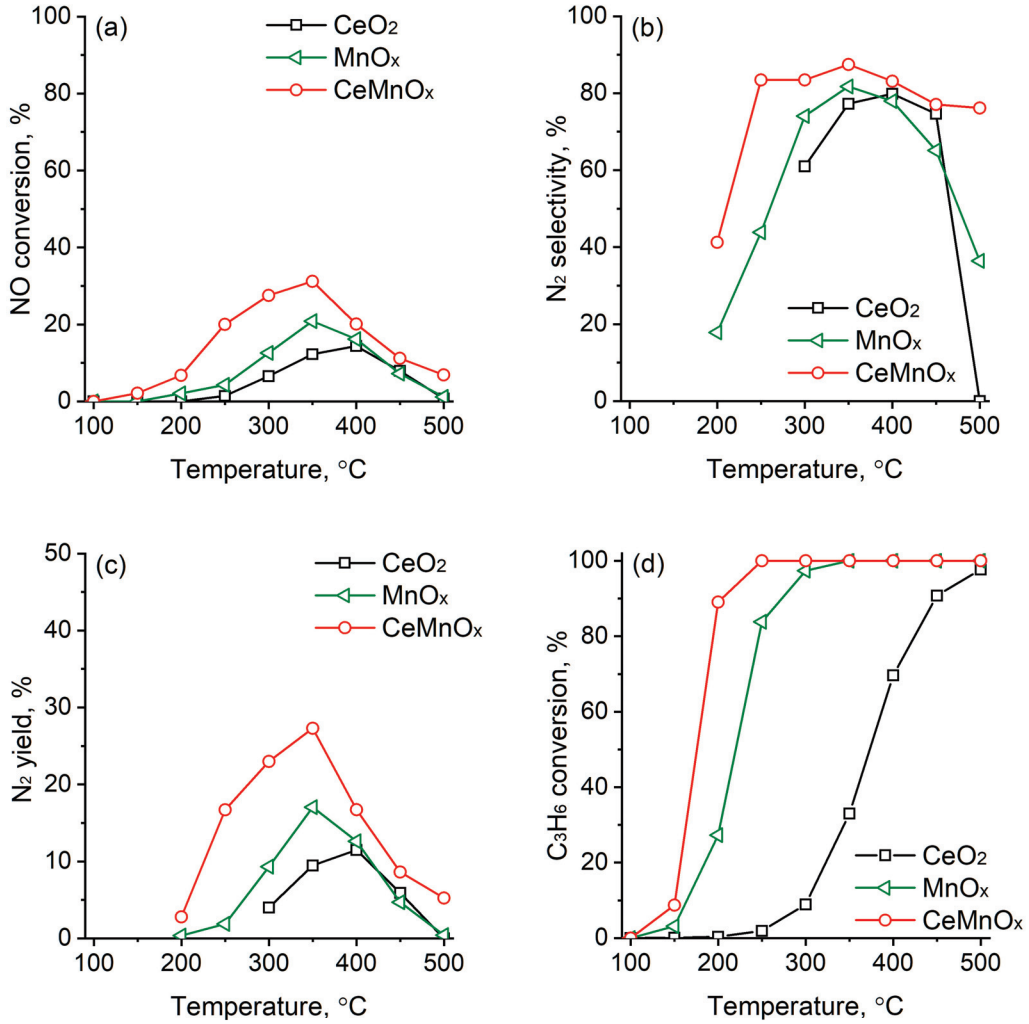

Figure 11. NO_x conversion (**a**), selectivity to N_2 (**b**), N_2 yield (**c**), and C_3H_6 conversion (**d**) over MnO_x, CeO_2 and $CeMnO_x$ oxide supports.

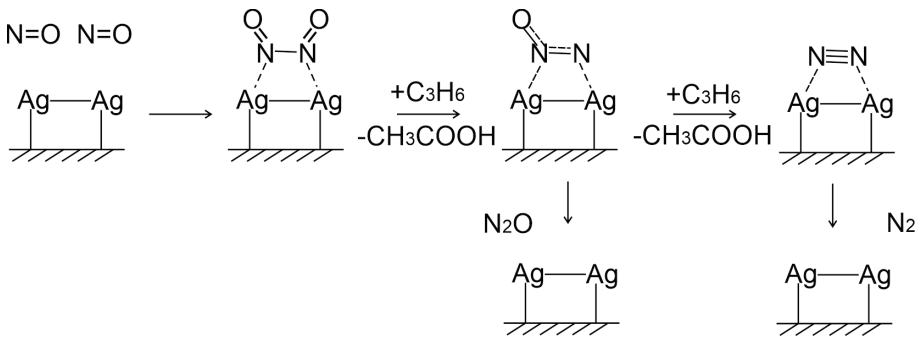

Scheme 1. Proposed scheme of NO reduction on Ag_2^+ clusters.

An important aspect to consider is the presence of H_2 in the NO-C_3H_6 reaction mixture [27]. In fact, it is well known that the addition of H_2 determines a promoting effect on the C_3H_6-SCR ("hydrogen effect") [58]. Such effect results in an increased percentages of strongly adsorbed and decomposed nitrates on the catalyst surface and in the conversion of these adsorbed species into –NCO and –CN, which are supported to be the key surface intermediates for the HC-SCR reaction [59,60].

In this respect, the reaction mixture containing 2.9% of hydrogen was used as a standard. To study the effect of hydrogen addition, the catalytic properties of $Ag/CeMnO_x$

and Ag/MnO_x samples, as the most perspective, were studied using H_2-free reaction mixture. Figure 12 shows the results obtained. The activity and selectivity of the Ag/MnO_x catalyst were notably lower without hydrogen in all temperatures studied (see Figure 10 for comparison). Whereas, the $Ag/CeMnO_x$ catalyst shows similar catalytic performances in the absence of hydrogen as compared with those in the presence of hydrogen.

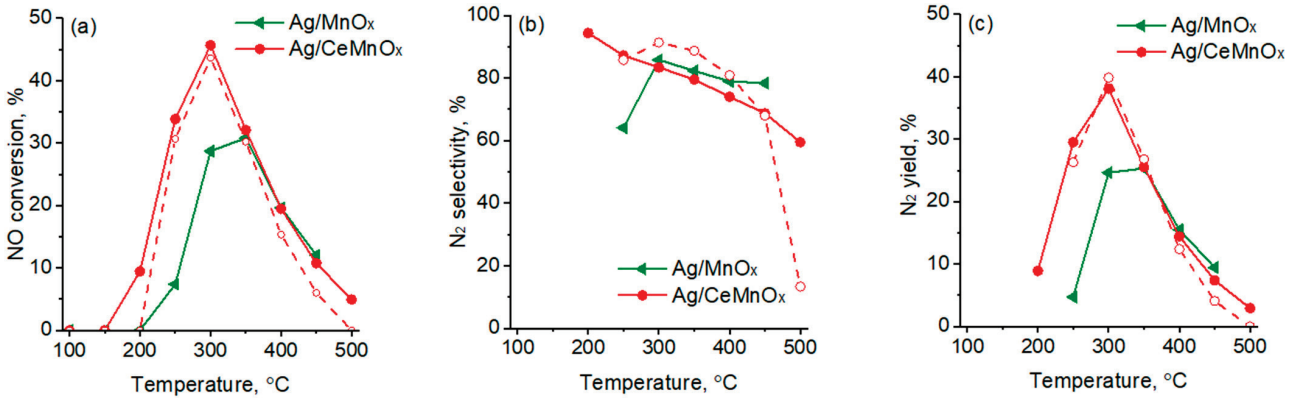

Figure 12. NO_x conversion (**a**), selectivity to N_2 (**b**), and N_2 yield (**c**) over Ag/MnO_x and $Ag/CeMnO_x$ catalysts without H_2 addition in the reaction mixture. Open symbols and dash line are data registered in presence of H_2 over the $Ag/CeMnO_x$ catalyst, reported for comparison.

To study the catalyst stability, the samples were thermally aged. Figure 13 shows the results on SCR study using standard reaction mixture obtained for aged samples. According to the data obtained, the thermal aging results in deactivation of the Ag/CeO_2 sample and notable decrease in catalytic efficiency of the Ag/MnO_x sample, while the performances of the $Ag/CeMnO_x$ catalyst was practically unchanged, which was assigned to a rather high stability of its phase composition and textural characteristics as compared with those of Ag/CeO_2 and Ag/MnO_x samples (for details see Supplementary Materials, Tables S1 and S2).

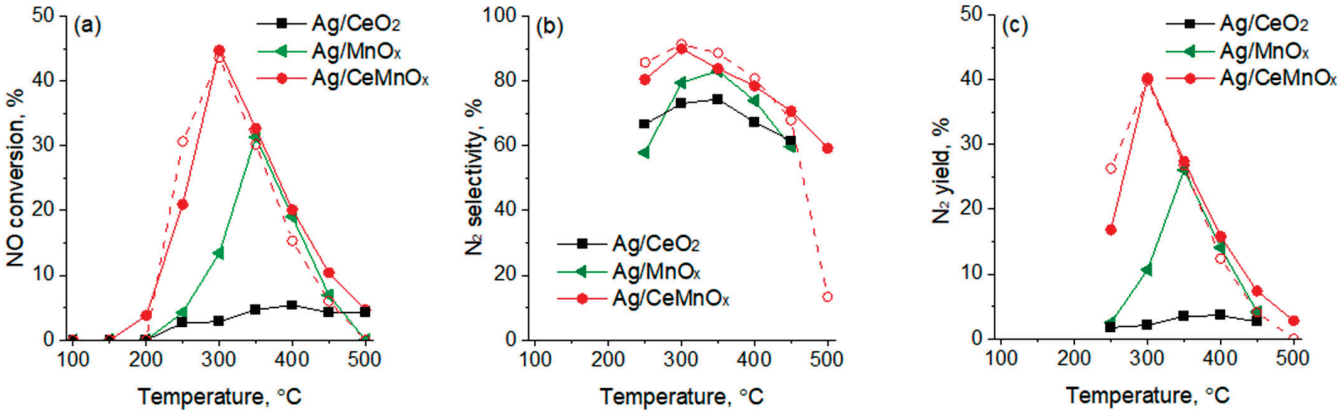

Figure 13. NO_x conversion (**a**), selectivity to N_2 (**b**), and N_2 yield (**c**) over aged Ag/MnO_x, Ag/CeO_2 and $Ag/CeMnO_x$ catalysts. Open symbols and dash line are data for the $Ag/CeMnO_x$ catalyst (not aged), reported for comparison.

Thereby, the results obtained indicate that the $1\%Ag/CeMnO_x$ showed the highest catalytic efficiency in both catalytic properties and stability among studied catalyst, with its activity and selectivity being comparable or superior as compared with those previously reported for $1\%Ag/CeZrO_x$ catalyst (Table 4) [27]. Thus, the $1\%Ag/CeMnO_x$ showed comparable NO conversion of 46% and significantly higher N_2 selectivity of 86% as compared with 50% NO conversion and 30% N_2 selectivity $1\%Ag/CeZrO_x$ under H_2-free conditions those resulting in superior overall efficiency (40% N_2 yield vs 15% N_2 yield). The hydrogen addition in the reaction mixture results in notable improvement of both activity

and selectivity of the 1%Ag/$CeZrO_x$ catalyst, with the NO conversion increasing up to 80%, N_2 selectivity increasing up to 60%, and N_2 yield increasing up to 48%. The effect of hydrogen addition on the 1%Ag/$CeMnO_x$ catalyst performance was less noticeable, with the NO conversion decreasing up to 44%, N_2 selectivity increasing up to 91%, and N_2 yield remaining 40%. Despite the slightly inferior overall efficiency of the 1%Ag/$CeMnO_x$ catalyst in these conditions, it showed high stability after aging, which makes it promising for further CH-SCR catalyst development.

Table 4. Comparison of catalytic efficiency (of the 1%Ag/$CeMnO_x$ catalysts with similar catalysts available literature data.

Catalyst	Reaction Conditions					NO Reduction Efficiency			Ref.
	NO, ppm	O_2, vol.%	C_3H_6, vol.%	H_2, vol.%	WHSV, mL g^{-1} h^{-1}	X(NO), %	S(N_2), %	Y(N_2), %	
1%Ag/$CeMnO_x$	1000	10	3600	2.9	25,000	44	91	40	This work
1%Ag/$CeMnO_x$	1000	10	3600	-	25,000	46	86	40	This work
1%Ag/$CeMnO_x$ (aged)	1000	10	3600	-	25,000	44	90	40	This work
1%Ag/$CeZrO_x$	700	3	700	0.5	45,000	80	60	48	[28]
1%Ag/$CeZrO_x$	700	3	700	-	45,000	50	30	15	[28]

WHSV is the weight hourly space velocity; X(NO) is NO conversion, S(N_2) is N_2 selectivity and Y(N_2) is yield.

As previously discussed and reported in literature [58], different Ag species such as isolated silver cations (Ag^+), oxidized silver clusters ($Ag_n^{\delta+}$), and metallic silver clusters (Ag_n^0) can been observed in the Ag catalysts and HC-SCR catalysts; the oxidized silver species (Ag^+ and/or $Ag_n^{\delta+}$) play an important role, in fact they are proposed to be the active species in the NO-SCR reaction with propene, whereas the Ag_n^0 metallic clusters are responsible for the nonselective oxidation of hydrocarbons. Thus, NO adsorption with dimer formation was shown to be favourable on the supported silver Ag_2^+ clusters followed by its reduction with HC or alcohol to form N_2 and N_2O [61]. The NO reduction activity was clarified to be controlled by partial oxidation of C_3H_8 mainly to surface acetates [59]. Scheme 1 presents the proposed scheme of NO reduction on $Ag_n^{\delta+}$, specifically Ag_2^+, clusters based on the literature data.

Based on the so far reported literature, the catalytic performance of supported Ag catalysts is controlled by many factors, including morphological, structural and electronic ones. In the present work, the citrate sol-gel method has produced a mixed oxide $CeMnO_x$ (with molar ratio Ce/Mn = 1) with "patchwork" nanodomain microstructure, where silver is uniformly distributed as Ag^+ and/or $Ag_n^{\delta+}$ species that are supposed provide NO adsorption to form N_2O_2 dimers that are subsequently reduced with propylene to form N_2 at low temperatures. At high temperatures (>300 °C), the competitive total propylene oxidation seems to lead to the decrease in the catalyst activity in the NO reduction.

4. Conclusions

The Ag/CeO_2, Ag/MnO_x, and $Ag/CeMnO_x$ catalyst with 1 wt.% Ag were successfully prepared using a combination of citrate sol-gel method for support synthesis and incipient wetness impregnation with $[Ag(NH_3)_2]NO_3$ aqueous solution to deposit the active component. The used approaches provided the formation in the $CeMnO_x$ of a characteristic "patchwork" domain microstructure that along with the presence of well dispersed $Ag^+/Ag_n^{\delta+}$ species strongly interacting with the support, produced a catalyst with higher NO-SCR performance and perfect stability compared to Ag/CeO_2 and Ag/MnO_x systems, achieving 44% NO conversion at 300 °C under a WSHV of 25,000 mL g^{-1} h^{-1} and selectivity to N_2 close to 90%. At temperatures above 300 °C, a high contribution from the C_3H_6 oxidation was observed for all catalysts. Since it is well agreed that for an efficient NO SCR catalyst it is required to increase the NO conversion values and to expand the temperature range of operation, it can be concluded that this achievement may be associated with the

investigation of different Ag loadings and as well with the decrease of CeO_2 molar fraction in a $CeMnO_x$ mixed oxide, while maintaining its microstructure.

Supplementary Materials: The following supporting information can be downloaded at: https://www.mdpi.com/article/10.3390/nano13050873/s1, Figure S1: HAADF STEM (a) and high resolution EDX mapping of indicated region (b) for the Ag/MnO_x sample; Figure S2: HRTEM image (a) and high resolution EDX mapping (b) for the $Ag/CeMnO_x$ sample. Table S1: Specific surface area (SSA) and total pore volume (V) of supports and catalysts determined by low-temperature nitrogen adsorption/desorption data; Table S2: Phase composition of aged samples and characteristics of their crystalline phases according to XRD data.

Author Contributions: Conceptualization, O.V.V. and L.F.L.; investigation, E.L.G., T.S.K., M.V.G., L.C., D.Y.S., G.P., L.S.K., O.A.S.; formal analysis, E.L.G., T.S.K., M.V.G., D.Y.S., L.C., G.P., L.S.K., O.A.S.; writing—original draft preparation, E.L.G., T.S.K.; project administration, O.V.V. and L.F.L. All authors have read and agreed to the published version of the manuscript.

Funding: This work was financially supported by the Ministry for Science and Education of the Russian Federation (Project No. 075-15-2021-1388) and by the Italian Ministry of Foreign Affairs and International Cooperation ("Progettazione di Catalizzatori Attivi a base di Ag-Pt depositati su Ce e Mn modificati con Y per il Post-Trattamento dei Gas di Scarico emessi dai Motori Diesel" Prot. MAE01538512021-10-26).

Data Availability Statement: No applicable.

Acknowledgments: The TEM studies were carried out using facilities of the shared research center "National center of investigation of catalysts" at Boreskov Institute of Catalysis. The authors acknowledge V.A. Svetlichnyi (Tomsk State University) for Raman spectroscopy study and M.A. Salaev (Tomsk State University) for language review.

Conflicts of Interest: The authors declare no conflict of interest.

References

1. Boretti, A. Advantages and Disadvantages of Diesel Single and Dual-Fuel Engines. *Front. Mech. Eng.* **2019**, *5*, 64. [CrossRef]
2. Reşitolu, I.A.; Altinişik, K.; Keskin, A. The pollutant emissions from diesel-engine vehicles and exhaust aftertreatment systems. *Clean Technol. Environ. Policy* **2015**, *17*, 15–27. [CrossRef]
3. Salaev, M.A.; Kulchakovskaya, E.V.; Liotta, L.F.; Vodyankina, O.V. Bimetallic Ag-based catalysts for low-temperature SCR: Quo vadis? *Appl. Catal. A* **2022**, *644*, 118815. [CrossRef]
4. Rodríguez-Fernández, J.; Tsolakis, A.; Ahmadinejad, M.; Sitshebo, S. Investigation of the deactivation of a NO_x-reducing hydrocarbon-selective catalytic reduction (HC-SCR) catalyst by thermogravimetric analysis: Effect of the fuel and prototype catalyst. *Energy Fuels* **2010**, *24*, 992–1000. [CrossRef]
5. Mrad, R.; Aissat, A.; Cousin, R.; Courcot, D.; Siffert, S. Catalysts for NO_x selective catalytic reduction by hydrocarbons (HC-SCR). *Appl. Catal. A* **2015**, *504*, 542–548. [CrossRef]
6. Gómez-García, M.A.; Pitchon, V.; Kiennemann, A. Pollution by nitrogen oxides: An approach to NO_x abatement by using sorbing catalytic materials. *Environ. Int.* **2005**, *31*, 445–467. [CrossRef]
7. Worch, D.; Suprun, W.; Gläser, R. Supported transition metal-oxide catalysts for HC-SCR $DeNO_x$ with propene. *Catal. Today* **2011**, *176*, 309–313. [CrossRef]
8. Napolitano, P.; Liotta, L.F.; Guido, C.; Tornatore, C.; Pantaleo, G.; La Parola, V.; Beatrice, C. Insights of Selective Catalytic Reduction Technology for Nitrogen Oxides Control in Marine Engine Applications. *Catalysts* **2022**, *12*, 1191. [CrossRef]
9. Liu, W.; Long, Y.; Zhou, Y.; Liu, S.; Tong, X.; Yin, Y.; Li, X.; Hu, K.; Hu, J. Excellent low temperature NH_3-SCR and NH_3-SCO performance over Ag-Mn/Ce-Ti catalyst: Evaluation and characterization. *Mol. Catal.* **2022**, *528*, 112510. [CrossRef]
10. Xu, J.; Qin, Y.; Wang, H.; Guo, F.; Xie, J. Recent advances in copper-based zeolite catalysts with low-temperature activity for the selective catalytic reduction of NO_x with hydrocarbons. *New J. Chem.* **2020**, *44*, 817–831. [CrossRef]
11. Miyadera, T. Alumina-supported silver catalysts for the selective reduction of nitric oxide with propene and oxygen-containing organic compounds. *Appl. Catal. B* **1993**, *2*, 199–205. [CrossRef]
12. Zhang, X.W.; Su, Y.a.-X.; Cheng, J.H.; Lin, R.; Wen, N.N.; Deng, W.Y.; Zhou, H. Effect of Ag on $deNO_x$ performance of SCR-C_3H_6 over Fe/Al-PILC catalysts. *J. Fuel Chem. Technol.* **2019**, *47*, 1368–1378. [CrossRef]
13. Grabchenko, M.V.; Mamontov, G.V.; Zaikovskii, V.I.; Parola VLa Liotta, L.F.; Vodyankina, O.V. The role of metal–support interaction in Ag/CeO_2 catalysts for CO and soot oxidation. *Appl. Catal. B* **2019**, *260*, 118148. [CrossRef]
14. Cao, F.; Xiang, J.; Su, S.; Wang, P.; Hu, S.; Sun, L. Ag modified Mn-Ce/γ-Al_2O_3 catalyst for selective catalytic reduction of NO with NH_3 at low-temperature. *Fuel Process. Technol.* **2015**, *135*, 66–72. [CrossRef]

15. Meunier, F.C.; Breen, J.P.; Zuzaniuk, V.; Olsson, M.; Ross, J.R.H. Mechanistic aspects of the selective reduction of NO by propene over alumina and silver-alumina catalysts. *J. Catal.* **1999**, *187*, 493–505. [CrossRef]
16. Kannisto, H.; Ingelsten, H.H.; Skoglundh, M. Ag-Al_2O_3 catalysts for lean NO_x reduction –Influence of preparation method and reductant. *J. Mol. Catal. A Chem.* **2009**, *302*, 86–96. [CrossRef]
17. Andreoli, S.; Deorsola, F.A.; Pirone, R. MnO_x-CeO_2 catalysts synthesized by solution combustion synthesis for the low-temperature NH_3-SCR. *Catal. Today* **2015**, *253*, 199–206. [CrossRef]
18. Sun, H.; Park, S.J. Recent advances in MnO_x/CeO_2-based ternary composites for selective catalytic reduction of NO_x by NH_3: A review. *Catalysts* **2021**, *11*, 1519. [CrossRef]
19. Ma, Y.; Mu, B.; Yuan, D.; Zhang, H.; Xu, H. Design of MnO_2/CeO_2-MnO_2 hierarchical binary oxides for elemental mercury removal from coal-fired flue gas. *J. Hazard. Mater.* **2017**, *333*, 186–193. [CrossRef]
20. Campbell, C.T.; Peden, C.H.F. Oxygen vacancies and catalysis on ceria surfaces. *Science* **2005**, *309*, 713–714. [CrossRef]
21. Kašpar, J.; Fornasiero, P.; Graziani, M. Use of CeO_2-based oxides in the three-way catalysis. *Catal. Today* **1999**, *50*, 285–298. [CrossRef]
22. Peña, D.A.; Uphade, B.S.; Smirniotis, P.G. TiO_2-supported metal oxide catalysts for low-temperature selective catalytic reduction of NO with NH_3: I. Evaluation and characterization of first row transition metals. *J. Catal.* **2004**, *221*, 421–431. [CrossRef]
23. Kapteijn, F.; Singoredjo, L.; Andreini, A.; Moulijn, J.A. Activity and selectivity of pure manganese oxides in the selective catalytic reduction of nitric oxide with ammonia. *Appl. Catal. B* **1994**, *3*, 173–189. [CrossRef]
24. Consentino, L.; Pantaleo, G.; La Parola, V.; Migliore, C.; La Greca, E.; Liotta, L.F. NH_3-NO SCR catalysts for engine exhaust gases abatement: Replacement of toxic $V2O_5$ with MnO_x to improve the environmental sustainability. *Top. Catal.* **2022**. [CrossRef]
25. Tang, X.; Zhang, Y.; Lei, Y.; Liu, Y.; Yi, H.; Gao, F. Promotional catalytic activity and reaction mechanism of Ag-modified $Ce_{0.6}Zr_{0.4}O_2$ catalyst for catalytic oxidation of ammonia. *J. Environ. Sci.* **2023**, *124*, 491–504. [CrossRef]
26. Ni, P.; Wang, X.; Li, H. A review on regulations, current status, effects and reduction strategies of emissions for marine diesel engines. *Fuel* **2020**, *279*, 118477. [CrossRef]
27. Duan, J.; Zhao, L.; Gao, S.; Li, X. New aspects on a low-medium temperature mechanism of H_2-assisted C_3H_6-SCR over xAg-CeZr catalyst. *Fuel* **2021**, *305*, 121574. [CrossRef]
28. Zhou, W.; Shao, Z.; Jin, W. Synthesis of nanocrystalline conducting composite oxides based on a non-ion selective combined complexing process for functional applications. *J. Alloys Compd.* **2006**, *426*, 368–374. [CrossRef]
29. Zhao, M.; Cai, W.; Li, J. Preparation and reaction mechanism of novel CexCoyCuz oxide composite catalysts towards oxidation of o-xylene. *J. Rare Earths* **2022**, *40*, 1573–1583. [CrossRef]
30. Grabchenko, M.V.; Dorofeeva, N.V.; Lapin, I.N.; La Parola, V.; Liotta, L.F.; Vodyankina, O.V. Study of Nickel Catalysts Supported on MnO_x–CeO_2 Mixed Oxides in Dry Reforming of Methane. *Kinet. Catal.* **2021**, *62*, 765–777. [CrossRef]
31. Atabak Asadi, A.; Behrouzifar, A.; Mohammadi, T.; Pak, A. Effects of Nano Powder Synthesis Methods, Shaping and Sintering Conditions on Microstructure and Oxygen Permeation of $La_{0.6}Sr_{0.4}Co_{0.2}Fe_{0.8}O_{3-d}$ (LSCF) Perovskite-type Membranes. *High Temp. Mater. Proc.* **2012**, *31*, 47–59. [CrossRef]
32. Bugrova, T.A.; Kharlamova, T.S.; Svetlichnyi, V.A.; Savel'eva, A.S.; Salaev, M.A.; Mamontov, G.V. Insights into formation of Pt species in Pt/CeO_2 catalysts: Effect of treatment conditions and metal-support interaction. *Catal. Today* **2021**, *375*, 36–47. [CrossRef]
33. Kibis, L.S.; Svintsitskiy, D.A.; Kardash, T.Y.; Slavinskaya, E.M.; Gotovtseva, E.Y.; Svetlichnyi, V.A.; Boronin, A.I. Interface interactions and CO oxidation activity of Ag/CeO_2 catalysts: A new approach using model catalytic systems. *Appl. Catal. A* **2019**, *570*, 51–61. [CrossRef]
34. Kibis, L.; Simanenko, A.; Stadnichenko, A.; Zaikovskii, V.; Boronin, A. Probing of Pd^{4+} Species in a PdO_x–CeO_2 System by X-Ray Photoelectron Spectroscopy. *J. Phys. Chem. C* **2021**, *125*, 20845–20854. [CrossRef]
35. Moulder, J.; Stickle, W.; Sobol, P.; Bombe, K.D. *Handbook of X-ray Photoelectron Spectroscopy*; Perkin-Elmer Corp.: Eden Prairie, MN, USA, 1992; 261p.
36. Thommes, M.; Kaneko, K.; Neimark, A.V.; Olivier, J.P.; Rodriguez-Reinoso, F.; Rouquerol, J.; Sing, K.S.W. Physisorption of gases, with special reference to the evaluation of surface area and pore size distribution (IUPAC Technical Report). *Pure Appl. Chem.* **2015**, *87*, 1051–1069. [CrossRef]
37. Taniguchi, T.; Watanabe, T.; Sugiyama, N.; Subramani, A.K.; Wagata, H.; Matsushita, N.; Yoshimura, M. Identifying defects in ceria-based nanocrystals by UV resonance Raman spectroscopy. *J. Phys. Chem. C* **2009**, *113*, 19789–19793. [CrossRef]
38. Derevyannikova, E.A.; Kardash, T.Y.; Stadnichenko, A.I.; Stonkus, O.A.; Slavinskaya, E.M.; Svetlichnyi, V.A.; Boronin, A.I. Structural Insight into Strong Pt–CeO_2 Interaction: From Single Pt Atoms to PtO_x Clusters. *J. Phys. Chem. C* **2019**, *123*, 1320–1334. [CrossRef]
39. Schilling, C.; Hofmann, A.; Hess, C.; Ganduglia-Pirovano, M.V. Raman Spectra of Polycrystalline CeO_2: A Density Functional Theory Study. *J. Phys. Chem. C* **2017**, *121*, 20834–20849. [CrossRef]
40. Schilling, C.; Ganduglia-Pirovano, M.V.; Hess, C. Experimental and Theoretical Study on the Nature of Adsorbed Oxygen Species on Shaped Ceria Nanoparticles. *J. Phys. Chem. Lett.* **2018**, *9*, 6593–6598. [CrossRef]
41. Yang, X.; Wang, X.; Zhang, G.; Zheng, J.; Wang, T.; Liu, X.; Shu, C.; Jiang, L.; Wang, C. Enhanced electrocatalytic performance for methanol oxidation of Pt nanoparticles on Mn_3O_4-modified multi-walled carbon nanotubes. *Int. J. Hydrogen Energy* **2012**, *37*, 11167–11175. [CrossRef]

42. Larbi, T.; Doll, K.; Manoubi, T. Density functional theory study of ferromagnetically and ferrimagnetically ordered spinel oxide Mn_3O_4. A quantum mechanical simulation of their IR and Raman spectra. *J. Alloys Compd.* **2016**, *688*, 692–698. [CrossRef]
43. Gao, T.; Fjellvåg, H.; Norby, P. A comparison study on Raman scattering properties of α- and β-MnO_2. *Anal. Chim. Acta* **2019**, *648*, 235–239. [CrossRef] [PubMed]
44. Julien, C.M.; Massot, M.; Poinsignon, C. Lattice vibrations of manganese oxides. Part I. Periodic structures. *Spectrochim. Acta A* **2004**, *60*, 689–700. [CrossRef] [PubMed]
45. Gao, T.; Norby, P.; Krumeich, F.; Okamoto, H.; Nesper, R.; Fjellvåg, H. Synthesis and properties of layered-structured Mn_5O_8 nanorods. *J. Phys. Chem. C* **2009**, *114*, 922–928. [CrossRef]
46. Aghbolaghy, M.; Soltan, J.; Chen, N. Role of Surface Carboxylates in the Gas Phase Ozone-Assisted Catalytic Oxidation of Toluene. *Catal. Lett.* **2017**, *147*, 2421–2433. [CrossRef]
47. Shim, S.-H.; LaBounty, D.; Duffy, T.S. Raman spectra of bixbyite, Mn_2O_3, up to 40 GPa. *Phys. Chem. Miner.* **2011**, *38*, 685–691. [CrossRef]
48. Huang, H.; Liu, J.; Sun, P.; Ye, S.; Liu, B. Effects of Mn-doped ceria oxygen-storage material on oxidation activity of diesel soot. *RSC Adv.* **2017**, *7*, 7406. [CrossRef]
49. Murugan, B.; Ramaswamy, A.V. Nature of Manganese Species in $Ce_{1-x}Mn_xO_{2-ä}$ Solid Solutions Synthesized by the Solution Combustion Route. *Chem. Mater.* **2005**, *17*, 3983–3993. [CrossRef]
50. Wang, H.; Luo, S.; Zhang, M.; Liu, W.; Wu, X.; Liu, S. Roles of oxygen vacancy and O in oxidation reactions over CeO2 and Ag/CeO_2 nanorod model catalysts. *J. Catal.* **2018**, *368*, 365–378. [CrossRef]
51. Chang, S.; Li, M.; Hua, Q.; Zhang, L.; Ma, Y.; Ye, B.; Huang, W. Shape-dependent interplay between oxygen vacancies and Ag–CeO2 interaction in Ag/CeO2 catalysts and their influence on the catalytic activity. *J. Catal.* **2012**, *293*, 195–204. [CrossRef]
52. Romeo, M.; Bak, K.; El Fallah, J.; Le Normand, F.; Hilaire, L. XPS Study of the reduction of cerium dioxide. *Surf. Interface Anal.* **1993**, *20*, 508–512. [CrossRef]
53. Chigane, M.; Ishikawa, M. Manganese Oxide Thin Film Preparation by Potentiostatic Electrolyses and Electrochromism. *J. Electrochem. Soc.* **2000**, *147*, 2246. [CrossRef]
54. Lei, K.; Han, X.; Hu, Y.; Liu, X.; Cong, L.; Cheng, F.; Chen, J. Chemical etching of manganese oxides for electrocatalytic oxygen reduction reaction. *Chem. Commun.* **2015**, *51*, 11599–11602. [CrossRef] [PubMed]
55. Fujiwara, M.; Matsushita, T.; Ikeda, S. Evaluation of Mn3s X-ray photoelectron spectroscopy for characterization of manganese complexes. *J. Electron Spectros. Relat. Phenom.* **1995**, *74*, 201–206. [CrossRef]
56. Waterhouse, G.I.N.; Bowmaker, G.A.; Metson, J.B. Oxidation of a polycrystalline silver foil by reaction with ozone. *Appl. Surf. Sci.* **2001**, *183*, 191–204. [CrossRef]
57. Tjeng, L.H.; Meinders, M.B.J.; van Elp, J.; Ghijsen, J.; Sawatzky, G.A.; Johnson, R.L. Electronic structure of Ag_2O. *Phys. Rev. B* **1990**, *41*, 3190–3199. [CrossRef] [PubMed]
58. Wang, J.; You, R.; Qian, K.; Pan, Y.; Yang, J.; Huang, W. Effect of the modification of alumina supports with chloride on the structure and catalytic performance of Ag/Al_2O_3 catalysts for the selective catalytic reduction of NO_x with propene and H_2/propene. *Chin. J. Catal.* **2021**, *42*, 2242–2253. [CrossRef]
59. Breen, J.P.; Burch, R. A review of the effect of the addition of hydrogen in the selective catalytic reduction of NO_x with hydrocarbons on silver catalysts. *Top. Catal.* **2006**, *39*, 53–58. [CrossRef]
60. Sazama, P.; Čapek, L.; Drobná, H.; Sobalík, Z.; Dědeček, J.; Arve, K.; Wichterlová, B. Enhancement of decane-SCR-NO_x over Ag/alumina by hydrogen. Reaction kinetics and in situ FTIR and UV-vis study. *J. Catal.* **2005**, *232*, 302–317. [CrossRef]
61. Matulis, V.E.; Ragoyja, E.G.; Ivashkevich, O.A.; Lyakhov, D.A.; Michels, D. DFT Study of NO Reduction Process on Ag/γ-Al_2O_3 Catalyst: Some Aspects of Mechanism and Catalyst Structure. *J. Phys. Chem. C* **2020**, *125*, 419–426. [CrossRef]

nanomaterials

MDPI

Article

Life Cycle Assessment as Support Tool for Development of Novel Polyelectrolyte Materials Used for Wastewater Treatment

George Barjoveanu [1], Carmen Teodosiu [1,*], Irina Morosanu [1], Ramona Ciobanu [1], Florin Bucatariu [1,2] and Marcela Mihai [1,2]

[1] Department of Environmental Engineering and Management, "Gheorghe Asachi" Technical University of Iasi, 73 D. Mangeron Street, 700050 Iasi, Romania
[2] "Petru Poni" Institute of Macromolecular Chemistry, 41A Grigore Ghica Voda Alley, 700487 Iasi, Romania
* Correspondence: cteo@ch.tuiasi.ro

Abstract: This life cycle assessment (LCA) study focused on comparing the environmental performances of two types of synthesis strategies for polyethyleneimine (PEI) coated silica particles (organic/inorganic composites). The classic layer-by-layer and the new approach (one-pot coacervate deposition) were the two synthesis routes that were tested for cadmium ions removal from aqueous solutions by adsorption in equilibrium conditions. Data from the laboratory scale experiments for materials synthesis, testing, and regeneration, were then fed into a life cycle assessment study so that the types and values of environmental impacts associated with these processes could be calculated. Additionally, three eco-design strategies based on material substitution were investigated. The results point out that the one-pot coacervate synthesis route has considerably lower environmental impacts than the layer-by-layer technique. From an LCA methodology point of view, it is important to consider material technical performances when defining the functional unit. From a wider perspective, this research is important as it demonstrates the usefulness of LCA and scenario analysis as environmental support tools for material developers because they highlight environmental hotspots and point out the environmental improvement possibilities from the very early stages of material development.

Keywords: one-pot coacervate deposition; layer-by-layer deposition; inorganic/organic composites; life cycle assessment; eco-design

Citation: Barjoveanu, G.; Teodosiu, C.; Morosanu, I.; Ciobanu, R.; Bucatariu, F.; Mihai, M. Life Cycle Assessment as Support Tool for Development of Novel Polyelectrolyte Materials Used for Wastewater Treatment. *Nanomaterials* **2023**, *13*, 840. https://doi.org/10.3390/nano13050840

Academic Editors: Marco Stoller and George Z. Kyzas

Received: 26 January 2023
Revised: 19 February 2023
Accepted: 22 February 2023
Published: 23 February 2023

1. Introduction

The discharge of a wide variety of pollutants into the aquatic environment from anthropogenic activities (i.e., agricultural, industrial, and urban waste) causes many concerns in relation to water resource quality, ecosystems, and human health [1]. Among the various water pollutants, heavy metal ions [2], pharmaceuticals [3,4], pesticides [5], dyes [6], and halogenated flame retardants [7] are part of the priority/emerging pollutants and are characterized by low concentrations (in the ng/L and μg/L range), toxicity, carcinogenic and mutagenic effects, and bio-accumulative behavior. These characteristics can generate significant impacts both on human health and living organisms in the aquatic environment and pose significant challenges for water/wastewater treatment technologies [8]. Numerous water and wastewater treatment processes have been developed and employed for their removal or destruction, for example, membrane processes [9–11], ion exchange [12], coagulation and flocculation processes [13], adsorption on different sorbents [14,15] and oxidation processes [16,17]. Due to cost-effectiveness, high efficiency, and ease of operation, adsorption is one of the most attractive and applied technologies worldwide [2,18]. Traditional sorbents, such as activated carbon, zeolites, clays, etc., are often incapable of providing high removal efficiencies of these pollutants due to their relatively low sorption capacity [18]. To improve the sorbent's performance, nanotechnology is used to shape or

modify materials based on carbon, bio-materials, metal oxides, silica, engineered nanomaterials, magnetic and non-magnetic nanoparticles, and nanocomposites [14,19]. These novel materials have unique properties such as high adsorption capacity, large surface area, surface-free energy, stability, selectivity, and reusability [20,21].

Many studies have investigated the performance of using composite materials for water and wastewater treatment. For example, Menazea et al. [22] studied the interaction between the chitosan/graphene oxide composite and divalent heavy metals (Ni^{2+}, Cu^{2+}, As^{2+}, $Cd^{2+,}$ and Pb^{2+}) as an effective removal from wastewater. The results indicate that graphene improves the stability of chitosan and its adsorption reactivity for heavy metal ions. Senguttuvan et al. [6] prepared a polypyrrole/zeolite nanocomposite by chemical oxidation and obtained good removal efficiency of reactive blue and reactive red from the synthetic solution.

To enhance their sorption capacity and selectivity, the surface of such sorbents needed to be functionalized with organic or inorganic reagents to provide adsorption sites [20]. For example, the silica microparticles surface was modified with a high number of amino ($–NH_2$) and carboxylic (–COOH) groups of polyelectrolytes [23], while magnetite (Fe_3O_4) nanoparticles were functionalized with thiol (–SH) and carboxylic (–COOH) groups using meso-2,3-dimercaptosuccinic acid [24]. Depending on the functional groups of nanocomposite sorbents, different interaction mechanisms with pollutants can occur, for example, electrostatics, coordinative bonds, and hydrophobic forces.

With respect to their synthesis, different methods were used to obtain nanocomposite sorbents, which were able to interact with inorganic/organic pollutants based on a combination of their structural durability and functional group availability. Nosike et al. [25] synthesized via one deposition a new mercury sorbent based on a zeolitic imidazolate framework (ZIF-90) assembled onto the poly(acrylic acid) (PAA) capped Fe_3O_4 nanoparticles and cysteine. The sorbent exhibited fast kinetics and a good sorption capacity for Hg^{2+}. Based on the emulsion templating concept, Semenova et al. [26] developed nanocomposite particles of polyethylenimine (PEI)–silica and investigated the adsorption capacity of copper ions. PEI-silica nanocomposites exhibit a great adsorption capacity for inorganic metals due to a large number of functional groups. Bucatariu et al. [27] fabricated the same type of composite utilizing a layer-by-layer (LbL) technique in which PEI and the PAA or PEI_4-Cu complex and PAA were alternately deposited and cross-linked with glutaraldehyde (GA) onto silica microparticles. The obtained multilayered composites were used in multiple sorption cycles for copper ions (Cu^{2+}) from an aqueous solution. The sorption experiments showed that the amount of loaded Cu^{2+} was dependent on the amount of the organic part, while the kinetics of sorption depended more on the number of functional groups available inside the $(PEI)_n$ film. Moreover, some review articles briefly present the nanocomposite sorbents used in water and wastewater remediation [21] and recent developments in the synthesis and characterization of composites based on polyelectrolytes [28]. Alternatively, Khan et al. [29] investigated the usage of green nanosorbents for the removal of pharmaceutical contaminants in water and wastewater systems.

However, most of these novel nanocomposite sorbents are still being studied on a laboratory scale. Furthermore, their potential environmental performance has not been sufficiently studied. Subsequently, there is a knowledge gap on the production feasibility, environmental performance, emissions, wastes, impacts on human health, and the development guidelines for these innovative materials. The development of these nanomaterials should be in accordance with the principles of *sustainable development* and *green chemistry* (waste prevention, design and use of safer chemicals, use of renewable energy and raw materials, and use of less hazardous chemicals) [8,30]. In order to support these principles and to evaluate environmental performance, life cycle assessments (LCA) could be applied. LCA enables the identification and quantification of the impacts generated on the environment, human health, as well as resources and emissions throughout the life span of a product or service (i.e., from raw material extraction, production, use, and disposal, including recycling and reuse) [31].

A recent study proposed and investigated how scenario-based LCA may be used to forecast potential environmental impacts and sustainability hot spots during the design and synthesis phases of two LbL synthesis routes to develop silica//PEI microparticles [8]. From then, the available literature found only a few LCA studies to evaluate the synthesis of nanocomposite sorbents for water/wastewater remediation. For instance, Lawal et al. [32] investigated the impact that was generated by the synthesis of hexagonal boron nitride-magnetite (Fe_3O_4) nanocomposites when used as adsorbents for the removal of Cr(VI) ions from aqueous solution, while Garcia-Gonzalez et al. [33] performed an LCA study to determine the environmental impacts associated with the production of silicate-titanate nanotube chitosan beads, the usage to remove cadmium from wastewater, and for recycling. The studies highlighted that electricity and chemical consumption were the main inputs contributing to the total impact at a laboratory scale production. However, most studies define approaches and strategies for safe design in the early production of innovative materials in the area of nanotechnology through LCA or combining LCA with risk assessment and socio-economic assessment [34–36].

The objective of this study is to investigate how LCA can be used to evaluate and compare the environmental performance of two synthesis routes to obtain nano-structured materials containing an inorganic silica core that is coated with cross-linked PEI. The two synthesis strategies are layer-by-layer polymer deposition and one-pot coacervate deposition. Our investigation considers the very early stages of product development and is aimed at identifying, quantifying, and comparing the environmental impacts that may arise from the chemicals, synthesis operations, and processes by means of LCA. Initial product testing (removal of Cd^{2+} ions from synthetic wastewater by adsorption at equilibrium) and sorbent regeneration are also included in the LCA analysis and used to define a comprehensive functional unit that could depict environmental impacts more objectively. Another study objective is to develop and use these early environmental profiles to investigate several scenarios related to the eco-design of these materials. This study brings new insight into how LCA can be used as a material design instrument that enables the evaluation of environmental aspects related to nanostructured material synthesis by comparing two different synthesis routes and evaluating three eco-design criteria.

2. Materials, Methods and Methodology

2.1. Composite Material Synthesis, Characterization and Testing

From a technical point of view, the synthesis goals were to obtain organic/inorganic composite materials that would combine the structural stability of inorganic support with a polymeric phase with a high affinity for heavy metal ions and other pollutant species. For this purpose and considering our previous experience [2,8,27,37], the silica microparticles have been used as inorganic support, and where the solid surface was covered (by two different methods) with the polymeric phase: (1) the layer-by-layer deposition of water-soluble PEI and PAA and (2) direct deposition of the organic part using an innovative one-pot interpolyelectrolyte coacervate precipitation, with less material and energy consumption and lack of toxic by-products formation, as presented in Figure 1.

In the layer-by-layer technique, polyelectrolyte films are alternatively deposited on silica microparticles. The procedure consists of introducing the silica core particles (4 g) in 200 mL of a PEI (M_w = 25,000 g·mol^{-1}) aqueous solution ($5 \cdot 10^{-3}$ mol·L^{-1}, pH = 9.5) for 1 h at room temperature, then by washing them in distilled water to remove the excess polycation and then introducing the newly formed silica/PEI composite in 200 mL of PAA (M_w = 10,000 g·mol^{-1}) solution ($5 \cdot 10^{-3}$ mol·L^{-1}, pH = 3.5). Finally, particles are thoroughly rinsed again with ultrapure water. This procedure was repeated until nine polymer layers were deposited onto the silica surface, forming the silica//$(PEI/PAA)_{4.5}$ composite.

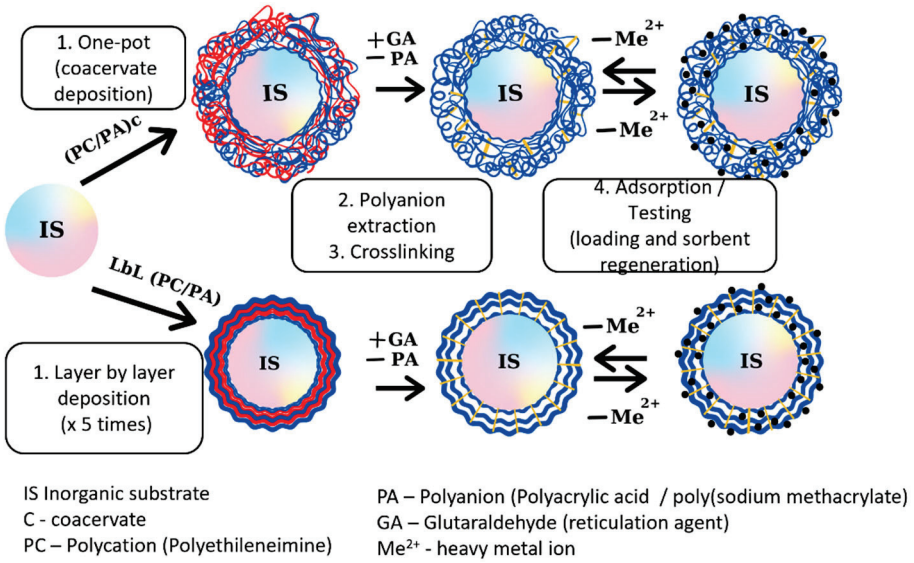

Figure 1. Inorganic/organic composite synthesis routes (adapted with permission after [2]; copyright 2022, Elsevier).

In the second strategy, the coacervate was generated in situ by the non-stoichiometric combination of PEI, used as polycation, and PAA or with poly(sodium methacrylate) (PMAA) (M_W = 1800 g·mol^{-1}), used as polyanions.

The second step of the one-pot synthesis through the in situ precipitation of the coacervate is similar to the LbL technique and consists of a chemical cross-linking reaction (in presence of glutaraldehyde, GA) at two different molar ratios between the aldehyde and amino groups, which yielded two cross-linking degrees (r = 0.1 and r = 1). The last synthesis step was the extraction of the unreacted polymeric cations (PEI) and anions (PAA or PMAA) from the cross-linked organic shell in a strongly basic medium.

These materials were tested in single-element sorption experiments, which targeted the removal of Cd^{2+} ions from aqueous solutions [2]. The influence of different parameters was investigated and enabled the estimation of the experimental maximum sorption capacity, as presented in Table 1 [2]. Subsequently, these data were used to calculate the functional unit (mg ions Cd^{2+} removed). It has to be noted that a total of eight nanostructured composites have been obtained by layer-by-layer and four by one-pot synthesis, respectively, but the LCA analysis only includes the materials with the best removal efficiency for Cd^{2+} ions (which are bolded in Table 1).

Table 1. Synthesis routes and experimental data (adapted from [2]).

Synthesis Method	Composite Material	r	Thermogravimetric Analysis		Experimental Data	Isotherm
			Organic Content, %	Calculated Maximum Sorption Capacity, mg Cd^{2+}/g Composite	Maximum Sorption Capacity, mg Cd^{2+}/g Composite Material	
LbL	IS/(PEI/PAA)$_{4.5}$	0.1	4.2	27.449	16.0	Sips
One-pot	IS/(PEI-PAA)$_c$	0.1	10.8	70.583	67	Toth
One-pot	IS/(PEI-PMAA)$_c$	0.1	15.7	102.607	69.6	Toth
LbL	IS/(PEI/PAA)$_{4.5}$	1	10.1	66.008	26.67	Toth
One-pot	IS/(PEI-PAA)$_c$	1	20.8	135.938	82.8	Toth
One-pot	IS/(PEI-PMAA)$_c$	1	15.5	101.300	76.2	Toth
One pot	Q/(PEI/PAA)$_c$	0.1	3	19.606	6	Toth

Note: IS—inorganic silica core, Q = quartz sand, PEI—polyethyleneimine, PAA—Polyacrylic acid, PMAA—poly(sodium methacrylate), c—coacervate, r—aldehyde to amino molar ratio.

2.2. Life Cycle Assessment Methodology

2.2.1. Goal and Scope Definition

The goal of the LCA analysis was to evaluate the potential environmental impacts caused by the production and use of nano-structured composite materials obtained by LbL and one-pot synthesis routes, which were subsequently used for the removal of Cd^{2+} ions from aqueous solutions. The analysis uses a *cradle-to-gate* approach which includes the following foreground processes: laboratory-scale synthesis processes for inorganic/organic composites and testing (adsorption) processes for the removal of Cd^{2+} ions from synthetic wastewaters. Testing has included repeated sorption/desorption cycles to evaluate the loss of the adsorbent and the evolution of the sorption capacity after repeated cycles. Testing data were used to compute the functional unit for the LCA study. The background system included processes for chemicals and energy production. The analysis did not include transport and disposal processes. Two functional units were defined and used to compare the two synthesis methods, i.e., 1 g of synthesized and purified composites to focus on the synthesis steps, and 1 mg of Cd^{2+} ions were removed to evaluate the heavy metal ion removal efficiency, which is the main functionality of the engineered materials.

2.2.2. Life Cycle Inventory

The life cycle inventory (LCI) data of the inorganic/organic composite materials synthesis was obtained during the laboratory scale experiments, as well as during their testing. The LCI data for the foreground system included primary data generated in the synthesis and testing procedures (repeated cycles of sorption Cd^{2+} ions sorption followed by sorbent regeneration), as presented in Table 2. The background system incorporates the production of electricity (considering the Romanian electricity mix), chemical production, and wastewater treatment, and these data were sourced from the Ecoinvent 3.3 database. As no additional co-products were obtained from the syntheses, all the environmental impacts were allocated to the obtained inorganic/organic composites.

Table 2. Inventory data per 1 g of silica//PEI composites.

No	Inventory Entries		IS/$(PEI/PAA)_{4.5}$ (r = 0.1 LbL)	IS/(PEI-PAA)c (r = 0.1 One Pot)	Comments/Ecoinvent Process
	Composite material	g	1	1	
	Materials/fuels				
1	Silica particle	g	0.99	0.99	SiO_2 sol gel method
2	Ultrapure water	g	2120	123.6	Water, ultrapure, at plant/GLO U
3	Poly(ethyleneimine)	mg	43	51	Ethylenediamine
4	Poly(acrylic acid)	mg	56	456	PAA-water dispersion (by radical polymerization)
5	Glutaryc anhydride	g	0.0135	0.06	Acetic anhydride from acetaldehyde
7	Sodium hydroxide	g	1.6	1.28	Sodium hydroxide (50% NaOH)
9	Hydrochloric acid	g	0.365	0.292	
	Emissions to water				
10	Amine, tertiary	g	0.01075	0.0102	
11	Glutaraldehyde	g	0.05	0.012	
12	Chemically polluted water	g	162.5	123.6	
13	Acrylic acid	g	0.09	0.0092	

Usually, to compile LCI, databases (e.g., Ecoinvent) are used because they provide easy-to-use data and comprise average data for the large-scale production of chemicals [38]. This, however, is of little help in the case of the particular lab-scale syntheses of highly engineered materials because these use special chemical compounds or special manufacturing synthesis (fine chemicals), which are not usually covered in these databases or are not scope-adequate in terms of their input/output structure or associated environmental impacts. To overcome these uncertainties, some of the inventory entries have been modeled individually in accordance with previous research studies [38,39]. PEI was modeled based on several data available in Eco-invent (ethylenediamine and ring opening polymerization

of aziridine); for the poly(acrilic acid), a radical polymerization reaction was modeled based on Zahran et al. [40] and Ristic et al. [41], while the glutaraldehyde was modeled as acetaldehyde. The silica particles used in the synthesis were commercially available, but they were modeled considering a sol-gel co-precipitation reaction protocol [42]. The output flows from these synthesis processes refer to the excess materials which were modeled as waterborne pollutants.

LCI analysis based on the data in Table 1 clearly shows that the one-pot synthesis route significantly uses fewer chemicals (with one magnitude order smaller values). With respect to the quantities used to obtain 1 g of nanocomposites, it may be noticed that the silica core particle accounted for 99% of the particle mass, and the ultrapure water which was used for repeated rinses (in the case of the LbL synthesis) was the chemical with the highest used quantity.

2.2.3. Life Cycle Impact Assessment

The life cycle impact assessment (LCIA) was performed according to the ISO 14040:2006 [43,44] recommendations at the level of classification and characterization steps by using the ReCiPe 2016 method at the midpoint. This LCIA method includes 18 impact categories [45]. SimaPro 9.1.0.11 software was used to compile the inventory and to perform the life cycle impact assessment. LCIA has considered the *cradle-to-gate* approach as previously presented and covered by the inventory description. Current LCIA methodologies do not account for the environmental impacts that are related to nanomaterials release into the environment because there is a lack of characterization factors, fate, and toxicity data related to these compounds.

3. Results and Discussion

3.1. Environmental Profiles

The two synthesis routes for the composite materials are very similar in terms of the chemicals involved but pretty different considering the operational steps they involve. The layer-by-layer technique comprises a series of successive submersions of particles in solutions and mild agitation and rinsing with ultrapure water, while the one-pot method only employs a single step for the polymeric coating of the inorganic support particle. It is important to note that no electricity or heating is required for any of these synthesis routes. One of the main advantages of these materials is that their synthesis occurs at a normal temperature and that no organic solvents are required, as PEI and PAA are among the water-soluble polymers. Considering the inventory modeling as presented before, the general environmental profiles for two similar particles are presented in Table 3.

Table 3. Environmental impacts of composite silica/PEI materials (per functional unit).

Impact Category	Unit	Symbol	Impacts Per 1 g IS/(PEI/PAA)$_{4.5}$—r = 0.1 (LBL)	Impacts Per 1 g IS/(PEI-PAA)c—r = 0.1 (One-Pot)	Impact Ratio One Pot/Lbl	Impacts Per 1 mg Cd^{2+} Removed byIS/(PEI/PAA)$_{4.5}$—r = 0.1 (LBL)	1 mg Cd^{2+} Removed by IS/(PEI-PAA)c—r = 0.1 (One-Pot)	Impact Ratio One Pot/Lbl
Global warming	kg CO_2 eq	CC	6.93×10^{-2}	6.94×10^{-2}	100.2%	4.33×10^{-3}	1.04×10^{-3}	23.9%
Stratospheric ozone depletion	kg CFC11 eq	OD	3.45×10^{-8}	3.40×10^{-8}	102.0%	2.07×10^{-9}	5.05×10^{-10}	24.4%
Ionizing radiation	kBq Co-60 eq	IR	3.46×10^{-3}	3.40×10^{-3}	98.1%	2.16×10^{-4}	5.07×10^{-5}	23.4%
Ozone formation, Human health	kg NOx eq	OF-HH	5.21×10^{-4}	5.20×10^{-4}	99.9%	3.25×10^{-5}	7.77×10^{-6}	23.9%
Fine particulate matter formation	kg PM2.5 eq	PM	1.37×10^{-4}	1.38×10^{-4}	100.6%	8.59×10^{-6}	2.06×10^{-6}	24.0%
Ozone formation, Terrestrial ecosystems	kg NOx eq	OF-ECO	7.58×10^{-4}	7.58×10^{-4}	100.0%	4.74×10^{-5}	1.13×10^{-5}	23.9%
Terrestrial acidification	kg SO_2 eq	TA	2.92×10^{-4}	2.94×10^{-4}	100.7%	1.82×10^{-5}	4.39×10^{-6}	24.0%
Freshwater eutrophication	kg P eq	FE	5.69×10^{-5}	3.17×10^{-5}	55.8%	3.56×10^{-6}	4.74×10^{-7}	13.3%

Table 3. *Cont.*

Impact Category	Unit	Symbol	Impacts Per 1 g IS/(PEI/PAA)$_{4.5}$—r = 0.1 (LBL)	Impacts Per 1 g IS/(PEI-PAA)c—r = 0.1 (One-Pot)	Impact Ratio One Pot/Lbl	Impacts Per 1 mg Cd^{2+} Removed byIS/(PEI/PAA)$_{4.5}$—r = 0.1 (LBL)	1 mg Cd^{2+} Removed by IS/(PEI-PAA)c—r = 0.1 (One-Pot)	Impact Ratio One Pot/Lbl
Marine eutrophication	kg N eq	ME	6.14×10^{-6}	2.81×10^{-6}	45.7%	3.84×10^{-7}	4.19×10^{-8}	10.9%
Terrestrial ecotoxicity	kg 1,4-DCB	TTOX	1.36×10^{-1}	1.37×10^{-1}	101.0%	8.48×10^{-3}	2.05×10^{-3}	24.1%
Freshwater ecotoxicity	kg 1,4-DCB	FTOX	1.46×10^{-3}	1.46×10^{-3}	99.9%	9.11×10^{-5}	2.17×10^{-5}	23.8%
Marine ecotoxicity	kg 1,4-DCB	MTOX	2.04×10^{-3}	2.05×10^{-3}	100.6%	1.27×10^{-4}	3.06×10^{-5}	24.0%
Human carcinogenic toxicity	kg 1,4-DCB	HC-TOX	2.05×10^{-3}	2.03×10^{-3}	99.3%	1.28×10^{-4}	3.03×10^{-5}	23.7%
Human non-carcinogenic toxicity	kg 1,4-DCB	HNonC-TOX	4.05×10^{-2}	4.08×10^{-2}	100.7%	2.53×10^{-3}	6.08×10^{-4}	24.0%
Land use	m2a crop eq	LAND	1.97×10^{-3}	1.96×10^{-3}	99.7%	1.23×10^{-4}	2.93×10^{-5}	23.8%
Mineral resource scarcity	kg Cu eq	MIN	1.10×10^{-4}	1.10×10^{-4}	100.2%	6.88×10^{-6}	1.65×10^{-6}	23.9%
Fossil resource scarcity	kg oil eq	FOS	2.87×10^{-2}	2.87×10^{-2}	100.0%	1.79×10^{-3}	4.28×10^{-4}	23.9%
Water consumption	m3	WAT	1.12×10^{-2}	9.17×10^{-3}	81.9%	7.00×10^{-4}	1.37×10^{-4}	19.6%

The data in Table 3 present the environmental impact values that were obtained by considering each functional unit of the LCA study (1 g composite material obtained and 1 mg Cd^{2+} ions removed). If one compares these environmental profiles on a g/g basis, it may be observed that the two syntheses routes generate similar impact values in most impact categories, with some difference in the freshwater and marine eutrophication and water use categories, where the one-pot synthesis route had less than half of the impacts conducted by the layer-by-layer route. If we refer to absolute impact values, 1 g of the composite material generates about 0.069 kg CO_2 eq in the climate change category, 0.134 kg 1,4-DCB in the terrestrial eco-toxicity category and 9.1–11.2 L of water in the water use category.

When comparing the composites considering the other functional unit (mg Cd^{2+} ions removed), it is clear that the one-pot synthesis generates considerably lower impacts than the layer-by-layer method; one-pot composites generate only around 24% of the LbL impacts, with the exception of the eutrophication categories, where the impacts are even less (10.9 and 13.3 %).

In Figure 2, the impact profile structure for obtaining composite materials is presented. The two impact profiles are similar, with the most important contributor being the silica core particle in most of the categories. This is, of course, due to the very high proportion (99%) of the silica core in the overall mass of the composite particles.

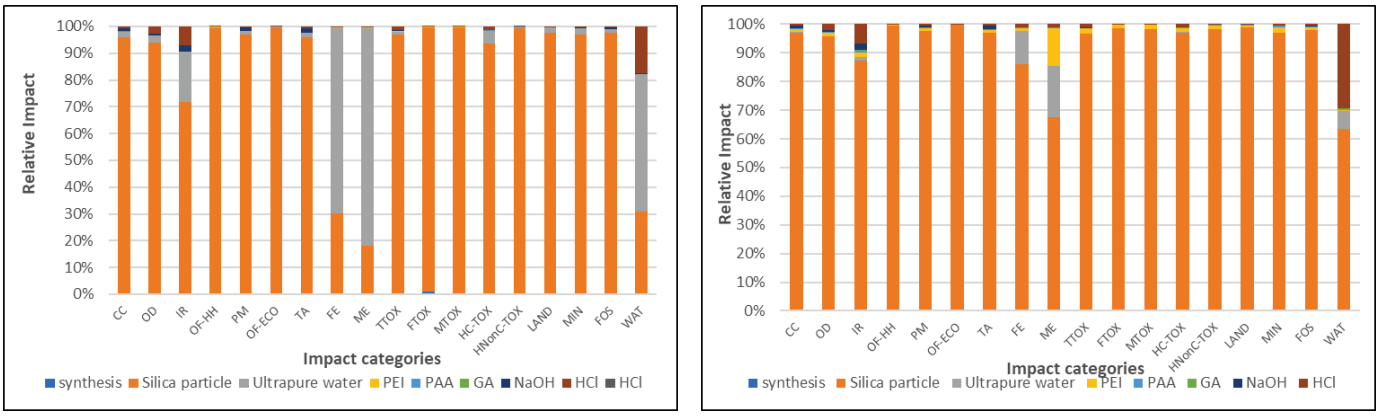

(**a**) (**b**)

Figure 2. Environmental profile structures of the composite materials (**a**). LbL- IS//(PEI/PAA)$_{4.5}$ (r = 0.1); (**b**) One-pot IS//(PEI/PAA)c (r = 0.1).

To better understand the contribution of other chemicals in the environmental profiles, in Figure 3, only the contribution of the polymeric part of the synthesized materials is displayed.

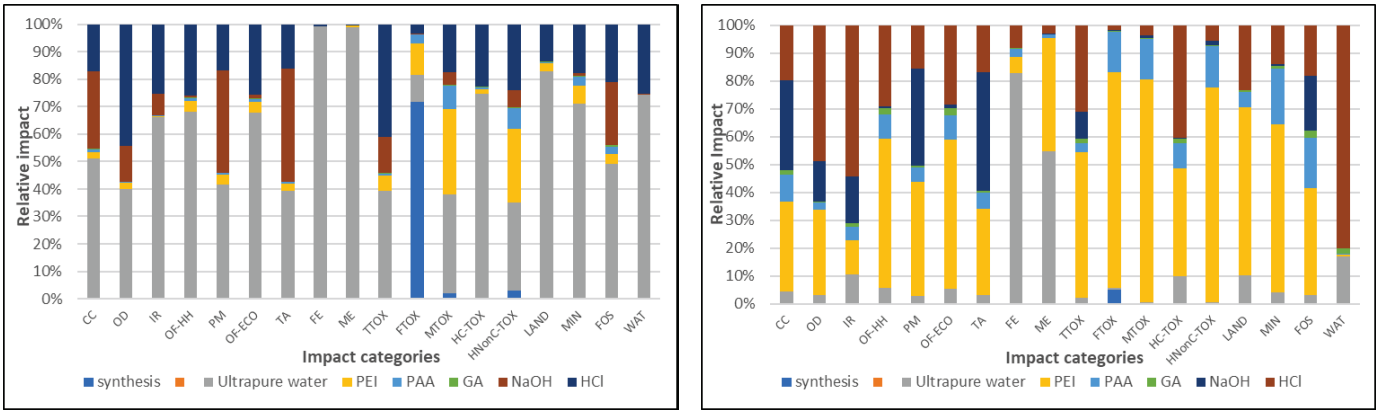

(**a**) (**b**)

Figure 3. Environmental profile structures of the polymeric particle coating materials (**a**). LbL-IS/(PEI/PAA)$_{4.5}$ (r = 0.1); (**b**) One-pot IS/(PEI/PAA)$_c$ (r = 0.1).

By analyzing the impact profile structures presented in Figure 3, one may notice that for the composite particles obtained by LbL (Figure 3a), the most important contributor is the use of ultrapure water, which has the highest impact in all categories, except on freshwater toxicity FTOX 9.8%. This is due to the fact that ultrapure water is used in large volumes for dilutions and repeated rinses in the case of LbL synthesis. Ultrapure water impacts are largely due to electricity use for its production and, as presented in Figure 3a, has the highest contribution in the marine (ME) and terrestrial (TE) eutrophication categories (over 99% of the total impact).

In addition to ultrapure water use, hydrochloric acid, and sodium hydroxide are also important contributors in both syntheses. These chemicals are used for the extraction of unreacted polymeric species and have a much higher impact than the actual species involved in obtaining the nanostructured materials, which only have minor contributions to the general impact profile.

In the case of the composites obtained by the one-pot route (Figure 3b), the PEI generated between 5.3 % (WAT) and 79.8% (TE) for most of the categories, making it the most important contributor among the chemicals. The second most important contributor was hydrochloric acid which, similarly to the PEI, generated high impacts in almost all categories. Hydrochloric acid was used as a pH regulator in the single-step synthesis and as an extractor for the unreacted PEI and PAA.

We may notice that the actual synthesis processes had only minor contributions in the toxicity-related categories, and this was due to the wastewater volumes generated after the nanostructured composite particles were rinsed and purified. These impacts account for a maximum of 71.7% for the LbL method and 5.1% for the one-pot route in the freshwater toxicity category (FTOX).

By analyzing these environmental profiles, it is possible to identify major contributors to different impact categories. The next step in this analysis would be to identify where changes should be made in the syntheses chain of operations. For this, in Figure 4, the individual contribution of each synthesis step is presented for the layer-by-layer deposition (Figure 4a) and the coacervate deposition (one-pot) synthesis (Figure 4b). These profiles exclude the contribution of the core silica particle because it was clear that these had the most important share in the total impact (Figure 2). The profiles in Figure 4a depict a greater impact of the actual synthesis step in the case of the layer-by-layer deposition method, as compared to the extraction and crosslinking phases. This situation is due to the large

quantities of water which were used to rinse the nanostructured composite particles after each layer deposition.

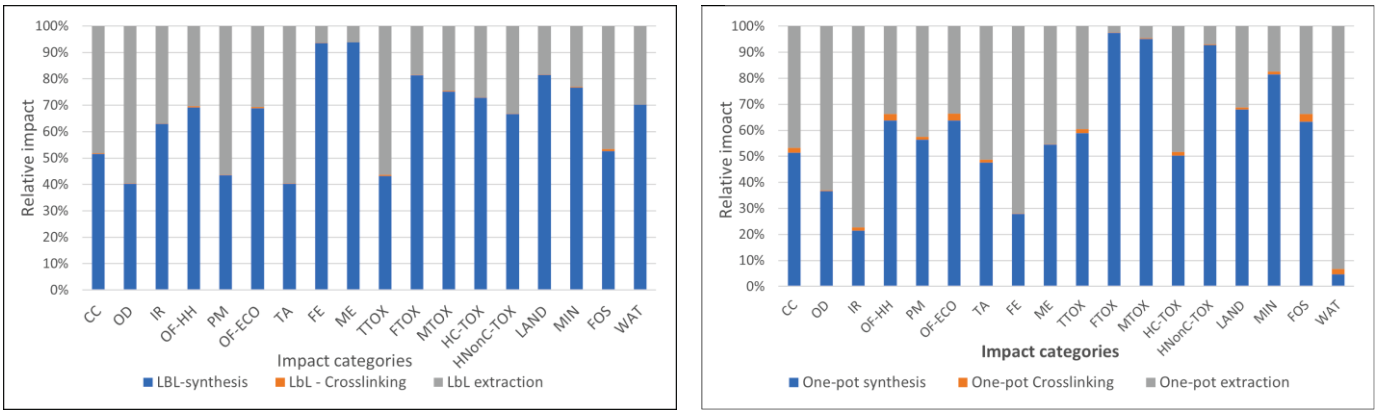

(**a**) (**b**)

Figure 4. Environmental impacts induced by the synthesis steps (**a**). LbL deposition; (**b**) One-pot synthesis).

In the case of the one-pot route, there is a more balanced distribution of impacts across categories between the synthesis and extraction process, while the crosslinking demonstrated a slightly higher share (Figure 4b).

3.2. Eco-Design Scenarios

The environmental analysis results, which were presented in the previous section, indicate the most important impact contributors that were used as a rationale for studying a series of eco-design scenarios aimed at minimizing the environmental impacts of the one-pot synthesis route. The LbL route has been excluded because it clearly had the worse environmental performance compared to the one-pot method (Table 1). Therefore, focusing on the one-pot reaction route, the scenarios are considered in their potential to replace some of the chemicals in the following sequence.

- Scenario 1: Replacing the silica support particle with inert (quartz) sand.
- Scenario 2: Changing the crosslinking agent concentration (CH_2 to NH_2 ratio from 1 to 0.1)
- Scenario 3: Replacing Poly(acrylic acid) with sodium poly(metacrylate).

Scenario 1 considers the replacement of the highly engineered silica support particles with simpler inert quartz particles. To investigate this scenario, the one-pot synthesis route was used to obtain a batch composite quartz/polymeric sorbent starting from a batch of selected sand (70 microns) which was coated with a PEI/PAA polymer in a similar fashion to the silica-cored materials [46]. This composite material was characterized and tested, and it showed very promising results in terms of polymeric content (approx. 3% wt), including very good stability (loss of sorption capacity of approximately 7% after 5 repeated sorption cycles of Cu^{2+} ions), and a good sorption capacity for Cd^{2+} ions (6 mg Cd^{2+} ions/g composite material). Compared to the previous attempts of synthesizing quartz-cored particles through the LbL method [37], these results were very promising from an operational point of view. However, if we compare the environmental impacts generated in scenario 1 with a reference situation given by a correspondent silica core particle, as presented in Figure 5, one may notice that the environmental situation does not improve.

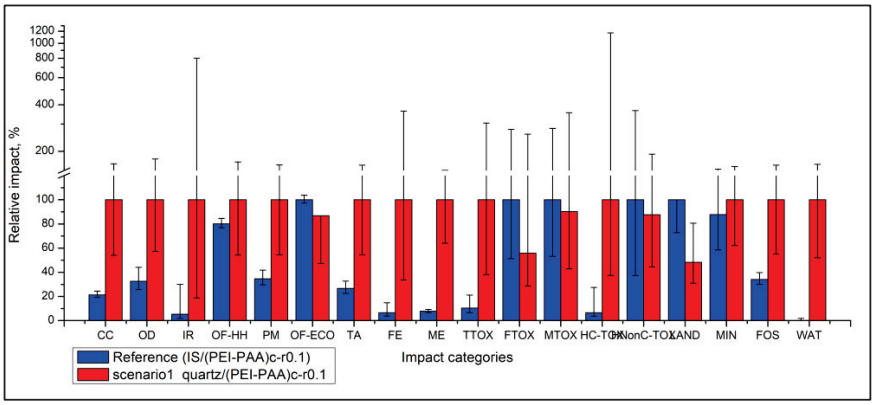

(**a**)

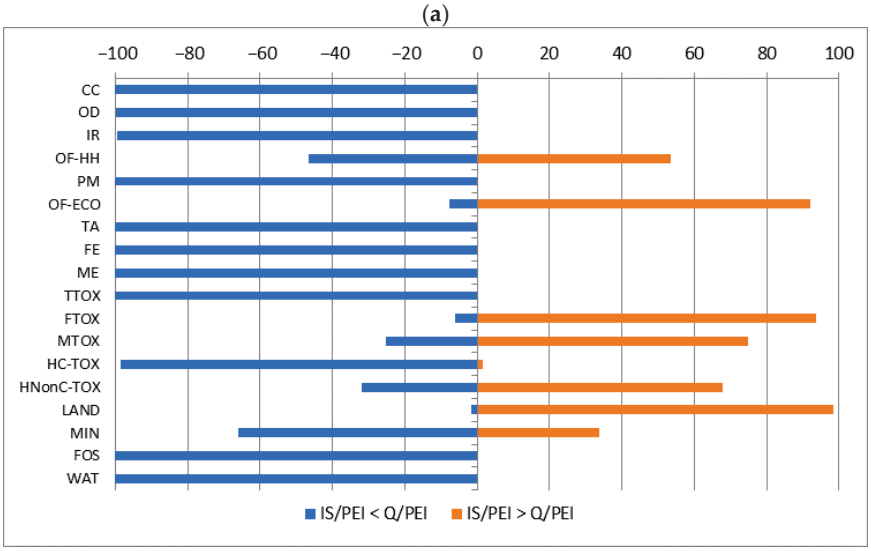

(**b**)

Figure 5. Environmental impacts according to the reference case and Scenario 1 (**a**). Actual impact values (**b**). Probability distribution of differences between the reference case $(IS/(PEI/PAA)_c$ (r = 0.1) and Scenario 1 $(quartz/(PEI/PAA)_c$ (r = 0.1)).

On the contrary, in most categories, the impacts increased because, on the one hand, the inert quartz-cored composite had a considerably lower retention capacity for cadmium ions (albeit much better than the previous LbL attempt), and, on the other hand, the specific impact profile had some high impacts (mainly due to electricity which is used in the initial sieving of the sand particles). Scenario 1 generated slightly lower impacts in the following categories: ozone formation (−14%), freshwater ecotoxicity (−45%), marine ecotoxicity (−10%), human non-carcinogenic toxicity (−13%), and land use (−52%).

It has to be noted that because these profiles are based on laboratory-scaled data, a high degree of uncertainty characterizes these scenario results. Uncertainty was evaluated by means of a Monte Carlo analysis (1000 rounds), which enabled the estimation of confidence intervals for the most likely impact value (usually the mean or median, depending on the fitted probability distribution), as well as some statistic parameters which describe the goodness of approximation. The uncertainty analysis is based on default standard uncertainty values as presented in the EcoInvent 3.3 database for background processes, while for the foreground data (used to compile the life cycle inventories), specific uncertainties were estimated as 10% of the coefficient of variability for each measure. In some cases, greater variability was considered. For example, by considering a uniform distribution of electricity-related variability (e.g., a 0.5, 1.0, or 1.5 kW powered motor for the sieving device), a very high uncertainty was obtained, especially in the impact categories related to electricity use (IR—ionizing radiation, FE—freshwater toxicity and HC_TOX human carcinogenic toxicity), as presented in Figure 5 where uncertainty is depicted as the

95% confidence interval for each impact category. This very high uncertainty hinders a comparison with the reference case, especially where the impact values of the compared situations (including the lower confidence limit) are similar. To overcome this drawback, a comparative Monte Carlo analysis includes that in which the runs estimate the probability that one event is more likely to occur than another based on individual variability data. Such a comparison is presented in Figure 5b, where the blue (negative) represents the probability that the reference case has lower impacts than Scenario 1, and the red bar (positive) represents the probability that the reference case is higher than Scenario 1. It was thus possible to make a clear distinction among the impact categories that were affected by the highest uncertainty: in the IR category, there was only a 0.4% chance that Scenario 1 would have a higher impact than the reference situation, while in the human carcinogenic toxicity category, this probability was 1.4%.

Scenario 2 considers reducing the concentration of the crosslinking agent with a 10-fold factor in an attempt to avoid strong composite cross-linking, which could generate a slightly looser polymeric layer over the core particle. Strong crosslinking is generally associated with the strong packing of polymeric chains, which translates into less accessibility for pollutant species to reach active sorption sites but improves the superficial density of functional groups [28,47]. On the contrary, low composite cross-linking degrees (e.g., 1:10) can improve the accessibility for active functional groups while lessening the stability of the organic layer. The environmental profiles that were presented previously demonstrated that the impact share of the crosslinking agent (glutaraldehyde) was small in all impact categories; therefore, whatever environmental benefit would this change create, it would come from improving the technical performance of the product. This was confirmed experimentally and can be observed in Table 1, where all the maximum sorption capacities increased when the crosslinking concentration increased (when comparing similarly structured materials).

In Figure 6, a comparison between a reference case which considers the removal of Cd^{2+} ions through sorption on particles with a 0.1 crosslinking ratio (CH_2 to NH_2-concentration), and Scenario 2, which considers the use of the same type of particle, but with a much higher crosslinking ratio (1:1) shows that from an environmental point of view, it is worth cross-linking the polymeric chains at stronger values, as the impacts decrease. By using a more concentrated crosslinking agent (1 M glutaraldehyde), it is possible to decrease environmental impacts by approximately 35% in all categories. This is because, in this case, both situations have similar uncertainties in terms of values, and an uncertainty analysis is not required.

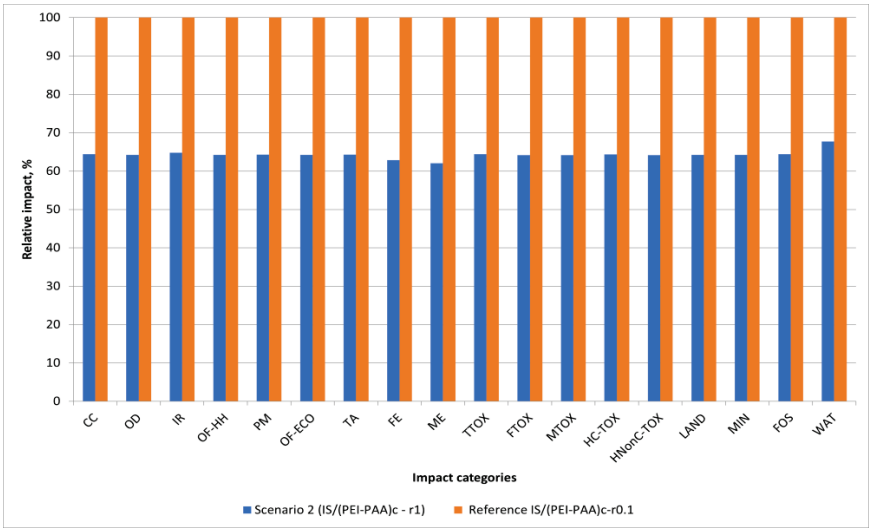

Figure 6. Scenario 2 vs. the reference case comparison of environmental impacts.

In Scenario 3, the replacement of the PAA with PMAA was studied. The results presented in Figure 7 demonstrate that by making this change, it is possible to have lower impact values from 7.91 to 9.26% in all categories, except for water consumption, where this difference was 14.33%.

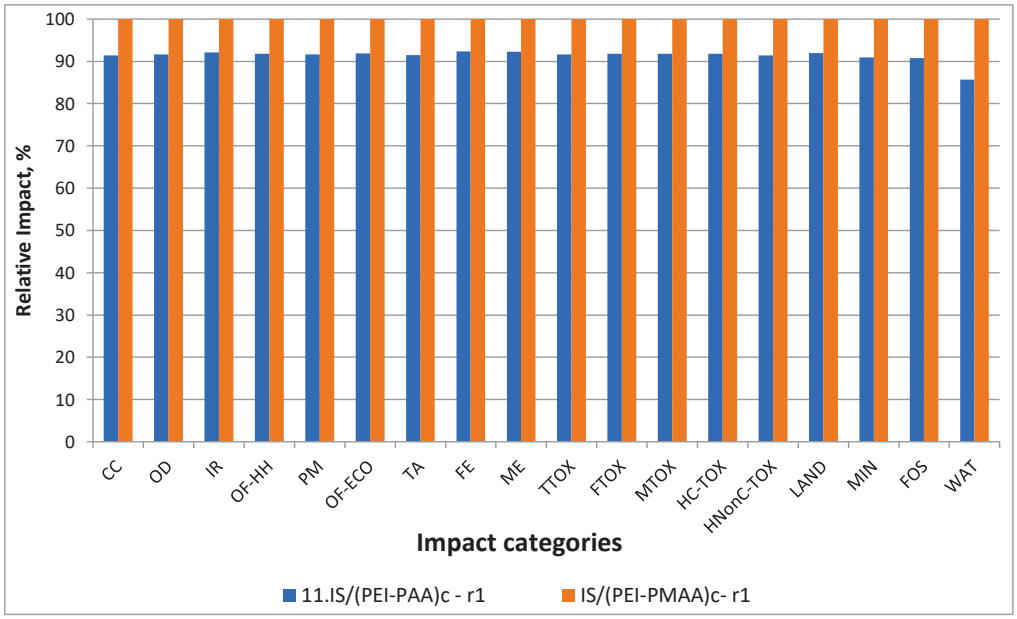

Figure 7. Scenario 3 vs. the reference case comparison of environmental impacts.

4. Conclusions

This study showcases how life cycle assessment can be used to evaluate the eco-design options for early-stage material development and engineering while allowing the environmental sustainability of novel materials when used for wastewater treatment processes to be evaluated. This LCA study is focused on the comparison of the technical and environmental performances of two types of synthesis strategies for PEI-coated silica particles (organic/inorganic composites), which were tested for Cd^{2+} ion removal from aqueous solutions. Laboratory experiments of materials] synthesis and testing (consisting of repeated cycles of pollutant loading and sorbent regeneration) enabled the identification and quantification of types and values of environmental impacts that were associated with these processes, and three eco-design strategies based on materials substitution were investigated. Concretely, the silica-core particle was found to have the most important contribution to the overall environmental impact profile. The scenario which had considered replacing the highly engineered porous silica core particle with a simpler quartz sand particle did not lead to better environmental performances, despite its promising functional performance. This evaluation demonstrated that the material functionality, as an expression of its technical performance, represented a key aspect in the representation and estimation of the environmental performance of novel materials. From a practical point of view and from the perspective of the material developer, it is important to consider as early as possible in the product development process the eco-design criteria that can evaluate the prospective environmental sustainability of novel materials. At the same time, the LCA results have pointed out that aspects such as functional unit definition, inventory data gaps, data estimation, and associated uncertainties have to be carefully considered and analyzed when interpreting the LCA results. Further research should include the investigation of environmental impacts that are associated with the nano-structured particles released in the environment, which are likely to occur during the use and post-use phases of their life cycle.

Author Contributions: Conceptualization, G.B. and F.B.; methodology G.B., data validation, C.T. and M.M.; formal analysis, G.B., F.B. and I.M.; Investigation, G.B., I.M., F.B., R.C., M.M. and C.T.; resources, C.T. and M.M.; writing—original draft preparation, G.B., R.C. and F.B.; writing—review and editing, G.B., F.B., M.M. and C.T.; visualization, G.B.; supervision, C.T. and M.M.; project administration, C.T.; funding acquisition, C.T. All authors have read and agreed to the published version of the manuscript.

Funding: This work was supported by a grant of the Ministry of Research, Innovation and Digitization, CNCS/CCCDI–UEFISCDI, project number PN-III-P4-ID-PCE-2020-1199, within PNCDI III, contract PCE 56/2021, "Innovative and sustainable solutions for priority and emerging pollutants removal through advanced wastewater treatment processes" (SUSTINWATER).

Institutional Review Board Statement: Not applicable.

Informed Consent Statement: Not applicable.

Data Availability Statement: The data presented in this study are available on request from the first author.

Conflicts of Interest: The authors declare no conflict of interest.

References

1. Ghiorghita, C.A.; Mihai, M. Recent Developments in Layer-by-Layer Assembled Systems Application in Water Purification. *Chemosphere* **2021**, *270*, 129477. [CrossRef]
2. Morosanu, I.; Paduraru, C.; Bucatariu, F.; Fighir, D.; Mihai, M.; Teodosiu, C. Shaping Polyelectrolyte Composites for Heavy Metals Adsorption from Wastewater: Experimental Assessment and Equilibrium Studies. *J. Environ. Manag.* **2022**, *321*, 115999. [CrossRef]
3. Zepon Tarpani, R.R.; Azapagic, A. Life Cycle Environmental Impacts of Advanced Wastewater Treatment Techniques for Removal of Pharmaceuticals and Personal Care Products (PPCPs). *J. Environ. Manag.* **2018**, *215*, 258–272. [CrossRef]
4. Phoon, B.L.; Ong, C.C.; Mohamed Saheed, M.S.; Show, P.L.; Chang, J.S.; Ling, T.C.; Lam, S.S.; Juan, J.C. Conventional and Emerging Technologies for Removal of Antibiotics from Wastewater. *J. Hazard. Mater.* **2020**, *400*, 122961. [CrossRef]
5. Mojiri, A.; Zhou, J.L.; Robinson, B.; Ohashi, A.; Ozaki, N.; Kindaichi, T.; Farraji, H.; Vakili, M. Pesticides in Aquatic Environments and Their Removal by Adsorption Methods. *Chemosphere* **2020**, *253*, 126646. [CrossRef] [PubMed]
6. Senguttuvan, S.; Janaki, V.; Senthilkumar, P.; Kamala-Kannan, S. Polypyrrole/Zeolite Composite—A Nanoadsorbent for Reactive Dyes Removal from Synthetic Solution. *Chemosphere* **2022**, *287*, 132164. [CrossRef]
7. Li, B.; Wang, K.; Ma, L.X.; Sun, S.J.; Jia, L.R.; Yuan, A.N.; Shen, J.M.; Qi, H.; Zhang, A.P. Deca-BDE and Alternative Halogenated Flame Retardants in a Wastewater Treatment Plant in Harbin (2009–2016): Occurrence, Temporal Trends, Seasonal Variation, and Fate. *Sci. Total Environ.* **2018**, *625*, 1156–1163. [CrossRef]
8. Barjoveanu, G.; Teodosiu, C.; Bucatariu, F.; Mihai, M. Prospective Life Cycle Assessment for Sustainable Synthesis Design of Organic/Inorganic Composites for Water Treatment. *J. Clean. Prod.* **2020**, *272*, 122672. [CrossRef]
9. Kim, S.; Chu, K.H.; Al-Hamadani, Y.A.J.; Park, C.M.; Jang, M.; Kim, D.H.; Yu, M.; Heo, J.; Yoon, Y. Removal of Contaminants of Emerging Concern by Membranes in Water and Wastewater: A Review. *Chem. Eng. J.* **2018**, *335*, 896–914. [CrossRef]
10. Abtahi, S.M.; Ilyas, S.; Joannis Cassan, C.; Albasi, C.; de Vos, W.M. Micropollutants Removal from Secondary-Treated Municipal Wastewater Using Weak Polyelectrolyte Multilayer Based Nanofiltration Membranes. *J. Membr. Sci.* **2018**, *548*, 654–666. [CrossRef]
11. Parida, V.K.; Saidulu, D.; Majumder, A.; Srivastava, A.; Gupta, B.; Gupta, A.K. Emerging Contaminants in Wastewater: A Critical Review on Occurrence, Existing Legislations, Risk Assessment, and Sustainable Treatment Alternatives. *J. Environ. Chem. Eng.* **2021**, *9*, 105966. [CrossRef]
12. Bezzina, J.P.; Ruder, L.R.; Dawson, R.; Ogden, M.D. Ion Exchange Removal of Cu(II), Fe(II), Pb(II) and Zn(II) from Acid Extracted Sewage Sludge–Resin Screening in Weak Acid Media. *Water Res.* **2019**, *158*, 257–267. [CrossRef]
13. Musteręț, C.P.; Morosanu, I.; Ciobanu, R.; Plavan, O.; Gherghel, A.; Al-Refai, M.; Roman, I.; Teodosiu, C. Assessment of Coagulation–Flocculation Process Efficiency for the Natural Organic Matter Removal in Drinking Water Treatment. *Water* **2021**, *13*, 3073. [CrossRef]
14. Aguilar-Pérez, K.M.; Avilés-Castrillo, J.I.; Ruiz-Pulido, G. Nano-Sorbent Materials for Pharmaceutical-Based Wastewater Effluents—An Overview. *Case Stud. Chem. Environ. Eng.* **2020**, *2*, 100028. [CrossRef]
15. Rathi, B.S.; Kumar, P.S. Application of Adsorption Process for Effective Removal of Emerging Contaminants from Water and Wastewater. *Environ. Pollut.* **2021**, *280*, 116995. [CrossRef] [PubMed]
16. Du, J.; Zhang, B.; Li, J.; Lai, B. Decontamination of Heavy Metal Complexes by Advanced Oxidation Processes: A Review. *Chin. Chem. Lett.* **2020**, *31*, 2575–2582. [CrossRef]
17. Maniakova, G.; Kowalska, K.; Murgolo, S.; Mascolo, G.; Libralato, G.; Lofrano, G.; Sacco, O.; Guida, M.; Rizzo, L. Comparison between Heterogeneous and Homogeneous Solar Driven Advanced Oxidation Processes for Urban Wastewater Treatment: Pharmaceuticals Removal and Toxicity. *Sep. Purif. Technol.* **2020**, *236*, 116249. [CrossRef]

18. Jangid, P.; Inbaraj, M.P. Applications of Nanomaterials in Wastewater Treatment. *Mater. Today Proc.* **2021**, *43*, 2877–2881. [CrossRef]
19. Jain, A.; Kumari, S.; Agarwal, S.; Khan, S. Water Purification via Novel Nano-Adsorbents and Their Regeneration Strategies. *Process Saf. Environ. Prot.* **2021**, *152*, 441–454. [CrossRef]
20. Jawed, A.; Saxena, V.; Pandey, L.M. Engineered Nanomaterials and Their Surface Functionalization for the Removal of Heavy Metals: A Review. *J. Water Process Eng.* **2020**, *33*, 101009. [CrossRef]
21. El-sayed, M.E.A. Nanoadsorbents for Water and Wastewater Remediation. *Sci. Total Environ.* **2020**, *739*, 139903. [CrossRef] [PubMed]
22. Menazea, A.A.; Ezzat, H.A.; Omara, W.; Basyouni, O.H.; Ibrahim, S.A.; Mohamed, A.A.; Tawfik, W.; Ibrahim, M.A. Chitosan/Graphene Oxide Composite as an Effective Removal of Ni, Cu, As, Cd and Pb from Wastewater. *Comput. Theor. Chem.* **2020**, *1189*, 112980. [CrossRef]
23. Bucatariu, F.; Schwarz, D.; Zaharia, M.; Steinbach, C.; Ghiorghita, C.A.; Schwarz, S.; Mihai, M. Nanostructured Polymer Composites for Selective Heavy Metal Ion Sorption. *Colloids Surf. A Physicochem. Eng. Asp.* **2020**, *603*, 125211. [CrossRef]
24. Kothavale, V.P.; Sharma, A.; Dhavale, R.P.; Chavan, V.D.; Shingte, S.R.; Selyshchev, O.; Dongale, T.D.; Park, H.H.; Zahn, D.R.T.; Salvan, G.; et al. Carboxyl and Thiol-Functionalized Magnetic Nanoadsorbents for Efficient and Simultaneous Removal of Pb(II), Cd(II), and Ni(II) Heavy Metal Ions from Aqueous Solutions: Studies of Adsorption, Kinetics, and Isotherms. *J. Phys. Chem. Solids* **2023**, *172*, 111089. [CrossRef]
25. Nosike, E.I.; Jiang, Z.; Miao, L.; Akakuru, O.U.; Yuan, B.; Wu, S.; Zhang, Y.; Zhang, Y.; Wu, A. A Novel Hybrid Nanoadsorbent for Effective Hg2+ Adsorption Based on Zeolitic Imidazolate Framework (ZIF-90) Assembled onto Poly Acrylic Acid Capped Fe3O4 Nanoparticles and Cysteine. *J. Hazard. Mater.* **2020**, *392*, 122288. [CrossRef]
26. Semenova, A.; Giles, L.W.; Vidallon, M.L.P.; Follink, B.; Brown, P.L.; Tabor, R.F. The Structure of Colloidal Polyethylenimine–Silica Nanocomposite Microparticles. *Particuology* **2023**, *76*, 86–100. [CrossRef]
27. Bucatariu, F.; Ghiorghita, C.-A.; Schwarz, D.; Boita, T.; Mihai, M. Layer-by-Layer Polyelectrolyte Architectures with Ultra-Fast and High Loading/Release Properties for Copper Ions. *Colloids Surf. A Physicochem. Eng. Asp.* **2019**, *579*, 123704. [CrossRef]
28. Bucatariu, F.; Teodosiu, C.; Morosanu, I.; Fighir, D.; Ciobanu, R.; Petrila, L.M.; Mihai, M. An Overview on Composite Sorbents Based on Polyelectrolytes Used in Advanced Wastewater Treatment. *Polymers* **2021**, *13*, 3963. [CrossRef]
29. Khan, A.H.; Khan, N.A.; Zubair, M.; Azfar Shaida, M.; Manzar, M.S.; Abutaleb, A.; Naushad, M.; Iqbal, J. Sustainable Green Nanoadsorbents for Remediation of Pharmaceuticals from Water and Wastewater: A Critical Review. *Environ. Res.* **2022**, *204*, 112243. [CrossRef]
30. García-Quintero, A.; Palencia, M. A Critical Analysis of Environmental Sustainability Metrics Applied to Green Synthesis of Nanomaterials and the Assessment of Environmental Risks Associated with the Nanotechnology. *Sci. Total Environ.* **2021**, *793*, 148524. [CrossRef]
31. Bârjoveanu, G.; Teodosiu, C.; Gîlcă, A.F.; Roman, I.; Fiore, S. Environmental Performance Evaluation of a Drinking Water Treatment Plant: A Life Cycle Assessment Perspective. *Environ. Eng. Manag. J.* **2019**, *18*, 513–522.
32. Lawal, U.; Kumar Allam, B.; Bahadur Singh, N.; Banerjee, S. Adsorptive Removal of Cr(VI) from Wastewater by Hexagonal Boron Nitride-Magnetite Nanocomposites: Kinetics, Mechanism and LCA Analysis. *J. Mol. Liq.* **2022**, *354*, 118833. [CrossRef]
33. Garcia Gonzalez, M.N.; Quiroga-Flores, R.; Börjesson, P. Life Cycle Assessment of a Nanomaterial-Based Adsorbent Developed on Lab Scale for Cadmium Removal: Comparison of the Impacts of Production, Use and Recycling. *Clean. Environ. Syst.* **2022**, *4*, 100071. [CrossRef]
34. Salieri, B.; Barruetabeña, L.; Rodríguez-Llopis, I.; Jacobsen, N.R.; Manier, N.; Trouiller, B.; Chapon, V.; Hadrup, N.; Jiménez, A.S.; Micheletti, C.; et al. Integrative Approach in a Safe by Design Context Combining Risk, Life Cycle and Socio-Economic Assessment for Safer and Sustainable Nanomaterials. *NanoImpact* **2021**, *23*, 100335. [CrossRef]
35. Subramanian, V.; Peijnenburg, W.J.G.M.; Vijver, M.G.; Blanco, C.F.; Cucurachi, S.; Guin, J.B. Chemosphere Approaches to Implement Safe by Design in Early Product Design through Combining Risk Assessment and Life Cycle Assessment. *Chemosphere* **2023**, *311*, 137080. [CrossRef]
36. Mech, A.; Gottardo, S.; Amenta, V.; Amodio, A.; Belz, S.; Bøwadt, S.; Drbohlavová, J.; Farcal, L.; Jantunen, P.; Małyska, A.; et al. Safe- and Sustainable-by-Design: The Case of Smart Nanomaterials. A Perspective Based on a European Workshop. *Regul. Toxicol. Pharmacol.* **2022**, *128*, 105093. [CrossRef]
37. Barjoveanu, G.; Teodosiu, C.; Mihai, M.; Morosanu, I.; Fighir, D.; Vasiliu, A.-M.; Bucatariu, F. Chapter 12—Life Cycle Assessment for Eco-Design in Product Development. In *Assessing Progress Towards Sustainability*; Elsevier: Amsterdam, The Netherlands, 2022; pp. 247–271. [CrossRef]
38. Althaus, H.; Chudacoff, M.; Hischier, R.; Jungbluth, N.; Osses, M.; Primas, A.; Hellweg, S. Life Cycle Inventories of Chemicals. *Final Rep. Ecoinvent Data* **2007**, *2*, 1–957.
39. Piccinno, F.; Hischier, R.; Seeger, S.; Som, C. Predicting the Environmental Impact of a Future Nanocellulose Production at Industrial Scale: Application of the Life Cycle Assessment Scale-up Framework. *J. Clean. Prod.* **2018**, *174*, 283–295. [CrossRef]
40. Zahran, M.A.; El-Mawgood, W.A.A.; Basuni, M. Poly Acrylic Acid: Synthesis, Aqueous Properties and Their Applications as Scale Inhibitor. *Elastomers Plast.* **2016**, *7–8*, 53–58.
41. Ristic, I.; Miletic, A.; Sad, N.; Govedarica, O. The Synthesis of Polyacrylic Acid With Controlled Molecular the Synthesis of Polyacrylic Acid With Controlled Molecular Weights. *Phys. Chem.* **2016**, *2016*, 685–688.

42. Azlina, H.N.; Hasnidawani, J.N.; Norita, H.; Surip, S.N. Synthesis of SiO_2 Nanostructures Using Sol-Gel Method. *Acta Phys. Pol. A* **2016**, *129*, 842–844. [CrossRef]
43. *ISO 14040*; Environmental Management—Life Cycle Assessment—Part 1: Principles and Framework. International Organization for Standardization: Geneva, Switzerland, 2006; p. 3.
44. *ISO 14044*; Environmental Management. Life Cycle Assessment. Requirements and Guidelines. International Organization for Standardization: Geneva, Switzerland, 2006.
45. Huijbregts, M.A.J.; Steinmann, Z.J.N.; Elshout, P.M.F.; Stam, G.; Verones, F.; Vieira, M.; Zijp, M.; Hollander, A.; van Zelm, R. ReCiPe2016: A Harmonised Life Cycle Impact Assessment Method at Midpoint and Endpoint Level. *Int. J. Life Cycle Assess.* **2017**, *22*, 138–147. [CrossRef]
46. Bucatariu, F.; Zaharia, M.M.; Petrila, L.M.; Simon, F.; Mihai, M. Sand/Polyethyleneimine Composite Microparticles: Eco-Friendly, High Selective and Efficient Heavy Metal Ion Catchers. *Colloids Surf. A Physicochem. Eng. Asp.* **2022**, *649*, 129540. [CrossRef]
47. Bucatariu, F.; Petrila, L.M.; Zaharia, M.M.; Simon, F.; Mihai, M. Sand/Polyethyleneimine Composites with Enhanced Sorption/Desorption Properties toward Pollutants. *Water* **2022**, *14*, 3928. [CrossRef]

nanomaterials

MDPI

Review

Noble Metals Functionalized on Graphene Oxide Obtained by Different Methods—New Catalytic Materials

Mihaela Iordache [1], Anisoara Oubraham [1,*], Ioan-Sorin Sorlei [1], Florin Alexandru Lungu [1], Catalin Capris [1], Tudor Popescu [2] and Adriana Marinoiu [1,*]

[1] National Research and Development Institute for Cryogenics and Isotopic Technologies—ICSI, 4 Uzinei Street, 240050 Râmnicu Vâlcea, Romania
[2] Faculty of Chemical Engineering and Biotechnologies, 011061 Bucharest, Romania
* Correspondence: anisoara.oubraham@icsi.ro (A.O.); adriana.marinoiu@icsi.ro (A.M.)

Abstract: In recent years, research has focused on developing materials exhibiting outstanding mechanical, electrical, thermal, catalytic, magnetic and optical properties such as graphene/polymer, graphene/metal nanoparticles and graphene/ceramic nanocomposites. Two-dimensional sp^2 hybridized graphene has become a material of choice in research due to the excellent properties it displays electrically, thermally, optically and mechanically. Noble nanomaterials also present special physical and chemical properties and, therefore, they provide model building blocks in modifying nanoscale structures for various applications, ranging from nanomedicine to catalysis and optics. The introduction of noble metal nanoparticles (NPs) (Au, Ag and Pd) into chemically derived graphene is important in opening new avenues for both materials in different fields where they can provide hybrid materials with exceptional performance due to the synergistical result of the specific properties of each of the materials. This review presents the different synthetic procedures for preparing Pt, Ag, Pd and Au NP/graphene oxide (GO) and reduced graphene oxide (rGO) composites.

Keywords: reduced graphene oxide (rGO); noble metal nanomaterials (NPs); catalytic activity

Citation: Iordache, M.; Oubraham, A.; Sorlei, I.-S.; Lungu, F.A.; Capris, C.; Popescu, T.; Marinoiu, A. Noble Metals Functionalized on Graphene Oxide Obtained by Different Methods—New Catalytic Materials. *Nanomaterials* **2023**, *13*, 783. https://doi.org/10.3390/nano13040783

Academic Editor: Supriya A. Patil

Received: 25 January 2023
Revised: 16 February 2023
Accepted: 17 February 2023
Published: 20 February 2023

1. Introduction

Polymer electrolyte membrane fuel cells (PEMFCs) represent one of the top researched power generation devices that convert the chemical energy of hydrogen directly into electricity [1]. Because this technology is clean as well as efficient, it provides an option for applications such as power generation on a large scale, co-generation of power and heat, backup and off-grid energy sources as well as transportation and mobile applications. Serving as one of the main problems that requires solving is the inferior kinetics of the oxygen reduction reaction (ORR) as well as the fuel cell reactions, which require a significant number of precious metals, leading to high costs of production. Poor performance and robustness of the catalysts being used as part of the electrodes is another significant problem to solve for PEMFCs [2]. Various materials and methods have also been proposed to solve these problems. Thus, one approach in this regard was replacing the carbon black in the catalyst layer with graphene. Over the last few years, numerous studies were carried out to evaluate the potential of using graphene-based materials in energy applications. Their large surface area, outstanding mechanical characteristics and superior electrical conductivity coupled with the workability of graphene have been the reasoning behind this attention [1]. Globally, there is a growing demand for nanostructured materials, as they are the key elements in enabling tools for renewable energy and hydrogen storage as well as indicator applications. Materials based on graphene have been shown to be very promising in achieving this goal due to their interesting properties, resulting in the conduction of a large number of theoretical and experimental studies [3]. With graphene being a flat monolayer of hexagonally arranged sp^2-bonded carbon atoms bundled in a 2D figure-like

network, it has been offered considerable attention from the experimental and the theoretical communities alike. Considering its superior electronic characteristics, graphene sheets offer potential solutions for the manufacturing of nanocomposites [4] and in the fabrication of field-effect transistors [5], dye-sensitized solar cells [6] as well as electrochemical sensors [7], electromechanical resonators [8] and lithium-ion batteries [4]. Graphene-based composite materials are capable of improving both electronic and thermal conductivity [9]. Moreover, graphene can provide stable mechanical support to active electrode materials, which can result in a potential composite for supercapacitor applications [10]. Noble metal nanoparticles (NPs) are a major topic for various fields such as electronics, sensing and catalysis as well as medicine and energy storage, as they exhibit unconventional physical and chemical properties [11]. In the last few decades, scientists have been especially interested in nano catalysis due to NPs satisfying nearly all the criteria of an ideal catalyst. They are of extremely small size and they present high surface-to-volume ratio, outstanding shape-dependent properties, uniformity in particle-size distribution while having a truly heterogenous nature and they are reusable with a near-constant efficiency [12]. The dispersion of metal nanoparticles on graphene sheets potentially offers a new way of developing catalytic, magnetic and optoelectronic materials [9]. However, the stability and catalytic activity of NP-based materials are limited due to their severe aggregation in aqueous media. More recently, graphene oxide (GO), which is a 2D material with a high specific surface area, when used as a platform to load NPs, has shown improvements in the stability and catalytic performance of the resulting NPs@GO nanocomposite [13]. Graphite oxide is a material that is produced through the oxidation of graphite leading to an increased interlayer spacing and the functionalization of its basal planes. Reproducible GO properties can be obtained depending on the state of preparation and on the graphene crystal, powders and particle size in relationship with the careful control of the water content of the applied acids, temperature conditions, length of time and drying conditions [3]. Graphene oxide (GO) is a two-dimensional carbon nanomaterial composed of carbon atoms organized in a hexagonal lattice, forming a flat sheet and containing oxygenated groups. GO has been a topic of interest for many applications (e.g., material science, nanomedicine, environmental technology and biotechnology) due to the extraordinary properties it exhibits, such as thermal resistance, electrical conductivity, optical transparency, chemical versatility and mechanical strength [14]. The GO-based materials also show remarkable properties, while chemical, thermal or other methods can be used in order to decrease the oxygen content, resulting in reduced graphene oxide (rGO). GO has been proven to be a very competent carbon support for the decoration of various metal nanoparticles due to it having significant surface area/active surface sites and its available nanosheets on both sides. The highly synergistic effect between nanoparticles and their uniform dispersion due to GO directly leads to an increase in the performance of the material [15]. The properties of both graphene and graphene oxide allows them to be used in several fields, especially for the preparation of nanocomposites and catalytic performances [16]. In noble metal/graphene nanocomposites using Pd, Pt, Au and Ag nanoparticles, the graphene oxide and metal salts are completely reduced. After decorating metal NPs on GO surfaces, the nonlinear optical properties can be significantly improved [3].

The novelty of this work is the comprehensive analysis of the state-of-the-art synthesis scalable methods for preparation of noble metals that are supported on graphene oxide. At the nano level, the compact atomic organization gives special properties for materials, such as electrical resistance or conductivity, precisely the properties for which noble metals are used. Noble metals represent limited group of metals including elements such as ruthenium, rhodium, palladium, silver, rhenium, osmium, iridium, platinum and gold. These elements are defined by two chemical properties that differentiate them from the rest of the metals—corrosion resistance and stability in oxidizing agents.

This work aims to update new synthesis methods of graphene functionalized with noble metals (Pt, Au, Ag and Pd) and to introduce new catalysts in fuel cell applications and renewable technologies. The paper undertakes an analysis of the recent research in the

field and highlight the advantages of using noble metal nanostructures in catalytic applications. This new information comes in addition to works from the literature that focus on biomedical applications or biosensors [17], diagnosis or therapy [18] and less in fields such as fuel cell technologies, renewable energy and hydrogen storage [19,20]. Thus, Section 2 will address the theme "Methods of Synthesis NPs@GO Nanocomposites", followed by Section 3 with examples of catalyst applications "Advantages and disadvantages of the synthesis methods of noble metals functionalized on graphene oxide" and ending with Section 4, "Conclusions".

2. Methods of Synthesis NPs@GO Nanocomposites

The last allotropic form of carbon graphene has demonstrated that it possesses remarkable physicochemical properties (specific surface area between 1500–2600 $m^2\ g^{-1}$) [21,22] that can be exploited for many electrochemical applications. Graphene possesses a single layer as a carbon sheet with the thickness of an atom. Graphene oxide (GO) represents the oxidized form of graphene and is considered in recent years as a suitable raw material for the manufacture of graphene. The most used method for obtaining graphene oxide, starting from graphite, is the Hummer chemical oxidation method. This method is shown schematically in Figure 1. This technique was also modified by other researchers in order to obtain an improved quality of graphene oxide. The obtained graphene oxide is subsequently dried and reduced using different reducing agents to improve electrical conductivity. To reduce graphene oxide, different reductants can be used (hydroiodic acid, hydrazine hydrate, hydrobromic acid, sodium borohydride, hydrochloric acid, sulfuric acid, ascorbic acid and dextrose) in order to eliminate the oxygen functional groups for the considerable improvement of electrical conductivity. The presence of different functional groups in graphene oxide influences the hydrophilic behavior, which is due to the level of oxidation. In addition, the multiple layers of GO are the consequence of a strong electrostatic charge but also of hydrophilicity, which can facilitate a good dispersion for anchored metals. The reduction in GO (specific surface area around 380–1000 $m^2\ g^{-1}$, peak at $2\theta = 11.2°$) [21] is a classical method for obtaining a graphene-like structure. Reduced graphene oxide can be obtained by different chemical, thermal or photo-thermal reduction methods. Depending on the methods used, the produced rGO (specific surface area between 389.9–670 $m^2\ g^{-1}$, peak at $2\theta = 25.8°$, electrical conductivity: 103.3 $S{\cdot}cm^{-1}$ and $I_D/I_G = 0.2$) [23] approaches more or less close to the pure graphene structure. Among the reducing agents we mention inorganic chemical agents (for example, sodium borohydride) or organic (for example, phenyl hydrazine hydrate or hydroxylamine). Thermal reduction usually takes place in an inert atmosphere at elevated temperatures.

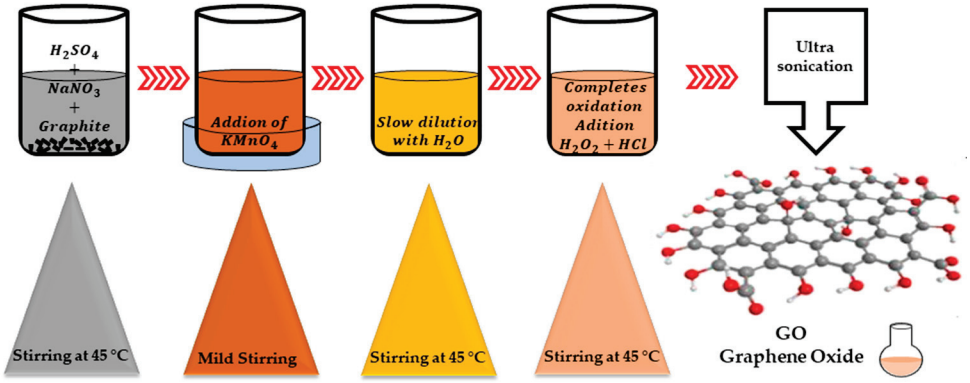

Figure 1. Hummer's method.

In order for graphene to be electrochemically active, it is often used to modify the carbon structure by functionalizing it with different types of noble metal elements. This functionalization will be dealt with in this review.

The reported methods aimed at the synthesizing of different metal nanoparticles (MNPs)/rGO nanocomposites involve chemical reduction, electrochemical deposition, thermally assisted method, photochemical reduction, microwave irradiation and sono-chemical reduction. In most of these methods, a suspension of GO based on water or ethanol is allowed to react with a metal precursor in the presence of a reducing agent such as hydrazine hydrate, ascorbic acid, sodium citrate or glucose in order to obtain a simultaneous reduction in both the metal ions and the GO resulting in the production of MNPs/rGO composites.

2.1. Chemical Reduction

Chemical reduction is the most commonly used method to effectively immobilize NPs on GO and rGO. This method involves noble metal ions in solution being reduced to NPs on GO nanowires through additional reductants such as $NaBH_4$, ascorbic acid, sodium citrate or hydrazine (Figure 2). Usually, the GO and rGO dispersion is firstly mixed with noble metal salt solutions, following which the noble metal ions begin adsorbing on the GO and rGO nanosheet surface through electrostatic interaction. Following this, the reducing agents in the mixture reduce the noble metal ions adsorbed in NPs on GO and rGO nanowires [24].

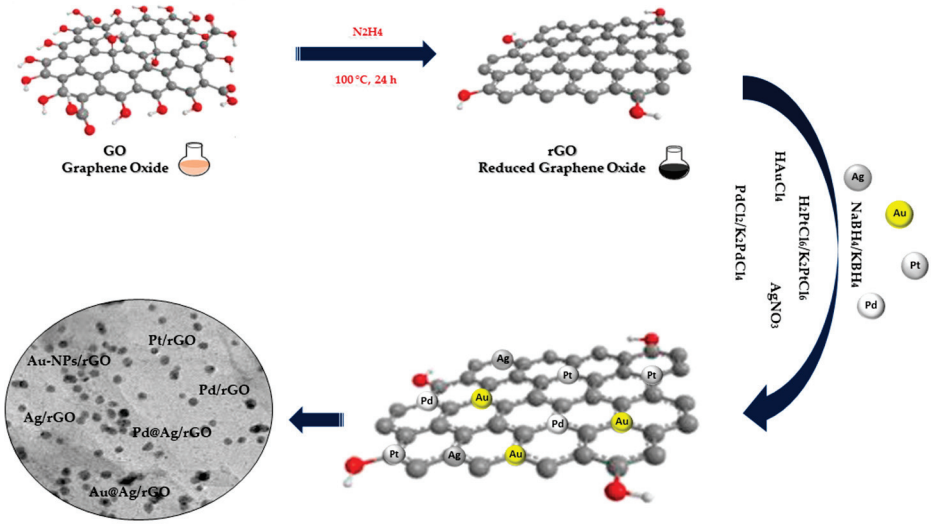

Figure 2. Chemical reduction synthesis of noble metal nanocomposites.

The three fundamental steps constituting the reduction process are as follows: (1) adsorption/reduction, (2) nucleation and (3) growth. The presence of oxygen-containing functional groups on the surface of the GO and rGO favors the adsorption of free metal ions through electrostatic interactions, followed by the reduction in metal ions by a reducing agent and finally the growth of NPs on the GO and rGO sheets. In spite of the formation of MNPs by chemical reduction being a facile process, this technique is limited due to difficulties sterned from size and morphology of the NPs, which can potentially result in polydisperse and large sizes of on GO and rGO surfaces [18].

Guo et al. [24], through the use of the chemical co-reduction method, synthesized a series of Pt-Ni/rGO catalysts with different Pt/Ni molar ratios and a total metal concentration of 0.99 mM. The production of these catalysts was performed through the rapid injection of KBH_4 to reduce H_2 $PtCl_6$ and $Ni(NO_3)_2$ in the experiment at a temperature of 273 K and in an N_2 atmosphere. X-ray powder diffraction (XRD) was used for the characterization of the detailed crystalline phases of the Pt-based NPs loaded on partially reduced GOs. The XRD results for the Pt/rGO catalyst displayed four diffraction peaks of (111), (200), (220) and (311). The peaks seen in the Pt_{40}-Ni_{60}/rGO catalyst model were shifted to a high angle range suggesting the formation of ally structured Pt-Ni BNPs loaded on rGO. Transmission electron microscope (TEM) images clearly visualized the uniform

distribution of the Pt and Pt-Ni NPs on the rGO with an average size of about 3.4 and 2.6 nm; these results were consistent with the ones from the Scherrer formula. This indicates that the size of the Pt_{40}-Ni_{60} BNPs of Pt_{40}-Ni_{60}/rGO catalyst could be reduced through the doping of Ni. Furthermore, the lattice stripe spacing of 0.220 nm can be assigned to the (111) lattice planes of Pt. The HRTEM image of Pt_{40}-Ni_{60} BNPs showed a lattice stripe spacing of 0.206 nm, value which is intermediary between the lattice spacing of crystalline Pt (111) at 0.226 nm and Ni (111) at 0.203 nm. This serves as a further indicator that the rGO-supported Pt-Ni BNPs possess an alloy structure. Moreover, elemental mapping images of the catalyst revealed that the C and O elements were uniformly distributed in the entire sample, and that Pt and Ni elements were aggregated into particles, thus serving as confirmation of the formation of alloy-structured Pt-Ni BNPs. After an XPS characterization of the Pt/rGO catalyst, the C 1s spectrum typically showed four peaks at 284.75, 284.86, 286.9 and at 287.6 eV, which assigned the characteristics of C-C, C=C, C-O and C=O, respectively. The fact that O 1s XPS spectrum can be deconvoluted into peaks corresponding to O=C (at 531.7 eV) and O-C (at 532.88 eV) can be used as an explanation for the incomplete reduction in the function groups (hydroxyl, carboxyl, etc.) of GO during the co-reduction process. Pairing peaks assigned to metallic Pt^0 $4f_{(7/2)}$ and Pt^0 $4f_{(5/2)}$ were located at 71.32 and 72.2 eV in the Pt 4f spectrum with one other pairing peak assigned to oxidized $Pt^{(2+)}$ $4f_{(7/2)}$and $Pt^{(2+)}$ $4f_{(5/2),}$ being located at 72.2 and 75.62 eV, respectively. The first pairing peaks in the Pt/rGO catalyst were found to have higher binding energies than the bulk Pt $4f_{(7/2)}$ and Pt $4f_{(5/2)}$ (71.1 eV and 74.4 eV, respectively) by approximately 0.22 eV and 0.1 eV, which is an indicator that the Pt NPs were positively charged.

In another study [25], cobalt was used in the fabrication of AgPdNPs supported on rGO. Firstly, $NaBH_4$ was used to reduce Pd $^{(2+)}$ and Co $^{(2+)}$ with the resulting amorphous $Co_3(BO_3)_2$ and AgPd on the surface of the rGO. The amorphous $Co_3(BO_3)_2$ can be removed simply through etching with H_3PO_4. Using this method, the prevention of the aggregation of AgPd nanoparticles is effective, thus obtaining well-dispersed AgPd nanoparticles. The rGO catalyst supported by the AgPd nanoparticles was used for the catalytic transfer hydrogenation of nitro-compounds at room temperature using H-COOH as hydrogen donor. This obtained catalyst has a high catalytic efficiency, which is a result of the highly dispersed bimetallic nanoparticles coupled with the synergistic interaction between the metallic nanoparticles and the support. TEM showed that the AgPd particles of $Ag_{0.1}Pd_{0.9}$/rGO catalyst were effectively dispersed on the rGO lamellar support. The obvious lattice fringe found in the representative high-resolution TEM image of $Co_6Ag_{0.1}Pd_{0.9}$/rGO demonstrated the good crystallinity of the AgPdNPs. It resulted in a lattice spacing of 0.23 nm, value between the (111) lattice spacing of face-centered cubic Ag at 0.24 nm and Pd at 0.22 nm. This implies that AgPd has formed as an alloy structure. It was found that the form of the AgPd nanoparticles was not uniform; however, there was a narrow size distribution averaging at 4.3 nm $\pm$ 0.9 nm. The XRD patterns of AgPd hybrids in $Co_6Ag_{0.1}Pd_{0.9}$/rGO catalysts observe a diffraction peak located between the Ag (111, 2 theta = 38.03 deg) and Pd (111, 2 theta = 40.10 deg) diffraction peaks, further suggesting the formation of the AgPd alloy. As AgPd has been incorporated by $Co_3(BO_3)_2$, no AgPd peak of $Co_6Ag_{0.1}Pd_{0.9}$/rGO could be observed, which is further attested by the TEM results. A nitrogen adsorption/desorption analysis was carried out at 77 K in order to determine the porosity of $Ag_{0.1}Pd_{0.9}$/rGO and $Co_6Ag_{0.1}Pd_{0.9}$/rGO. $Co_6Ag_{0.1}Pd_{0.9}$/rGO was found to have a low specific surface area of approximately 6 m^2 g^{-1}, which was attributed to the high amount of $Co_3(BO_3)_2$ occupying the surface of the rGO. By comparison, in $Co_6Ag_{0.1}Pd_{0.9}$/rGO, an increased absorption of nitrogen (310 m^2 g^{-1}) can be observed. After removing $Co_3(BO_3)_2$ by etching with H_3PO_4, $(Co_6)Ag_{0.1}Pd_{.0.9}$/rGO results in high porosity, which serves in facilitating reactant diffusion to the metal nanoparticles. $(Co_6)Ag_{0.1}Pd_{0.9}$/rGO presents a higher surface area (278 m^2 g^{-1}) than $Ag_{0.1}Pd_{0.9}$/rGO (135 m^2 g^{-1}). XPS measurement results showed that Ag and Pd alike in the $(Co_6)Ag_{0.1}Pd_{.0.9}$/rGO catalyst are found in reduced states. The electronic states of Pd^0, 3d5/2 and 3d3/2 can be detected at 335.83 eV and 341.11 eV, respectively. The spectra of the Ag 3d and Pd 3d observed

attest that $(Co_6)Ag_{0.1}Pd_{0.9}$/rGO is made of metallic Ag and Pd, serving as additional confirmation of the effective synthesis of the AgPd alloy. Pd^{2+} peaks were detected at 338.14 eV and 343.48 eV, which can be attributed to the oxidation of metallic Pd in an environment containing oxygen.

Abbasi and co-workers [26] synthesized Pd nanoparticles using $PdCl_2$ and $NaBH_4$ as a strong reducing agent and polyvinyl alcohol (PVA) as stabilizing agent. During the chemical process, the palladium Pd^{2+} from the salt solution was reduced to Pd° as nanoparticles. A total of 120 mL of distilled water, 0.88 mL of freshly prepared 2% polyvinyl alcohol (PVA) solution and 2.15 mL of 0.02 M $PdCl_2$ solution were immediately added, resulting in a yellow-brown solution. A 0.1 M $NaBH_4$ solution (0.86 mL) was then slowly added to the reaction mixture while stirring vigorously. Observing an immediate color change to brown served as an indicator for the formation of Pd NPs. Following UV–Vis spectroscopic analysis, the palladium nanoparticles present the absorption spectrum of 4.1 p.m. It was found that the absorption peak of the Pd^{2+} precursor no longer appears at 420 nm, with this peak disappearing being an indicator for the complete reduction in the Pd^{2+} nanoparticles to Pd°. After three measurements, a size of 122 nm was found. The zeta potential of the palladium nanoparticles was immediately at -3.91 ± 3.85 mV, as shown. Regarding the stability of Pd NPs, although the zeta potential showed lower values, the synthesized nanoparticles were stable at room temperature and did not show any sign of agglomeration during the last 12 months.

Shu et al. [27] used a mildly tempered process of oxidation to obtain the in situ oxidation of PdIr alloy on NGs (nitrogen-doped graphene), (PdIrO/NGs). K_2PdCI_4 (36.6 mg) and $H_2IrCl_6 \cdot 6H_2O$ (7.7 mg) were dispersed in deionized water and then mixed under strong stirring. The obtained solution was added to the NGs dispersion with stirring, and then the $NaBH_4$ mixture was slowly dispersed into the aqueous solution. The obtained dispersion reacted in an ice bath under an N_2 atmosphere for 300 min. The powder resulting from vacuum filtration, washing and lyophilization was calcined at 250 °C to obtain PdIrO/NGs. The same steps excluding calcination were used to synthesize the PdIrO/NGs catalyst. The XRD patterns of PdIrO/NGs, PdIr/NGs and Pd/NGs showed a broad peak between 20° and 30°, which was identifiable as the proprietary peak of NGs. The two diffraction peaks of 39.4° and 45.8° for Pd/NGs were found to correspond to the (111) and (200) planes of metallic Pd, respectively. The pattern revealed through XRD of PdIrO/NGs, which evidently showed a positive shift of the diffraction peak between 39.4° and 40.7° in comparison to the peak of Pd/NGS, it was an indicator of the high formation quality of the Pd-Ir alloy. In addition, in the XRD pattern of $PdIrO/NG_S$, three diffraction peaks can be clearly observed at 33.9°, 41.9° and 54.8°, which correlate to the (101), (110) and (112) planes of PdO. Following the XPS analysis, a deconvolution of the Pd 3d spectra was discovered into two groups at 340.6 eV 335.3 eV, whereas the peaks discovered at 342.4 eV and 336.9 eV in the spectra may relate to $PdO/_{2/2}$ and Pd $3d_{5/2}$. A significant increase in the concentration of PdO and IrO_2 in $PdIrO/NG_S$ can be observed, meaning that the alloy was oxidized. TEM analysis showed a uniform monodispersion of the nanoparticles on the NGS surface with a slight decrease in particle size observed after alloy formation and with a significant increase following calcination. EDS mapping demonstrated the homogeneous dispersion of C, N, O, Pd and Ir in $PdIrO/NG_S$. BET (Brunauer–Emmett–Teller type IV) isotherms indicated that additional mesopores can be obtained in $PdIrO/NG_S$, as they are in agreement with the pore dimension distribution curves. The largest specific surface area is that of $PdIrO/NG_S$, with a higher limit of 122.4 $m^2\ g^{-1}$ while $PdIrO/NG_S$, with a value of 96.9 $m^2\ g^{-1}$ and with a value of 40.9 $m^2\ g^{-1}$, have lower surface areas. This demonstrates that large BET surfaces and meso-porous structure are used to improve electrocatalytic activity.

Teffu et al. [28] synthesized Pd-rGO using electroless palladium deposition by immersing the rGO in a sodium hypophosphite-based plating bath. The electroless plating bath, which contained 50 mL of sodium hypophosphite (10 g L^{-1}) as reducing agent and 5 g of rGO, was subjected to constant stirring (300 rpm) for 30 min at 50 °C, followed by

adding $PdCl_2$, 160 mL of NH_4OH (28%) and 27 g of NH_4Cl, respectively. A total of 50 mL of plating solution was added to the bath solution and the mixture was stirred for 30 min to allow Pd plating on the surface of the rGO sheets. The mixture was filtered, washed with ultrapure water and dried overnight at 80 °C. As observed from the XRD patterns in the case of Pd-rGO, the characteristic peak at 2θ = 24° is attributed to the (002) planes of the chemically reduced GO stack, which is an indicator for the effective reduction in GO by hydrazine hydrate. At the same time, it was found that the two diffraction peaks centered at 2θ of 39 and 45° can be attributed to the (111) and (200) reflections of the Pd nanoparticles, respectively. Investigation on the thermal stability of the fabricated Pd-rGO nanocomposite was performed using thermogravimetric analysis (TGA), with the results concluding that Pd-rGO shows a 15% loss of weight for the entire investigated temperature range (up to 560 °C). At 100 °C, the slight lost weight was caused by the loss of adsorbed water, while the losses of up to 400 °C are a result of the decomposition of residual hydroxyl and carboxyl functional groups. The FTIR spectra of Pd-rGO nanocomposite showed, as is expected, either the disappearance or the significantly reduced intensity of the FTIR peaks belonging to rGO after the reduction process, which serves as confirmation of the formation of Pd nanoparticles on rGO. Further observation showed very low band intensities in Pd-rGO, with some even disappearing, with reference to the rGO spectrum. This implied that the palladium incorporation on the rGO is on the surface of the graphene oxide sheets.

Rajkumar et al. synthesized [29] NP Au@Pt by two chemical methods. Au@Pt NPs were initially synthesized using Fren's method: $HAuCl_4$ was placed in a triple-neck flask connected to a condenser under strong stirring. This was heated to a boil, following which a solution of sodium citrate was quickly inserted and then the mixture was brought to a boiling temperature again. The boiling process was maintained for 10 min, with stirring being maintained for an additional 15 min post removal of the heat source. This solution was then naturally cooled to room temperature. Seed-mediated growth was the second method used to synthesize Au@Pt NPs. H_2PtCl_6, deionized water and prepared Au-NPs were mixed in a beaker. This obtained mixture was refrigerated afterward to 4 °C followed by slowly adding $NaBH_4$ under stirring to obtain Au@Pt NPs. The nanostructures and morphology of multi-walled carbon nanotubes (MWCNTs) and GO/MWCNT dispersion were conducted by TEM and showed interlaced tubular structures with an average diameter of approx. 20 nm. Several lamellar structures integrated with carbon nanotubes (CNTs) could be observed upon the supplementation of GO, essentially scattering the CNTs. The Au-NPs showed a typical spherical structure with a particle diameter of approximately 13 nm. The reduction by hydroxyl groups of chloruretic ions on sodium citrate resulted in the formation of Au NPs. Synthesizing Au@Pt NPs resulted in a slightly increased particle size while for GO/MWCNT/Au@Pt NPs, the successive drop method was employed in the copper mesh. Au@Pt NPs were pre-applied on the GO/MWCNT surface, thus a new three-dimensional sensing interface for glucose sensing was constructed. Spectra obtained through Raman of MWCNTs, GO/MWCNTs and GO/MWCNTs compatible with Au@Pt NPs showed all characteristic Raman bands of MWCNTs at 1572 cm^{-1} and 1345 cm^{-1} relating to G and D bands. D comes from the disordered carbon structure, and the G band from sp^2 hybridized carbon atoms. The intensity ratios (I_G/I_D) of the two peaks (G and D) have different values for different samples, with 0.93, 0.85 and 0.72 for MWCNT, GO/MCNT and GO/MWCNT/Au@Pts NPs, respectively. The escalation in ID indicated an expansion of the disordered carbon structure when supplementing GO and Au@Pts NPs, which demonstrated the effective construction of GO/MWCNT/Au@Pt NPs.

2.2. Thermally Assisted Method

The thermally assisted method is one of the important methods used to fabricate NPs@GO nanocomposites more simply at high temperature (Figure 3) [13]. Thermally assisted synthesis is an easy and efficient method used to immobilize NPs on GO. The speed of the process makes the size and the distribution of the NPs@GO, in this case, difficult to control.

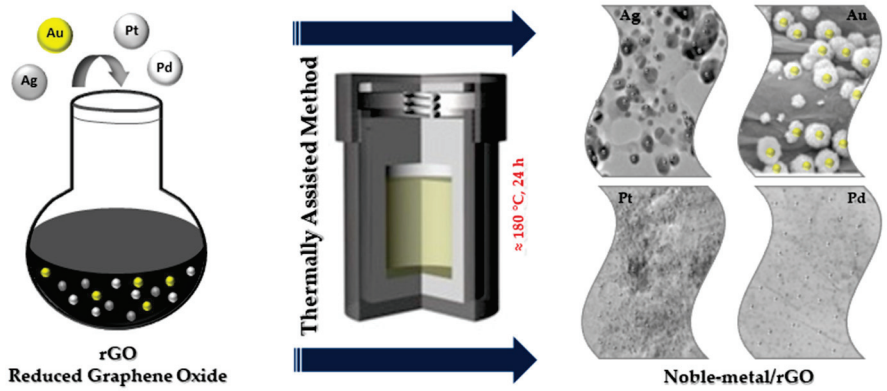

Figure 3. Thermally assisted synthesis of noble metal nanocomposites.

Abdulhusain et al. [30] prepared Ag-ZnO-rGO ternary nanocomposites by an in situ hydrothermal process in the presence of 1,8-diamino-3,6-dioxaoctane (DDO). The nano-photocatalysts possessing attractive physicochemical properties led to the idea of using a different procedure for the enhancement of Ag-ZnO-rGO nanocomposite properties in applications related to water treatment. Preparation of the appropriate nanocomposites at a lower temperature and for a shorter time have led to in situ synthesis being the chosen method. A 1,8-diamino-3,6-dioxaoctan was utilized in the synthesizing of the ternary Ag-ZnO-rGO nanocomposites, since the generous DDO carbon chain acts as a limiting factor to the accumulation of nanostructures. Firstly, graphene oxide was dispersed in distilled water resulting in solution A. Following this, zinc nitrate hexahydrate was in an aqueous mixture containing DDO, which resulted in solution B. The next step was the preparation of the silver nitrate aqueous solution. Finally, solutions A and B were mixed, while also pouring ethanol into the mixture. The resulting transparent suspension was placed in an autoclave and conditioned at 140 °C for an interval of 120 min. The collected precipitate was washed several times with distilled water and ethanol before being dried. The percentage weight of Ag was adjusted in order to attain the product with the highest performance. Moreover, studies were conducted on the effect of 1, 8-diamino-3, 6-dioxaoctan on the size distribution, morphology and purity of the product. Finally, the nanocomposite was exposed to degradation using a pollutant (RhB—rhodamine-B) in order to study its photocatalytic activity. Studies were performed to evaluate the changes in photocatalytic performance of the product by varying the pH and the concentration of Ag and the dye itself, respectively. The largest percentage of dye degradation was observed at a concentration of 10 ppm, with the pH of the mixture regulated to 11. The increased performance of the photocatalyst in alkaline media can be attributed to absorbed hydroxyl anions at the surface of the photocatalyst. Based on kinetic studies, photocatalytic reactions follow pseudo-first order with holes and hydroxyl radicals being critical active agents for photocatalysis. It is worth noting that the used synthesis process for this type of nanocomposite can be further applied for the rest of the nanocomposites due to its simplicity and eco-friendliness.

Rudra et al. used the thermally assisted method in synthesizing Au-Mn_3O_4-decorated graphene oxide and Au-Mn_3O_4 nanocomposite [31]. It was synthesized as follows: GO was added to distilled water in a beaker and sonicated for 30 min and this solution was then placed into screw cap tubes. Afterward, manganese acetate was added to the reaction mixture and the gold (III) solution. In order to balance the pH, sodium acetate was added to the solution. The screw cap tubes were stored in modified hydrothermal (MTH) conditions for 24 h. The sample was then washed several times with deionized water before being dried under vacuum to result in the Au-Mn_3O_4-decorated GO nanocomposites. The XRD results showed that the diffraction peaks correspond to (101), (112), (200), (103), (211), (204), (105), (303), (321), (224), (116), (305) and (413) planes of the Mn_3O_4, respectively. The peak positions at 2θ = 38.45°, 44.34°, 64.47°, 77.35° and 81.70° support the presence of Au (0) with the corresponding planes being 111, 200, 220, 311 and 222. Raman analysis shows a

sharp peak at 658 chm^{-1} for the Au-Mn_3O_4/GO composites, which was attributed to the Mn_3O_4 decorated on the GO. The material's morphological features and elemental contents were investigated using TEM and EDX analysis. The GO image shows the typical flake-like layered material whereas the image of the $AuMn_3O_4$ composite has a nanorod morphology owing to the growth of Mn_3O_4 nanorods from the Au (0) nucleation centers.

Wang et al. presented the preparation of Ag/CeO_2 anchored on reduced graphene oxide (rGO) nanocomposite. Ag/CeO_2-rGO is considered to be a simple, recyclable and sustainable photocatalyst for the esterification of aldehydes at room temperature under visible light irritation [15]. The catalyst was prepared as follows: 5 mmol of $Ce(NO_3)_3 \cdot 6H_2O$ and 0.5 mmol of $AgNO_3$ were slowly added to 1.8 mg mL^{-1} GO aqueous solution with constant stirring and followed by the addition of 0.5 mmol polyethylene glycol molecular weight 4000 (PEG 4000) and 20 mmol urea. The reaction mixture was transferred to an autoclave for the hydrothermal reaction at 185 °C for about 24 h. After cooling in the autoclave, the obtained solid sample was washed with deionized water and ethanol, then dehydrated at 50 °C in a hot air oven for 12 h. XRD analysis showed two additional peaks at 25.5 and 38.19 degrees, corresponding to the (002) plane of rGO and (111) planes with metallic phases of Ag. The specific surface area of reduced graphene oxide-embedded Ag/CeO_2 was found to be 292.6 m^2/g with a maximum of the pores in ranges from 5 to 15 nm.

Das et al. synthesized using thermally assisted method Pt-M/GNPs (graphene nanoplatelets) (M = Ni, Fe and Cu) of catalysts. The adsorption isotherm showed that the use of 0.2 g of metal precursor over 0.1 g of GNPs yielded the highest metal loading [1]. Pt-M/GNPs catalysts were characterized from a physical point of view using XRD analysis, thermogravimetric analysis (TGA), inductively coupled plasma mass spectrometry analysis (ICP-MS), high resolution transmission electron microscopy analysis (HRTEM) and Raman analysis. XRD was used on the synthesized catalyst samples to determine the development of metal crystal structures on the GNPs support. The samples were scanned between $10° < 2\theta < 90°$. The distinct diffraction for the Pt/GNP catalyst corresponds to the (111), (200), (220) and (311) planes of Pt in the face-centered cubic crystal structure. TGA analyses were carried out between at a temperature ranging from 25 to 1000 °C with a 10 °C min^{-1} heating rate under air atmosphere. TGAs were used on the GNPs support material in order to determine the total metal loading. The results showed that the weight content of the metal nanoparticles (Pt-Ni, Pt-Fe and Pt-Cu) were approximately 24.0–30.0 wt%. ICP-MS analysis was employed in order to establish the composition of the Pt-M/GNPs catalysts. The results showed that the Pt loading (% by weight) was between 17.5% and 25.4% and the metal loading (% by weight)was 3.40% Ni, 1.40% Fe and 3.20% Cu. The particle size and morphology were investigated using TEM, considering its capability for imaging at an atomic scale. The average particle size was found to be 1.7 nm for Pt-Ni/GNPs, 1.6 nm for Pt-Fe/GNPs and 2.1 nm for Pt-Cu/GNPs. Raman spectroscopy was used to find I_D/I_G, the ratio between the intensities of the D band and the G band, a measure commonly employed to characterize the defect concentration in samples of graphene. The I_D/I_G values of the Pt-Ni/GNPs, Pt-Fe/GNPs and Pt-Cu/GNPs catalysts were discovered to be 0.230, 0.340 and 0.470, respectively [1].

Xue et al. used the thermally assisted method to anchor Pt nanocrystals onto three-dimensional (3D) porous boron and nitrogen double-doped reduced graphene oxide–carbon nanotube frameworks (Pt/BNrGO-CNT) [32]. They used the solvothermal method to obtain different BNrGO/CNT feeding ratios in the 3D Pt/BNrGO-CNT catalysts. To obtain this result, a mixture of CNT powder and GO solution $NH_4[BF_4]$ is reacted for 24 h at 180 °C inside a high-pressure reactor. Afterward, a formulated $(BNrGO)_5$-$(CNT)_5$ support material is inserted into the ethylene–glycol mixture containing K_2PtCl_4, and additional processing at 120 °C is performed for a duration of 12 h in order to obtain the final product. Another ration of BNrGO-CNT was also prepared. The results obtained through ICP-MS determined the Pt loadings for the Pt/$(BNrGO)_3$-$(CNT)_7$, Pt/$(BNrGO)_5$-$(CNT)_5$, Pt/$(BNrGO)_7$-$(CNT)_3$, Pt/$(BNrGO)_9$-$(CNT)_1$, Pt/rGO, Pt/CNT and Pt/C catalysts at 18.20, 18.80, 18.70, 19.40, 18.40, 19.00 and 19.60 wt%, respectively. Pt particles show

interplanar spacings of 0.223 nm and 0.195 nm, accurately corresponding to the (111) and (200) planes of face-centered cubic Pt crystals. Through TEM it can be observed that the Pt/BNrGO-CNT hybrid is composed mainly of the four types of elements (C, B, N and Pt), with these four components being uniformly distributed throughout the whole sheets. XRD reveals that the aforementioned diffraction peak appears at approximately $2\theta = 25.0^\circ$ for Pt/rGO and Pt/BNrGO-CNT. The three characteristic diffraction peaks of metallic Pt correspond to the (111), (200) and (220) crystal planes within the cubic Pt structure. The intensity ration between D and G (I_D/I_G) of the GO, rGO and Pt/rGO samples was determined as 0.87, 1.04 and 0.96, respectively, proving the presence of several topological flaws in the carbon structures. Conversely, the I_D/I_G of Pt/BNrGO-CNT proved a low 0.76, hinting towards the fact that the incorporation of low-defect CNTs into the rGO skeletons can be used as a means of reducing the density of defects of the hybrid system. The specific surface areas are 226 $m^2\ g^{-1}$ and 240 $m^2\ g^{-1}$ for Pt/BNrGO-CNT and BNrGO-CNT hybrids, respectively.

Grad et al. prepared Pd/rGO and Pd-Au/rGO catalysts through wet impregnation of GO using an aqueous mixture of metal salts. The resulting mixture of GO and metal ions was then processed through thermal treatment in (H_2 + Ar) mixture [33]. The Pd/rGO catalyst was prepared using GO and $PdCl_2$ solution in diluted HCl by wet impregnation, resulting in 10 wt.% palladium on rGO. The target Pd-Au/rGO with metal concentrations of 7.5 wt.% Pd and 2.5 wt.% Au was obtained similarly through wet impregnation, employing a mixture comprising $PdCl_2$ and $HAuCl_4$ aqueous solutions. In both cases, the impregnated samples were dried at ambient temperature followed by thermal reduction in Ar. Afterward, it was thermal treated in a (H_2 + Ar) mixture (10 vol.% H_2) for 30 min at 250 °C. The resulting surface areas determined using the BET method are 210 m^2/g for Pd/rGO and 206 m^2/g for Pd-Au/rGO. The XRD profiles for both of the catalysts display the (002) graphene reflexion situated at 23° for Pd/rGO and at 23.7° for the Pd-Au bimetallic catalyst, as well as the metal reflexions: Pd (111) at 39.9°, Pd (200) at 46.4° for Pd/rGO and one metal reflexion situated at 38.9° for Pd-Au/rGO. Size of the metal crystallite calculated by XRD is 5 nm for Pd/rGO and 3.5 nm for Pd-Au/rGO. The bimetallic catalyst displays a distance between the carbon layers of 0.378 nm, whereas the Pd/rGO catalyst displays a distance of 0.386 nm, with the medium number of graphene layers for Pd/rGO being 4 and for Pd-Au/rGO being 5.5. The burning temperature for the palladium containing catalyst is 517 °C, while the Pd-Au bimetallic has a much lower value at 447 °C. The I_D/I_G intensity ratio of the D and G bands is 0.90 for Pd/rGO and 0.85 for Pd-Au/rGO; values were obtained from Raman spectra [33].

2.3. Microwave Irradiation Method

In recent years, microwave irradiation has been used as an eco-friendly method in the synthesizing organic, inorganic and inorganic–organic hybrid materials due to its well-known advantages over conventional synthetic methods. The size as well as distribution of NPs synthesized using the light or microwave irradiation method could be easily controlled compared to reductant-assisted or thermal-assisted reduction method, by changing the intensity, power and irradiation time of the light or microwave (Figure 4). Another important property of microwave irradiation synthesis is that along with the reduction in metals, simultaneous reduction in graphene oxide is possible [13].

Wojnicki et al. synthesized Au/rGO. They first dissolved metallic gold in aqua regia to obtain the Au(III) chloride complex [34]. A Magnum II (Ertec, Poland) 600 W microwave-heated digestion system was used to obtain Au/rGO. The parameters of the microwave-heated digestion system were set to a temperature of 523 K using microwaves at a frequency of 2.45 GHz for 10 min. The pressure in the reaction vessel increased from atmospheric to approximately 40 bar. XRD showed that the intensity of diffraction lines ascribed to GO (001) and graphite (002) crystal planes was much smaller when compared to the intensity of Au (111) line. The average value of the AuNPs diameter was calculated at 12 nm. The high-resolution Au spectrum confirmed the presence of metallic gold by XPS. XPS peaks

were ascribed to Au 4 $f_{7/2}$ with a binding energy 84 eV and spin-orbit energy shift of 3.7 eV. The ratio of the intensities of the D and G bands (I_D/I_G) presented by the Raman spectra of the investigated samples proved to be equal to 0.60 for GO, 0.63 for rGO and 0.81 for Au/rGO, respectively. The obtained I_D/I_G values are directly proportional with the number of structural defects in the sample.

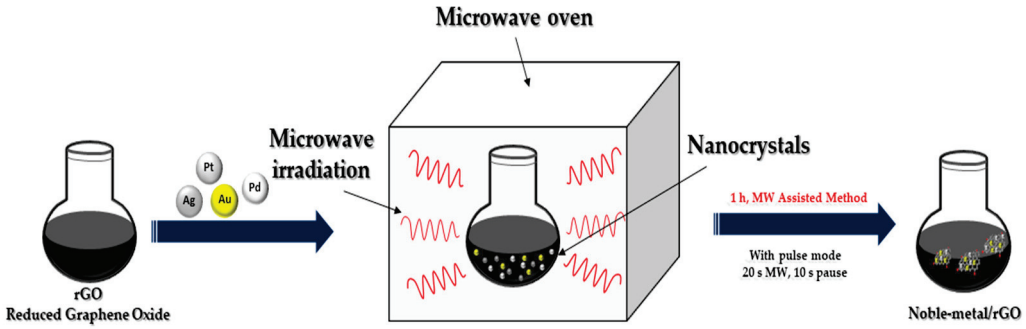

Figure 4. Microwave irradiation synthesis of noble metal nanocomposites.

Gold nanoparticles decorated on rGO were prepared using the microwave-assisted process (MW). The procedure has demonstrated remarkable advantages as eco-friendly method for Au/rGOs obtaining with simultaneous reduction in graphene oxide and formation of gold nanoparticles by an innovative one-step process. The characterization of prepared samples demonstrated good chemical stability and controllable morphology. The samples were used for membrane electrode assembly development and tested in operation of proton exchange membrane fuel cells. The electrochemical stability of the innovative Au/rGO-based cathode was analyzed using several accelerated stress tests (ASTs) by considering the cycling potential protocol. The electrochemical analysis considering the I-V study, cyclic and linear voltammetry has provided improved performances in comparison with the standard commercial cathode. The aggressive AST indicated an excellent stability; thus, the authors reported an improved electrocatalyst for oxygen reduction reaction with higher stability and durability for fuel cells. Moreover, the paper indicates the possibility of extending the protocol using the microwave-assisted process for obtaining other noble metal nanoparticles supported on rGO [35–39].

A single-step route to obtain platinum/platinum-cobalt uniformly distributed nanoparticles supported on reduced graphene oxide was developed recently. This route provides significant advantages such as its low cost, low time-consuming nature and high yield in comparison to state-of-the-art chemical methods used to prepare efficient Pt/rGO catalyst. The morphology of prepared samples has been evaluated by specific techniques, while the electro catalytic durability has been evaluated using the electrochemical performances in fuel cells [40,41]. Significant performance and stability in PEM fuel cells was demonstrated. The produced Pt-rGO-based membrane electrode assemblies were studied for stability under fuel starvation in comparison with commercial Pt/C-based membrane electrode assemblies. The electro-chemical activity was studied and the electrochemical response indicated the higher stability during degradation test under fuel starvation in comparison with commercial Pt/C catalyst. These results extend the applicability of described preparation protocol to other noble/transition metal nanoparticles supported on graphene-based materials.

2.4. Ultrasonication Method

The ultrasonic method (Figure 5) leads to the rapid heating of the liquid to temperatures of 5000 K in a few nanoseconds, resulting in microbubbles with an effective effect. These microbubbles act as chemical reactors. Oxidative and reducing radicals are generated in the cavitation effect during sonolysis. Sonication in the range of 20 to 1000 kHz leads to the formation of MNPs from metal precursor solution. The collapse of these microbubbles

leads to the generation of high temperatures inside the bubbles [18]. Ultrasonic testing techniques are widely accepted for testing materials in many industries, including power generation, steel, aluminum, titanium production, airframe manufacturing, jet engine manufacturing and shipbuilding [42].

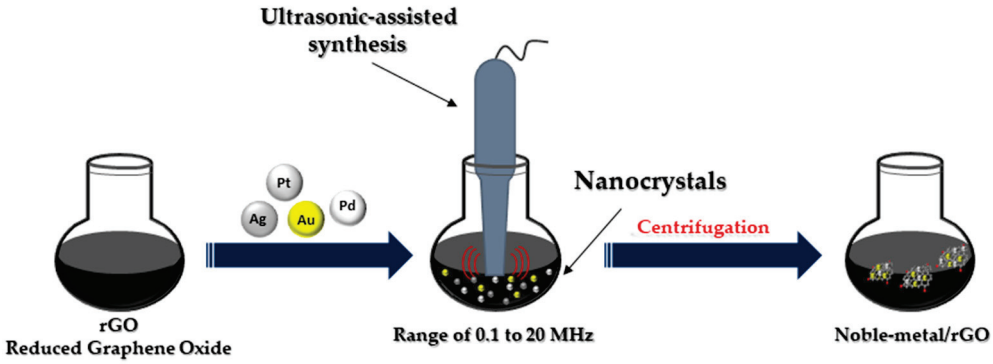

Figure 5. Ultrasonic-assisted synthesis of noble metal nanocomposites.

Li et al. synthesized the AuPs/rGO through a mixture of 4 mg/mL GO suspension and 0.48 mg/mL AuPs solution with a volume ratio of 1:1; it was then sonicated for 1 h. After the AuPs/rGO was reduced by hydroiodic acid, it was washed with deionized water and then dried in air. The images of AuPs/rGO composite by SEM showed the uniform distribution of the AuPs on the surface of rGO. XRD measurements and the corresponding calculated results are consistent with the SEM images. The AuPs composites are inserted into the layered graphene sheets. The diffraction peak is 2θ = 8.84° for rGO to 2θ = 7.86° for AuPs-rGO. XRD measurements are consistent with the SEM images. The Raman spectra of both the AuPs-rGO and pure rGO film show a wide band at 2400 cm^{-1}~3200 cm^{-1} [43].

Tran et al. prepared the Ag/GO nanocomposites through the ultrasonication method. Ag/GO nanocomposites were synthesized with GO, double-distilled water and sonicated for a duration of 10 min, after which $AgNO_3$ was added. Centrifugation at 12,000 rpm was used to separate the final Ag/GO nanocomposites, which were then washed with double-distilled water [44]. The FTIR spectrum of GO reveals several proprietary peaks situated at 3224, 1724, 1226 and 1050 cm^{-1} for hydroxyl -OH, carboxyl -COOH, epoxy C-O-C and alkoxyl C-O. After anchoring with AgNPs, the epoxy stretching mode at 1226 cm^{-1} is no longer present, while peaks that are indicative of different oxygen functional groups remain well-preserved. Nanocomposites of GO and Ag/GO reveal a diffraction peak at 2θ of 10.1° in the XRD patterns relating to the (002) crystal plane of GO nanosheets. In addition to the distinctive diffraction peak of GO, the Ag/GO nanocomposites also exhibit a number of separate peaks at 2θ of 38.1, 44.2, 64.5 and 77.5 degrees, which can be attributed to the (111), (200), (220) and (311) facets of typical fcc metallic Ag (JCPDS No. 04-0783), respectively. The patterns revealed by XRD demonstrate the effective adhesion of AgNPs to GO nanowires. The I_D/I_G ratio of the GO increased from 0.87 to 0.92 when the GO was anchored with AgNPs. The C/O atomic ratio found in the Ag/GO nanocomposites is greater than that of the GO, with the values obtained by XPS analysis being 2.6 for Ag/GO and 2.0 for GO. FTIR showed the characteristic peaks for Ag/GO centered at 284.8, 287.0 and 288.5 eV, respectively, for C=C, C-O and C=O. XPS analyses determined an atomic percentage of Ag of 2.46.

Bi et al. prepared PCN-222 and Ag^+-decorated PCN-222 (zirconium-metalloporphyrinic metal–organic framework) using $ZrCl_4$, meso-tetra(4-carboxyphenyl) porphine, benzoic acid and $AgNO_3$. The solution was ultrasonically dispersed and dissolved in a mixture of N, N-dimethylformamide and acetic acid. Preparing the Ag^+-decorated PCN-222@EDTA-GO-CS (CS-chitosan) foam required $AgNO_3$, $ZrCl_4$, H_2TCPP and benzoic acid that were ultrasonically solvable in the N, N-dimethylformamide [45]. The Ag^+-decorated PCN-222 showed clear crystal lattices and the TEM-EDS mappings revealed the even dispersion of

Ag, C, N, O and Zr elements. The characteristic peaks of PCN-222 at 1709, 1640, 1603, 1549, 1402, 967, 801 and 719 cm^{-1} were obtained through the use of FT-IR spectra. The peaks in binding energies at 367.5 eV and 373.5 eV arose from the presence of Ag+ ions.

Mehmandoust et al. prepared Pt/CQDs@rGO nanocomposite (CQDs—carbon quantum dots) by ultrasonication method [46]. The Pt/CQDs@rGO nanocomposite is prepared using the GO dispersion, aqueous sodium citrate and ammonia solution for the CQDs, following which H_2PtCl_6 was added to the solution. In the XRD patterns, the characteristic peaks of (002) obtained at 11.0° (d002 = 0.85 nm), 28.9° and 24.0° were for GO, CQDs and Pt/CQDs/rGO, respectively. After the reduction process, the diffraction peaks are observed at, respectively, 46.9°, 55.7° and 81.6°, corresponding to (111), (200) and (220) planes of the face-centered cubic (fcc) structure of Pt. The crystallite sizes of GO, CQDs and Pt/CQDs@rGO are 54 nm, 17 nm and 38 nm, respectively. The large crystallite size of Pt/CQDs@rGO shows the aggregation of Pt nanoparticles. D and G bands have been detected using Raman spectroscopy at 1350 cm−1 and 1580 cm^{-1} for graphene oxide, 1350 cm^{-1} and 1580 cm^{-1} in the case of GQDs and at 1357 cm^{-1} and 1590 cm^{-1} for Pt/N-CQDs@rGO nanocomposite. The values of the ratios between the intensities of the D and G bands (I_D/I_G) are 0.88 and 0.94 and have been calculated for GO and Pt/CQDs@rGO, respectively. The EDX investigation exhibits all essential elements such as C, O, Na, Cl and Pt individually from Pt/CQDs@rGO nanocomposite.

Mariappan et al. presented the study of Ag/rGO prepared with glucose, vitamin C and $NaBH_4$ as reducing agents through the ultrasonication method [47]. The Ag/rGO is prepared using GO, polyvinylpyrrolidone is dispersed in double-distilled water by continuous sonication for 2 h and afterward, $AgNO_3$ and glucose are added. The same experimental procedure is repeated for vitamin C and $NaBH_4$. The Ag/rGO samples have peaks at 2θ values of 38.13°, 44.34°, 66.44° and 77.44°, which agree with the cubic crystal structure of the Ag NPs. The grain sizes of the Ag NPs are 28 nm, 25 nm and 22 nm for GAg_G, GAg_V and GAg_S, respectively. Through Raman spectroscopy, a graphitic band (G band) at 1590 cm^{-1} and a disorder band (D band) at 1365 cm^{-1} can be observed. The absorption bands at 257 nm for GAg_G, 268 nm for GAg_S and 270 nm for GAg_V. I_D/I_G ratios have been measured at 1.26 for GAg_S, 1.19 for GAg_V and 0.94 GAg_G.

Aljafari et al. prepared Pd/GO using the sonication technique. This process used GO, palladium acetate and glucose. The pH was adjusted using NaOH [48]. The diffraction peaks noticed at 40.1°, 46.6°, 68.0°, 82.1° and 86.4° match with Pd (111), Pd (200), Pd 220), Pd (311) and Pd (222), respectively. The absorption bands for Pd NPs are 260 nm and for Pd/rGO are 265 nm.

Mao et al. [49] synthesized the graphene oxide sheets decorated by silver nanoparticles using the sonication method. This process used graphene oxide colloid, $AgNO_3$ and cetyl trimethylammonium bromide. The final product is graphene oxide sheets that are decorated by silver nanoparticles. The peaks at 38.31°, 44.41°, 63.51° and 77.71° can be assigned to the (111), (200), (220) and (311) crystalline planes of silver, respectively, which shows that the silver nanoparticles are composed of pure crystalline silver. The particle diameter of silver nanoparticles is about 10 nm. The band of silver nanoparticles is at about 414 nm.

For the preparation of graphene materials doped with metal nanomaterials, the synthesis methods are very important to ensure the best dispersion of the metal particles and the narrowest distribution of their size, because both significantly affect the electrocatalytic activity.

In Table 1 we presented the synthesis method according to the noble metals used. In conclusion, we can state that the chemical reduction method is specific to the noble metal Pd, the thermally assisted method is specific to the noble metals Au, Ag and Pt, the microwave-assisted method is specific to the noble metals Au and Pt and the ultrasonication method is specific to all four noble metals present in our study (Au, Ag, Pt and Pd).

Table 1. Synthesis method depending on the nature of the introduced metal.

Metals	Method	References
$Pt_{40}Ni_{60}$/rGO	Chemical reduction	[24]
$(Co_6)Ag_{0.1}Pt_{0.9}$/rGO		[25]
PdNPs		[26]
PdIrO/NGs		[27]
Pd-rGO		[28]
Au@PdNPs		[29]
AgZnO-rGO	Thermally assisted method	[30]
$AuMn_3O_4$-rGO		[31]
Ag/CeO_2-rGO		[15]
Pt-Cu/GNPs		[1]
Pt-Ni/GNPs		[1]
Pt-Fe/GNPs		[1]
Pt-BNrGO		[32]
Pd/rGO		[33]
Pt-Au/rGO		[33]
Au/rGO	Microwave-assisted method	[34–39]
Pt/rGO		[40,41]
Au/rGO	Ultrasonication	[43]
Ag/GO		[44]
Ag-PCN-222		[45]
Pt-CQDs/rGO		[46]
Ag/rGO		[47]
Pd/rGO		[48]
Ag/rGO		[49]

3. Advantages and Disadvantages of the Synthesis Methods of Noble Metals Functionalized on Graphene Oxide

In recent years, different methods have been proposed for the synthesis of nanoparticles deposited on a graphene support. The choice of the most suitable method has the greatest importance in terms of the structure and catalytic efficiency of the catalysts. Table 2 presents the advantages, disadvantages and applications of the most known methods used in the synthesis of nanoparticles deposited on a graphene support.

Table 2. Advantages and disadvantages of the synthesis methods of noble metals functionalized on graphene oxide.

Method	Advantages	Disadvantages	Application	Ref.
Ultrasonication	■ High temperature (5000 K) in a few nanoseconds; ■ Friendly environmental conditions; ■ Dual frequency conditions are used to substantially reduce the likelihood of any physical damage to the graphene sheets.	o Low concentration of GO suspension for overcoming the activation energy barrier; o Particle size dimensions are difficult to control during ultrasonication.	- Fuel cell application; - Biomedical application; - Electrochemical sensor applications.	[50–53]

Table 2. *Cont.*

Method	Advantages	Disadvantages	Application	Ref.
Thermally assited method	■ Possibility of variation of the electronic properties of the graphene oxide photoreduction composite; ■ Photo-electrochemical reduction process is simple and also inexpensive; ■ Increase in charge redox reaction and ion diffusion via photovoltaic effect.	o The level of reduction in certain groups on the surface of graphene oxide is not very relevant.	- Supercapacitor application; - Hydrogen production; - Electrochemical sensor applications.	[54–57]
Pulsed laser ablation in liquids (PLAL)	■ Could provide a green synthesis strategy of GO metal nanocomposites; ■ Short reaction time—from several hours to a few minutes; ■ Does not involve toxic chemicals.	o Lack of optimized parameters of the PLAL method for improving the yield and desired properties of carbon nanomaterials; o The importance of the effect of the liquid carrier medium on the GO optical properties.	- Biomedical application; - Photovoltaic applications; - Electrochemical sensor applications.	[58–61]
Chemical reduction	■ Uses green reductants; ■ Low cost implementation.	o High loss of mechanical integrity of freeze-dried nanosheets; o Presence of a quantity of metal impurities after reduction.	- Biomedical application; - Fuel cell applications; - Sensor applications.	[62–65]
Electrochemical deposition	■ Simple, efficient and fast technique; ■ Can control the size of noble metal nanoparticles and the deposition time.	o Moderate–intrinsic electrocatalytic properties.	- Optical application; - Fuel cell applications; - Electrochemistry applications.	[66–69]
Microwave-assisted synthesis	■ Uniform and fast heating technique; ■ Uniform dispersion of a smallest particle size; ■ High electrocatalytic activity of nanoparticles.	o Long and time-consuming to complete a reaction; o Process set up is difficult to realize.	- Fuel cell applications; - Supercapacitors application; - Electrochemistry applications.	[70–73]
Seed mediated growth method	■ Small-size nanoparticle synthesis; ■ Well-controllable growth rate.	o Possible agglomeration and unreliable electrostatic attraction of metal precursors and GO.	- Electrochemistry applications; - Fuel cell applications.	[74–77]
Ex situ synthesis	■ Present the advantages of easy filtration, good shape and size control of the nanosheets.	o Linking agent is required, because the metal nanoparticle and graphene sheets are synthesized separately; o Aggregation of the metal nanoparticles before their attachment onto the GO can be a problem.	- Electron emission applications; - Electrochemistry applications; - Fuel cell applications.	[78–81]

In conclusion, the most valuable method among the preparation methods of graphene-deposited nanomaterial catalysts is microwave field irradiation, especially due to the short synthesis time, the fast and uniform heating and the significant challenge in controlling uniformity of the metal nanoparticle's decoration on the graphene surface. By applying irradiation in the microwave field, under the influence of temperature, homogeneous reaction centers are formed in the reaction medium at the interface between the irradiation-sensitive graphene support and the metal precursor. Additionally, the presence of a

reducing agent in the reaction medium means that the precursor can be converted to its metallic form by microwave irradiation.

The qualities of noble metals have demonstrated a special efficiency in the electrocatalytic activity and the electrochemical stability of compounds based on carbon and graphene oxide. In order to improve the oxygen reduction reaction (ORR) and the quality of hydrogen adsorption and desorption, a higher electrochemical active surface area (ECSA) of the catalyst based on noble metals is necessary. The intrinsic increase in the active surface is proportional to the metal content in the chemical compound and to the dispersion of metal nanoparticles on the rGO sheets. The uniform distribution and surface morphology of noble metal nanoparticles on rGO have an effect on the ORR. An excessive reaction energy can cause an agglomeration of the noble metal nanoparticles, leading to particle sizes over 10 nm and the suppression of catalytic activity by reducing the active surface. Figure 6 present the trend of noble metal nanocomposites synthesis methods in different applications. Thus, it can be seen that the most applications of graphene functionalized with noble metals are in applications with fuel cells, renewable energy sources (photovoltaics, production of green hydrogen) and supercapacitors.

The trend of noble metal nanocomposites synthesis methods in different applications

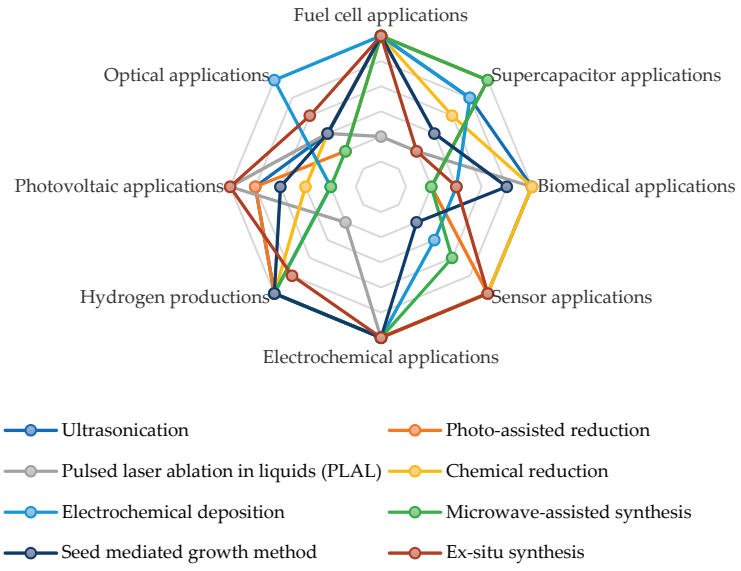

Figure 6. The trend of noble metal nanocomposites synthesis methods in different applications.

4. Conclusions

This review presents the most used and up-to-date methods for the synthesis of graphene functionalized with noble metals (Pt, Ag, Pd and Au) as well as the relevant methods for the characterization of catalysts. The potential of capitalizing on the improved catalytic properties of graphene functionalized with noble metals was also discussed. The studies presented in this review were carried out in order to understand how the metal–support interaction drives chemical catalysis. The preparation technique, the type and amount of metal, the nature of the support, the type of dopant and the technique of applying the catalyst, all these are dependent on the metal–support relationship. Following this review, it was found that the noble metals demonstrated a special efficiency in the electrocatalytic activity and the electrochemical stability of the compounds based on carbon and graphene oxide. It was also observed that to improve the oxygen reduction reaction (ORR) and the quality of hydrogen adsorption and desorption, a higher electrochemical active surface area (ECSA) of the noble metal catalyst is required. The uniform distribution and surface morphology of noble metal nanoparticles on rGO were

found to have an effect on the ORR. Most applications of noble metal functionalized graphene are in fuel cells, renewable energy (photovoltaic, green hydrogen production) and supercapacitor applications.

Author Contributions: All authors have contributed by investigating the literature. Conceptualization, M.I. and A.M.; Methodology, A.M. and A.O.; Software, I.-S.S.; Validation, A.M. and M.I.; Investigation, M.I., A.M., A.O. and I.-S.S.; Resources, A.M. and M.I.; Data curation, A.M. and M.I.; Writing—original draft preparation, M.I. and A.M.; Writing—review and editing, M.I., A.O., I.-S.S., C.C.; Visualization, I.-S.S., C.C. and F.A.L., T.P.; Supervision, A.M.; Project administration, M.I., A.M.; Funding acquisition, M.I., A.M. All authors have read and agreed to the published version of the manuscript.

Funding: This work was supported by the Ministry of Research, Innovation and Digitization of Romania, projects PN 23 15 01 04 and PN 23 15 01 03, by the Romanian Executive Agency for Higher Education Research.

Data Availability Statement: Not applicable.

Conflicts of Interest: The authors declare no conflict of interest.

References

1. Daş, E.; Gürsel, S.A.; Yurtcan, A.B. Simultaneously deposited Pt-alloy nanoparticles over graphene nanoplatelets via supercritical carbon dioxide deposition for PEM fuel cells. *J. Alloys Compd.* **2021**, *874*, 159919. [CrossRef]
2. Branco, C.M.; El-kharouf, A.; Du, S. Materials for Polymer Electrolyte Membrane Fuel Cells (PEMFCs): Electrolyte Membrane, Gas Diffusion Layers, and Bipolar Plates. In *Reference Module in Materials Science and Materials Engineering*; Elsevier: Amsterdam, The Netherlands, 2017; pp. 1–11.
3. Moafi, A.; Heidari, O.; Soltannia, B.; Wlodarski, W.; Shahi, F.; Parvin, P. Reduction of metal nanoparticle decorated flexible graphene oxide by laser at various temperatures and under selected atmospheres. *Carbon Trends* **2022**, *6*, 100140. [CrossRef]
4. Khan, B.M.; Oh, W.C.; Nuengmatch, P.; Ullah, K. Role of graphene-based nanocomposites as anode material for Lithium-ion batteries. *Mater. Sci. Eng. B* **2023**, *287*, 116141. [CrossRef]
5. Park, D.; Lee, D.; Kim, H.J.; Yoon, D.S.; Hwang, K.S. Scalable Functionalization of Polyaniline-Grafted rGO Field-Effect Transistors for a Highly Sensitive Enzymatic Acetylcholine Biosensor. *Biosensors* **2022**, *12*, 279. [CrossRef]
6. Paranthaman, V.; Sundaramoorthy, K.; Chandra, B.; Muthu, S.P.; Alagarsamy, P.; Perumalsamy, R. Investigation on the Performance of Reduced Graphene Oxide as Counter Electrode in Dye Sensitized Solar Cell Applications. *Phys. Status Solidi* **2018**, *215*, 1800298. [CrossRef]
7. Huang, Z.; Song, H.; Feng, L.; Qin, J.; Wang, Q.; Guo, B.; Wei, L.; Lu, Y.; Guo, H.; Zhu, D.; et al. A novel ultrasensitive electrochemical sensor based on a hybrid of rGO/MWCNT/AuNP for the determination of lead(II) in tea drinks. *Microchem. J.* **2023**, *186*, 108346. [CrossRef]
8. Pang, J.; Le, X.; Pang, K.; Dong, H.; Zhang, Q.; Xu, Z.; Gao, C.; Fu, Y.; Xie, J. Highly precision carbon dioxide acoustic wave sensor with minimized humidity interference. *Sens. Actuators B Chem.* **2021**, *338*, 129824. [CrossRef]
9. Yusof, N.M.; Ibrahim, S.; Rozali, S. Synthesis of graphene oxide-cobalt oxide hybrid materials for gas sensors application. *Mater. Today Proc.* **2022**, *66*, 2680–2684. [CrossRef]
10. Majumdar, S.; Sen, P.; Ray, R. Graphene oxide induced high dielectricity in CS/PMMA solid polymer electrolytes and the enhanced specific capacitance with Ag decorated $MnCoFeO_4$ nanoparticles anchored graphene sheets in hybrid solid-state supercapacitors. *Mater. Res. Bull.* **2022**, *151*, 111814. [CrossRef]
11. Higgins, M.C.M.; Ghobadi, S.; Rojas, J.V.; Castano, C.E. X-ray synthesis of noble metal nanoparticles onto 2D and 3D graphene oxide supports. *Appl. Surf. Sci.* **2020**, *528*, 146313. [CrossRef]
12. Hemmati, S.; Heravi, M.M.; Karmakar, B.; Veisi, H. Green fabrication of reduced graphene oxide decorated with Ag nanoparticles (rGO/Ag NPs) nanocomposite: A reusable catalyst for the degradation of environmental pollutants in aqueous medium. *J. Mol. Liq.* **2020**, *319*, 114302. [CrossRef]
13. Yang, W.; Pan, M.; Huang, C.; Zhao, Z.; Wang, J.; Zeng, H. Graphene oxide-based noble-metal nanoparticles composites for environmental application. *Compos. Commun.* **2021**, *24*, 100645. [CrossRef]
14. Krishnaraj, C.; Kaliannagounder, V.K.; Rajan, R.; Ramesh, T.; Kim, C.S.; Park, C.H.; Liu, B.; Yun, S.-I. Silver nanoparticles decorated reduced graphene oxide: Eco-friendly synthesis, characterization, biological activities and embryo toxicity studies. *Environ. Res.* **2022**, *210*, 112864. [CrossRef] [PubMed]
15. Wang, Y.; Lu, C.-Y.; Yin, Z.-F. Reduced graphene oxide decorated with Ag/CeO_2 nanocomposite towards room temperature photocatalytic esterification of aldehydes. *Mater. Lett.* **2020**, *270*, 127723. [CrossRef]
16. Abbas, A.M.; Abid, M.A.; Abbas, K.N.; Aziz, W.J.; Salim, A.A. Photocatalytic activity of Ag-ZnO nanocomposites integrated essential ginger oil fabricated by green synthesis method. *J. Phys. Conf. Ser.* **2021**, *1892*, 012005. [CrossRef]

17. Jiříčková, A.; Jankovský, O.; Sofer, Z.; Sedmidubský, D. Synthesis and Applications of Graphene Oxide. *Materials* **2022**, *15*, 920. [CrossRef]
18. Darabdhara, G.; Das, M.R.; Singh, S.P.; Rengan, A.K.; Szunerits, S.; Boukherroub, R. Ag and Au nanoparticles/reduced graphene oxide composite materials: Synthesis and application in diagnostics and therapeutics. *Adv. Colloid Interface Sci.* **2019**, *271*, 101991. [CrossRef]
19. Usman, M.R. Hydrogen storage methods: Review and current status. *Renew. Sustain. Energy Rev.* **2022**, *167*, 112743. [CrossRef]
20. Burkholder, M.B.; Rahman, F.B.A.; Chandler, E.H., Jr.; Regalbuto, J.R.; Gupton, B.F.; Tengco, J.M.M. Metal supported graphene catalysis: A review on the benefits of nanoparticular supported specialty sp2 carbon catalysts on enhancing the activities of multiple chemical transformations. *Carbon Trends* **2022**, *9*, 100196. [CrossRef]
21. Zhang, S.; Wang, H.; Liu, J.; Bao, C. Measuring the specific surface area of monolayer graphene oxide in water. *Mater. Lett.* **2020**, *261*, 127098. [CrossRef]
22. Nam, P.T.; Van Khanh, N.; Thom, N.T.; Phuong, N.T.; Van Trang, N.; Xuyen, N.T.; Thai, V.Q.; Tuan, V.A.; Thanh, D.T.M. Synthesis of reduced graphene oxide for high-performance supercapacitor. *Vietnam. J. Chem.* **2018**, *56*, 778–785. [CrossRef]
23. Mohan, V.B.; Jayaraman, K.; Bhattacharyya, D. Brunauer–Emmett–Teller (BET) specific surface area analysis of different graphene materials: A comparison to their structural regularity and electrical properties. *Solid State Commun.* **2020**, *320*, 114004. [CrossRef]
24. Guo, J.; Li, X.; Duan, H.; Zhang, H.; Jia, Q.; Zhang, S. Graphene supported Pt–Ni bimetallic nanoparticles for efficient hydrogen generation from KBH_4/NH_3BH_3 hydrolysis. *Int. J. Hydrog. Energy* **2022**, *47*, 11601–11610. [CrossRef]
25. Kaur, A.; Kaur, G.; Singh, P.P.; Kaushal, S. Supported bimetallic nanoparticles as anode catalysts for direct methanol fuel cells: A review. *Int. J. Hydrog. Energy* **2021**, *46*, 15820–15849. [CrossRef]
26. Abbasi, Z.; Saeed, W.; Shah, S.M.; Shahzad, S.A.; Bilal, M.; Khan, A.F.; Shaikh, A.J. Binding efficiency of functional groups towards noble metal surfaces using graphene oxide–metal nanoparticle hybrids. *Colloids Surfaces A Physicochem. Eng. Asp.* **2020**, *611*, 125858. [CrossRef]
27. Shu, J.; Li, R.; Lian, Z.; Zhang, W.; Jin, R.; Yang, H.; Li, S. In-situ oxidation of Palladium–Iridium nanoalloy anchored on Nitrogen-doped graphene as an efficient catalyst for methanol electrooxidation. *J. Colloid Interface Sci.* **2022**, *605*, 44–53. [CrossRef] [PubMed]
28. Teffu, D.M.; Ramoroka, M.E.; Makhafola, M.D.; Makgopa, K.; Maponya, T.C.; Seerane, O.A.; Hato, M.J.; Iwuoha, E.I.; Modibane, K.D. High-performance supercabattery based on reduced graphene oxide/metal organic framework nanocomposite decorated with palladium nanoparticles. *Electrochim. Acta* **2022**, *412*, 140136. [CrossRef]
29. Rajkumar, M.; Devadas, B.; Chen, S.-M.; Yeh, P.-C. Single step electrochemical fabrication of highly loaded palladium nanoparticles decorated chemically reduced graphene oxide and its electrocatalytic applications. *Colloids Surfaces A Physicochem. Eng. Asp.* **2014**, *452*, 39–45. [CrossRef]
30. Abdulhusain, Z.H.; Alshamsi, H.A.; Salavati-Niasari, M. Silver and zinc oxide decorated on reduced graphene oxide: Simple synthesis of a ternary heterojunction nanocomposite as an effective visible-active photocatalyst. *Int. J. Hydrog. Energy* **2022**, *47*, 34036–34047.
31. Rudra, S.; Deka, N.; Nayak, A.K.; Pradhan, M.; Dutta, G.K. Facile hydrothermal synthesis of Au-Mn_3O_4 decorated graphene oxide nanocomposites for solid-state supercapacitor. *J. Energy Storage* **2022**, *50*, 104615. [CrossRef]
32. Xue, Y.; Zhang, H.; Xiong, J.; He, H.; Huang, H. Well-dispersive Pt nanocrystals anchored onto 3D boron and nitrogen double-doped reduced graphene oxide–carbon nanotube frameworks as efficient electrocatalysts for methanol oxidation. *J. Electroanal. Chem.* **2022**, *921*, 116705. [CrossRef]
33. Grad, O.; Mihet, M.; Coros, M.; Dan, M.; Lazar, M.D.; Blanita, G. Reduced graphene oxide modified with noble metal nanoparticles for formic acid dehydrogenation. *Catal. Today* **2021**, *366*, 41–47. [CrossRef]
34. Wojnicki, M.; Michorczyk, B.; Wojtaszek, K.; Kutyła, D.; Kołczyk-Siedlecka, K.; Małecki, S.; Wrzesińska, A.; Kozanecki, M.; Kwolek, P.; Gajewska, M.; et al. Zero waste, single step methods of fabrication of reduced graphene oxide decorated with gold nanoparticles. *Sustain. Mater. Technol.* **2022**, *31*, e00387. [CrossRef]
35. Marinoiu, A.; Andrulevicius, M.; Tamuleviciene, A.; Tamulevicius, T.; Raceanu, M.; Varlam, M. Synthesis of well dispersed gold nanoparticles on reduced graphene oxide and application in PEM fuel cells. *Appl. Surf. Sci.* **2020**, *504*, 144511. [CrossRef]
36. Marinoiu, A.; Andrulevicius, M.; Tamuleviciene, A.; Tamulevicius, T.; Carcadea, E.; Raceanu, M.; Varlam, M. High performance catalytic system with enhanced durability in PEM fuel cell. *Int. J. Hydrog. Energy* **2020**, *45*, 10409–10422. [CrossRef]
37. Marinoiu, A.; Raceanu, M.; Andrulevicius, M.; Tamuleviciene, A.; Tamulevicius, T.; Nica, S.; Bala, D.; Varlam, M. Low-cost preparation method of well dispersed gold nanoparticles on reduced graphene oxide and electrocatalytic stability in PEM fuel cell. *Arab. J. Chem.* **2020**, *13*, 3585–3600. [CrossRef]
38. Lazar, O.-A.; Marinoiu, A.; Raceanu, M.; Pantazi, A.; Mihai, G.; Varlam, M.; Enachescu, M. Reduced Graphene Oxide Decorated with Dispersed Gold Nanoparticles: Preparation, Characterization and Electrochemical Evaluation for Oxygen Reduction Reaction. *Energies* **2020**, *13*, 4307. [CrossRef]
39. Marinoiu, A.; Andrei, R.; Vagner, I.; Niculescu, V.; Bucura, F.; Constantinescu, M.; Carcadea, E. One Step Synthesis of Au Nanoparticles Supported on Graphene Oxide Using an Eco-Friendly Microwave-Assisted Process. *Mater. Sci.* **2020**, *26*, 249–254. [CrossRef]
40. Marinoiu, A.; Carcadea, E.; Sacca, A.; Carbone, A.; Sisu, C.; Dogaru, A.; Raceanu, M.; Varlam, M. One-step synthesis of graphene supported platinum nanoparticles as electrocatalyst for PEM fuel cells. *Int. J. Hydrog. Energy* **2021**, *46*, 12242–12253. [CrossRef]

41. Marinoiu, A.; Raceanu, M.; Carcadea, E.; Andrulevicius, M.; Tamuleviciene, A.; Tamulevicius, T.; Capris, C.; Varlam, M. Efficient method to obtain Platinum–Cobalt supported on graphene oxide and electrocatalyst development. *Int. J. Hydrog. Energy* **2020**, *45*, 26226–26237. [CrossRef]
42. Available online: https://www.bindt.org/What-is-NDT/Ultrasonic-methods (accessed on 26 August 2022).
43. Li, J.; Xiang, Y.; Ma, W.; Fu, X.; Huang, Y.; Li, G. Gold particles decorated reduced graphene oxide for low level mercury vapor detection with rapid response at room temperature. *Ecotoxicol. Environ. Saf.* **2021**, *228*, 112995. [CrossRef] [PubMed]
44. Tran, N.T.; Tu, T.N.; Nguyen, H.T.; Phan, D.T.; Hoang, V.C. One-step and surfactant-less synthesis of highly dispersed Ag nanoparticles on graphene oxide as highly effective catalyst for removal of organic dyes. *Synth. Met.* **2020**, *269*, 116550. [CrossRef]
45. Bi, C.; Zhang, C.; Ma, F.; Zhu, L.; Zhu, R.; Qi, Q.; Liu, L.; Dong, H. Development of 3D porous Ag+ decorated PCN-222 @ graphene oxide-chitosan foam adsorbent with antibacterial property for recovering U(VI) from seawater. *Sep. Purif. Technol.* **2022**, *281*, 119900. [CrossRef]
46. Mehmandoust, M.; Erk, N.; Karaman, O.; Karimi, F.; Bijad, M.; Karaman, C. Three-dimensional porous reduced graphene oxide decorated with carbon quantum dots and platinum nanoparticles for highly selective determination of azo dye compound tartrazine. *Food Chem. Toxicol.* **2021**, *158*, 112698. [CrossRef] [PubMed]
47. Mariappan, S.M.; Eswaran, M.K.; Schwingenschlögl, U.; Thangeeswari, T.; Vinoth, E.; Shkir, M.; Said, Z.; Karthikeyan, B. Impact of reducing agents on the ammonia sensing performance of silver decorated reduced graphene oxide: Experiment and first principles calculations. *Appl. Surf. Sci.* **2021**, *558*, 149886. [CrossRef]
48. Aljafari, B.; Arulmani, S.; Takshi, A.; Anandan, S. Sonochemical decoration of palladium on graphene carpet for electrochemical methanol oxidation. *J. Electroanal. Chem.* **2022**, *913*, 116289. [CrossRef]
49. Mao, A.; Zhang, D.; Jin, X.; Gu, X.; Wei, X.; Yang, G.; Liu, X. Synthesis of graphene oxide sheets decorated by silver nanoparticles in organic phase and their catalytic activity. *J. Phys. Chem. Solids* **2012**, *73*, 982–986. [CrossRef]
50. Vinodgopal, K.; Neppolian, B.; Salleh, N.; Lightcap, I.V.; Grieser, F.; Ashokkumar, M.; Ding, T.T.; Kamat, P.V. Dual-frequency ultrasound for designing two-dimensional catalyst surface: Reduced graphene oxide–Pt composite. *Colloids Surf. A Physicochem. Eng. Asp.* **2012**, *409*, 81–87. [CrossRef]
51. Sontakke, A.D.; Purkait, M.K. A brief review on graphene oxide Nanoscrolls: Structure, Synthesis, characterization and scope of applications. *Chem. Eng. J.* **2021**, *420*, 129914. [CrossRef]
52. Tafoya, J.P.V.; Doszczeczko, S.; Titirici, M.M.; Sobrido, A.B.J. Enhancement of the electrocatalytic activity for the oxygen reduction reaction of boron-doped reduced graphene oxide via ultrasonic treatment. *Int. J. Hydrog. Energy* **2022**, *47*, 5462–5473. [CrossRef]
53. Ruiz-Camacho, B.; Palafox-Segoviano, J.A.; Pérez-Díaz, P.J.; Medina-Ramírez, A. Synthesis of supported Pt nanoparticles by sonication for ORR: Effect of the graphene oxide-carbon composite. *Int. J. Hydrog. Energy* **2021**, *46*, 26027–26039. [CrossRef]
54. Andryushina, N.S.; Stroyuk, A.L.; Ustavytska, O.O.; Kurys, Y.I.; Kuchmy, S.Y.; Koshechko, V.G.; Pokhodenko, V.D.; Stroyuk, O. Graphene Oxide Composites with Silver Nanoparticles: Photochemical Formation and Electrocatalytic Activity in the Oxidation of Methanol and Formaldehyde. *Theor. Exp. Chem.* **2014**, *50*, 155–161. [CrossRef]
55. Hu, J.Y.; Li, Z.; Zhai, C.Y.; Wang, J.F.; Zeng, L.X.; Zhu, M.S. Plasmonic photo-assisted electrochemical sensor for detection of trace lead ions based on Au anchored on two-dimensional g-C_3N_4/graphene nanosheets. *Rare Met.* **2021**, *40*, 1727–1737. [CrossRef]
56. Pattananuwat, P.; Khampuanbut, A.; Haromae, H. Novel electrode composites of mixed bismuth-iron oxide/graphene utilizing for photo assisted supercapacitors. *Electrochim. Acta* **2021**, *370*, 137741. [CrossRef]
57. Hernández-Majalca, B.C.; Meléndez-Zaragoza, M.J.; Salinas-Gutiérrez, J.M.; López-Ortiz, A.; Collins-Martínez, V. Visible-light photo-assisted synthesis of GO-TiO_2 composites for the photocatalytic hydrogen production. *Int. J. Hydrog. Energy* **2019**, *44*, 12381–12389. [CrossRef]
58. Menazea, A.; Ahmed, M. Silver and copper oxide nanoparticles-decorated graphene oxide via pulsed laser ablation technique: Preparation, characterization, and photoactivated antibacterial activity. *Nano-Struct. Nano-Objects* **2020**, *22*, 100464. [CrossRef]
59. Moqbel, R.A.; Gondal, M.A.; Qahtan, T.F.; Dastageer, M.A. Synthesis of cadmium sulfide-reduced graphene oxide nanocomposites by pulsed laser ablation in liquid for the enhanced photocatalytic reactions in the visible light. *Int. J. Energy Res.* **2018**, *42*, 1487–1495. [CrossRef]
60. Yogesh, G.K.; Shukla, S.; Sastikumar, D.; Koinkar, P. Progress in pulsed laser ablation in liquid (PLAL) technique for the synthesis of carbon nanomaterials: A review. *Appl. Phys. A* **2021**, *127*, 810. [CrossRef]
61. Ghavidel, E.; Sari, A.H.; Dorranian, D. Experimental investigation of the effects of different liquid environments on the graphene oxide produced by laser ablation method. *Opt. Laser Technol.* **2018**, *103*, 155–162. [CrossRef]
62. Guex, L.G.; Sacchi, B.; Peuvot, K.F.; Andersson, R.L.; Pourrahimi, A.M.; Ström, V.; Farris, S.; Olsson, R.T. Experimental review: Chemical reduction of graphene oxide (GO) to reduced graphene oxide (rGO) by aqueous chemistry. *Nanoscale* **2017**, *9*, 9562–9571. [CrossRef]
63. Ambrosi, A.; Chua, C.K.; Khezri, B.; Sofer, Z.; Webster, R.D.; Pumera, M. Chemically reduced graphene contains inherent metallic impurities present in parent natural and synthetic graphite. *Proc. Natl. Acad. Sci. USA* **2012**, *109*, 12899–12904. [CrossRef]
64. Kurian, M. Recent progress in the chemical reduction of graphene oxide by green reductants–A Mini review. *Carbon Trends* **2021**, *5*, 100120. [CrossRef]
65. Pareek, A.; Sravan, J.S.; Mohan, S.V. Exploring chemically reduced graphene oxide electrode for power generation in microbial fuel cell. *Mater. Sci. Energy Technol.* **2019**, *2*, 600–606. [CrossRef]

66. Berbeć, S.; Żołądek, S.; Wasilewski, P.; Jabłońska, A.; Kulesza, P.; Pałys, B. Electrochemically Reduced Graphene Oxide–Noble Metal Nanoparticles Nanohybrids for Sensitive Enzyme-Free Detection of Hydrogen Peroxide. *Electrocatalysis* **2020**, *11*, 215–225. [CrossRef]
67. Kong, B.-S.; Geng, J.; Jung, H.-T. Layer-by-layer assembly of graphene and gold nanoparticles by vacuum filtration and spontaneous reduction of gold ions. *Chem. Commun.* **2009**, *16*, 2174–2176. [CrossRef] [PubMed]
68. Liu, G.; Xiong, Z.; Yang, L.; Shi, H.; Fang, D.; Wang, M.; Shao, P.; Luo, X. Electrochemical approach toward reduced graphene oxide-based electrodes for environmental applications: A review. *Sci. Total Environ.* **2021**, *778*, 146301. [CrossRef] [PubMed]
69. Pushkareva, I.; Pushkarev, A.; Kalinichenko, V.; Chumakov, R.; Soloviev, M.; Liang, Y.; Millet, P.; Grigoriev, S. Reduced Graphene Oxide-Supported Pt-Based Catalysts for PEM Fuel Cells with Enhanced Activity and Stability. *Catalysts* **2021**, *11*, 256. [CrossRef]
70. Hassan, H.M.A.; Abdelsayed, V.; Khder, A.E.R.S.; AbouZeid, K.M.; Terner, J.; El-Shall, M.S.; Al-Resayes, S.I.; El-Azhary, A.A. Microwave synthesis of graphene sheets supporting metal nanocrystals in aqueous and organic media. *J. Mater. Chem.* **2009**, *19*, 3832–3837. [CrossRef]
71. Shih, K.-Y.; Wei, J.-J.; Tsai, M.-C. One-Step Microwave-Assisted Synthesis of PtNiCo/rGO Electrocatalysts with High Electrochemical Performance for Direct Methanol Fuel Cells. *Nanomaterials* **2021**, *11*, 2206. [CrossRef]
72. Rosli, N.H.A.; Lau, K.S.; Winie, T.; Chin, S.X.; Chia, C.H. Microwave-assisted reduction of graphene oxide for an electrochemical supercapacitor: Structural and capacitance behavior. *Mater. Chem. Phys.* **2021**, *262*, 124274. [CrossRef]
73. Faraji, S.; Ani, F.N. Microwave-assisted synthesis of metal oxide/hydroxide composite electrodes for high power supercapacitors—A review. *J. Power Sources* **2014**, *263*, 338–360. [CrossRef]
74. Jiang, T.; Wang, X.; Tang, S.; Zhou, J.; Gu, C.; Tang, J. Seed-mediated synthesis and SERS performance of graphene oxide-wrapped Ag nanomushroom. *Sci. Rep.* **2017**, *7*, 9795. [CrossRef] [PubMed]
75. Wei, J.; Hu, Y.; Liang, Y.; Kong, B.; Zheng, Z.; Zhang, J.; Jiang, S.P.; Zhao, Y.; Wang, H. Graphene oxide/core–shell structured metal–organic framework nano-sandwiches and their derived cobalt/N-doped carbon nanosheets for oxygen reduction reactions. *J. Mater. Chem. A* **2017**, *5*, 10182–10189. [CrossRef]
76. Gao, Y.; Gu, J.; Li, L.; Zhao, W.; Li, Y. Synthesis of gold nanoshells through improved seed-mediated growth approach: Brust-like, in situ seed formation. *Langmuir* **2016**, *32*, 2251–2258. [CrossRef] [PubMed]
77. He, L.-L.; Song, P.; Feng, J.-J.; Fang, R.; Yu, D.-X.; Chen, J.-R.; Wang, A.-J. Porous dandelion-like gold@ palladium core-shell nanocrystals in-situ growth on reduced graphene oxide with improved electrocatalytic properties. *Electrochim. Acta* **2016**, *200*, 204–213. [CrossRef]
78. Sun, B.; Wu, J.; Cui, S.; Zhu, H.; An, W.; Fu, Q.; Shao, C.; Yao, A.; Chen, B.; Shi, D. In situ synthesis of graphene oxide/gold nanorods theranostic hybrids for efficient tumor computed tomography imaging and photothermal therapy. *Nano Res.* **2017**, *10*, 37–48. [CrossRef]
79. Zahed, M.A.; Barman, S.C.; Sharifuzzaman, M.; Xuan, X.; San Nah, J.; Park, J.Y. Ex Situ Synthesis of Hexagonal NiO Nanosheets and Carboxyl-Terminated Reduced Graphene Oxide Nanocomposite for Non-Enzymatic Electrochemical Detection of $H_2O_2$and Ascorbic Acid. *J. Electrochem. Soc.* **2018**, *165*, B840. [CrossRef]
80. Alaefour, I.; Shahgaldi, S.; Zhao, J.; Li, X. Synthesis and Ex-Situ characterizations of diamond-like carbon coatings for metallic bipolar plates in PEM fuel cells. *Int. J. Hydrog. Energy* **2021**, *46*, 11059–11070. [CrossRef]
81. Kakaei, K.; Rahnavardi, M. Synthesis of nitrogen-doped reduced graphene oxide and its decoration with high efficiency palladium nanoparticles for direct ethanol fuel cell. *Renew. Energy* **2021**, *163*, 1277–1286. [CrossRef]

MDPI
St. Alban-Anlage 66
4052 Basel
Switzerland
www.mdpi.com

Nanomaterials Editorial Office
E-mail: nanomaterials@mdpi.com
www.mdpi.com/journal/nanomaterials

Academic Open
Access Publishing

mdpi.com

ISBN 978-3-7258-0594-5